frontiers | Research Topics

Advancement in hydrological modeling and water resources management for achieving Sustainable Development Goals (SDGs)

Edited by
Vikram Kumar, Jahangeer Jahangeer, Rajneesh Singh and Prabhat Kumar Singh Dikshit

Published in
Frontiers in Water
Frontiers in Environmental Science

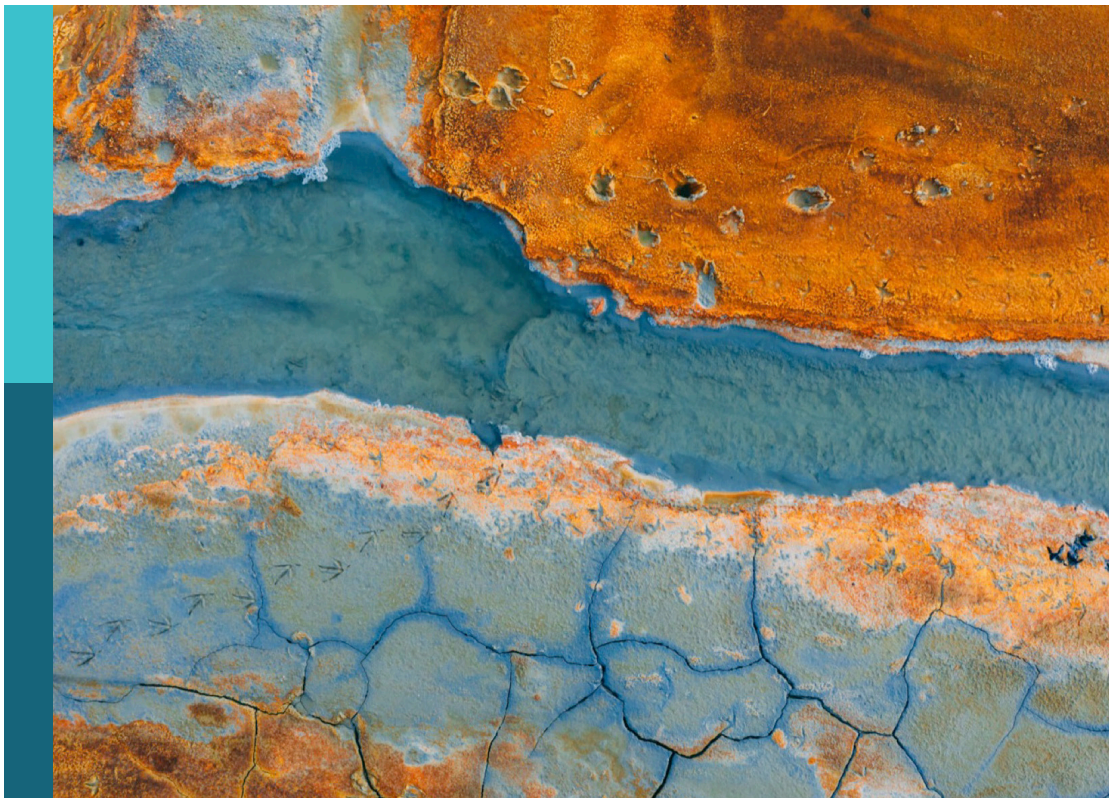

ISSN 1664-8714
ISBN 978-2-8325-6252-9
DOI 10.3389/978-2-8325-6252-9

About Frontiers

Frontiers is more than just an open access publisher of scholarly articles: it is a pioneering approach to the world of academia, radically improving the way scholarly research is managed. The grand vision of Frontiers is a world where all people have an equal opportunity to seek, share and generate knowledge. Frontiers provides immediate and permanent online open access to all its publications, but this alone is not enough to realize our grand goals.

Frontiers journal series

The Frontiers journal series is a multi-tier and interdisciplinary set of open-access, online journals, promising a paradigm shift from the current review, selection and dissemination processes in academic publishing. All Frontiers journals are driven by researchers for researchers; therefore, they constitute a service to the scholarly community. At the same time, the *Frontiers journal series* operates on a revolutionary invention, the tiered publishing system, initially addressing specific communities of scholars, and gradually climbing up to broader public understanding, thus serving the interests of the lay society, too.

Dedication to quality

Each Frontiers article is a landmark of the highest quality, thanks to genuinely collaborative interactions between authors and review editors, who include some of the world's best academicians. Research must be certified by peers before entering a stream of knowledge that may eventually reach the public - and shape society; therefore, Frontiers only applies the most rigorous and unbiased reviews. Frontiers revolutionizes research publishing by freely delivering the most outstanding research, evaluated with no bias from both the academic and social point of view. By applying the most advanced information technologies, Frontiers is catapulting scholarly publishing into a new generation.

What are Frontiers Research Topics?

Frontiers Research Topics are very popular trademarks of the *Frontiers journals series*: they are collections of at least ten articles, all centered on a particular subject. With their unique mix of varied contributions from Original Research to Review Articles, Frontiers Research Topics unify the most influential researchers, the latest key findings and historical advances in a hot research area.

Find out more on how to host your own Frontiers Research Topic or contribute to one as an author by contacting the Frontiers editorial office: frontiersin.org/about/contact

Advancement in hydrological modeling and water resources management for achieving Sustainable Development Goals (SDGs)

Topic editors

Vikram Kumar — Planning and Development, Govt. of Bihar, India

Jahangeer Jahangeer — University of Nebraska-Lincoln, United States

Rajneesh Singh — University of Minnesota Twin Cities, United States

Prabhat Kumar Singh Dikshit — Indian Institute of Technology (BHU), India

Citation

Kumar, V., Jahangeer, J., Singh, R., Dikshit, P. K. S., eds. (2025). *Advancement in hydrological modeling and water resources management for achieving Sustainable Development Goals (SDGs)*. Lausanne: Frontiers Media SA.

doi: 10.3389/978-2-8325-6252-9

Table of contents

frontiers | Frontiers in Water

TYPE Editorial
PUBLISHED 10 April 2025
DOI 10.3389/frwa.2025.1599795

OPEN ACCESS

EDITED AND REVIEWED BY
Jianshi Zhao,
Tsinghua University, China

*CORRESPONDENCE
Rajneesh Singh
✉ itsrajneeshs@gmail.com

RECEIVED 25 March 2025
ACCEPTED 31 March 2025
PUBLISHED 10 April 2025

CITATION
Kumar V, Jahangeer J, Singh R and Dikshit PKS (2025) Editorial: Advancement in hydrological modeling and water resources management for achieving Sustainable Development Goals (SDGs). *Front. Water* 7:1599795.
doi: 10.3389/frwa.2025.1599795

Editorial: Advancement in hydrological modeling and water resources management for achieving Sustainable Development Goals (SDGs)

Vikram Kumar[1], Jahangeer Jahangeer[2], Rajneesh Singh[3]* and Prabhat Kumar Singh Dikshit[4]

[1]Bihar Mausam Sewa Kendra (BMSK), Planning and Development Department, Patna, India, [2]Community and Regional Planning Program, University of Nebraska Lincoln, Lincoln, NE, United States, [3]Department of Hydrology, Indian Institute of Technology, Roorkee, Uttarakhand, India, [4]Department of Civil Engineering, Indian Institute of Technology (Banaras Hindu University), Varanasi, India

KEYWORDS

water quality, surface water, groundwater, sediment transport, climate change, streamflow, nature based solutions (NbS)

Editorial on the Research Topic
Advancement in hydrological modeling and water resources management for achieving Sustainable Development Goals (SDGs)

The sustainable management of our existing water resources is of utmost importance as water is a fundamental resource for life and critical for food security, sanitation, and human wellbeing. At the global scale, the United Nations Sustainable Development Goals (SDGs), particularly SDG 6 (Clean Water and Sanitation), SDG 2 (Zero Hunger), SDG 13 (Climate Action), and SDG 15 (Life on Land), directly needs a serious effort toward effective management of water resources. This Research Topic titled "*Advancement in Hydrological Modeling and Water Resources Management for Achieving Sustainable Development Goals (SDGs)*" explores the crucial role that hydrological monitoring and modeling along with the innovative water resources management practices play in achieving these SDGs. The integration of advance hydrological tools and models with water resources planning and management strategies is crucial for decision maker to and minimize the impacts of climate change which is a global issue. In this Research Topic, emerging challenges, and its solutions has been showcasing from different region which are as follows:

Hydrological modeling: the foundation of effective water resources management

Hydrological models have long been instrumental in predicting and developing an understanding of the distribution of water and water quality challenges within the environment. Several articles in Research Topic brings advancement in hydrological modeling which offers better simulations, thereby improving predictions of hydrological behavior under various scenarios. Integrating hydrological models with climate models

permits more accurate predictions of future water availability in the face of climate change, helping policymakers design more effective strategies for water management and climate resilient infrastructure. Such models provide an understanding of how a minor shift in temperature, precipitation patterns, and extreme weather events can affect local and regional water resources planning. For instance, a study featured in Research Topic utilizes advanced downscaling techniques to improve climate projections, particularly in regions susceptible to water stress. By using bias-corrected regional climate model (RCM) data, the study offers valuable insights into how climate change may influence water availability, highlighting at-risk areas and providing decision-makers with the tools to anticipate challenges and plan accordingly aligning with SDG 13–15.

Groundwater resources: vulnerability assessment and protection

To date, groundwater remains one of the most important sources of freshwater, facilitating water for domestic purpose, agriculture use, and industrial use, especially in regions with limited surface water. However, groundwater resources are dwindling due to over-extraction, pollution, and climate change. Several articles in Research Topic highlight the need for improved methods to assess and protect groundwater resources. For example, one study discusses the use of Geographic Information Systems (GIS) and the DRASTIC model to assess groundwater vulnerability to contamination. This approach helps identify areas where groundwater is at risk, allowing for targeted protection measures, such as land-use regulations or establishing buffer zones around vulnerable aquifers. Such innovative approaches to groundwater management may prove vital to ensure that groundwater resources remain available for future generations aligning with SDG6 and SDG13.

Streamflow and sediment transport modeling for flood control and ecosystem health

Streamflow and sediment transport models are crucial for predicting flooding events, managing river systems, and conserving a healthy aquatic ecosystem. Accurate simulation of water flow through catchments and movement of sediments through rivers can help reduce the impacts of floods, prevent soil erosion, and preserve water quality. In this Research Topic, several articles explore the application of the Soil and Water Assessment Tool (SWAT) to simulate streamflow and sediment transport. One such case study in the Song River basin, using the SWAT model to predict how land use and climate changes will affect water and sediment dynamics in the region. This type of understanding is crucial for developing flood control strategies, as it helps identify areas at risk, which may be of high importance for designing flood protection infrastructure. The study further elucidates the need for integrated land and water management approaches, considering the complex interactions between hydrological systems and human activities. Such study also helps in ensuring that river ecosystems remain resilient, supporting biodiversity, and providing ecosystem services like water purification and carbon sequestration aligning with SDG 3,11–13, and SDG15.

Nature-based solutions and ecosystem services for resilient urban water systems

With the growth in urban population, the need for a sustainable and climate resilient water system is becoming more pressing. Traditional approaches for water management, such as dams and pipelines, are observed to be less effective in addressing the multifaceted challenges of modern cities. In response, the concept of nature-based solutions (NbS) is gradually gaining momentum. These solutions utilize natural resources associated with often biologically mediated processes, such as wetlands, forests, and green infrastructure, to manage water resources and enhance resilience to climate change. An article in Research Topic explores the role of NbS in urban water management, specifically focusing on their ability to provide multiple ecosystem services, including flood regulation, water quality enhancement, and temperature moderation. The study integrates NbS into urban planning to create more cost-effective, resilient, and sustainable cities, aligning with SDG 11.

Addressing droughts in a changing climate

Droughts represent themselves as a threat to water security, agriculture, and the ecosystem. With climate change's influence on the frequency and intensity of drought events, our ability to predict and manage drought conditions becomes imperative. A study featured in this Research Topic explains the use of drought models for the prediction of drought conditions in semi-arid regions. Through the analysis of historical data and advanced modeling techniques, this research facilitates early warning signals, allowing communities and governments to take proactive measures, such as water rationing or the implementation of drought-resistant crop varieties. Such efforts contribute toward SDG 2 (Zero Hunger) and SDG 6 (Clean Water and Sanitation) by ensuring food and water security.

Advancements in wastewater treatment and water reuse technologies

Innovative technologies promoting the reuse of water are pivotal to addressing the challenge of water scarcity. Several articles in this Research Topic discuss advancements in wastewater treatment processes, focusing on development of efficient and affordable technologies for treatment of wastewater to meet with the water demand and water quality standards for reuse. Such innovations are crucial for reduced burden on freshwater

resources, particularly in regions facing water scarcity. Reusing treated wastewater for non-potable purposes, such as irrigation, industrial use, or landscape irrigation, can help conserve valuable freshwater resources and contribute to the achievement of SDG 12 (Responsible Consumption and Production) and SDG 6 (Clean Water and Sanitation).

Gender equality and inclusive water management

Women are often most disproportionately affected by water scarcity and water-related challenges. However, their involvement in water management decision-making processes has often been limited. An article from this Research Topic emphasizes the importance of integrating gender considerations into water management practices, ensuring that women have equal opportunities to participate in water governance and decision-making. Through gender equality in water management, the policies and interventions can become more inclusive, effective, and sustainable, supporting SDG 5 (Gender Equality) and SDG 6 (Clean Water and Sanitation).

Conclusion: bridging science, policy, and practice for sustainable water management

The articles in this Research Topic underscore the transformative potential of advanced hydrological modeling and innovative water management techniques toward achieving the SDGs the United Nations (UN) set up. By incorporating climate change projections, improving groundwater vulnerability assessments, utilizing nature-based solutions, and enhancing water reuse technologies, the world would be better equipped to address the challenges of water scarcity, pollution, and extreme weather events. Moreover, these advancements are not solely the domain of scientists and engineers as, policymakers and communities should also work together to translate these scientific insights into effective, actionable strategies. The synergy between science, policy, and practice is imperative for a sustainable and resilient water future. As we look toward the future, it is evident that achieving the SDGs will need more ongoing innovation, collaboration, and commitment. Through continued research, the adoption of best practices, and the integration of science into policy and governance, we can move toward a world where water resources are managed sustainably, equitably, and effectively.

Author contributions

VK: Writing – review & editing, Formal analysis, Writing – original draft, Visualization. JJ: Writing – original draft, Formal analysis, Writing – review & editing, Visualization. RS: Writing – review & editing, Formal analysis, Writing – original draft, Visualization. PD: Writing – review & editing.

Conflict of interest

The authors declare that the research was conducted in the absence of any commercial or financial relationships that could be construed as a potential conflict of interest.

Publisher's note

frontiers | Frontiers in Water

TYPE Methods
PUBLISHED 01 December 2023
DOI 10.3389/frwa.2023.1279444

OPEN ACCESS

EDITED BY
Jahangeer Jahangeer,
University of Nebraska-Lincoln, United States

REVIEWED BY
Mohamed Mwabumba,
Nelson Mandela African Institution of Science and Technology, Tanzania
Apoorv Verma,
Indian Institute of Technology Roorkee, India

*CORRESPONDENCE
Chunqiao Song
✉ cqsong@niglas.ac.cn

RECEIVED 18 August 2023
ACCEPTED 07 November 2023
PUBLISHED 01 December 2023

CITATION
Luo S and Song C (2023) Uncertainties on the combined use of ICESat and ICESat-2 observations to monitor lake levels.
Front. Water 5:1279444.
doi: 10.3389/frwa.2023.1279444

Uncertainties on the combined use of ICESat and ICESat-2 observations to monitor lake levels

Shuangxiao Luo[1,2] and Chunqiao Song[2,3,4]*

[1]Faculty Geography Resource Sciences, Sichuan Normal University, Chengdu, China, [2]Key Laboratory of Watershed Geographic Sciences, Nanjing Institute of Geography and Limnology, Chinese Academy of Sciences, Nanjing, China, [3]University of Chinese Academy of Sciences, Nanjing (UCASNJ), Nanjing, China, [4]University of Chinese Academy of Sciences, Beijing, China

Lake water level is an important variable to indicate lake hydrological balances and climate change impacts. Benefiting from the launch of the laser altimeters ICESat and ICESat-2, higher spatial-resolution elevation measurements have opened new possibilities for monitoring lake levels globally over the past two decades. However, uncertainties on the combined use of two-generation satellite laser measurements have not yet been investigated specifically. This study aimed to summarize the important technique notes on water level data processing by integrating the ICESat and ICESat-2 altimetry measurements. We mainly focused on the effect of geoid height, water masks for extracting altimetry footprints, and the 9-year data gap between the two generations of satellites on water level change estimates. We compared the influences of the above three factors in different situations by selecting typical lakes worldwide as study cases. The results showed that: (1) In the combination of ICESat and ICESat-2 products, geoid heights need to be recalculated for each footprint based on its longitude and latitude in order to replace the geoid values of the original products when calculating orthometric heights. It is necessary because the default geoids in both generations of products (ICESat and ICESat-2) exhibit a systematic deviation; (2) To balance the accuracy and efficiency, the small water mask in the low-level year is recommended to extract the potential footprints in comparison with the laborious processing of time-varying water masks; (3) The 9-year data gap between ICESat and ICESat-2 observations may cause inevitable overestimations or underestimations of the long-term change rate of lake levels with a non-linear trajectory, yet it has few effects on lakes with (near) linear trending or fluctuating changes.

KEYWORDS

ICESat, ICESat-2, lake, satellite altimetry, water level

1 Introduction

Lakes, as the key component of the hydrosphere, participate in the global hydrological cycle. Climate change and human activities significantly affect lake formation, development, expansion, and shrinkage. Monitoring the long-term lake variations is important to understand the climatic and anthropogenic impacts on water resources. Global lakes have changed rapidly in the past decades, according to growing evidence (Pham-Duc et al., 2020). However, long-term *in situ* lake-level data are usually unavailable due to the sparse gauge observations. Remote sensing techniques have demonstrated great potential for monitoring

lake-level changes and understanding the driving mechanisms (Song et al., 2015b; Jiang et al., 2019; Mi et al., 2019; Yao et al., 2019; Luo et al., 2021; Xu N. et al., 2022).

In the past few decades, numerous studies have investigated lake water level changes on a regional or global scale via satellite altimeters (Song et al., 2015a, 2023; Cretaux et al., 2016; Jiang et al., 2017; Lei et al., 2017; Qiao et al., 2019; Shu et al., 2020; Chen et al., 2021). Multi-source radar altimetry missions provide lake elevation measurements with a temporal coverage of more than 20 years, such as TOPEX/POSEIDON (1992–2005), ERS-1/2 (1991–2000/1995–2011), Envisat (2002–2012), Jason-1/2/3 (2001–2013/2008-/2016-), CryoSat-2 (2010-), SARAL (2013-), and Sentinel-3 (2016-) (Schwatke et al., 2015; Shen et al., 2020; Feng et al., 2023). Radar altimeters are suitable for monitoring large lakes due to their coarse footprints and large inter-track spacing gaps. In contrast, the Ice, Cloud, and Land Elevation Satellite (ICESat) data have been widely applied to monitor global lakes at a finer scale by benefiting from its small footprint diameter of ∼70 m. However, the investigation time period is impeded by the short temporal coverage of ICESat data (2003–2009). Thus, it is rather necessary to seek an approach to synthesizing multiple altimetry datasets for monitoring global lake dynamics. ICESat-2, launched in September 2018, is the follow-on mission of ICESat. Compared to radar altimetry, this satellite has the characteristics of multi-beam and high-resolution photon-counting observation, and its laser footprints are ∼17 m and separated by ∼0.7 m. Thus, combining the observations of two laser altimetry satellites, ICESat and ICESat-2, can reveal the temporal and spatial change characteristics of global lake levels over the past two decades (Feng et al., 2022; Luo et al., 2022).

However, the accuracy of the synthesized altimetry data from different instrument measurements and potential elevation bias is the major concern for monitoring lake changes. There have been several global-scale lake-level datasets synthesizing multi-source altimeter observations, such as the River and Lake Database (Berry et al., 2005), the Global Reservoir and Lake Monitor (G-REALM) (Birkett et al., 2011), HYDROWEB (Cretaux et al., 2011), and the Database for Inland Waters (DAHITI) (Schwatke et al., 2015). These datasets have been successfully applied to tracking the hydrological dynamics of lakes on regional or global scales (Dubey et al., 2015; Song et al., 2015a; Tan et al., 2017; Luo et al., 2019; Schwatke et al., 2020; Liang et al., 2023). These data products all emphasized the importance of data integration for multi-source radar altimetry measurements (e.g., correction of inconsistent geoid heights). For laser altimetry data processing, a few previous studies have explored the influences of lake water masks on extracting satellite altimetry potential footprints. For example, Xu et al. (2020) analyze the effects of using different buffers to obtain water masks and conclude that the buffer width set at ∼100 m for the narrow lake can obtain the highest altimetry accuracy. However, the method to join the two-generation satellite laser measurements has not yet been investigated comprehensively. The inundation extents of most lakes exhibit strong intra-annual and inter-annual variations, and accurately extracting lake elevation points is a critical prerequisite for obtaining reliable water levels. After thoroughly considering the key processes involved in altimetry data processing, three crucial aspects were identified for the joint processing of ICESat and ICESat-2 data: the geoid height, the water mask used to extract altimetry points, and the 9-year data gap between the two satellite missions. Through experimentation, the best method for extracting water levels was selected among these three key aspects. Other potential influencing factors, such as the efficient number of altimetry footprints or the water level data sampling interval, were excluded after initial testing, as their impacts on water level change rates exist in local-scale lakes or can be reduced by the setting of statistical thresholds. Therefore, this study aims to summarize the three important technique notes on water level data processing by integrating the ICESat and ICESat-2 altimetry measurements.

2 Study data

2.1 Lake water level data

2.1.1 Lake water level time series from laser altimetry

The ICESat laser altimeter was launched in January 2003, and its small footprints allow for measuring elevations effectively at a fine scale. The Release-34 GLAH14 product (February 2003–October 2009) of the National Snow and Ice Data Center (NSIDC) is applied in this study. ICESat-2 ATL13, a dataset for inland water surface height, was applied to monitor lake water level changes in 2018–2020. The version-5 datasets of ICESat-2 ATL13 are available at NSIDC.

2.1.2 Radar altimetry dataset for cross-evaluating lake water levels

In this study, the lakes with the HYDROWEB water level data over the period of 2003–2020 were selected for cross-evaluation on the synthesized ICESat/ICESat-2 measurements. HYDROWEB, initiated by LEGOS (Cretaux et al., 2011), is a website that provides water level time series of global lakes, reservoirs, and rivers based on multiple altimetry missions, such as TOPEX/Poseidon, ENVISAT, and Sentinel-3B. In this study, potential instrument biases between different products (ICESat/ICESat-2 data and the validation data) and geoid differences were removed by using the validation data as a reference.

2.1.3 *In situ* data for lake water level validation

In this study, the available *in situ* data were applied to validate the water levels of ICESat/ICESat-2. *In situ* data for Dauphin Lake and Lake Erie were collected from the website of the Government of Canada and the TIDES and CURRENTS websites of the National Oceanic and Atmospheric Administration, respectively. *In situ* water level data for Qinghai Lake were obtained from Xu F. et al. (2022). The *in situ* data in this study have been organized to closely match a monthly temporal resolution.

2.2 Lake masks for extracting altimetry footprints

Three types of commonly used water mask data were applied to compare the effects of different water masks on extracting potential altimetry footprints, including the historically maximum

water extent, the stationary water body data product (e.g., the HydroLAKES dataset), and time-varying dynamic water inundation masks.

The Global Surface Water (GSW) dataset, which applies Landsat imageries from March 1984 to the present to identify changes in the surface water area, was used to obtain the first type of water mask (Pekel et al., 2016). This study employed surface water occurrences from GSW to map the maximum water extents (all locations ever mapped as water during the observation period) of lakes from 1984 to 2020.

We chose the HydroLAKES dataset, which includes 1,427,688 lakes (>0.1 km^2), to obtain the small water mask of lakes at low water levels. Lake polygons (including all attributes) of HydroLAKES are available in a shapefile format (Messager et al., 2016). One of the primary sources of HydroLAKES is the Shuttle Radar Topography Mission (SRTM) Water Body Data, which provided the extent of the water inundation in February 2000. As there are many lakes that have been expanding in the past 20 years (Luo et al., 2022), their water extents from HydroLAKES data can be used as small water masks for conservatively extracting on-lake footprints.

The monthly water frequency data produced by the Global Land Analysis and Discovery Laboratory (Pickens et al., 2020) were used to derive dynamic lake water masks. The water mask corresponding to the ICESat/ICESat-2 measurements data in the same month was chosen to filter on-lake altimetry footprints.

3 Methods

Lake water levels can be obtained from on-lake footprint elevations by an overlay analysis of the lake water mask and altimetry tracks. The averaging elevations of footprints are calculated based on ellipsoid and geoid heights. After obtaining the orthometric height of each observation date, the lake-level change rate is calculated via the linear fitting of the water level time series during the observation periods (e.g., 2003–2009 and 2018–present of ICESat/ICESat-2). Therefore, we focused on investigating the influences of three key data-processing procedures on estimating lake water levels based on ICESat/ICESat-2 observations, including the selection of geoid models, different water masks for filtering footprints, and the 9-year data gap (2010–2018) of water level time series (Figure 1).

As shown in Figure 1, the orthometric height based on the geoid (H) is calculated by subtracting the geoid height relative to the ellipsoid system (N) from the ellipsoid height (h). The geoid is the shape that the ocean surface would take under the Earth's gravity without considering other effects such as winds and tides. This surface is recombined with the mean ocean surface and extends into the continent's interior (Gauss, 1828). The EGM, published by the National Geospatial-Intelligence Agency (NGA), is a series of geopotential models of the Earth. The EGM reference frames include EGM84, EGM96, EGM2008, and EGM2020 (Barnes et al., 2015). Both EGM96 and EGM2008 are the commonly used geoid reference systems. Therefore, the geoids of these two reference systems are adopted and compared in this study.

The procedure for obtaining the long-term lake water levels based on ICESat/ICESat-2 is summarized as follows. First, water masks were used to extract potential lake footprints from the laser altimeter. Second, the normalized median absolute deviation (NMAD) method was applied to remove the errors from the clouds, lake surface waves, snow, or saturated reflected signals (Hoehle and Hoehle, 2009). Data processing using the NMAD method includes the following steps: (1) calculating the median of all water levels within 1 day, (2) computing the absolute deviations of each factor from the median value, (3) determining the median of these absolute deviations (MAD), and (4) multiplying by a constant of 1.4826, and removing water levels that exceed the range ([median-MAD, median+MAD]). We excluded lake levels with fewer than five altimetry footprints on each observation date to reduce the height bias derived from insufficient measurement times. To further eliminate potential outliers in water levels, we tested the water level processing results of multiple lakes and chose a threshold of 0.3 m. Then, lakes with the water level standard deviation of each observation date larger than 0.3 m (depending on the uncertainty range relative to lake-level changes) were also removed. Third, we computed the lake water level on each observation date by averaging the remainder of the footprint elevations. Finally, the water level change rate based on the time series data was obtained via the robust fitting method (Holland and Welsch, 1977).

4 Results and analyses

4.1 The effect of geoid selection on estimating lake levels and change rates

Orthometric height is approximated by subtracting geoid height from ellipsoid height. An accurate geoid model is needed for converting ellipsoidal heights to orthometric heights. Therefore, the main function of the geoid is deemed to be a reference surface for the water level in geodesy, and the geoid heights at different locations of one lake may be quite different (Li and Gotze, 2001). This height difference is more obvious in large water bodies because large lakes span more spatial domains. Thus, we chose Lake Erie (25,768 km^2), one of the Great Lakes in North America, as the research case to investigate the effect of geoid on lake water levels. Then, we considered four scenarios of the geoid reference, including no use of the geoid (1), default geoid heights contained in the NASA data product (2), recalculation of geoid by the EGM96 model (3), or EGM2008 model (4). The EGM2008/EGM96 geoid heights were recalculated based on the longitude and latitude of each footprint by using the NGA tool. To validate the integration of ICESat and ICESat-2 under various scenarios, we compared the time-series waveforms and water level change rates with those of *in situ* water level data.

The water level time series in the four scenarios show that the lake levels without considering geoid height are significantly disorganized (Figure 2A), and the seasonal signal of water level is not reasonable in both ICESat and ICESat-2 periods (Figure 2B). As shown in Figures 2A, C, there is an obvious systematic deviation between the ICESat and ICESat-2 water levels (based on the

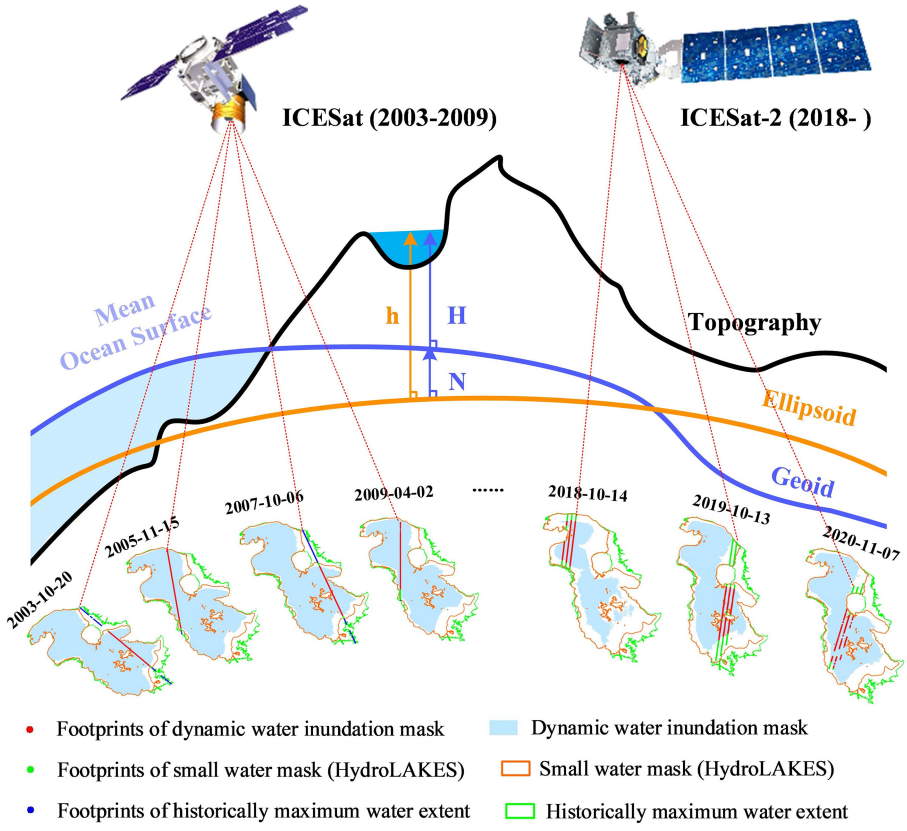

FIGURE 1
Framework of lake-level calculations, including geoid, different water masks, and the 9-year gap between ICESat/ICESat-2.

default EGM 2008 geoids provided by the ICESat and ICESat-2 products). Therefore, the water level change rate is obviously overestimated based on the original geoid of the product. From Figures 2D–F, the water levels based on the EGM2008 and EGM96 geoids have comparable change patterns and the same water level change rate, which is rather consistent with the *in situ* data. According to the user guidebook for ICESat and ICESat-2 raw products, although both of the datasets were processed with the EGM2008 geoids, there is a systematic bias when combining the two-time series (2003–2009 and 2018–present). It could be due to the inconsistent usage of different spherical harmonic coefficients of the EGM2008 model applied in ICESat and ICESat-2 products (not stated in the product manual). In previous studies, deviations in the water levels of some lakes on the Tibetan Plateau were also mentioned. Zhang et al. (2019) mentioned that for Qinghai Lake, ICESat aligns well with *in situ* measurements, and the lake level derived from HYDROWEB is slightly higher than both ICESat and station observations. In the case of Selin Co and Nam Co, the elevations from ICESat/ICESat-2 are slightly higher than those from HYDROWEB, possibly due to altimeter instrument biases and geoid variations. Therefore, it is important to obtain orthometric heights via a consistent geoid model, and it is necessary to recalculate geoids when obtaining lake water levels from ICESat/ICESat-2.

4.2 The effect of water mask on estimating lake levels and change rates

Lake levels are calculated generally by averaging on-lake footprints filtered by water masks. The water mask selection is a key step that affects altimetry accuracy, especially for lakes with remarkable changes in water inundation extent. Due to limitations such as the scarcity of hydrological monitoring stations, remote locations, and constraints related to data politics, obtaining long-term and large-scale *in situ* data on water levels is challenging, particularly for small lakes. Radar altimetry satellites, with footprints ranging from 0.3 to 8 km, are well-suited for long-term water level monitoring of large lakes. However, their coverage is limited to medium- and small-sized lakes. Small lakes are difficult to monitor with *in situ* data or radar altimetry satellite datasets, but reference data are needed for lake water level verification. It only makes sense to discuss using different time periods of lake inundation extents as masks for extracting potential water levels when the lake area changes are significant. Therefore, we chose a large lake (Lake Urmia in Central Asia) with obvious inundation area changes as the study case, to compare the effect of different water masks on the lake-level estimates. Lake Urmia is an endorheic salty lake in Iran, and its area was ~4,600 km^2 in 2000. Persistent drought and groundwater pumping cause the

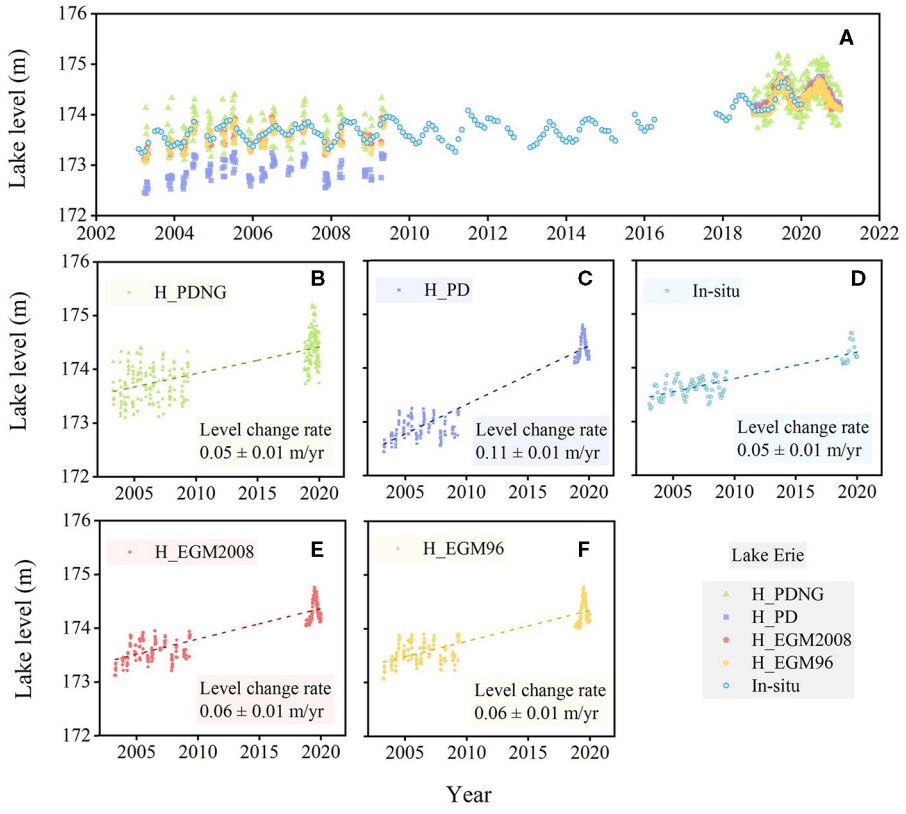

FIGURE 2
Time series of water levels under four different scenarios and comparison with *in situ* data **(A)**. H_PDNG: no use of the geoid **(B)**, H_PD: the water level based on the product-default geoid **(C)**, the *in situ* water level **(D)**, H_EGM2008: the water level based on recalculated geoid by EGM2008 **(E)**, and H_EGM96: the water level based on recalculated geoid by EGM96 **(F)**.

continuous shrinkage of the lake. Thus, we set three different types of water masks historically maximum water extent, a small water mask (HydroLAKES data, representing the status of ~2000), and a monthly dynamic inundation mask. The historically maximum water extent may obtain as many observation opportunities as possible and add the observation times for some lakes. The small water mask (e.g., HydroLAKES data) has the advantages of easy access and a large number of lakes. The conservative water mask makes it easy to eliminate the outliers of water level data in the following process. The dynamic water masks can track the expansion or shrinkage of the lake and avoid including the "polluted" footprints of the lakeshore. There is a trade-off between the temporal-spatial resolution of the water level and the efficiency of data processing in the mask choice. Therefore, it is important to compare the water level time series and water level change rate under the three mask scenarios. In this study, we calculated the orthometric heights from ICESat/ICESat-2 data for each type of mask based on the recalculated geoid (EGM2008) and the WGS84. We validated the integration of ICESat and ICESat-2 data under different water masks by comparing the absolute difference in water levels and change rate with validation data. The water level data obtained from three different masks have all been processed to remove outliers using the NAMD method. During the satellite mission periods (2003–2009 and 2018–2020), the historically maximum water extent, small water mask, and dynamic water inundation mask for Lake Urmia derived observations 110 times (717,701 footprints), 109 times (710,340 footprints), and 106 times (584,666 footprints), respectively (Table 1). The comparison of the water level change rate shows that the result from maximum water extent (−0.17 ± 0.01 m/year in Figure 3B) is the most deviated from the reference value (−0.14 ± 0.01 m/year in Figure 3E). The results from the small water mask and dynamic water inundation mask are roughly consistent (Figure 3).

Furthermore, we compared the number of footprints and water levels from the three masks on the same observation date in Lake Urmia. The results under three different mask scenarios show that footprints derived from historically maximum water extent are nearly twice the number from small water masks and dynamic water inundation masks (Table 2; Figure 4). Specifically, the water level from the maximum water extent (1,274.61 m) is far from the reference value (1,272.69 m) under the same geographical reference system (see), while the water level results acquired in October 2005 based on the HydroLAKES lake mask (1,272.79 m) and dynamic mask (1,272.57 m) were basically consistent. The absolute difference between the water level results of three water masks and the reference value (HYDROWEB) is 1.92, 0.10, and 0.12 m, respectively.

TABLE 1 Statistics of lake-level monitoring results from three water masks in the period of 2003–2009 and 2018–2020 in Lake Urmia.

Mask	Historically maximum water extent	Small water mask (HydroLAKES)	Dynamic water inundation mask	HYDROWEB (reference)
Observation dates	110	109	106	-
Footprints	717,701	710,340	584,666	-
Water level change rate	-0.17 ± 0.01 m/yr	-0.15 ± 0.01 m/yr	-0.16 ± 0.01 m/yr	-0.14 ± 0.01 m/yr

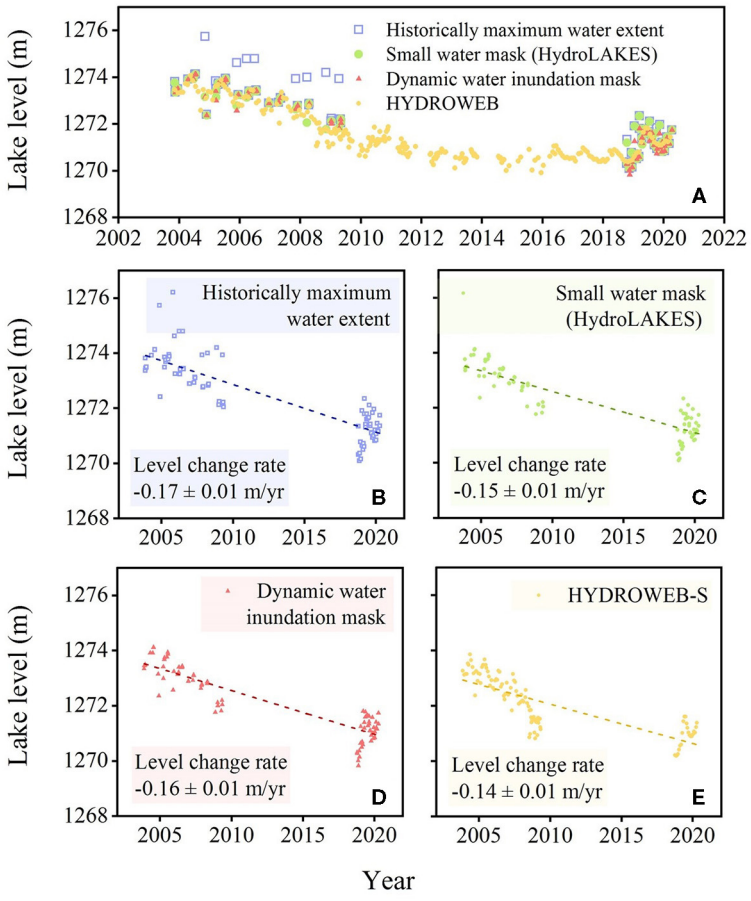

FIGURE 3
(A–E) Time series of water levels under three different water masks. HYDROWEB-S (e) means the sparse HYDROWEB based water level time series. The intermediate period is removed, and the monitoring period is consistent with ICESat/ICESat-2.

4.3 The effect of the 9-year data gap on estimating lake levels and change rates

The advantages of ICESat and ICESat-2 mainly lie in their capability to monitor small and medium-sized lakes with high accuracy. Combining the two generations of laser altimetry satellites can achieve the two-decade monitoring of ~7,000 lakes over 10 km² globally (Luo et al., 2022). However, there is a 9-year data gap between the two satellites from 2010 to 2018, which inevitably induces some uncertainties in estimating the water level change rates. Therefore, to quantify the influence of the 9-year data gap on the water level change rate, we selected lakes with different time-series patterns for comparison. Considering that different lakes are experiencing varying impacts due to the data gap, we selected lakes with relatively stable water levels, seasonal fluctuations, and drastic inter-annual or decadal trending changes. Correspondingly, Dauphin Lake, Garabogazkol Lake, Hulun Lake, Qinghai Lake, and Migriggyangzham Co were selected as the study cases for investigating the effect of the 9-year data gap on estimating the water level change rate. We applied the HydroLAKES dataset, a small water mask, to extract the footprints and finally obtained the water level time series referred to as EGM2008 and WGS84. We assessed the influence of the 9-year data gap on deriving water level time series through the integration of ICESat and ICESat-2 data by comparing water level change rates with validation data. The results indicate that the correlation between the validation data and ICESat/ICESat-2 data for the five lakes is consistently above 0.99. The average absolute error between these five datasets

TABLE 2 Statistics of lake-level monitoring results from three water masks on the same observation date in Lake Urmia.

Mask	Historically maximum water extent	Small water mask (HydroLAKES)	Dynamic water inundation mask	HYDROWEB (reference)
2005_10_25_footprints	650	348	304	-
2005_10_25_water_level	1,274.61 m	1,272.79 m	1,272.57 m	1,272.69 m

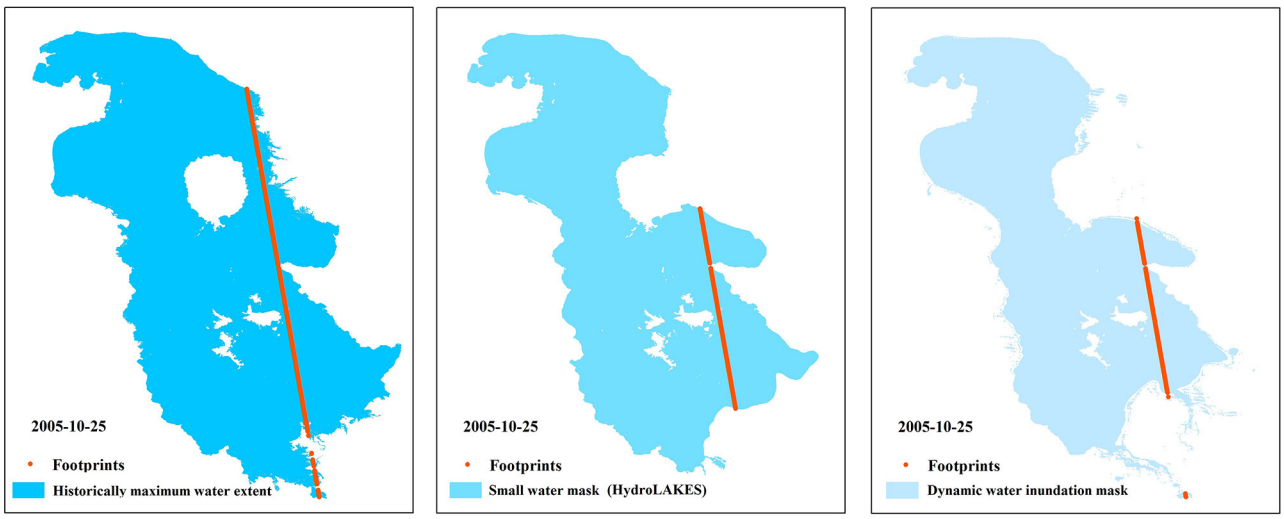

FIGURE 4
Altimetry footprints of Lake Urmia by three different water masks based on the observations carried out on October 25, 2005.

and the validation data is 0.01 m/year, which is lower than the typical calculation error for water level change rates. The specific comparison results are shown in Figure 5. For the relatively stable water level pattern in 2010–2018, such as Dauphin Lake, or the water level pattern in Garabogazkol Lake with seasonal fluctuation, the 9-year data gap had a limited effect on the change rate estimation. For the water level pattern with large fluctuations in 2010–2018 such as Hulun Lake, the data gap led to an obvious underestimation of the results. For the water level pattern with small fluctuations in 2010–2018, such as Qinghai Lake, the data gap caused an overestimation of the water level change rate. For the water level pattern with a near-linear increase in 2010-2018, such as Migriggyangzham Co, there is little effect on the change rate estimation.

5 Summary and concluding remarks

The development of satellite laser altimetry opens new possibilities for monitoring global lake levels at a finer scale. The joint use of ICESat and ICESat-2 laser altimetry data can facilitate the near two-decade detection of lake water level changes. In this study, we summarize three primary data-processing procedures (geoid height, water mask for extracting potential footprints, and the 9-year data gap between the two generations of laser altimetry satellites) impacting lake-level estimates when integrating the ICESat and ICESat-2 altimetry measurements. The major conclusions and suggestions are organized as follows.

Geodetic reference needs to be considered when constructing the time series of lake water levels. We suggest recalculating the geoid heights of ICESat and ICESat-2 altimetry data using the consistent geoid model (e.g., EGM2008 and EGM96) rather than the default geoid heights of product data. The comparison results of different water masks for extracting altimetry footprints showed that the maximum water extent would introduce larger errors, while the results based on the dynamic mask and the small water mask are basically comparable. However, the mapping of dynamic water masks is a laborious task, especially for the investigation of lakes at regional or global scales. The smaller water mask is recommended to extract the potential on-lake altimetry footprints when the lake is at lower water level. The lake mask should be selected according to the different hydrological characteristics of the study regions. For example, for the expanding lakes on the Tibetan Plateau, it is suitable to choose the water extent around the year 2000 to extract the on-lake footprints during the period 2003–2020. However, in Central Asia, where most lakes are shrinking, it would be better to obtain water extents derived from more recent satellite imagery.

The 9-year data gap between ICESat and ICESat-2 observations may result in an overestimation or underestimation of the water level change rate for lakes with non-linear expansion/contraction. However, it has a limited effect on lakes with (near-) linear change or seasonal fluctuation. Thus, it is very crucial to develop methods for filling the data gap. For example, we can establish the lake hypsometric curve by fitting the lake area and water level changes and reconstructing the missing water levels from the consecutive

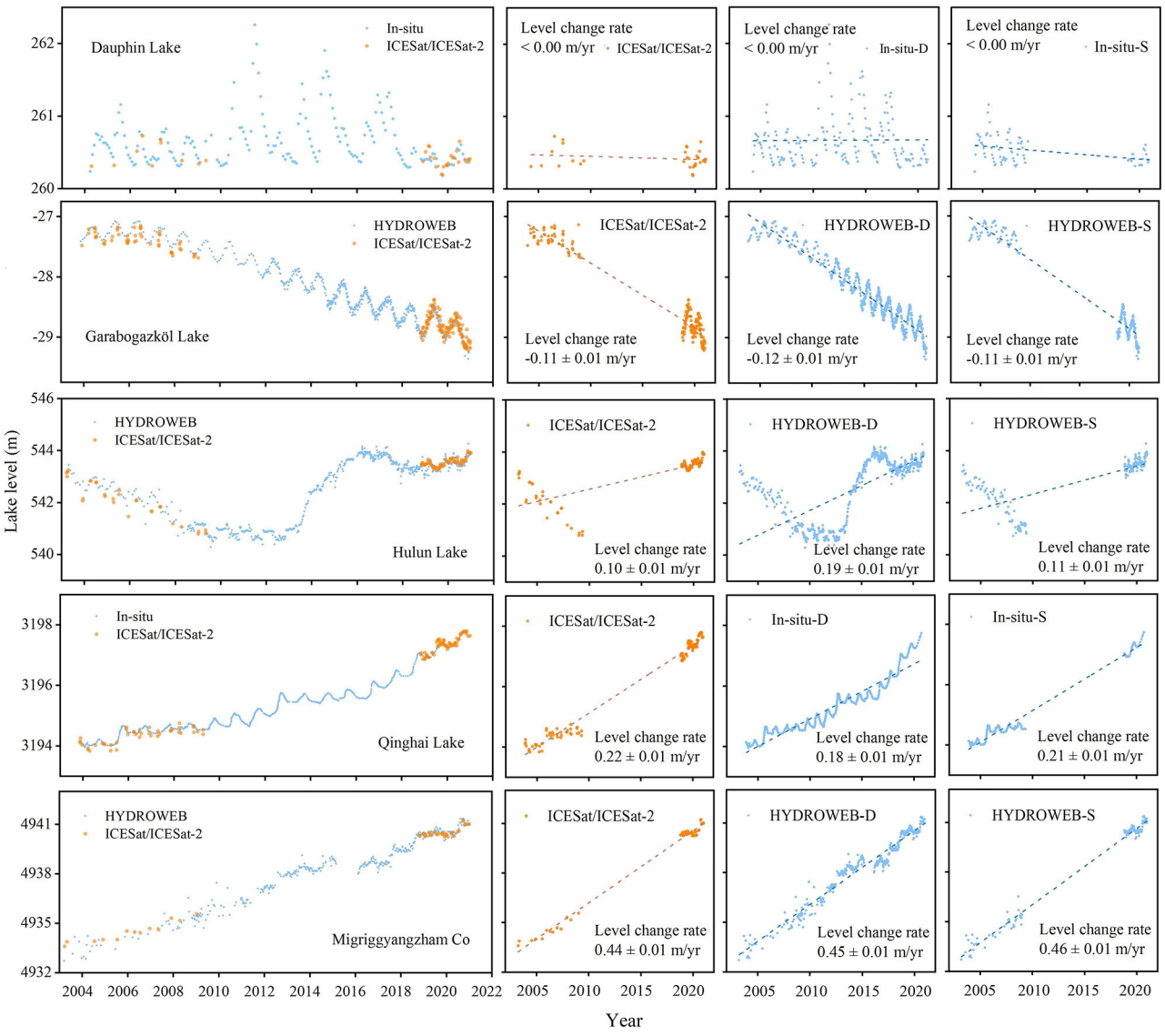

FIGURE 5
Effect of a 9-year data gap on the water level change rate from lakes with different water level change patterns. Dauphin Lake, Garabogazkol Lake, Hulun Lake, Qinghai Lake, and Migriggyangzham Co represent the stable, seasonal, large, small, and linear fluctuation patterns of water levels in 2003–2020, respectively.

time series of lake areas. In addition, integration of the water levels from other altimetry satellites, such as CryoSat-2 (2010–present), is also an effective solution. However, this method is more suitable for large lakes due to the coarser footprints of CryoSat-2. In addition, overlaying lake shorelines on DEMs can be applied to extract lake levels for supplementing the data gap. It should be mentioned that there could be other possible data-processing procedures affecting the accuracy of lake level and change rate estimates when integrating ICESat and ICESat-2 data, for instance, the linear fitting method, data sampling intervals (e.g., the monthly or seasonal data composite), and methods of removing height outliers. All of these procedures should be considered cautiously for generating accurate lake-level estimates from the altimetry satellite observations.

Data availability statement

The data used in the study can be found in the https://doi.org/10.6084/m9.figshare.24456358.v1.

Author contributions

SL: Data curation, Methodology, Visualization, Writing – original draft. CS: Funding acquisition, Project administration, Supervision, Writing – review & editing.

Funding

The author(s) declare financial support was received for the research, authorship, and/or publication of this article. This study was supported by the National Key Research and Development Program of China (Grant Nos. 2022YFF0711603 and 2019YFA0607101), the Strategic Priority Research Program of the Chinese Academy of Sciences (Grant Nos. XDA23100102 and XDA28020503), and the National Natural Science Foundation of China (Grant Nos. 41971403 and 41801321).

Acknowledgments

We are grateful to the National Snow and Ice Data Center for providing ICESat/ICESat-2 data (https://nsidc.org/data/icesat, https://nsidc.org/data/atl13/versions/5), LEGOS for providing lake-level data (http://hydroweb.theia-land.fr/), the website Government of Canada for providing *in situ* data of Dauphin Lake (https://wateroffice.ec.gc.ca/mainmenu/historical_data_index_e.html), the website TIDES and CURRENTS for providing *in situ* data of Lake Erie (https://tidesandcurrents.noaa.gov/stations.html?type=Water+Levels), the Global Land Analysis and Discovery Laboratory for providing the monthly water frequency data (https://glad.umd.edu/dataset/global-surface-water-dynamics), Messager for providing the small water mask of the lakes (https://www.hydrosheds.org/page/hydrolakes), the Joint Research Center for providing the maximum water extent of the lakes (https://global-surface-water.appspot.com/), and the National Geospatial-Intelligence Agency for providing a tool of calculating geoid heights (https://earth-info.nga.mil/).

Conflict of interest

The authors declare that the research was conducted in the absence of any commercial or financial relationships that could be construed as a potential conflict of interest.

Publisher's note

All claims expressed in this article are solely those of the authors and do not necessarily represent those of their affiliated organizations, or those of the publisher, the editors and the reviewers. Any product that may be evaluated in this article, or claim that may be made by its manufacturer, is not guaranteed or endorsed by the publisher.

References

Barnes, D., Factor, J. K., Holmes, S. A., Ingalls, S., Presicci, M. R., Beale, J., et al. (2015). *Earth Gravitational Model 2020*. American Geophysical Union Fall meeting 2015 abstract id. G34A–03.

Berry, P. a. M., Garlick, J. D., Freeman, J. A., and Mathers, E. L. (2005). Global inland water monitoring from multi-mission altimetry. *Geophys. Res. Lett.* 32, 814. doi: 10.1029/2005GL022814

Birkett, C., Reynolds, C., Beckley, B., and Bradley, D. (2011). From research to operations: the USDA global reservoir and lake monitor. *Coastal Altimetry* 19–50.

Chen, T., Song, C., Ke, L., Wang, J., Liu, K., Wu, Q., et al. (2021). Estimating seasonal water budgets in global lakes by using multi-source remote sensing measurements. *J. Hydrol.* 593, 125781. doi: 10.1016/j.jhydrol.2020.125781

Cretaux, J. F., Abarca-Del-Rio, R., Berge-Nguyen, M., Arsen, A., Drolon, V., Clos, G., et al. (2016). Lake volume monitoring from space. *Surv. Geophys.* 37, 269–305. doi: 10.1007/s10712-016-9362-6

Cretaux, J. F., Jelinski, W., Calmant, S., Kouraev, A., Vuglinski, V., Berge-Nguyen, M., et al. (2011). SOLS: a lake database to monitor in the Near Real Time water level and storage variations from remote sensing data. *Adv. Space Res.* 47, 1497–1507. doi: 10.1016/j.asr.2011.01.004

Dubey, A. K., Gupta, P. K., Dutta, S., and Singh, R. P. (2015). An improved methodology to estimate river stage and discharge using Jason-2 satellite data. *J. Hydrol.* 529, 1776–1787. doi: 10.1016/j.jhydrol.2015.08.009

Feng, Y., Yang, L., Zhan, P., Luo, S., Chen, T., Liu, K., et al. (2023). Synthesis of the ICESat/ICESat-2 and CryoSat-2 observations to reconstruct time series of lake level. *Int. J. Digital Earth* 16, 183–209. doi: 10.1080/17538947.2023.2166134

Feng, Y., Zhang, H., Tao, S., Ao, Z., Song, C., Chave, J., et al. (2022). Decadal lake volume changes (2003–2020) and driving forces at a global scale. *Remote Sens.* 14, 1032. doi: 10.3390/rs14041032

Gauss, C. F. (1828). *Bestimmung des Breitenunterschiedes zwischen den Sternwarten von Göttingen und Altona: durch Beobachtungen am Ramsdenschen Zenithsector*. Bei Vandenhoeck und Ruprecht.

Hoehle, J., and Hoehle, M. (2009). Accuracy assessment of digital elevation models by means of robust statistical methods. *ISPRS J. Photogram. Remote Sens.* 64, 398–406. doi: 10.1016/j.isprsjprs.2009.02.003

Holland, P. W., and Welsch, R. E. (1977). Robust regression using iteratively re-weighted least-squares. *Commun. Statis. A Theory Methods* 6, 813–827. doi: 10.1080/03610927708827533

Jiang, L., Andersen, O. B., Nielsen, K., Zhang, G., and Bauer-Gottwein, P. (2019). Influence of local geoid variation on water surface elevation estimates derived from multi-mission altimetry for Lake Namco. *Remote Sens. Environ.* 221, 65–79. doi: 10.1016/j.rse.2018.11.004

Jiang, L., Nielsen, K., Andersen, O. B., and Bauer-Gottwein, P. (2017). Monitoring recent lake level variations on the Tibetan Plateau using CryoSat-2 SARIn mode data. *J. Hydrol.* 544, 109–124. doi: 10.1016/j.jhydrol.2016.11.024

Lei, Y., Yao, T., Yang, K., Sheng, Y., Kleinherenbrink, M., Yi, S., et al. (2017). Lake seasonality across the Tibetan Plateau and their varying relationship with regional mass changes and local hydrology. *Geophys. Res. Lett.* 44, 892–900. doi: 10.1002/2016GL072062

Li, X., and Gotze, H. J. (2001). Ellipsoid, geoid, gravity, geodesy, and geophysics. *Geophysics* 66, 1660–1668. doi: 10.1190/1.1487109

Liang, X., Song, C., Liu, K., Chen, T., and Fan, C. (2023). Reconstructing centennial-scale water level of large Pan-Arctic lakes using machine learning methods. *J. Earth Sci.* 34, 1218–1230. doi: 10.1007/s12583-022-1739-5

Luo, S., Song, C., Ke, L., Zhan, P., Fan, C., Liu, K., et al. (2022). Satellite laser altimetry reveals a net water mass gain in global lakes with spatial heterogeneity in the early 21st century. *Geophys. Res. Lett.* 49, 676. doi: 10.1029/2021GL096676

Luo, S., Song, C., Liu, K., Ke, L., and Ma, R. (2019). An effective low-cost remote sensing approach to reconstruct the long-term and dense time series of area and storage variations for large lakes. *Sensors* 19, 4247. doi: 10.3390/s19194247

Luo, S., Song, C., Zhan, P., Liu, K., Chen, T., Li, W., et al. (2021). Refined estimation of lake water level and storage changes on the Tibetan Plateau from ICESat/ICESat-2. *Catena* 200, 105177. doi: 10.1016/j.catena.2021.105177

Messager, M. L., Lehner, B., Grill, G., Nedeva, I., and Schmitt, O. (2016). Estimating the volume and age of water stored in global lakes using a geo-statistical approach. *Nat. Commun.* 7, 13603. doi: 10.1038/ncomms13603

Mi, H., Fagherazzi, S., Qiao, G., Hong, Y., and Fichot, C. G. (2019). Climate change leads to a doubling of turbidity in a rapidly expanding Tibetan lake. *Sci. Total Environ.* 688, 952–959. doi: 10.1016/j.scitotenv.2019.06.339

Pekel, J.- F., Cottam, A., Gorelick, N., and Belward, A. S. (2016). High-resolution mapping of global surface water and its long-term changes. *Nature* 540, 418. doi: 10.1038/nature20584

Pham-Duc, B., Sylvestre, F., Papa, F., Frappart, F., Bouchez, C., Cretaux, J. F., et al. (2020). The Lake Chad hydrology under current climate change. *Sci. Rep.* 10, 5498. doi: 10.1038/s41598-020-62417-w

Pickens, A. H., Hansen, M. C., Hancher, M., Stehman, S. V., Tyukavina, A., Potapov, P., et al. (2020). Mapping and sampling to characterize global inland water dynamics from 1999 to 2018 with full Landsat time-series. *Remote Sens. Environ.* 243, 111792. doi: 10.1016/j.rse.2020.111792

Qiao, B., Zhu, L., Wang, J., Ju, J., Ma, Q., Huang, L., et al. (2019). Estimation of lake water storage and changes based on bathymetric data and altimetry data and the association with climate change in the central Tibetan Plateau. *J. Hydrol.* 578, 124052. doi: 10.1016/j.jhydrol.2019.124052

Schwatke, C., Dettmering, D., Bosch, W., and Seitz, F. (2015). DAHITI - an innovative approach for estimating water level time series over inland waters using multi-mission satellite altimetry. *Hydrol. Earth Syst. Sci.* 19, 4345–4364. doi: 10.5194/hess-19-4345-2015

Schwatke, C., Dettmering, D., and Seitz, F. (2020). Volume variations of small inland water bodies from a combination of satellite altimetry and optical imagery. *Remote Sens.* 12, 1606. doi: 10.3390/rs12101606

Shen, M., Duan, H., Cao, Z., Xue, K., Qi, T., Ma, J., et al. (2020). Sentinel-3 OLCI observations of water clarity in large lakes in eastern China: Implications for SDG 6, 3.2 evaluation. *Remote Sens. Environ.* 247, 111950. doi: 10.1016/j.rse.2020.111950

Shu, S., Liu, H., Beck, R. A., Frappart, F., Korhonen, J., Xu, M., et al. (2020). Analysis of Sentinel-3 SAR altimetry waveform retracking algorithms for deriving temporally consistent water levels over ice-covered lakes. *Remote Sens. Environ.* 239. 111643. doi: 10.1016/j.rse.2020.111643

Song, C., Huang, B., and Ke, L. (2015a). Heterogeneous change patterns of water level for inland lakes in High Mountain Asia derived from multi-mission satellite altimetry. *Hydrol. Proc.* 29, 2769–2781. doi: 10.1002/hyp.10399

Song, C., Ye, Q., Sheng, Y., and Gong, T. (2015b). Combined ICESat and cryoSat-2 altimetry for accessing water level dynamics of Tibetan lakes over 2003-2014. *Water* 7, 4685–4700. doi: 10.3390/w7094685

Song, L., Song, C., Luo, S., Chen, T., Liu, K., Zhang, Y., et al. (2023). Integrating ICESat-2 altimetry and machine learning to estimate the seasonal water level and storage variations of national-scale lakes in China. *Remote Sens. Environ.* 294, 113657. doi: 10.1016/j.rse.2023.113657

Tan, C., Ma, M., and Kuang, H. (2017). Spatial-temporal characteristics and climatic responses of water level fluctuations of global major lakes from 2002 to 2010. *Remote Sens.* 9, 20150. doi: 10.3390/rs9020150

Xu, F., Zhang, G., Yi, S., and Chen, W. (2022). Seasonal trends and cycles of lake-level variations over the Tibetan Plateau using multi-sensor altimetry data. *J. Hydrol.* 604, 127251. doi: 10.1016/j.jhydrol.2021.127251

Xu, N., Ma, Y., Wei, Z., Huang, C., Li, G., Zheng, H., et al. (2022). Satellite observed recent rising water levels of global lakes and reservoirs. *Environ. Res. Lett.* 17, 074013. doi: 10.1088/1748-9326/ac78f8

Xu, Y., Gu, S., Yin, Z., Lin, J., Zhao, J., Zhu, X., et al. (2020). Obtaining accurate water level measurements in lakes: analysis of changes in ICESat altimetry accuracy with buffer changes. *IEEE Access* 8, 81090–81100. doi: 10.1109/ACCESS.2020.2991228

Yao, F., Wang, J., Wang, C., and Cretaux, J.- F. (2019). Constructing long-term high-frequency time series of global lake and reservoir areas using Landsat imagery. *Remote Sens. Environ.* 232, 111210. doi: 10.1016/j.rse.2019.111210

Zhang, G., Chen, W., and Xie, H. (2019). Tibetan plateau's lake level and volume changes from NASA's ICESat/ICESat-2 and landsat missions. *Geophys. Res. Lett.* 46, 13107–13118. doi: 10.1029/2019GL085032

frontiers | Frontiers in Water

TYPE Original Research
PUBLISHED 08 January 2024
DOI 10.3389/frwa.2023.1323139

OPEN ACCESS

EDITED BY
Hafzullah Aksoy,
Istanbul Technical University, Türkiye

REVIEWED BY
Aldo Fiori,
Roma Tre University, Italy
Mohammad Najafzadeh,
Graduate University of Advanced Technology, Iran

*CORRESPONDENCE
Vikram Kumar
✉ 25.vikram@gmail.com

RECEIVED 17 October 2023
ACCEPTED 08 December 2023
PUBLISHED 08 January 2024

CITATION
Kumar V and Sen S (2024) Rating curve development and uncertainty analysis in mountainous watersheds for informed hydrology and resource management. *Front. Water* 5:1323139. doi: 10.3389/frwa.2023.1323139

Rating curve development and uncertainty analysis in mountainous watersheds for informed hydrology and resource management

Vikram Kumar* and Sumit Sen

Department of Hydrology, Indian Institute of Technology, Roorkee, India

Accurate measurement of continuous stream discharge poses both excitement and challenges for hydrologists and water resource planners, particularly in mountainous watersheds. This study centers on the development of rating curves utilizing the power law at three headwaters of the lesser Himalayas—Aglar, Paligaad, and Balganga—through the installation of water level recorders for stage measurement and salt dilution for discharge measurement from 2014 to 2016. The stream stage–discharge relationship, crucially known as the rating curve, is susceptible to numerous factors in mountainous watersheds that are often challenging to comprehend or quantify. Despite significant errors introduced during the rating curve development, such as stemming from observations, modeling, and parameterization, they are frequently overlooked. In this study, acknowledging the inherent uncertainty, we employ the maximum-likelihood method to assess uncertainty in the developed rating curve. Our findings reveal substantial inconsistency in the stage–discharge relationship, particularly during high flows. A novel contribution of this study is introducing a weighing factor concept that correlates uncertainty with the morphological parameters of the watershed. The higher value of the weighting factor in Paligaad (0.37) as compared to Balganga (0.35) and less in the case of Aglar (0.27) will have more uncertainty. The authors contend that precise rating curves and comprehensive uncertainty analyses can mitigate construction costs, foster robust decision-making, and enhance the perceived credibility of decisions in hydrology and water resource management.

KEYWORDS

rating curve, Himalayas, uncertainty, weighing factor, water resource management

Introduction

Appropriate quantification of stream discharge is, arguably, essential for designing canals, dams, and other hydraulic structures and effectively managing water resources, which thus affects economic returns. Discharge is a crucial variable and challenging to continuously monitor along many major streams to manage flood and high flow (Kumar and Sen, 2023). Understanding discharge variation during low flow conditions is equally important to state the environmental flow requirement and cope with water quality or pollutant releases (Najafzadeh et al., 2023).

Alteration in stream discharge may result from adequate rainfall and aquifer recharge, which may also be affected by the intensity and duration of precipitation, seasonality, and timing of flow (Beavis et al., 2010; Kumar and Shanu, 2017; Kumar and Sen, 2018; Kumar and Paramanik, 2020). In mountains, quantification is rarely done due to sparse field-based measurements in rugged terrain, and instrumentation safety threatens public health, food production, regional water resources policy, and security (Kumar and Sen, 2023). Despite the importance of mountainous catchments in providing freshwater, little is known about understanding discharge variation and hydrological processes (Scanlon et al., 2006; Viviroli et al., 2007; Nanda et al., 2018). Since mountains are also called water towers for human beings and are equally crucial for the ecosystem, it becomes essential to monitor them at the regional and national levels (United Nations, 2011; Kumar and Sen, 2020; Najafzadeh et al., 2021). To develop a scientifically based plan or policy for any stream, it is essential to quantify the discharge dynamics at ungauged streams by setting up a rating curve (*RC*) and ascertaining the presence of uncertainty in the rating curve (*RC*). Quantification of discharge and development of rating curve (*RC*) are gradually growing because of their extensive use in predicting the impact of land use/land cover (LULC), flood forecasting, climate change studies, operation of the dam, and other hydraulic structures and finding out the discharge of adjacent or similar ungauged watersheds.

To create a rating curve (RC) for an ungauged stream, it is necessary to establish an empirical relationship between the discharge of the stream (Q) and the corresponding gauge height (H). Appropriate site selection for gauging and discharge measurement is an essential predictor for developing and maintaining rating curves (*RCs*). The straightforward exercise is to monitor multiple paired measurements of stream discharge and gauge height (*Q, H*) to develop a relationship and estimate the parameters. While establishing the rating curve (RC) parameters, the fundamental hypothesis of best fitting of the curve is that stream discharge and gauge height (*Q, H*) are mutually independent and have the same probability distribution. Most of the time, this hypothesis is invariably false while developing a rating curve (*RC*). Access to gauging location can often impact the frequency, timing, and accuracy of (*Q, H*) measurements (Najafzadeh and Anvari, 2023). In addition to the location of gauging, sometimes during the monsoon season (July–September), there is intense rainfall or long rainfall spells which restrict access to field sites and discharge of measurements. Currently, a rating curve (*RC*) is being developed based on stream profile without measuring stream discharge and gauge height (*Q, H*) (Szilagyi et al., 2005; Perumal et al., 2007, 2010; Christopher et al., 2010), using additional parameters other than the stage (H) (Sahoo and Ray, 2006), based on the capabilities of remote sensing (Birkhead and James, 1998) and uncertainty present in rating curves (Clarke, 1999; Jalbert et al., 2011). According to United States Geological Survey (USGS) guidelines, the difference between measured and predicted discharges should be <10% to accept the estimated discharge at the site. When an error in modeled discharge is <30% of the observed discharge, the generic rating curve (*GRC*) could be used (Kevin, 2012). The main objective for developing the *GRC* is to generate a rating curve (*RC*) with some minor adjustments in the parameters to reduce the stream discharge and gauge height (*Q, H*) measurement.

Understanding the dynamic stream system in mountains poses numerous challenges and causes many problems while measuring the stream discharge and gauge height (*Q, H*). Thus, it becomes very challenging to measure the stage and stochastic nature of discharge preciously. Therefore, stream discharge (*Q*) not only depends on the stage (*H*) but also depends on the profile (geometry and slope) and roughness of the stream with morphometry of the watershed. The relationship between stream discharge and gauge height (Q, H) for a stream cross section is not always the same because stream discharge is often influenced by many parameters that are not easy to measure (Sefe, 1996). Hence, power law $Q = a(h + ho)^c$ to develop a rating curve for a particular cross section is not exact but an approximation (Henderson, 1966). The rating curve (*RC*) changes shape from a parabolic to a different form, influencing the parameters over the specific limit (Guven and Aytek, 2009), which are difficult to find and sometimes impossible to obtain the correct values. Imprecise or inaccurate estimation of rating curve (*RC*) parameters leads to overestimation or underestimation of a design flood with higher failure risks and costs. If the presence of error or uncertainty in the rating curve (*RC*) is quantified well, it could enhance the discharge assessment and ensure positive decision-making. Quantifying the uncertainty in the rating curve (*RC*) as a standard protocol can indirectly protect money and increase decision-making credibility. Representative confidence bound for uncertainty measurement relies on gauge location and stream profile (Westerberg et al., 2011).

Broadly, uncertainty in the rating curve (*RC*) can be classified as follows:

i) *Observational uncertainty* is associated with the primary observation used (e.g., stage and discharge) for developing rating curves, which usually involves errors due to both as well as instrumental errors.

ii) *Model uncertainty* is linked with the formulation of power law for rating curve development with approximations involved in mathematical equations.

iii) *Parameter uncertainty* is caused by failure to decide input parameters involved in model development due to insufficient data.

To analyze the above-described uncertainty in stream discharge measurement, Domeneghetti et al. (2012) proposed an outline and showed uncertainty effects on the calibration of the model. Pappenberger et al. (2006) developed a decision tree model to represent different uncertainty causes. According to Montanari (2007), other uncertainty methods can be categorized into (a) analytical methods (Tung, 1996), (b) approximation methods (Melching, 1992), (c) methods based on the analysis of model errors (Montanari and Brath, 2004), (d) Monte Carlo methods (Kuczera and Parent, 1998), (e) Bayesian methods (Beven and Binley, 1992), and (f) methods based on fuzzy set concept (Maskey et al., 2004).

The stage measurement, recorded using a water level recorder placed in a stilling well, usually causes fewer errors than stream discharge, which involves calculating clearance by measuring the velocity of the whole stream cross section (Pelletier, 1988; Clarke, 1999). Inadequate temporal measurement of stream stage (*H*) for an average daily discharge poses additional doubt and error (Petersen-Overleir et al., 2009). During peak stream discharge,

it is hard to monitor flashy and uncontrolled turbulent flows, which are often challenging to accurately measure and are also the source of uncertainty (Leonard et al., 2000; Shrestha et al., 2007). Among the traditional methods for discharge measurement, evaluating stream discharge by the salt dilution method proves better, especially in mountainous or remote areas where it is not easy to find a suitable hydrologic profile (Radulovic et al., 2008). Additionally, the stream discharge (*Q*) measurements using salt dilution can be accurate at ∼±5 % (Day, 1976). The objective of this study was threefold: (1) to develop a rating curve for three different headwater streams (Aglar, Paligaad, and Balganga) in the lesser Himalayas. The developed stage–discharge relationship can later be used for computing stream discharge by monitoring the stage alone (2) to estimate the uncertainty involved in the developed stage–discharge relationship. Uncertainty measurement was applied using the evaluation of codes that state the uncertainty of each gauging at 95% confidence intervals and (3) to develop a concept of weighing factor to correlate the uncertainty with the morphometry of watershed, which governs the flow behavior with the sensitive parameter. The detailed rating curve and uncertainty analysis of mountains, especially in the Himalayas, which are considered water towers, play a crucial role in better quantifying water availability for agriculture, optimal planning, and managing water resources. The authors believe that the above analysis delivers a suitable method for hydrology and water resource practitioners to evaluate the rating curve and stream discharge uncertainty.

Methodology and data

The three headwaters in the lesser Himalayas, viz., Aglar, Paligaad, and Balganga, have been instrumented since April 2014 to collect continuous rainfall and stage measurements. Stream discharge is also measured from time to time to develop a rating curve (*RC*). Basic statistical characteristics, such as minimum and maximum, for these three sites are represented in Table 1. A detailed description of the study methodology is described subsequently below.

Measurement of stage and discharge

Stage measurements of the streams have been monitored with an automatic water level sensor (AWLS) placed in a stilling well made up of perforated pipes (Figure 1). The AWLS is a capacitance-based water level recorder with a data logger (Odyssey, Ltd). It has been recording the water depth in a stream from the stream bed at a 15-min interval since April 2014 at Aglar and Paligaad and since June 2014 at Balganga.

The recorded stream depth from the sensors was downloaded every once or twice a month to avoid data loss. Recorded data are verified with visual measurements on the data's downloading. With the increase in stream discharge, the surplus water in the stream leads the stream to expand laterally and the stream's depth to increase. Discharge in all the streams is being measured by salt dilution, which is a well-known method for mountainous catchment and where current metering may be inaccurate. In this method, a known amount of sodium chloride solution (NaCl) is injected into the stream, concurrently measuring the electrical conductivity (EC) at regular intervals downstream. Using the concept of mass conservation, the discharge Q (m^3/S) from the stream is estimated using Equation (1):

$$Q = \frac{M_s}{\int_0^T (C_t - C_o)dt} \quad (1)$$

where M_s is the weight of sodium chloride injected in kg, T is the time of passage of the salt slug in seconds, and C_o and C_t are the concentration of sodium chloride at time zero and time t in kg/m^3, respectively. NaCl was chosen as a tracer because of its low cost, non-toxic nature, and ready availability at the site, and because it can be precisely measured by an EC meter. In the mountainous region, discharge measurement using slug injection can be precise within ∼± 5%. The use of salt dilution technique for discharge measurement is restricted up to 15 m^3/s due to environmental considerations (Church, 1973).

Rating curve development

To address the issues of cost, time constraints, and the impracticality of continuous stream discharge monitoring during high flows, an alternative approach involving continuously observing the stage, which is relatively easier to monitor, has been suggested. Subsequently, the stage data can be converted to stream discharge using the stage–discharge power equation, commonly referred to as the rating curve. The observed value of the stream stages and corresponding discharges were plotted on arithmetic and logarithmic graphs. The plotted graph represents the combined consequence of a wide range of depth and discharge parameters. If the stage–discharge relationship for a gauging section does not change with time, the control is said to be "permanent." If it changes with respect to time, it is called "shifting control." The ideal control channel situation is when the energy gradient line is parallel to the water surface gradient and to the bed gradient line. Hydraulics formulas for the control section and channel can be represented as a power law (ISO 1100, 2010; World Meteorological Organization, 2010), and the power law parameters are assumed to be constant (Subramanya, 2006),

$$Q = a(h + h_o)^c \quad (2)$$

where Q is the discharge of the stream, h is the water depth in the stream, usually says stage, "a" is a power law coefficient that relates to the features of the controlling section or channel, h_o is an offset, and "*c*" is an exponent related to the type of hydraulic control (Le Coz et al., 2014).

The best-fit curve, which governs the value of a, h_o, and *c* in Equation (2) for a given depth range, can be obtained using the least square error method. For this, considering the logarithmic scale, Equation (2) becomes

$$ln\, Q = ln\, a + c \times ln\,(h + h_o) \quad (3)$$

TABLE 1 Statistical characteristics of daily discharge for the study area.

Station	Area (km^2)	Minimum (m^3/s)	Maximum (m^3/s)	Average (m^3/s)	Standard deviation (m^3/s)
Aglar	99.65	0.220	2.460	0.580	0.281
Paligaad	59.78	0.120	9.030	0.980	1.331
Balganga	13.12	0.004	0.520	0.079	0.058

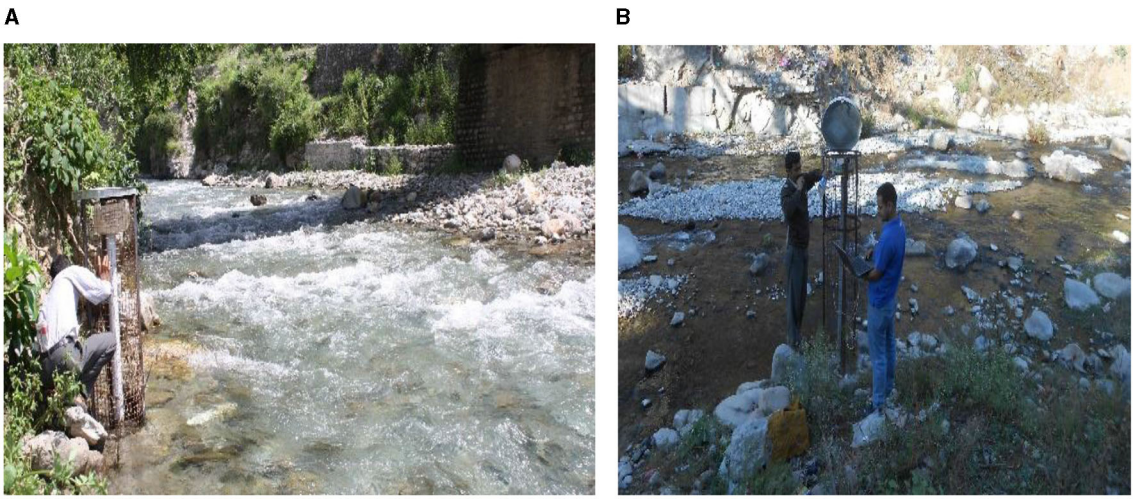

FIGURE 1
(A) Medium flow condition and AWLS in a PVC pipe. **(B)** Data downloading from the Odyssey data logger.

A linear trend line equation between "log Q" (Y-axis) and "log (h – h_o)" (X-axis) was well fitted in MATLAB, the slope of this line gives "b," and Y-intercept gives "log a" (and thereby "a"). Thus, the stage–discharge relationship is developed in Equation (3). This developed relationship for all three gauging locations is considered an epitome of all the channel characteristics. Occasionally, the stage–discharge curve is in a parabolic shape, which changes to a composite curve and vice versa, and the parameters vary through the limit (Guven and Aytek, 2009). Thus, it is not simple to estimate the rating curve parameters (a, h_o, and *c*) for all cases, and it is occasionally challenging to obtain the actual values. Generally, at least 15 sets of stage-discharge are needed to develop a rating curve, including low to high flows.

Assessment of uncertainty in rating curves

Estimating uncertainty in the rating curve (RC) initiated from false measurement or the method described in the earlier section built from less stage–discharge pair measurements is significant to understand. On considering that an error (ε) in power law, Equation (2) can be written as

$$Q = a(h + h_o)^c(1 + \varepsilon) \tag{4}$$

The basic assumption in Equation (4) is that ε is generally distributed with zero mean value and constant variance (σ^2). No correlated errors are assumed ($\mathrm{cov}[\varepsilon_i, \varepsilon_j] = 0$) for different samples of stage discharge. On log transformation, Equation (4) becomes Equation (5)

$$lnQ = ln(a) + c \times ln(h + h_o) + \varepsilon \tag{5}$$

On minimizing the ε term (Equation 6), which is our objective,

$$S^2 = \sum \varepsilon^2 = \sum [ln(Q_i) - (\ln(a) + c * ln(h + ho)]^2 \tag{6}$$

The following equations can be used for assessing power model rating curve relationship uncertainty in estimated discharges for a specific level (H = b), calculating variance (Equations 7–10)

$$var\ (\ln(Q_i)\,|H{=}b) = D_i{}^T * var\ (\theta *) * D_i \tag{7}$$

$$D_i = \left[1,\ ln\left(b + H_o\right),\ \frac{c}{\left(b + H_o\right)}\right] \tag{8}$$

$$var\,(Q) = Q^2 var\left[\ln(Q)\right] \tag{9}$$

$$var\left(\theta^*\right) = I^{-1} \tag{10}$$

To get the value of $var\,(\theta^*)$, first, the (I) has to be solved, which is the Fischer information matrix, translated by Venetis (1970), using Equations (11) and (12)

$$I = -\begin{bmatrix} \frac{\partial^2 l}{\partial \ln(a)^2} & \frac{\partial^2 l}{\partial ln(a)\partial c} & \frac{\partial^2 l}{\partial ln(a)\partial H_0} & 0 \\ \frac{\partial^2 l}{\partial ln(a)\partial c} & \frac{\partial^2 l}{\partial a^2} & \frac{\partial^2 l}{\partial a \partial H_0} & 0 \\ \frac{\partial^2 l}{\partial ln(a)\partial H_0} & \frac{\partial^2 l}{\partial ln(a)\partial H_0} & \frac{\partial^2 l}{\partial H_0^2} & 0 \\ 0 & 0 & 0 & \frac{\partial^2 l}{\partial \sigma^2} \end{bmatrix} \tag{11}$$

$$l = -\frac{n}{2}\ln\left(2\pi\sigma^2\right) - \frac{1}{2\sigma^2}\sum\left(\ln\left(Q_i\right) - \left(\ln\left(a\right) + c * ln\left(H_i + H_o\right)\right)\right)^2 \tag{12}$$

Then, the value of variance, Equation (13) is estimated using the standard error of regression (se) relation

$$\sigma \approx se = \sqrt{\frac{S^2}{n-k}} \tag{13}$$

The process of analyzing uncertainty in the rating curve holds considerable importance in investigations involving risks and the overall consistency of water and hydrology-related projects. By taking uncertainty into consideration, it provides valuable support to hydraulic design modelers. These professionals can then use this information to plan and design operational models, helping them anticipate and forecast potential deficiencies in the future. In essence, considering uncertainty enhances the reliability and effectiveness of hydraulic design and risk management in water-related projects.

Result and discussion

Rating curve development

The link between stream water level (stage) and stream discharge (Q, H) is influenced by the character of the stream channel and its bank. With the increase in stream discharge, the excess water causes the stream to expand, leading to the rise in stream depth and the widening of stream banks. Multiple data points of stage and discharge (Q, H) were highly correlated after the quality control was used to obtain a rating curve (RC). The river stage and corresponding discharge value of all these gauging stations were measured from September 2014 to December 2015. A non-linear curve fitting algorithm in MATLAB using the function "nlinfit" and the power equation shown in Equation (3) has been used to develop the rating curve (RC).

The developed stage–discharge relationship with the coefficient of determination is shown in Figure 2, and the rating curve power law coefficients are shown in Table 2. In our understanding, developed (Q, H) can be considered the best approximation of stage and discharge data series for the best fit of the curve. The shape of the (Q, H) curve is inhibited by analyzing constraints based on field collected data. Extrapolation of the curve other than the calibrated range should be realistic and sustained by accompanying evidence.

From the monitored (Q, H) data for three streams, the non-linear relationships between stage and discharge were similar for Aglar and Paligaad, which have relatively lower relief ratio (0.002 and 0.004) as compared to Balganga, which has relief ratio (0.007), and the rating curve (RC) parameters are different for the three gauging stations. For unconfined bedrock streams (Aglar and Paligaad), the coefficients of determination (R^2) are 0.92 and 0.86, whereas the Balganga is confined between the control section with $R^2 = 0.90$. Understanding the channel geometry that governs the (Q, H) relationship is fundamental in developing stage–discharge relationships. The rating curve for the Balganga, where the flow is low compared to Aglar and Paligaad, is usually influenced by section control. High flow in the Paligaad is influenced by channel control, whereas the combination of section and channel control influences Aglar. As the depth of water increases in Paligaad, the control section gets submerged because of these higher flows and no longer controls the relationship between the stage and discharge (Q, H). The flow in streams is then controlled either by an additional downstream control section or by the channel profile and Manning's roughness (i.e., channel control). In addition, the channel's control dimension will differ, subject to the stream discharge. Usually, the coefficients of power law "a" and "c" are explicit to some stream channel characteristics, which can be correlated with the physical features of the river. "a" is a scaling factor that embraces the river width and the Manning coefficient. As it can be inferred from Table 2, the value of "a" is higher for Paligaad (15.93), followed by Aglar (3.35) and Balganga (0.0014). "c" embraces the stream geometry and displays the type of control in the relationship between the stage and discharge (Q, H). A higher value of "c" (1.63) in the case of Balganga indicates a section control, and a lower value of "c" (1.2) in the case of Aglar indicates channel control.

Furthermore, the point of zero flow (H_0) is challenging to determine in deep rivers and mountainous watersheds where rocky profiles exist. The observed discharge was not fixed for all gauging sites for a specific stage and showed differing discharge trends. There is variability in the rating parameters at different stages and stations. The presence of seasonal components at all gauging sites has been observed; it is primarily noticeable at the Aglar and Paligaad gauging sites. The discharge from the stream for a particular water height may change by more than one factor. To validate the computed stream discharge by the salt dilution method at Aglar, Balganga, and Paligaad, the cross-sectional details at these gauging stations were plotted, and the stream velocities were precisely measured by a current meter to obtain the discharge values (Figure 3). Riverbed configurations of all these rivers have different flow resistances; therefore, all these have other (Q, H) associations. The resistance to flow commonly increases with an increase in discharge, with noticeable discontinuities in the course of transitions between channel profiles.

This well-developed relationship between the stage and discharge (Q, H) and its effectiveness with respect to changes in the river behavior must be an issue for future investigation. With limited observation, it is challenging to identify a particular cause for the variability in future. The interchange of scour and fill sequences in the riverbed, with deposition throughout the

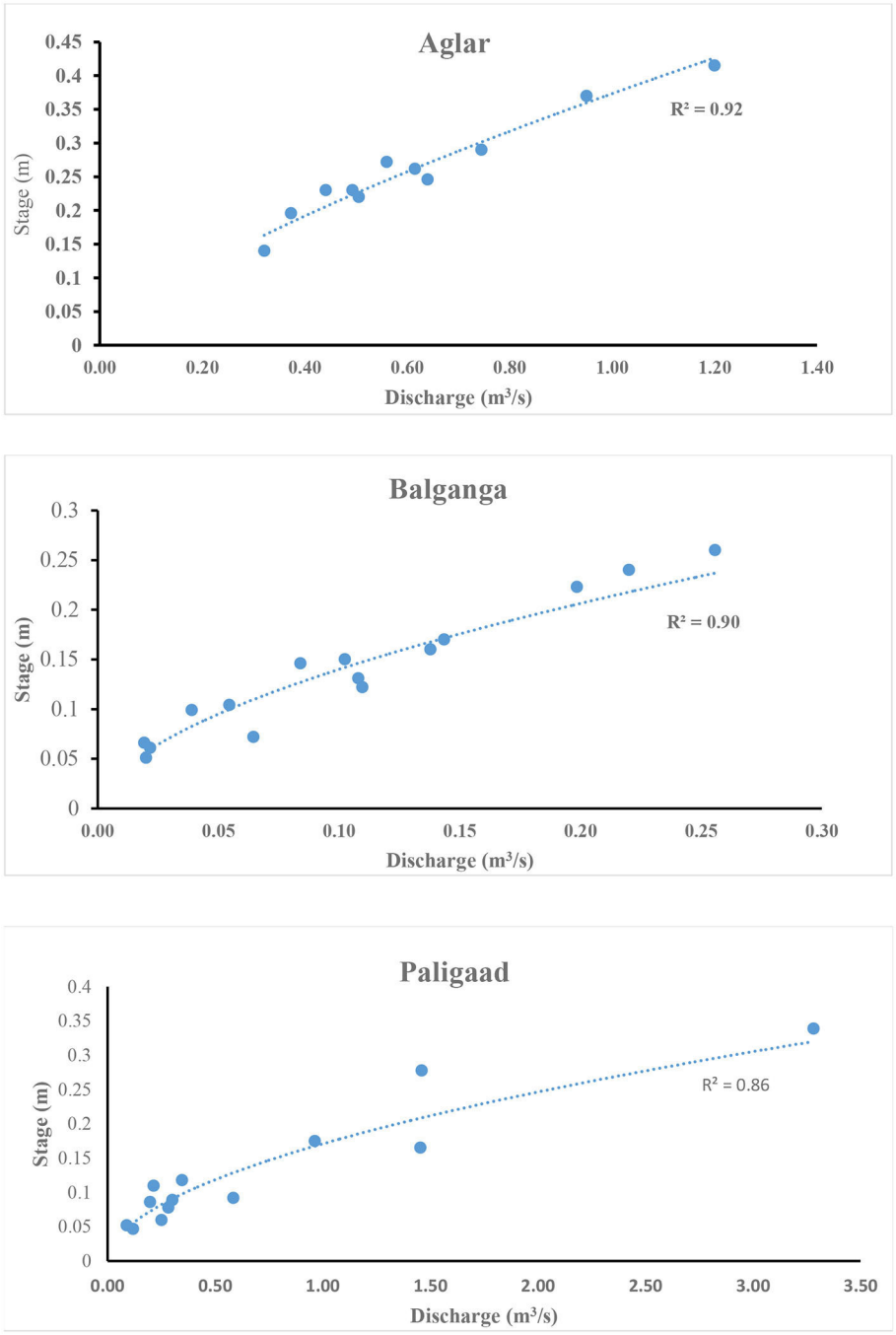

FIGURE 2
Stage–discharge relationship for different ungauged streams of the Aglar watershed.

non-rainy season and rate of erosion and subsequent deposition during the rainy season, has the ability to alter the river channel's conveyance and, consequently, its hydraulic properties. On the other hand, vegetation changes could also play an essential role by yielding a modified friction slope as it might mature on the side of the river throughout the non-rainy season. In the case of steep-slope mountainous rivers, the effect of backwater can be much less, and one can ignore this. In this study, an attempt has not been made to elucidate the different processes or grouping techniques that contribute to the inconsistency in the stage and discharge relationship (Q, H). Instead, a relationship has been developed that was not available. Continuous monitoring of the gauging stations will reveal the variability in (Q, H) in the future.

TABLE 2 Rating curve coefficients of the Aglar sub-watersheds.

Coefficients	Aglar	Paligaad	Balganga
c	1.270	1.635	1.6136
a	3.3523	15.937	2.33

Uncertainty analysis

The stream discharge evaluations from the developed rating curve (RC) in the present study were subjected to some uncertainties because of any of the sources of errors mentioned in the introduction. The inconsistency in these rating curves (RC) was more pronounced than what present estimation methods permit for. It is generally advised to adjust the parameters of the rating curve (RC) if the resulting developed rating curve (RC) shows a change of more than 5% compared to the observed discharge.

For systematically designed section controls, the actual gauge height of zero flow (Q = 0) will be nearly the same as the exact gauge height of zero discharge (Q = 0). Even though caution has been taken for data recording as described in the methodology, recorded data contain sets with few outliers. A depth of stream that deviates by more than 2 cm is considered an outlier and hence not used in this analysis. The daily fluctuations in the recorded stage variation exhibited that the maximum depth in stream flow commonly occurred between midnight and morning (10:00 AM) in the wet period. In contrast, the pattern is different in the dry period, with less depth between late night and morning (10:00 AM) compared to the wet period. This diurnal discrepancy in stage (depth) recording highlighted the prerequisite for considering the uncertainty in discharge measurement at different times with only a few stage measures during the day.

In the absence of any past uncertainty data of discharge in the mountainous watershed or any evidence about the sources of uncertainty in the rating curve (RC) in the Aglar watershed, the uncertainty in discharge measurement was estimated to be 11.9% in Aglar, 28% in Balganga, and 43% in Paligaad (Figure 4). Paligaad stream is flashy compared to Balganga and Aglar, so the promising discharge measurement consists of only a few measurements, and the error is as much as 43%. Our outcome from the uncertainty analysis is that uncertainty in the stage–discharge relationship will be greater where fewer data (pairs of Q and H) are observed for rating curve generation during the high flows. Additionally, in the case of the Paligaad, the 95% uncertainty prediction interval (bound) is much more comprehensive for larger stage measurement values than Aglar and Balganga (Figure 4) due to less observation during high and flashy stream flow.

The magnitude of the errors in the rating curve is measured by a pair of (Q, H) that is bound between the uncertainties. For the determination of the confidence intervals band of uncertainty, it is presumed that the residuals around the developed relationship have a normal distribution with fixed variance value; Figure 4 represents the overall uncertainty in different confidence intervals. The error arising from a lack of sufficient stage–discharge measurements, resulting in the inability to accurately differentiate between high and low discharge levels, can have significant implications. This study sheds light on the effectiveness of measures in various streams, each characterized by its unique parameters, in discerning how high or low flow measurements can impact our comprehension of water availability. Such limitations in measurement precision could potentially lead to misconceptions about critical hydrological processes that are crucial for converting

The geomorphology of the watershed has a significant role in the transformation of rainfall to stream discharge and associated processes. For example, the reaction from a poor drainage network with good vegetation cover will be slower than that of a well-developed drainage network with less vegetation cover. From the geomorphology point of view, the average width/depth ratio for all the monitoring stations is <12; therefore, according to cross-sectional and plan view, these streams are either of A, E, and G categories as per Rosgen (1996) Classification. "A" types of river are initiated within the valley. Due to intrinsic channel gradient, this type of river has a great sediment transport potential and relatively less sediment storage capability. Although "A" type

FIGURE 3
Cross-sectional plotting and discharge measurement using the current meter.

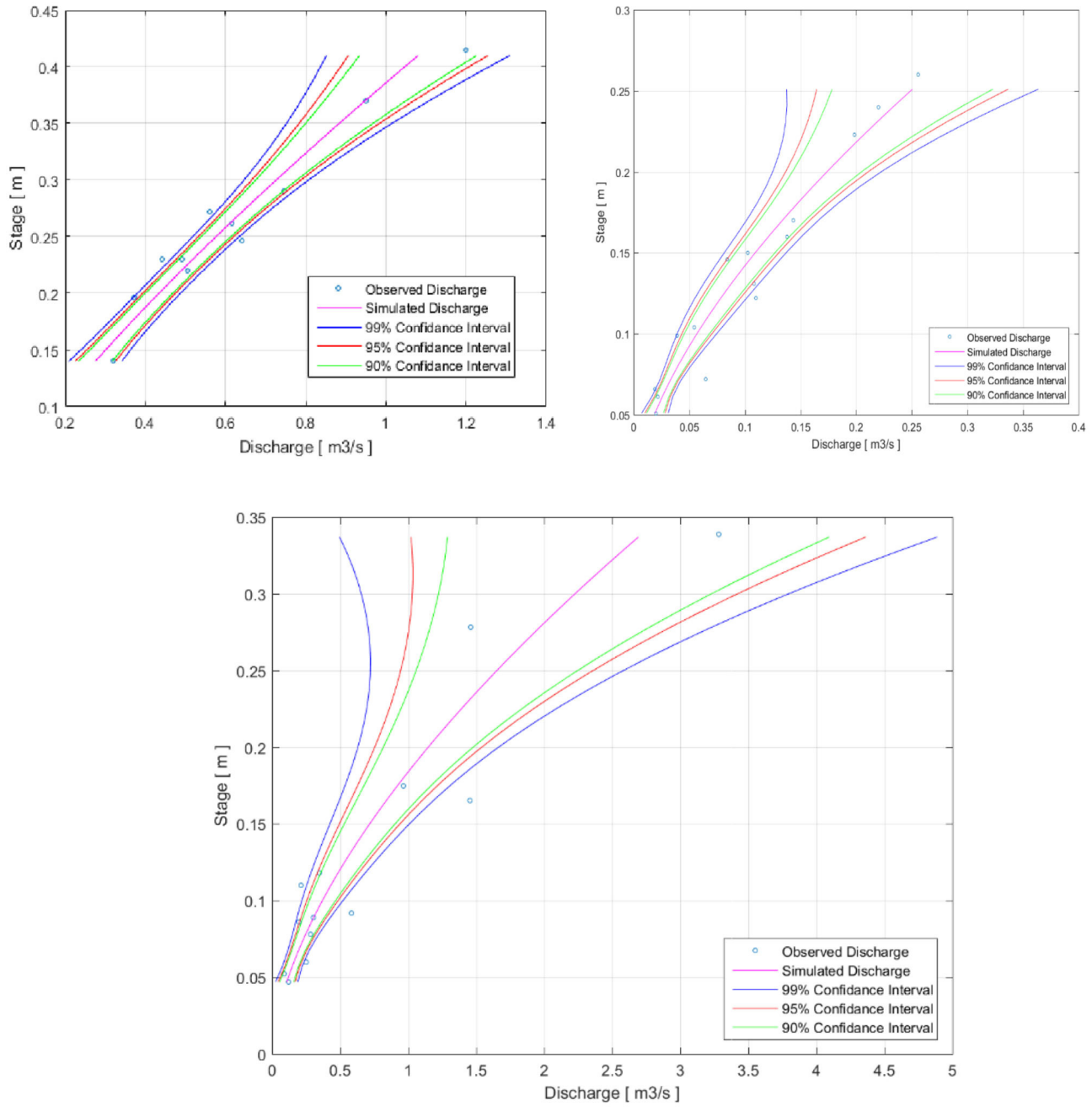

FIGURE 4
Uncertainty in different confidence intervals for Aglar sub-watersheds.

streams follow low-order streams, which can range from first order to fifth order or larger, located at the upper catchment, the "E" stream type characterizes the developmental "end-point" of stream channel stability for specific alluvial streams undergoing a natural dynamic order of system evolution. This stream type exhibits very low channel width/depth ratios and very high channel sinuosity, resulting in a significant meander width ratio. The other type "G" is entrenched with a low-to-moderate channel sinuosity. Channel gradients are generally steeper than 0.02, with very high bank erosion rates and sediment delivery ratios. In conclusion, Aglar shows low sensitivity to disturbance, excellent recovery potential, low sediment delivery, less erosion possibility, and reasonable influence of vegetation. In contrast, Paligaad is highly sensitive to disruption and has good recovery potential, moderate stream bank potential, and very high leverage of vegetation.

A weighting factor is developed in the present study to understand the influence of catchment geomorphology on uncertainty. The geomorphological parameters considered are area of watershed (A), drainage density (D), relief ratio (R), form factor (F), and elongation ratio (E), and its corresponding values for each watershed are summarized in Table 3. The weighting factors for the calculation are given in Equations (14) and (15)

TABLE 3 Morphological parameters of the Aglar sub-watershed.

Morphological parameters	Aglar	Paligaad	Balganga
Drainage density (D)	0.27	0.32	0.31
Relief ratio (R)	0.02	0.04	0.07
Elongation ratio (E)	0.18	0.21	0.19
Form factor (F)	1.59	1.43	0.61
Area (km^2) (A)	99.65	59.78	13.12
Weighing factor value (W_i)	**0.27**	**0.37**	**0.35**

Bold is done to highlight the calculated values which was the point of interest.

$$W_i = \frac{k_i}{\sum_i^I k_i} \tag{14}$$

$$k_i = \frac{A_i \times D_i \times R_i}{F_i \times E_i} \tag{15}$$

where I is the number of sub-catchments (3 in the present case).

The higher the value of W_i, the more the uncertainty will be; thus, there is a chance of more error in Paligaad (0.37) as compared to Balganga (0.35) and less in the case of Aglar (0.27). The confirmation presented by developing the weighing factor in this study supports the degree of uncertainty in the estimation of stage–discharge data. It could be further reduced by investments in hydrometric field instrumentations, particularly by generating more and more data and developing new methods based on data, technologies, and techniques for high flow measurements and winter stream flow monitoring. The above findings also meant that the monitored number of stage–discharge measures for rating curve generation should be more than 25 to compensate for the large uncertainty requirements.

This study mainly aimed at estimating uncertainty propagated into instant discharge values obtained from rating curves built from low-density discharge measurements. Further research envisages revising the rating curve with discharge measurement during high flows and reducing the uncertainty propagation in daily and monthly discharge values. The improved rating curve with less error will result in better hydrological modeling and calculations, such as water scarcity indexes or flood designs used for hydraulic structure dimensioning.

Conclusion

Assessing the relationship between stage and discharge data and errors in the developed relationship should be considered a significant step in quantifying water resources in any watershed. As the vital parameter, i.e., discharge in the Aglar watershed or lesser Himalayan rivers, is derived from the stage–discharge relationships only (rating curves), this hydrometric data collection (stage and discharge) is one of the most reliable, consistent, and attractive for unraveling and understanding the hydrological process and quantifying water availability.

Thus, the present study focuses on rating curve development using power law at three headwaters of lesser Himalayas (Aglar, Paligaad, and Balganga) by means of installing a water level recorder for stage measurement and salt dilution for discharge measurement between 2014 and 2016.

- In the presence of uncertainty as inherent, an attempt has also been made to ascertain uncertainty in developed rating curves using the maximum-likelihood method.
- Analysis of the monitored (Q, H) data for three streams, the non-linear relationships between stage and discharge were similar for Aglar and Paligaad, which have relatively lower relief ratios (0.002 and 0.004) as compared to Balganga, which has a relief ratio (0.007), and the rating curve (RC) parameters are different for the three gauging stations.
- For unconfined bedrock streams (Aglar and Paligaad), the coefficients of determination (R^2) are 0.92 and 0.86, whereas the Balganga is confined between the control section with $R^2 =$ 0.90. A comparatively higher value of the power law coefficient "c" (1.63) in the case of Balganga indicates a section control, and a lower value of "c" (1.2) in the case of Aglar indicates channel control.
- The diurnal fluctuations in the recorded stage variation exhibited uncertainty in the rating curve, which highlights the uncertainty analysis in the rating curve. Furthermore, a weighting factor is developed to understand the influence of catchment geomorphology on uncertainty. The higher value of the weighting factor will be the uncertainty; thus, there are chances of more error in Paligaad (0.37) as compared to Balganga (0.35) and less in the case of Aglar (0.27).
- The extent of uncertainty due to high flow remains indeterminate because no field data were collected due to the flashy nature of the flow.

The above rating curve development and uncertainty analysis are expected to inspire the design of forthcoming research required to overcome this scarcity of data at high flows. This preliminary study would become the benchmark for further research and help policy creators and watershed administrators to improve planning and management related to water in rural parts of the lesser Himalayas or other mountainous catchments.

Data availability statement

The raw data supporting the conclusions of this article will be made available by the authors, without undue reservation.

Ethics statement

Written informed consent was obtained from the individual(s) for the publication of any identifiable images or data included in this article.

Author contributions

VK: Writing—original draft. SS: Conceptualization, Project administration, Supervision, Validation, Writing—review & editing.

Funding

The author(s) declare financial support was received for the research, authorship, and/or publication of this article. The authors would like to acknowledge the Indian Institute of Technology, Roorkee, for funding under grant # F.I.G-100582 and the Department of Science and Technology under grant # SER-776 toward field visits and instrumentation.

Acknowledgments

The authors thank Mr. Sumer Panwar, Aliva Nanda, and Vijay Jirwan for their field support.

Conflict of interest

The authors declare that the research was conducted in the absence of any commercial or financial relationships that could be construed as a potential conflict of interest.

Publisher's note

All claims expressed in this article are solely those of the authors and do not necessarily represent those of their affiliated organizations, or those of the publisher, the editors and the reviewers. Any product that may be evaluated in this article, or claim that may be made by its manufacturer, is not guaranteed or endorsed by the publisher.

References

Beavis, S. G., Roberts, J., and Ellis, D. J. (2010). Water-dependent ecosystems: the ecological consequences of irrigation infrastructure refurbishment. Waterlines Report Series No 33.

Beven, K., and Binley, A. (1992). The future of distributed models: model calibration and uncertainty prediction. *Hydrol. Proces.* 6, 279–298. doi: 10.1002/hyp.3360060305

Birkhead, A. L., and James, C. S. (1998). Synthesis of rating curves from local stage and remote discharge monitoring using non-linear muskingum routing. *J. Hydrol.* 205, 52–65. doi: 10.1016/S0022-1694(97)00131-5

Christopher, F. S., Jeffrey, T. C., and Stephen, M. W. (2010). *The Continuous Slope-Area Method for Computing Event Hydrographs, Scientific Investigations Report*, U. S. Geological Survey. Available online at: https://pubs.usgs.gov/sir/2010/5241/sir2010-5241

Church, M. (1973). Some tracer techniques for streamflow measurements. *Tech. Bull. Br. Geornorphol.* Res. *Group*. 12, 72.

Clarke, R. T. (1999). Uncertainty in the estimation of mean annual flood due to rating-curve in definition. *J. Hydrol.* 222, 185–190. doi: 10.1016/S0022-1694(99)00097-9

Day, T. J. (1976). On the precision of salt dilution gauging. *J. Hydrol.* 31, 293–306. doi: 10.1016/0022-1694(76)90130-X

Domeneghetti, A., Castellarin, A., and Brath, A. (2012). Assessing rating-curve uncertainty and its effects on hydraulic model calibration. *Hydrol. Earth Syst. Sci.* 16, 1191–1202. doi: 10.5194/hess-16-1191-2012

Guven, A., and Aytek, A. (2009). New approach for stage-discharge relationship: gene-expression programming. *J. Hydrol. Eng.* 14, 812–820. doi: 10.1061/(ASCE)HE.1943-5584.0000044

Henderson, F. M. (1966). *Open Channel Flow*. New York, NY: The Macmillan Company.

ISO 1100 (2010). *Hydrometry - Measurement of Liquid Flow in Open Channels Part 2: Determination of the Stage-Discharge Relationship*. Geneva: ISO, 20.

Jalbert, J., Mathevet, T., and Favre, A. C. (2011). Temporal uncertainty estimation of discharges from rating curves using a variographic analysis. *J. Hydrol.* 397, 83. doi: 10.1016/j.jhydrol.2010.11.031

Kevin, S. (2012). "Developing rating curves for bedrock step-pool rivers using sparse data," in *Proceedings of The National Conference On Undergraduate Research (NCUR) 2012*. Ogden Utah: Weber State University.

Kuczera, G., and Parent, E. (1998). Monte Carlo assessment of parameter uncertainty in conceptual catchment models: the Metropolis algorithm. *J. Hydrol.* 211, 69–68. doi: 10.1016/S0022-1694(98)00198-X

Kumar, V., and Paramanik, S. (2020). Application of high-frequency spring discharge data: a case study of Mathamali spring rejuvenation in the Garhwal Himalaya. *Water Supply* 20, 3380–3392. doi: 10.2166/ws.2020.223

Kumar, V., and Sen, S. (2018). Evaluation of spring discharge dynamics using recession curve analysis: a case study in data-scarce region, Lesser Himalayas, India. *Sust. Water Resour. Manage.* 4, 539–557. doi: 10.1007/s40899-017-0138-z

Kumar, V., and Sen, S. (2020). Assessment of spring potential for sustainable agriculture: a case study in lesser Himalayas. *Appl. Eng. Agric.* 36, 11–24. doi: 10.13031/aea.13520

Kumar, V., and Sen, S. (2023). Hydrometeorological field instrumentation in Lesser Himalaya to advance research for future water and food security. *Environ. Monitor. Assess.* 195, 1162. doi: 10.1007/s10661-023-11625-8

Kumar, V., Shanu, and Jahangeer. (2017). Statistical distribution of rainfall in Uttarakhand, India. *Appl. Water Sci.* 7, 4765–4776. doi: 10.1007/s13201-017-0586-5

Le Coz, J., Renard, B., Bonnifait, L., Branger, F., and Boursicaud, R. (2014). Combining hydraulic knowledge and uncertain gaugings in the estimation of hydrometric rating curves: a Bayesian approach. *J. Hydrol.* 509, 573–587. doi: 10.1016/j.jhydrol.2013.11.016

Leonard, J., Mietton, M., Najib, H., and Gourbesville, P. (2000). Rating curve modelling with Manning's equation to manage instability and improve extrapolation. *Hydrol. Sci. J.* 45, 739–750. doi: 10.1080/02626660009492374

Maskey, S., Guinot, V., and Price, R. K. (2004). Treatment of precipitation uncertainty in rainfall runoff modelling: a fuzzy set approach. *Adv. Water Resour.* 27, 889–898. doi: 10.1016/j.advwatres.2004.07.001

Melching, C. S. (1992). An improved first-order reliability approach for assessing uncertainties in hydrological modelling. *J. Hydrol.* 132, 157–177. doi: 10.1016/0022-1694(92)90177-W

Montanari, A. (2007). What do we mean by 'uncertainty'? The need for a consistent wording about uncertainty assessment in hydrology. *Hydrol. Process.* 21, 841–845. doi: 10.1002/hyp.6623

Montanari, A., and Brath, A. (2004). A stochastic approach for assessing the uncertainty of rainfall-runoff simulations. *Water Resour. Res.* 40, W01106. doi: 10.1029/2003WR002540

Najafzadeh, M., Ahmadi-Rad, E. S., and Gebler, D. (2023). Ecological states of watercourses regarding water quality parameters and hydromorphological parameters: deriving empirical equations by machine learning models. *Stochastic Environ. Res. Risk Assess.* 8, 1–24. doi: 10.1007/s00477-023-02593-z

Najafzadeh, M., and Anvari, S. (2023). Long-lead streamflow forecasting using computational intelligence methods while considering uncertainty issue. *Environ. Sci. Pollut. Res.* 30, 84474–84490. doi: 10.1007/s11356-023-28236-y

Najafzadeh, M., Noori, R., Afroozi, D., Ghiasi, B., Hosseini-Moghari, S. M., Mirchi, A., et al. (2021). A comprehensive uncertainty analysis of model-estimated longitudinal and lateral dispersion coefficients in open channels. *J. Hydrol.* 603, 126850. doi: 10.1016/j.jhydrol.2021.126850

Nanda, A., Sen, S., Jirwan, V., Sharma, A., and Kumar, V. (2018). Understanding plot-scale hydrology of lesser himalayan watershed—a field study and HYDRUS-2D modelling approach. *Hydrol. Proc.* 32, 1254–1266. doi: 10.1002/hyp.11499

Pappenberger, F., Matgen, P., Beven, K. J., Henry, J. B., Pfister, L., Fraipont, P., et al. (2006). Influence of uncertain boundary conditions and model structure on flood inundation predictions. *Adv. Water Resour.* 29, 1430–1449. doi: 10.1016/j.advwatres.2005.11.012

Pelletier, P. (1988). Uncertainties in the single determination of river discharge: a literature review. *Can. J. Civil Eng.* 15, 834–850. doi: 10.1139/l88-109

Perumal, M., Moramarco, T., Sahoo, B., and Barbetta, S. (2007). A methodology for discharge estimation and rating curve development at ungauged river sites. *Water Resour. Res.* 43. doi: 10.1029/2005WR004609

Perumal, M., Moramarco, T., Sahoo, B., and Barbetta, S. (2010). On the practical applicability of the VPMS routing method for rating curve development at ungauged river sites. *Water Resour. Res.* 46. doi: 10.1029/2009WR008103

Petersen-Overleir, A., Soot, A., and Reitan, T. (2009). Bayesian rating curve inference as a streamflow data quality assessment tool. *Water Resour. Manage.* 23, 1835–1842. doi: 10.1007/s11269-008-9354-5

Radulovic, M., Radojevic, D., Devic, D., and Blecic, M. (2008). *Discharge Calculation of the Spring Using Salt Dilution Method – Application Site Bolje Sestre Spring (Montenegro)*. Available online at: http://balwois.com/balwois/administration/full_paper/ffp-1257.pdf (accessed July 24, 2013).

Rosgen, D. L. (1996). A classification of natural rivers: reply to the comments by JR Miller and JB Ritter. *Catena* 27, 301–307. doi: 10.1016/0341-8162(96)00018-5

Sahoo, G. B., and Ray, C. (2006). Flow forecasting for a Hawaii stream using rating curves and neural networks. *J. Hydrol.* 317, 63–80. doi: 10.1016/j.jhydrol.2005.05.008

Scanlon, B. R., Keese, K. E., Flint, A. L., Flint, L. E., Gaye, C. B., Edmunds, W. M., et al. (2006). Global synthesis of groundwater recharge in semiarid and arid regions. *Hydrol. Proc.* 20, 3335–3370. doi: 10.1002/hyp.6335

Sefe, F. T. K. (1996). A study of the stage-discharge relationship of the Okavango River at Mohembo, Botswana. *Hydrol. Sci. J.* 41, 97–116. doi: 10.1080/02626669609491481

Shrestha, R. R., Bardossy, A., and Nestmann, F. (2007). Analysis and propagation of uncertainties due to the stage-discharge relationship: a fuzzy set approach. *Hydrol. Sci. J.* 52, 595–610 doi: 10.1623/hysj.52.4.595

Subramanya, K. (2006). *Engineering Hydrology*. New Delhi: Tata McGraw-Hill.

Szilagyi, J., Balint, G., Gauzer, B., and Bartha, P. (2005). Flow routing with unknown rating curves using a state-space reservoir-cascade-type formulation. *J. Hydrol.* 311, 219. doi: 10.1016/j.jhydrol.2005.01.017

Tung, Y. K. (1996). "Uncertainty and reliability analysis," in *Water Resources Handbook*, ed L. W. Mays (New York, NY: McGraw-Hill), 7.1–7.65.

United Nations (2011). *Challenges and Opportunities for Water in the Transition to a Green Economy International UN-water Conference Water in the Green Economy in Practice: Towards Rio 20, 3–5*. Available online at: https://www.un.org/waterforlifedecade/green_economy_2011/

Venetis, C. (1970). A note on the estimation of the parameters in logarithmic stage-discharge relationships with estimates of their error. *Int. Assoc. Sci. Hydrol.. Bulletin* 15, 105. doi: 10.1080/02626667009493957

Viviroli, D., Durr, H. H., Messerli, B., Meybeck, M., and Weingartner, R. (2007). Mountains of the world, water towers for humanity: typology, mapping, and global significance. *Water Resour. Res.* 43, 5653. doi: 10.1029/2006WR005653

Westerberg, I. K., Guerrero, J. L., Younger, P. M., Beven, K. J., Seibert, J., Halldin, S., et al. (2011). Calibration of hydrological models using flow duration curves. *Hydrol. Earth Syst. Sci.* 152205–2227. doi: 10.5194/hess-15-2205-2011

World Meteorological Organization (2010). *Manual on Stream Gauging. Volume II—Computation of Discharge.* Geneva: WMO, 195.

frontiers | Frontiers in Water

TYPE Original Research
PUBLISHED 26 February 2024
DOI 10.3389/frwa.2024.1360515

OPEN ACCESS

EDITED BY
Rajneesh Singh,
University of Minnesota Twin Cities,
United States

REVIEWED BY
Manoj Chandra Garg,
Amity University, India
Anamika Yadav,
Assam University, India

*CORRESPONDENCE
Dorothee Spuhler
✉ dorothee.spuhler@ost.ch
Regula Meierhofer
✉ regula.meierhofer@eawag.ch

RECEIVED 23 December 2023
ACCEPTED 07 February 2024
PUBLISHED 26 February 2024

CITATION
Bouman L, Spuhler D, Bünzli M-A, Melad A III, Diop L, Coelho O and Meierhofer R (2024) The water flow diagram. *Front. Water* 6:1360515. doi: 10.3389/frwa.2024.1360515

The water flow diagram

Lukas Bouman[1], Dorothee Spuhler[2]*, Marc-André Bünzli[3], Amancio Melad III[4,5], Lamine Diop[6], Osmar Coelho[7] and Regula Meierhofer[1]*

[1]Department of Sanitation, Water and Waste for Development, Swiss Federal Institute of Aquatic Science and Technology (Eawag), Duebendorf, Switzerland, [2]UMTEC Institut für Umwelt- und Verfahrenstechnik, University of Applied Sciences of Eastern Switzerland (OST), Rapperswil, Switzerland, [3]Thematic Cooperation Water, Swiss Agency for Development and Cooperation, Bern, Switzerland, [4]UNESCO-IHE Institute for Water Education, Delft, Netherlands, [5]De La Salle University (DLSU), Manila, Philippines, [6]Gaston Berger University, Saint-Louis, Senegal, [7]Center for Sustainable Development, Brasilia Federal University, Brasilia, Brazil

Introduction: The Water Flow Diagram (WFD) is a novel advocacy and communication tool that presents urban water supply and management in a simple visualization. Rapid urbanization, growing populations, and the climate crisis increase the pressure on water resources, particularly in urbanized areas. The WFD aims to foster a dialogue around conflict of interests and opportunities among different stakeholders, and trigger actions toward more sustainable urban water management (UWM), as well as a water secure future.

Method: The WFD is produced from data on water abstraction, water use of different sectors, water treatment, water recycling and contamination risks. The data were obtained from government services, wastewater and water utilities, large industries, universities and reports of intergovernmental organizations. If these sources did not have data, reports from NGOs or consultants, comparable contexts, default values or expert judgements were considered. The annual water flows are presented in a Sankey Diagram. An intuitive color code highlights the flows as "problematic" or "appropriate" and points to areas where UWM practices should be improved.

Results and conclusions: The final diagrams are a concise instrument that identifies challenges of UWM in the four application cases presented in this article. Key challenges that became evident included: pollution from agricultural production, the lack of wastewater and sanitation infrastructure, high water losses in the distribution networks, water exports leading to a lack in local supply and sewer overflows during heavy rainfalls. Opportunities identified were the need to: invest in sanitation and wastewater to protect resources, create coordination bodies to align conflict of interests, and/or invest in blue-green infrastructure for rainwater retention. The WFD triggered local actions, such as in-depth discussions between relevant actors, the formation of integrated water use committees and the interest of the national ministry in Senegal to replicate the diagram for other locations. This article presents the methodology, discusses the four case studies and deliberates on the prospective use of the WFD.

KEYWORDS

integrated water resource management, human right to water and sanitation, community engagement, decision support, advocacy

1 Introduction

Growing population and climate change increase the pressure on water resources, particularly in urbanized areas. The world's population exceeded eight billion in 2022 (Nandagiri, 2023) with 56% living in cities (WorldBank, 2023). The United Nations predict that 68% of the over nine billion people will live in cities by 2050

(Habitat, 2022). Urbanized areas alter the water cycle. Overall runoff volumes increase (Dunne and Leopold, 1978; Arnold Jr and Gibbons, 1996) and are less buffered than in non-urbanized areas, resulting in higher peak discharges during heavy rainfalls (Dunne and Leopold, 1978; Packman, 1980; Konrad, 2003). Due to climate change, extreme events, such as heavy rainfalls and droughts, will increase (Field, 2012). Furthermore, groundwater recharge has reduced due to an increase in impervious area (O'Driscoll et al., 2010). At the same time, groundwater abstraction has increased, particularly in developing countries, where groundwater is usually a safer alternative to surface water (McGrane, 2016). On the other hand, exfiltration from malfunctioning water supply and sewerage can increase and contaminate groundwater tables (Jacobson, 2011). On the qualitative aspects, many different contaminants originate from cities, such as heavy metals (McGrane, 2016), microbial contaminants (Kay et al., 2007), elevated nutrient loadings, volatile organic compounds, nanoparticles and micropollutants, such as pesticides, pharmaceuticals (Heberer et al., 2002) and polycyclic aromatic hydrocarbons (PAHs) from vehicular emissions (Van Metre et al., 2000).

Such stress factors impair sustainable urban water management (UWM) and restrain progress toward the Sustainable Development Goals (SDG), including SDG 6: clean water and sanitation, SDG 11: sustainable cities and communities and SDG 13: climate action. Therefore, it is important to accelerate the shift to sustainable management of urban water resources. Tools are needed to foster communication among stakeholders and to support advocacy and adequate planning decisions. A collectively created visualization of the urban water flows, including challenges and opportunities, could make a decisive contribution toward an earlier adoption of sustainable UWM schemes.

Because the sector did not have a useful tool to visualize water flows, researchers and development experts from the Swiss Community of Practice around water (Aguasan) jointly created the Water Flow Diagram (WFD). The rationale was that a well-crafted diagram could instantly and memorably communicate a connection that might otherwise demand an extensive and quickly forgettable explanation (Platts and Hua Tan, 2004). Based on this hypothesis, three criteria were defined for the diagram: it should: (i) be applicable without the need for any programming skills; (ii) allow for a quick identification of the challenges and opportunities through an easily understandable graphic, and (iii) be based on a participatory approach that includes data collection, interpretation and action planning. The main stakeholders of the participatory process should include: private and industrial water users, agricultural companies and small farmers, water related decision makers, water rights defenders, utilities, policy makers, urban planners, civil society, and NGOs.

2 Materials and methods

An extensive literature review on existing tools and instruments that visualize urban water balances led to the conception of the WFD. The tool was further developed in an iterative co-creation process through several case studies. At each step, feedback from different experts was collected and injected into the next stage of development.

2.1 Existing urban water balance tools

A selection of tools that visualize water and wastewater flows documented in literature and/or highlighted by experts in the sector is presented in Table 1.

The Water Flow Charts by the Lawrence Livermore National Laboratory use Sankey Diagrams to represent annual water balances for states or an entire country (Kaiper, 2004). They provide an intuitive overview of state-wide or nation-wide water flows in a visual format. The diagrams do not reveal whether or not the water is treated before use or discharge, nor if the management practices are appropriate. The methodology of how these water balances are put together is not publicly available.

In the sanitation sector, the Shit Flow Diagram was developed by the Sustainable Sanitation Alliance (Peal et al., 2020). It uses a flow diagram approach to visualize which proportions of the fecal sludge and wastewater in a city are safely or not safely managed. To communicate the latter, an intuitive color code is used. No special skills or programming skills are necessary to make such a diagram.

The City Water Balance by the Environmental Protection Agency of the United States uses an intuitive Sankey Diagram approach to track the major pathways of urban water. Values for data that is lacking are estimated (Erban et al., 2018). On the basis of the diagram, the viewer cannot judge whether the water management practices are appropriate or not. Since the compilation of the data is based on the software environment *R*, the user needs programming skills to apply it.

The Best Practice Water Balance of the International Water Association provides a useful volumetric overview for water utilities from the source to the water distribution, focusing on non-revenue water (Lambert, 2002). The output, however, is not visualized in a graphic. Neither the wastewater nor the water quality are considered in the water balance.

In addition, a variety of computer models have been developed to simulate water balances in urban areas. For example the Dynamic Urban Water Simulation Model (DUWSiM) by the University College Dublin, Ireland (Willuweit and O'Sullivan, 2013), the Urban Volume and Quality (UVQ) model by the Commonwealth Scientific and Industrial Research Organization, Australia (Mitchell and Diaper, 2006), the Water Evaluation and Planning System by the Stockholm Environment Institute, USA (Sieber and Purkey, 2015) the LiWatool by the Institute for Automation and Communication, Germany (Schütze and Robleto, 2010) and the Integrated Urban Water Model by the Colorado State University. They predict water demand and available water and/or storm water and wastewater production. Some of them include water quality. While some models simulate the micro environment (street level), others simulate the macro level (watershed). These computer-based models can be very useful for engineers, modelers and planners, but require substantial programming and software skills. Most of the models do not have visual outputs that can easily be disseminated and understood by a diverse audience.

10.3389/frwa.2024.1360515

TABLE 1 Selection of existing urban water balance tools (white cells = favorable characteristics, gray = partly favorable characteristics, black = unfavorable characteristics).

	Water flow charts	Shit flow diagram	City water balance	IWA water balance	Computer models
Institution	Lawrence Livermore National Laboratory	Sustainable Sanitation Alliance	US Environmental Protection Agency	International Water Association	Various institutions
Sectors covered	Water source, use and discharge	Wastewater and Sanitation	Complete	Water supply	Depends on the model
Intuitive*	Yes	Yes	Yes	Medium	No
Visualization	Sankey diagram	Flow Diagram	Sankey diagram	None	Typically none
Provides a judgement of current practices	No	Yes	No	No	Depends on the model
Programming and software skills needed for the application	No	No	Yes	No	Yes

*Intuitive: Can be understood without expert knowledge and/or specific training and has elements that help to make the instrument easy to understand, e.g., a color code.

2.2 Expert consulting

The development of the WFD tool was based on a co-creation approach. Starting with a first draft, practitioners were regularly engaged and the diagram and underlying methodology were created in an iterative process. The practitioners consulted included water and wastewater experts, WASH specialists, practitioners, water users, utility managers and graphic designers. Practitioner engagement took place through bilateral conversations on specific parts of the diagram, in two online workshops, in regular meetings of Aguasan—a Swiss community of practice of organizations working in the WASH sector—and at five different international water conferences (Stockholm World Water Week, United Nations Water Week, World Water Forum, All Systems Connect Symposium and the Global Water Operators Partnerships Alliance Congress). The inputs collected during these consultations informed the further development of the methodology.

2.3 The water flow diagram methodology

Yearly water balances are illustrated with *Sankey Diagrams*, which consists of "nodes" that are connected with "flows." The width of a flow is proportional to its quantity, in this case, the annual water flow from one process to another. It is read from left to right to follow the path of the water flows along the water use chain. The unit of the volumes indicated is 1,000 m^3/year. Six different functional groups for the processes were defined: source, drinking water treatment and distribution, use (domestic, public, industrial and agricultural), wastewater transport and treatment, discharge, and reuse. Inside every functional group, there are standard options to choose from corresponding to the nodes in the Sankey Diagram. The structure is presented in Figure 1. If there are significant reasons to add a node to the standard structure, it can simply be added manually.

The color code was defined as appropriate or problematic on the basis of the adequacy of the water quality and quantity of a flow, and its use or destination. The evaluation was done by the local project teams together with the researchers from Eawag. Four water qualities were defined: uncontaminated, microbiologically contaminated, biochemically contaminated and chemically contaminated. For every section of the water flow between two nodes, the water quality was categorized as problematic (red) or appropriate (green). For example, if microbiologically contaminated water was treated by a microbial treatment, the UWM was categorized as appropriate. However, if chemically contaminated water was treated by a microbial treatment, the UWM was categorized as problematic. Furthermore, the default output water quality for every node was defined based on the input water quality and the node itself, unless the data indicated otherwise.

If there was no information about the water quality, it was colored gray. Categorization into appropriate and problematic flows was also done regarding water quantity. For example, water losses in the distribution system of up to 10% were considered as appropriate, whereas higher losses were categorized as problematic. Furthermore, the SDG 6 principle that safely managed water needs to be available on the premises was taken into account. Therefore, unpiped water was categorized as a problematic UWM. A detailed guide to judge the appropriateness of the UWM practices for every combination of flow and node is attached to the user manual (Bouman and Spuhler, 2023). Every case study team applied this detailed guide in close exchange with the Eawag experts throughout the process.

The system boundary of a WFD is defined at the beginning of every analysis. For the cases studies presented here, the municipal boundaries or the service area of utilities were used. In systems with narrower system boundaries and a higher population density, a stronger focus is put on the assessment of water management practices in the urban areas. However, the water flows represented in a WFD always interact with the water flows, stocks, practices and water quality outside of its system boundaries. In diagrams of less densely populated areas, the assessment focuses more on the impact of large scale water use and landuse on the water availability and water quality. Even an entire catchment area of a city could be within the system boundaries of the WFD.

Various *data sources* can be used to compose a WFD. Potential data sources are government services, (waste) water utilities,

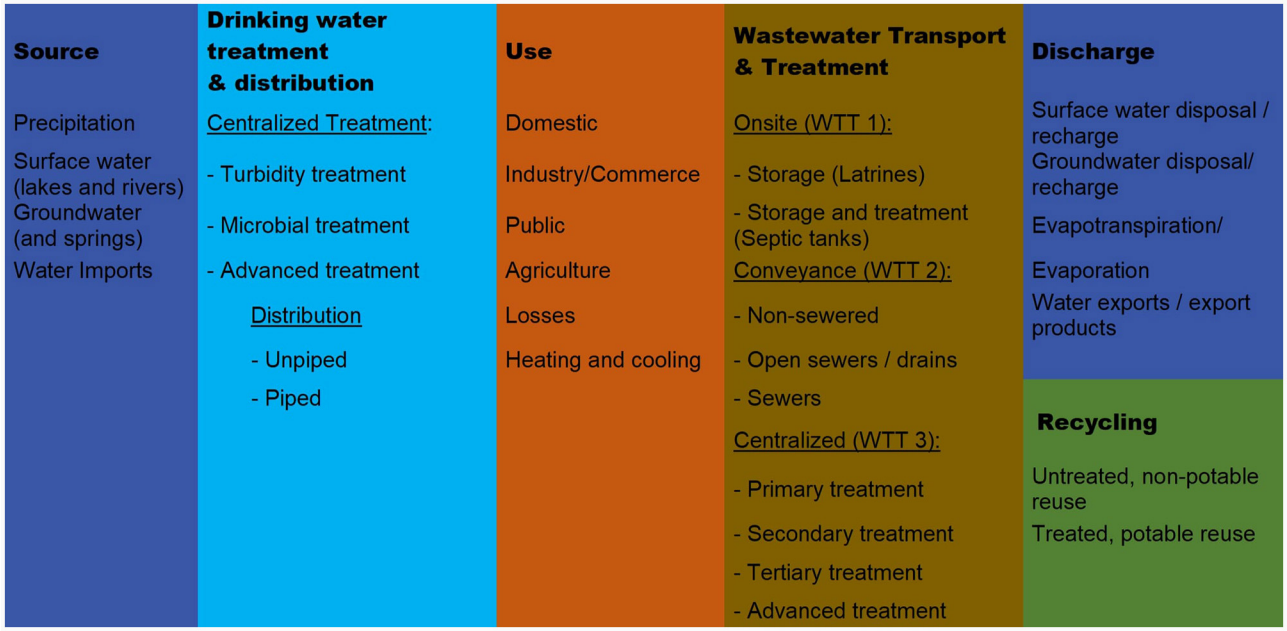

FIGURE 1
Structure of the Water Flow Diagram with six functional groups and the standard nodes.

agencies, universities and large industrial users. If higher quality data are not accessible, reports from consultants, NGOs or intergovernmental organizations might serve as data sources. If such reports are not available, estimations for default values can be drawn from comparable contexts or expert judgements. Experts included either generalists with multiple years of international experience in the water or sanitation sectors or specialists, such as employees of a water utility or members of a farmer's association with solid expertise of a specific aspect of the diagram. In all of the case studies, except for Bern, data from one particular year were used. In the case of Bern, the average values of a timeline of 5 years were used for the diagram. The validity of the data was discussed during the appropriation meeting (see procedure in the following paragraph) where all the stakeholders discussed and approved the final WFD. An important element in the validation process of a WFD was that the water flows in the diagram needed to be fully balanced. As storage of water in one node is not possible, all the water flowing into a node also has to be shown as flowing out. Basing the analysis on the water balance permits the stakeholders to analyse, discuss and recheck the quantities of water flows that are estimated, especially in cases where data of lower reliability are used.

The WFDs were composed during an iterative and *participatory process*. The stakeholders included the municipality and administrative authorities, utilities and technical services, different private and industrial water users, civil society, researchers, planners, and NGOs. The goal of the participatory process was to build a common understanding of the water management and its challenges. This understanding would then become the basis for broadly supported key action points. Stakeholders were involved in the initial data collection, validation of different evolving versions of the diagram, and, finally, the definition and adoption of action points. The procedure followed was different from case to case and is described in Section 2.4.

The procedure to develop a WFD consists of the following steps:

1. *Ignite the process*: a partner organization was found, the system boundaries defined and ideally, a support statement of the municipality obtained.
2. *Collect data*: data was collected from government services, wastewater and water utilities, large industries, universities, NGOs or consultants, secondary sources, or expert judgements. In some circumstances, primary data collection was conducted.
3. *Draft WFD*: the data was compiled in an Excel template that was then used to generate the Sankey Diagram, using an open access online tool (sankeymatic.com), which was then graphically edited in PowerPoint.
4. *Conduct appropriation meeting*: the draft WFD was discussed by all interested stakeholders, the main messages defined and potential indicators and actions elaborated on.
5. *Finalize WFD*: the diagram with the learnings from the appropriation meeting was finalized, disseminated and actions to improve the UWM were proposed.

2.4 Case studies

The following describes how WFD diagrams were developed in the four case study locations: Bern, Switzerland, Rio Pardo de Minas, Brazil, Santa Maria Bulacan, Philippines and in suburbs of Dakar, Senegal.

2.4.1 Bern, Switzerland

The capital of Switzerland was the first case study location. Bern is a relatively small city with a well-developed UWM. The city boundaries were used as system boundaries and included an area of 51 km^2 and 135,000 inhabitants, corresponding to a density of 2,630 inhabitants per km^2. The necessary data was readily available from the wastewater and drinking water utilites and the cantonal office and data from the years 2015–2020 were used. The participatory process in Bern, however, was not as central as in other locations since the case study served as proof of concept. The wastewater and drinking water utilites and the cantonal office were also involved in the process of defining the diagram and validating it. The Mayor of the city supported the process with a letter of support and a video message.

2.4.2 Rio Pardo de Minas, Brazil

Rio Pardo de Minas is a municipality in the northeast of the Brazilian state of Minas Gerais. Its main economic activities are agriculture and small industries. The municipal boundaries were used as system boundaries. The area included 3,130 km^2 and 31,000 inhabitants, with a low population density of 10 inhabitants per km^2. Information was collected from local partner organizations and from the municipality. In addition, the National Water Agency database of water use rights was consulted. The participatory process was led by the local office of a Swiss NGO. Co-creation workshops were organized with the following local organizations: the Rural Workers Union of Rio Pardo de Minas, the North of Minas Gerais Alternative Agriculture Center, and the Rio Pardo de Minas Farmers Union. The Mayor of the city supported the process and the appropriation meeting was planned at the municipality level.

2.4.3 Santa Maria Bulacan, Philippines

The municipality of Santa Maria lies in the Philippian province Bulacan. Over 90% of the economic activities are in the service sector, with marginal industry, agriculture and fishery sectors. The municipal boundaries were used as system boundaries. The areas included 91 km^2 and 289,820 inhabitants, corresponding to a population density of 3,188 inhabitants per km^2. The data was obtained from the Municipal Local Government Unit of Santa Maria Bulacan, the Santa Maria Water District, private water concessionaires, the Maynilad Water Academy, the National Irrigation Association and the municipality's Socioeconomic Plan. After the collection of data and the composition of the diagram, an appropriation meeting was conducted in Santa Maria, Bulacan. It was attended by the members of the Integrated Safe Water, Sanitation, and Hygiene (iWASH) Council and the iWASH Technical Working Group of the local government. Participants from the local government included the Municipal Administrator, the Municipal Planning and Development Coordinator, the Municipal Agriculturist, and the Municipal Environment and Natural Resources Officer. The inputs from the meeting were used to validate assumptions that had to be made due to the data gaps in the diagram.

2.4.4 Suburbs of Dakar, Senegal

Diender, Kayar and Keur Moussa are three communities in the suburbs of Dakar. Agriculture is the predominant economic activity in this water scarce area, and part of the available groundwater is exploited for the water supply of Dakar. The municipal boundaries were used as system boundaries. Diender consisted of an area of 118 km^2 with 43,465 inhabitants (368 inhabitants/km^2), while Kayar comprised an area of 16 km^2 and 33,383 inhabitants (2,086 inhabitants/km^2) and Keur Moussa stretched out on 222 km^2 with 69,168 inhabitants (312 inhabitants/km^2). The participatory process was led by a consultant of the local office of a Swiss NGO supported by two local partner organizations, the Environment Development Action for Natural Land Protection (ENDA Pronat) and the Federation of Agropastoralists of Diender (FAPD). The data was obtained from the Water Resources Management and Planning Department, the Office of Rural Water Wells, the Association of Borehole Users, the National Water Company of Senegal, Eau du Sénégal (water utility of urban and peri-urban areas in Senegal), and the World Health Organization. The local partner organizations planned and facilitated the meetings between the consultant, the community stakeholders, the sub-prefecture and the technical services, as well as the meeting for input from the local communities. All the meetings were held at the community level to take the voices of the most disadvantaged sections of the population into account.

3 Results

A WFD was produced for each case study location.

In Figure 2 the WFD of Bern is presented. Almost all flows are green (appropriate UWM). Abstracted groundwater was treated with ultraviolet light and distributed to private households, industry, public buildings, fountains and hydrants. The industries used some negligible volumes of untreated water for their processes. Approximately 5% of treated water was lost during the distribution in the piped network, which was below the threshold of 10% for problematic UWM defined in the user guide (Bouman and Spuhler, 2023). This, therefore, could be considered as appropriate UWM. All buildings are connected to a centralized sewer system. Most wastewater was appropriately treated in an advanced wastewater treatment plant before being discharged into the river Aare. Groundwater and river water were abstracted, used for heating and cooling, and discharged again to the water bodies without quality change. Approximately 173,000 m^3 of piped water per year were used in agriculture (in addition to rain-fed water supply to the fields). The water, after use by agriculture, sometimes polluted the groundwater and surface water. Small volumes of water were exported by industry (concrete factory) and agriculture. The most interesting finding of the WFD was that ~15% of the total wastewater in the sewer system was discharged to the river Aare without treatment, which was relatively high compared to the Swiss average of 3%–4% (Staufer and Ort, 2012). The discharge happened only during heavy rainfall events, when sewer and plant capacities were exceeded. The diagram identified that improvements of the combined sewer overflow should be implemented. Potential measures for improvement

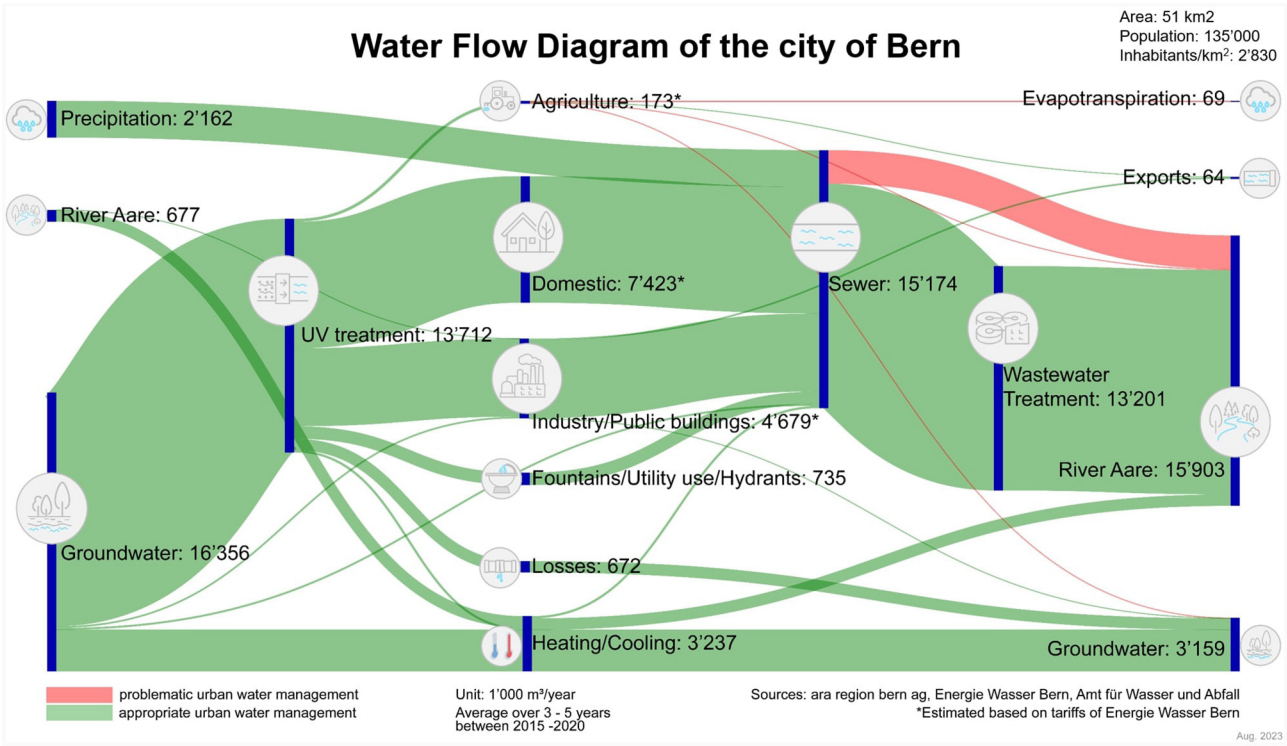

FIGURE 2
Water Flow Diagram of the city of Bern, Switzerland. *Percentages estimated on the basis of tariff levels.

consist of infrastructure adaptions or the installation of blue-green infrastructure to reduce immediate run-off after heavy rainfalls.

In the case study in Rio Pardo, initially, the system boundaries chosen were of the urban populated area. Because the partner organization was particularly interested to show the water allocation among the different sectors of the entire municipality, the system boundaries were widened to the municipality. Consequently, also less populated, rural areas were included in the WFD. The water flow diagram in Rio Pardo da Minas (Figure 3) identified a majority of water flows as problematic (red). Irrigation for agriculture operated by large agrobusinesses producing cash crops consumed almost 100% of the water. The water, potentially contaminated with pesticides and fertilizers due to inadequate agricultural practices, infiltrated into groundwater and surface water. Irrigation methods caused an estimated 70% of water losses due to evapotranspiration. It was estimated that 5% of the water input into agriculture was exported with the agricultural products. The proportion of domestic, industrial and public uses of the overall water consumption were minor. Nevertheless, they polluted the surface water and groundwater, since for a large proportion of this water, there was no appropriate treatment of the wastewater. Approximately 25% of the water was lost in the piped distribution network. Although the urban dimension of the water flow is hardly visible in this WFD, its visualization triggered an intensive dialogue on water utilization and water rights amongst different relevant stakeholders and the municipality. First, the WFD was discussed in workshops together with local partner organizations as described in Section 2.4. During the subsecutive appropriation meeting at the municipal level, where the diagram was presented to the city Mayor and his Secretary, dozens of miners stormed the city auditorium and demanded to stop the activity. They argued that the analysis of the utilization of water pose a threat to the local economy. Due to this conflict, the meeting at the city auditorium was terminated and discussions about the WFD were continued only with unions and NGOs. During these discussions, it was agreed that the situation had to first calm down before making another attempt at presenting the WFD at the municipal level.

In Santa Maria, Bulacan, in the Philippines (Figure 4) ~30% of the drinking water originated from surface water, whereas 70% came from groundwater. After chlorination, the piped water was distributed to the different users. The domestic sector used 41% of the treated water, the industrial sector 12%, the public sector 1%, agriculture 34 and 12% were lost in the distribution network. 1% of the water used by the domestic sector was not treated prior to use. There was no sewer system and the wastewater was either collected in septic tanks (93%) and in pit latrines (4%) or was collected in open channels and directly discharged to the surface water (3%). The pit latrines were unlined and, therefore, polluted water from the pit latrines leaked into the groundwater. A small proportion of septic tanks were regularly emptied with trucks and the sludge exported, but it is unknown what happens to the rest of them (gray flow). Agriculture accounted for the major part of the water consumption. In Santa Maria, rain-fed agriculture was considered in the diagram in contrast to the other case studies. It was estimated that 19,712 m^3 per year of precipitation fed into agriculture lands and that 60% of the water

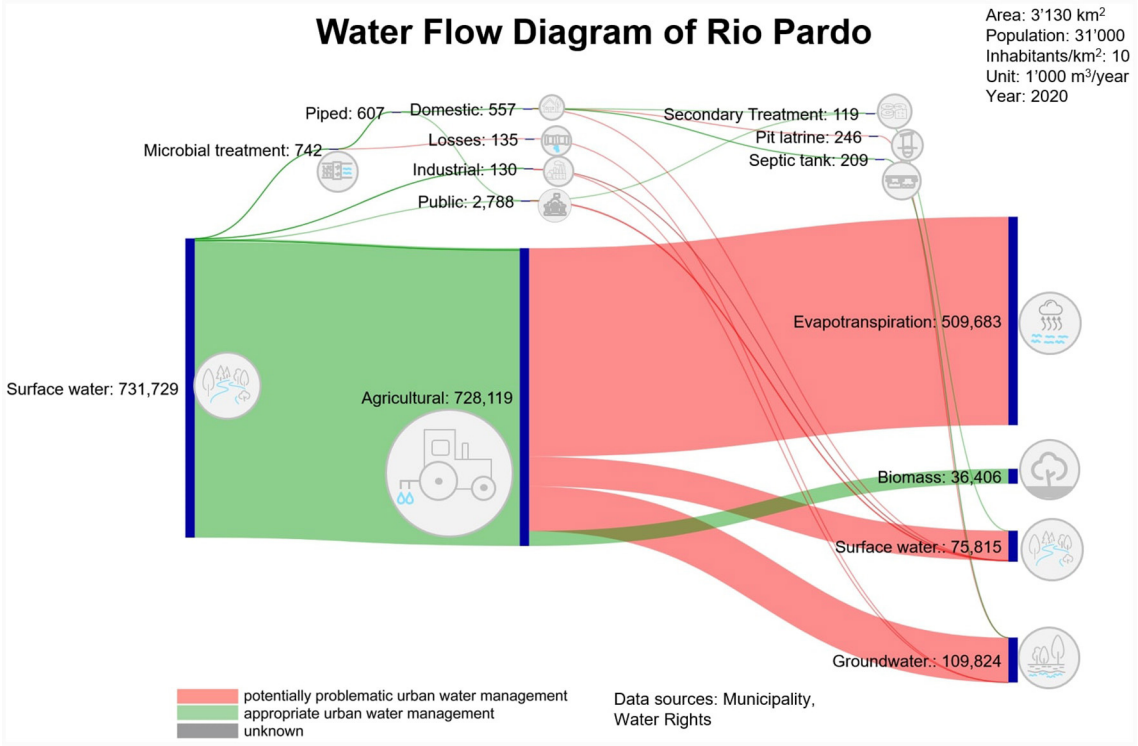

FIGURE 3
Water Flow Diagram of Rio Pardo de Minas, Brazil.

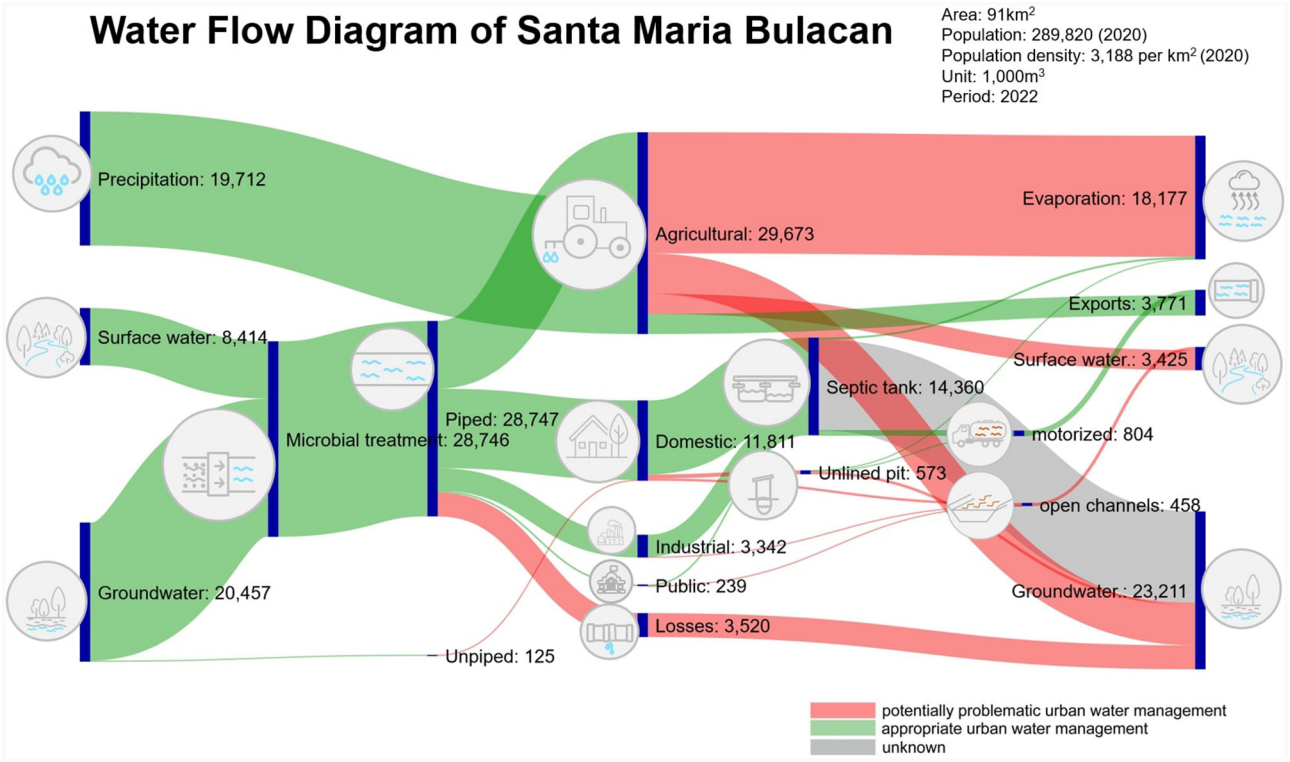

FIGURE 4
Water Flow Diagram of Santa Maria, Bulacan, Philippines.

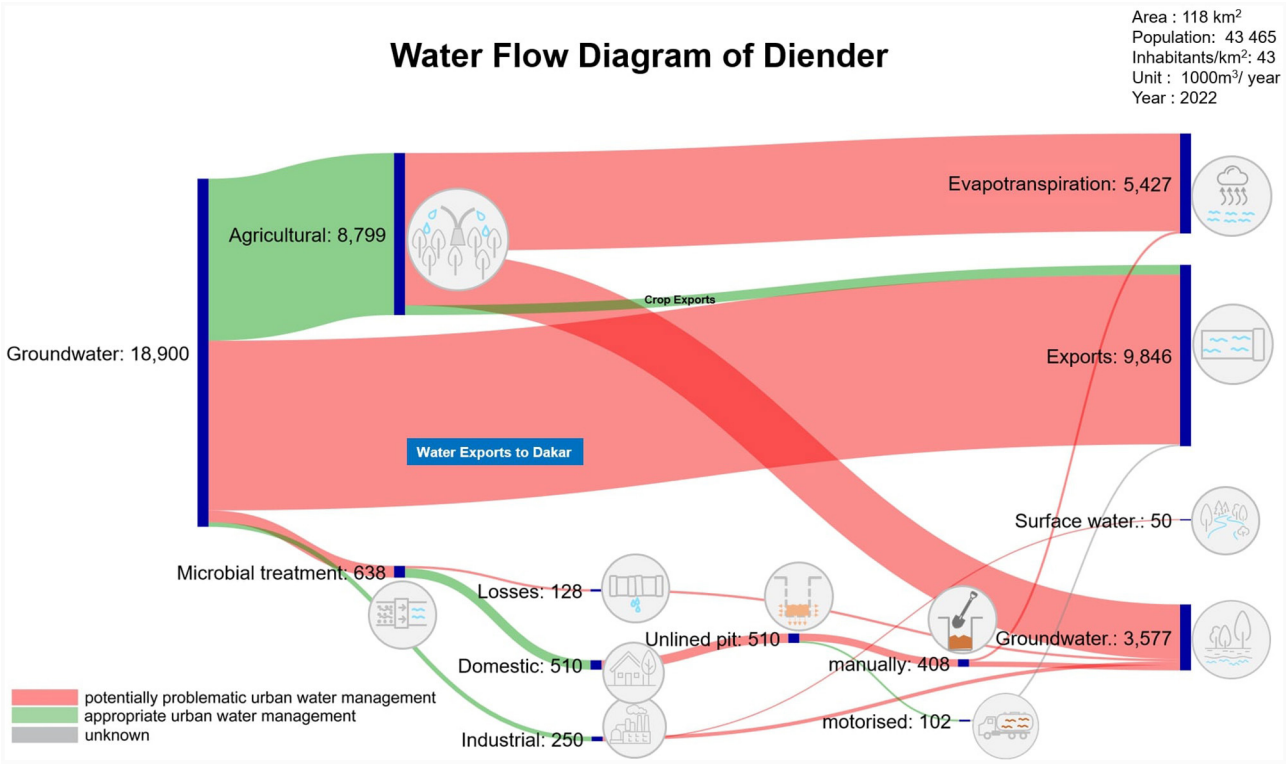

FIGURE 5
Water Flow Diagram of the municipality of Diender, Senegal.

used in agriculture evapotranspirated, partly because inappropriate irrigation techniques were used in the area. Additionally, it was estimated that 10% of the polluted agricultural water flew into surface water bodies, 20% into groundwater and 10% of the water from agriculture was exported as agricultural products.

Figure 5 shows the WFD of Diender, one of three diagrams from Senegal. More than half of the pumped groundwater was exported to the city of Dakar. Another 47% of the water was used for agriculture. The water that was used in agriculture was probably polluted with pesticides and fertilizers, and would have a negative impact on the groundwater. The evapotranspiration rate was estimated to be 60% because of inadequate irrigation methods in the area. Furthermore, it was estimated that 5% of the water was exported as agricultural products. Similar to the findings from the example of Rio Pardo de Minas, the water consumption for domestic, public and industrial uses were minor. Nevertheless, inappropriate sanitation systems threaten the surface water resources and the groundwater on which the city of Dakar depends. The participative process of collecting data, analyzing the diagram and formulating potential measures in Dakar was characterized by a very active stakeholder engagement at the meetings held at the community level, which were organized and facilitated by the local partner organizations. The process effectively highlighted issues in water management that had been raised by the civil society for quite some time and achieved support to mitigate these issue from the authorities. A result of the process was the formation of a committee for integrated water resources management planning in the three communities, that consists of members from the utilities and civil society. Furthermore, the Ministry of Water and Sanitation in Senegal expressed interest to replicate the WFD in other communities and to use it in local water resource management plans.

4 Limitations

The applied methodology has some limitations. First, the coefficients for evapotranspiration and runoff of water to surface water and groundwater after agricultural use are difficult to measure or estimate. In the presented case studies, rough estimations were used that were derived from literature and expert consulting. Second, stakeholder consultations revealed that the irrigation and land management methods were not water efficient. Therefore, the flow toward evapotranspiration were coded as problematic (red). A better judgement is not possible without doing a more systematic assessment of the situation on the ground. Third, it was assumed that the water running off after agricultural use was contaminated with pesticides; however, this assumption is not based on solid evidence. Lastly, the specificity of the WFDs are limited and the conclusions that can be drawn from them are general. Spatial conclusions on where, for example, water resources are being polluted or where there are leakages in the distribution network cannot be made, nor can the extent of pollution be determined. An explanatory description that accompanies the WFD can overcome this limitation to some extent. However, the WFD was designed as a communication and

advocacy tool that is based locally availably data sets that can be limited in precision. Therefore a detailed and precise assessment of hydrological processes is not possible.

5 Discussion

In all four case studies, the WFDs depicted the water sources used by the cities, highlighted if the water treatment was adequate and revealed how much water was allocated among the different sectors. While in Bern and Santa Maria, groundwater and surface water were abstracted to be treated, only river water was used in Rio Pardo and only groundwater in Diender. Except for the case study of Bern, where the narrower system boundaries excluded a larger part of the non-urbanized areas, the major part of water in the other three case studies was used by agriculture. For example, in the case of Rio Pardo de Minas, agriculture used up to 64,000 L/day per person. The domestic water use was 150 L/day per person in Bern, 112 L/day per person in Santa Maria Bulacan, 49 L/day per person in Rio Pardo de Minas and 32 L/day per person in Diender. In addition, except for Bern, the losses in the distribution networks were higher than 10% and therefore, categorized as problematic UWM practices. At all locations, open water resources were threatened by polluted water either from agriculture or from the lack of wastewater and sanitary infrastructure. The extent of polluted water reaching open water bodies varied across the locations, and not surprisingly was higher in less developed regions, such as in the suburbs of Dakar or Rio Pardo de Minas. Bern was the only study site where a comprehensive sewer system was in place and where the pollution of the water resources due to heavy rainfall events that overflow sewer system, sending the water directly to the river, was limited. The other study sites had primarly onsite sanitation systems installed. Polluted water leaking from those systems threatened groundwater and surface water bodies. In none of the study sites were signficiant amounts of water recycled.

The selection of *system boundaries* had a large impact on the conclusions that could be drawn from the diagram. If the system boundaries included large rural areas, one of the main conclusions was that a large part of the water was used by agriculture. Consequently, the impact of UWMs in systems with large rural areas was more difficult to depict and evaluate, as most urban flow arrows were too small to be compared. Yet, setting narrow system boundaries around an urban area would not show the agricultural and sometimes also industrial activities that take place outside the city boundaries. Water related activities outside city boundaries are relevant for the urban population because they impact the availability of water and the amount allocated to the different sectors and they influence water quality. One possibility to overcome this challenge is to prepare a WFD that represents the whole water catchment area of a city and a separate "zoom-in" diagram of the urban area.

The *participatory processes* required much time to identify all relevant stakeholders and to integrate them into each step of the process. This was especially the case in Rio Pardo de Minas and Diender where the processes to compose and discuss the WFD were highly participatory. A precondition to be able to conduct the participatory approach was that institutions and organizations were willing to participate and openly share the data. A clear explanation of the goal of the participatory process, a detailed explanation of the purpose of the WFD and an official support statement by political leaders were helpful to bring stakeholders on board. Since the goal of this study was to analyse the practical application of the WFD as a tool, the participatory processes were not analyzed in detail.

In all locations, the WFD triggerd a *dialogue around sustainable water management*. In Senegal, for example, the participatory discussion of the WFD led to the formation of a committee for water resource management in which the local administrative authorities were strongly involved. Furthermore, the Ministry of Water and Sanitation was interested in replicating the WFD in other communities. The experience in Rio Pardo highlighted that the utilization of water by different stakeholders is a sensitive issue and that a successful participary dialogue needs to be based on a comprehensive understanding of the subject matter and the trust of the stakeholders in the participatory process and dialogue. The protest of the miners revealed that, it needs to be communicated transparently that the WFD can highlight challenges in water management but solutions have to be identified during a joint process.

The following insights were gained regarding the application criteria outlined in the introduction:

i. The WFD methodology consists of a guide and an Excel-based data file that can be uploaded to an open online tool to make the Sankey Diagram. Final adjustments can be made in PowerPoint. During the case studies, the tools proved to be easy-to-use for people without any programming skills. Basic computer literacy and analytical skills were sufficient to produce the WFDs.
ii. In each of the case studies, the development of a WFD was initiated by different actors: researchers in Bern, a local NGO in Dakar, an international NGO in Brazil and a private consultant in collaboration with the public utility in the Philippines. Also, the settings were different with e.g., different system boundaries, population densities varying by a factor of more than 300, different main water sources, including full supply from groundwater, full supply from surface water to a balanced supply from three different sources, and different associated water challenges. In all four cases, the WFD demonstrated its capacity to visualize the challenges of a city's UWM in a single diagram, created the basis for a common understanding of these challenges, and showed opportunities for improvement. Despite its systematic approach, the results of the WFD depended on the expertise of local stakeholders and the assumptions made such as system bounderies, data estimations, and the judgement of the flows in "appropriate" or "problematic" UWM practices.
iii. In all four cases, the participatory process brought together different stakeholders and initiated consultation and joint action planning. The experiences made during these participatory processes confirmed the suitability of the WFD to be used as a tool to trigger communication about water management and to facilitate concerted negotiations toward solutions.

On the basis of insights gained during the implementation of the case studies, which confirmed the tool's compliance with the design criteria and its effect on triggering corrective measures in UWM, there should be a broader dissemination of the tool to a larger community of users. In addition, the

following measures are suggested to extend the applicability of the tool:

Firstly, the total precipitation within the system boundaries could be included in an updated version of the WFD. Precipitation plays an increasingly important role in UWM, since rainfall patterns are more and more influenced by climate change. The diagram could also highlight the potential impacts of climate hazards by showing which areas of the UWM are vulnerable to heavy rainfall, drought and other climate related hazards, providing stakeholders with a tool to identify measures contributing to climate resilience. However, including precipitation in WFDs adds complexity to the diagram in the form of additional flows and nodes, and would require more data to be gathered. The advantages and disadvantages of including precipitation would need to be assessed carefully and would differ from case to case.

Secondly, an adapted version of the WFD could be developed where the system boundaries are shifted from an urban focus to the watershed level. This would allow for the consequences of land use changes on larger scales to be made visible. Remote sensing data could be used to estimate evapotranspiration and runoff, based on land cover and slope. The improved version could also show the coefficients for run-off and evapotranspiration in more detail in order to allow for the making of more evidence-based estimations of evapotranspiration, runoff and infiltration, particularly for agricultural water use. The trade-off in a diagram with wider system boundaries is that the urban water flows become less visible, as discussed earlier in this section.

Thirdly, the WFD could be used to visualize scenarios. The diagram could show how policies or interventions, for example, cause land use changes that affect urban water flows or the hydrologic cycle on the watershed level. Also, the diagram could be part of long-term monitoring at regular intervals to make changes in UWM visible. However, the diagram cannot attribute the changes to certain strategies or interventions. The changes in UWM might be caused by a certain strategy or intervention, but might as well be due to other factors, such as changing urban dynamics, changing water needs or data consistency.

Fourthly, a better understandiung of the steps required for successfully steering the participatory process and providing more specific guidance to the implementation partners will improve the application of the WFD.

Lastly, a more user friendly web application that can make WFDs more easily available could be developed.

The experiences gained during the participatory processes to develop the WFDs in the four presented cases revealed that the methodology applied for the WFD yields a suitable tool for the understanding of water flows and that it can be useful in the planning of improvements to an integrated UWM. Users can easily comprehend the tool and the information provided in the diagram facilitates the participatory processes.

Data availability statement

The datasets generated for this study can be found in the Eawag Research Data Institutional Collection. For each case study, there is a separate repository with the data and Supplementary material. Bern, Switzerland: https://doi.org/10.25678/000BZD, Rio Pardo de Minas, Brazil: https://doi.org/10.25678/000BYC, Diender, Senegal: https://doi.org/10.25678/000BXB, Santa Maria Bulacan, Philippines: https://doi.org/10.25678/000BWA. Further inquiries can be directed to the corresponding author.

Author contributions

LB: Conceptualization, Data curation, Investigation, Methodology, Software, Visualization, Writing – original draft, Writing – review & editing. DS: Conceptualization, Investigation, Methodology, Writing – original draft, Writing – review & editing. M-AB: Conceptualization, Funding acquisition, Methodology, Supervision, Writing – original draft, Writing – review & editing. AM: Investigation, Methodology, Writing – review & editing. LD: Investigation, Methodology, Writing – review & editing. OC: Investigation, Methodology, Writing – review & editing. RM: Funding acquisition, Methodology, Project administration, Supervision, Writing – original draft, Writing – review & editing.

Funding

The author(s) declare financial support was received for the research, authorship, and/or publication of this article. This research was possible through funding by the Swiss Agency for Development and Cooperation, the City of Bern and the aid organization of the Swiss protestant churches (HEKS/EPER). Open access funding by Swiss Federal Institute of Aquatic Science and Technology (Eawag).

Acknowledgments

The authors would like to thank all the stakeholders in the different case studies for contributing to the making of the Water Flow Diagrams, the water experts who provided valuable feedback on how to improve the methodology, as well as HEKS/EPER for the consistent support.

Conflict of interest

The authors declare that the research was conducted in the absence of any commercial or financial relationships that could be construed as a potential conflict of interest.

Publisher's note

All claims expressed in this article are solely those of the authors and do not necessarily represent those of their affiliated organizations, or those of the publisher, the editors and the

reviewers. Any product that may be evaluated in this article, or claim that may be made by its manufacturer, is not guaranteed or endorsed by the publisher.

Supplementary material

The Supplementary Material for this article can be found online at: https://www.frontiersin.org/articles/10.3389/frwa.2024.1360515/full#supplementary-material

SUPPLEMENTARY TABLE 1
Data_bern.

SUPPLEMENTARY TABLE 2
Inventory_wfd_bern.

SUPPLEMENTARY TABLE 3
Inventory_wfd_riopardo.

SUPPLEMENTARY TABLE 4
Inventory_wfd_santamaria.

SUPPLEMENTARY TABLE 5
Inventory_wfd_diender.

SUPPLEMENTARY FIGURE 1
System_boundaries_bern.

SUPPLEMENTARY FIGURE 2
System_boundaries_diender.

SUPPLEMENTARY FIGURE 3
System_boundaries_riopardo.

SUPPLEMENTARY FIGURE 4
System_boundaries_santamaria.

References

Arnold Jr, C. L., and Gibbons, C. J. (1996). Impervious surface coverage: the emergence of a key environmental indicator. *J. Am. Plan. Assoc.* 62, 243–258. doi: 10.1080/01944369608975688

Bouman, L., and Spuhler, D. (2023). *Water Flow Diagram - Quick guide*. Eawag. Available online at: www.sandec.ch/wfd (accessed February 14, 2024).

Dunne, T., and Leopold, L. B. (1978). *Water in Environmental Planning*. New York, NY: Macmillan.

Erban, L. E., Balogh, S. B., Campbell, D. E., and Walker, H. A. (2018). An R package for open, reproducible analysis of urban water systems, with application to Chicago. *Open Water* 5:26. doi: 10.3389/fbuil.2019.00124

Field, C. B. (2012). *Managing the Risks of Extreme Events and Disasters to Advance Climate Change Adaptation: Special Report of the Intergovernmental Panel on Climate Change*. Cambridge, MA: Cambridge University Press. doi: 10.1017/CBO9781139177245

Habitat, U. (2022). *Envisaging the Future of Cities, World Cities Report 2022, UN Human Settlements Programme*. Available online at: https://unhabitat.org/sites/default/files/2022/06/wcr_2022.pdf (accessed February 14, 2024).

Heberer, T., Reddersen, K., and Mechlinski, A. (2002). From municipal sewage to drinking water: fate and removal of pharmaceutical residues in the aquatic environment in urban areas. *Water Sci. Technol.* 46, 81–88. doi: 10.2166/wst.2002.0060

Jacobson, C. R. (2011). Identification and quantification of the hydrological impacts of imperviousness in urban catchments: a review. *J. Environ. Manag.* 92, 1438–1448. doi: 10.1016/j.jenvman.2011.01.018

Kaiper, G. (2004). *Water Flow Charts-2000*. Livermore, CA: Lawrence Livermore National Lab (LLNL).

Kay, D., Edwards, A. C., Ferrier, R. C., Francis, C., Kay, C., Rushby, L., et al. (2007). Catchment microbial dynamics: the emergence of a research agenda. *Prog. Phys. Geogr.* 31, 59–76. doi: 10.1177/0309133307073882

Konrad, C. P. (2003). Effects of *Urban Dev*elopment on *Floods*. Tacoma: US Geological Survey. doi: 10.3133/fs07603

Lambert, A. O. (2002). International report: water losses management and techniques. *Water Sci. Technol. Water Supply* 2, 1–20. doi: 10.2166/ws.2002.0115

McGrane, S. J. (2016). Impacts of urbanisation on hydrological and water quality dynamics, and urban water management: a review. *Hydrol. Sci. J.* 61, 2295–2311. doi: 10.1080/02626667.2015.1128084

Mitchell, V. G., and Diaper, C. (2006). Simulating the urban water and contaminant cycle. *Environ. Model. Softw.* 21, 129–134. doi: 10.1016/j.envsoft.2005.03.003

Nandagiri, R. (2023). *8 Billion Lives, Infinite Possibilities: The Case for Rights and Choices*. New York, NY: UNFPA.

O'Driscoll, M., Clinton, S., Jefferson, A., Manda, A., and McMillan S. (2010). Urbanization effects on watershed hydrology and in-stream processes in the southern United States. *Water* 2, 605–648. doi: 10.3390/w2030605

Packman, J. (1980). *The Effects of Urbanisation on Flood Magnitude and Frequency*. Wallingford: Institute of Hydrology

Peal, A., Evans, B., Ahilan, S., Ban, R., Blackett, I., Hawkins, P., et al. (2020). Estimating safely managed sanitation in urban areas; lessons learned from a global implementation of excreta-flow diagrams. *Front. Environ. Sci.* 8:1. doi: 10.3389/fenvs.2020.00001

Platts, K., and Hua Tan, K. (2004). Strategy visualisation: knowing, understanding, and formulating. *Manag. Decis.* 42, 667–676. doi: 10.1108/00251740410538505

Schütze, M., and Robleto, G. (2010). *Challenges of Water and Wastewater Management in the Desert Megacity of Lima/Peru-How Can Macromodelling Help?* Durham, NC: NOVATECH.

Sieber, J., and Purkey, D. (2015). *WEAP User Guide*. Somerville, MA: Stockholm Environment Institute, U.S. Center.

Staufer, P., and Ort, C. (2012). "*Mikroverunreinigungen aus diffusen Quellen: Faktenblatt, Diffuse Mikroverunreinigungs-Emissionen aus Siedlungen (DIMES)*," in *German (Fact sheet, Diffuse micropollutantemissions from urban areas (DIMES))*. Study for the Swiss Federal Office for the Environment (FOEN), Eawag, Dübendorf, Switzerland. Available online at: https://www.dora.lib4ri.ch/eawag/islandora/object/eawag%3A14774 (accessed February 14, 2024).

Van Metre, P. C, Mahler, B. J., and Furlong, E. T. (2000). Urban sprawl leaves its PAH signature. *Environ. Sci. Technol.* 34, 4064–4070. doi: 10.1021/es991007n

Willuweit, L., and O'Sullivan, J. J. (2013). A decision support tool for sustainable planning of urban water systems: presenting the dynamic urban water simulation Model. *Water Res.* 47, 7206–7220. doi: 10.1016/j.watres.2013.09.060

WorldBank (2023). *Urban Development*. Available online at: https://www.worldbank.org/en/topic/urbandevelopment/overview (accessed February 14, 2024).

frontiers | Frontiers in Water

TYPE Original Research
PUBLISHED 18 April 2024
DOI 10.3389/frwa.2024.1380761

OPEN ACCESS

EDITED BY
Jahangeer Jahangeer,
University of Nebraska-Lincoln, United States

REVIEWED BY
Akshay Chaudhary,
Chitkara University, India
Abhijit Biswas,
Assam University, India
Mohit Kumar,
PEC University of Technology Chandigarh, India, in collaboration with reviewer AB

*CORRESPONDENCE
Aditya Kapoor
✉ adityain2003@gmail.com;
✉ aditya.kapoor@iitrpr.ac.in

RECEIVED 02 February 2024
ACCEPTED 01 April 2024
PUBLISHED 18 April 2024

CITATION
Kapoor A and Kashyap D (2024) Inverse problem assisted multivariate geostatistical model for identification of transmissivity fields.
Front. Water 6:1380761.
doi: 10.3389/frwa.2024.1380761

Inverse problem assisted multivariate geostatistical model for identification of transmissivity fields

Aditya Kapoor[1]* and Deepak Kashyap[2]

[1]Department of Civil Engineering, Indian Institute of Technology Ropar, Rupnagar, India, [2]Retired, Rupnagar, India

Groundwater models often require transmissivity (*T*) fields as an input. These *T* fields are commonly generated by performing univariate interpolation of the *T* data. This *T* data is derived from pumping tests and is generally limited due to the large costs and logistical requirements. Hence *T* fields generated using this limited data may not be representative for a whole study region. Groundwater models often require transmissivity (*T*) fields as an input. These *T* fields are commonly generated by performing univariate interpolation (using kriging, IDW etc.) of the *T* data. This *T* data is derived from pumping tests and is generally limited due to the large costs and logistical requirements. Hence, the *T* fields generated using this limited data may not be representative for the whole study region. This study presents a novel cokriging based methodology to generate credible *T* fields. Cokriging - a multivariate geostatistical interpolation method permits incorporation of additional correlated auxiliary variables for the generation of enhanced fields. Here abundantly available litholog derived saturated thickness data has been used as secondary (auxiliary) data given its correlation with the primary *T* data. Additionally, the proposed methodology addresses two operational problems of traditional cokriging procedure. The first operational problem is the poor estimation of variogram and cross-variogram parameters due to sparse *T* data. The second problem is the determination of relative contributions of primary and secondary variable in the estimation process. These two problems have been resolved by proposing a set of novel non-bias conditions, and linking the interpolator with a head based inverse problem solution for credible estimation of these parameters. The proposed methodology has been applied to Bist doab region in Punjab (India). Additionally, base line studies have been performed to elucidate the superiority of the proposed cokriging based methodology over kriging in terms of head reproducibility.

KEYWORDS

cokriging, geostatistics, groundwater modeling, inverse problem, parameter estimation

1 Introduction

Distributed groundwater flow models are being increasingly used for regional planning of groundwater development (McKinney and Lin, 1994; Marino, 2001; Bhattacharjya and Datta, 2005; Miller et al., 2009; Ghosh and Kashyap, 2012; Singh et al., 2016; Escriva-Bou et al., 2020; Zeinali et al., 2020; Maliva et al., 2021; Mamo et al., 2021; Izady et al., 2022; Bailey et al., 2023). These models invariably require values of transmissivity (*T*) at the spatial grid cells.

Pumping tests can provide data of these values only at a limited number of locations due logistical difficulties and large expenses involved. The present practice for bridging this data gap is centered around two broad strategies *viz.* interpolation alone, or joining of interpolation with an inverse problem (IP) solution. The former practice involves interpolating cell values of T (or hydraulic conductivity) employing only the available measured values (Anderson et al., 2015; Dickson et al., 2019). The latter practice invokes the interpolator and also a flow model so that more information can be used to obtain better estimates of T using historical head measurements through the use of an optimizer (Yeh, 2015). Employing measured T values and historical head fields, it aims at producing hydraulically consistent T field that has better predictive capability, than would be obtained using T values alone.

Commonly used interpolation functions include finite element linked basis functions (Yoon and Yeh, 1976), spline, polynomial (Chapra and Canale, 2010; Yao et al., 2014; Adhikary et al., 2017), and geostatistical tools viz. kriging (RamaRao et al., 1995; Kitanidis, 1997; Oliver and Webster, 2015; Kavusi et al., 2020; Cui et al., 2021; Kapoor and Kashyap, 2021; Senoro et al., 2021; Panagiotou et al., 2022; Júnez-Ferreira et al., 2023) and cokriging (Aboufirassi and Mariño, 1984; Ahmed and de Marsily, 1987; Ahmed et al., 1988; Kitanidis, 1997; Wackernagel, 2003; Belkhiri et al., 2020; Zawadzki et al., 2021; Zhao et al., 2022; Christelis et al., 2023). The present study centers around cokriging, that is a multivariate form of the univariate geostatistical tool kriging (Kitanidis, 1997; Oliver and Webster, 2015). Kriging is the best linear unbiased interpolator of a regionalized stationary variable preserving its measured values. The interpolation is based upon the spatial statistics of measured values. The spatial statistics is estimated by a variogram which depicts auto-semivariance of the variable as a function of the separation distance. The interpolated value is expressed as a linear combination of the measured values, and the weights are estimated from the requirements of minimized mean square error and the unbiasedness of the interpolation.

Cokriging, based upon similar concepts, introduces an additional stationary regionalized secondary variable (B) that is *a priori* known to be correlated to the variable subjected to interpolation (termed as primary variable). The spatial statistics in this case are defined in terms of variograms of the primary and secondary variables, and cross-variogram between the primary and secondary variables. The latter describes the variation of cross-semivariance between T and B as a function of the separation distance. The interpolated value in this case is expressed as linear combination of the measured values of the primary and secondary variables as expressed in Eq. 1.

$$T_o = \sum_i \alpha_i T + \sum_j \beta_j B_j \quad (1)$$

Where T_o is the interpolated value of primary variable at an unsampled location, T_i and B_j is the ith and jth measurements of the primary and secondary variable, respectively. The set of weights- α and β appearing there in are derived from the twin requirements of minimized mean square error and the unbiasedness of the estimation. Cokriging has been used for generating T (or hydraulic conductivity) fields with varying secondary variables like hydraulic head (Kitanidis and Vomvoris, 1983; Yeh et al., 1995), specific capacity (Aboufirassi and Mariño, 1984; Ahmed and de Marsily, 1987), electrical conductivity (Ahmed et al., 1988).

The T fields emanating from interpolation approach may not always be capable of simulating realistic heads and velocity fields due to limited number of measurements, and inaccuracies in the measurements themselves. This problem is overcome by taking recourse to the joined interpolator- inverse problem (IP) solutions. IP solutions are typically based upon linked simulation optimization (LSO) approach (Gannett et al., 2012; Alam and Umar, 2013; Davis et al., 2015). The simulator component of the IP is further joined to the chosen interpolator treating nodal transmissivities as the unknown IP decision variables. The associated dimensionality problem (Yeh, 2015) is overcome by restricting the number of unknown nodal transmissivities to a manageable limit in the context of non-linear optimization. The chosen nodal points may be the sites of measured T values (pumping test sites) or un-sampled locations termed as pilot points (RamaRao et al., 1995; Anderson et al., 2015). The former strategy permits moderation of the measured values as per prescribed plausibility criteria (RamaRao et al., 1995) to render them optimally consistent with the historical heads and the flow equation. The reported studies invoking interpolator-IP joining have generally used kriging (Certes and de Marsily, 1991; LaVenue and Pickens, 1992; RamaRao et al., 1995; Jazaei et al., 2019) treating the geostatistical parameters to be known *a priori*. These solutions typically aim at reaching optimal estimates of the decision variables that yield least-squares of the mismatch between the simulated and the observed head fields (RamaRao et al., 1995; Anderson et al., 2015). The estimates are expected to provide a transmissivity field that is optimally consistent with the observed head fields and the governing differential equation, and hence is capable of producing credible heads and velocity fields. Yeh et al. (1995) has presented an alternative form of the interpolator-IP joining for ensuring this consistency wherein transmissivity is cokriged by employing T and heads as primary and secondary variables, respectively. Consistency of the T field with the flow equation is ensured by iteratively simulating additional heads, treating the measured values as constant heads. The T field is re-cokriged iteratively employing the measured T and the enhanced data base of head values. This approach is similar to the interpolator-IP methodology that permits generation of consistent head and transmissivity fields.

Although cokriging has been in vogue for some time, the authors came across two major operational problems while implementing it for the generation of T fields treating B as the secondary variable. The first one relates to generation of the geostatistical parameters. The parameters essentially emanating from the spatial statistics of measured values of T and B, comprise variogram parameters of T and B, and cross-variogram parameters of the cross variogram between T and B. Variograms depict variation of auto-semivariance (say of T or B) with the separation distance. Variograms of T and B are typically derived from the respective measured values, and the cross-variogram from co-located measurements of T and B. It may be recalled that cokriging essentially permits supplementing sparse data of primary variable (say T) by abundantly available measurements of the

Abbreviations: BL, baseline; ESA, European space agency; IADI, iterative alternating direction implicit; IP, inverse problem; LSO, linked simulation optimization; LULC, land use land cover; SHD, secondary hydrogeological data; SUMT, sequentially unconstrained minimization technique; SC, specific capacity; T, transmissivity (primary variable); OW, observation well.

correlated secondary variable (say *B*). This pattern of data availability inherently inhibits a robust development of the variogram of the primary variable due to sparseness of its data. In addition, the development of the cross-variogram also gets compromised on account of still sparser co-located measurements of the primary and secondary variables. This conjecture is well honored by the variogram of *T* and cross variogram of *T-SC* (specific capacity – chosen as the secondary variable) presented by Aboufirassi and Mariño (1984). Results from the present study (presented subsequently) are also consistent with it. This problem to some extent has been addressed by Ahmed et al. (1988) by supplementing the poorly available data of the primary variable through univariate interpolation – which may jeopardize the advantage of the multivariate interpolation. The variograms and cross-variograms may also be generated analytically (Yeh et al., 1995), but the underlying assumptions may not always hold.

The other problem with the implementation of cokriging arises from the requirement of setting up/formulating unbiasedness conditions. These conditions, requiring the expectation of the interpolated value (Eq. 1) to be equal to the mean value of the primary variable ($\overline{T}$), is expressed by the following equation by Eq. 2.

$$E\left[\sum_i \alpha_i TP_i + \sum_j \beta_j BP_j\right] = \overline{T} \tag{2}$$

Where *TP* and *BP* are the measured data of primary and secondary variable. Assuming both *TP* and *BP* to be first order stationary, the unbiasedness condition is simplified to the following form by Eq. 3.

$$\sum_i \alpha_i \overline{TP} + \sum_j \beta_j \overline{BP} = \overline{T} \tag{3}$$

Under a common scenario of the primary and secondary variables having different means and dimensions (or having indeterminate dimensions due to the log-transformation), the only way Eq. 3 can be satisfied with dimensional propriety is to split it into following two equations (Isaaks and Srivastava, 1989; Wackernagel, 2003).

$$\sum_i \alpha_i = 1 \tag{4}$$

$$\sum_j \beta_j = 0 \tag{5}$$

Eq. 5 read with Eq. 1 essentially implies that the mean contribution of the secondary variable values towards the interpolation is constrained to zero on account of the dimensional inconsistency. This may trivialize the role of secondary variable in the interpolation process. Further, it may also lead to unexpected/unrealistic negative estimates (Isaaks and Srivastava, 1989).

It follows from the preceding discussion that the data derived variogram of *T* and cross-variogram of *T-B* may not be credible due to the data sparseness. Accordingly, these spatial statistics parameters are treated as the IP decision variables in the proposed interpolator-IP method. Alternative non-biasedness conditions are proposed that ensure an optimal role for the primary as well as the secondary variable. The relative roles of the participating variables are quantified by introducing a distribution parameter. This unknown parameter is also treated as a decision variable. For the sake of dimensional propriety, the cokriging is conducted without taking log transforms of the participating variables. This may to some extent compromise the maximum likelihood of the solution since log transformed variables may follow Gaussian distribution more closely. Nevertheless, the solution with somewhat compromised Gaussian distribution requirement may be viewed as based upon minimization of the weighted sum of squares of the interpolation errors (Hoeksema and Kitanidis, 1985). This compromise may be considered as a tradeoff between the requirement of assigning optimal role to abundant data of secondary variable and ensuring likelihood of the solution. The deterioration of the solution on account of some loss of likelihood may be compensated by improved solution by way of by letting the secondary variable measurements play their due role in the interpolation process. This is amply illustrated in the model application wherein a much larger role (70%) of the *BP* data is depicted by the optimized weighing parameter – quite consistent with its data size (58 *BP* data points against only 15 *TP* measurements). The solution may also improve by way of avoiding negative weights of secondary variables and the consequent deterioration of the solution (Isaaks and Srivastava, 1989). Although mostly the IP-kriging joining studies require the geostatistical parameters to be known *a priori*, a few studies have incorporated their estimation in the IP solution (terming them as *hyperparameters*) in the context of 3-D transient hydraulic tomography (Cardiff and Barrash, 2011) and estimation of aquifer diffusivity and Richard's equation parameters (Rai and Tripathi, 2019).

Alternate IP decision variables/parameters are proposed notwithstanding the current practice of considering the nodal transmissivities as the IP decision variables treating the geostatistical parameters of the interpolator to be known *a priori*. However as shall be demonstrated subsequently, the geostatistical parameters, especially in the context of cokriging may not always be known credibly. As such, the present study essentially explores another option regarding choice of the IP decision variables in the framework of the interpolator- IP method. Invoking cokriging as the interpolator, the proposed method treats certain poorly known (or unknown) structural parameters of the interpolator as the IP decision variables. This approach thus, simultaneously calibrates the interpolator and provides the desirable hydraulic consistency between the transmissivity and the observed head fields, without modifying the data base of measured *T* or head values. However, the approach is based on the assumption of a good correlation between Transmissivity and saturated thickness. The correlation between the two is honored as long as the hydraulic conductivity of the conducting material is more or less lies in a close range.

The methodology has been illustrated by applying it to Bist doab which is an interbasin falling in the state of Punjab (India). The area has a relatively sparse transmissivity data base that is supplemented by abundantly available well logs. Therefore, it is quite suitable for illustrating the proposed cokriging based model.

2 Present study

The present study focuses on developing a model for generating *T* fields employing a multivariate geostatistical interpolation technique cokriging, joined with a head based inverse problem (IP) solution. The

joining aims at estimation of poorly known/unknown parameters of cokriging, ensuring optimal consistency between the transmissivity field and the heads. The model has been designed to interpolate T using the measured values of transmissivity and the correlated variable (B) representing the permeable part of the saturated-thickness (termed from now on as saturated thickness for the sake of brevity). In accordance with cokriging nomenclature, T and B are treated as the primary and the secondary variable, respectively. This multivariate approach is useful since a T field generated exclusively from pumping test values of transmissivity (TP data) may not be hydrogeologically realistic due to the sparseness of pumping tests. On the other hand, a T field interpolated compositely from sparse TP data and usually abundant values of the saturated thickness (BP data) may turn out to be more realistic. The interpolated value (T_o) in this case is expressed as linear combination of the measured values of T and B as per the following equation.

$$\mathrm{T_o} = \sum_i \alpha_\mathrm{i} \mathrm{TP_i} + \sum_j \beta_\mathrm{j} \mathrm{BP_j} \tag{6}$$

The set of weights- α and β appearing there in are derived from the twin requirements of minimized mean square error and the unbiasedness of the estimation. These requirements appear in the form of set of equations that are also known as cokriging equations.

2.1 Model development

Two segments of the proposed model viz. T-B cokriging and its joining with IP are discussed in the following Sections.

2.1.1 Proposed T-B cokriging

In the present study, cokriging has been employed to generate the transmissivity field treating pumping test derived transmissivities (TP) as primary variable data and lithologs derived saturated thickness (BP) as secondary variable data. Recalling that cokriging is essentially applicable to the first order stationary data only (Olea, 2018), it is necessary to identify the trends (if any) in (TP) and (BP) data and subtract them from the respective raw data to arrive at the de-trended data (TP_D and BP_D) respectively (this step has been illustrated subsequently). The envisaged cokriging interpolates detrended transmissivity (T_{Do}) at an unsampled/target location (x_o) as a weighted sum of TP_D and BP_D data as follows.

$$\mathrm{T_{Do}} = \sum_{\mathrm{i=1}}^{\mathrm{n}} \alpha_\mathrm{i} \mathrm{TP_{Di}} + \sum_{\mathrm{j=1}}^{\mathrm{m}} \beta_\mathrm{j} \mathrm{BP_{Dj}} \tag{7}$$

Where, n, m = number of TP_D and BP_D data points within a prescribed search radius, α_i(dimensionless) = unknown weight assigned to ith TP_D data, and β_j($\mathrm{LT^{-1}}$) = unknown weight assigned to jth BP_D data. Further, the trended transmissivity at target location (T_o) is estimated by adding the corresponding trend ξ_o.

$$\mathrm{To} = \mathrm{TDo} + \xi o \tag{8}$$

These weights are derived from the criterion of the minimization of variance of estimation error and ensuring unbiasedness of the interpolation (Kitanidis, 1997). These two criteria jointly lead to a set of $(n+m)$ normal equations (Wackernagel, 2003) in terms of semivariance (γ_{TT}) of T, semivariance (γ_{BB}) of B, and cross-semivariance (γ_{TB}) of T and B.

Discrete point values of the functions γ_{TT}, γ_{BB} and γ_{TB} for varying Euclidean distance (h) are obtained by "pairing" the (TP_D), (BP_D) and (TP_D-BP_D) data points with varying h. Subsequently parameters (say $\boldsymbol{\theta}_1$, $\boldsymbol{\theta}_2$ and $\boldsymbol{\theta}_3$ respectively) of the chosen theoretical models are estimated by least-squares criterion. The most-commonly used theoretical models are Gaussian, exponential and hole-effect model (Kitanidis, 1997).

2.1.2 Unbiasedness equations

From the dimensional consideration, the coefficients (α_i) appearing in the interpolation equation (Eq. 1) are dimensionless. And the other set of coefficients (β_j) have dimension of hydraulic conductivity ($\mathrm{LT^{-1}}$). Accordingly, following two equations are presented to ensure the unbiasedness of the interpolation.

$$\sum_i \alpha_\mathrm{i} = \lambda \tag{9}$$

$$\sum_j \beta_\mathrm{j} = (1-\lambda)\mathrm{K}* \tag{10}$$

Where, λ = an unknown dimensionless parameter and K^* = a representative local hydraulic conductivity. In the present study K^* has been indexed as ($\overline{TP}_D/\overline{BP}_D$). Where, $\overline{TP}_D$, $\overline{BP}_D$ = arithmetic means of TP_D and BP_D values invoked in the interpolation equation (Eq. 6). The parameter λ (value lying between 0 and 1) is viewed as a distribution factor indexing the relative contributions of TP and BP data (as TP_D and BP_D) towards the estimation of T_{Do} and hence T_o.

The corresponding expectation ($\overline{T}_{Do}$) of interpolated detrended transmissivity (Eq. 6) is as follows by Eq. 11.

$$\overline{\mathrm{T}}_{\mathrm{Do}} = \sum_{\mathrm{i=1}}^{\mathrm{n}} \alpha_\mathrm{i} \overline{\mathrm{TP}}_\mathrm{D} + \sum_{\mathrm{j=1}}^{\mathrm{m}} \beta_\mathrm{j} \overline{\mathrm{BP}}_\mathrm{D} \tag{11}$$

Where $\overline{TP}_D$ = mean detrended transmissivity and $\overline{BP}_D$= mean detrended saturated thickness Eq. 12.

Using Eqs. 8, 9 the expectation is rewritten as follows by Eq. 12.

$$\overline{\mathrm{T}}_{\mathrm{Do}} = \lambda \overline{\mathrm{TP}}_\mathrm{D} + (1-\lambda)\mathrm{K}^* \overline{\mathrm{BP}}_\mathrm{D} \tag{12}$$

Recalling that $\overline{TP}_D$= $K^*\overline{BP}_D$, the expectation turns out to be equal to the mean value.

$$\overline{\mathrm{T}}_{\mathrm{Do}} = \overline{\mathrm{TP}}_\mathrm{D} \tag{13}$$

Thus, Eqs. 9, 10 apart from ensuring the dimensional consistency, lead to unbiased interpolation by preserving the mean transmissivity. Further, they ensure data-driven flexible weighting of the relative contributions from (T) and (B) data towards the interpolation. Optimal value of the distribution parameter (λ) is arrived at through

the envisaged inverse problem solution – as discussed in the subsequent Section.

2.1.3 Joining of cokriging with IP

As discussed earlier, sparseness of (*TP*) data may lead to relatively unreliable estimation of parameters of *T* variogram ($\boldsymbol{\theta}_1$) and *T*-*B* cross-variogram ($\boldsymbol{\theta}_3$). Further, the distribution parameter (λ) incorporated in the unbiased equations also needs to be estimated. In the present model these issues have been addressed by joining the *T*-*B* cokriging with a head-based IP solution. The IP is designed to yield optimal estimates of these poorly known/unknown hyperparameters ($\boldsymbol{\theta}_1$, $\boldsymbol{\theta}_3$ and λ), designating them henceforth as IP parameters/decision variables ($\boldsymbol{\Omega}$). The proposed IP model comprising a head simulator linked to an optimizer, aims at arriving at such estimates of the IP parameters which minimize the mismatch (quantified by *Z* – refer Eq. 1) between the observed and simulated head fields. The simulated head field (*h*) is generated by solving an appropriate differential equation governing groundwater flow (e.g., MODFLOW). The simulation requires *T* field and other data comprising recharge/withdrawals, boundary conditions, aquifer parameters etc. Further, historical head fields are required for computing the mismatch function (*Z*). These related data (other than *T* field) are termed herein as secondary hydrogeological data (SHD) and are assumed to be known *a priori*. The *T* field can in-turn be derived from discrete point (*TP*, *BP*) data and the cokriging parameters. The latter may comprise known parameters ($\boldsymbol{\theta}_2$) and poorly determined/unknown ones ($\boldsymbol{\Omega} = \boldsymbol{\theta}_1$, $\boldsymbol{\theta}_3$ and λ). Therefore, for given set of [(SHD), $\boldsymbol{\theta}_2$ and (*TP* and *BP*) data] *Z* would be an exclusive function of ($\boldsymbol{\Omega}$). As such the inverse problem is posed as optimization problem presented in Eq. 14.

$$Minimize\ Z = \sum_i (\hat{h}_i - h_i)^2 \tag{14}$$

with respect to $\boldsymbol{\Omega}$.

Where, h_i= observed head at *i*th space–time point, and h_i= corresponding simulated head. This minimization requires linkage of a simulator with an optimizer within the framework of LSO (linked simulation optimization) approach. In this approach, an optimizer is linked to a simulator. The optimizer algorithmically generates trial set of decision variable and this trial set is employed by simulator to compute state variables. This process is continued until the objective function is minimized (or maximized) as per the criteria adopted. The simulator comprises three components viz. computation of *T* field, simulation of corresponding head fields, and finally computation of *Z*.

It may be noted that unlike kriging, the cokriging (Eq. 7 along with Eq. 8) is not an "exact" interpolator due to participation of *BP* data in the interpolation of *T*. As such, the IP-cokriged transmissivities at the sampling points will not match with the corresponding measured values – which nonetheless is quite a common scenario in practical calibrations (Davis et al., 2015). The mismatch will increase as λ decreases due to associated increasing role of *BP* data (and consequent decreasing role of *TP* data) in the interpolation process. However, with excessively diminished role of *TP* data the generated *T* field may display large departure from the *TP* data and hence may not be plausible. This situation may be tackled by enforcing an additional objective function (Z_1) depicting the departure and conducting multi-objective minimization of *Z* and Z_1. This has been illustrated in the example presented in the following "Model Application" Section.

2.2 Model application

The model discussed in the preceding Sections has been illustrated by applying it to Bist doab which is an interbasin bounded by perennial rivers Satluj and Beas, and Shivalik mountains (Figure 1). Details of the illustration are included in the following text.

2.2.1 Study area

The study area spanning over 8,040 km^2 is inhabited by 5.26 million people (Economic and Statistical Organization, Government of Punjab, 2016). In terms of Land Use and Land Cover, approximately 80% of the geographical area in this region is covered by agricultural tracts. The detailed LULC analysis for the study area has been performed using ESA WorldCover (Zanaga et al., 2022) dataset in Google Earth Engine. ESA WorldCover provides a global LULC map for the year 2021 at a 10 m resolution. It provides 11 classes such as tree cover, shrubland, grassland, cropland, builtup area, bare lands, snow etc. Additional details for the same are presented in the Supplementary material. The underlying aquifer is composed of alluvium deposits consisting dominant sand strata with intermittent clay layers. Since the clay layers are nearly horizontal and spatially intermittent, the formation may be deemed to be a single horizontally isotropic unconfined aquifer. As per reported data, its saturated thickness varies from 42 m to 156 m and the transmissivity from 540 m^2/day to 1830 m^2/day from north-east to south-west (Central Ground Water Board, 2009; Singh et al., 2013). The area is served by southwest monsoon system with normal rainfall varying from 432 mm in southwest region to 759 mm in the north-east. A large part of annual rainfall (about 77%) occurs during monsoon season extending from June to October. The groundwater resource is primarily derived from the rainfall recharge with a relatively smaller contribution from two canal systems serving the area. The area is subjected to intensive groundwater development with about 95% of the withdrawals utilized for meeting irrigation demands. Contribution of the canal systems towards the irrigation demands is quite small. Rice and wheat are major crops of the area, with the former cultivated during monsoon season (locally referred as kharif season) and the latter in non-monsoon season (locally referred as rabi season). Consequent to the intensive agricultural groundwater development, especially for water intensive rice crop, the area is experiencing a watertable decline.

2.2.2 Data base

The envisaged cokriging requires sample *T* data (*TP*) and the sample *B* data (*BP*). Further, the proposed IP solution requires historical head fields and the corresponding withdrawals, recharge and boundary conditions. These data were gathered from several state and central government water resources agencies. Pumping test based *TP* data from 15 test sites (Figure 1) and well-log derived *BP* data from 58 bore sites were employed for the study. The available well logs were rather elementary

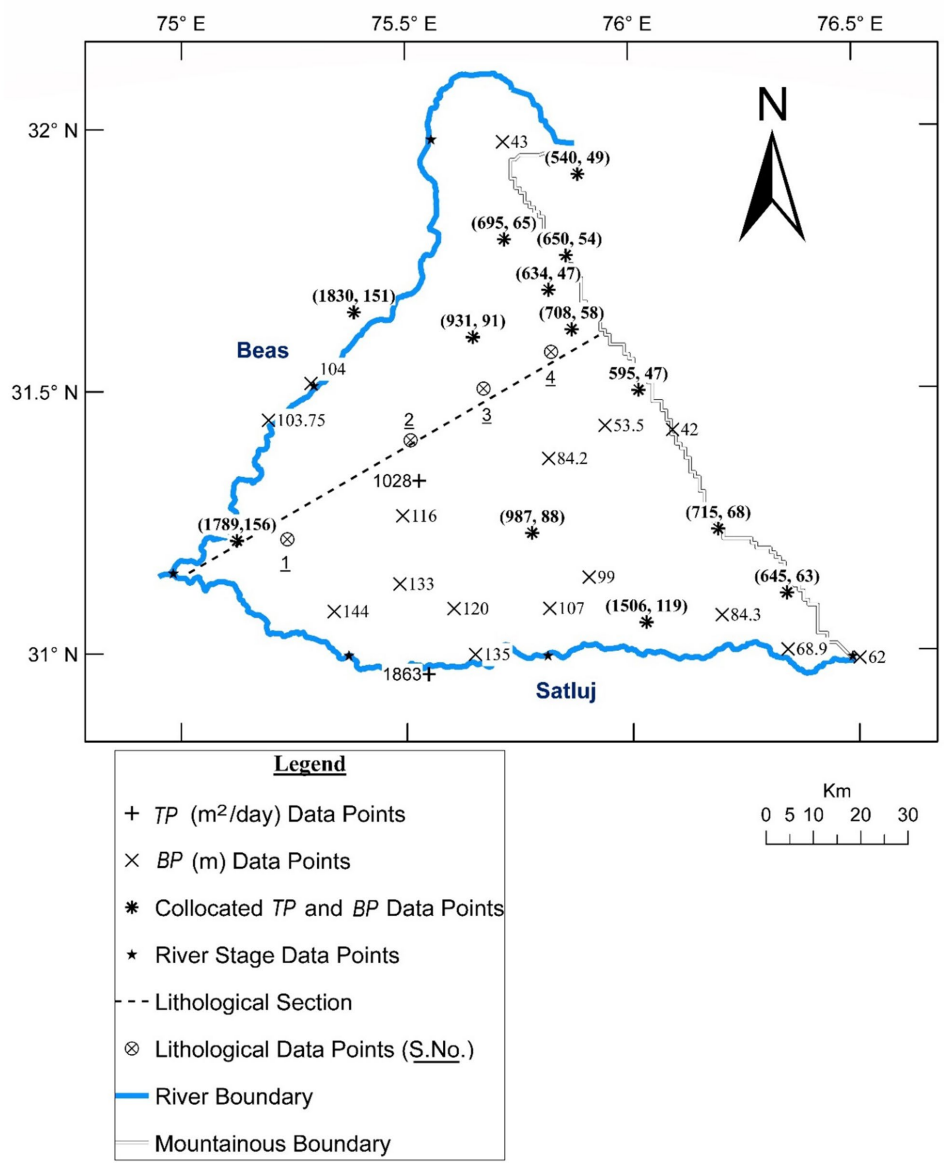

FIGURE 1
Index map of study area.

displaying only "sand" and "clay" layers – broadly referring to permeable and non-permeable fractions, respectively. The saturated thickness values (*BP*) were arrived at by adding all the 'sand' thicknesses captured in the respective well logs. A few well log sites along with the corresponding values of saturated thickness are shown in Figure 1. Lithological profile for a representative section (refer Figure 1) along north-east direction is shown in Figure 2. Thirteen of the fifteen (*TP*) points have co-located (*BP*) points – leading to as many co-located (*TP-BP*) data points (Figure 1).

Watertable data comprises observations from 91 wells at six discrete times over a period of three years extending from June-2014 to October-2016. These discrete times represent three pre-monsoon and two post-monsoon states. River stage data from six locations (three on Satluj, two on Beas and one at the confluence) at the same discrete times were employed for assigning the boundary conditions (Figure 1). The study area comprises 29 administrative blocks (Figure 3) and seasonal blockwise recharge/withdrawals and block-wise specific yield data were derived from published reports (CGWB, 2013).

2.2.3 Correlation between primary and secondary variables

The proposed cokriging model is an interpolator of the primary variable transmissivity (T) wherein the saturated thickness (B) is incorporated as the secondary variable. Although the correlation between variables T and B is depicted by the definition of T (i.e., $T = KB$), additional analyses were conducted to establish the necessary correlation between their respective sample values. As a first step, the co-located T and B data are plotted on linear scales (Figure 4). The scatter-points display a consistent rise of T as B increases – implying a positive correlation between the two. The points tend to fall between two enveloping

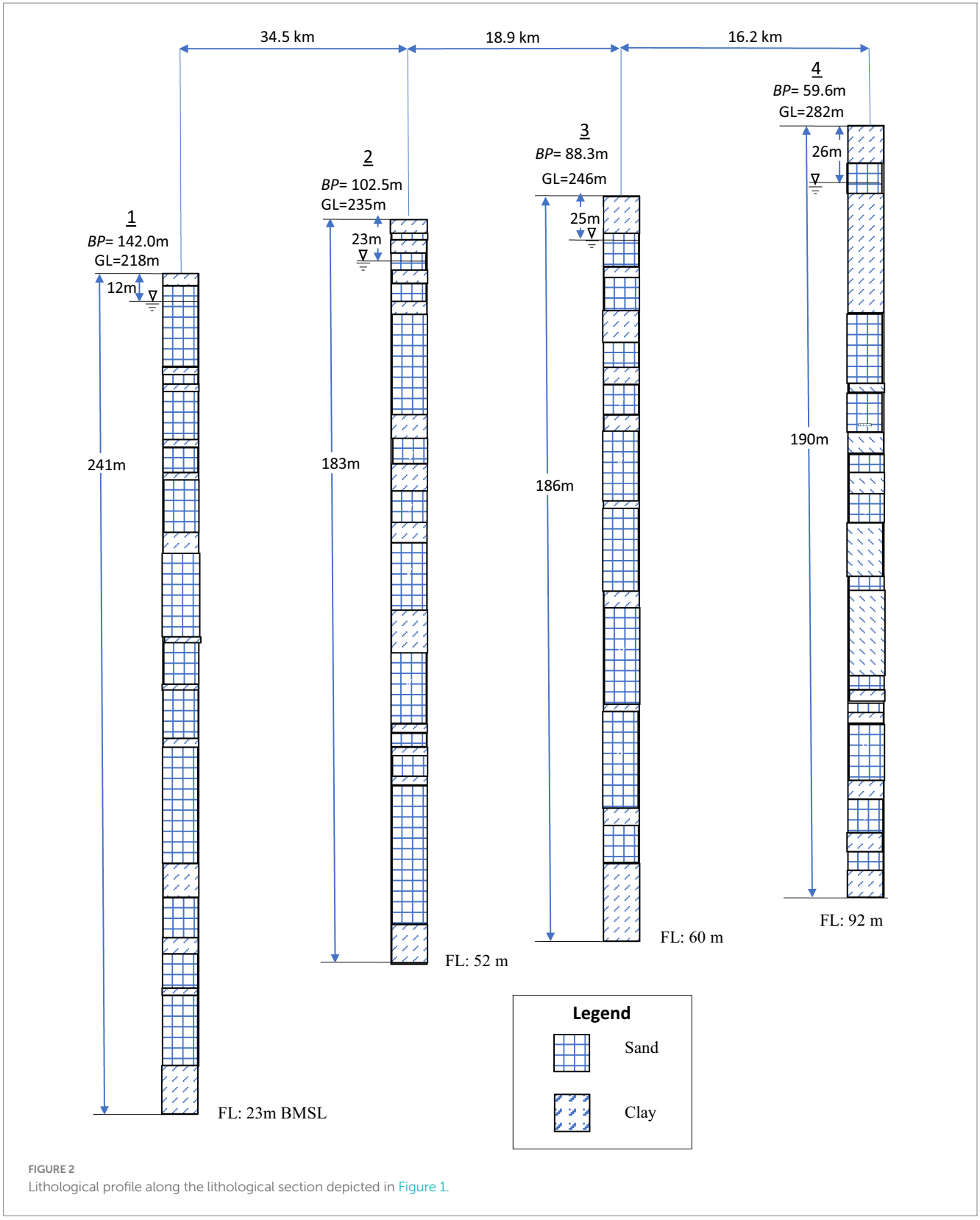

FIGURE 2
Lithological profile along the lithological section depicted in Figure 1.

straight lines ($TP = 10.2BP$, and $TP = 13.5BP$) – implying that K may be varying in the range (10.2 to13.5 m/day) in the region encompassed by the measurement points. Further, the correlation between T and B was established objectively by developing a cross- correlogram (Wackernagel, 2003) between T and B (Figure 5). This figure depicts the variation of the coefficient of correlation between T and B as a function of separation distance (h). It may be seen that a strong correlation (0.91) exists between co-located ($h = 0$) T and B values. The correlation vanishes asymptotically at a distance of about 35 km.

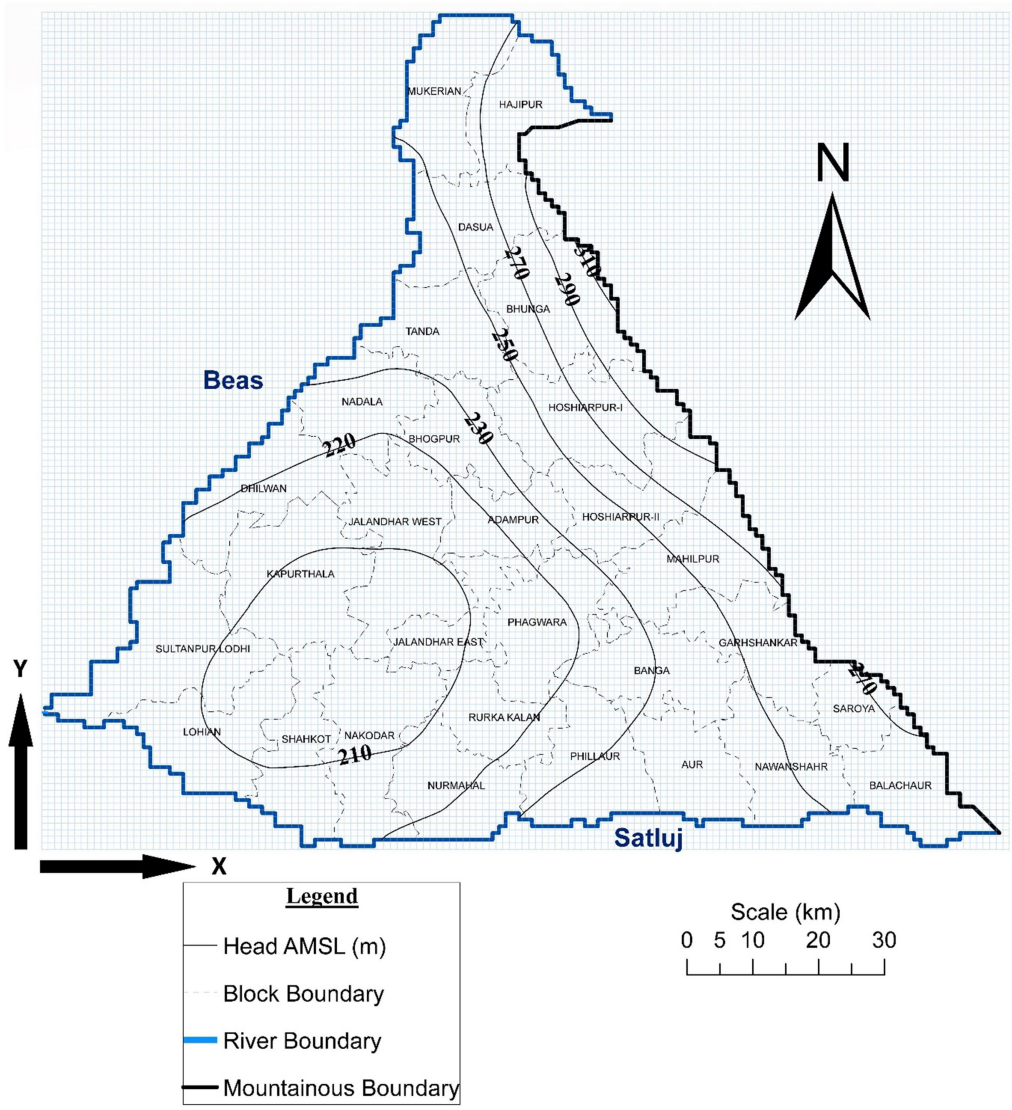

FIGURE 3
Block Boundaries and adopted initial condition.

2.2.4 Detrending raw data

The available data (*TP* and *BP*) were detrended to fulfill the requirement of first order stationarity. Detrending has been performed by fitting least-squares 2-D plane equations in terms of X and Y (Figure 3), through *TP(X,Y)* and *BP(X,Y)* data points. Parameters of these planes viz., intercepts (T_0 and B_0 respectively) and gradients (trends) in x and y directions (I_{XT} and I_{YT}; I_{XB} and I_{YB} respectively) were estimated by regression analyses (Table 1). Finally, *T* and *B* data were detrended by simply subtracting the trend terms derived from the respective gradients.

2.2.5 Generation of variograms/cross-variogram

These geostatistical attributes were generated employing the detrended data of TP_D (15 Nos.), BP_D (58 Nos.) and co-located (TP_D and BP_D) (13 Nos.). These data were utilized for developing experimental values of semivariances (γ_{TT}, $\gamma_{BB}$and γ_{TB}) for an array of separating distances (*h*). These discrete point data of experimental variograms/cross-variogram are presented in Figures 6–8 respectively.

Subsequently a theoretical model was fitted to each experimental variogram/cross-variogram by the least squares approach. The models were selected from an array of reported models (Kitanidis, 1997), on the basis of the "best" least-squares fit characterized by highest R^2. The reported models have two main characteristics viz. sill (σ^2) and range (*R*). Whereas the sill is the limiting value of the semivariance as *h* tends to infinity, the range is the distance (*h*) at which the semivariance equals 95% of the sill. Gaussian and exponential variogram models (Kitanidis, 1997) were adopted for *T* and *B*, respectively. Gaussian cross-variogram model was adopted for *T-B* cross variogram Estimated geostatistical parameters for these models are presented in Table 2.

As expected, R^2 for the model of *B* variogram is higher apparently on account of large number of sample (*BP*) points. On the other hand, the statistic values for the models of *T* variogram and *T-B*

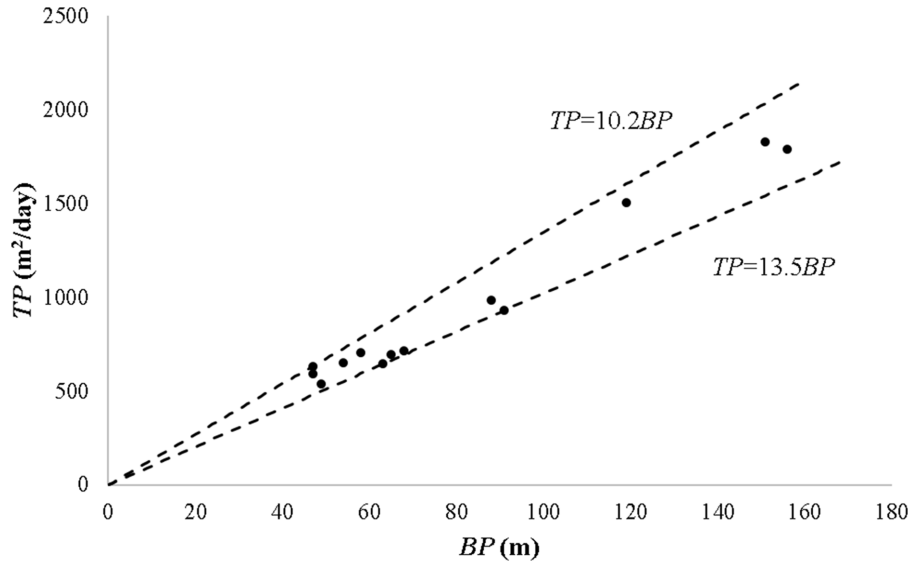

FIGURE 4
Variation in hydraulic conductivity.

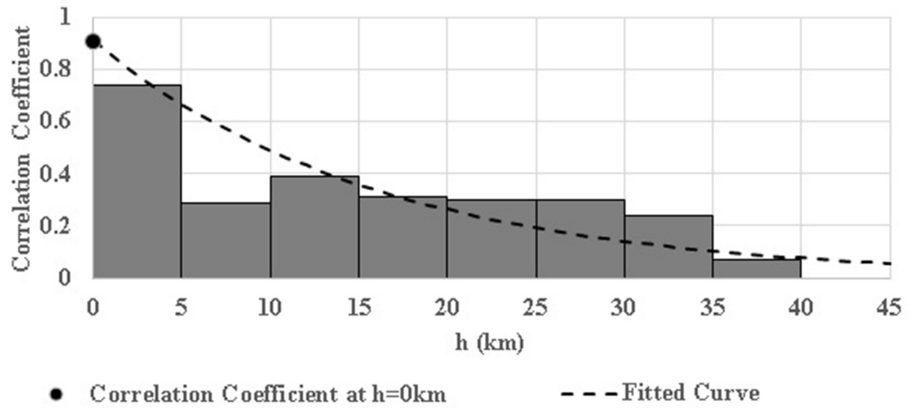

FIGURE 5
Cross-correlogram depicting variation in *T-B* cross-correlation coefficient with separating distance (*h*).

cross-variogram are lower owing to fewer sample points of (*TP*) and (*TP-BP*) data. This substantiates the need for refining the estimates of the model parameters of *T* variogram (termed as $\boldsymbol{\theta}_1$) and those of *T-B* cross-variogram (termed as $\boldsymbol{\theta}_3$). As such, the parameters ($\boldsymbol{\Omega}$) of the IP solution are defined as follows by Eq. 15.

$$\Omega = \left[\left(\sigma^2_{TT}, L_{TT}, \sigma^2_{TB}, L_{TB}, \lambda\right)\right] \tag{15}$$

2.2.6 Interface of cokriging with IP

The cokriging model of *T* discussed in the preceding Sections was linked to a groundwater flow model of the study area for the estimation of the envisaged parameters ($\boldsymbol{\Omega}$) of the IP problem. The groundwater flow model employed in the present study is based upon a numerical solution of the differential equation presented in Eq. 16.governing two dimensional horizontal in an isotropic confined aquifer Eq. 16.

$$\frac{\partial}{\partial X}\left(T\frac{\partial h}{\partial X}\right)+\frac{\partial}{\partial Y}\left(T\frac{\partial h}{\partial Y}\right)-W=\left(S_y\right)\frac{\partial h}{\partial t} \tag{16}$$

Where, T = isotropic transmissivity, h = head, X, Y = orthogonal cartesian coordinate, W = sink term, S_y = specific yield. Employing "current" values of ($\boldsymbol{\Omega}$), the T term appearing in above equation is cokriged as per Eqs. 7, 8 using the sample points (*TP* and *BP*) falling within the respective search radius (=7/4L_{TT}). This confined flow equation incorporating isotropic transmissivity as a time-averaged flow parameter has been invoked for modeling the unconfined flow assuming (i) horizontal isotropy, (ii) small enough temporal fluctuation of h and (iii) flat spatial gradients honoring Dupuit-Forchheimer assumptions. The adopted flow equation was solved to

TABLE 1 Detrending parameters.

Parameter	T_o	I_{XT}	I_{YT}	B_o	I_{XB}	I_{YB}
Value	1,293 m^2/day	−11 m^2/day/km	8.3 m^2/day/km	95 m	−8.1 m/km	6.7 m/km

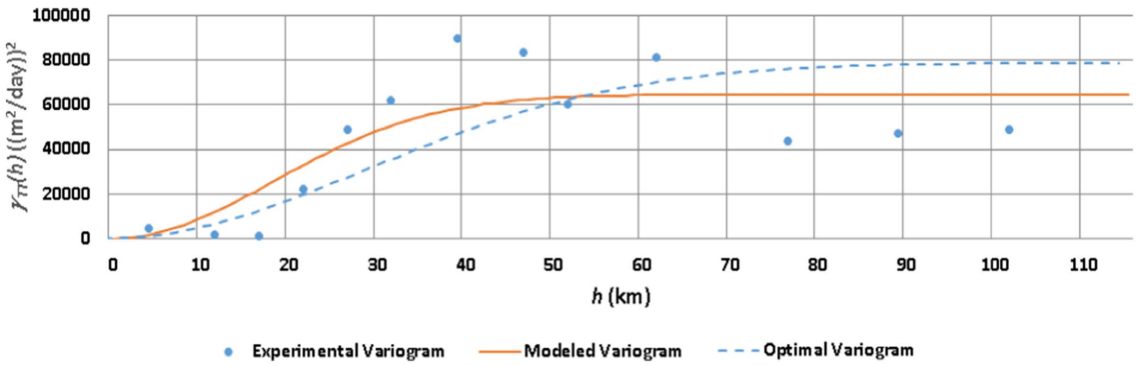

FIGURE 6
Experimental, modeled and IP-derived optimal *T* variograms.

simulate the head fields at advancing discrete times using IADI based finite difference method. The flow model was externally linked to an optimizer based upon SUMT algorithm (Fiacco and McCormick, 1990) to facilitate the estimation of (**Ω**).

Adopting a spatial discretization of 1,000 m, a finite difference grid (Figure 3) comprising 8,350 active nodes and 418 boundary nodes was superposed over the study area. Recalling that the head data are available at six discrete times (over a period of three years extending from June-2014 to October-2016), the June-2014 head field was treated as the initial condition (Figure 3). Head fields at the following five discrete times (until October 2016) were simulated adopting a time interval of 15 days. The boundary conditions at the river boundary nodes were assigned as per the available river stage data. Neuman boundary condition was assigned along the mountainous boundary. The necessary flux rate was derived from the prevailing hydraulic gradients. The forcing function vector (*W*) was derived from the available recharge/withdrawal data.

The vector of poorly known/unknown parameters (**Ω**) was estimated by minimizing the mismatch between the observed and the simulated head fields of October 2016. Accordingly, the IP is defined as the following optimization problem (Eq. 17).

$$Minimize\ Z = \sum_{i=1}^{na}\left(\hat{h}_i - h_i\right)^2 \text{ wrt.Five decision variables } \left[\Omega = \left(\sigma^2_{TT}, L_{TT}, \sigma^2_{TB}, L_{TB}, \lambda\right)\right] \quad (17)$$

Where, *na* = number of active nodes, $\hat{h}_i$ = observed head at *i*th active node at October 2016, and h_i=simulated head at *i*th active node at October 2016. Constraints were assigned to ensure non-negativity of all the five variables. Further, the fifth decision variable (λ) was contrained as in Eq. 18.

$$0 \le \lambda \le 1 \quad (18)$$

3 Results

Recalling that the poorly known/unknown cokriging parameters (***Ω***) are treated as the IP parameters (and hence decision variables of the proposed optimization problem), their initial and the optimized values along with the corresponding objective function values are presented in Table 3. It may be seen that the parameters undergo a substantial variation leading to a reduction of the objective function from 1954 m^2 to 1,609 m^2. The corresponding cokriged-IP *T* field is presented in Figure 9.

It may be noted that the resultant optimal value of λ is quite low (0.07)—apparently on account of relatively sparse and some-what clustered *T* data. This implies that the interpolation of *T* has been largely governed by *BP* data with a relatively smaller role of *TP* data. This in turn has led to large mismatch between the interpolated and sampled *T* values at the sampling points (Figure 9). Although this kind of mismatch is quite common in practical calibrations (Davis et al., 2015), attempt was made to control it as much as possible to enhance plausibility (RamaRao et al., 1995) of the cokriged *T* field without significantly compromising upon the optimality of *Z*. This was done enforcing representing T mismatch as expressed in Eq. 19.

$$Minimize\ Z1 = \frac{1}{n}\sum_n \left|\frac{T_{oi} - TP_i}{TP_i}\right| \times 100 \quad (19)$$

Where, TP_i, T_{oi} = measured and IP-cokriged transmissivity at *i*th sampling location, respectively, and *n* = number of sampled *TP* data.

The multi-objective minimization of *Z* and Z_1 was conducted by applying the principle of Pareto front optimization (Goodarzi et al., 2014; Rao, 2019) which in the present context would imply

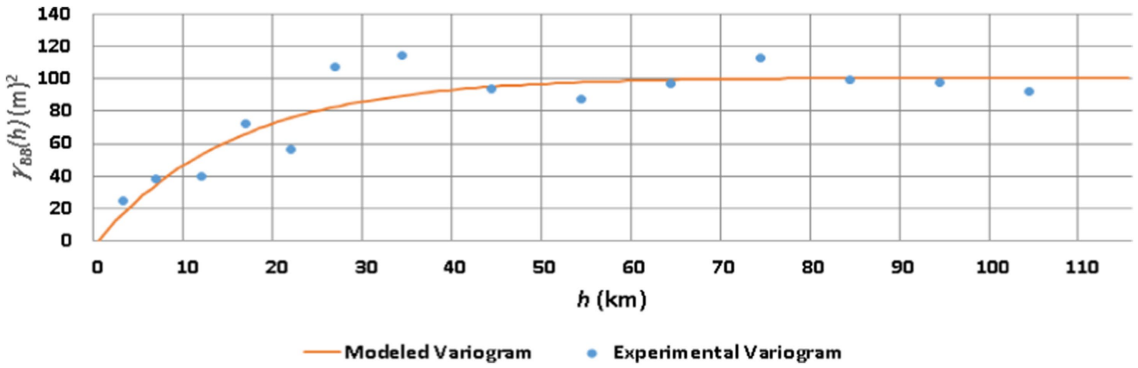

FIGURE 7
Experimental and modeled *B* variograms.

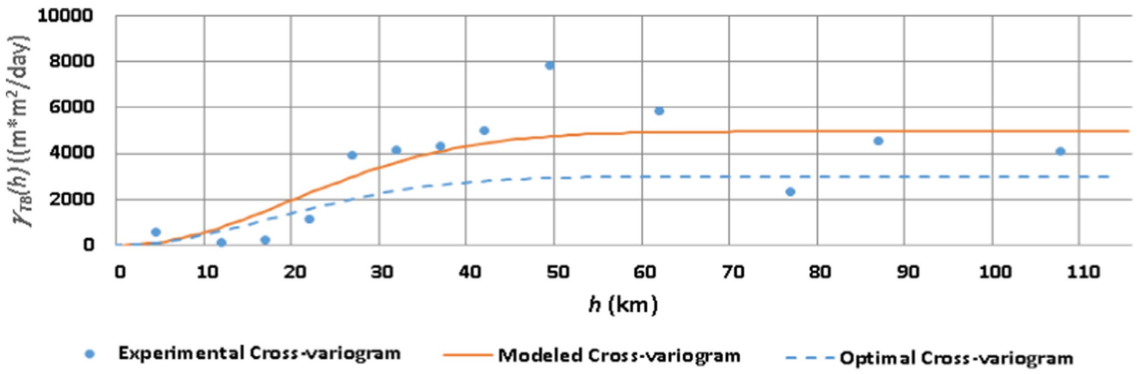

FIGURE 8
Experimental, modeled and IP-derived (Optimal) *T*-*B* cross-variograms.

minimizing Z without undue degradation of Z_1. A Pareto front depicting variation of Z and Z_1 at increasing λ values is presented in Figure 10. The front clearly shows that ($\lambda = 0.07$) though an optimal solution in context of Z compromises on minimization of Z_1. As λ increases from 0.07 to 0.3, increase of Z is minimal (1,609 to 1,631 m^2) with a notable decrease in Z_1. However, as λ increases beyond 0.3, Z increases rapidly with a pronouncedly larger gradient. Thus, ($\lambda = 0.3$) may be deemed to be the Pareto front optimal solution since around it there is no way of decreasing Z without increasing Z_1 sharply. As such, the optimal value of the decision variable λ was modified to 0.3. Incidentally this value of λ also nearly equals the ratio of B and T data. The corresponding modified T field is superposed over the initial T ($\lambda = 0.07$) field (Figure 9). The former field though still displaying departure from the sampled T values, honors them more closely as compared to the latter one. The departure is more pronounced in central-south-western region wherein T data are sparse but B data are well available.

The contours of the simulated heads corresponding to the modified T field at the target time (October 2016) are presented in the Supplementary Figure S2. However, since the residuals ($h_i - h_i$) are not discernible in these contours because of the scale effect, the spatial distribution of the nodal residuals is depicted explicitly in Supplementary Figure S3. The variograms and cross-variogram derived from the initial and optimal parameters, along with the experimental points, are presented in Figures 6–8.

TABLE 2 Estimated parameters of models of variograms and cross-variogram.

Estimated model parameters	γ_{TT}	γ_{BB}	γ_{TB}
σ^2	6.45×10^{-4} (m^2/day)^2	101 m^2	4.95×10^{-3} m $\times$ m^2/day
L	25.5 km	15.4 km	27 km
R^2	0.68	0.81	0.48

4 Discussion of results

Results presented in Table 3 reveal that parameters L_{TT} and λ change significantly as the cokriging interpolator is joined with the envisaged IP solution. The assigned initial value (25.5 km) of L_{TT} emanates from regression of limited number of experimental points with rather low R^2 (0.68). The optimized value (42 km) is significantly higher implying a substantially enhanced range ($R = 7/4L_{TT}$). This indicates that the spatial auto-correlation of T extends over much

TABLE 3 Initial and optimal geostatistical parameters.

Parameter	σ^2_{TT}	L_{TT}	σ^2_{TB}	L_{TB}	λ	Z
Initial value	6.45×10^4 $(m^2/day)^2$	25.5 km	4.95×10^3 $(m\times m^2/day)$	27 km	1	1954 m^2
Optimal value	7.87×10^4 $(m^2/day)^2$	42 km	3.01×10^3 $(m\times m^2/day)$	26 km	0.07	1,609 m^2

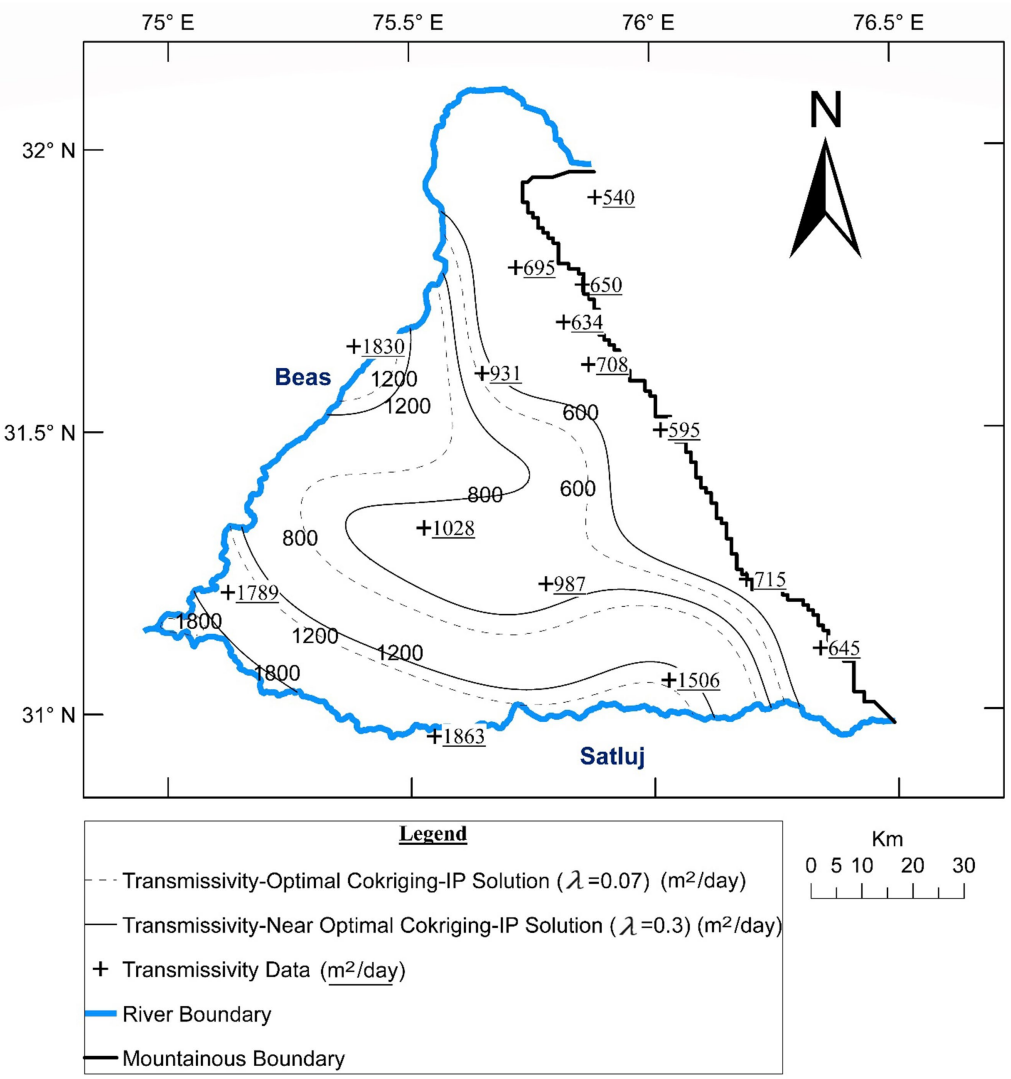

FIGURE 9
Optimal and pareto-front (near-optimal) transmissivity fields.

longer distance than what is revealed by the limited *TP* data. The distribution parameter (λ) is near- optimized as 0.30 – implying a larger weight to the *BP* data as compared to the *TP* data. This weighing proportion seems to be reasonable in view of the relative sparseness of *TP* data. The transmissivity field emanating from the proposed approach has resulted in much improved reproduction of the observed head field – evidenced by improved *Z* (Table 3).

For gaining additional insight, hydraulic conductivity (*K*) field was generated (Figure 11) by dividing the IP-cokriged *T* field by the kriged *B* field (Figure 12). The *K* field displays a variation from 7 to 15 m/day which extends beyond the range of 10.2 to 13.5 m/day depicted in Figure 4. Recalling that Figure 4 is derived from the limited co-located *T-B* data, the expansion of the *K* range is accomplished through IP-cokriging assisted interplay between the head and (*T, B*) data including the ones among the latter that are not co-located. This facilitates production of more realistic *K* and *T* fields. For example, this has permitted capture of hydrogeologically consistent low *K* in the interior zone and high *K* near river Satluj (shown as sites A and B in Figure 11) in spite of absence of any co-located *T-B* data there.

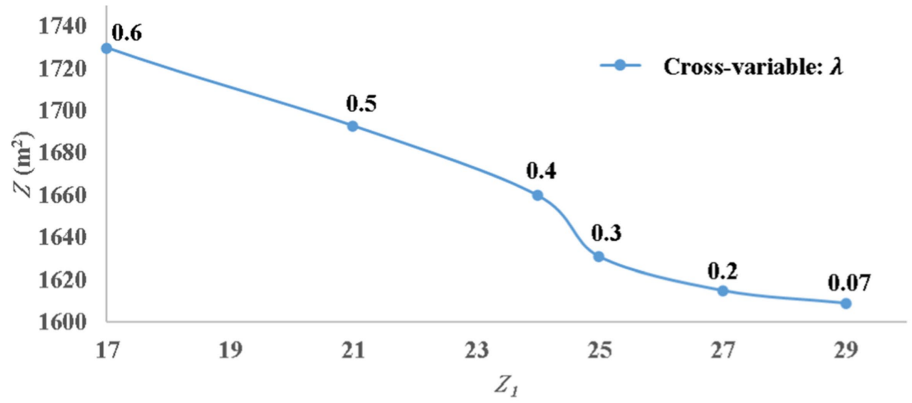

FIGURE 10
Computed pareto front.

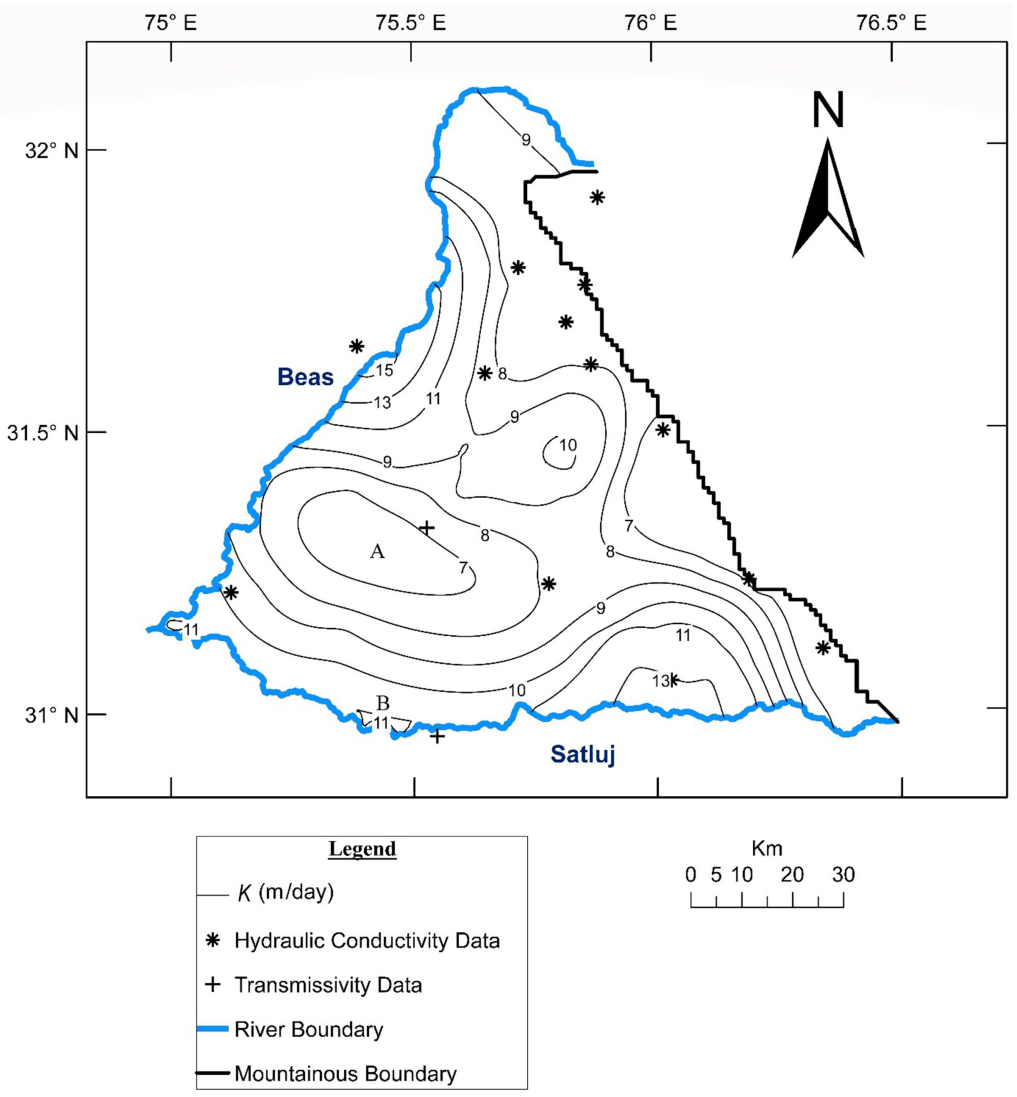

FIGURE 11
K field emanating from proposed model and *B* field (refer Figure 12).

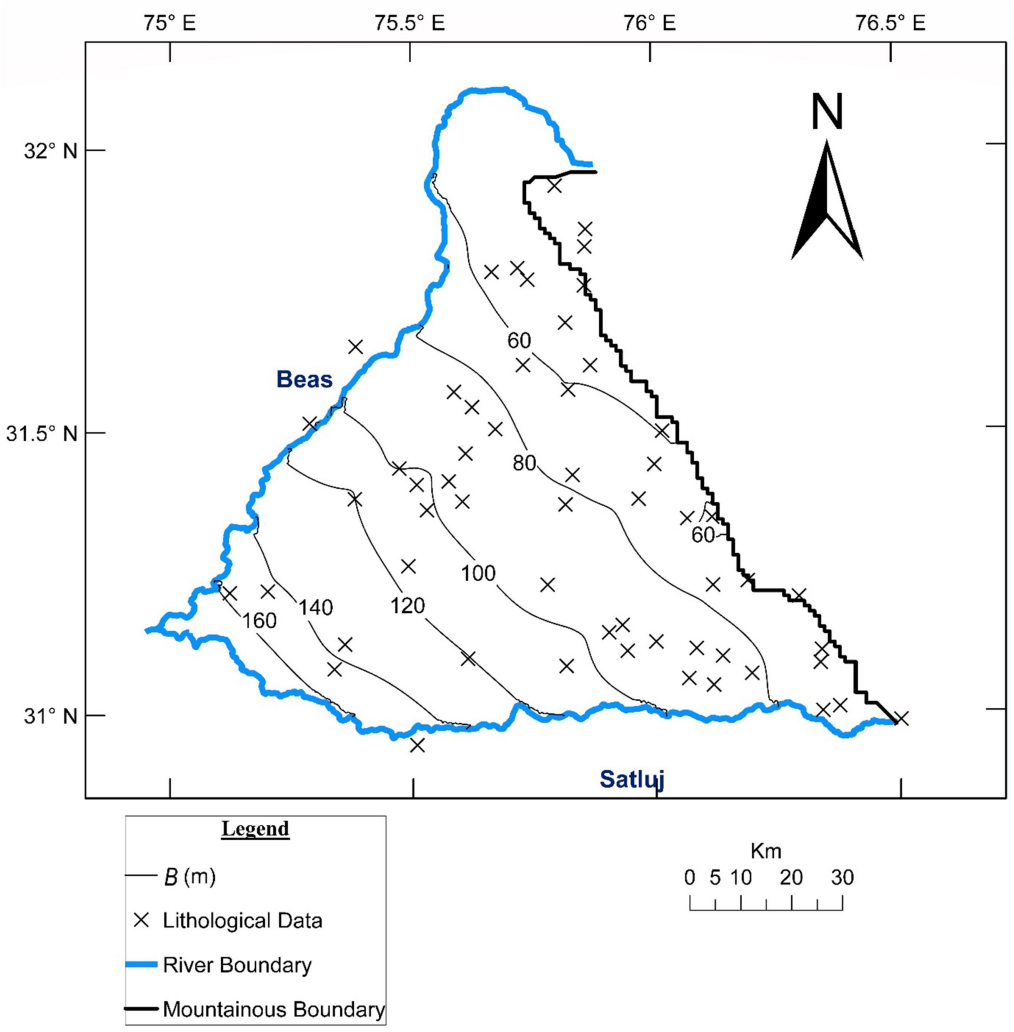

FIGURE 12
B Field obtained by kriging the *BP* data.

TABLE 4 *Z* (m^2) at target and non-target times.

Discrete time	Oct-14	Jun-15	Oct-15	Jun-16	Oct-2016 (target time)
Proposed model ($\lambda = 0.30$)	758	1,670	2,360	2,279	1,631
BL1	949	1783	2,411	2,437	1928
BL2	893	1811	2,416	2,435	1921

5 Validation of *T* field

It may be recalled that while solving the envisaged IP, the head field of the June 2014 was treated as the initial condition and the fields of the following five discrete times (until October 2016) were simulated. However, the head based IP solution was defined in terms of the mismatch between the observed and the simulated fields of October 2016 only—not using the observed head fields of four intervening discrete times. As such, October 2016 and the four preceding simulation times are henceforth termed as target and non-target times, respectively. Validity of the optimal parameter estimates (and hence of the resulting *T* field) has been linked to the reproduction of the observed fields at the non-target times.

Values of the mismatch parameter *Z* (Eq. 13) at the target as well as non-target times are presented in Table 4. It may be seen that *Z* values at the non-target times are not conspicuously higher than the optimized value (1,631 m^2) corresponding to the target time. The time series of the observed and simulated heads at four typical locations OW1, OW2, OW3, OW4 (Supplementary Figure S3) are presented in Supplementary Figure S4. Again, the observed head time series are quite well reproduced at the target as well as non-target times. These

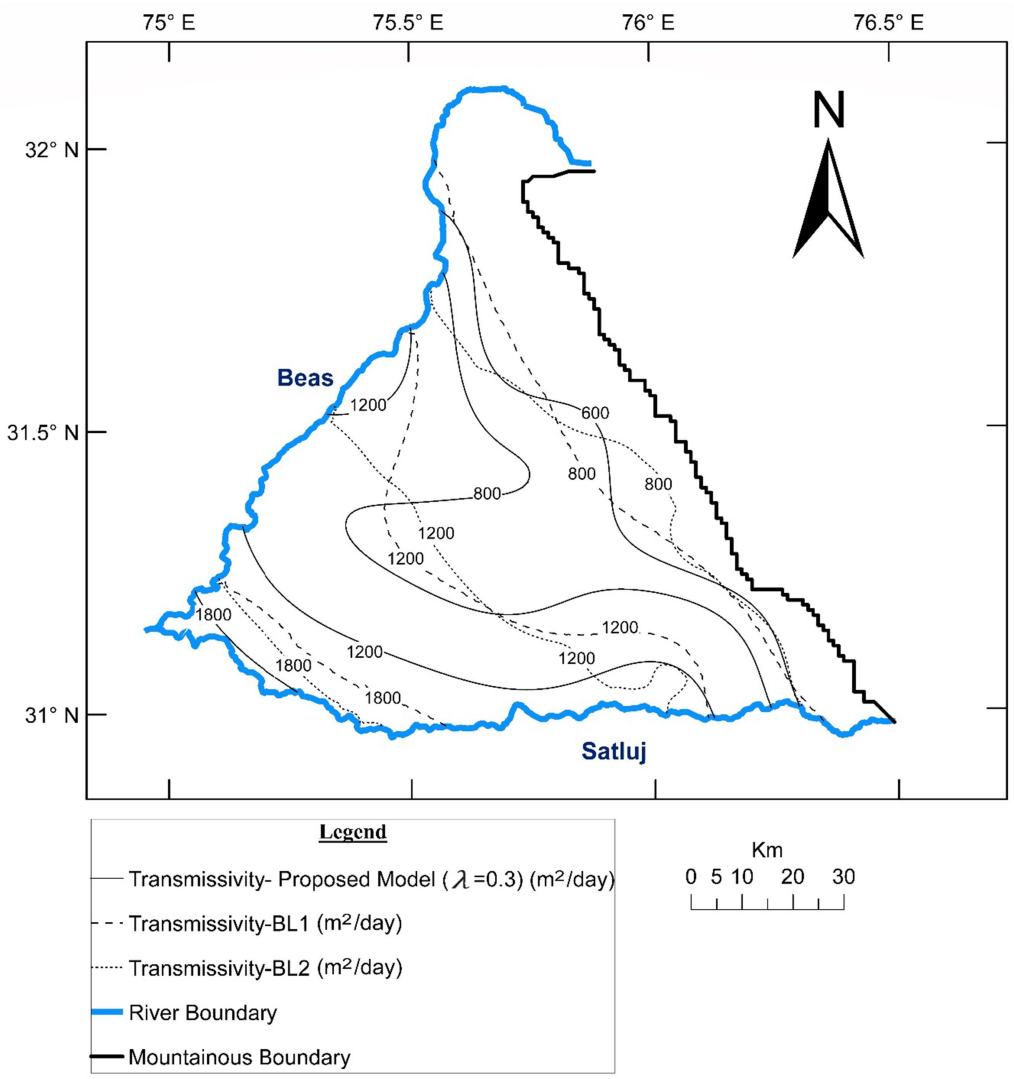

FIGURE 13
Transmissivity fields (proposed model, BL1 and BL2).

inferences validate the parameter estimation and the consequent transmissivity field.

6 Baseline studies

The proposed model for generation of *T* field invokes a cokriging-IP based solution. However, there could be relatively simpler/practice-oriented modeling options viz. (i) kriging of *TP* and (ii) kriging of *K*(=*TP*/*BP*) and *BP*, and multiplying the two to obtain *T* field. Performance metrics of these baseline options (termed, respectively, as BL1and BL2) were compared with those of the proposed model. As a first step towards the comparison, an alternative *T* field was generated using the baseline model under reckoning. This was subsequently employed for simulating the head fields at five discrete times viz. four non-target times and the target time (October 2016) referred to in the Validation Section.

The transmissivity fields emanating from the proposed model, BL1 and BL2 are presented in Figure 13. Corresponding values of the mismatch parameter (*Z*) were derived from these head fields (Table 4). It may be seen that compared to BL1 and BL2, the proposed model yields significantly reduced *Z* values at all discrete times including the non-target ones. This clearly demonstrates superiority of the proposed model over BL1 and BL2. It may also be seen that in spite of using additional data, BL2 does not lead to significantly lower *Z* values in comparison to those from BL1. It may be seen that BL1 and BL2 lead to almost similar transmissivity fields (Figure 13). It may be inferred that independent usage of *T* and *B* data does not provide any value addition over using only *T* data. It is the synergic and simultaneous deployment of both *T* and *B* data that improves the credibility of resulting *T* fields.

The generated *T* field has also been informally validated by invoking the corresponding *K* field (Refer Figure 12) that was computed by dividing the proposed *T* field by *B* field. The field displays *K* variation from 7 to 15 m/day which falls in the broad range for sands (Domenico and Schwartz, 1990). Recalling that *B* represents cumulative 'sand' thickness, this may be deemed to be an elementary validation of the generated *T* field.

7 Conclusion

The proposed IP-joined cokriging interpolator permits credible generation of transmissivity fields even when the primary T data are sparse. The data sparseness is overcome by simultaneously invoking data of other T-correlated secondary variable B, and moderating the unknown/poorly known cokriging parameters. In the present study, combination of sparse T data with abundantly available saturated thickness values has been shown to be work well. However, recourse can be taken to other secondary variables like formation loss parameter (derived from step-drawdown tests), geophysical resistivity etc. The prevalent practice of IP solution is generally aimed at moderating the available T data or estimating T values at stipulated un-gauged locations. However, as has been demonstrated in this study, the IP solution can also be used for modification of poorly known geostatistical parameters of cokriging, apart from estimating the unknown ones. The study reveals that adopting IP- joined cokriging in place of kriging may lead to a substantial improvement in the reproduction of the observed head fields. This in turn may imply enhanced head prediction capability of the generated transmissivity fields.

Data availability statement

The raw data supporting the conclusions of this article will be made available by the authors, without undue reservation.

Author contributions

AK: Conceptualization, Data curation, Formal analysis, Investigation, Methodology, Resources, Software, Validation, Visualization, Writing – original draft, Writing – review & editing. DK: Conceptualization, Funding acquisition, Investigation, Methodology, Project administration, Resources, Software, Supervision, Validation, Visualization, Writing – original draft, Writing – review & editing, Formal analysis.

Funding

The author(s) declare that no financial support was received for the research, authorship, and/or publication of this article.

Acknowledgments

The data used in the present study was gathered from Water Resources Organization, Punjab; Department of Agriculture, Punjab; and Central Groundwater Board, Chandigarh. Authors are thankful to Chief Engineer K.S. Takshi, Mr. Neeraj Pandit and Mr. Tejdeep Singh from these organizations for their help and meaningful discussions. Authors are also thankful to Indian Institute of technology Ropar for providing the facilities to perform this research.

Conflict of interest

The authors declare that the research was conducted in the absence of any commercial or financial relationships that could be construed as a potential conflict of interest.

Publisher's note

All claims expressed in this article are solely those of the authors and do not necessarily represent those of their affiliated organizations, or those of the publisher, the editors and the reviewers. Any product that may be evaluated in this article, or claim that may be made by its manufacturer, is not guaranteed or endorsed by the publisher.

Supplementary material

The Supplementary material for this article can be found online at: https://www.frontiersin.org/articles/10.3389/frwa.2024.1380761/full#supplementary-material

References

Aboufirassi, M., and Mariño, M. A. (1984). Cokriging of aquifer transmissivities from field measurements of transmissivity and specific capacity. *J. Int. Assoc. Math. Geol.* 16, 19–35. doi: 10.1007/BF01036238

Adhikary, S. K., Muttil, N., and Yilmaz, A. G. (2017). Cokriging for enhanced spatial interpolation of rainfall in two Australian catchments. *Hydrol. Process.* 31, 2143–2161. doi: 10.1002/hyp.11163

Ahmed, S., and de Marsily, G. (1987). Comparison of geostatistical methods for estimating transmissivity using data on transmissivity and specific capacity. *Water Resour. Res.* 23, 1717–1737. doi: 10.1029/WR023i009p01717

Ahmed, S., de Marsily, G., and Talbot, A. (1988). Combined use of hydraulic and electrical properties of an aquifer in a geostatistical estimation of transmissivity. *Groundwater* 26, 78–86. doi: 10.1111/j.1745-6584.1988.tb00370.x

Alam, F., and Umar, R. (2013). Groundwater flow modelling of Hindon-Yamuna interfluve region, western Uttar Pradesh. *J. Geol. Soc. India* 82, 80–90. doi: 10.1007/s12594-013-0113-8

Anderson, M. P., Woessner, W. W., and Hunt, R. J. (2015). *Applied groundwater modeling: Simulation of flow and advective transport*. Amsterdam, Netherlander: Academic press.

Bailey, R. T., Abbas, S., Arnold, J., White, M., Gao, J., and Čerkasova, N. (2023). Augmenting the national agroecosystem model with physically based spatially distributed groundwater modeling. *Environ. Model Softw.* 160:105589. doi: 10.1016/j.envsoft.2022.105589

Belkhiri, L., Tiri, A., and Mouni, L. (2020). Spatial distribution of the groundwater quality using kriging and co-kriging interpolations. *Groundw. Sustain. Dev.* 11:100473. doi: 10.1016/j.gsd.2020.100473

Bhattacharjya, R. K., and Datta, B. (2005). Optimal management of coastal aquifers using linked simulation optimization approach. *Water Resour. Manag.* 19, 295–320. doi: 10.1007/s11269-005-3180-9

Cardiff, M., and Barrash, W. (2011). 3-D transient hydraulic tomography in unconfined aquifers with fast drainage response. *Water Resour. Res.* 47:367. doi: 10.1029/2010WR010367

Central Ground Water Board (2009). *Report of the working group on methodology for assessment of development potential of deeper aquifers*. Faridabad: Central Ground Water Board, pp.26–27.

Certes, C., and de Marsily, G. (1991). Application of the pilot point method to the identification of aquifer transmissivities. *Adv. Water Resour.* 14, 284–300. doi: 10.1016/0309-1708(91)90040-U

Chapra, S. C., and Canale, R. P., (2010). *Numerical methods for engineers*. Boston: McGraw-Hill Higher Education. ISBN: 978-0073401065

Christelis, V., Kopsiaftis, G., Regis, R. G., and Mantoglou, A. (2023). An adaptive multi-fidelity optimization framework based on co-kriging surrogate models and stochastic sampling with application to coastal aquifer management. *Adv. Water Resour.* 180:104537. doi: 10.1016/j.advwatres.2023.104537

Cui, T., Pagendam, D., and Gilfedder, M. (2021). Gaussian process machine learning and kriging for groundwater salinity interpolation. *Environ. Model Softw.* 144:105170. doi: 10.1016/j.envsoft.2021.105170

CGWB, (2013). Dynamic Groundwater Resources of Punjab. Central Groundwater Board and Water Resources and Environment Directorate of Punjab. Chandigarh.

Davis, K. W., Putnam, L. D., and LaBelle, A. R. (2015). *Conceptual and numerical models of groundwater flow in the Ogallala and Arikaree aquifers, pine ridge Indian reservation area, South Dakota, water years 1980-2009 (no. 2014-5241)*. Reston, Virginia, USA: US Geological Survey.

Dickson, N. E., Comte, J. C., Koussoube, Y., Ofterdinger, U. S., and Vouillamoz, J. M. (2019). Analysis and numerical modelling of large-scale controls on aquifer structure and hydrogeological properties in the African basin (Benin, West Africa). *Geol. Soc. Lond., Spec. Publ.* 479, 81–100. doi: 10.1144/SP479.2

Domenico, P. A., and Schwartz, F. W., (1990). *Physical and chemical hydrogeology*, John Wiley & Sons, New York, 824.

Economic and Statistical Organization, Government of Punjab, (2016). District Domestic Product Of Punjab (2011-12 To 2015-16). [online] EPOSB. Available at: https://www.esopb.gov.in/static/PDF/Publications/State-Income/DDP-2011-12TO2015-16.pdf (Accessed 15 May 2020).

Escriva-Bou, A., Hui, R., Maples, S., Medellín-Azuara, J., Harter, T., and Lund, J. R. (2020). Planning for groundwater sustainability accounting for uncertainty and costs: an application to California's Central Valley. *J. Environ. Manag.* 264:110426. doi: 10.1016/j.jenvman.2020.110426

Fiacco, A. V., and McCormick, G. P. (1990). Nonlinear programming: sequential unconstrained minimization techniques. *Soc. Indus. Appl. Math.* 12, 593–594. doi: 10.1137/1012119

Gannett, M. W., Wagner, B. J., and Lite, K. E. (2012). *Groundwater simulation and management models for the upper Klamath basin, Oregon and California*. Reston, Virginia, USA: US Department of the Interior, US Geological Survey.

Ghosh, S., and Kashyap, D. (2012). Kernel function model for planning of agricultural groundwater development. *J. Water Resour. Plan. Manag.* 138, 277–286. doi: 10.1061/(ASCE)WR.1943-5452.0000178

Goodarzi, E., Ziaei, M., and Hosseinipour, E. Z., (2014). *Introduction to optimization analysis in hydrosystem engineering*. New York, NY: Springer International Publishing.

Hoeksema, R. J., and Kitanidis, P. K. (1985). Analysis of the spatial structure of properties of selected aquifers. *Water Resour. Res.* 21, 563–572. doi: 10.1029/WR021i004p00563

Isaaks, E. H., and Srivastava, R. M. (1989). An Introduction to Applied Geostatistics. *Oxford University Press, New York*, 413.

Izady, A., Joodavi, A., Ansarian, M., Shafiei, M., Majidi, M., Davary, K., et al. (2022). A scenario-based coupled SWAT-MODFLOW decision support system for advanced water resource management. *J. Hydroinf.* 24, 56–77. doi: 10.2166/hydro.2021.081

Jazaei, F., Waldron, B., Schoefernacker, S., and Larsen, D. (2019). Application of numerical tools to investigate a leaky aquitard beneath urban well fields. *Water* 11:5. doi: 10.3390/w11010005

Júnez-Ferreira, H. E., Hernández-Hernández, M. A., Herrera, G. S., González-Trinidad, J., Cappello, C., Maggio, S., et al. (2023). Assessment of changes in regional groundwater levels through spatio-temporal kriging: application to the southern basin of Mexico aquifer system. *Hydrogeol. J.* 31, 1405–1423. doi: 10.1007/s10040-023-02681-y

Kapoor, A., and Kashyap, D. (2021). Parameterization of pilot point methodology for supplementing sparse transmissivity data. *Water* 13:2082. doi: 10.3390/w13152082

Kavusi, M., Khashei Siuki, A., and Dastourani, M. (2020). Optimal design of groundwater monitoring network using the combined election-kriging method. *Water Resour. Manag.* 34, 2503–2516. doi: 10.1007/s11269-020-02568-7

Kitanidis, P. K. (1997). *Introduction to geostatistics: Applications in hydrogeology*. Cambridge, United Kingdom: Cambridge University Press.

Kitanidis, P. K., and Vomvoris, E. G. (1983). A geostatistical approach to the inverse problem in groundwater modeling (steady state) and one-dimensional simulations. *Water Resour. Res.* 19, 677–690. doi: 10.1029/WR019i003p00677

LaVenue, A. M., and Pickens, J. F. (1992). Application of a coupled adjoint sensitivity and kriging approach to calibrate a groundwater flow model. *Water Resour. Res.* 28, 1543–1569. doi: 10.1029/92WR00208

Maliva, R. G., Manahan, W. S., and Missimer, T. M. (2021). Climate change and water supply: governance and adaptation planning in Florida. *Water Policy* 23, 521–536. doi: 10.2166/wp.2021.140

Mamo, S., Birhanu, B., Ayenew, T., and Taye, G. (2021). Three-dimensional groundwater flow modeling to assess the impacts of the increase in abstraction and recharge reduction on the groundwater, groundwater availability and groundwater-surface waters interaction: a case of the rib catchment in the Lake Tana sub-basin of the upper Blue Nile River, Ethiopia. *J. Hydrol. Reg. Stud.* 35:100831. doi: 10.1016/j.ejrh.2021.100831

Marino, M. A. (2001). "Conjunctive management of surface water and groundwater" in *Regional management of water resources Journal of the International Association for Mathematical Geology*, vol. 268, 165–173.

McKinney, D. C., and Lin, M. D. (1994). Genetic algorithm solution of groundwater management models. *Water Resour. Res.* 30, 1897–1906. doi: 10.1029/94WR00554

Miller, N. L., Dale, L. L., Brush, C. F., Vicuna, S. D., Kadir, T. N., Dogrul, E. C., et al. (2009). Drought resilience of the California Central Valley surface-ground-water-conveyance system 1. *J. Am. Water Res. Ass.* 45, 857–866. doi: 10.1111/j.1752-1688.2009.00329.x

Olea, R. A. (2018). *A practical primer on geostatistics (no. 2009–1103)*. New York, USA: Reston, Virginia, USA: US Geological Survey.

Oliver, M. A., and Webster, R. (2015). *Basic steps in Geostatistics: the variogram and kriging, springer briefs in agriculture*. 2211-808X, vol. *1* Springer.

Panagiotou, C. F., Kyriakidis, P., and Tziritis, E. (2022). Application of geostatistical methods to groundwater salinization problems: a review. *J. Hydrol.* 615:128566. doi: 10.1016/j.jhydrol.2022.128566

Rai, P. K., and Tripathi, S. (2019). Gaussian process for estimating parameters of partial differential equations and its application to the Richards equation. *Stoch. Env. Res. Risk A.* 33, 1629–1649. doi: 10.1007/s00477-019-01709-8

RamaRao, B. S., LaVenue, A. M., De Marsily, G., and Marietta, M. G. (1995). Pilot point methodology for automated calibration of an ensemble of conditionally simulated transmissivity fields: 1. Theory and computational experiments. *Water Resour. Res.* 31, 475–493. doi: 10.1029/94WR02258

Rao, S. S. (2019). *Engineering optimization: theory and practice*. Hoboken, New Jersey: John Wiley & Sons.

Senoro, D. B., de Jesus, K. L. M., Mendoza, L. C., Apostol, E. M. D., Escalona, K. S., and Chan, E. B. (2021). Groundwater quality monitoring using in-situ measurements and hybrid machine learning with empirical Bayesian kriging interpolation method. *Appl. Sci.* 12:132. doi: 10.3390/app12010132

Singh, A., Panda, S. N., Kumar, K. S., and Sharma, C. S. (2013). Artificial groundwater recharge zones mapping using remote sensing and GIS: a case study in Indian Punjab. *Environ. Manag.* 52, 61–71. doi: 10.1007/s00267-013-0101-1

Singh, A., Panda, S. N., Saxena, C. K., Verma, C. L., Uzokwe, V. N., Krause, P., et al. (2016). Optimization modeling for conjunctive use planning of surface water and groundwater for irrigation. *J. Irrig. Drain. Eng.* 142:04015060. doi: 10.1061/(ASCE)IR.1943-4774.0000977

Wackernagel, H. (2003). *Multivariate Geostatistics*. Berlin, Heidelberg: Springer Berlin Heidelberg.

Yao, L., Huo, Z., Feng, S., Mao, X., Kang, S., Chen, J., et al. (2014). Evaluation of spatial interpolation methods for groundwater level in an arid inland oasis, Northwest China. *Environ. Earth Sci.* 71, 1911–1924. doi: 10.1007/s12665-013-2595-5

Yeh, W. W. (2015). Optimization methods for groundwater modeling and management. *Hydrogeol. J.* 23, 1051–1065. doi: 10.1007/s10040-015-1260-3

Yeh, T. C. J., Gutjahr, A. L., and Jin, M. (1995). An iterative cokriging-like technique for ground-water flow modeling. *Groundwater* 33, 33–41. doi: 10.1111/j.1745-6584.1995.tb00260.x

Yoon, Y. S., and Yeh, W. G. (1976). Parameter identification in an inhomogeneous medium with the finite-element method. *Soc. Pet. Eng. J.* 16, 217–226. doi: 10.2118/5524-PA

Zanaga, D., Van De Kerchove, R., Daems, D., De Keersmaecker, W., Brockmann, C., Kirches, G., et al., (2022). *ESA WorldCover 10 m 2021 v200*. Zenodo.

Zawadzki, J., Fabijańczyk, P., and Treichel, W. (2021). Monitoring of groundwater quality with cokriging of geochemical and geoelectrical measurements. *Multidiscip. Aspects Prod. Eng.* 4, 97–106. doi: 10.2478/mape-2021-0009

Zeinali, M., Azari, A., and Heidari, M. M. (2020). Multiobjective optimization for water resource management in low-flow areas based on a coupled surface water–groundwater model. *J. Water Resour. Plan. Manag.* 146:04020020. doi: 10.1061/(ASCE)WR.1943-5452.000118

Zhao, Z., Zhang, L., and Bi, E. (2022). Spatial interpolation of highly skewed data of the Junggar Basin phreatic groundwater through the multi-scale cokriging model. *Earth Sci. Inf.* 15, 1737–1748. doi: 10.1007/s12145-022-00835-2

frontiers | Frontiers in Water

TYPE Original Research
PUBLISHED 15 May 2024
DOI 10.3389/frwa.2024.1401689

OPEN ACCESS

EDITED BY
Rajneesh Singh,
University of Minnesota Twin Cities, United States

REVIEWED BY
Rohitash Yadav,
Birsa Agricultural University, India
Aditya Kapoor,
Indian Institute of Technology Roorkee, India
Abhishek Majumder,
Tripura University, India

*CORRESPONDENCE
Abhijit Biswas
abhi.021983@gmail.com

RECEIVED 15 March 2024
ACCEPTED 04 April 2024
PUBLISHED 15 May 2024

CITATION
Yadav A, Roy SM, Biswas A, Swain B and Majumder S (2024) Modelling and prediction of aeration efficiency of the venturi aeration system using ANN-PSO and ANN-GA. *Front. Water* 6:1401689. doi: 10.3389/frwa.2024.1401689

Modelling and prediction of aeration efficiency of the venturi aeration system using ANN-PSO and ANN-GA

Anamika Yadav[1], Subha M. Roy[2], Abhijit Biswas[3]*, Bhagaban Swain[3] and Sudipta Majumder[4]

[1]Department of Agricultural Engineering, Triguna Sen School of Technology, Assam University, Silchar, Assam, India, [2]Smart Aquaculture Research Center, Chonnam National University, Yeosu, Republic of Korea, [3]Department of Computer Science and Engineering, Triguna Sen School of Technology, Assam University, Silchar, Assam, India, [4]Department of Computer Science and Engineering, Institute of Engineering and Technology, Dibrugarh University, Dibrugarh, Assam, India

The significance of this study involves the optimisation of the aeration efficiency (AE) of the venturi aerator using an artificial neural network (ANN) technique integrated with an optimisation algorithm, i.e., particle swarm optimisation (PSO) and genetic algorithm (GA). To optimise the effects of operational factors on aeration efficiency by utilising a venturi aeration system, aeration experiments were conducted in an experimental tank with dimensions of $90\,\text{cm} \times 55\,\text{cm} \times 45\,\text{cm}$. The operating parameters of the venturi aerator include throat length (TL), effective outlet pipe (EOP), and flow rate (Q) to estimate the efficacy of the venturi aerator in terms of AE. A 3–6-1 ANN model was developed and integrated with the PSO and GA techniques to find out the best possible optimal operating variables of the venturi aerator. The coefficient of determination (R^2), root mean square error (RMSE), and mean absolute error (MAE) determined from the experimental and estimated data were used to assess and compare the performance of the ANN-PSO and ANN-GA modelling. It is shown that ANN-PSO provides a better result as compared to ANN-GA. The operational parameters, TL, EOP, and Q, were determined to have the most optimum values at 50 mm, 6 m, and 0.6 L/s, respectively. The optimised aeration efficiency of the venturi was found to be 0.105 kg O_2/kWh at optimum operational circumstances. In fact, the neural network having an ideal design of (3-6-1) and a correlation coefficient value that is extremely close to unity has validated the results indicated above.

KEYWORDS

venturi aeration, ANN-PSO, genetic algorithm, soft computing, optimisation

Highlights

- Performance evaluation of artificial neural network–particle swarm optimisation (ANN-PSO) and artificial neural network–genetic algorithm (ANN-GA) techniques to optimise the operating variables of venturi.
- Soft computing methods are used for the estimation of aeration efficiency.
- A comparison of the ANN-PSO technique with the ANN-GA approach.

1 Introduction

India is the third-largest fish producer worldwide, contributing 7.56% of the world's food supply, and its production has increased consistently over the past 10 years on average. In 2019, the overall aquaculture production increased by 1.5% compared to the previous year, reaching 4,421.22 thousand metric tonnes (FAO, 2019). In semi-intensive and intensive aquaculture, applications of aeration practises are crucial to maintaining microclimate conditions that are compatible with the physiological needs of the cultivated species. Aerators mainly distribute gas bubbles that enable oxygen to move to the water. The economic viability and productivity of commercial aquaculture farming depend significantly on the condition of the water quality. Dissolved oxygen (DO) is the most crucial parameter of the water quality that might affect aquaculture production and the survival rate of all aquatic species. Temperature and DO are interrelated parameters, and temperature variations can result in a more significant difference in the amount of DO in ponds (Dayıoğlu, 2022). According to a thumb rule, the optimal values of DO for the majority of aquatic species at sea level are considered as 50% saturation concentration in freshwater bodies, or 5 mg/L and 4 mg/L at temperatures of 15°C and 26°C, respectively (Roy et al., 2022; Yadav and Roy, 2023). In particular, the cold water and warm water species require DO concentrations between 7 mg/L and 9 mg/L and between 4 mg/L and 7 mg/L for proper growth and reproduction (Roy et al., 2021b, 2022). The existence possibility of aquatic species can increase using artificial aeration techniques in pond culture (Pawar et al., 2009). Aquaculture ponds have always used artificial aeration, i.e., surface, diffused, and gravity aeration, but in recent years, attention to venturi aeration has greatly expanded to generate fine bubbles and microbubbles (Navisa et al., 2014; Cheng et al., 2019; Sangeeta and Tiwari, 2019; Roy et al., 2020, 2021a; Luxmi et al., 2022). One of the most cost-effective aerators for small-scale aqua farmers is the venturi aerator. The venturi aeration system is a widely used technique in water engineering including aquaculture, which works on Bernoulli's principle (Baylar and Ozkan, 2006). The venturi aeration has a unique design to supply an abundant amount of air through entrainment at the narrower section of the venturi called the throat section. The venturi aeration is a highly efficient technique to increase the oxygen transfer ability through the production of many tiny bubbles. The aeration effectiveness is defined by the amount of gas and liquid interface area of contact that is primarily governed by the size of liquid film between gas molecules and liquid film (Yadav et al., 2020, 2021). Prior to inserting into the whole water volume, venturi aerators are primarily designed to mix air and water together at the throat of the venturi through inserted air holes (Baylar and Emiroglu, 2003; Gupta et al., 2016; Li et al., 2017; Sun et al., 2017; Sihag et al., 2021). The venturi aeration system can be utilised in various fields or industries such as water treatment plants, agriculture fields, fertiliser application, integrated irrigation systems, hatchery farms, and recirculating aquaculture systems (Omary et al., 2020; Wang et al., 2022). The venturi is highly efficient and provides significant benefits to the farmers as low power is needed to operate, is durable and compatibly cheaper, and requires less maintenance (Mahmud et al., 2020).

According to the results found from past studies, a venturi aerator performs best amongst all aeration systems with a standard aeration efficiency (SAE) value of 0.5 to 3.0 kg O2 / kWh. The optimum SAE was reported using venturi in a circular geometry tank as 1.7 to 2.05 kg O2 / kWh (Zhang et al., 2020). Both geometrical and dynamic characteristics may affect the aeration system's performance. It was found that the rate of oxygen entrainment and its transmission efficiency increase with pipe diameter and water velocity for all ratios of venturi throat to inlet and outlet diameter (Yadav et al., 2019). Ghomi et al. (2009) investigated several varying geometrical limits of venturi to regulate the SAE value. The maximum SAE value for each depth (20, 40, and 60 cm) and the angle ($0, 22.5,$ and 45^{Y}) of aeration was found to be at 14 mm diameter along with the coefficient value (R^2) of 0.958. Sanghani et al. (2014) examined the impact of geometrical factors of venturi on the throat length, the inlet and outlet angles, and the diameter ratio of the inlet, throat section, and pressure gradient. Baylar and Ozkan (2006) observed that the pressure was reduced at the throat by increasing the inlet pressure. The increased inlet pressure and contraction ratio lead to frequent increases in mass flow rates, and the reverse flow occurs in the contracted segment of the venturi (Zhang, 2017).

Recently, according to the review of literature, several research studies have been conducted on soft computing techniques based on artificial neural network (ANN), particle swarm optimisation (PSO), and genetic algorithm (GA) modelling in a variety of applications of aeration system (Bagatur and Onen, 2014; Kumar et al., 2018; Garg and Jain, 2020; Roy et al., 2021b). The ANN is a useful tool for simulating complex processes with dynamic interaction between the components that affect outcomes (Omid et al., 2009; Pareek et al., 2021). The ANN techniques can be utilised to identify the most effective process variables for maximising output. Roy et al. (2022) worked on the hybrid ANN-PSO approach to improve the geometric and dynamic characteristics of the designed cascade aerator pooled circular type to increase the aeration efficiency. Dayev et al. (2022) worked on soft computing methods to evaluate the capability of advanced computing approaches to accurately find out the air flow rate in a wet gas mixture, mainly in circumstances when the monitoring of such quantities using conventional models is actually difficult to adopt practically. Furthermore, ANN models have been employed by Mjalli et al. (2007) to evaluate the efficacy of the aeration system adopted in wastewater treatment facilities. When it comes to application, developed ANN models are far superior to response surface methodology (RSM) (Roy et al., 2021a). Garg and Jain (2020) investigated that the ANN outperforms the RSM for evaluating performance and analysis of variables of extracting biofuel via seaweed. In comparison with regression analysis, artificial neural networks are more generalisable, less susceptible to variability and anomalies, and can manage flawed information or data (Luk et al., 2001; Haykin, 2009). The literature cited above demonstrates that the ANN modelling may be effectively applied to simulate the operational characteristics of the aquaculture aeration system (Pareek et al., 2023a,b). However, a number of statistical approaches were successfully used for the optimisation of the aeration system, whereas the PSO and other comparatively more sophisticated optimisation algorithms have not yet been the subject of research. This optimisation method has been successfully used to solve a variety of issues in the physical world (Roy et al., 2022). In addition, other soft computing methods such as genetic expression programming (GEP), multiple linear and non-linear regressions, neuro-fuzzy, neural network, artificial intelligence (AI) models, and Gaussian process regression (GPR) models have been utilised to assess the effectiveness of AE of weirs and water jet system (Onen, 2014; Pareek et al., 2023a,b).

According to the research study that is currently available, past research was primarily used to estimate oxygenating characteristics and capacity. In contrast, a recent study supports the development of ANN, based on soft computing models, which draws their power to increase the AE of venturi. Furthermore, to improve the AE, the venturi aerator's operational variables were further combined with an ANN model using PSO and GA gradient techniques. The geometrical design and operating variables of the proposed venturi aerator might affect aeration performance. No analogous studies using soft computing techniques on venturi aeration for the primary aim of aquaculture have been found. In order to attain the greatest possible aeration efficiency, the present study aimed to identify the design parameters (throat length and extended outlet pipe length) and operative parameter (flow rate) of the venturi aeration system.

Furthermore, the present study assesses to optimise the aeration efficiency of the venturi aeration system in terms of aeration efficiency using the ANN model integrated with PSO and GA techniques. Furthermore, the effectiveness of the ANN-PSO and ANN-GA techniques has been examined and compared.

1.1 Paper representation

This article is organised as follows: Section 2 presents a theoretical analysis based on the two-film theory to determine the overall oxygen mass transfer rate, standard oxygen transfer rate, and standard aeration efficiency.

Section 3 encompasses materials and methods, including the experimental setup, experimental design, and procedure to evaluate the performance of venturi aeration. In addition, this section discusses the artificial neural network integrated with particle swarm optimisation and genetic algorithm technique and the performance analysis.

A detailed summary of the results and discussions is discussed in Section 4, which includes performance evaluation of the developed models, ANN modelling, PSO, a comparison between the integrated models, and the effects of operating parameters on aeration efficiency.

Section 5 discusses the conclusion of this article, including the authors' perspectives on the subject of the study and potential directions for further research.

2 Theoretical analysis

The two-film theory is the most frequently employed technique to determine the oxygen transfer rate, which is applicable in the two-phase system consisting of a gas phase and a liquid phase (Lewis and Whitman, 1924; Treybal, 1985). The variation in the oxygen concentration affects the transfer rate of oxygen mass from the atmosphere into the water interface with respect to time can be represented by Equation 1 (Metcalf et al., 1979).

$$\frac{dC}{dt} = K_L \frac{A}{V}(C_s - C) = K_L a(C_s - C), \tag{1}$$

where C_s = steady saturation concentration (mg/l) of DO in water bodies at standard temperature and pressure, C = oxygen content in water, and $\frac{A}{V} = a =$ specific area . Further integrating Equation 1 at $C = C_0$ to C and $t = 0$ to t can be rewritten as Equations 2, 3:

$$\int_{C_0}^{C} \frac{dC}{C_s - C} = (K_L a)\int_0^t dt, \tag{2}$$

$$\ln\left(\frac{C_s - C_t}{C_s - C_0}\right) = -(K_L a)t. \tag{3}$$

The oxygen transfer coefficient at T°C, $K_L a_T$ may be stated as follows using the two-film theory as Equation 4.

$$K_L a_T = \frac{\ln(C_s - C_0) - \ln(C_s - C_t)}{t}, \tag{4}$$

where ln = natural logarithm, C_s = saturation concentrations of dissolved oxygen (mg/l), C_0 and C_t = oxygen concentration at initial time, $t = 0$ and t, respectively. The graph between $\ln(Cs - Ct)$ and t represents a linear slope, which determines the $K_L a_T$ value (ASCE, 2007), and can be represented by Equation 5.

$$K_L a_{20} = K_L a_T \times \theta^{(20-T)}, \tag{5}$$

where $K_L a_{20}$ = coefficient of mass transfer at a standard temperature of 20°C (h^{-1}), $K_L a_T$ = coefficient of mass transfer at T °C (h^{-1}), θ = constant for pure water as 1.024 (Boyd, 1998; ASCE, 2007), and T = temperature of water (°C). Efficiency and durability are the most important factors to take into account whilst selecting an aerator for daily use in aquaculture farms. The standard oxygen transfer rate (SOTR) and standard aeration efficiency (SAE) measurements can be used to evaluate the proposed aerator's performance (Boyd and Ahmad, 1987). The SOTR is the amount of oxygenation capacity of an aeration system with respect to time at a standard pressure of 1.01325 bar and a standard temperature of 20°C, the primary DO concentration level of 0 mg/L, and clear tap water (APHA, 1985). The SAE is the ratio between SOTR and the required power (P, kW) to run the aerator (Lawson and Merry, 1993). Both the SOTR and SAE can be calculated by Equations 6, 7, respectively.

$$SOTR = K_L a_{20} \times (C_s - C_0) \times V \times 10^{-3}, \tag{6}$$

$$SAE = \frac{SOTR}{P} = \frac{K_L a_{20} \times (C_s - C_0) \times V \times 10^{-3}}{P}. \tag{7}$$

The following Equations 8, 9 may be used to derive the oxygen transfer rates (OTR) and aeration efficiency (AE) from SOTR and SAE, respectively (Boyd, 1998):

$$OTR = \alpha\left(\frac{\beta C_{sTW} - C_L}{C_{S20}}\right) \times SOTR, \tag{8}$$

$$AE = \alpha\left(\frac{\beta C_{sTW} - C_L}{C_{s20}}\right)\theta^{(T-20)} \times SAE, \quad (9)$$

where α and β are the correction factors.

3 Materials and methods

3.1 Experimental setup and approach

A 220 L volume of an experimental tank with measurements of 90 cm × 55 cm × 45 cm was operated with the venturi for oxygenating the full volume of water (Figure 1). The venturi circulates water with the help of pipe fittings in a closed-loop system with an associated pump, valves, water metre, and pressure gauge. The well-known sections of the venturi are divided into three distinct parts, namely, converging, throat, and diverging. The converging section is connected with the narrow section at the neck of the venture, and it terminates with the diverging section as an outlet of the venturi. Each of the sections of the venturi may be separated from one another. Another extended outlet pipe (EOP) is also connected with the diverging section to supply oxygenated water into the full volume of the water tank. Both converging and diverging sections were fabricated with the same length of 100 mm. The middle section of the venture, i.e., throat consists of five sets of different lengths, namely, 10 mm, 20 mm, 30 mm, 40 mm, and 50 mm . In total, four different extended outlet pipe lengths were designated in the current study to see the performance of aeration efficiency, i.e., 2 m, 4 m, 6 m, and 8 m.

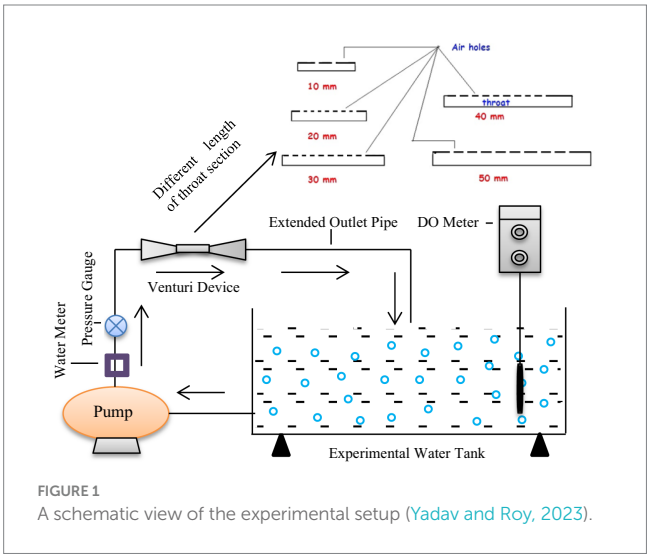

FIGURE 1
A schematic view of the experimental setup (Yadav and Roy, 2023).

3.2 Experimental design and procedure

All the experiments were conducted using a 1-HP centrifugal pump, which circulates water by venturi in a closed-loop manner with connecting extended outlet pipes of various lengths. The throat section produces a vacuum and makes it possible for air entry from air holes due to the pressure reduction. As a result, the air bubbles mix with water that flows via the venturi to the outlet pipe and continues to travel in the water tank. The experiments were conducted at three different flow rates (Q) of 0.30 L/s, 0.60 L/s, and 0.90 L/s for all sets of design parameters (throat length, TL; and extended outlet pipe, EOP). Table 1 presents the planned experiments to improve the venturi aeration system's aeration efficiency. A total of 60 experiments were performed with three replicates to optimise the aeration efficiency of the venturi aerator. With a 5% threshold of significance, substantial model parameters were found using the analysis of variance (ANOVA). In the current study, the AE of the venturi aeration system was analysed and compared using integrated models, i.e., ANN-PSO and ANN-GA. The extended outlet pipe (EOP), throat length (TL), and flow rate (Q) are the independent variables, and the dependent variable is chosen as AE to determine the model response.

In this analysis, pure tap water was initially deoxygenated using non-steady re-aeration experiments (ASCE, 2007). Each experiment utilised clean tap water that was deoxygenated to reduce the DO of each milligramme per litre employing 10 mg of sodium sulphite and 0.1 mg of cobalt chloride as a catalyst per litre volume of water (Boyd, 1998). The EXTECH DO metre 407,510 was used to measure the temperature, and DO level datasets for each set of operations were carried out at 1 min of an identical interval until 80% of DO saturation was attained. For each DO saturation measurement that was acquired, the measurements for the DO deficiencies were also produced. Furthermore, the graphical representation amongst natural log deficits (ordinate) and aeration time (abscissa) represents the best-fit gradient line to assess K_La_T. The gradient line was additionally improved by a 20°C temperature correction factor. Moreover, the oxygen transfer ability of the venturi has been estimated by K_La_{20}, OTR, and AE using Equations 5–7, respectively.

TABLE 1 Experimental schedule to determine the AE of the venturi aeration system.

S. No.	Parameters	Number of variables	Levels
A.	Independent parameters		
1.	Extended outlet pipe (EOP)	4	2, 4, 6, and 8 m with an interval of 2 m
2.	Throat length (TL)	5	10, 20, 30, 40, and 50 mm at an interval of 10.0 mm
3.	Water flow rate (Q)	3	0.30, 0.60, and 0.90 L/s at an interval of 0.30 L/s
B.	Dependent parameters		
1.	AE (kg O_2/kWh)		---

3.3 Artificial neural network integrated with particle swarm optimisation and genetic algorithm technique

The artificial neural network (ANN) is a data processing system that distributes data uniformly and has certain traits and features that are comparable to the neural structure of the human brain (Haykin, 1999; Mohanty et al., 2010; Yadav and Roy, 2023). An ANN includes an input layer (independent variables), a hidden layer, and an output layer (dependent variables); each layer contains a variety of processing components. An increasingly popular solution to conventional modelling methodologies and a more accurate tool to utilise with complicated non-linear interactions is the ANN, which relies on the idea of real-world neurons as well. An average neural system is fully interconnected, meaning that every single neuron in a single layer has a link to all the other neurons in each layer above it (Kumar et al., 2002). The process of the data information modelling approach starts using basic analysing units before scaling up to more complicated ones, modifying balanced inputs to make neural networks more effective. The effectiveness of an ANN multilayer model relies on both the number of neurons and connections and is affected by how the information is received, processed, and subsequently processed in hidden layers (Karri and Sahu, 2018). The available research shows that most researchers utilise a gradient-based optimisation technique called feed-forward neural network development with a conventional back-propagation strategy (Rumelhart et al., 1986).

The AE of the venturi aerator was considered as a result of the model with its selected operational parameters, i.e., TL, EOP, and Q, which were used as model inputs. A total of 70% of the 60 data points were applied for training, whilst the rest of the 30% were employed for network setting. In the present study, the experimental dataset of a 70:30 splitting ratio was used (Roy et al., 2022; Yadav and Roy, 2023). The optimal network layout for the ANN model was discovered to be 3–6-1 as presented in Figure 2. In the current study, the overfitting issue was resolved by standardising the experimental findings using min–max normalisation before utilising them for ANN training.

The particle swarm optimisation (PSO) modelling integrated with ANN is a cutting-edge, accurate, and experimental approach. A kind of meta-heuristic model called ANN-PSO can be utilised to build realistic models and deal with non-uniform multi-component interactions between dependent and independent variables (Yadav and Roy, 2023). The PSO requires fewer parameter adjustments than any other optimisation approach available and is simpler to implement (Eberhart and Shi, 2001). Furthermore, if the target function includes a single attribute and several local minima/maxima, the ideal value may be reached using the PSO method (Roy et al., 2021b). As PSO is a naturalistic exploration method as opposed to gradient-based optimisation, it has the drawback of being a sluggish procedure (Roy et al., 2021b). On the other hand, complicated non-linear optimisation issues are frequently solved using mathematical techniques such as genetic algorithm-based optimisation (ANN-GA) and ANN modelling. In the present study, ANN was integrated with PSO and GA algorithms separately to generate data of ANN using various amounts of neurons in the middle-hidden layer whilst taking into account the sample estimates for PSO and GA (Ghose et al., 2023). The movement of the points in space may be understood by their velocities, which also have the potential to hold their local and global best values (Jun et al., 2020). Each particle kept its location and modified velocity based on its own flight performance along with that of other elements in the search space to identify the most efficient result. The updated velocities and orientations of every single particle as it travels to the local optimal point (pbest) and global best point (gbest) are computed using the following Equations 10, 11.

$$v_i^{k+1} = wv_i^k + c_1 r_1 \left(pbest_i - x_i^k \right) + c_2 r_2 \left(gbest - x_i^k \right), \tag{10}$$

$$x_i^{k+1} = x_i^k + v_i^{k+1}, \tag{11}$$

where, $i = 1, 2, \ldots N$; N = population size, v_i^k = flow rate of the element i at iteration k; x_i^k = element position i at iteration k; $pbest_i$ = personal best of element i; $gbest$ = best point in the community; w = weight of inertia; c_1 and c_2 = coefficients; and r_1 and r_2 = random numbers uniformly scattered in the range (0, 1) (Figure 3).

Holland (1992) established the genetic algorithm (GA), a meta-heuristic optimisation method that utilises the ideas of the natural selection process and heredity. It is employed to resolve optimisation issues that are both confined and uncontrolled. Using statistical modifications, GA may continually adjust the number of distinctive approaches whilst searching over enormous solution spaces. The GA technique consists of three crucial processes, including the first group creation, genetic operator training (reproduction, crossover, and mutation), and evaluation according to a group's fitness value (Yang et al., 2020). The genetic algorithm identifies people at random within the existing population at each stage, treating them as a pair of parents to create progeny for the generations to come. Over succeeding generations, the population progresses in the direction of the optimal solution. It is possible to choose an adequate goal function by using a mixed genetic algorithm. The ability of ANN models to estimate the future is improved by the multidirectional searching technique used in GA (Figure 4).

In this study, the highest possible swarm size was set at 10 random particles produced and 50 iterations. The values taken for w, c_1, and c_2 are 0.8, 1.05, and 1.05, respectively. The programme was run by MATLAB-2013a to execute the ANN-PSO and ANN-GA techniques. Although the MATLAB PSO method employs an optimisation strategy, its goal is to maximise AE, which is expressed as a similar minimising problem, as follows:

$$objective\ function = \underset{X \in X^T}{\text{minimise}} \left(\frac{1}{F(X)} \right), \tag{12}$$

where $X = [X_1, X_2, X_3]^T$ = selected resolution vector and $F(X)$ = result of the ANN. The limits are specified as $10 \le X_1(TL) \le 50, 2 \le X_2(EOP) \le 8$, and $0.3 \le X_3(Q) \le 0.9$.

3.4 Performance analysis of the developed models

To evaluate the efficacy of the developed ANN and linear regression (LR) models, the coefficient of determination (R^2), root mean square error (RMSE), and mean absolute error (MAE) were used as indicators of effectiveness. The variables used in the produced

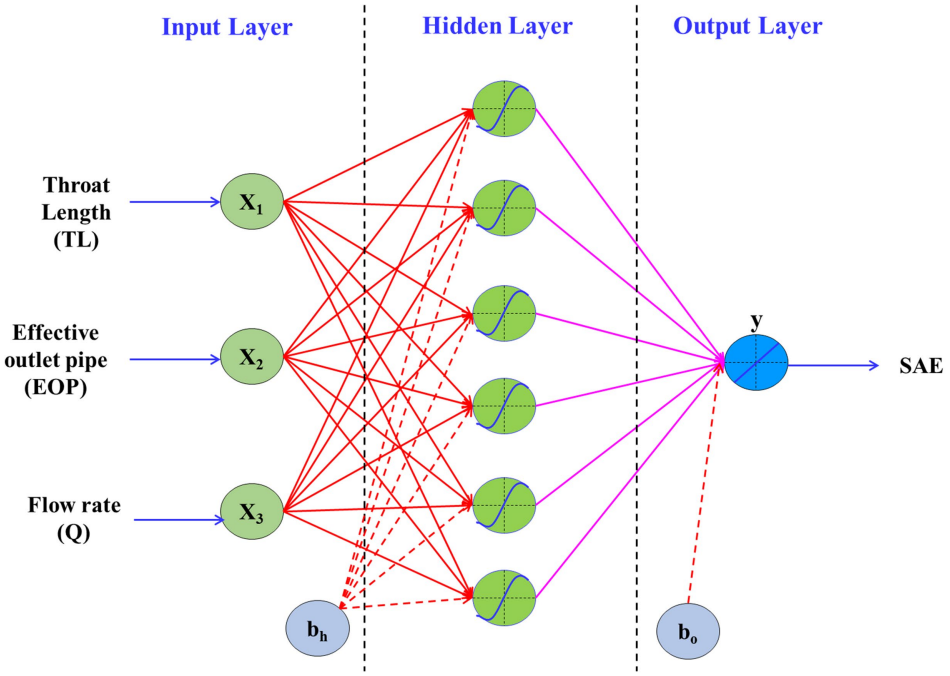

FIGURE 2
Topology of the 3-6-1 ANN model.

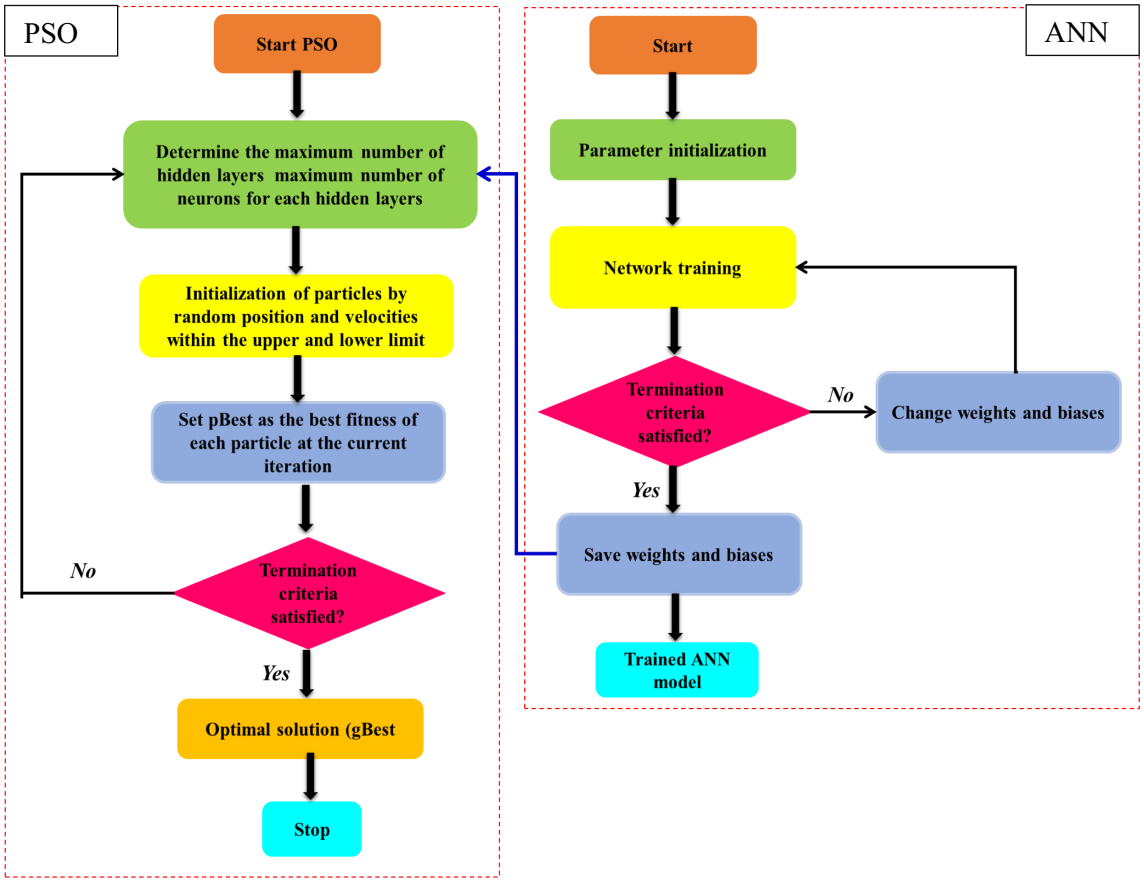

FIGURE 3
Flowchart of the ANN-PSO techniques.

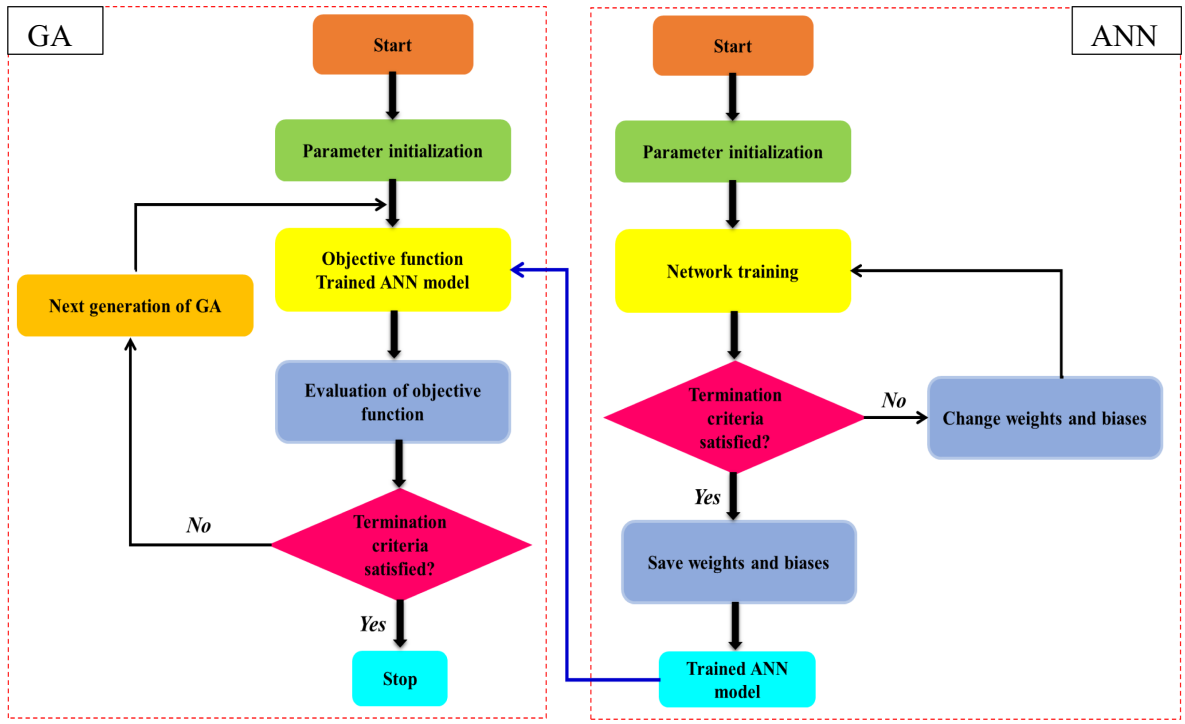

FIGURE 4
Flowchart of the ANN-GA techniques.

models were compared, and the algorithm of high coefficients of R^2 and fewer values of MAE and RMSE was determined as the best fit. The following Equations 13, 14, 15 were used to calculate R^2, RMSE, and MAE, respectively:

$$R^2 = \frac{\sum_{i=1}^{N}\left(O_i-\bar{O}\right)\left(P_i-\bar{P}\right)}{\sqrt{\sum_{i=1}^{N}\left(O_i-\bar{O}\right)^2\sum_{i=1}^{N}\left(P_i-\bar{P}\right)^2}}, \quad (13)$$

$$\mathrm{RMSE} = \sqrt{\frac{\sum_{i=1}^{N}(Oi-Pi)2}{N}}, \quad (14)$$

$$\mathrm{MAE} = \frac{1}{N}\sum_{i=1}^{N}|O_i-P_i|, \quad (15)$$

where N is the total amount of observations, Oi and Pi are the observable and projected values, respectively, and the bar represents the variable's mean.

4 Results and discussion

4.1 Modelling and linear regression analysis for AE

The linear regression analysis utilises a total of 60 observed responses; the model was developed using the least square method. A linear regression model was developed for several responses of AE using the investigated dataset. The linear relationship between AE and independent operative variables, i.e., TL, EOP, and Q, is depicted in the regression Equation 16.

$$\begin{aligned} AE\left(\frac{kg\ O_2}{kWh}\right) = {} & 0.0173 + 0.0098\times EOP + 0.0053 \\ & \times Q + 0.001\times TL - 9.317\times10^{-4} \\ & \times EOP^2 - 0.0042\times Q^2 + 2.505 \\ & \times10^{-6}\times TL^2 - 5.165\times10^{-4} \\ & \times EOP\times Q - 9.525\times10^{-6} \\ & \times EOP\times TL - 3.301\times10^{-5}\times Q\times TL. \end{aligned} \quad (16)$$

The linear regression Equation 16 specifies the hypothesis model that fits well in between the independent variables and AE. The linear regression equation is a second-order polynomial, which has a high coefficient of correlation (R^2) value, demonstrating that a significant relationship is feasible. The p-value and the R^2 value were estimated as 0.972 and 0.005, respectively. The above findings are supported by the value of the modified coefficient of correlation (R^2 adj.), 0.976. The 97.25% probability from the analysis indicates that the independent variables (TL, EOP, and Q) of the LR model are highly significant.

According to the statistical results (Table 2), every component of the linear model (TL, EOP, and Q), as well as the quadratic model term (TL2, EOP2, and Q2), has statistical significance at the 97.25% level of confidence. There is no statistical significance ($p > 0.05$) for the interacting model variables (EOP×Q), (EOP×TL), and (Q×TL).

TABLE 2 Estimated regression coefficients for AE (kg O_2/kWh).

Terms	Coefficient	SE coefficient	T	P
Constant	0.075297	0.000964	78.081	0.000
EOP (m)	−0.000194	0.000529	−0.367	0.716
Q (L/s)	−0.001017	0.000483	−2.109	0.040
TL (mm)	0.022789	0.000557	40.900	0.000
EOP (m)× EOP (m)	−0.008386	0.000886	−9.460	0.000
Q (L/s)×Q (L/s)	−0.000385	0.000836	−0.461	0.647
TL (mm)× TL (mm)	0.001002	0.000942	1.064	0.292
EOP (m)×Q (L/s)	−0.000465	0.000647	−0.718	0.476
EOP (m)× TL (mm)	−0.000572	0.000748	−0.765	0.448
Q (L/s)×TL (mm)	−0.000198	0.000682	−0.290	0.773

*S = 0.00305179, Significance level at R^2 = 97.25%, R^2 (pred) = 96.02%, R^2 (adj) = 96.76%.

TABLE 3 ANOVA for AE (kgO_2/kWh).

Terms	DF	Seq SS	Adj SS	Adj MS	F	*P*
Regression	9	0.016479	0.016479	0.001831	196.60	0.000
Linear	3	0.015622	0.015622	0.005207	559.13	0.000
EOP (m)	1	0.000001	0.000001	0.000001	0.13	0.716
Q (L/s)	1	0.000041	0.000041	0.000041	4.45	0.040
TL (mm)	1	0.015579	0.015579	0.015579	1672.80	0.000
Squares	3	0.000846	0.000846	0.000282	30.28	0.000
EOP × EOP	1	0.000833	0.000833	0.000833	89.49	0.000
Q × Q	1	0.000002	0.000002	0.000002	0.21	0.647
TL × TL	1	0.000011	0.000011	0.000011	1.13	0.292
Interaction	3	0.000011	0.000011	0.000004	0.39	0.757
EOP × Q	1	0.000005	0.000005	0.000005	0.52	0.476
EOP × TL	1	0.000005	0.000005	0.000005	0.58	0.448
Q × TL	1	0.000001	0.000001	0.000001	0.08	0.773
Residual Error	50	0.000466	0.000466	0.000009		
Total	59	0.016945				

The results of the *p* values are an easy approach for evaluating the importance of various coefficients. The significance of the associated coefficient increases with decreasing P. The correlation between the variables is extremely significant ($F = 196.60$; $p = 0.000$), according to the ANOVA (Table 3) of the best-fitted estimated model. According to the results of the present study, the model term TL ($p = 0.000$) is significant ($p < 0.05$), whereas, the other model terms, EOP ($p = 0.716$) and Q ($p = 0.040$) are not significant ($p > 0.005$). The quadratic terms EOP × EOP ($p = 0.000$) are significant ($p < 0.05$), whilst the other quadratic terms Q × Q ($p = 0.647$) and TL × TL ($p = 0.292$) have a poor fit and are considered non-significant ($p > 0.05$). Additionally, the interaction between the independent variables (EOP × Q, EOP × TL, and Q × TL) has no apparent impact on the AE ($p > 0.005$). Consequently, it may be concluded that the proposed model satisfactorily matches the results of the experiments (Pareek et al., 2023a,b).

4.2 Artificial neural network modelling

Artificial neural network (ANN), which gets their inspiration from the way the human brain functions, may be used to predict outcomes for a variety of activities, including analytical and numerical modelling involving a variety of data types. The ANN depends on an awareness of the statistical fundamentals of the events underlying the procedure, and it has significant benefits over traditional modelling approaches (Figure 5). The development of the best back-propagation training technique, the establishment of the appropriate number of neurons, and verifying and testing the model, all three processes were employed to develop the perfect ANN modelling structure (Kedia et al., 2022). The ANN aims to predict available capabilities using real data by replicating the organic nervous system, which replicates data on somebody's cognitive processes. The ANN often results in an inundation of previous experience data. Once the model was successfully constructed using the trial and error method, the minimum MSE was found between the target value and the ANN model's forecast value of AE (Yadav and Roy, 2023). The neural network correlation network indicates the projected and targeted datasets, i.e., the training dataset, the testing dataset, and the complete experimental dataset for the ANN model as shown in Figure 5. The ANN model's coefficient value of R^2 for the training dataset, the validation dataset, the testing dataset, and the overall prediction was observed to be 0.98855, 0.97891, 0.98320, and 0.98545, respectively (Figure 5). From Figure 5, the R^2 value between the measured and anticipated responses for the data analysis phases (training, validation, and testing) is close to 1. Hence, the implementation of the ANN was deemed to be very satisfying and robust to estimate the AE values. The highest possible AE value of 0.1050 kg O_2/kWh was found using the expected TL, EOP, and Q values of 50 mm, 6 m, and 0.6 L/s, respectively.

The MSE versus the number of epochs is displayed and is presented in Figure 6. In epoch 8, the value 0.000016445 represents the prime substantial performance. During the training phase, the neural network divides the source and target dataset into three individual data, i.e., training, validation, and testing samples. Using training samples, the network is instructed, and variables are changed in response to errors. The network's ability to make predictions is assessed using validation samples, and training ceases when it hits the point of saturation. Furthermore, network evaluation is performed before, during, and after training using testing data. Figure 6 shows a green, blue, and red line for validation, training, and testing, respectively. The green colour of the ring circle denotes the network's peak validation effectiveness. On the other hand, the generalisation comes to an end and the training is ended after 19 epochs. It changes throughout retraining as a result of the network regularly splitting the source and target datasets.

Figure 7 displays training state plots for the gradient values, mutation (mu), and validation cheques for ANN. A gradient depicts

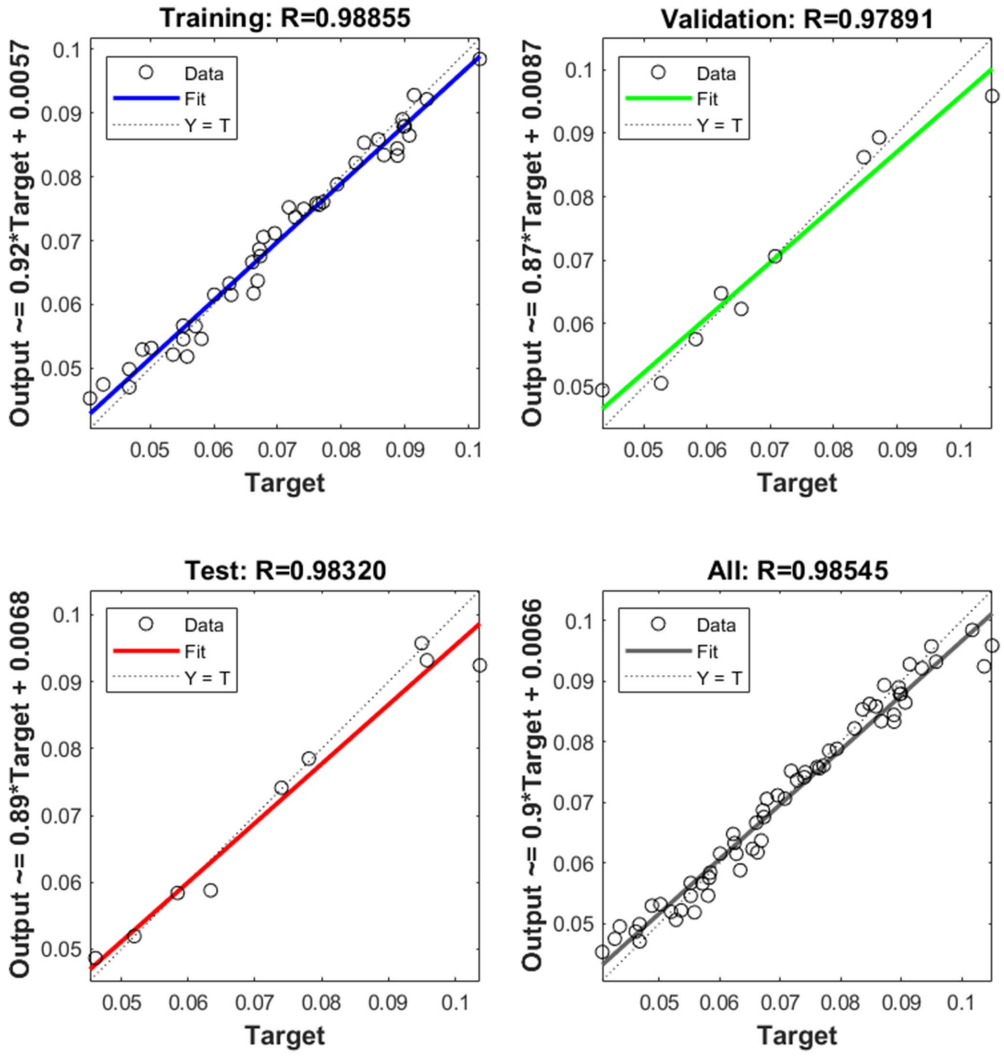

FIGURE 5
Training, validation, test, and overall scatter plots of ANN model for various stages.

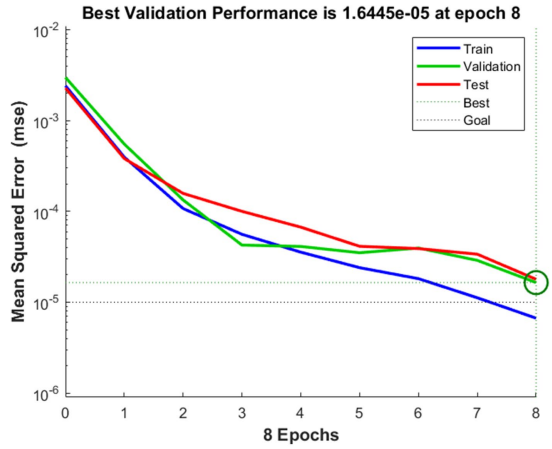

FIGURE 6
The best validation graph of the network.

the tangent's slope on a function graph. It suggests that there is a rapid rate of increase in the direction that the parameter under consideration is moving. Error convergence is directly influenced by the back-propagation neural network that was constructed to use the controlling parameter called mutation (mu). A validation cheque halted the learning process of the neural network. A variety of validation tests will be carried out based on how frequently the neural network is iterated (Roy et al., 2023). The gradient's magnitude and the number of validation cheques needed to end the training are displayed in Figure 7A. As training approaches the performance threshold, the gradient becomes very small. The training phase will end if the gradient's magnitude is less than 0.00001, which can be modified by adjusting the parameter. The mutation is shown against the increasing number of iterations in Figure 7B. This graphic demonstrates how training improves and the network error decreases. Based on Figure 7C, the number of validation cheques indicates how many rounds the validation performance fails to decline in succession. The training will end once this number hits 8 in the current scenario.

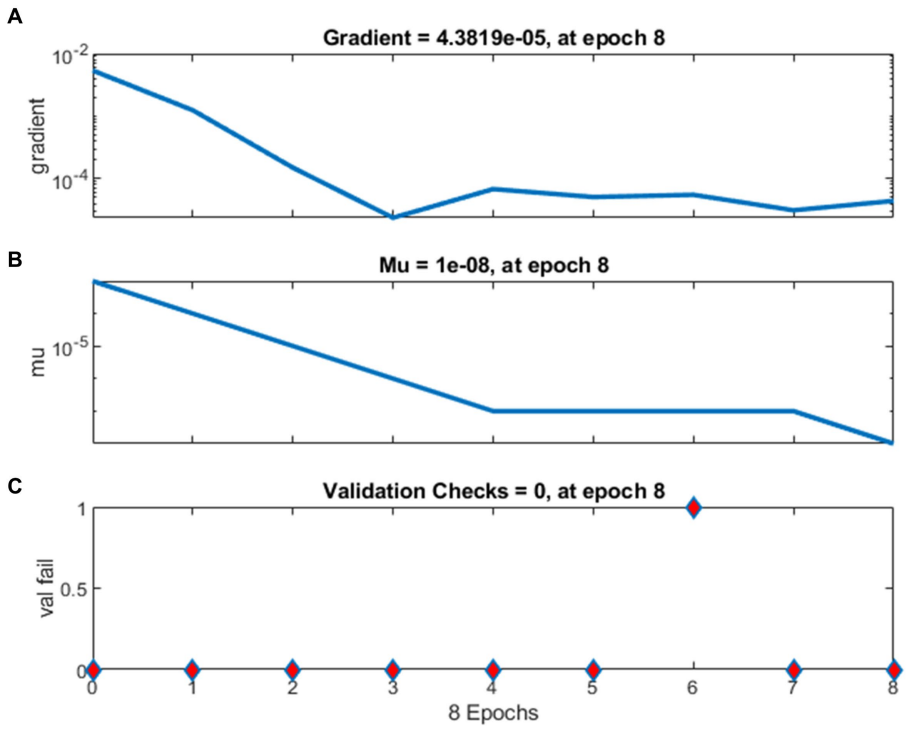

FIGURE 7
Training state plots for **(A)** gradient, **(B)** mutation, and **(C)** validation cheques.

TABLE 4 **Performance indicators of the ANN models in the prediction of aeration efficiency.**

Model	Data	Performance standard		
		R^2	RMSE	MAE
ANN-PSO	Training data	0.988	0.020	0.090
	Testing data	0.983	0.029	0.176
ANN-GA	Training data	0.972	2.567	1.980
	Testing data	0.912	3.675	3.123

4.3 Particle swarm optimisation

The design parameters (TL and EOP) and operational parameters (Q) of the venturi aeration system were optimised using the most reliable prediction model and PSO in order to obtain the highest acceptable AE. The PSO algorithm scatters its elements all over a hyperdimensional search area. Every cluster member serves as an alternate solution to the optimisation problem by evaluating the desired function at that member's present location. Engelbrecht (2007) defined that the positioning of elements within the search region is altered in accordance with people's social-psychological propensity to imitate others' accomplishments. Every single particle in a cluster is therefore driven for movement by fusing some aspect of its previous existence with the expertise of those around it.

4.4 A comparison between ANN-PSO and ANN-GA models

The developed ANN-PSO and ANN-GA models were predicted and compared based on statistical characteristics datasets of training and testing by model parameters, i.e., R^2, RMSE, and MAE. Table 4 displays these model evaluation indicators of created models. The high R^2 value for training and testing and the low value of RMSE and MAE indicate the significant performance of two values between experimental AE values.

The ANN-PSO model has a high R^2 value for training and testing and a low value of RMSE and MAE compared to the ANN-GA model indicating a better prediction of AE values. Therefore, it can be concluded that the performance of ANN-PSO is better than ANN-GA. Table 5 displays and compares the optimal parameters produced by the combined ANN-PSO and ANN-GA methods. The developed models ANN-PSO and ANN-GA are used to select the suitable operating conditions and aids to find out the AE of the venturi aerator. A maximum deviation of 5.714% of the anticipated and actual values of AE from ANN-PSO is presented in Table 5.

Table 6 displays the optimum parameters using the combined ANN-PSO method, which has been compared with the results of the earlier experimental research study (Yadav and Roy, 2023). The created ANN-PSO model may be used to estimate the accessible

TABLE 5 Optimised limits by ANN-PSO and ANN-GA.

Model	TL	EOP	Q (L/s)	Aeration efficiency (kg O_2/kWh)		
				Predicted	Observed	Deviation (%)
ANN-PSO	5.026	48.0100	0.601	0.996	0.105	5.714%
ANN-GA	5.426	50.0000	0.68	0.993	0.105	5.714%

TABLE 6 A comparison of the SAE values of the integrated ANN-PSO technique with the previous dataset.

SAE (kg O_2/kWh) value using the ANN-PSO algorithm		Deviation (%)
Present study	Previous study (Yadav and Roy, 2023)	
0.996	0.902	7.09

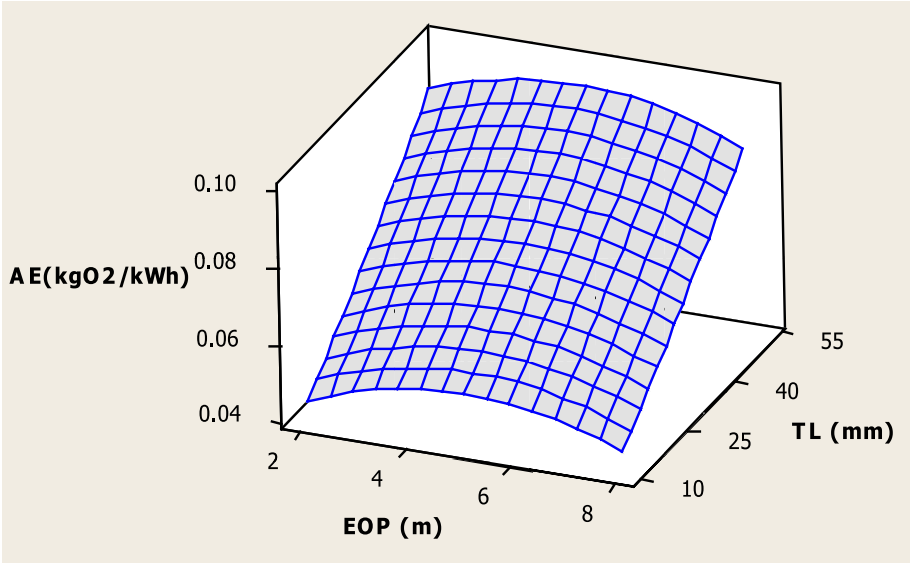

FIGURE 8
Interactive response surface plot of EOP and TL on SAE.

aeration effectiveness of the venturi aeration system and to determine the proper operating parameters.

4.5 Effects of operating parameters (TL, EOP, and Q) on AE

The combined effect of operating parameters as EOP and TL on AE is shown in Figure 8, the combined effect of EOP and Q on AE is shown in Figure 9, and the combined effect of Q and TL on AE is shown in Figure 10. It can be clearly seen from Figure 8 that the AE steadily rises with the increase in the extended outlet pipe (EOP) from 2 m to 6 m and then drops again to 8 m of EOP. It can also be found that the AE rises rapidly with increasing throat length (TL) up to 50 mm. This is due to the fact that by increasing the throat length (TL = 10 mm to 50 mm), more vacuum is created that facilitates the maximum pressure reduction resulting in more oxygen transfer rate and aeration efficiency. When the effective outlet pipe increases, the air bubbles get dispersed resulting in the reduction of aeration efficiency. The maximum AE was found at 6 m EOP and 50 mm TL.

Figure 9 shows a relation between EOP and Q on AE. It can be seen from Figure 9 that AE increases with the increasing EOP up to 6 m. However, after 6 m of EOP, the AE values decline when it reaches to the maximum EOP of 8 m. In addition, it was found the AE values are influenced by varying the flow rate (Q). The AE value increases with an increase in Q value up to 0.6 L/s. For further increase in the Q from 0.6 L/s to 0.9 L/s, the AE starts to decrease mainly at the EOP of 8 m. This is due to the fact that the increasing discharges create more turbulence and aid in enhancing the transfer rate of oxygen. Furthermore, at the maximum 8 m EOP, inserted air bubbles get dispersed without affecting the oxygen transfer, which reduces the AE of the venturi. Therefore, it can be concluded that the Q is primarily responsible for transferring air into the water (Yadav et al., 2021).

Furthermore, the effect of Q and TL on AE is presented in Figure 10. Figure 10 indicates very clearly that with an increase in the TL of the venturi, the AE increases at every increasing Q. The maximum AE value was found at 50 mm of TL for all increasing flow rates (Q = 0.3 L/s, 0.6 L/s, and 0.9 L/s). The reason behind that the increasing TL provides a high air entrainment rate, that obvious improves the oxygen transfer capability of the venturi with the increasing Q. The maximum SAE value was determined to be 0.105 kg

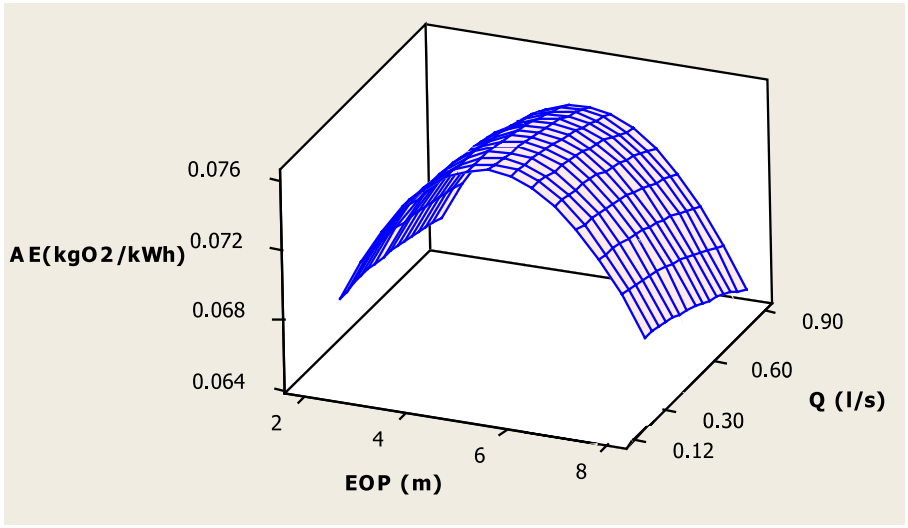

FIGURE 9
Interactive response surface plot of EOP and Q on SAE.

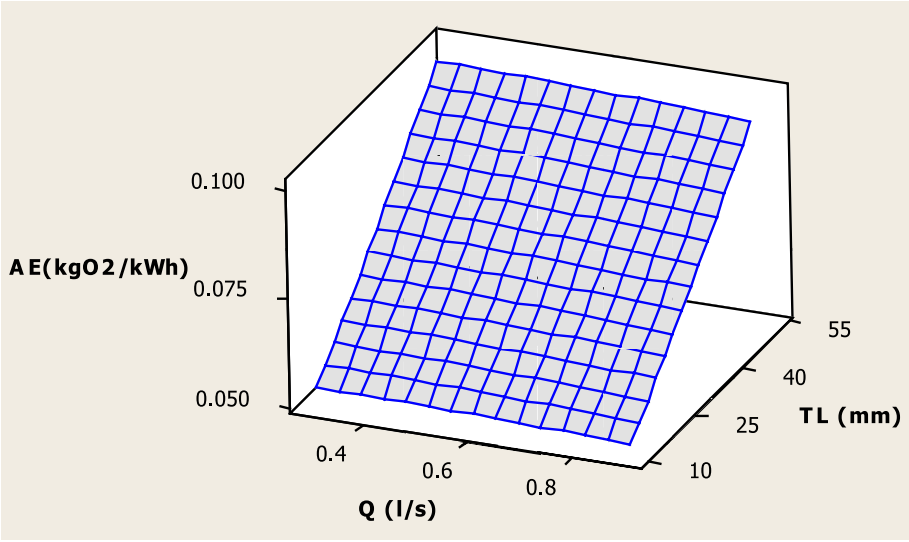

FIGURE 10
Interactive response surface plot of Q and TL on SAE.

O_2/kWh, when operating at 0.6 L/s flow rate with a 6 m effective output pipe and a 50 mm throat length of the venturi.

5 Future scope

The venturi aeration system and its applications have been constrained by several challenges related to air entrainment in water and wastewater treatment. The challenges associated with air bubble formation limit the ability to produce stable fine bubbles in large quantities as existing techniques sometimes require expensive specialist equipment (Yuan et al., 2024). Furthermore, this study may be expanded to highlight the restrictions on turbulence that occurs in the throat section of the venturi, by capturing the intricate cavitation phenomena. By clarifying the difficulties encountered in applying turbulence models to air entrainment via venturi systems, this study offers a foundation for further research endeavours focussed on optimising mathematical expressions (Devkota et al., 2024). This methodical technique can significantly increase numerical simulation accuracy and bring computational findings more closely aligned with empirical data. The results of this study will assist in simulating aeration efficiency through venturi aeration by helping to choose the most suitable venturi settings in the fields of aquaculture and wastewater treatment. This may help to enhance

the functionality and design of the venturi. The results of this study might be helpful in the design and improvement of industrial systems that employ the aeration phenomena. Furthermore, this study might serve as a starting point for further investigations into the technical and industrial uses of venturi systems and their design and optimisation.

6 Conclusion

The effectiveness of the venturi aeration system has been introduced as an effective optimisation strategy for evaluating the aeration efficiency (AE) using hybrid prediction modelling techniques, i.e., artificial neural network–particle swarm optimisation (ANN-PSO) and artificial neural network–genetic algorithm (ANN-GA). From the developed ANN integrated with PSO and GA, the operating parameters, i.e., TL, EOP, and Q, were optimised at 50 mm, 6 m, and 0.6 L/s, respectively, in order to maximise the AE. The highest AE was found as 0.105 kgO_2/kWh to exist under optimal operating circumstances. From the overall finding, it can be concluded that the performance of ANN-PSO is better than ANN-GA, due to the accuracy of ANN-PSO being more based on a 5.714% deviation. The suggested hybrid model is also easy to use and can take into consideration an inclusive range of factors affecting the efficacy of aerators. The developed ANN-PSO and ANN-GA models may be utilised to determine the optimal operating parameters for different aerators and anticipate the aeration efficiency of the venturi aerator. Notably, the integrated model's primary constraint is its applicability to particular regions that are similar or that have only slight variations under any of the circumstances.

Data availability statement

The raw data supporting the conclusions of this article will be made available by the authors, without undue reservation.

Author contributions

AY: Conceptualization, Data curation, Formal analysis, Investigation, Methodology, Project administration, Resources, Software, Supervision, Validation, Visualization, Writing – original draft, Writing – review & editing. SR: Conceptualization, Data curation, Formal analysis, Methodology, Validation, Visualization, Writing – review & editing. AB: Conceptualization, Data curation, Formal analysis, Methodology, Resources, Software, Supervision, Validation, Visualization, Writing – original draft, Writing – review & editing. BS: Investigation, Project administration, Software, Supervision, Validation, Visualization, Writing – review & editing. SM: Data curation, Formal analysis, Investigation, Resources, Software, Supervision, Validation, Visualization, Writing – review & editing.

Funding

The author(s) declare that no financial support was received for the research, authorship, and/or publication of this article.

Conflict of interest

The authors declare that the research was conducted in the absence of any commercial or financial relationships that could be construed as a potential conflict of interest.

Publisher's note

References

APHA. (1985). *Standard methods for the examination of water and wastewater, 16th Edn.* Washington, DC: APHA.

ASCE. (2007). *Standard measurement of oxygen transfer in clean water*. Virginia: American Society of Civil Engineers.

Bagatur, T., and Onen, F. (2014). A predictive model on air entrainment by plunging water jets using GEP and ANN. *KSCE J. Civ. Eng.* 18, 304–314. doi: 10.1007/s12205-013-0210-7

Baylar, A., and Emiroglu, M. (2003). Air entrainment and oxygen transfer in a venturi. *Proc. ICE Water Marit. Eng.* 156, 249–255. doi: 10.1680/wame.2003.156.3.249

Baylar, A., and Ozkan, F. (2006). Applications of venturi principle to water aeration systems. *Environ. Fluid Mech.* 6, 341–357. doi: 10.1007/s10652-005-5664-9

Boyd, C. E. (1998). Pond water aeration systems. *Aquac. Eng.* 18, 9–40. doi: 10.1016/S0144-8609(98)00019-3

Boyd, C. E., and Ahmad, T. (1987). *Evaluation of aerators for channel catfish farming, bulletin 584*. Alabama: Alabama Agricultural Experiment Station, Auburn University, p. 52.

Cheng, X., Xie, Y., Zhu, D., and Xie, J. (2019). Modeling re-oxygenation performance of fine-bubble–diffusing aeration system in aquaculture ponds. *Aquac. Int.* 27, 1353–1368. doi: 10.1007/s10499-019-00390-6

Dayev, Z., Shopanova, G., Toksanbaeva, B., Yetilmezsoy, K., Sultanov, N., Sihag, P., et al. (2022). Modeling the flow rate of dry part in the wet gas mixture using decision tree/kernel/non-parametric regression-based soft-computing techniques. *Flow Meas. Instrum.* 86:102195. doi: 10.1016/j.flowmeasinst.2022.102195

Dayıoğlu, M. A. (2022). Experimental study on design and operational performance of solar-powered venturi aeration system developed for aquaculture–a semi-floating prototype. *Aquac. Eng.* 98:102255. doi: 10.1016/j.aquaeng.2022.102255

Devkota, H. R., Jha, D. K., Joshi, T. P., and Shrestha, S. (2024). Applications of Nanobubble aeration Technology for Aquaculture Practices: a review. *Nepal. J. Agric. Sci.*:223.

Eberhart, E., and Shi, Y. (2001). *Particle swarm optimization: Developments, applications and resources. Proceedings of the 2001 congress on evolutionary computation (IEEE cat. No.01TH8546), Seoul, Korea (south)*. 81–86.

Engelbrecht, A. P. (2007). *Computational intelligence: An introduction. 2nd Edn.* West Sussex: John Wiley and Sons Ltd.

FAO. (2019). *The state of food and agriculture 2019. Moving forward on food loss and waste reduction*. Rome: FAO, p. 182.

Garg, A., and Jain, S. (2020). Process parameter optimization of biodiesel production from algal oil by response surface methodology and artificial neural networks. *Fuel* 277:118254. doi: 10.1016/j.fuel.2020.118254

Ghomi, M. R., Sohrabnejad, M., and Ovissipour, M. R. (2009). An experimental study of nozzle diameters, aeration depths and angles on standard aeration efficiency (SAE) in a venturi aerator. *Water Pract. Technol.* 4, 1–8. doi: 10.2166/wpt.2009.043

Ghose, A., Gupta, D., Nuzelu, V., Rangan, L., and Mitra, S. (2023). Optimization of laccase enzyme extraction from spent mushroom waste of Pleurotus florida through ANN-PSO modeling: an ecofriendly and economical approach. *Environ. Res.* 222:115345. doi: 10.1016/j.envres.2023.115345

Gupta, B., Nayak, A. K., Kandar, T. K., and Nair, S. (2016). Investigation of air–water two phase flow through a venturi. *Exp. Thermal Fluid Sci.* 70, 148–154. doi: 10.1016/j.expthermflusci.2015.07.012

Haykin, S. (1999). *Neural network: A comprehensive foundation*. Englewood Cliffs, NJ: Prentice-Hall Inc..

Haykin, S. (2009). *Neural networks and learning machines. 3rd Edn.* India: Pearson Education.

Holland, J. H. (1992). *Adaptation in natural and artificial systems*. London: MIT Press.

Jun, L. Y., Karri, R. R., Yon, L. S., Mubarak, N. M., Bing, C. H., Mohammad, K., et al. (2020). Modeling and optimization by particle swarm embedded neural network for adsorption of methylene blue by jicama peroxidase immobilized on buckypaper/polyvinyl alcohol membrane. *Environ. Res.* 183:109158. doi: 10.1016/j.envres.2020.109158

Karri, R. R., and Sahu, J. N. (2018). Modeling and optimization by particle swarm embedded neural network for adsorption of zinc (II) by palm kernel shell based activated carbon from aqueous environment. *J. Environ. Manag.* 206, 178–191. doi: 10.1016/j.jenvman.2017.10.026

Kedia, N. K., Kumar, A., and Singh, Y. (2022). Prediction of underground metro train-induced ground vibration using hybrid PSO-ANN approach. *Neural Comput. Applic.* 35, 8171–8195. doi: 10.1007/s00521-022-08093-5

Kumar, M., Raghuwanshi, N. S., Singh, R., Wallender, W. W., and Pruitt, W. O. (2002). Estimating evapotranspiration using artificial neural network. *J. Irrig. Drain. Eng.* 128, 224–233. doi: 10.1061/(ASCE)0733-9437(2002)128:4(224)

Kumar, M., Ranjan, S., and Tiwari, N. K. (2018). Oxygen transfer study and modeling of plunging hollow jets. *Appl Water Sci* 8:740. doi: 10.1007/s13201-018-0740-8

Lawson, T. B., and Merry, G. E. (1993). Procedures for evaluating low-power surface aerators under field conditions, in: Techniques for modern aquaculture. Proceedings of an Aquacultural Engineering Conference, ASAE, Michigan, USA, p. 511.

Lewis, W. K., and Whitman, W. G. (1924). Principles of gas absorption. *Ind. Eng. Chem. Res.* 16, 1215–1220. doi: 10.1021/ie50180a002

Li, J. J., Song, Y. C., Yin, J. L., and Wang, D. Z. (2017). Investigation on the effect of geometrical parameters on the performance of a venturi type bubble generator. *Nucl. Eng. Des.* 325, 90–96. doi: 10.1016/j.nucengdes.2017.10.006

Luk, K. C., Ball, J. E., and Sharma, A. (2001). An application of artificial neural networks for rainfall forecasting. *Math. Comput. Model.* 33, 683–693. doi: 10.1016/S0895-7177(00)00272-7

Luxmi, K. M., Tiwari, N. K., and Ranjan, S. (2022). Application of soft computing approaches to predict gabion weir oxygen aeration efficiency. *ISH J. Hydraul. Eng.* 29, 244–258. doi: 10.1080/09715010.2022.2050311

Mahmud, R., Erguvan, M., and MacPhee, D. W. (2020). Performance of closed loop venturi aspirated aeration system: experimental study and numerical analysis with discrete bubble model. *Water* 12, 16–37. doi: 10.3390/w12061637

Metcalf, L., Eddy, H. P., and Tchobanoglous, G. (1979). *Wastewater engineering: Treatment, disposal, and reuse*, New York: McGraw-Hill.

Mjalli, F. S., Al-Asheh, S., and Alfadala, H. E. (2007). Use of artificial neural whites network black-box modeling for the prediction of wastewater treatment plants performance. *J. Environ. Manag.* 83, 329–338. doi: 10.1016/j.jenvman.2006.03.004

Mohanty, S., Jha, M. K., Kumar, A., and Sudheer, K. P. (2010). Artificial neural network modeling for groundwater level forecasting in a river island of eastern India. *Water Resour. Manag.* 24, 1845–1865. doi: 10.1007/s11269-009-9527-x

Navisa, J., Sravya, T., Swetha, M., and Venkatesan, M. (2014). Effect of bubble size on aeration process. *Asian J. Sci. Res.* 7, 482–487. doi: 10.3923/ajsr.2014.482.487

Omary, R., Li, H., Tang, P., Issaka, Z., and Chao, C. (2020). Review of venturi injector application technology for efficient fertigation in irrigation system. *Int. J. Curr. Microbiol. App. Sci.* 9, 46–61. doi: 10.20546/ijcmas.2020.901.006

Omid, M., Asghar, M., and Omid, M. H. (2009). An intelligent system for sorting pistachio nut varieties. *Expert Syst. Appl.* 36, 11528–11535. doi: 10.1016/j.eswa.2009.03.040

Onen, F. (2014). Prediction of penetration depth in a plunging water jet using soft computing approaches. *Neural Comput. & Applic.* 25, 217–227. doi: 10.1007/s00521-013-1475-y

Pareek, C. M., Singh, N., Tewari, V. K., Dhruw, L. K., and Singh, H. D. (2023a). Classification of broken maize kernels using artificial neural network-assisted image-processing approach. *J. Biosyst. Eng.* 48, 55–68. doi: 10.1007/s42853-022-00173-7

Pareek, C. M., Tewari, V. K., and Machavaram, R. (2023b). Multi-objective optimization of seeding performance of a pneumatic precision seed metering device using integrated ANN-MOPSO approach. *Eng. Appl. Artif. Intell.* 117:105559. doi: 10.1016/j.engappai.2022.105559

Pareek, C. M., Tewari, V. K., Machavaram, R., and Nare, B. (2021). Optimizing the seed-cell filling performance of an inclined plate seed metering device using integrated ANN-PSO approach. *Artif. Intell. Agric.* 5, 1–12. doi: 10.1016/j.aiia.2020.11.002

Pawar, N. A., Jena, J. K., Das, P. C., and Bhatnagar, D. D. (2009). Influence of duration of aeration on growth and survival of carp fingerlings during high density seed rearing. *Aquaculture* 290, 263–268. doi: 10.1016/j.aquaculture.2009.02.030

Roy, S. M., Jayraj, P., Machavaram, R., and Mal, B. C. (2021a). Diversified aeration facilities for effective aquaculture systems–a comprehensive review. *Aquac. Int.* 29, 1181–1217. doi: 10.1007/s10499-021-00685-7

Roy, S. M., Pareek, C. M., Kim, T., and Mal, B. C. (2023). Artificial intelligence-based approach for improving the aeration efficiency of a perforated plate aeration system. *Multiscale Multidiscip. Model. Exp. Des.* 1, 1–14. doi: 10.1007/s41939-023-00250-0

Roy, S. M., Pareek, C. M., Machavaram, R., and Mukherjee, C. K. (2022). Optimizing the aeration performance of a perforated pooled circular stepped cascade aerator using hybrid ANN-PSO technique. *Inf. Proc. Agric.* 9, 533–546. doi: 10.1016/j.inpa.2021.09.002

Roy, S. M., Tanveer, M., Gupta, D., Pareek, C. M., and Mal, B. C. (2021b). Prediction of standard aeration efficiency of a propeller diffused aeration system using response surface methodology and an artificial neural network. *Water Supply* 21, 4534–4547. doi: 10.2166/ws.2021.199

Roy, S. M., Tanveer, M., Mukherjee, C. K., and Mal, B. C. (2020). Design characteristics of perforated tray aerator. *Water Supply* 20, 1643–1652. doi: 10.2166/ws.2020.069

Rumelhart, D. E., Hinton, G. E., and Williams, R. J. (1986). Learning representations by back propagating errors. *Nature* 323:533. doi: 10.1038/323533a0

Sangeeta, S. R., and Tiwari, N. K. (2019). Aeration efficiency evaluation of modified small Parshall flume using M5P and adaptive neuro-fuzzy. *Sustain. Eng. Proc. EGRWSE* 30, 243–252. doi: 10.1007/978-981-13-6717-5_24

Sanghani, C. R., Jayani, D. C., Jadvani, N. R., Dobariya, H. N., and Jasoliya, K. R. (2014). Effect of geometrical parameters of venturimeter on pressure drop. *Int J. Sci. Res. Sci. Eng. Technol.* 2, 865–868.

Sihag, P., Dursun, O. F., Sammen, S. S., Malik, A., and Chauhan, A. (2021). Prediction of aeration efficiency of Parshall and modified venturi flumes: application of soft computing versus regression models. *Water Supply* 21, 4068–4085. doi: 10.2166/ws.2021.161

Sun, L. C., Mo, Z. Y., Zhao, L., Liu, H. T., Guo, X., Ju, X. F., et al. (2017). Characteristics and mechanism of bubble breakup in a bubble generator developed for a small TMSR. *Ann. Nucl. Energy* 109, 69–81. doi: 10.1016/j.anucene.2017.05.015

Treybal, R. E. (1985). *Mass transfer operations. 5th Edn.* New York: Mc Graw Hill.

Wang, H., Wang, J., Li, G., Mo, Y., and Zhang, Y. (2022). Performance test of Venturi aerators for subsurface drip irrigation. *J. Irrig. Drain. Eng.* 148:06022001. doi: 10.1061/(ASCE)IR.1943-4774.0001660

Yadav, A., Kumar, A., and Sarkar, S. (2019). Design characteristics of venturi aeration system. *Int. J. Innov. Technol. Explor. Eng.* 8, 63–70. doi: 10.35940/ijitee.J9929.0981119

Yadav, A., Kumar, A., and Sarkar, S. (2020). An experimental study to evaluate the efficacy of air entrainment holes on the throat of a venturi aeration system. *Aquac. Int.* 28, 1057–1068. doi: 10.1007/s10499-020-00511-6

Yadav, A., Kumar, A., and Sarkar, S. (2021). Performance evaluation of venturi aeration system. *Aquac. Eng.* 93:102156. doi: 10.1016/j.aquaeng.2021.102156

Yadav, A., and Roy, S. M. (2023). An artificial neural network-particle swarm optimization (ANN-PSO) approach to predict the aeration efficiency of venturi aeration system. *Smart Agric. Technol.* 4:100230. doi: 10.1016/j.atech.2023.100230

Yang, H., Hasanipanah, M., Tahir, M. M., and Bui, D. T. (2020). Intelligentprediction of blasting-induced ground vibration using ANFIS optimized by GA and PSO. *Nat. Resour. Res.* 29, 739–750. doi: 10.1007/s11053-019-09515-3

Yuan, J., Zeng, T., Liu, Z., and Li, W. (2024). Experimental research on a gas liquid mixing oxygen increasing device based on microbubbles. *Int. J. Mech. Elect. Eng.* 2, 7–12. doi: 10.62051/ijmee.v2n1.02

Zhang, J. X. (2017). Analysis on the effect of venturi tube structural parameters on fluid flow. *AIP Adv.* 7:065315. doi: 10.1063/1.4991441

Zhang, C., Song, B., Shan, J., Ni, Q., Wu, F., and Wang, S. (2020). Design and optimization of a new tube aeration device. *Aquac. Int.* 28, 985–999. doi: 10.1007/s10499-020-00507-2

frontiers | Frontiers in Environmental Science

TYPE Policy Brief
PUBLISHED 21 June 2024
DOI 10.3389/fenvs.2024.1398822

OPEN ACCESS

EDITED BY
Vikram Kumar,
Planning and Development, Govt. of Bihar, India

REVIEWED BY
Prakash Kumar Jha,
Mississippi State University, United States
Sayantan Sarkar,
Texas A and M AgriLife Research, United States

*CORRESPONDENCE
Ankit Chandra,
ankitchandra@nebraska.edu

RECEIVED 10 March 2024
ACCEPTED 24 May 2024
PUBLISHED 21 June 2024

CITATION
Chandra A and Brozović N (2024), Shifting dynamics and environmental implications of the irrigation pump market in India.
Front. Environ. Sci. 12:1398822.
doi: 10.3389/fenvs.2024.1398822

Shifting dynamics and environmental implications of the irrigation pump market in India

Ankit Chandra[1]* and Nicholas Brozović[1,2]

[1]Daugherty Water for Food Global Institute at the University of Nebraska, Lincoln, NE, United States, [2]Department of Agricultural Economics, University of Nebraska-Lincoln, Lincoln, NE, United States

India is the world's largest user of groundwater for irrigation, with approximately 32 million pumps running on diesel, electric, and solar power. Subsidized electricity has led to an increase in the adoption of electric pumps by farmers, with increasing electrification rates and rising diesel costs contributing to the trend. Government subsidies have been instrumental in enhancing smallholder irrigation pump access. However, subsidies on irrigation pumps may exacerbate undesirable groundwater depletion. In smallholder settings where the capital needed to purchase irrigation equipment exceeds farmers' means, "irrigation-as-a-service" and "rental pumps" with organized and affordable volumetric pricing could offer viable solutions. This policy brief provides key learnings on the Indian irrigation pump market and its policy and environmental implications, based on semi-structured interviews and secondary data collected.

KEYWORDS

smallholder, irrigation pump, policy, finance, solar, groundwater, environment

1 Introduction

Irrigation is a crucial tool for addressing climate change impacts on agricultural production within the framework of the Sustainable Development Goals (SDGs). As a result, irrigation continues to be a policy focus in many developing economies where drought occurs. At a country level, India is the largest user of groundwater for irrigation (Balasubramanya and Buisson, 2022). A large market for small mechanized water pumping equipment exists, with an estimated 32 million irrigation pumps already operating that use diesel, electric, or solar power (IEA, 2022). The irrigation pump market in India was valued at around $1.1 billion in 2022 (Arizton, 2020). It is expected to reach $1.6 billion by 2027, with a compound annual growth rate of 8.4%.

Amidst the rapid growth and proliferation of mechanized irrigation pumps in India, groundwater overexploitation is an ongoing concern, exacerbated by the difficulty of enforcing groundwater governance systems for millions of spatially-distributed smallholder farmers. The long-term economic and environmental implications of widespread, often uncoordinated, irrigation adoption include greenhouse gas emissions and water quality degradation associated with irrigation. Government subsidies, public-private partnerships, and blended financial models to improve irrigation access have played key roles in improving the productivity of smallholder agriculture (Shah, 2007; Singh et al., 2014; Bassi, 2018). As a result of investments in the irrigation sector the net irrigated area in India, estimated at 20.85 million hectares in 1950–51 (Singh et al., 2014), increased to 70.4 million hectares in 2020–21 (FAO AQUASTAT, 2020).

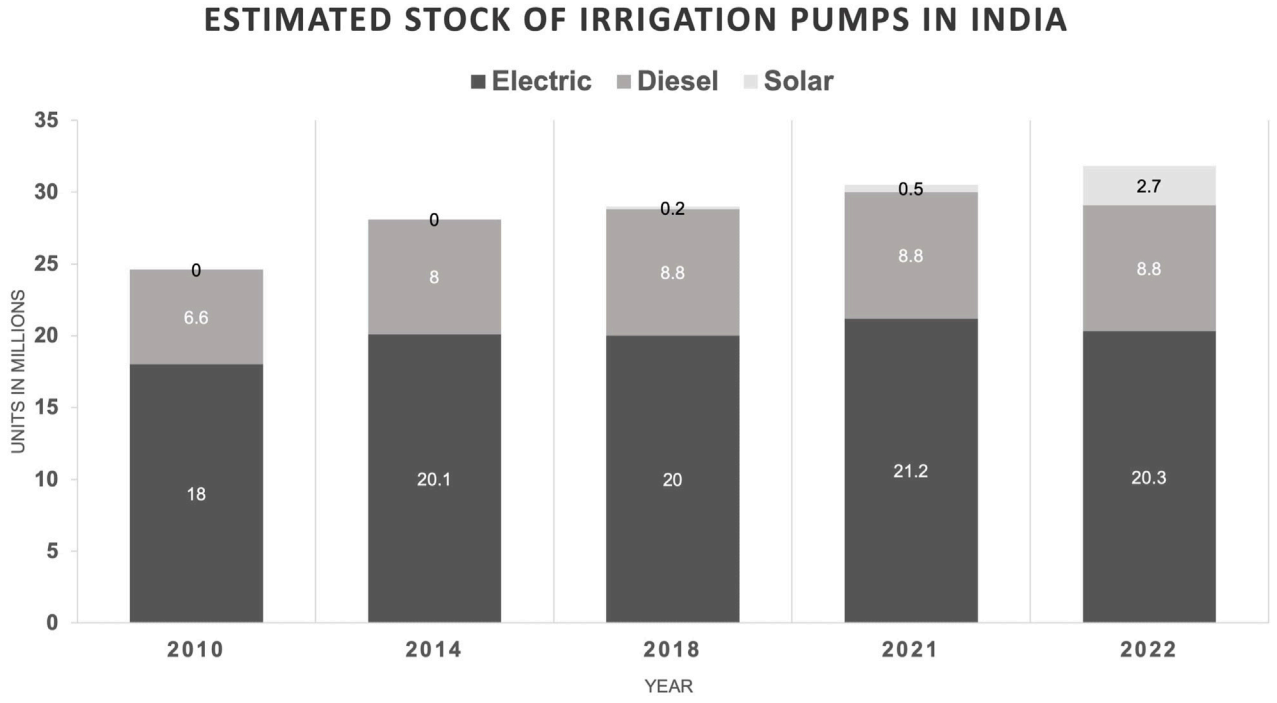

FIGURE 1
Distribution of estimated number of installed irrigation pumps in India (2010-22), adapted from IEA, 2022.

Despite the importance of private-sector dominated irrigation pump markets in India, there is limited research on the structure and key trends in these markets, including the relative influence of private and government interventions. In this policy brief, we combine data from semi-structured interviews with farmers and irrigation stakeholders and relevant secondary data to highlight and contextualize key trends emerging in Indian irrigation pump markets.

Twenty six irrigating farmers (owners of diesel and electric pumps) and irrigation dealers were interviewed in the states of Bihar and Uttar Pradesh. These two states represent typical smallholder provinces in Northern India and contain a high density of diesel and electric pumps (Singh et al., 2014). The interviews were used to provide context around the lived experience of people involved in different parts of the business ecosystem that provides irrigation pumps to smallholder farmers. The insights obtained speak to the role of government policies, as well as of private sector business strategy, in determining the trajectory of irrigation pump adoption across space and time. Although we conducted interviews within a narrow region rather than the entire country, the findings still offer insights into broader trends and patterns. While irrigation policies and guidelines vary in every state in India–even within states–the typical challenges of power and irrigation pump subsidies, unregulated use of groundwater, and the adoption of new technology in an attempt to curb water use concerns remain similar across the country. Some caution may be needed in extrapolating these findings to the national level, as regional differences and unique circumstances within individual states may influence outcomes differently.

2 Key findings

2.1 Shifts in the irrigation pump market

Irrigation in India predominantly depends on groundwater pumped through about 9 million diesel and 21 million electric pumps (IEA, 2022). These pumps are small and generally individually operated. Over the past decade, the irrigation pump market has shifted from diesel to electric irrigation pumps (Figure 1), with a growing focus on solar irrigation pumps (SIPs).

Indian farmers prefer electric pumps for a variety of reasons. Compared to diesel, which is costly, electric grid-connected pumps are cheaper. Over time, the average diesel prices have surged from Rs. 38.5 per liter ($0.46/ltr) in January 2010 to Rs. 89 per liter ($1.07/ltr) in January 2024 (Open Government Data, 2024). Several states offer subsidized or free electricity. Additionally, electric pumps have lower operational and maintenance costs. The farmers we interviewed said they did not need to worry about their electric pumps being stolen because they are installed with a one-time submersible pump set. In many states, with water tables located 300–800 feet deep, tube wells with submersible pump sets are the best option to access groundwater for irrigation. However, the rapid implementation of electric pumps has led to the excessive withdrawal of groundwater in multiple states in India, particularly in Punjab, Haryana, Rajasthan, Andhra Pradesh, and Uttar Pradesh (Standing Committee on Water Resources, 2022).

In an attempt to reduce overextraction of groundwater, the government is considering whether to discourage electric pumps.

Farmers may be required to obtain permits from the state government in the near future if they wish to drill. This represents a change from the current regulatory framework, where no permits are required. The government is also considering introducing measures such as pre-paid cards for energy, allowing charging for electricity used for irrigation and restricting power supply (Standing Committee on Water Resources, 2022). The outcomes of these potential future policy changes and associated pilot programs will be keenly observed. However, implementing these programs might be challenging due to the current absence of widespread metering of tube wells as well as regional issues such as power theft (Chaudhari et al., 2021).

Recently, both government and private entities have promoted the adoption of solar irrigation pumps (SIPs), especially to replace diesel pumps, as a means to reduce carbon emissions and groundwater depletion (Balasubramanya et al., 2024). However, diesel pumps are not scrapped as a condition of new solar pump sales. Thus, the number of available diesel-based irrigation pumps is generally unchanged by solar pump adoption and farmers who own SIPs still use diesel pumps for irrigation due to easy access and operability. Simultaneously, there is an increased emphasis on connecting solar projects to the electric grid with the goal of selling surplus electricity to energy distribution companies (DISCOMs) and creating an alternative revenue source for farmers (Balasubramanya and Buisson, 2022). Nevertheless, farmers might not sell surplus solar energy to the grid unless the tariff is sufficiently high after meeting their own pumping needs, particularly if their neighbors also have unmet pumping needs for irrigation.

The adoption of SIPs at the farm level is still in its infancy. Around 0.2 million SIPs were installed by the end of 2019. The number was expected to expand to 3 million installations by 2022 (Yashodha et al., 2021; IEA, 2022). While the total number of SIPs installed is uncertain due to lags in targeted installations and unreported sales, there is clear positive trend in the expansion of solar irrigation.

2.2 Government subsidies and financial support for irrigation pumps

Various institutions, including the government, are making efforts to promote the widespread adoption of SIPs by offering a range of subsidies and credit options. Additionally, there are a variety of subsidies for purchasing other kinds of irrigation pumps. Pump subsidies are meant to provide relief for smallholder farmers who irrigate, and these vary from state to state. The recent expansion of solar irrigation is due, in large part, to India's flagship agri-solarization program, "Pradhan Mantri Kisan Urja Suraksha evam Uthhaan Mahabhiyan" (PM-KUSUM). The program allows Central and State Government to provide a 60% subsidy for SIPs. Typically, of the remaining cost, 30% is provided through agricultural loans and farmers bear 10%. However, the level of subsidies and farmers' initial investments vary at the state level. For example, in Bihar, the government provides a subsidy of 75%. In the neighboring states, Jharkhand and Uttar Pradesh, the government provides a 60% subsidy. Economic theory would suggest that differential subsidies might lead to arbitrage across state borders. Traders or individuals can purchase the pump in the region with lower prices and then resell it in the region with higher prices, earning a profit from the price difference. This type of arbitrage can potentially distort the intended impacts of the subsidy scheme at a state level.

Even with the available subsidies, smallholder farmers still bear relatively high initial capital expenses. Banks play a crucial role in lending, but the interest from commercial banks to provide credit to smallholders for irrigation equipment financing has been limited to date. Even with subsidies, the high cost of SIPs, loans, and collateral requirements likely has a detrimental impact on adoption and market share. For example, for a 5 hp SIP in Uttar Pradesh where the expected cost is Rs. 2,73,137 ($3,277), the Central and State governments contribute Rs. 1,63,882 ($1,966), while farmers must contribute the remaining amount of Rs. 1,09,255 ($1,311) (Uttar Pradesh Dept. of Agriculture, 2023). For a farming household, this amount is a substantial sum, especially where the average monthly farmer household income is Rs. 8,000 ($96 per month) (Ministry of Agriculture and Farmers Welfare, 2022).

While SIPs have the potential to reduce emissions and lower irrigation costs, empirical evidence suggests a mix of successes and failures with solar irrigation projects in India (Mongabay, 2023). This is primarily because of high initial investment costs, together with technical issues such as lower pump capacity and flow rate in comparison to diesel pumps, inferior quality and small size of solar PV modules sourced in Indian markets, and lack of after-sales support (Source: Personal communications, January 2022).

Another potentially problematic aspect of solar pump use is that, with no variable costs of producing water and no incentives to manage natural resources in place, farmers have no reason to be careful in how much they pump and will likely overdraw groundwater (Bassi, 2018). As seen in Figure 2, only 18%–25% of wells are deemed safe for water extraction in the northwest region with a similar trend in some southern states. Currently, these regions have high concentrations of solar pumps (Bridge to India, 2021) which potentially aggravate the groundwater depletion situation.

Beyond the high levels of subsidization of electricity, subsidies are also provided for the purchase of electric and diesel pumps within some states. For example, in Bihar and Madhya Pradesh, there is up to a 50% subsidy (Rs. 8,000 or $96, whichever is lesser) on electric irrigation pump sets. Government regulators have stopped electric pump subsidies in Punjab, Haryana, Rajasthan, Karnataka, Tamil Nadu, and Uttar Pradesh to discourage farmers from pumping due to the overextraction of groundwater in these states and associated declining groundwater tables.

Typically, each state government decides subsidy levels depending on its budget situation and on local politics. For instance, in Bihar, pump subsidies were put on hold during the COVID-19 pandemic. They were revived in 2022 with changes in the agricultural budget and policies, and with the launch of subsidy distributions through Online Farm Mechanization Application Software (OFMAS) by the State Department of Agriculture in Bihar. Farmers are required to apply for subsidies through the OFMAS platform. OFMAS makes the application process easier and more transparent than previously. Farmers need to register

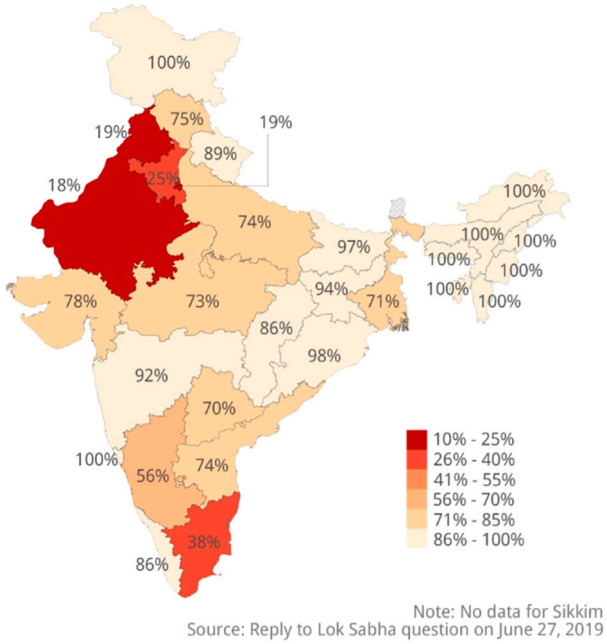

FIGURE 2
Indian map showing the states that are deemed safe for water extraction from irrigation wells. In the northwest region, only 18%–25% of wells are classified as safe (Adapted from CGWB).

and provide details of their land holdings and crops. Once the application is approved, the subsidy is facilitated through pump manufacturers, who supply irrigation equipment to the farmer. In many states, farmers apply for subsidies through irrigation dealers and distributors during "Krishi mela" (a district-level event organized by the state government during the *Rabi* and *Kharif* cropping season). Farmers receive their subsidy within 45–60 days of application through Direct Benefit Transfer (DBT). DBT is a mode of paying subsidies straight into the bank accounts of beneficiaries, seen as one of the most promising pathways to enhance the efficiency of subsidy programs (Source: Personal communication with Bihar Government Officials, December 2022).

There are government subsidies for diesel pumps in some regions, especially where the electricity supply for irrigation is irregular (Source: Personal communications, December 2022). Controversially, these subsidies often carry a political motive, often neglecting the physical reality of depleting natural resources. Subsidies on diesel pump irrigation are employed as a tool to secure political support and appease voter bases. The result of such an approach is the proliferation of diesel pumps, aggravating environmental problems. Overall, the wide range of implemented policies creates tensions between the adoption of irrigation pumps and pathways to achieve multiple SDGs through agriculture.

2.3 Informal water markets to irrigation service provision

Informal, unregulated, and localized water markets have existed in different parts of India for decades (Bajaj et al., 2023). Informal water market arrangements allow irrigation pump owners to sell water to other farmers at a mutually agreed-upon price. In a typical setup, farmers own portable irrigation pumps and rent them to other local farmers for irrigation, acting as water sellers. Pump or hosepipe rentals provide access to irrigation to those smallholder farmers who cannot afford their own well and pumping equipment. Water markets are popular among Indian farmers and encourage investment in tube wells and other irrigation equipment through the prospect of profitable water sales. In a state like Uttar Pradesh, which has the highest number of farmers in the country and in which around 80% of agricultural area is irrigated, about half of farmers either rent borewells through pipelines or purchase water from large land-owning farmers for their irrigation needs (Jain and Shahidi, 2018).

The equity, scale, and nature of water market transactions vary across space and time and with the choice of crops. For instance, in Samastipur village in Bihar, a farmer currently charges Rs. 160 ($1.92) per hour for renting his diesel pump, whereas for an electric or submersible pump, the charge is Rs. 80–90 ($0.96–$1.10) per hour. In Vaishali village, also situated in Bihar, the water charge is roughly Rs. 200 ($2.40) per acre per hour for diesel pumps. Water buyers usually take 3–4 irrigation sessions in a season and end up paying between Rs. 6,000–8,000 ($72–$96) per acre per season for 10 h of irrigation, including labor charges. Similarly, in Uttar Pradesh, water buyers primarily rely on diesel motor pumps where the rental rate is Rs. 130-200 ($1.60–$2.40) per hour. (Source: Personal communications, August 2021).

Where smallholder farmers lack capital or credit to invest in irrigation equipment, alternatives such as "irrigation-as-a-service" or "shared pump" concepts can provide access to water for agriculture. By sharing mobile irrigation equipment across

multiple sites and users, such approaches allow for higher capacity utilization of the irrigation equipment, spreading fixed costs over multiple users and potentially increasing the accessibility of irrigation to the poorest smallholders. While the implementation and analysis of irrigation-as-a-service in India is still limited, preliminary observations suggest that some existing irrigation-as-a-service startups, such as AgriRain and Oorja, are providing value to their smallholder customers and to village level micro-entrepreneurs.

3 Policy recommendations

Current agricultural water policies and governance in India create challenges to long-term food and water security. Subsidies on electricity have resulted in large-scale adoption of electric pumps, which has led to groundwater overextraction and depletion of aquifers. In many parts of India, agricultural water use is still heavily subsidized through both energy pricing and irrigation equipment subsidies. Such price distortions provide farmers with little incentive to invest in water-saving technologies or to adopt efficient irrigation practices. Rethinking agricultural policies that subsidize energy can play a crucial role in addressing the broader issue of groundwater depletion. However, it is understood that this might entail significant political resistance. Therefore, it is also important to consider how to develop programs for farmers that hold the potential to reduce water and energy use without increasing poverty (Mitra et al., 2023).

Furthermore, while there is a push from both governmental and private entities to promote the expansion of SIPs, current solar strategy and program designs are deployed by the energy department (e.g., State Renewable Energy Development Agencies or nodal agencies) mainly to increase energy intensity and to decrease the electricity subsidy burden. As water, energy, and food are interlinked, it might be beneficial to design cohesive solar program strategies in conjunction with water departments (e.g., Central Ground Water Board) and other agricultural or environmental stakeholders. Doing so could lead to a comprehensive consideration of groundwater extraction, emissions reduction, and beneficial crop choices in a systems approach.

Groundwater is a state subject in India, which means that state governments are responsible for managing and regulating groundwater resources within their respective territories. The central government provides guidelines and support to the states, but state governments have found it challenging to enforce groundwater regulations. Challenges related to agricultural water use are often local and context specific. Groundwater governance in India often fails to involve local communities (Shunglu et al., 2022), with decisions being made by government agencies without adequate local consultation. Understanding behavioral and decision-making aspects on a community level while considering the links between crop choices, groundwater availability, and irrigation technology adoption can play an important role in improving sustainable irrigation. Studies involving experimental games have shown that, when the links between crop choice and groundwater depletion are made explicit, farmers can act cooperatively to address groundwater issues (Meinzen-Dick et al., 2016).

Overall, there is a need for more localized policies monitoring groundwater, increasing the adoption of metered tube wells, incentivizing crop choices, and data collection to understand the status of groundwater resources in different parts of the country. Monitoring and data collection and distribution, whether done by government, nongovernmental, or private sector organizations, can help in making informed decisions on groundwater management. There is also a clear need to collect more evidence on business models for irrigation-as-a-service as a means to provide profitable and sustainable access to water for smallholders.

Author contributions

AC: Writing–original draft, Writing–review and editing. NB: Supervision, Validation, Writing–review and editing.

Funding

The author(s) declare that no financial support was received for the research, authorship, and/or publication of this article.

Conflict of interest

The authors declare that the research was conducted in the absence of any commercial or financial relationships that could be construed as a potential conflict of interest.

Publisher's note

Supplementary material

The Supplementary Material for this article can be found online at: https://www.frontiersin.org/articles/10.3389/fenvs.2024.1398822/full#supplementary-material

References

Arizton (2020) *Indian pump market- industry outlook and forecast 2021-2026. 248*. Available at: https://www.arizton.com/market-reports/pump-market-india-market-size-analysis (Accessed February 25, 2024).

Bajaj, A., Singh, S. P., and Nayak, D. (2023). Are farmers willing to pay for groundwater irrigation? Insights from informal groundwater markets in Western Uttar Pradesh. India. *Agric. Water Manag.* 288, 108458. doi:10.1016/j.agwat.2023.108458

Balasubramanya, S., and Buisson, M. C. (2022). Positive incentives for managing groundwater in the presence of informal water markets: perspectives from India. *Environ. Res. Lett.* 17, 101001. doi:10.1088/1748-9326/ac914f

Balasubramanya, S., Garrick, D., Brozović, N., Ringler, C., Zaveri, E., Rodella, A.-S., et al. (2024). Risks from solar-powered groundwater irrigation. *Science* 383, 256–258. doi:10.1126/science.adi9497

Bassi, N. (2018). Solarizing groundwater irrigation in India: a growing debate. *Int. J. Water Resour. Dev.* 34 (1), 132–145. doi:10.1080/07900627.2017.1329137

Bridge to India (2021). Review: India solar pumps market-current status and outlook. Available at: https://bridgetoindia.com/reviews-india-solar-pumps-market-current-status-and-outlook/ (Accessed February 05, 2024).

Chaudhuri, S., Parakh, D., Roy, M., and Kaur, H. (2021). Groundwater-sourced irrigation and agro-power subsidies: boon or bane for small/marginal farmers in India? *Groundw. Sustain. Dev.* 15, 100690. doi:10.1016/j.gsd.2021.100690

Food and Agricultural Organization of the United Nations (FAO) (2020) *Aquastat*. Available at: https://data.apps.fao.org/aquastat/?lang=en (Accessed March 28, 2024).

IEA (2022) *The estimated stock of agricultural irrigation pumps in India, 2010-2022*. Paris: IEA. Available at: https://www.iea.org/data-and-statistics/charts/estimated-stock-of-agricultural-irrigation-pumps-in-india-2010-2022 (Accessed February 05, 2024).

Jain, A., and Shahidi, T. (2018) *Adopting solar for irrigation farmers' perspectives from Uttar Pradesh*. New Delhi: Council on Energy, Environment and Water. Available at: http://www.ceew.in/sites/default/files/CEEW-Adopting-Solar-for-Irrigation-Farmers-Perspectivesfrom-UP-Report-17Jan18.pdf.

Meinzen-Dick, R., Chaturvedi, R., Domènech, L., Ghate, R., Janssen, M. A., Rollins, N. D., et al. (2016). Games for groundwater governance: field experiments in Andhra Pradesh, India. *Ecol. Soc.* 21 (3), art38. doi:10.5751/ES-08416-210338

Ministry of Agriculture & Farmers Welfare (2022). Income of farmers: state-wise/UT-wise Average monthly income per agricultural household (Considering paid out expenses only) during the agricultural year July 2018 June 2019. Available at: https://pib.gov.in/PressReleasePage.aspx?PRID=1884228 (Accessed February 05, 2024).

Mitra, A., Balasubramanya, S., and Brouwer, R. (2023). Can cash incentives modify groundwater pumping behaviors? Evidence from an experiment in Punjab. *Am. J. Agric. Econ.* 105 (3), 861–887. doi:10.1111/ajae.12340

Mongabay (2023). Solar pumps offer financial relief to West Bengal farmers, but growth is slow. Available at: https://india.mongabay.com/2023/06/solar-pumps-offer-financial-relief-to-west-bengal-farmers-but-growth-is-slow/ (Accessed April 23, 2024).

Open Government Data Platform India (2024). Year-wise details of retail sales price (RSP) of petrol and diesel in Delhi. Available at: https://data.gov.in/resource/year-wise-details-retail-sales-price-rsp-petrol-and-diesel-delhi-01-04-2005-01-08-2023 (Accessed March 28, 2024).

Shah, T. (2007). Crop per drop of diesel? Energy squeeze on India's smallholder irrigation. *Econ. Political Wkly.* 42 (39), 4002–4009. doi:10.2307/40276478

Shunglu, R., Köpke, S., Kanoi, L., Nissanka, T. S., Withanachchi, C. R., Gamage, D. U., et al. (2022). Barriers in participative water Governance: a critical analysis of community development approaches. *Water* 14 (5), 762. doi:10.3390/w14050762

Singh, O. P., Singh, R., and Singh, M. (2014). Impact of farm sector electricity subsidy on water use efficiency and water productivity in India. *Indian J. Agric. Econ.* 69 (3). doi:10.22004/ag.econ.229844

Standing Committee on Water Resources 2022-23 (2022) *Groundwater: a valuable but diminishing resource*. Available at: https://loksabhadocs.nic.in/lsscommittee/Water%20Resources/17_Water_Resources_22.pdf (Accessed February 25, 2024).

Yashodha, Y., Sanjay, A., and Mukherji, A. (2021) *Solar irrigation in India: a situation analysis report*. Colombo, Sri Lanka: International Water Management Institute IWMI, 29. doi:10.5337/2021.217

frontiers | Frontiers in Environmental Science

TYPE Original Research
PUBLISHED 21 August 2024
DOI 10.3389/fenvs.2024.1436848

OPEN ACCESS

EDITED BY
Jahangeer Jahangeer,
University of Nebraska-Lincoln, United States

REVIEWED BY
Ahmed S. El-Shafie,
Qatar University, Qatar
Manoj Garg,
Amity University, India

*CORRESPONDENCE
Shuhang Zhang,
ZSHmailgo@163.com

RECEIVED 22 May 2024
ACCEPTED 05 August 2024
PUBLISHED 21 August 2024

CITATION
Li Z, Zhang S, Zhu G and Xing J (2024) Use of graphene oxide for the removal of norfloxacin and ceftriaxone antibiotics from aqueous solution: process optimization using response surface approach.
Front. Environ. Sci. 12:1436848.
doi: 10.3389/fenvs.2024.1436848

Use of graphene oxide for the removal of norfloxacin and ceftriaxone antibiotics from aqueous solution: process optimization using response surface approach

Zhihui Li[1], Shuhang Zhang[2]*, Guina Zhu[1] and Jie Xing[2]

[1]Qingyang Prefectural Center for Disease Control and Prevention, Qingyang, Gansu, China, [2]Qingyang People's Hospital, Qingyang, Gansu, China

In this research, graphene oxide (GO) as an adsorbent was used to remove norfloxacin and ceftriaxone antibiotics from aqueous solutions. All environmental factors affecting removal (e.g., pH, adsorbent mass, contact time, and concentration) were optimized in a discontinuous system. The design of experiments and the optimization of variables were carried out using the response surface method (RSM). The results of the analysis of variance (ANOVA) and the regression coefficients of the quadratic terms indicated that the responses were significantly affected by all the studied variables ($P < 0.05$). Also, the quadratic polynomial model results corresponded to empirical data with a high coefficient of determination (i.e., $R^2 > 0.99$ for both antibiotics). Besides, the adjusted R^2 (R^2-adj > 0.98 for both antibiotics) was close to R^2 values, indicating a good and acceptable statistical model. According to the results, the optimal removal of antibiotics by GO occurs in conditions of pH of 8, 0.034 g of the adsorbent mass, a sonication time of 20 min, and a concentration of 25 mg L^{-1}. In these conditions, the maximum removal efficiencies of ceftriaxone and norfloxacin were equal to 95.87% and 98.64%, respectively. GO was recovered in five adsorption/desorption processes, and the removal efficiency declined very slightly after using the adsorbent for five cycles. Therefore, it is concluded that GO is an efficient and acceptable adsorbent for removing ceftriaxone and norfloxacin from aqueous environments.

KEYWORDS

central composite design, norfloxacin, ceftriaxone, response surface method, ultrasound-assisted removal

1 Introduction

The presence of pollutants of organic origin in water resources is considered a serious threat to the environment and human health (Singh et al., 2022). Pharmaceutical compounds account for a type of these pollutants entering surface and underground water sources, mainly through sewage and urban/industrial effluents. Due to their high stability, the presence of pharmaceutical substances in the environment not only causes disturbances in the standard wastewater treatment processes in treatment systems but also

exerts toxic effects on humans and other living organisms; hence, their removal is of interest to researchers (Jäger et al., 2018; Farhat et al., 2022).

Among the wide range of pharmaceutical pollutants, antibiotics are widely used in medicine and veterinary medicine because of their antimicrobial effects (Bilal et al., 2023). These organic compounds enter the environment not only through effluent from the pharmaceutical industry but also due to an incomplete metabolism mechanism during the treatment period. In this respect, the persistent presence of antibiotics in the aquatic environment and their bioaccumulation leads to microbial and bacterial resistance (Wydro et al., 2023; Wysowska et al., 2024).

As an antibiotic of the third generation of cephalosporins, ceftriaxone ($C_{18}H_{18}N_8O_7S_3$) is used to kill many bacteria and to treat bacterial infections such as meningitis, gonorrhea-induced infections, pneumonia, and orthopedic surgeries (Nguyen et al., 2022). The main side effects of ceftriaxone include skin and digestive complications, dyspnea, increased blood platelet levels, anaphylactic shock, anaphylactoid reactions, and cardiac arrest. These effects have severe effects on patient's life-threatening in many cases. Unfortunately, the excessive use of ceftriaxone in unnecessary cases (e.g., colds) is an important factor for the increased occurrence of the drug's side effects. Ceftriaxone may also cause severe intestinal disorders such as diarrhea or abdominal cramps (Tao et al., 2024). Research has shown that some of these highly consumed antibiotics enter the wastewater treatment systems in their original form daily through the renal biliary excretion system of the patients under treatment (Noman et al., 2022).

As the second generation of fluoroquinolones, the antibiotic norfloxacin ($C_{16}H_{18}FN_3O_3$) is used to treat various infections, particularly urinary infections (Liu et al., 2022). This antibiotic prevents the function of a bacterial enzyme involved in DNA replication called DNA gyrase and topoisomerase II and inhibits the multiplication of bacterial DNA. The side effects of norfloxacin include nausea, headache, fatigue, arthritis, gastrointestinal bleeding, depression, and indigestion (Swidan and Rubin, 2020). This drug can cause severe side effects such as tendon irritation or rupture and nervous system problems. Tendon problems may appear a long time after treatment and can lead to lifelong disability in severe cases (Sharma et al., 2008). Multiple fluoroquinolone family antibiotics and their modified by-products in drinking water, surface and underground water, and wastewater have currently caused major concerns (Hiasa, 2018; Bhatt and Chatterjee, 2022).

These pollutants not only do not vanish in wastewater treatment systems but also kill effective microbes in biological treatment, leading to the ineffectiveness of wastewater treatment systems (Pei et al., 2019; Madhusoodanan, 2022). Due to their resistance to biological decomposition, these compounds enter the environment (particularly water sources) through wastewater treatment plants (Kim et al., 2023). Researchers have frequently addressed the entry of these antibiotics into the environment in the concentration range of ng L^{-1} to μg L^{-1} (Dorival-García et al., 2013). Therefore, it is necessary to adopt appropriate treatment methods to eliminate or reduce such antibiotics before entering the environmental resources.

Various methods, such as chemical precipitation, biological processes, ion exchange, membrane filtration, and electrochemical techniques, are available for antibiotic-containing wastewater treatment (Molinari et al., 2020; Uluseker et al., 2021; Spit et al., 2022; Li J. et al., 2023; Vinayagam et al., 2023; da Silva Júnior et al., 2024). The efficiency of these methods is limited due to the high cost, long treatment time, toxicity of chemicals, prohibition in wide applications, and limited access in developing countries, making it necessary to use alternative techniques (Ahmed et al., 2021). Adsorption is among the low-cost methods of high interest used for reducing some pollutants for various reasons such as low cost, flexibility, simplicity of design, ease of operation, insensitivity to toxic pollutants, and the availability of a wide range of inexpensive adsorbents compared to other treatment methods (Tony, 2022; Dutta et al., 2024).

Different adsorbents, including natural and synthetic adsorbents, are used in adsorption method. A group of synthetic adsorbents used for this purpose is graphene oxide (GO). The identified unique properties of this adsorbent (e.g., a high surface area, special functional groups on the surface, and high absorption capacity) have nowadays directed attention toward using this material as an adsorbent (Wang et al., 2018; Krishna et al., 2023).

Yang et al. (2022) used the GO adsorbent to remove enrofloxacin and rhodamine B. They obtained the optimum conditions as a pH of 7, optimal contact time of 23 min, and removal of ˃92.5% for both analytes. The GO adsorbent performed well in enrofloxacin and rhodamine B removal from an aqueous solution with maximum adsorption capacities of 45.035 and 107.230 mg g^{-1} for enrofloxacin and rhodamine B, respectively (Yang et al., 2022).

Kadhim et al. (2020) modified the polyether sulfone (PES) membrane using the GO adsorbent. They used the PES/GO adsorbent to remove Acid Black and Rose Bengal. They presented evidence that this adsorbent could efficiently remove the mentioned dyes. The performance of the PES/GO adsorbent showed a removal rate of >99% for both dyes (Kadhim et al., 2020).

Madadrang et al. (2012) removed Pb (II) through the silanization reaction between N-(trimethoxysilylpropyl) ethylenediamine triacetic acid (EDTA-silane) and hydroxyl groups on the GO surface to improve the removal technique. The results showed that the adsorption capacity of the adsorbent to remove Pb (II) was equal to 479 mg g^{-1} (Madadrang et al., 2012).

Yang et al. (2011) used GO to remove methylene blue from aqueous solutions. They reported that using the hematite powder adsorbent could remove more than 99% of methylene blue from aqueous solutions, with an adsorption capacity of 714 mg g^{-1} (Yang et al., 2011).

This study reports using GO as an adsorbent to remove ceftriaxone and norfloxacin from aqueous solutions. The surface characteristics of the adsorbent and operating variables in the adsorption process, including pH of the solution, concentration, time, and mass of the adsorbent, were investigated in this research.

2 Materials and methods

2.1 Chemicals, reagents, and instrumentation

The materials used in this study include laboratory-grade chemicals without the need for further purification. A stock

solution of the antibiotics (1,000 mg L^{-1}) was prepared in double distilled water (DDW). Working solutions were prepared by diluting the stock solution. In all experiments, DDW was used to prepare solutions and reagents. The pH of the solution was adjusted using 0.1 M HCl and 0.1 M NaOH. The pH was measured by a pH meter (Metrohm 632). The adsorbent was separated from the mixture with an Andreas Hettich D72 centrifuge. The residual concentration of antibiotics was quantified using a (DR6000) UV-VIS spectrophotometer. The GO adsorbent was characterized with a scanning electron microscope (SEM, Cambridge Stereoscan S360), a Fourier transform infrared spectrophotometer (FTIR, Thermo Nicolet Avatar 370), x-ray powder diffraction (XRD, Philips XPERT MPD), and Brunauer-Emmett-Teller (BET, NOVA 2000e) techniques.

2.2 Synthesis of GO

GO was synthesized using the Hummers method. According to this method, 23 mL of concentrated sulfuric acid was added to 1 g of graphite powder, and the resulting mixture was stirred at 5°C for 20 min. The color of the solution is black due to the presence of graphite. Then, 0.5 g of sodium nitrate was added to the solution and stirred at 20°C for 30 min. Next, 3 g of potassium permanganate was added to the mixture gradually during 1 h. The graphite oxidation process was completed by stirring the mixture on a stirrer for 3 h. At this stage, the color of the solution turned dark green. Afterward, 100 mL of DDW was added to the solution and stirred for some time, followed by adding about 5 mL of hydrogen peroxide to neutralize the excess permanganate. Finally, the GO obtained from the solution was separated using a centrifuge at 2,500 rpm. The separated GO was washed with DDW several times. Graphite oxide was converted to graphene oxide by heating it in an ultrasonic bath with a power of 400 W for 30 min. Next, the precipitate was separated from the liquid through centrifugation. Finally, GO powder was obtained by drying the resulting precipitate completely in an oven with a maximum temperature of 80°C for 24 h (Omar et al., 2023).

2.3 Experimental design

Using design methods in any research helps manage the order and number of required tests before starting the tests such that the least number of tests are needed in the shortest time. Using this method, in turn, saves time, reduces material consumption, and improves accuracy (Li X. et al., 2023).

Statistical and multivariate engineering techniques such as the response surface method (RSM) are among the widely used design methods in wastewater treatment. Studies employ RSM to build models free from problems existing in the method of changing one factor at a time (OFAT) and can simultaneously examine and optimize the effect of multiple factors (Maldonado et al., 2023). Compared to OFAT, the advantages of RSM include prioritizing the importance of factors, reducing the number of tests, determining the interaction between factors, providing a mathematical relationship between factors to reach the response, and predicting new answers by changing the factors (Shojaei et al., 2021a; He et al., 2023).

TABLE 1 The CCD of independent variables.

Variables	Unit	Symbols	Level of variables				
			−α	−1	0	+1	+α
Concentration	mg L^{-1}	A	20	40	60	80	100
pH of solution	—	B	3	5	7	9	11
Adsorbent mass	g	C	0.01	0.02	0.03	0.04	0.05
Sonication time	min	D	5	10	15	20	25

The built models may also be applied to access the linear or quadratic effects of the tested factors and various graphs, including the interaction graphs between the factors. RSM includes factors, levels, and responses (Veza et al., 2023).

Factors are actually the variables affecting the results of tests, namely environmental factors such as pH, contact time, adsorbent mass, and adsorbent concentration in adsorption processes. The levels refer to the range of factor changes, including the minimum, maximum, and average values of the factors. The responses deal with the necessary values for the outputs.

Among the RSM design methods, the central composite design (CCD) method was chosen in the present study due to the greater number of levels. In this design, the factors have five levels defined as -α, −1, 0, +1, and +α. Here, +α and -α are the maximum and minimum values of each factor, respectively (Amin et al., 2023). In this method, four important and influential factors (i.e., pH, adsorbent mass, contact time, and concentration) were simultaneously optimized using Design-Expert V.12 software. This design allows the responses to be modeled by fitting a second-order polynomial, which can be expressed as (Equation 1).

$$Y = \beta_0 + \sum_{i=1}^{k} \beta_i X_i + \sum_{i=1}^{k} \beta_{ii} X_i^2 + \sum_{i \le j}^{k} \sum_{j} \beta i j X_i X_j + e \quad (1)$$

where β0, βi, βii, and βij are the constant, linear, square, and interaction coefficients of the factors, respectively. Xi and Xj are independent variables, and e is the unpredicted error. Y (R%) is the response. In the CCD design, the number of tests is calculated using Equation 2.

$$N = 2^k + 2K + nc \quad (2)$$

where k is the number of independent variables, and nc is the number of central points. According to the mentioned inputs, the model determined 30 tests for each antibiotic. Table 1 shows the test design matrix of CCD to remove antibiotics. The number of responses defined for the Design-Expert software included the removal percentages of ceftriaxone and norfloxacin (Table 2).

2.4 Removal of ceftriaxone and norfloxacin from aqueous solution by GO

This empirical study was conducted discontinuously on a laboratory scale in 250-mL Erlenmeyer flasks. Operating factors, including pH (3–11), contact time (5–25 min), concentration

10.3389/fenvs.2024.1436848

TABLE 2 The CCD with their corresponding experimental and predicted removal.

Variables					Ceftriaxone		Norfloxacin	
Run	A	B	C	D	Observed	Predicted	Observed	Predicted
1	−2	0	0	0	82.57	82.13	92.25	90.32
2	1	−1	−1	1	40.43	41.22	40.06	40.70
3	1	1	−1	−1	36.39	38.22	35.87	36.78
4	1	−1	1	−1	37.62	38.39	41.41	41.20
5	0	0	0	0	71.5	71.71	78.05	75.47
6	2	0	0	0	42.69	40.60	37.49	36.63
7	0	2	0	0	58.79	56.92	61.5	59.52
8	−1	1	−1	1	71.06	71.55	76.64	78.17
9	1	1	1	−1	47.65	48.53	49.29	51.40
10	−1	−1	1	1	80.85	80.28	79.11	79.52
11	−1	1	−1	−1	54.8	54.85	61.57	61.45
12	−1	−1	1	−1	58.29	59.14	66.73	67.64
13	0	0	−2	0	44.37	43.46	45.54	44.64
14	0	0	0	0	69.62	71.71	75.48	75.47
15	0	0	0	2	76.43	75.28	79.77	78.58
16	0	0	0	0	74.22	71.71	73.02	75.47
17	1	−1	1	1	54.17	55.38	48.91	50.50
18	−1	1	1	−1	68.94	69.41	75.4	76.08
19	0	0	0	0	72.37	71.71	76.47	75.47
20	−1	1	1	1	89.01	90.30	89.16	90.99
21	1	1	−1	1	50.36	50.77	50.35	50.92
22	0	−2	0	0	37.75	37.10	41.67	40.86
23	0	0	0	−2	42.97	41.60	54.16	52.56
24	1	1	1	1	64.43	65.27	64.48	63.73
25	1	−1	−1	−1	28.46	28.43	29.95	29.59
26	−1	−1	−1	1	61.47	61.86	70.35	69.71
27	−1	−1	−1	−1	44.5	44.92	53.96	56.02
28	0	0	0	0	70.19	71.71	73.19	75.47
29	0	0	2	0	73.79	72.18	70.95	69.07
30	0	0	0	0	72.38	71.71	76.62	75.47

(20–100 mg L^{-1}), and the adsorbent mass (0.01–0.05 g), were investigated in this research. The removal process of antibiotics was implemented with GO in an ultrasonic bath. For each test, 150 mL of the sample with an antibiotic concentration of 25 mg L^{-1} was first poured into the Erlenmeyer flask. If needed, 0.1 M NaOH or 0.1 M HCl solutions were used to adjust the pH of the samples. Next, a determined volume of the GO adsorbent was weighed and added to the sample in an Erlenmeyer flask, and the suspension was heated in an ultrasonic bath for a defined period. After the determined contact time, centrifugation was applied to separate adsorbent particles from the sample. The antibiotic concentration in the final solution was measured by a spectrophotometer. The antibiotic removal percentage was calculated using Equation 3.

$$\%Removal = \frac{C_0 - C_e}{C_0} \times 100 \quad (3)$$

where C_0 and C_e are the initial and final concentrations of the antibiotic (after the adsorption process), respectively.

TABLE 3 The ANOVA of remove ceftriaxone and norfloxacin.

Source	DF	Ceftriaxone				Norfloxacin			
		Sum of squares	Mean square	F-value	*P*-value	Sum of squares	Mean square	F-value	*P*-value
Model	14	7566.90	540.49	201.55	<0.0001	8376.49	598.32	153.20	<0.0001
A	1	2586.90	2586.90	964.64	<0.0001	4323.39	4323.39	1107.03	<0.0001
B	1	589.35	589.35	219.76	<0.0001	522.11	522.11	133.68	<0.0001
C	1	1237.40	1237.40	461.42	<0.0001	894.99	894.99	229.17	<0.0001
D	1	1701.01	1701.01	634.30	<0.0001	1,015.30	1,015.30	259.97	<0.0001
AB	1	0.0189	0.0189	0.0071	0.9342	3.10	3.10	0.79	0.3872
AC	1	18.13	18.13	6.76	0.0201	0.0000	0.0000	6.40	0.9980
AD	1	17.20	17.20	6.41	0.0230	6.66	6.66	1.70	0.2114
BC	1	0.1139	0.1139	0.0425	0.8395	9.09	9.09	2.32	0.1479
BD	1	0.0588	0.0588	0.0219	0.8842	9.18	9.18	2.35	0.1460
CD	1	17.62	17.62	6.57	0.0216	3.26	3.26	0.83	0.3755
A^2	1	183.48	183.48	68.42	<0.0001	246.62	246.62	63.14	<0.0001
B^2	1	1046.33	1,046.33	390.17	<0.0001	1095.49	1095.49	280.50	<0.0001
C^2	1	331.00	331.00	123.43	<0.0001	594.30	594.30	152.17	<0.0001
D^2	1	302.12	302.12	112.66	<0.0001	167.99	167.99	43.01	<0.0001
Residual	15	40.23	2.68			58.58	3.91		
Lack of Fit	10	26.32	2.63	0.9462	0.5622	38.40	3.84	0.9515	0.5595
Pure Error	5	13.91	2.78			20.18	4.04		
Cor Total	29	7607.13				8435.07			

Model Summary Statistics						
	Ceftriaxone			Norfloxacin		
Precision	R^2	R^2-Adj	R^2-Pred	R^2	R^2-Adj	R^2-Pred
	0.9947	0.9898	0.9774	0.9931	0.9866	0.9703

3 Results and discussion

3.1 Characterization of the GO adsorbent

The FT-IR technique is a powerful characterization method used to determine functional groups in a substance. Supplementary Figure S1 A shows the FT-IR spectrum of GO. The FT-IR pattern recorded at room temperature was measured in the range of 4,000–500 cm^{-1}. The peak at 3,400 cm^{-1} belongs to the presence of the hydroxyl group, 1730 cm^{-1} corresponds to carboxyl groups, 1,650 cm^{-1} is assigned to the carbon-carbon double bond (C = C), and 1,220 cm^{-1} refers to epoxy rings on the surface of GO. The carbon-oxygen bond also creates the 1,050 cm^{-1} peak. SEM was applied to determine the morphology of the GO adsorbent. According to the SEM image of GO (Supplementary Figure S1 B), the adsorbent surface is layered with the layers overlapped on each other. Due to the π-π bond between the benzene rings on the surface of GO, bonding is possible between different adsorbent layers, forming multilayer GO in this case. Supplementary Figure S1 C represents the N_2 adsorption and desorption isotherm for GO. The surface area of GO and the total volume of its cavities were measured using the BET method. The obtained surface area of GO, the holes' total volume, and the holes' average diameter were equal to 260.8 m^2 g^{-1}, 0.254 cm^3 g^{-1}, and 3.85 nm, respectively. According to the IOPAC, adsorbents with pore sizes between 2 and 50 nm are called mesoporous. Therefore, GO falls under the mesoporous adsorbents. The structure of GO was identified using the XRD analysis. The obtained results of the XRD pattern of GO (Supplementary Figure S1 D) show that the main peak at 2θ = 11.3° belongs to the GO (002) plane, and a weak peak at 2θ = 43° results from the un-laminated graphite.

10.3389/fenvs.2024.1436848

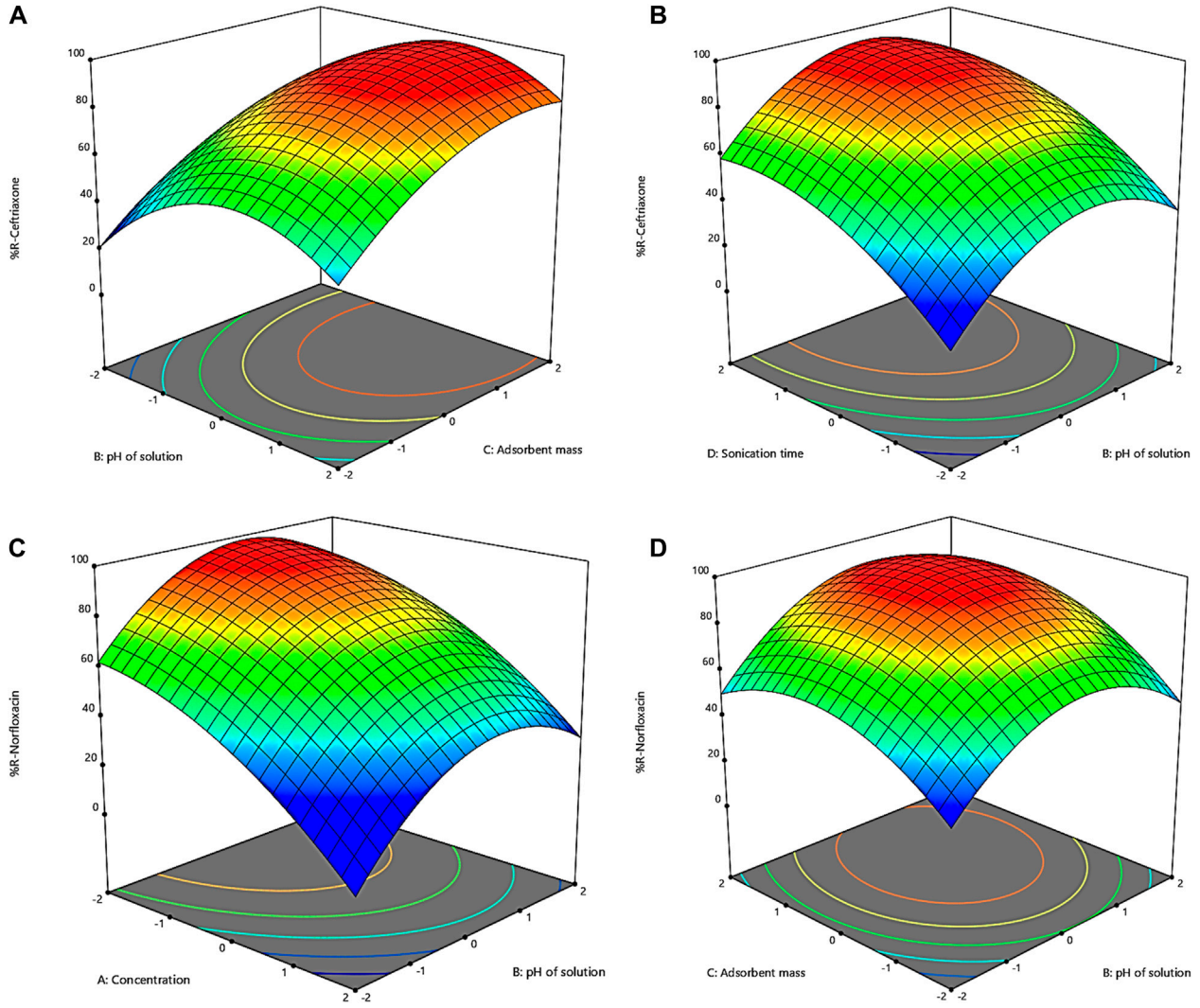

FIGURE 1
Three-dimensional plots of interactions for removal of **(A)** and **(B)** ceftriaxone; **(C,D)** norfloxacin.

3.2 Statistical analysis

Table 3 represents the ANOVA data for ceftriaxone and norfloxacin removal. After entering the required information into the software and running the model, the usefulness and appropriateness of the model should be evaluated in terms of application in the removal process of antibiotics. These assessments can be done using the ANOVA table data provided by the model. In this table, the *P*-value shows the effect of the factors on the response; the higher its value, the lower the effect of the factor. Therefore, if the *P*-value is >0.05 in a model, it means a very low impact of the factors on the obtained response, thereby rendering the model inappropriate. On the other hand, when the *P*-value is <0.05, the confidence level of the model is >95%, meaning favorable conditions (Di Leo and Sardanelli, 2020; Li Z. et al., 2023). According to Table 3, the *P*-value of the model is <0.0001 for both antibiotics, suggesting that the model is acceptable. The F-value represents a measure of the significance or validity of the model, and a higher value indicates more significance of the model. The F-value was high for both models, suggesting that the model is generally significant and acceptable.

Lack of fit (LOF) means the degree of compatibility of the model with real data, which should not be significant. The most ideal model is the one in which the model's fit with the laboratory data is statistically significant, and its incompatibility is not significant. Since such an ideal state can be seen for both antibiotics, it can be concluded that the models produced for both antibiotics and the responses provided by these models are in good agreement with the laboratory data. The coefficient of determination (R^2) should also be controlled in addition to examining the *P*-value and F-value. The closer R^2 is to 1, the better the model corresponds to the laboratory data. In addition to the R^2, this software provides two other coefficients of determination: 1) one belonging to the laboratory data, known as the adjusted R^2 (R^2-Adj) and 2) the prediction of the model responses, called the prediction R^2 (R^2-Pred). The difference between these two values should be less than 0.2 for the model to be acceptable (Yin et al., 2023). It can also be seen that this agreement is established in Table 3.

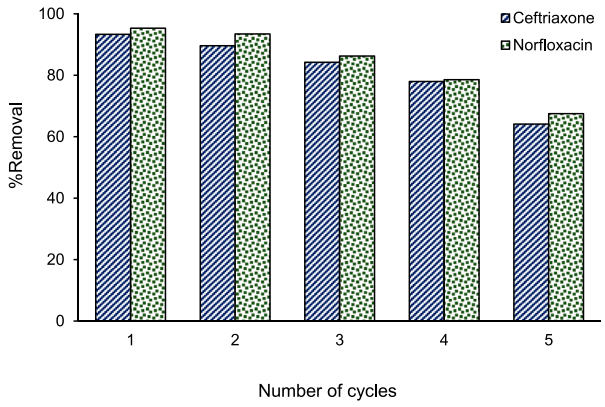

FIGURE 2
Regeneration studies of GO adsorbent.

In addition to examining the numbers in the ANOVA table, the obtained graphs should also be verified to visually evaluate the appropriate agreement of the model results with the laboratory data. Supplementary Figure S2 shows the real and predicted values for the response of the removal percentage of norfloxacin and ceftriaxone. Obviously, a good agreement exists between the predicted values of the model and the laboratory data because the laboratory-obtained points are distributed near the normal line. Among the useful outputs provided by the software is a mathematical equation between the factors affecting the removal (i.e., pH, contact time, adsorbent mass, and concentration) to reach the response. Equations 4, 5 are polynomial functions illustrating significant relationships between experimental variables and responses in the experimental design.

$$\text{Removal of ceftriaxone} = +71.71 - 10.38A + 4.95B + 7.18C + 8.41D - 0.03AB - 1.06AC - 1.03AD + 0.08BC - 0.06BD + 1.04CD - 2.58A^2 - 6.17B^2 - 3.47C^2 - 3.31D^2 \quad (4)$$

$$\text{Removal of norfloxacin} = +75.47 - 13.42A + 4.66B + 6.10C + 6.50D + 0.44AB - 0.01AC - 0.64AD + 0.75BC + 0.75BD - 0.45CD - 2.99A^2 - 6.31B^2 - 4.65C^2 - 2.47D^2 \quad (5)$$

where *A*, *B*, *C*, and *D* were concentration, pH, adsorbent mass, and sonication time, respectively.

3.3 Three-dimensional plots

Design-Expert software can also provide three-dimensional levels of the influence of factors on the response and exhibit the influence level of each factor on the response in colored forms. Figures 1A–D present the three-dimensional response surface for the effect of two factors simultaneously on the antibiotic removal rate. Accordingly, all four factors have a maximum area, indicating the influence of each factor on the response.

Figure 1A shows the effect of pH changes on ceftriaxone removal by the GO adsorbent. The range of pH changes was chosen to be from 3 to 11. Figure 1A shows that ceftriaxone has a low removal percentage in the acidic range. In other words, the reactions between the adsorbent and the adsorbate are low in these conditions. The removal percentage increases with rising pH toward neutral; however, the removal percentage declines with the continued ascending trend of pH. These observations can be attributed to the type of bond between ceftriaxone and the adsorbent, which is related to the surface charge of the adsorbent because this bond is electrostatic. The lowest negative charge for the GO adsorbent exists at acidic pHs. Therefore, an increase in both pH and the negative charge of the adsorbent allows for more bonds between the cationic molecule and GO, leading to increased adsorption (Zhang et al., 2016). The decrease in adsorption at pHs >7 is due to water ionization in the basic environment. Since the adsorbent is a hydrophilic substance, it shows a greater reaction affinity to water than ceftriaxone molecules. Indeed, water molecules and ceftriaxone molecules compete to seize the negative charges of the adsorbent surface in basic conditions, and the presence of this competitor lowers antibiotic adsorption (Olusegun et al., 2023).

To investigate the effect of the adsorbent mass on the removal of ceftriaxone, values of 0.01 to 0.05 g were chosen for the adsorbent. Figure 1A illustrates the effect of changes in the adsorbent mass on the ceftriaxone removal rate by the GO adsorbent. According to Figure 1A, the removal efficiency of ceftriaxone increased with increasing the adsorbent from 0.01 g to 0.05 g. The elevated efficiency with increasing the adsorbent mass can be attributed to the expanded surface of the adsorbent in contact with GO. This increased surface, in turn, amplifies the number of available adsorption sites for pollutant adsorption (Shojaei et al., 2021b). As can be inferred from Figure 1A, an amount of 0.034 g was optimal for the GO adsorbent. Moreover, this part of the study showed that the removal efficiency was not significantly affected by increasing the GO mass by more than 0.034 g.

Figure 1B shows the effect of contact time on the ceftriaxone removal rate by the GO adsorbent. The contact time was examined in the range of 5–25 min. According to Figure 1B, the contact time changes have two slopes in times <20 min and >20 min. The first part has a high slope, indicating the rapid adsorption process in this period. From the beginning to the first 20 min, the surface sites of the adsorbent are filled with ceftriaxone, and a rapid connection is established between ceftriaxone molecules and the GO adsorbent. After 20 min, the removal rate decreases because the sites are occupied on the adsorbent surface, making it necessary for ceftriaxone molecules to penetrate the adsorbent and fill the internal sites and pores (Anjum et al., 2019). Since GO is a mesoporous adsorbent with a pore diameter of about 3.8 nm and relatively large ceftriaxone molecules, penetration into the pores may be difficult. Therefore, a very low slope of the graphs can be seen in the second part. This slope suggests that a contact time of more than 20 min does not significantly affect removal, and it is not economical to use longer times. As mentioned above, an optimal contact time of 20 min was estimated for ceftriaxone.

Figure 1C represents the effect of norfloxacin concentrations on the GO adsorbent's removal efficiency. The impact of concentration on the removal efficiency of norfloxacin was investigated in the range of 20–100 mg L^{-1}. According to Figure 1C, the removal

TABLE 4 Effects of influence substances on the removal of ceftriaxone and norfloxacin (N = 3).

Foreign ions	Added as	Tolerable concentration (w/w)	Ceftriaxone	Norfloxacin
Cl^-	KCl	1,000	98.24 ± 1.6	98.09 ± 2.2
Ba^{2+}	$BaCl_2$	800	98.15 ± 1.7	98.54 ± 1.1
Ca^{2+}	$CaCl_2$	600	96.68 ± 2.1	97.04 ± 1.8
Ag^+	$AgNO_3$	100	97.06 ± 1.3	97.35 ± 1.4
Ni^{2+}	$Ni(NO_3)_2$	50	97.16 ± 2.0	96.56 ± 1.5

TABLE 5 Removal of ceftriaxone and norfloxacin from the environmental samples (N = 3).

Samples	Ceftriaxone	Norfloxacin
Tap water	93.89 ± 1.5	95.88 ± 1.2
Wastewater	89.95 ± 2.1	98.55 ± 1.0
Groundwater	91.65 ± 1.3	94.43 ± 2.2

efficiency decreased due to insufficient surface to adsorb higher concentrations of norfloxacin by increasing the norfloxacin concentration from 20 to 100 mg L^{-1}. Based on the results, norfloxacin molecules at low concentrations interacted with the adsorption sites on the surface of the adsorbent, resulting in a higher removal percentage. At higher concentrations, the removal efficiency decreases due to the saturation of the active sites of the adsorbent (Ali et al., 2016). As shown in Figures 1A, C concentration of 25 mg L^{-1} was determined as the optimal dose for norfloxacin.

3.4 Optimal conditions of removal

In addition to modeling the removal process, the removal conditions can be optimized using the RSM. The optimal removal conditions were assessed using the numerical software optimization technique in RSM. If the goal is to maximize the removal rate, the presented model with a utility of 1 will reach this goal. In this case, the removal efficiencies of ceftriaxone and norfloxacin will be 93.50% and 97.44%, respectively, with the adsorbent mass, contact time, concentration, and pH values of 0.034 g, 20 min, 25 mg L^{-1}, and 8, respectively (Supplementary Table S1). The prediction of the model was validated by conducting the experimental tests under optimal conditions. The experimental results of ceftriaxone and norfloxacin removal were 95.87% and 98.64%, respectively, confirming the model's accuracy.

3.5 Regeneration of GO adsorbent

A major aspect of an ideal adsorbent is that it can be used frequently. In fact, the reuse ability of an adsorbent in the adsorption process is valuable when a significant decrease is not observed in its efficiency. In this respect, an adsorbent with the possibility of recovery can significantly reduce the total costs of the removal process. In this research, the reusability of the GO adsorbent was examined by preparing some solutions containing ceftriaxone and norfloxacin. After using the GO adsorbent to remove antibiotics, it was separated from the solutions by centrifugation. The separated adsorbent was washed with 2 mL of methanol and finally dried in an oven at 85°C. This reuse cycle of GO in adsorption/desorption processes was repeated 5 times. Figure 2 presents the changes in the removal percentages of ceftriaxone and norfloxacin using recovered GO. In the first reuse cycle of the GO adsorbent, the removal efficiency decreased very slightly for both antibiotics. Although the removal efficiency declined by about 30% in the fifth reuse cycle of adsorbent, a significant removal rate with removal percentages of >64% was obtained for both antibiotics. Therefore, this adsorbent could well remove ceftriaxone and norfloxacin in five cycles of use.

3.6 Interference studies

The effect of possible interferences of various cations and anions in the removal of antibiotics was investigated to evaluate the method's applicability in removing norfloxacin and ceftriaxone in the presence of external ions. For this purpose, the signal of the sample solution was first measured in the absence of interfering species under optimal conditions. The obtained analytical signal was measured three times to calculate the average of the signals and the standard deviation. The possible interfering effect of each species was assessed by adding the target ion to the initial solution with a w/w ratio of 1,000 times compared to the antibiotics. Next, the corresponding analytical signal was obtained by performing the removal process on this solution. If the decomposition signal obtained in the presence of interfering species was not in the range of ±5%, it meant that the target ion was interfering with the existing ratio. Otherwise, the weight ratio of the interfering species would be reduced to the extent that the decomposition signal would be in the range of ±5%. The results (Table 4) show that when the species are present in the sample as much as 1,000 times of antibiotics, they do not interfere seriously in removing antibiotics.

3.7 Application to real samples

A synthetic sample was used to evaluate the proposed method's efficiency in removing ceftriaxone and norfloxacin. These samples were prepared using tap water, wastewater, and groundwater as fixed textures. In this procedure, specific doses of the antibiotics were added to a fixed volume of water samples to prepare synthetic samples. The resulting samples were examined using the proposed

TABLE 6 Literature comparison of removal for ceftriaxone and norfloxacin.

Analyte	Adsorbent	Amount	pH	Time	Removal/Adsorption	Ref.
Ceftriaxone	EC/AD process	0.75 g	7.5	12.5 min	100%	Noudeh et al. (2023)
	nZVI/$SrFe_{12}O_{19}$	0.15 g	5	8 min	98%	Amiri et al. (2020)
	O_3/UV/Fe_3O_4@TiO_2	2 g	9	30 min	92.40%	Hashemi et al. (2022)
	NBent-NTiO_2-Chit	0.2 g	5	10 min	93.5%	Mahmoud et al. (2020)
	GO	0.034 g	8	20 min	95.87%	This study
Norfloxacin	$CoFe_2O_4$@TiO_2-MMIP	0.4 g	7	60 min	91.1%	Fang et al. (2021)
	MgO/Chit/GO	0.01 g	7	360 min	1,000 mg g^{-1}	Nazraz et al. (2019)
	PDMPs	0.01 g	6.6	97 min	317 mg g^{-1}	Wan et al. (2018)
	HAP@CT	0.5 g	7	120 min	92%	Nayak et al. (2022)
	GO	0.034 g	8	20 min	98.64%	This study

method under optimal conditions. Each measurement was performed in triplicate. The standard increase method was used in the measurements. The results in Table 5 indicate the ability of GO to remove ceftriaxone and norfloxacin from water samples.

3.8 Comparison with other adsorbents

Table 6 compares the performance of the GO adsorbent with other adsorbents for ceftriaxone and norfloxacin removal. The experimental results revealed that the GO adsorbent was comparable with the other adsorbents for ceftriaxone and norfloxacin removal. The adsorbent consumption rate of the proposed method was considerably lower than that of other studies. Moreover, the duration of the current study on antibiotic removal was shorter than the other ones because the sonication process significantly increases the process efficiency. Additionally, using the RSM method dramatically reduces the number of tests, thereby saving time and the adsorbent amount. Therefore, the GO adsorbent performed well in ceftriaxone and norfloxacin removal from water samples.

4 Conclusion

In this research, the effectiveness of GO adsorbent in removing ceftriaxone and norfloxacin was investigated in laboratory conditions. The CCD-based RSM was used to model and optimize ceftriaxone and norfloxacin removal. The effects of adsorbent mass (0.01, 0.02, 0.03, 0.04, and 0.005 g), pH (3, 5, 7, 9, and 11), concentration (20, 40, 60, 80, and 100 mg L^{-1}), and sonication time (5, 10, 15, 20, and 25 min) were evaluated as independent variables and the removal rate as the dependent variable (response). Significant process variables were obtained as quadratic regression models for the response ($p < 0.0001$). An $R^2 > 0.99$ was calculated for removal modeling by the CCD method for ceftriaxone and norfloxacin. The results showed that the antibiotic concentration and the adsorbent mass in the removal process had the most negative and positive effects. The best process conditions were obtained as a pH of 8, an adsorbent mass of 0.034 g, a sonication time of 20 min, and a concentration of 25 mg L^{-1}. The removal efficiencies were equal to 95.87% and 98.64% for ceftriaxone and norfloxacin, respectively, under optimal conditions. The interference studies revealed that external ions did not seriously interfere with antibiotics removal when they were present in the sample as much as 1,000 times the antibiotics. The removal rates of ceftriaxone and norfloxacin were in the range of 89.95% to 98.55% for environmental samples under optimum conditions. The results of this study demonstrated that the GO adsorbent has a good ability to remove ceftriaxone and norfloxacin from aqueous solutions. Moreover, CCD and RSM proved a good ability in modeling, predicting, and optimizing the behavior of parameters affecting the process.

Data availability statement

The original contributions presented in the study are included in the article/Supplementary Material, further inquiries can be directed to the corresponding author.

Author contributions

ZL: Data curation, Formal Analysis, Writing–original draft. SZ: Supervision, Writing–review and editing. GZ: Conceptualization, Data curation, Formal Analysis, Writing–original draft. JX: Data curation, Formal Analysis, Writing–original draft.

Funding

The author(s) declare that no financial support was received for the research, authorship, and/or publication of this article.

Acknowledgments

The authors are grateful to Qingyang Prefectural Center for Disease Control and Prevention for their kind support.

Conflict of interest

The authors declare that the research was conducted in the absence of any commercial or financial relationships that could be construed as a potential conflict of interest.

Publisher's note

All claims expressed in this article are solely those of the authors and do not necessarily represent those of their affiliated organizations, or those of the publisher, the editors and the reviewers. Any product that may be evaluated in this article, or claim that may be made by its manufacturer, is not guaranteed or endorsed by the publisher.

Supplementary material

The Supplementary Material for this article can be found online at: https://www.frontiersin.org/articles/10.3389/fenvs.2024.1436848/full#supplementary-material

References

Ahmed, S. F., Mofijur, M., Nuzhat, S., Chowdhury, A. T., Rafa, N., Uddin, M. A., et al. (2021). Recent developments in physical, biological, chemical, and hybrid treatment techniques for removing emerging contaminants from wastewater. *J. Hazard. Mater.* 416, 125912. doi:10.1016/j.jhazmat.2021.125912

Ali, R. M., Hamad, H. A., Hussein, M. M., and Malash, G. F. (2016). Potential of using green adsorbent of heavy metal removal from aqueous solutions: adsorption kinetics, isotherm, thermodynamic, mechanism and economic analysis. *Ecol. Eng.* 91, 317–332. doi:10.1016/j.ecoleng.2016.03.015

Amin, I. S., Neysari, A. N., Althomali, R. H., Musad Saleh, E. A., Baymakov, S., Radie Alawady, A. H., et al. (2023). Development of microextraction methods for the determination of sulfamethoxazole in water and biological samples: modelling, optimization and verification by central composite design. *Front. Environ. Sci.* 11, 1242730. doi:10.3389/fenvs.2023.1242730

Amiri, S., Reza Sohrabi, M., and Motiee, F. (2020). Optimization removal of the ceftriaxone drug from aqueous media with novel zero-valent iron supported on doped strontium hexaferrite nanoparticles by response surface methodology. *ChemistrySelect* 5 (19), 5831–5840. doi:10.1002/slct.202000285

Anjum, H., Johari, K., Gnanasundaram, N., Appusamy, A., and Thanabalan, M. (2019). Impact of surface modification on adsorptive removal of BTX onto activated carbon. *J. Mol. Liq.* 280, 238–251. doi:10.1016/j.molliq.2019.02.046

Bhatt, S., and Chatterjee, S. (2022). Fluoroquinolone antibiotics: occurrence, mode of action, resistance, environmental detection, and remediation–A comprehensive review. *Environ. Pollut.* 315, 120440. doi:10.1016/j.envpol.2022.120440

Bilal, H., Li, X., Iqbal, M. S., Mu, Y., Tulcan, R. X. S., and Ghufran, M. A. (2023). Surface water quality, public health, and ecological risks in Bangladesh—a systematic review and meta-analysis over the last two decades. *Environ. Sci. Pollut. Res.* 30 (40), 91710–91728. doi:10.1007/s11356-023-28879-x

da Silva Júnior, A. H., de Oliveira, C. R. S., Wolff Leal, T., Pellenz, L., de Souza, S. M. D. A. G. U., de Souza, A. A. U., et al. (2024). Reviewing perovskite oxide-based materials for the effective treatment of antibiotic-polluted environments: challenges, trends, and new insights. *Surfaces* 7 (1), 54–78. doi:10.3390/surfaces7010005

Di Leo, G., and Sardanelli, F. (2020). Statistical significance: p value, 0.05 threshold, and applications to radiomics—reasons for a conservative approach. *Eur. Radiol. Exp.* 4, 18–8. doi:10.1186/s41747-020-0145-y

Dorival-García, N., Zafra-Gómez, A., Navalón, A., González, J., and Vílchez, J. L. (2013). Removal of quinolone antibiotics from wastewaters by sorption and biological degradation in laboratory-scale membrane bioreactors. *Sci. Total Environ.* 442, 317–328. doi:10.1016/j.scitotenv.2012.10.026

Dutta, L., Sethi, G. K., and Dey, S. (2024). A comprehensive and critical assessment on the efficiency of natural and synthetic adsorbents for the removal of recalcitrant malachite green from water: present level and future perspectives. *Korean J. Chem. Eng.* 1-19. doi:10.1007/s11814-024-00114-4

Fang, L., Miao, Y., Wei, D., Zhang, Y., and Zhou, Y. (2021). Efficient removal of norfloxacin in water using magnetic molecularly imprinted polymer. *Chemosphere* 262, 128032. doi:10.1016/j.chemosphere.2020.128032

Farhat, B., Chrigui, R., Rebai, N., and Sebei, A. (2023). Analysis of hydrochemical characteristics and assessment of organic pollutants (PAH and PCB) in El Fahs plain aquifer, northeast of Tunisia. *Environ. Sci. Pollut. Res.* 30 (35), 84334–84356. doi:10.1007/s11356-023-28216-2

Hashemi, S. Y., Yegane Badi, M., Pasalari, H., Azari, A., Arfaeinia, H., and Kiani, A. (2022). Degradation of Ceftriaxone from aquatic solution using a heterogeneous and reusable O3/UV/Fe3O4@ TiO2 systems: operational factors, kinetics and mineralisation. *Int. J. Environ. Anal. Chem.* 102 (18), 6904–6920. doi:10.1080/03067319.2020.1817909

He, X., Chen, X., Wang, X., and Jiang, L. (2023). Optimization of activated carbon production from corn cob using response surface methodology. *Front. Environ. Sci.* 11, 1105408. doi:10.3389/fenvs.2023.1105408

Hiasa, H. (2018). DNA topoisomerases as targets for antibacterial agents. *DNA topoisomerases Methods Protoc.* 1703, 47–62. doi:10.1007/978-1-4939-7459-7_3

Jäger, T., Hembach, N., Elpers, C., Wieland, A., Alexander, J., Hiller, C., et al. (2018). Reduction of antibiotic resistant bacteria during conventional and advanced wastewater treatment, and the disseminated loads released to the environment. *Front. Microbiol.* 9, 2599. doi:10.3389/fmicb.2018.02599

Kadhim, R. J., Al-Ani, F. H., Al-Shaeli, M., Alsalhy, Q. F., and Figoli, A. (2020). Removal of dyes using graphene oxide (GO) mixed matrix membranes. *Membranes* 10 (12), 366. doi:10.3390/membranes10120366

Kim, J. W., Hong, Y. K., Ryu, S. H., Kwon, O. K., Lee, Y. B., and Kim, S. C. (2023). Development of analytical method for veterinary antibiotics and monitoring of residuals in agricultural environment. *Appl. Biol. Chem.* 66 (1), 20. doi:10.1186/s13765-023-00777-3

Krishna, R. H., Chandraprabha, M. N., Samrat, K., Murthy, T. K., Manjunatha, C., and Kumar, S. G. (2023). Carbon nanotubes and graphene-based materials for adsorptive removal of metal ions–a review on surface functionalization and related adsorption mechanism. *Appl. Surf. Sci. Adv.* 16, 100431. doi:10.1016/j.apsadv.2023.100431

Li, J., Bai, H., Qiao, H., Du, C., Yao, P., Zhang, Y., et al. (2023). Causal effects of COVID-19 on cancer risk: a Mendelian randomization study. *J. Med. Virol.* 95 (4), e28722. doi:10.1002/jmv.28722

Li, X., Wang, B., Liu, F., and Yu, G. (2023). Occurrence and removal of pharmaceutical contaminants in urine: a review. *Water* 15 (8), 1517. doi:10.3390/w15081517

Li, Z., Zhao, R., Chen, X., Jiao, Y., and Chen, Z. (2023). Design approach for tuning the hybrid region of 3D-printed heterogeneous structures: modulating mechanics and energy absorption capacity. *ACS Appl. Mater. Interfaces* 15 (6), 7686–7699. doi:10.1021/acsami.2c17753

Liu, C., Xie, Y., Jiao, Y., Du, Y., Zheng, Q., and Sun, Y. (2022). Visible-light-driven nanoscale zero-valent iron loaded rGO/g-C3N4 for fluoroquinolone antibiotics degradation in water. *Front. Environ. Sci.* 10, 1065770. doi:10.3389/fenvs.2022.1065770

Madadrang, C. J., Kim, H. Y., Gao, G., Wang, N., Zhu, J., Feng, H., et al. (2012). Adsorption behavior of EDTA-graphene oxide for Pb (II) removal. *ACS Appl. Mater. Interfaces.* 4 (3), 1186–1193. doi:10.1021/am201645g

Madhusoodanan, J. (2022). How persister bacteria evade antibiotics, prolong infections. *Proc. Natl. Acad. Sci.* 119 (41), e2215617119. doi:10.1073/pnas.2215617119

Mahmoud, M. E., El-Ghanam, A. M., Mohamed, R. H. A., and Saad, S. R. (2020). Enhanced adsorption of Levofloxacin and Ceftriaxone antibiotics from water by assembled composite of nanotitanium oxide/chitosan/nano-bentonite. *Mater. Sci. Eng.* 108, 110199. doi:10.1016/j.msec.2019.110199

Maldonado, I., Vega Quispe, A. P., Merma Chacca, D., and Zirena Vilca, F. (2022). Optimization of the elimination of antibiotics by Lemna gibba and Azolla filiculoides using response surface methodology (RSM). *Front. Environ. Sci.* 10, 940971. doi:10.3389/fenvs.2022.940971

Molinari, R., Lavorato, C., and Argurio, P. (2020). Application of hybrid membrane processes coupling separation and biological or chemical reaction in advanced wastewater treatment. *Membranes* 10 (10), 281. doi:10.3390/membranes10100281

Nayak, A., Bhushan, B., and Kotnala, S. (2022). Fabrication of chitosan-hydroxyapatite nano-adsorbent for removal of norfloxacin from water: isotherm and kinetic studies. *Mater. Today Proc.* 61, 143–149. doi:10.1016/j.matpr.2021.07.356

Nazraz, M., Yamini, Y., and Asiabi, H. (2019). Chitosan-based sorbent for efficient removal and extraction of ciprofloxacin and norfloxacin from aqueous solutions. *Microchim. Acta.* 186, 459–9. doi:10.1007/s00604-019-3563-x

Nguyen, P. V., Aubry, C., Boudaoud, N., Gaubert, A., Langlois, M. H., Marchivie, M., et al. (2022). Oligonucleotide solid nucleolipid nanoparticles against antibiotic resistance of ESBL-producing bacteria. *Pharmaceutics* 14 (2), 299. doi:10.3390/pharmaceutics14020299

Noman, E. A., Mohamed, R. M. S. R., Al-Gheethi, A. A., Al-Shaibani, M. M., Al-Wrafy, F. A., Al-Maqtari, Q. A., et al. (2022). Antibiotics and antibiotic-resistant bacteria in greywater: challenges of the current treatment situation and predictions of future scenario. *Environ. Res.* 212, 113380. doi:10.1016/j.envres.2022.113380

Noudeh, G. D., Asdaghi, M., Noudeh, N. D., Dolatabadi, M., and Ahmadzadeh, S. (2023). Response surface modeling of ceftriaxone removal from hospital wastewater. *Environ. Monit. Assess.* 195 (1), 217. doi:10.1007/s10661-022-10808-z

Olusegun, S. J., Osial, M., Souza, T. G., Krajewski, M., Rodrigues, G. L., Marek, P., et al. (2023). Comparative characteristics and enhanced removal of tetracycline and ceftriaxone by Fe3O4-lignin and Fe3O4-carbon-based lignin: mechanism, thermodynamic evaluation, and DFT calculation. *J. Mol. Liq.* 371, 121075. doi:10.1016/j.molliq.2022.121075

Omar, H., Malek, N. S. A., Nurfazianawatie, M. Z., Rosman, N. F., Bunyamin, I., Abdullah, S., et al. (2023). A review of synthesis graphene oxide from natural carbon based coconut waste by Hummer's method. *Today Proc.* 75, 188–192. doi:10.1016/j.matpr.2022.11.427

Pei, M., Zhang, B., He, Y., Su, J., Gin, K., Lev, O., et al. (2019). State of the art of tertiary treatment technologies for controlling antibiotic resistance in wastewater treatment plants. *Environ. Int.* 131, 105026. doi:10.1016/j.envint.2019.105026

Sharma, P. C., Saneja, A., and Jain, S. (2008). Norfloxacin: a therapeutic review. *Int. J. Chem. Sci.* 6 (4), 1702–1713.

Shojaei, S., Nouri, A., Baharinikoo, L., Farahani, M. D., and Shojaei, S. (2021a). Removal of the hazardous dyes through adsorption over nanozeolite-X: simultaneous model, design and analysis of experiments. *Polyhedron.* 196, 114995. doi:10.1016/j.poly.2020.114995

Shojaei, S., Shojaei, S., Band, S. S., Farizhandi, A. A. K., Ghoroqi, M., and Mosavi, A. (2021b). Application of Taguchi method and response surface methodology into the removal of malachite green and auramine-O by NaX nanozeolites. *Sci. Rep.* 11 (1), 16054. doi:10.1038/s41598-021-95649-5

Singh, A. K., Kaur, R., Verma, S., and Singh, S. (2022). Antimicrobials and antibiotic resistance genes in water bodies: pollution, risk, and control. *Front. Environ. Sci.* 10, 830861. doi:10.3389/fenvs.2022.830861

Spit, T., van der Hoek, J. P., de Jong, C., van Halem, D., de Kreuk, M., and Perez, B. B. (2022). Removal of antibiotic resistance from municipal secondary effluents by ozone-activated carbon filtration. *Front. Environ. Sci.* 10, 834577. doi:10.3389/fenvs.2022.834577

Swidan, S., and Rubin, M. (2020). "Herbal and supplement use in pain management," in *Advanced therapeutics in pain medicine* (CRC Press), 301–322. Available at: https://www.taylorfrancis.com/chapters/edit/10.1201/9780429504891-19/herbal-supplement-use-pain-management-sahar-swidan-mara-rubin.

Tao, E., Zhou, H., Zheng, M., Zhao, Y., Zhou, J., Yuan, J., et al. (2024). Ceftriaxone-induced severe hemolytic anemia, renal calculi, and cholecystolithiasis in a 3-year-old child: a case report and literature review. *Front. Pharmacol.* 15, 1362668. doi:10.3389/fphar.2024.1362668

Tony, M. A. (2022). Low-cost adsorbents for environmental pollution control: a concise systematic review from the prospective of principles, mechanism and their applications. *J. Dispers. Sci. Technol.* 43 (11), 1612–1633. doi:10.1080/01932691.2021.1878037

Uluseker, C., Kaster, K. M., Thorsen, K., Basiry, D., Shobana, S., Jain, M., et al. (2021). A review on occurrence and spread of antibiotic resistance in wastewaters and in wastewater treatment plants: mechanisms and perspectives. *Front. Microbiol.* 12, 717809. doi:10.3389/fmicb.2021.717809

Veza, I., Spraggon, M., Fattah, I. R., and Idris, M. (2023). Response surface methodology (RSM) for optimizing engine performance and emissions fueled with biofuel: review of RSM for sustainability energy transition. *Results Eng.* 18, 101213. doi:10.1016/j.rineng.2023.101213

Vinayagam, V., Palani, K. N., Ganesh, S., Rajesh, S., Akula, V. V., Avoodaiappan, R., et al. (2023). Recent developments on advanced oxidation processes for degradation of pollutants from wastewater with focus on antibiotics and organic dyes. *Environ. Res.* 117500. doi:10.1016/j.envres.2023.117500

Wan, Y., Liu, X., Liu, P., Zhao, L., and Zou, W. (2018). Optimization adsorption of norfloxacin onto polydopamine microspheres from aqueous solution: kinetic, equilibrium and adsorption mechanism studies. *Sci. Total Environ.* 639, 428–437. doi:10.1016/j.scitotenv.2018.05.171

Wang, X., Liu, Y., Pang, H., Yu, S., Ai, Y., Ma, X., et al. (2018). Effect of graphene oxide surface modification on the elimination of Co (II) from aqueous solutions. *Chem. Eng. J.* 344, 380–390. doi:10.1016/j.cej.2018.03.107

Wydro, U., Wołejko, E., Luarasi, L., Puto, K., Tarasevičienė, Ž., and Jabłońska-Trypuć, A. (2023). A review on pharmaceuticals and personal care products residues in the aquatic environment and possibilities for their remediation. *Sustainability* 16 (1), 169. doi:10.3390/su16010169

Wysowska, E., Wiewiórska, I., and Kicińska, A. (2024). The problem of health risk resulting from the presence of pharmaceuticals in water used for drinking purposes: a review. *J. Ecol. Eng.* 25 (5), 244–256. doi:10.12911/22998993/186371

Yang, J., Shojaei, S., and Shojaei, S. (2022). Removal of drug and dye from aqueous solutions by graphene oxide: adsorption studies and chemometrics methods. *NPJ Clean. Water.* 5 (1), 5. doi:10.1038/s41545-022-00148-3

Yang, S. T., Chen, S., Chang, Y., Cao, A., Liu, Y., and Wang, H. (2011). Removal of methylene blue from aqueous solution by graphene oxide. *J. Colloid Interface Sci.* 359 (1), 24–29. doi:10.1016/j.jcis.2011.02.064

Yin, S., Yan, Z., Chen, X., Yan, R., Chen, D., and Chen, J. (2023). Mechanical properties of cemented tailings and waste-rock backfill (CTWB) materials: laboratory tests and deep learning modeling. *Constr. Build. Mater.* 369, 130610. doi:10.1016/j.conbuildmat.2023.130610

Zhang, X., Shen, J., Zhuo, N., Tian, Z., Xu, P., Yang, Z., et al. (2016). Interactions between antibiotics and graphene-based materials in water: a comparative experimental and theoretical investigation. *ACS Appl. Mater. Interfaces.* 8 (36), 24273–24280. doi:10.1021/acsami.6b09377

frontiers | Frontiers in Environmental Science

TYPE Original Research
PUBLISHED 21 October 2024
DOI 10.3389/fenvs.2024.1458858

OPEN ACCESS

EDITED BY
Jahangeer Jahangeer,
University of Nebraska-Lincoln, United States

REVIEWED BY
Sughosh Madhav,
Jamia Millia Islamia, India
Qizi Fu,
Hunan University, China
Mohammad Zakwan,
Maulana Azad National Urdu University, India

*CORRESPONDENCE
Xiang Zhang,
zhangxiang@whu.edu.cn

RECEIVED 03 July 2024
ACCEPTED 09 October 2024
PUBLISHED 21 October 2024

CITATION
Liu J, Zhang X and Gui H (2024) Comparative assessment of pollution control measures for urban water bodies in urban small catchment by SWMM.
Front. Environ. Sci. 12:1458858.
doi: 10.3389/fenvs.2024.1458858

Comparative assessment of pollution control measures for urban water bodies in urban small catchment by SWMM

Jie Liu[1,2], Xiang Zhang[2,3]* and Haijiao Gui[2,3]

[1]School of Architecture and Civil Engineering, Chengdu University, Chengdu, China, [2]Hubei Key Laboratory of Water System Science for Sponge City Construction, Wuhan University, Wuhan, China, [3]State Key Laboratory of Water Resources Engineering and Management, Wuhan University, Wuhan, China

Under the current increasingly serious water pollution situation in urban, the comprehensive treatment and protecting measures in urban small catchment are the necessary step to the water pollution treatment, not only focus on the water bodies themself. In this paper, the Luojiagang river channel and its catchment in Wuhan, which has been heavily impacted by water pollution, are taken as an example for the comparative assessment of pollution control measures in order to explore the effective and sustainable schemes including the LID (Low Impact Development---LID) by using SWMM model (Storm Water Management Model---SWMM). Through the comparison of pollution treatment measures based on scenarios simulation with the baseline scenarios, it was found that the reduction effects of pollutant peak concentrations at the outlet node of Luojiagang River had the decreasing order of: the combined measures (COS) > LID control > the water diversion from Donghu Lake (WAD) > the sewage treatment (SET) > the sediment dredging (SED), and the reduction effects of total pollutant load had the decreasing order of: LID > COS > SET > SED > WAD. The results show that the control of non-point source pollution is the key for the improvement of water quality in Luojiagang River, and LID plays important role in the reduction of both pollutant peak concentrations and load. This study has the implication for the decision making of the water pollution controlling schemes in urban small catchment.

KEYWORDS

urban, SWMM model, water pollution treatment, scenario simulation, Wuhan

1 Introduction

With the rapid expansion of cities and the growth of population, the issue of water pollution has become a matter of great concern that cannot be overlooked (Huang et al., 2019). Over 80% of urban rivers have demonstrated considerable levels of pollution, with some exhibiting a blackened and unpleasant odor (Qu and Fan, 2010). The occurrence of eutrophication and foul odors in urban water bodies has not only impacted the local environment but also the quality of life for residents in the surrounding areas. Furthermore, the water quality-induced water shortage poses a significant threat to the safety of urban water supply (Tao and Xin, 2014). Frequent incidents of urban water pollution reflect the gravity of the situation, making the treatment and management of urban water pollution a necessity for safeguarding economic and social development, as well as rebuilding ecological

civilization. Urban landscapes and the unplanned urbanization are host to a suite of contaminants that impact on water quality, where the major contributors to pollution and the novel contaminants continue to pose new challenges to comprehensive assessment, monitoring and treatment regimes (McGrane, 2016; Khan et al., 2022).

During recent years, the significant changes have been observed in the structure and water cycle of urban water systems through the construction of rainwater and sewage pipelines, water diversion projects, and gate operations (Grimm et al., 2008; Li Q. et al., 2019). The natural water network in urban areas has been transformed into a complex water network that combines natural and engineering features through a series of construction projects such as channels, gates, and pumping stations (Follstad Shah et al., 2019; Gessner et al., 2014; McGrane, 2016). In addition to its own water system connectivity, the complex urban water network is closely related to the processes of water intake, water use, and wastewater discharge, which makes its water cycle processes very complex (Kuhlemann et al., 2020), and its hydrological processes and pollution patterns are influenced by both natural factors and human intervention. Moreover, the complex urban water network is influenced by multiple sources of pollution, including point and non-point source, even the pollution arising from misconnections (Revitt and Ellis, 2016), posing additional challenges to urban water pollution management. The processes of pollutant generation, transmission and treatment in urban water networks and the impact of human regulation on the water environment need further exploration (Ehleringer et al., 2016).

The implementation of water pollution control in urban water networks involves a combination of point source pollution control, non-point source pollution control, and water body restoration measures. To address point-source pollution, an approach that involves collecting and treating wastewater is adopted, complemented by a range of policies and technologies to mitigate industrial pollution sources (Pan and Tang, 2021). Facing the challenges of the non-point sources, that are mainly produced by the untreated runoff (Charters et al., 2021; Müller et al., 2020) from impermeable urban surfaces, LID (Low Impact Development---LID) practices has gained significant popularity (Rong et al., 2021). Techniques such as bioretention cells, pervious pavements, and green roofs have demonstrated their effectiveness in several studies (Baek et al., 2015; Seo et al., 2017; Zhu et al., 2019; Liu et al., 2019; Liu, 2020). Due to the complexity of urban water issues, de Oliveira et al. (2022) pointed out that traditional engineering approaches alone (gray infrastructure) are not able to meet all the challenges of sustainability posed by growing urban population and consumption. A mix of green (such as LID), blue and grey infrastructures is likely to result in the best adaptation strategy as these three alternatives tend to complement each other (Alves et al., 2019). In China, the construction of sponge cities has emerged as a promising approach towards reducing urban waterlogging and non-point source pollution (Li Z. et al., 2019; Nguyen et al., 2019), in which the combination of gree, blue and grey is emphasized. But in practise, the combination of gree, blue and grey still exists many difficulties, such as how to determine the combining schemes and assess their effects assessment for the decision making etc.

In this context, a study taking a urban small catchment in Wuhan as an example is carried out for the comparison and analyzing of the effects of different water pollution treatment measures, which can provide valuable guidance to the decision making of the water pollution contoling schemes in urban small catchment. The detailed tasks in this paper include: (1) establishing a hydrological and water quality model of the Luojiagang catchment based on SWMM; (2) simulating the evolution trend of water quality in the catchment under different treatment measures, including LID and traditional engineering approaches; and (3) comparing and assessing the effects of different treatment measures to provide a reference for actual water environment treatment options.

2 Material and methods

2.1 Study area

The Luojiagang catchment, which includes the two main rivers, the Luojiagang River and the Shahugang River, is situated in Wuhan's core city and extends across three administrative districts: Hongshan, Wuchang, and Qingshan (Figure 1). Its total size is roughly 27.91 km^2. With a 3.85 km overall length, the Luojiagang River begins at Shahugang River in the south and terminates at Luojialu Pumping Station in the east. The Luojiagang River divides the Shahugang River into two sections, the eastern section of which begins at Xudong Street and receives tailwater discharge from the upstream Shahu Sewage Treatment Plant and the midstream Erlangmiao Sewage Treatment Plant as well as sporadic domestic sewage discharge, and the western section of which begins at Renhe Road and is connected to the Donghu Lake by the Xingouqu River. During the flood season, the Xingou gate is opened, thereby permitting the influx of water accumulated in the East Lake to cascade into the Shahugang River. The eastern and western sectors of the Shahugang River converge and amalgamate into the Luojiagang River, culminating in the eventual discharge of the waterway into the Yangtze River. The surface of the Luojiagang catchment exhibits relatively gentle terrain with locally concentrated high-rise buildings. The elevation of the region ranges between 11.46 m and 40.36 m. The majority of the catchment is urbanized. Overall, impermeable surfaces constitute a significant proportion of the study area, resulting in high runoff coefficients, short runoff formation times, limited infiltration capacities, and intensified pollutant scouring.

Luojiagang catchment faces substantial water environmental issues due to domestic sewage discharge, overflow merging, and indiscriminate garbage dumping, leading to the formation of a black-odorous water body. In recent years, a significant portion of the Luojiagang catchment has had sewage collection pipelines constructed and pollution outlets along the riverbanks intercepted to mitigate the impact of combined sewer overflows on the water body. Additionally, a comprehensive channel remediation project has been implemented to align with the requirements of the Donghu Lake Ecological Water Network Project. The implementation of the above measures has yielded initial results in the treatment of foul-smelling water in Luojiagang River. However, the issue of water pollution has not been completely eradicated. In order to further investigate the specific causes of pollution in Luojiagang and analyze the water quality trend of the river under different treatment measures, this

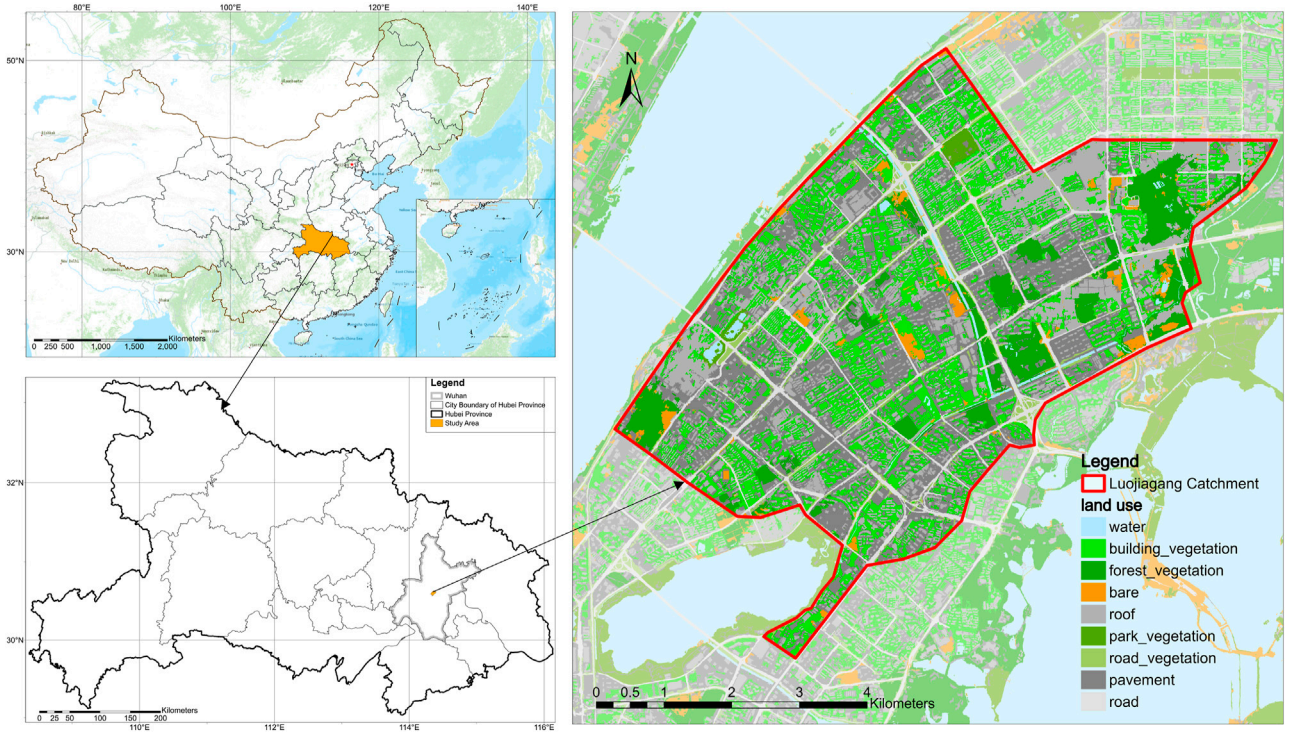

FIGURE 1
The geographical location and land use of Luojiagang catchment.

study will conduct hydrological and water quality simulations of the Luojiagang catchment based on the SWMM model. The findings will serve as a reference for future treatment efforts.

2.2 SWMM model

The Storm Water Management Model (SWMM) was developed by the United States Environmental Protection Agency (EPA) as a dynamic rainfall-runoff simulation program. It models the runoff volume and water quality of a single rainfall event or a long-term sequence by constructing catchments, drainage pipes, rainwater nodes, and treatment facilities (Gironás et al., 2010).

The basic operating unit of the SWMM model is the sub-catchment, which can be used to simulate hydrological and hydraulic processes, water quality, and sewage in various forms. Each sub-catchment is divided into three parts: impervious areas without depression storage, impermeable areas with depression storage, and pervious areas. SWMM provides three infiltration models, namely, Horton infiltration formula, Green-Ampt infiltration formula, and the Soil Conservation Service (SCS) Curve Number method. The pipe network section offers three runoff simulation methods: steady flow, kinematic wave, and dynamic wave. The steady flow method is the simplest to calculate as it maintains a constant flow at each time step. The kinematic wave method takes into account the pipe channel equation and uses hydraulic continuity and momentum conservation equations for calculation. The dynamic wave method considers additional factors such as node water flow, continuity equation, among others. Each method has its pros and cons and should be applied based on specific requirements.

The SWMM software can simulate the entire process of pollutant generation, runoff, and migration. By subdividing sub-catchments into different land use areas, it can simulate the pollution transmission of drainage systems by setting pollutant accumulation and washout characteristics for each land use type. The accumulation process refers to the continuous increase of pollutants on the surface caused by natural and human activities before rainfall occurs. SWMM software primarily employs power function models, exponential function models, and saturation function models to simulate pollutant accumulation. The washout process involves erosion of the underlying soil layer during runoff production and the dissipation of certain pollutants. The SWMM software mainly uses exponential function models, performance curve washout models, and event mean concentration function models to simulate pollutant washout.

2.3 Scenario definition

Due to severe pollution in Luojiagang River, four treatment measures are proposed based on the current situation and treatment conditions of non-point water pollution in the cathment, which include water diversion from Donghu Lake (WAD), sewage treatment (SET), sediment dredging (SED), and LID control (LID). Each measure has three levels of intensity, and a combination of low, medium, and high levels of intensity are set according to the actual situation for simulating the water environmental trend in Luojiagang

River through hydrodynamic and water quality modeling. The baseline scenario (BAS) has a water diversion flow from Donghu Lake of 3 m^3/s, a total nitrogen release rate of 268 $mg/m^2/d$, and a total phosphorus release rate of 158 $mg/m^2/d$ for sediment, without direct discharge sewage treatment and LID facilities.

Because the water quality of Donghu Lake is better than that of Luojiagang River, scientifically diverting water from Donghu Lake to the Yangtze River through Luojiagang River during the rainy season can not only prevent urban waterlogging but also improve the water quality of Luojiagang River. Considering the actual factors of water diversion project construction, the low, medium, and high water diversion discharges are set at 5 m^3/s (WAD1), 7 m^3/s (WAD2), and 9 m^3/s (WAD3), respectively.

A sewage interception pipeline has been installed along the west side of Luojiagang River to collect wastewater and discharge it into the Erlangmiao Sewage Treatment Plant. However, the degree of interception still needs improvement, and direct discharge of untreated sewage into the river still occurs in some areas. In light of the limited proportion of combined sewers in the study area and the high treatment efficacy of the local sewage treatment plant, the main measure of sewage treatment is set to collect and treat direct sewage in this study. To this end, the low, medium, and high direct sewage treatment rates were set to 20% (SET1), 40% (SET2), and 60% (SET3), respectively.

Sediment dredging is a common engineering measure to control black and odorous water bodies (Gu et al., 2016; Liu et al., 2015). The sediment of Luojiagang River and Shahugang River is seriously polluted because of the discharge of tail water and direct sewage from sewage plants all year round. Sediment dredging in these two rivers is an approach for pollution control in this area. The low, medium, and high sediment release rates were set at 80% (SED1), 50% (SED2), and 20% (SED3) of the baseline scenario.

The construction of sponge cities has become an essential part of environmental protection policies across various cities (Nguyen et al., 2019). It aims to reduce runoff levels and minimize pollution caused by rainfall runoff. To achieve this goal, many cities use low-impact development measures (LID) to build decentralized and small-scale sponge structures, including rain gardens, green roofs, bioretention cells, and artificial wetlands, among others (Hu et al., 2019). In this study, bioretention cells are chosen as a typical example of LID control measures for simulation due to their varying forms and strong applicability. Combining information from relevant literature (Rossman and Simon, 2022; Huang et al., 2022; Li et al., 2021) and the study area, the twelve parameters of the bioretention cells were determined (Table 1). The area proportions of low, medium, and high LID control were set at 10% (LID1), 20% (LID2), and 30% (LID3), respectively.

The above scenarios are single scenarios, and the simulated pollution control rate can reflect the treatment effect of each measure. In practice, the remediation of water environment is usually a systematic project, which requires multiple means to work at the same time. In order to examine the effectiveness of different pollution control measures in the actual management of water environments, this study combines the single scenarios previously examined into three combination scenarios: COS1, COS2, and COS3. COS1 is comprised of the scenarios WAD1, SET1, SED1, and LID1, and the remaining two combinations are similar.

Rainfalls with return periods of 0.25, 1, and 5 years were selected to represent light rain, moderate rain, and heavy rain in Wuhan City for water quality simulation analysis under different scenarios (Figure 2). For simplification, the BAS with a 1a rainfall return period was abbreviated as "1a-BAS", and similar abbreviations were used for the other scenarios.

3 Model setup and calibration

3.1 Model setup

The SWMM model was constructed with hydrological, water quality, and hydraulic modules. The hydrological module simulates surface runoff processes, the water quality module modeled the accumulation and flushing processes of pollutants in the underlying surface, and the hydraulic module was used to simulate the transport of water and pollutants.

The Luojiagang catchment was divided into 54 sub-catchments using a manual division method based on pipe network structure, the location of rainwater wells, topography, and land use. The land use types in the study area were categorized into five types: roofs, pavements, hard ground surfaces, construction land, and green land, of which the first three were impermeable surfaces and the latter two are permeable surfaces. The infiltration process in the permeable areas was calculated using the Horton model. The runoff calculation for surface runoff was based on the nonlinear reservoir method, where the continuity equation and Manning's formula were solved iteratively to obtain the runoff volume.

Due to the complex structure of the stormwater and sewage pipe networks in the study area, the kinematic wave model was selected for network simulation. The accumulation process of pollutants was

TABLE 1 Parameters setting for the bioretention cell.

Layers of bioretention cell	Parameters			
Surface layer	Storage depth (mm)	Vegetation volume fraction	Surface roughness (Mannings n)	Surface slope (%)
	60	0.15	0.5	0.4
Soil layer	Thickness (mm)	Porosity	Field capacity	Wilting point
	700	0.5	0.2	0.1
Storage layer	Thickness (mm)	Void Ratio	Seepage rate (mm/hr)	Clogging factor
	400	0.75	300	0

Note: the meaning of the twelve parameters can be found in the Storm Water Management Model User's Manual Version 5.2 (Rossman and Simon, 2022).

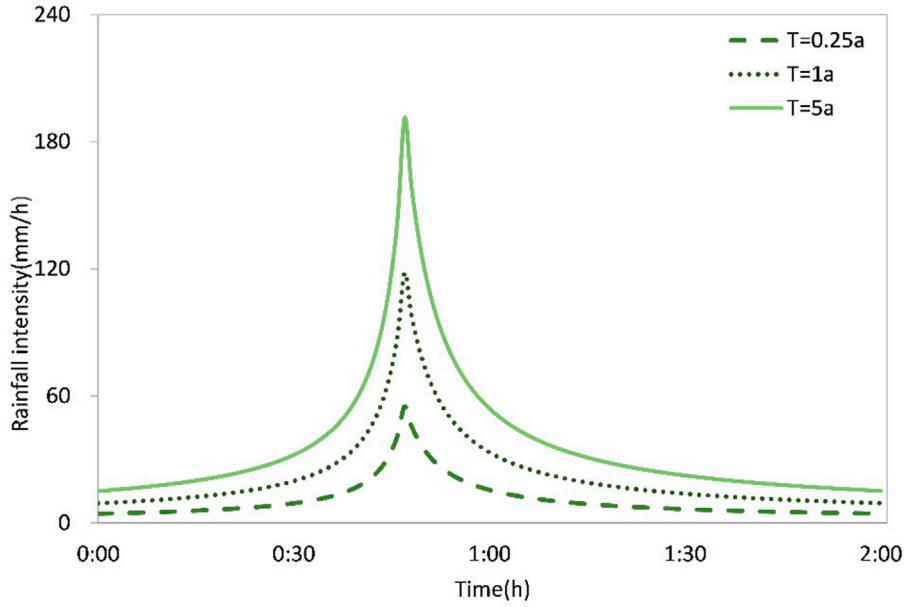

FIGURE 2
The design rainfall with different return periods (based on the Wuhan local standard: rainstorm intensity formula and design rainstorm profile of Wuhan, DB4201/T 641-2020).

modeled using the saturation function, and the flushing process was modeled using the exponential function. Key factors affecting water quantity and quality in the study area, such as the discharge of Donghu Lake, domestic sewage, sewage treatment plant operations, pump station discharges, and pollutant releases from sediment were integrated into the sub-catchments and the pipe network framework to construct a SWMM-based hydrological and water quality model for the Luojiagang catchment (Figure 3).

3.2 Model calibration

The SWMM model required the setting of numerous parameters, some of which can be obtained from actual engineering data and software such as ArcGIS, referred to as data parameters, while other parameters need to be obtained by referring to the value range of relevant literature and through parameter calibration, referred to as empirical parameters. The initial values of each parameter were determined based on different data, and then the model parameters were calibrated according to actual measured data (the initial values and calibrated values of hydrological, hydraulic, and water quality parameters are shown in Tables 2–4).

Water quality simulation was based on water quantity simulation, so the calibration and adjustment of hydrological and hydraulic parameters were required first. The Nash-Sutcliffe efficiency coefficient was used as the evaluation index for calibration of hydrological and hydraulic parameters, and a value closer to 1 indicated better simulation performance, and $NSE_{threshold}$ = 0.65 has been reported in the literature as a lower limit of a valid goodness-of-fit (Ritter and Muñoz-Carpena, 2013). The period from June 11 to June 30, 2019 was designated as the calibration period, while the period from May 14 to May 31, 2019 was identified as the validation period. Daily precipitation data measured at the Hubei University precipitation station was inputted, and the measured discharge at the Luojiagang catchment export node J16 was compared with the simulated discharge (Figure 4) to determine the simulation performance of the parameters. After multiple parameter adjustments, the Nash efficiency coefficient during the calibration period was calculated to be 0.81, and during the verification period, it was 0.75, meeting the simulation requirements of the model. Although the Nash efficiency coefficient indicated that the model has the satisfied accuracy, the more rainfall-runoff events are still needed for the calibration and validation in order to guarantee the accuracy of the model under the different rainfall scenario in future.

In terms of water quality parameter calibration, the relative error was utilized as the performance indicator for simulated parameters. Calibration and validation were conducted by comparing the simulated and measured concentrations at river nodes J16, J19, J43, and J56 on June 6, 2019 and May 11, 2019, respectively (Figure 5). Following numerous adjustments, the relative error's absolute value ranged from 3.10% to 15.79% during calibration and 0.56%–15.14% during validation (Figure 6). Accounting for measurement and monitoring errors and various interfering factors affecting river water quality, the degree of accuracy achieved was adequate to fulfill this model's simulation requirements.

4 Results and discussion

A hydrological and water quality model for the Luojiagang catchment based on SWMM was established to simulate the water dynamics and water quality conditions during the rainy season, and TN and TP were used as typical pollutants. Single and combined scenarios were designed for the four measures of East Lake water

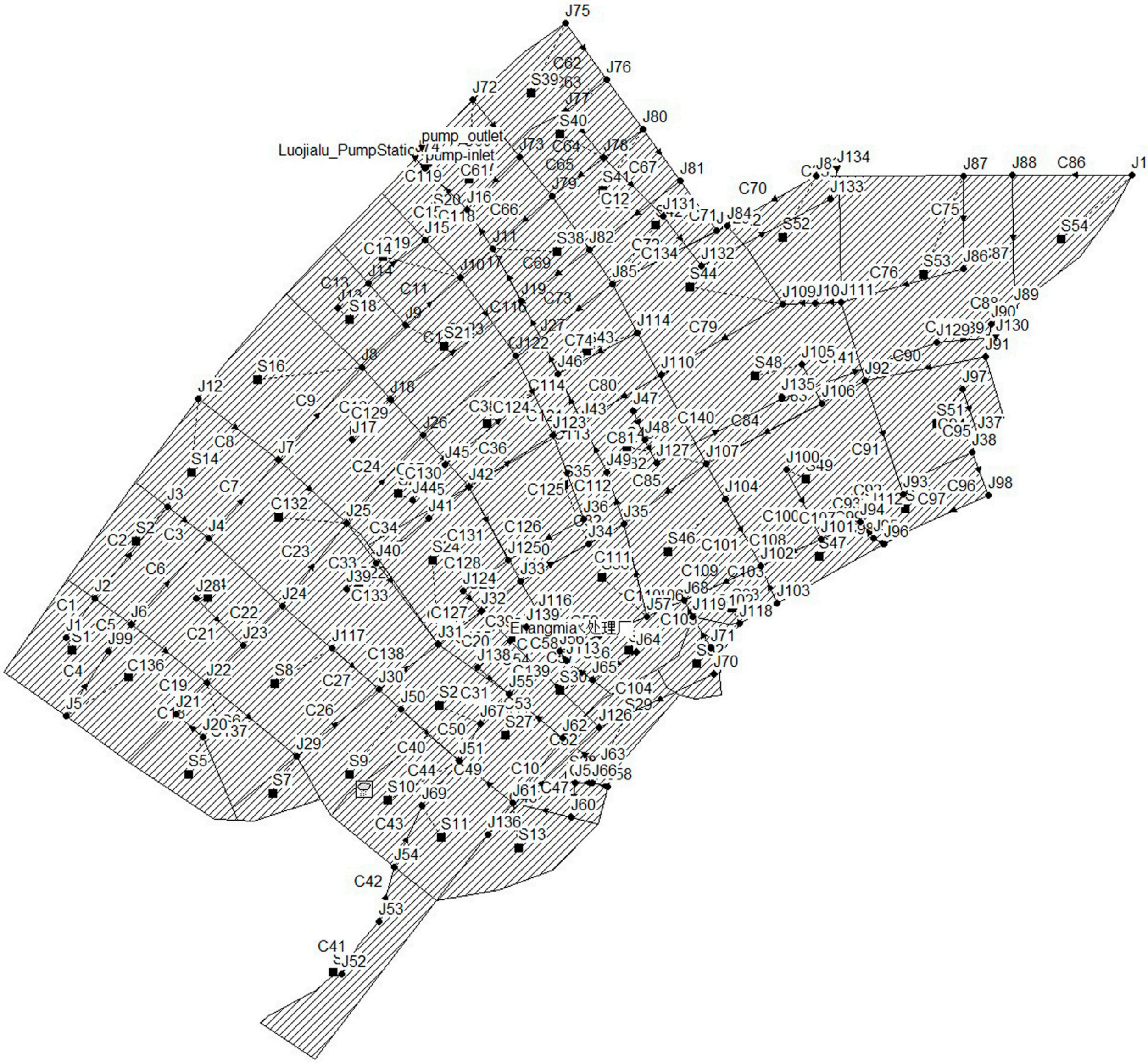

FIGURE 3
SWMM model of the Luojiagang catchment.

diversion, sewage treatment, dredging of sediment, and sponge city governance to simulate the trend of the water environment in Luojiagang River. By analyzing the pollution reduction effect of each governance measure and identifying the key links of pollution in the Luojiagang catchment, the purpose of providing scientific references for the water environment management in the Luojiagang catchment was achieved.

4.1 Analysis of the baseline scenario

In order to analyze the variation process and the rules of the runoff discharge and pollutants concentration in different rainfall intensity events in the Luojiagang catchment, the three baseline scenarios (BAS) of rainfall were selected respectively as the designing rainfall with a return period of 0.25, 1, and 5 years (Figure 2). The baseline scenarios of the land use types, the sub-catchments, the channels and the pipe network framework were kept the same as the situation of SWMM model setup and calibration, which were described by the paramenters in Tables 2–4. Then, the treatment scenarios (defined in Section 2.3), the water diversion from Donghu Lake (WAD), the sewage treatment (SET), the sediment dredging (SED) and the LID control (LID), will be applied for the scenario analysis of the effects of water pollution treatments which are compared with the baseline scenarios. By the comparisons, the function of the treatment scenarios will be evaluated, and the treatment scheme will be recomended.

By inputting the three disigning rainfall into the SWMM model, the runoff process at the J16 outlet node of the Luojiagang catchment was obtained (Figure 7). It was observed that the

TABLE 2 Adjustment of hydrological and hydraulic parameters.

	Parameter	Ranges	unit	Initial value	Calibrated value
Horton moddel	Max.Infil.Rate	25-80	mm/h	70	65.8
	Min.Infil.Rate	0-10	mm/h	3.8	2.8
	Decay constant	2-7	/	4	4
	Drytime	1-7	day	7	6
Subcatchment	N-imperv	0.011-0.033	/	0.013	0.012
	N-perv	0.05-0.8	/	0.24	0.23
	Des-imperv	0.2-10	mm	2	2.35
	Des-perv	2-7	mm	5	5.6
	Zero-imperv	5-85	%	25	25
Conduit	Manning-N	0.011-0.026	/	0.012	0.013
Channel	Manning-N	0.011-0.4	/	0.04	0.04

TABLE 3 Adjustment of pollutants cumulative model parameters.

Land use type	Parameter	Initial value		Calibrated value	
		TN	TP	TN	TP
Roof	Max. Buildup (kg/hm^2)	12	1.0	15	0.8
	Half-saturated cumulative time (d)	8	8	5	5
Pavement	Max. Buildup (kg/hm^2)	10	0.8	14	1
	Half-saturated cumulative time (d)	8	8	5	5
Hard ground surface	Max. Buildup (kg/hm^2)	10	0.8	10	1
	Half-saturated cumulative time (d)	8	8	5	5
Construction land	Max. Buildup (kg/hm^2)	14	1.2	16	1.5
	Half-saturated cumulative time (d)	8	8	5	5
Green land	Max. Buildup (kg/hm^2)	13	1.1	16	1
	Half-saturated cumulative time (d)	8	8	5	5

discharge hydrograph at the outlet node J16 exhibited a double peak, with a smaller first peak and a larger second peak. The first peak was generated by direct rainfall on the river channel and rainfall runoff from the surrounding catchments of the river channel, while the second peak appeared after the rainfall had ended and was generated by rainfall on the underlying surface of the catchment through the pipe network, reflecting the lag effect of the urban drainage system on rainfall.

In accordance with observed trends, higher volumes of rainfall correspond to earlier peak times, while smaller amounts of rainfall correspond to later peak times. In the scenario 0.25a-BAS, the second peak was relatively smooth, but when the rainfall intensity was greater, the runoff line showed a gap, indicating that some areas were limited by the overcurrent capacity of the pipe network. In the scenario 5a-BAS, the second peak showed a slightly gradual plateau, indicating that the pipe network of the catchment had reached its maximum overcurrent capacity and excess rainfall runoff was stored in rainwater wells, forming a stable flow in the pipe network. In the scenario 5a-BAS, some simulated rainwater nodes overflowed, indicating that the rainwater pipe network system in the study area needs to be improved.

From the outlet node J16 water quality process simulation (Figure 8), it was observed that the concentrations of TN and TP exhibited similar trends with a bimodal distribution of water quality. The first peak was mainly formed by surface runoff near the river channel during early rainfall events, when most surface pollutants were washed into the river, resulting in high levels of water pollution, reflecting an initial rain effect. While the second peak has a relatively low pollution degree due to the large rainfall and less residual surface pollutants.

In the scenarios 0.25a-BAS, the two peaks were smoother with smaller differences in peak values. However, the higher rainfall intensity resulted in more pronounced flushing effects, leading to the significantly higher and sharper first peak values. As the accumulation of pollutants on the underlying surface was

TABLE 4 Adjustment of pollutants washoff model parameters.

Land use type	Parameter	Initial value		Calibrated value	
		TN	TP	TN	TP
Roof	Washoff coefficient	0.008	0.005	0.01	0.006
	Washoff exponent	1.6	1.6	1.8	1.9
Pavement	Washoff coefficient	0.008	0.005	0.008	0.006
	Washoff exponent	1.5	1.5	1.8	1.7
	Street cleaning removal efficiency	60%	60%	60%	60%
Hard ground surface	Washoff coefficient	0.006	0.004	0.01	0.005
	Washoff exponent	1.5	1.5	1.8	1.7
Construction land	Washoff coefficient	0.007	0.005	0.009	0.008
	Washoff exponent	1.4	1.4	1.9	1.8
Green land	Washoff coefficient	0.005	0.002	0.008	0.002
	Washoff exponent	1.2	1.2	1.8	1.4

constant, the second peak values decreased as the rainfall intensity increased. Since other factors influencing water quality in the study area remained consistent, the analysis of the baseline scenario simulation reflected the impact of surface source pollution brought about by rainfall runoff in the study area under different rainfall intensities. The number of drought days in the early stage of this study was 10 days. Based on the simulated water quality process, it was evident that a significant volume of pollutants accumulated on the underlying surface, and the initial rainwater carried a high degree of pollution, which exerted a substantial impact on the water environment of the river. It was noteworthy that the river retained a considerable level of contamination even after 2 h of rainfall, and the pollution did not return to pre-rainfall levels until 12 h later. The contamination of the river resulting from a 2-h bout of precipitation had yet to revert to its pre-rainfall state, even after 12 h had elapsed, indicating that reducing surface source pollution is of utmost importance for water environment management in the Luojiagang catchment.

4.2 Pollutant concentration processes in different treatment scenarios

Based on the analysis of the scenario BAS, rainfall with a return period of 0.25, 1, and 5 years was selected to represent light rain, moderate rain, and heavy rain in Wuhan for the water quality simulation analysis under different treatment measures.

After comparing the pollutant concentrations and runoff processes under different treatment measures (Figure 9), it can be observed that due to the ongoing processes of water diversion from Donghu Lake, direct sewage discharge, and the release of endogenous pollutants, dilution of pollutants through WAD, SET, and SED has already played a significant role in reducing the concentration of pollutants prior to rainfall, while LID facilities had no impact on the concentration of pollutants in the river before rainfall, as their role was primarily focused on the storage and purification of rainfall runoff.

Of the four treatment measures, including WAD, SET, SED, and LID, the first three primarily impacted pollutant concentration. Under these three treatment measures, the pollutant concentrations of varying treatment intensities tended to converge during rainfall processes due to the fact that the constant water diversion discharge proportionally reduces as the runoff from rainwater accelerates, the constant direct discharge of sewage proportionally reduces, and the introduction of non-point source pollution reduces the proportion of endogenous pollution, respectively.

LID differed from the previous three measures in that it had a significant reduction effect on both runoff volume and pollutant concentration (Figures 9G, H; Figure 10). LID had a significant effect on reducing the first peak discharge, indicating the effectiveness of LID facilities in increasing infiltration and decreasing surface runoff. During rainfall conditions with a return period of 5 years, LID3 displayed a smooth curve. Similarly, under a return period of 0.25 years, LID aided in reducing the fluctuation of the runoff hydrograph, which pointed towards its ability to significantly minimize the overflow of the pipeline network. Additionally, during a rainfall event, pollutant reduction effect of LID increased with the rise in the rainfall intensity and reached its peak when the rainfall reached its peak. Afterward, it gradually reverted to the initial level.

Upon comparing the results of different rainfall return periods, it was found that the total runoff increased as the return period increased. This resulted in a decline of both the dilution effect of WAD and the attenuation effect of SED on pollutants, along with a reduction in the direct discharge contribution to pollution in the Luojiagang catchment. Consequently, the dilution effect of SET on pollution also diminished. Particularly in scenario 5a-SET3, pollutant concentration showed a small difference before the peak arrival as compared to scenario 5a-BAS. A smaller return

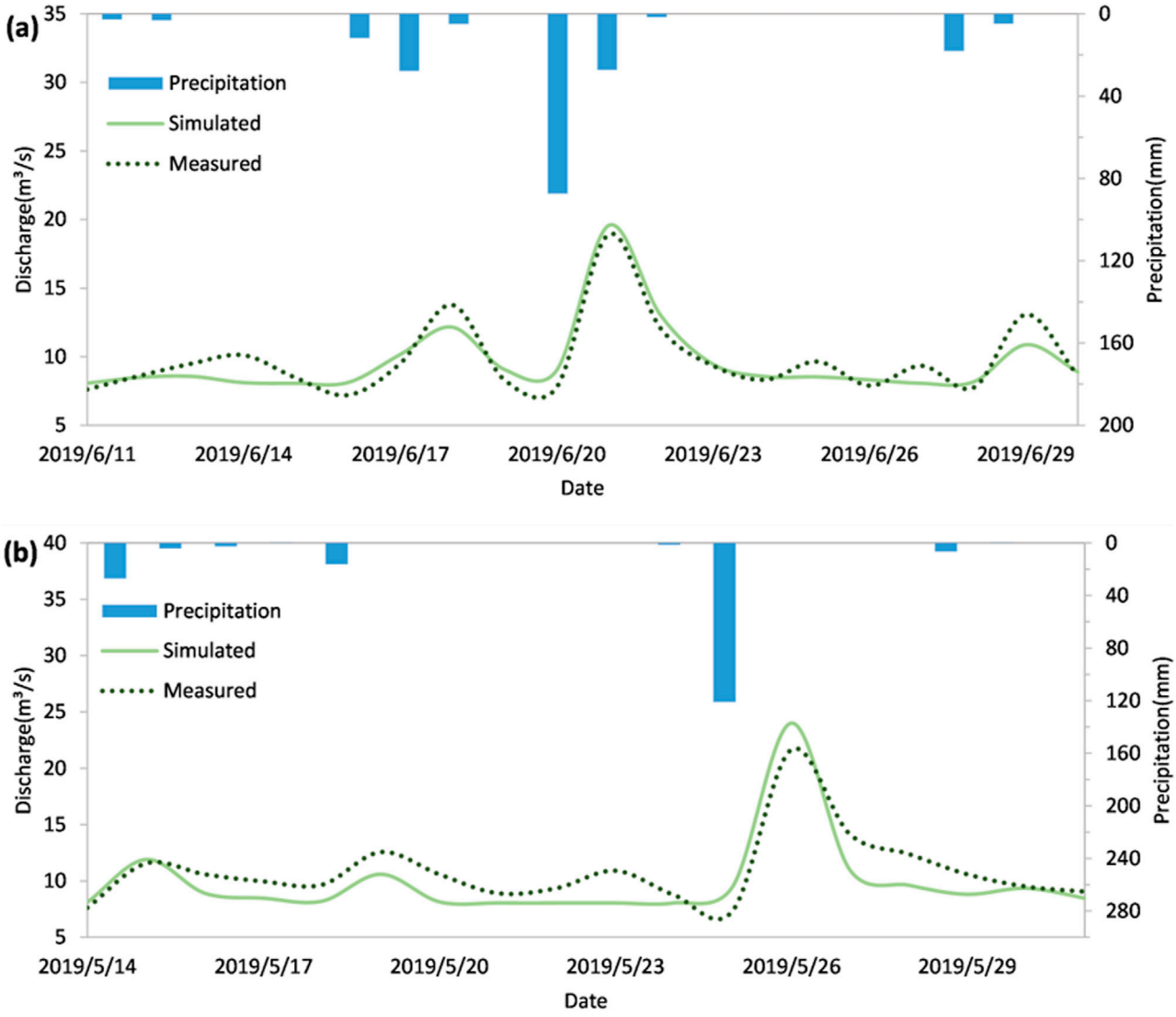

FIGURE 4
The measured discharge compared with the simulated discharge at the Luojiagang catchment export node J16 in **(A)** calibration and **(B)** validation.

period resulted in a delayed peak concentration time for the four treatment measures of WAD, SET, SED, and LID.

Upon evaluation of the pollution reduction effects of various measures, it was discovered that the concentration of total nitrogen and total phosphorus exhibited significant decrease in scenarios LID3, without changing the trend. The results suggested that LID facilities prove to be an effective means of reducing non-point source pollution in the Luojiagang catchment. LID demonstrated the most significant decrease in pollutant concentration, in coherence with previous analyses. Non-point source pollution accounted for a notable portion of pollution in the Luojiagang catchment and mitigating it could alleviate the pollution situation. Furthermore, WAD exhibited a significant reduction in pollutant concentration that ranked second, indicating that enhancing hydrological connectivity can prove an effective means of curbing pollution in the Luojiagang River. In contrast, SET and SED exhibited minimal decrease in pollutant concentration relative to the baseline scenario, signaling that point source wastewater discharge and endogenous pollution constitute a small fraction of pollution in the Luojiagang catchment.

4.3 Comparison of pollutant reduction rates and treatment effects

The pollution reduction rates, including (i) the reduction rate of pollutant peak concentration and (ii) the reduction rate of total pollutant contents within 24 h after the start of rain (in the following referred to as peak reduction rate and total reduction rate), were calculated across various scenarios in relation to the baseline scenario (Figure 11). This enabled a quantitative evaluation of the effectiveness of different pollution control measures and

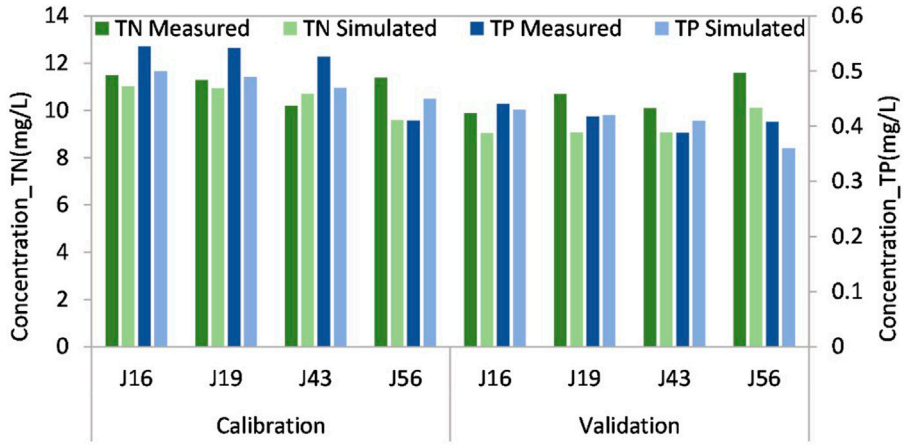

FIGURE 5
The comparison of measured and simulated concentrations of TN and TP at nodes J16, J19, J43, and J56.

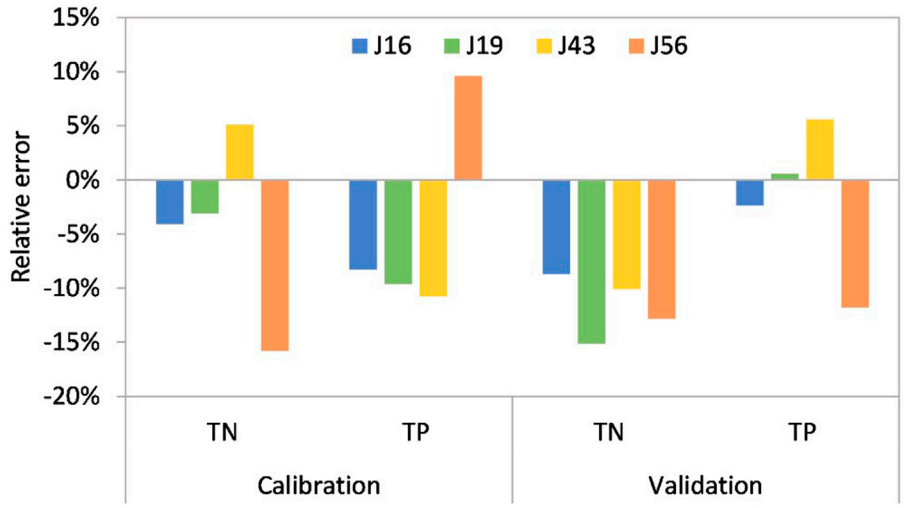

FIGURE 6
The relative error between measured and simulated concentrations at nodes J16, J19, J43, and J56.

intensities, which differed from the qualitative analysis based on the pollution concentration process line in the previous section. The peak reduction rates for each treatment scenario are ranked from highest to lowest as follows: COS > LID > WAD > SET > SED, and the total reduction rates are ranked from highest to lowest as follows: LID > COS > SET > SED > WAD. These rankings highlighted the efficacy of various measures in addressing water pollution in the Luojiagang catchment. Furthermore, non-point source pollution was the most prominent contributor to pollution levels in the area, while domestic sewage and endogenous pollution played a relatively minor role.

An increase in discharge at Luojiagang River, attributed to the water diversion from Donghu Lake, resulted in a rise in the overall amount of pollutants passing through the outlet node. The peak reduction rate also increased in proportion to the diversion volume, reflecting the significance of hydrological connectivity in river water environments and proving the efficacy of the Great Donghu Lake ecological water network connection project in enhancing water quality within urban rivers. The peak reduction rate recorded the highest value in scenario 1a-WAD, indicating that the WAD plays the best role under moderate rainfall conditions. In practical applications, it is crucial to consider construction costs and the safety of the river during the rainy season while determining a reasonable route and volume for water diversion. Simply opting for higher diversion rates is not always the most feasible solution. It should be noted that while the WAD had the lowest total reduction rate in the simulated scenarios, the dilution effect of pollution is just one aspect of the purpose. Furthermore, the water diversion will also have an impact on the river and lake community structures (Dai et al., 2020). More importantly, the Donghu Lake Ecological Water

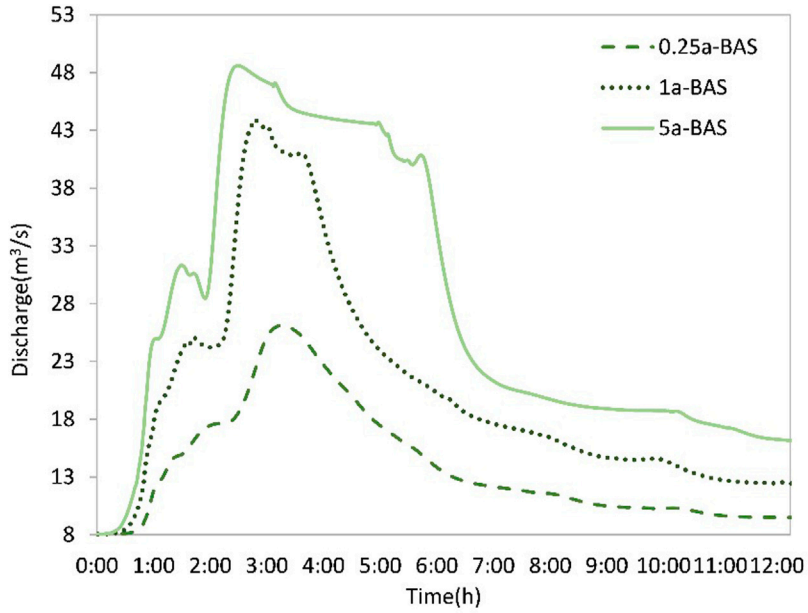

FIGURE 7
The discharge hydrograph at outlet node J16 of the Luojiagang catchment in baseline scenario with a return period of 0.25a, 1a, and 5a respectively.

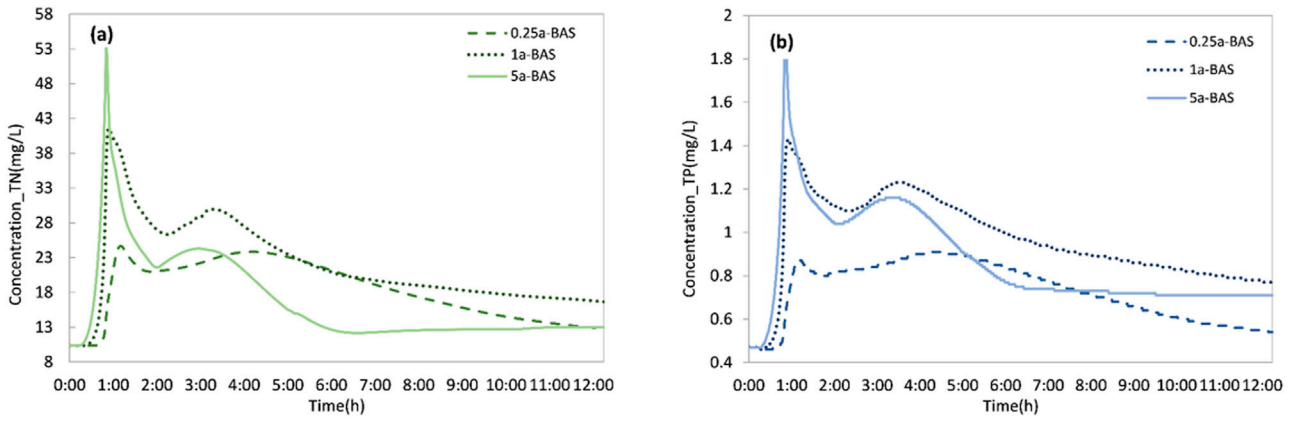

FIGURE 8
The evolution of **(A)** TN and **(B)** TP concentration at node J16 in baseline scenario.

Network Project can establish a hydraulic connection between the Yangtze River and Donghu Lake through water diversion (Guo and Kang, 2012), laying the foundation for ecological restoration projects.

The higher the degree of sewage treatment, the higher the peak reduction rate and total reduction rate. The smaller the rain intensity, the higher the reduction rate of peak concentrations of pollutants and the total reduction rate of sewage treatment measures. At present, most of the areas in the Luojiagang catchment have realized rainwater and sewage diversion, and the degree of domestic sewage interception is high. The direct sewage not connected to the sewage network should be further investigated and rectified to improve the sewage treatment rate.

The lower the release rate of pollutants in the sediment, the lower the pollutant concentration in the Luojiagang catchment, with the best water pollution control effect under light rain conditions. The impact of sediment dredging on the pollutant concentration in the river is very small, which reflects the effectiveness of previous endogenous pollution control work. Furthermore, the dredging effect was represented as a decrease in the endogenous release rate in the simulation. However, the practical application of dredging in different regions yielded inconsistent results. In some cases, dredging effectively reduced pollution loads (Chen et al., 2018), while in others, various complex factors such as dredging technology, dredging depth, and the environmental conditions of the water body itself

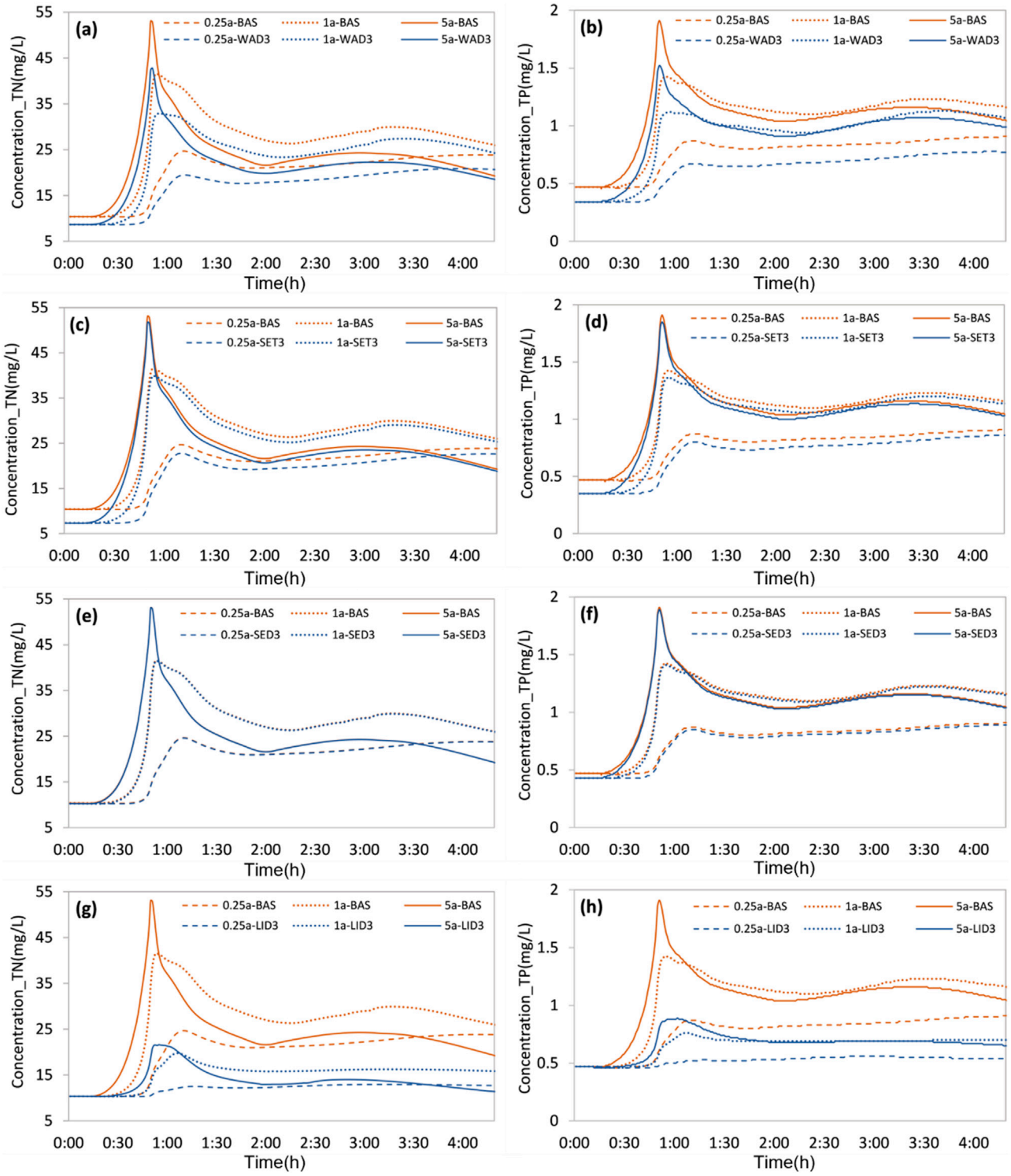

FIGURE 9
The evolution of TN **(A, E, G)** and TP **(B, F, H)** concentration at node J16 in different scenario: WAD **(A, B)**, SET **(C, D)**, SED **(E, F)**, and LID **(G, H)**.

influenced the effectiveness of pollution control after dredging (Chen et al., 2020; Weng, 2017; Zhu et al., 2022). Dredging alone cannot achieve long-term pollution control effectiveness, which requires reducing external loads (Liu et al., 2016

As the area of LID facilities increased, the peak reduction rates and total reduction rates also increased. The peak reduction rates of LID were highest during heavy rainfall, while the total reduction rates were highest during moderate rainfall. LID measures showed

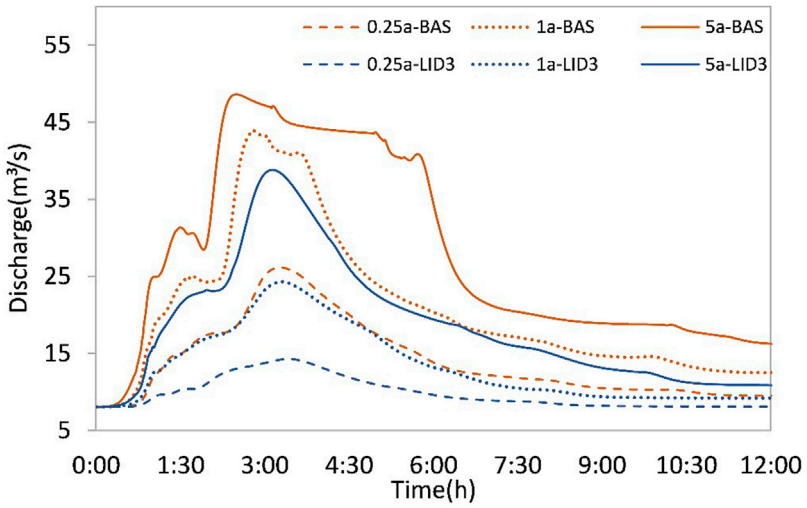

FIGURE 10
The flow process at node J16 in the scenario LID1 ~ LID3.

significant effectiveness in reducing both pollutant peak concentration and total pollutant load, indicating the importance of non-point source pollution in river pollution in urban centers and highlighting the necessity of sponge city construction. When the construction area of LID facilities accounted for 10%, the peak reduction rate of TN reached over 30%. Nevertheless, the peak reduction rates increase became less pronounced as the construction area of LID facilities rose to 20% or 30%. Therefore, the LID with a construction area of 10% was a cost-effective solution with good treatment results. Water management efforts in the Luojiagang catchment should focus on promoting the construction of LID facilities, enhancing urban vegetation, optimizing rainfall utilization, and strengthening pollution source regulations (e.g., roads, and construction sites, garbage, sewage, and dry-wet deposition at rainwater outlets) to diminish non-point source pollution. The effectiveness of LID facilities in controlling pollutants is influenced by various factors, not just the construction area mentioned here. In practical applications, factors such as the type of LID facility, functional design criteria, engineered design features, plant growth, and cost control all need to be further considered (Beryani et al., 2021; Glaister et at., 2017; Chaves et al., 2024).

The peak reduction rates by combined measures were higher than those of any individual measure, while the total reduction rates were second only to LID control. Notably, the total reduction rates achieved under combined conditions are equivalent to the sum of each individual condition, demonstrating that the impact of each measure is independent. This result denotes that the collective reduction in emissions accomplished by the diverse measures can be aggregated, thereby enabling the selection of the optimal and feasible conglomeration of remedial measures to alleviate pollution from varying origins, and ultimately achieve an enhanced water environment governance effect.

The treatment scenarios set in the SWMM simulation for this study are relatively simple and do not take into account the actual situation for more detailed settings. Specifically, the water diversion measures only consider the changes in water flow rate, and do not take into account the changes in pollutant levels caused by the changes in hydraulic conditions such as flow velocity resulting from water diversion (Yang et al., 2021). In addition, the sediment dredging is reflected in the variation of endogenous release rate, but actual engineering conditions were not taken into account. Moreover, the LID control measures were only represented by biological retention ponds and only considered the area of deployment, without taking into account more types of LID facilities and detailed deployment plans, which can impact the effectiveness of LID measures (Lee et al., 2022; Ma and Zhao, 2022). However, our goal is not to form a detailed treatment plan but to focus on the presentation effects of the four measures in the Luojiagang catchment. Therefore, simple scenario settings can still serve as a reference for water environment management in the region.

5 Conclusion

Under the current increasingly serious water pollution situation in urban, the comprehensive treatment and protecting measures in urban small catchment are the necessary step to the water pollution treatmen, not only focus on the water bodies themself. The comprehensive water pollution control measures, including the LID source control in a catchment and the treatment measures of the polluted water bodies, are getting more and more attention. But the effects evaluation and planning decision of the different schemes are facing the challenges of the complicated variety of the water pollution control measures and their combination. In order to explore the effects of the water pollution control measures and help the planning decision making, in this study, the Luojiagang river channel and its catchment in Wuhan, which has been heavily impacted by water pollution, are taken as an example for the comparative assessment of pollution control measures including the LID by using SWMM model. The results of this study provided

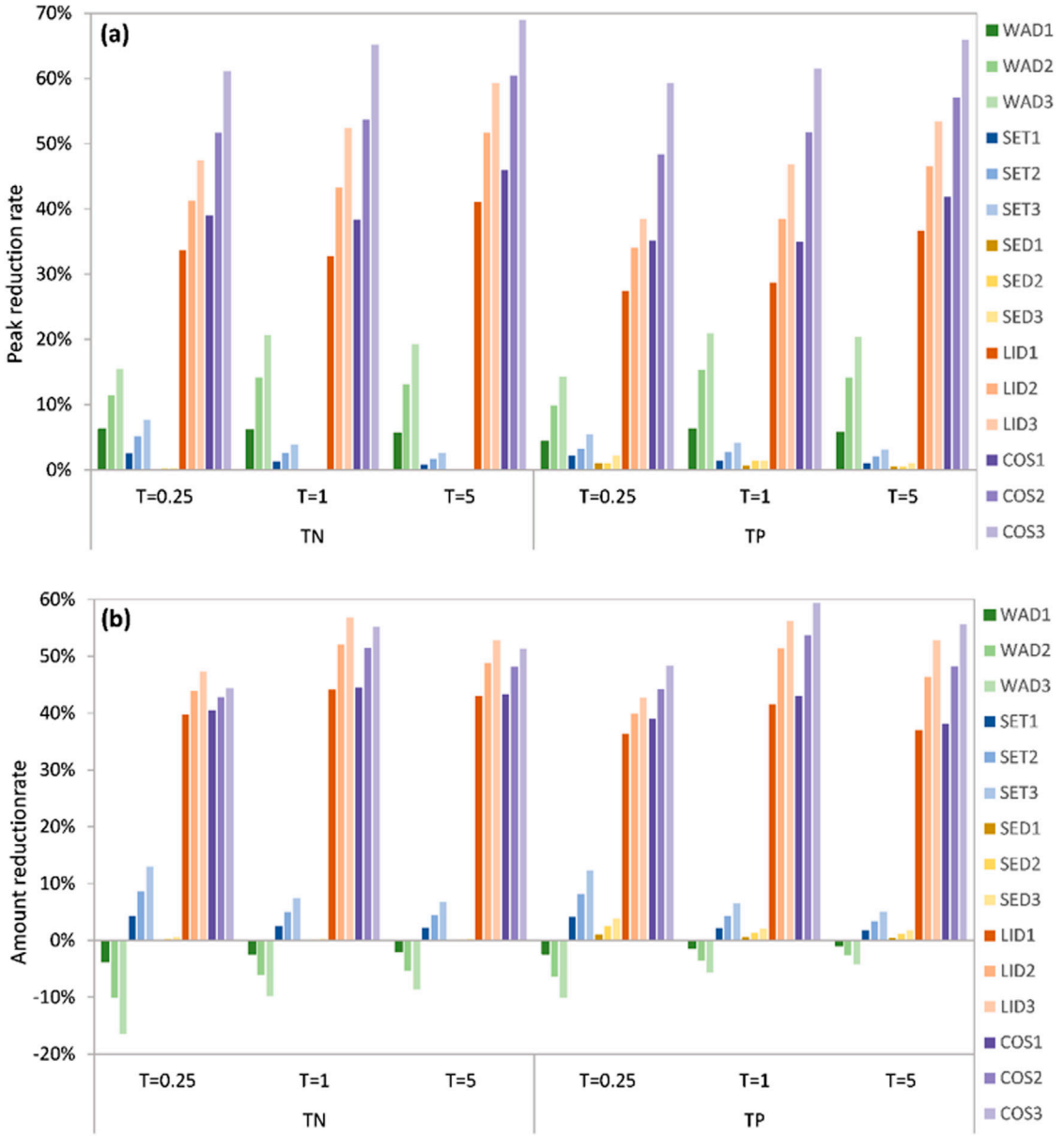

FIGURE 11
The **(A)** peak reduction rate and **(B)** total reduction rate in various scenarios.

scientific reference and practicable guidance for the water environment management in urban small catchment, and the following conclusions can be drawn.

(1) Through the comparison of pollution treatment measures based on scenarios simulation with the baseline scenarios, it was found that the reduction effects of pollutant peak concentrations at the outlet node of Luojiagang River had the decreasing order of: COS > LID control > WAD > SET > SED, and the reduction effects of total pollutant load had the decreasing order of: LID > COS > SET > SED > WAD.

(2) The results show that the control of non-point source pollution is the key for the improvement of water quality in Luojiagang River, and LID plays important role in the reduction of both pollutant peak concentrations and load. Therefore, while promoting the construction of LID facilities, it is essential to target non-point source pollution control.

(3) The total pollutant reduction rate of the combined measures was basically equal to the sum of the individual measures, indicating that the effects of various measures are independent and their governance effects can be overlapped.

(4) This study shows the implication for the decision of the water pollution contoling schemes in urban small catchment. In order to create a practical and comprehensive water environment management plan, future study will give more thought to the actual engineering conditions and further refine the model, especially in terms of the layout plan for LID facilities.

Data availability statement

The original contributions presented in the study are included in the article/supplementary material, further inquiries can be directed to the corresponding author.

Author contributions

JL: Conceptualization, Methodology, Writing–original draft. XZ: Funding acquisition, Project administration, Resources, Writing–review and editing. HG: Data curation, Investigation, Visualization, Writing–review and editing.

Funding

The author(s) declare that financial support was received for the research, authorship, and/or publication of this article. This research was supported by the Key Research and Development Program of Hubei Province (No. 2021BCA128), the Ministry of Water Resources of the People's Republic of China (SKS-2022014).

Conflict of interest

The authors declare that the research was conducted in the absence of any commercial or financial relationships that could be construed as a potential conflict of interest.

Publisher's note

All claims expressed in this article are solely those of the authors and do not necessarily represent those of their affiliated organizations, or those of the publisher, the editors and the reviewers. Any product that may be evaluated in this article, or claim that may be made by its manufacturer, is not guaranteed or endorsed by the publisher.

References

Alves, A., Gersonius, B., Kapelan, Z., Vojinovic, Z., and Sanchez, A. (2019). Assessing the Co-Benefits of green-blue-grey infrastructure for sustainable urban flood risk management. *J. Environ. Manag.* 239, 244–254. doi:10.1016/j.jenvman.2019.03.036

Baek, S.-S., Choi, D.-H., Jung, J.-W., Lee, H.-J., Lee, H., Yoon, K.-S., et al. (2015). Optimizing low impact development (LID) for stormwater runoff treatment in urban area, Korea: experimental and modeling approach. *Water Res.* 86, 122–131. doi:10.1016/j.watres.2015.08.038

Beryani, A., Goldstein, A., Al-Rubaei, A. M., Viklander, M., Hunt III, W. F., and Blecken, G. T. (2021). Survey of the operational status of twenty-six urban stormwater biofilter facilities in Sweden. *J. Environ. Manage.* 297, 113375. doi:10.1016/j.jenvman.2021.113375

Charters, F. J., Cochrane, T. A., and O'Sullivan, A. D. (2021). The influence of urban surface type and characteristics on runoff water quality. *Sci. Total Environ.* 755, 142470. doi:10.1016/j.scitotenv.2020.142470

Chaves, M. T. R., Farias, T. R. L., and Eloi, W. M. (2024). Comparative analysis of bioretention design strategies for urban runoff infiltration: a critical overview. *Eco. Eng.* 207, 107352. doi:10.1016/j.ecoleng.2024.107352

Chen, C., Kong, M., Wang, Y.-Y., Shen, Q.-S., Zhong, J.-C., and Fan, C.-X. (2020). Dredging method effects on sediment resuspension and nutrient release across the sediment-water interface in Lake Taihu, China. *Environ. Sci. Pollut. Res.* 27, 25861–25869. doi:10.1007/s11356-019-06192-w

Chen, M., Cui, J., Lin, J., Ding, S., Gong, M., Ren, M., et al. (2018). Successful control of internal phosphorus loading after sediment dredging for 6years: a field assessment using high-resolution sampling techniques. *Sci. Total Environ.* 616–617, 927–936. doi:10.1016/j.scitotenv.2017.10.227

Dai, J., Wu, S., Wu, X., Lv, X., Sivakumar, B., Wang, F., et al. (2020). Impacts of a large river-to-lake water diversion project on lacustrine phytoplankton communities. *J. Hydrology* 587, 124938. doi:10.1016/j.jhydrol.2020.124938

de Oliveira, J. A. P., Bellezoni, R. A., Shih, W., and Bayulken, B. (2022). Innovations in urban green and blue infrastructure: tackling local and global challenges in cities. *J. Clean. Prod.* 362, 132355. doi:10.1016/j.jclepro.2022.132355

Ehleringer, J. R., Barnette, J. E., Jameel, Y., Tipple, B. J., and Bowen, G. J. (2016). Urban water – a new frontier in isotope hydrology. *Isotopes Environ. Health Stud.* 52, 477–486. doi:10.1080/10256016.2016.1171217

Follstad Shah, J. J., Jameel, Y., Smith, R. M., Gabor, R. S., Brooks, P. D., and Weintraub, S. R. (2019). Spatiotemporal variability in water sources controls chemical and physical properties of a semi-arid urban river system. *JAWRA J. Am. Water Resour. Assoc.* 55, 591–607. doi:10.1111/1752-1688.12734

Gessner, M. O., Hinkelmann, R., Nützmann, G., Jekel, M., Singer, G., Lewandowski, J., et al. (2014). Urban water interfaces. *J. Hydrology* 514, 226–232. doi:10.1016/j.jhydrol.2014.04.021

Gironás, J., Roesner, L. A., Rossman, L. A., and Davis, J. (2010). A new applications manual for the Storm water management model (SWMM). *Environ. Model. and Softw.* 25, 813–814. doi:10.1016/j.envsoft.2009.11.009

Glaister, B. J., Fletcher, T. D., Cook, P. L., and Hatt, B. E. (2017). Interactions between design, plant growth and the treatment performance of stormwater biofilters. *Eco. Eng.* 105, 21–31. doi:10.1016/j.ecoleng.2017.04.030

Grimm, N. B., Faeth, S. H., Golubiewski, N. E., Redman, C. L., Wu, J., Bai, X., et al. (2008). Global change and the ecology of cities. *Science* 319, 756–760. doi:10.1126/science.1150195

Gu, X., Chen, K., Zhang, L., and Fan, C. (2016). Preliminary evidence of nutrients release from sediment in response to oxygen across benthic oxidation layer by a long-term field trial. *Environ. Pollut.* 219, 656–662. doi:10.1016/j.envpol.2016.06.044

Guo, X. M., and Kang, L. (2012). Research on tactics of water diversion of lake dong. *Adv. Mater. Res.* 356–360, 2358–2361. doi:10.4028/www.scientific.net/amr.356-360.2358

Hu, M., Zhang, X., Li, Y., Yang, H., and Tanaka, K. (2019). Flood mitigation performance of low impact development technologies under different storms for retrofitting an urbanized area. *J. Clean. Prod.* 222, 373–380. doi:10.1016/j.jclepro.2019.03.044

Huang, J., Zhang, Y., Arhonditsis, G. B., Gao, J., Chen, Q., Wu, N., et al. (2019). How successful are the restoration efforts of China's lakes and reservoirs? *Environ. Int.* 123, 96–103. doi:10.1016/j.envint.2018.11.048

Huang, J. J., Xiao, M., Li, Y., Yan, R., Zhang, Q., Sun, Y., et al. (2022). The optimization of Low Impact Development placement considering life cycle cost using Genetic Algorithm. *J. Environ. Manag.* 309, 114700. doi:10.1016/j.jenvman.2022.114700

Khan, I., Zakwan, M., Koya Pulikkal, A., and Lalthazula, R. (2022). Impact of unplanned urbanization on surface water quality of the twin cities of Telangana state, India. *Mar. Pollut. Bull.* 185, 114324. doi:10.1016/j.marpolbul.2022.114324

Kuhlemann, L.-M., Tetzlaff, D., and Soulsby, C. (2020). Urban water systems under climate stress: an isotopic perspective from Berlin, Germany. *Hydrol. Process.* 34, 3758–3776. doi:10.1002/hyp.13850

Lee, J., Kim, J., Lee, J. M., Jang, H. S., Park, M., Min, J. H., et al. (2022). Analyzing the impacts of sewer type and spatial distribution of LID facilities on urban runoff and non-point source pollution using the Storm water management model (SWMM). *Water* 14, 2776. doi:10.3390/w14182776

Li, G., Xiong, J., Zhu, J., Liu, Y., and Dzakpasu, M. (2021). Design influence and evaluation model of bioretention in rainwater treatment: a review. *Sci. Total Environ.* 787, 147592. doi:10.1016/j.scitotenv.2021.147592

Li, Q., Wang, F., Yu, Y., Huang, Z., Li, M., and Guan, Y. (2019). Comprehensive performance evaluation of LID practices for the sponge city construction: a case study in Guangxi, China. *J. Environ. Manag.* 231, 10–20. doi:10.1016/j.jenvman.2018.10.024

Li, Z., Xiao, J., Evaristo, J., and Li, Z. (2019). Spatiotemporal variations in the hydrochemical characteristics and controlling factors of streamflow and groundwater in the Wei River of China. *Environ. Pollut.* 254, 113006. doi:10.1016/j.envpol.2019.113006

Liu, C., Shao, S., Shen, Q., Fan, C., Zhou, Q., Yin, H., et al. (2015). Use of multi-objective dredging for remediation of contaminated sediments: a case study of a typical heavily polluted confluence area in China. *Environ. Sci. Pollut. Res.* 22, 17839–17849. doi:10.1007/s11356-015-4978-5

Liu, C., Zhong, J., Wang, J., Zhang, L., and Fan, C. (2016). Fifteen-year study of environmental dredging effect on variation of nitrogen and phosphorus exchange across the sediment-water interface of an urban lake. *Environ. Pollut.* 219, 639–648. doi:10.1016/j.envpol.2016.06.040

Liu, J. H. (2020). "Discussion on urban non-point source pollution simulation and prevention measures," in *Tianhe district of Guangzhou under the background of sponge city construction* (Guangzhou, China: Guangdong University of Technology).

Liu, W., Wei, W., Chen, W., Deo, R. C., Si, J., Xi, H., et al. (2019). The impacts of substrate and vegetation on stormwater runoff quality from extensive green roofs. *J. Hydrology* 576, 575–582. doi:10.1016/j.jhydrol.2019.06.061

Ma, Y., and Zhao, H. (2022). The role of spatial patterns of low impact development in urban runoff pollution control within parcel based catchments. *Front. Environ. Sci.* 10, 926937. doi:10.3389/fenvs.2022.926937

McGrane, S. J. (2016). Impacts of urbanisation on hydrological and water quality dynamics, and urban water management: a review. *Hydrological Sci. J.* 61, 2295–2311. doi:10.1080/02626667.2015.1128084

Müller, A., Österlund, H., Marsalek, J., and Viklander, M. (2020). The pollution conveyed by urban runoff: a review of sources. *Sci. Total Environ.* 709, 136125. doi:10.1016/j.scitotenv.2019.136125

Nguyen, T. T., Ngo, H. H., Guo, W., Wang, X. C., Ren, N., Li, G., et al. (2019). Implementation of a specific urban water management - sponge City. *Sci. Total Environ.* 652, 147–162. doi:10.1016/j.scitotenv.2018.10.168

Pan, D., and Tang, J. (2021). The effects of heterogeneous environmental regulations on water pollution control: quasi-natural experimental evidence from China. *Sci. Total Environ.* 751, 141550. doi:10.1016/j.scitotenv.2020.141550

Qu, J., and Fan, M. (2010). The current state of water quality and technology development for water pollution control in China. *Crit. Rev. Environ. Sci. Technol.* 40, 519–560. doi:10.1080/10643380802451953

Revitt, D. M., and Ellis, J. B. (2016). Urban surface water pollution problems arising from misconnections. *Sci. Total Environ.* 551, 163–174. doi:10.1016/j.scitotenv.2016.01.198

Ritter, A., and Muñoz-Carpena, R. (2013). Performance evaluation of hydrological models: statistical significance for reducing subjectivity in goodness-of-fit assessments. *J. Hydrology* 480, 33–45. doi:10.1016/j.jhydrol.2012.12.004

Rong, G., Hu, L., Wang, X., Jiang, H., Gan, D., and Li, S. (2021). Simulation and evaluation of low-impact development practices in university construction: a case study of Anhui University of Science and Technology. *J. Clean. Prod.* 294, 126232. doi:10.1016/j.jclepro.2021.126232

Rossman, L. A., and Simon, M. A. (2022). *Storm water management model User's manual version 5.2, center for environmental solutions and emergency response office of research and development*. Washington, DC: US Environmental Protection Agency. Available at: https://www.epa.gov/system/files/documents/2022-04/swmm-users-manual-version-5.2.pdf.

Seo, M., Jaber, F., Srinivasan, R., and Jeong, J. (2017). Evaluating the impact of low impact development (LID) practices on water quantity and quality under different development designs using SWAT. *Water* 9, 193. doi:10.3390/w9030193

Tao, T., and Xin, K. (2014). Public health: a sustainable plan for China's drinking water. *Nature* 511, 527–528. doi:10.1038/511527a

Weng, J. (2017). Post-dredging effect assessment based on sediment chemical quality in urban rivers of Yangzhou. *Environ. Monit. Assess.* 189, 246. doi:10.1007/s10661-017-5963-x

Yang, H., Wang, J., Li, J., Zhou, H., and Liu, Z. (2021). Modelling impacts of water diversion on water quality in an urban artificial lake. *Environ. Pollut.* 276, 116694. doi:10.1016/j.envpol.2021.116694

Zhu, L., Zhang, H., Li, Y., Sun, W., Song, C., Wang, L., et al. (2022). Dredging effects on nutrient release of the sediment in the long-term operational free water surface constructed wetland. *J. Environ. Manage.* 322, 116160. doi:10.1016/j.jenvman.2022.116160

Zhu, Z., Chen, Z., Chen, X., and Yu, G. (2019). An assessment of the hydrologic effectiveness of low impact development (LID) practices for managing runoff with different objectives. *J. Environ. Manage.* 231, 504–514. doi:10.1016/j.jenvman.2018.10.046

frontiers | Frontiers in Environmental Science

TYPE Original Research
PUBLISHED 11 November 2024
DOI 10.3389/fenvs.2024.1487469

OPEN ACCESS

EDITED BY
Jahangeer Jahangeer,
University of Nebraska-Lincoln, United States

REVIEWED BY
Shamshad Ahmad,
District Water Testing Laboratory Jal Nigam, India
Aditya Kapoor,
Indian Institute of Technology Roorkee, India

*CORRESPONDENCE
Atul Kumar Rahul,
atulcivil.iitbhu@gmail.com

RECEIVED 28 August 2024
ACCEPTED 28 October 2024
PUBLISHED 11 November 2024

CITATION
Priyadarshee A, Rahul AK, Kumar V, Kumar A and Kumar N (2024) Spatial variation in water quality of the Burhi Gandak River: a multi-location assessment.
Front. Environ. Sci. 12:1487469.
doi: 10.3389/fenvs.2024.1487469

Spatial variation in water quality of the Burhi Gandak River: a multi-location assessment

Akash Priyadarshee[1], Atul Kumar Rahul[1]*, Vijay Kumar[1], Ashish Kumar[1] and Niraj Kumar[2]

[1]Department of Civil Engineering, MIT Muzaffarpur, Muzaffarpur, India, [2]Motihari College of Engineering Motihari, Bihar, India

The Burhi Gandak River, a significant tributary of the Ganga River and a vital water source in Bihar, India, is facing critical water quality degradation due to rapid population growth, urbanization, and industrial activities. This study conducts a detailed water quality assessment of the river, focusing on the effects of these anthropogenic factors across different locations, seasons, and industrial zones. Water samples were collected and analyzed for key parameters, including pH, total dissolved solids (TDSs), total hardness (TH), biological oxygen demand (BOD), and dissolved oxygen (DO). The results indicate significant spatial and temporal variations, with water quality deteriorating notably in areas like Samastipur and Khagaria, where industrial and urban activities are more concentrated. For instance, BOD levels increased from 7.5 mg/L to 9.5 mg/l as the river flows through urban Samastipur, signaling a decline in water quality. Additionally, sugar mills located along the river contribute to higher pollution levels during operational months, especially in Lauria and Sugauli. Seasonal analysis shows that the lean season experiences the highest levels of degradation, while monsoon floods increase suspended solids due to sediment inflow. These findings emphasize the urgent need for improved regulation of industrial discharge and urban waste management to protect the water quality of the Burhi Gandak River and the livelihoods dependent on it.

KEYWORDS

water quality, urbanization, industrialization, Burhi Gandak, Ganga

1 Introduction

Rivers are a vital source of water for drinking, industrial, and irrigation purposes (Prakash et al., 2020). The River Ganga is one of the most important rivers in India, having agricultural, industrial, transportation, tourism, mythological, and ecological significance (Trivedi, 2010). In India, the northern plain is developed by the Ganga River and its tributaries, and it serves approximately 330 million people in India (India-WRIS, 2010). Bihar is one of the states situated in the northern plain of India. In Bihar, there are many important tributaries of the Ganga River, like Gandak, Kosi, Sone, Burhi Gandak, and Ghagara (Sinha and Friend 1994). The Burhi Gandak River is a tributary of the Ganga River. It is also known as 'Sikrahna' in Bihar and is one of the tributaries that completely flows in Bihar (Singh et al., 2018). It originates from Chautarwa Chaur near Bishambharpur in the district of West Champaran, Bihar (Kumar, 2020). Burhi Gandak passes through the districts of West Champaran, East

Champaran, Muzaffarpur, Samastipur, and Khagaria. The last district of Burhi Gandak is Khagaria, where it joins the River Ganga near Gogri Jamalpur. The total length of Burhi Gandak is 580 km, and its catchment area is 12,021 sq. km (Mishra, 2018). Originating from the Himalayas, it carries a substantial load of detritus. Through this stretch, the river exhibits consistent sinuosity, indicating its mature stage. Its primary source of water is rainfall, with the monsoon season in September bringing heavy precipitation, leading to seasonal floods nearly every year (Philip and Gupta, 2008). Masan, Balor, Pandai, Sikta, Tilawe, and Tiur are the left tributaries, and Dhanauti, Kohra, and Danda are the right tributaries of the Burhi Gandak River (Kumar, 2018). Sinha and Dayal (1980) have shown through the study that the Burhi Gandak River has changed its course many times in history. The river's reliance on robust physicochemical characteristics of water underscores the critical importance of preserving water quality, making it a matter of utmost significance (Verma, 2018a; 2018b).

In recent decades, many cities and towns, like Motihari and Muzaffarpur, have developed along the banks of the Burhi Gandak. The population in these towns is growing rapidly. The population of Muzaffarpur and Motihari districts is approximately 4.8 million and 5 million, respectively (Village and Town Directory, 2011). The population density of these areas is more than 1200 persons/km^2. So, because of this, urban activities are also increasing. Industries in these cities and towns are growing rapidly. These regions are fertile lands, and the water of Burhi Gandak is being used for irrigation purposes. These areas have agriculture-based industries such as litchi processing, sugar industry and dairy, manufacturing industries such as leather and textile, food processing industry, engineering and metal works, and chemical industries (Muzaffarpur- District Industrial Potential Survey, 2011). Due to urbanization and industrial growth, huge amounts of wastewater are being generated and polluting the river water. Pollution of rivers presents a growing challenge in India, as noted by Bhargava (1987). Like many others, the Ganga River faces contamination primarily from human sewage, animal waste, agricultural runoff, population growth, toxic waste, and industrial pollutants, as highlighted by Bhardwaj et al. (2010). This pollution poses significant threats to both human health and biodiversity, as emphasized by Lantzy and Mackenzie (1979), Nriagu (1979), and Ross (1994). Rivers can be tainted by degradable substances such as organic matter (e.g., flowers and wood) and non-degradable materials, including plastics, electronic waste, and metals. Understanding the physical and chemical attributes of river water is essential for evaluating its quality and determining its suitability for various purposes, such as public water supply, agriculture, and industry, as outlined by Dwivedi and Pathak (2007).

Researchers like Kumar and Mishra (2015) and Sharma and Choudhary (2014, 2016) have conducted studies on the water quality of the Burhi Gandak River. A study of the tributaries of Ganga along with Burhi Gandak shows a pH value of 7.1–8.7 and a DO of 0.7–10.7 (India-WRIS, 2010). Ali and Roy (2024) investigated the impact of the Muzaffarpur City land change on the urban runoff and the water quality of Burhi Gandak. These studies do not deal with the impact of urbanization and industrialization on various water quality parameters. Kumar (2020) has conducted a hydrobiological study on the Burhi Gandak River near the urban area of Samastipur. Furthermore, the limited regions of the rivers were considered in all these studies. The present study investigates the water quality in different regions of the Burhi Gandak River. In addition, the impact on the water quality of Burhi Gandak by urbanization and industrialization is investigated. The findings from this paper will contribute to a deeper understanding of the water quality challenges faced by the Burhi Gandak River. By identifying critical factors influencing degradation, particularly in urbanized and industrialized areas, this study lays the groundwork for informed policy decisions and more effective management strategies. Future research can be built on this foundation to establish real-time water quality monitoring systems and develop predictive models to anticipate seasonal variations, especially during lean seasons. Moreover, this research can guide local authorities in prioritizing pollution control measures, enhancing community awareness, and fostering sustainable practices to preserve the river's water quality. Additionally, these insights may serve as a reference for addressing water quality challenges in other tributaries of the Ganga River and beyond, encouraging further collaborative efforts to improve the ecological health of the region's waterways.

2 Materials and methods

2.1 Study area

As mentioned earlier, Burhi Gandak originates from the West Champaran District and meets Ganga in the Khagaria District. Considering this, five places were selected to collect the water quality data of the Burhi Gandak River. These places are near Lauria, Sugauli, Muzaffarpur, Samastipur, and Khagaria. Figure 1 shows the map of the places from where water quality data were collected. The coordinates of the places are shown in Table 1. Burhi Gandak originates from the district of West Champaran. So, Lauria, a small town from West Champaran, which is on the bank of the Burhi Gandak River, was selected for the study. It is approximately 28 km from the district headquarters and is one of the important Buddhist archaeological sites. The next location selected on the downstream side was Sugauli. It is situated in East Champaran. Both Lauria and Sugauli are famous for the sugar industry.

The next sites selected for study were Muzaffarpur and Samastipur. Both are significant cities in North Bihar. As per the 2011 census of India, the population of Muzaffarpur City is more than three lakh, and the population density is 13,285 persons per sq km. Both Muzaffarpur and Samastipur are important from the industrial activity point of view. The last location selected in the study is Khagaria. Burhi Gandak meets the Ganga River in the district of Khagaria. Considering this, the last location was selected. Figure 2 illustrates the delineated watershed of the Burhi Gandak River, incorporating the hierarchical stream ordering and designated data collection points. The stream order classification effectively highlights the hydrological network's structure, while the marked data collection sites provide critical reference points for subsequent spatial and hydrological analyses within the watershed.

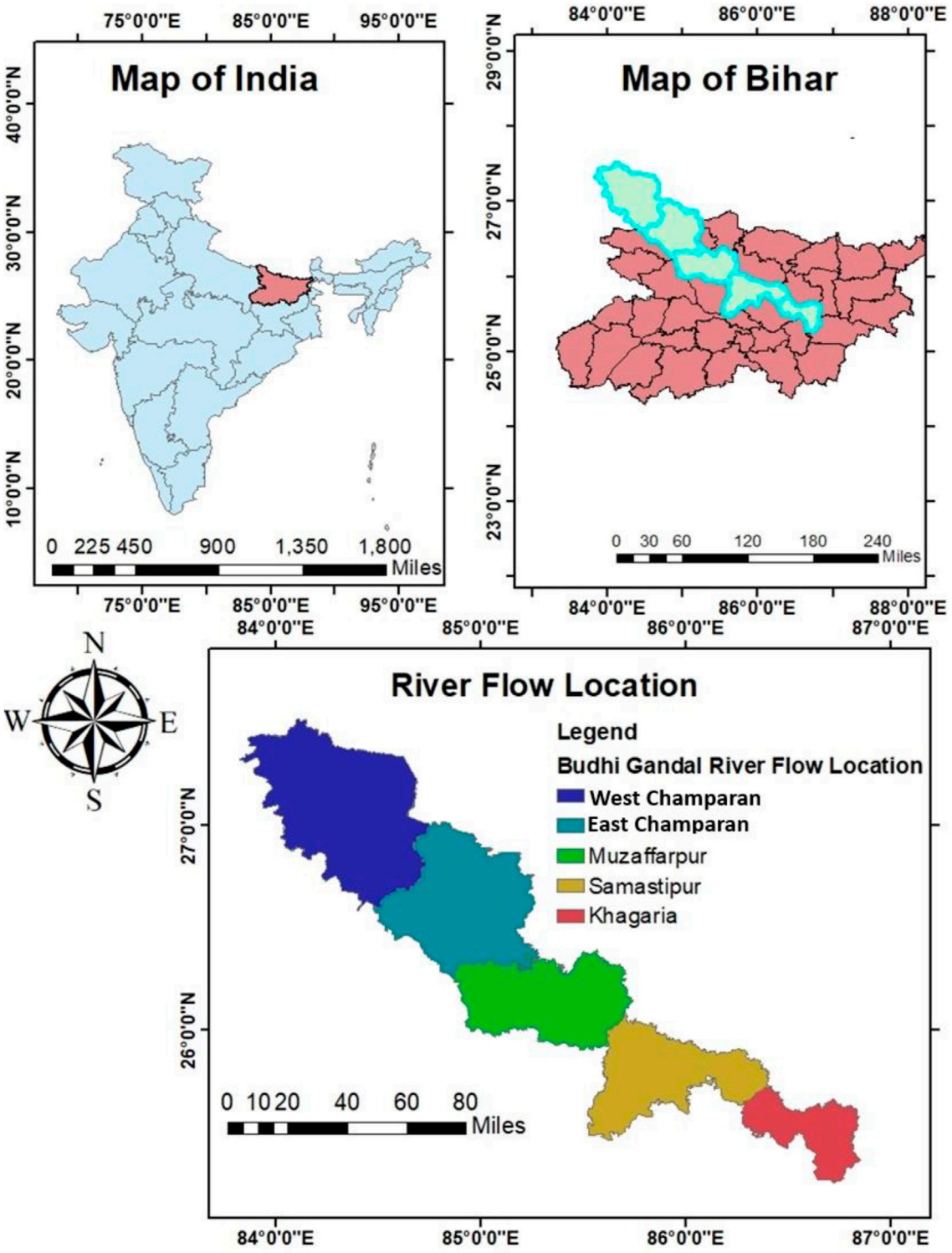

FIGURE 1
Study area of the Burhi Gandak River.

2.2 Geomorphological and hydrological details

The Burhi Gandak River displays various geomorphic features, including point bars, oxbow lakes, meander scars, and abandoned channels. In the middle and downstream sections, notable features include river terraces, point bars, floodplain deposits, and natural levee deposits. The river channel becomes shallower as it flows upstream but deepens downstream. The Burhi Gandak River exhibits pronounced meandering characteristics, particularly in

TABLE 1 Coordinates of the study area selected.

S. No.	Study area	Coordinate
1	Lauria, West Champaran	27.010738 N, 84.399,714 E
2	Sugauli, East Champaran	26.787,606 N, 84.738,613 E
3	Muzaffarpur	26.1,512,117 N, 85.374,329 E
4	Samastipur	25.870,205 N, 85.779,357 E
5	Khagaria	25.49,497,222 N, 86.4,638,611 E

Samastipur and Begusarai districts. Throughout these areas, the river channel frequently divides and reunites downstream, creating an anastomosing channel pattern. In the proximal, middle, and distal sections, the slope gradients of the Burhi Gandak River measure 69.0, 12.0, and 8.60 cm/km, respectively (Singh and Singh, 2005). The valley width ranges from 20 to 800 m, being narrowest in the proximal part and widest in the distal part.

The annual rainfall data of the study regions considered in this study is presented in Figure 2. The rainfall data presented in this study are from 1971 to 2022. It can be observed that the average annual rainfall for all the locations considered in this study is more than 1000 mm. It indicates that a sufficient amount of rainfall is obtained in the catchment area of Burhi Gandak. Most of the rainfall in this region occurs during the monsoon season. The annual average rainfall data from 1971 to 2020 show that West Champaran receives the maximum rainfall among all the locations selected. West Champaran is located in the Tarai region of the Himalayas. This increases the rainfall in this region. These data further show that Samastipur is getting a relatively lesser amount of rainfall among the sites considered. However, rainfall data from 2019 to 2022 show that the average annual has decreased for all the locations. However, Muzaffarpur has the highest reduction in rainfall. It has become a place with the lowest rainfall among all the considered locations. It is difficult to estimate the possible cause of it with limited data. However, recently, the highest growth in industrialization and urbanization has taken place in Muzaffarpur City among all the selected cities. This might be one of the major causes of the reduction in rainfall.

The land use land cover (LULC) map for the study area was generated using ArcGIS, leveraging satellite imagery and a digital elevation model (DEM) for enhanced spatial accuracy. After preprocessing the imagery, supervised classification was employed to delineate key land cover types, including agricultural, forest, urban, and water bodies. The integration of DEM data provided critical topographical context, refining land classification, particularly in areas with varied elevations. This synergy of LULC and DEM in ArcGIS enabled precise spatial analysis, which is essential for environmental and topographical assessments. Figure 3 shows the LULC map of Bihar. The LULC map indicates the land and its utilization, like forest area, crop area, and urban area. It can be observed in Figure 4 that most of the regions have similar rainfall patterns. Table 2 shows the area of the

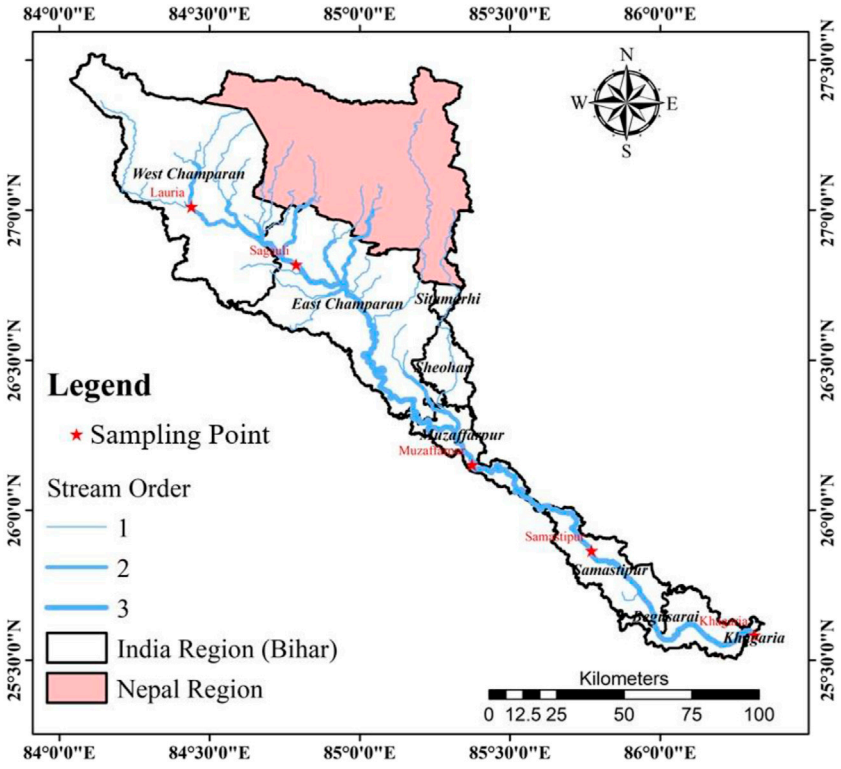

FIGURE 2
Watershed of the river with a sampling point location for all locations.

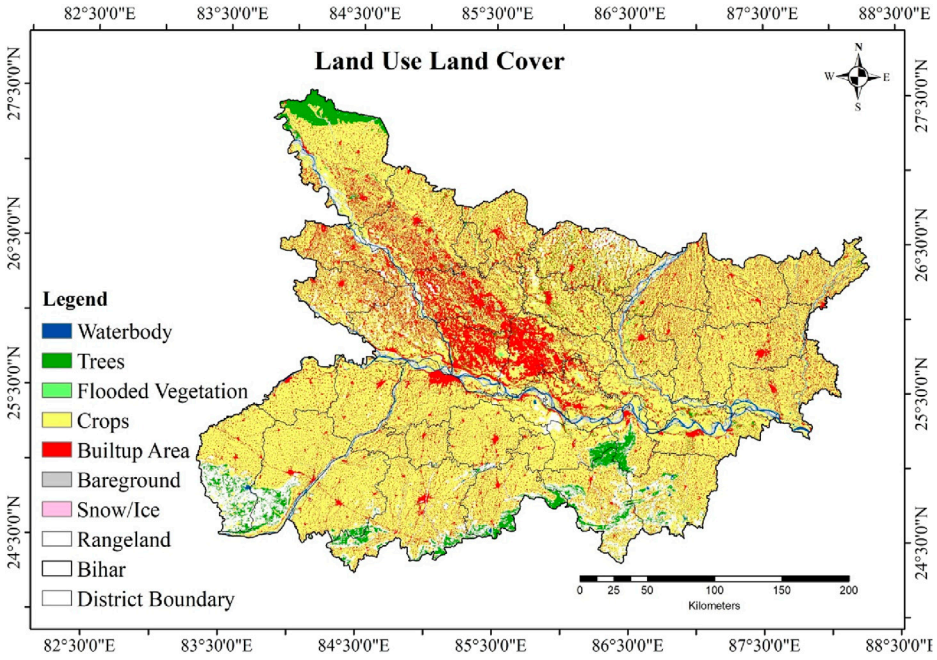

FIGURE 3
2023 LULC map of Bihar.

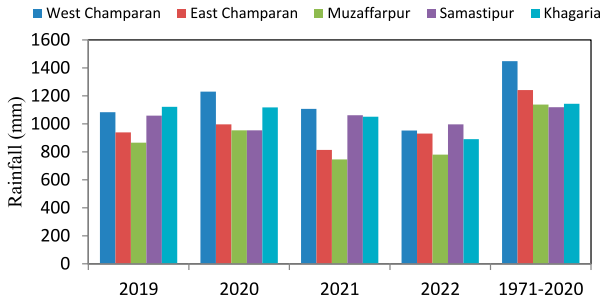

FIGURE 4
Rainfall data for different districts from 1971 to 2022 (MOES, 2010; DES, 2022).

different LULC classes. It shows that agricultural cropland covers the highest area. The district, except for West Champaran, through which Burhi Gandak flows, has mainly cropland or buildup area. The northern part of West Champaran is covered with forest areas.

To understand the impact of urbanization, industrial activities, and location on the water quality of the Burhi Gandak River, data related to geomorphology and hydrology were collected from the available literature and the official government websites of the government of Bihar and India after this water quality-related data were collected. For this purpose, results from the laboratory tests and data from the literature were used. The water quality data of Lauria, Sugauli, and Muzaffarpur were obtained from the laboratory test results, while data of Samastipur and Khagaria

TABLE 2 LULC information of Bihar.

LULC class	Area (sq.km)	LULC class	Area (sq.km)
Builtup, urban	896.84	Builtup, rural	5,436.53
Builtup, mining	238.27	Agriculture, cropland	66,981.4
Agriculture, plantation	2,949.69	Agriculture, fallow	2,851.74
Forest, deciduous	4,565.14	Forest, forest plantation	5.41
Forest, scrub forest	1,302.12	Grass/grazing	17.31
Barren/unculturable/wastelands, Salt affected land	3.43	Barren/unculturable/wastelands, Gullied/ravinous land	71.36
Barren/unculturable/wastelands, scrub land	2,484.95	Barren/unculturable/wastelands, sandy area	49.23
Barren/unculturable/wastelands, barren rocky	93.42	Wetlands/water bodies, coastal wetland	1984.19
Wetlands/water bodies, river/stream/canals	4,034.47	Wetlands/water bodies, reservoir/lakes/ponds	203.36

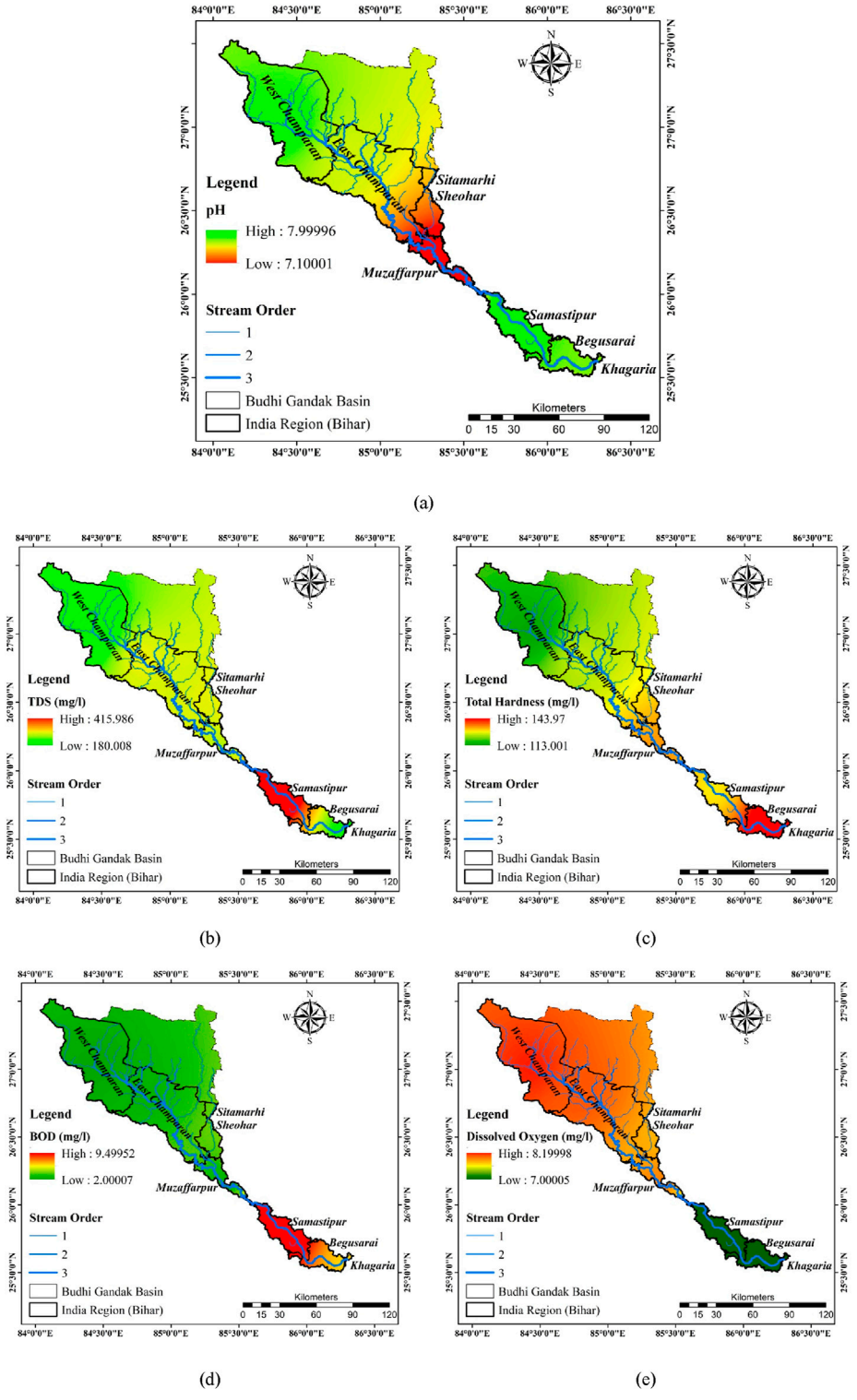

FIGURE 5
River water quality at different locations (Sharma and Choudhary, 2016; Kumar and Mishra, 2015), **(A)** variation in pH in different locations, **(B)** variation in TDS in different locations, **(C)** variation in TH in different location, **(D)** variation in BOD on different location, and **(E)** variation in DO on different location.

were obtained from the available literature. The data obtained from the literature were confirmed through the laboratory test performed on the sample obtained from the mentioned location through random sampling.

3 Results and discussion

As mentioned earlier, to evaluate the impact of different conditions like location, industrialization, urbanization, and

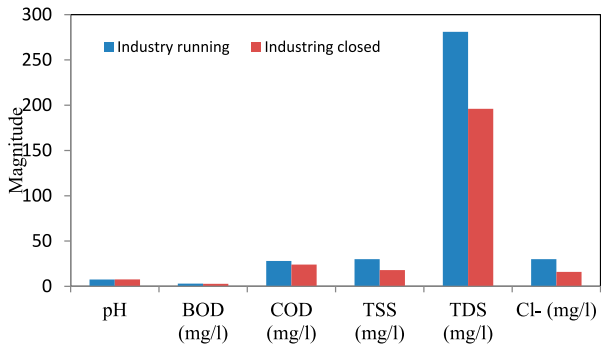

FIGURE 6
Variation in different parameters for closed and running industry for river water near Sugauli.

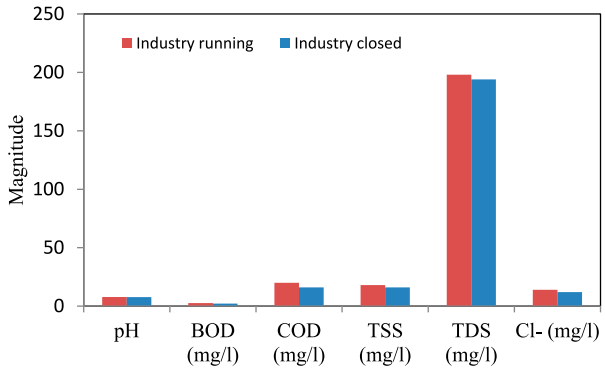

FIGURE 7
Variation in different parameters for closed and running industry for river water near Lauria.

season's water quality, data were collected from the direct testing of the water sample or the literature available. The impact of these factors is discussed in the following section.

3.1 Impact of location

The variations in the pH, total dissolved solids (TDSs), total hardness (TH), biological oxygen demand (BOD), and dissolved oxygen (DO) for different locations are presented in Figure 5. It can be observed that all these water quality parameters vary significantly from one location to another. The pH value of the water is 7.1, while it is 7.8 for Lauria and Khagaria (Fig, 4a), with Samastipur exhibiting the highest pH levels. Furthermore, TDS and BOD are also highest in Samastipur (4b, 4d). For Lauria and Khagaria, TDS values are almost in a similar range, but Sugauli and Muzaffarpur show relatively high TDS values. TH for all locations is in the range of 113–144 mg/L (4d). The variation in the DO value, as presented in Figure 5E, shows that the DO of water in Lauria, Sugauli, and Muzaffarpur is around 8. However, in Samastipur and Khagaria, it decreases to around 7. All the places have good DO levels. The presence of DO is important for aquatic life. So, the present condition of DO indicates that Burhi Gandak is satisfactory from the aquatic life point of view. Furthermore, we can conclude that the quality of the river water heavily depends on the local conditions. So, there is always a requirement for local control of human activities to improve or maintain the quality of water.

The impact of the industry on the water quality of rivers can be understood by comparing the results shown in Figures 6, 7. Figure 6 shows the result of the water quality of Sugauli, and Figure 7 shows the water quality results of Lauria. Both of the places have sugar plants near the banks of the Burhi Gandak River. Sugar plants do not operate for the full year. They start in November and close in March. So, to understand the impact of the industry on the water quality of the river, water samples were collected and tested during the operational and shutdown seasons of the industry. It can be observed for both places that degradation in water quality took place when the industry was running. The quality parameters of water are within permissible limits in all cases. However, it can be concluded from Figures 6, 7 that due to industrial activity, water quality is affected. There is a requirement for

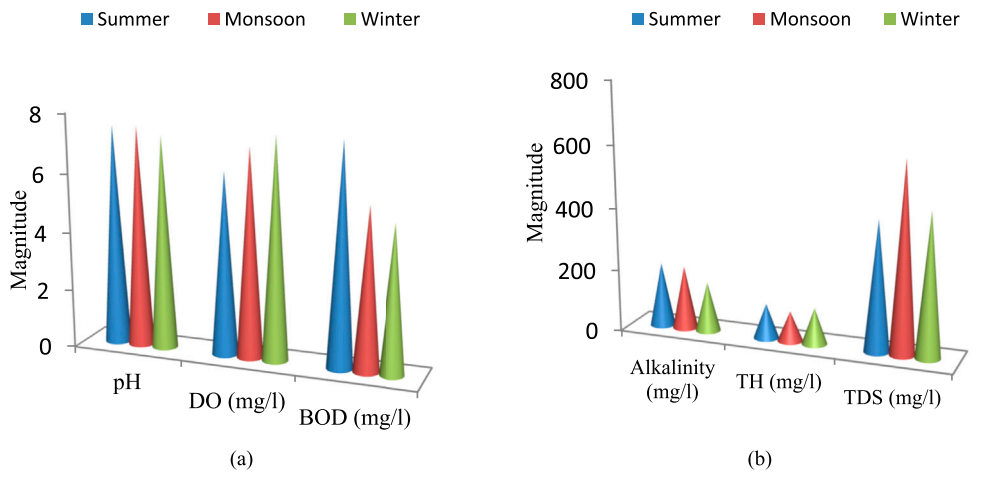

FIGURE 8
Variation in the different parameters in **(A)** and **(B)** for river water at the entry point of Samastipur (Kumar and Prasad, 2022).

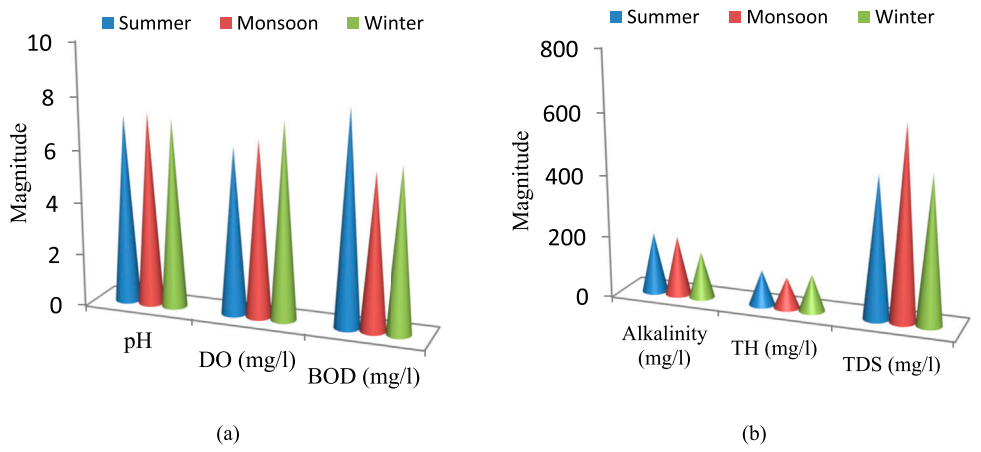

FIGURE 9
Variation in the different parameters in **(A)** and **(B)** for river water at the midpoint of Samastipur (Kumar and Prasad, 2022).

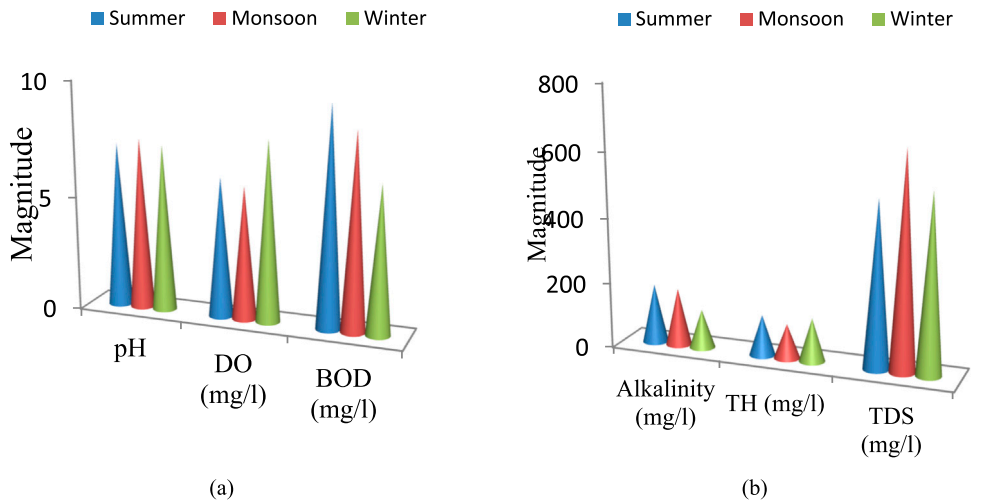

FIGURE 10
Variation in the different parameters in **(A)** and **(B)** for river water at the exit point of Samastipur (Kumar and Prasad, 2022).

proper supervision of these industries so that they maintain the quality of the water coming from their effluent treatment plants.

3.2 Impact of urbanization

The impact of urbanization can be understood by comparing the results of water quality presented in Figures 8–10. Figure 8 indicates the water quality of the river for all the seasons collected from the entry point of Samastipur City. Figure 9 shows the water quality for all the seasons of the river collected from the midpoint of the city, while Figure 10 shows the water quality for all the seasons at the endpoint of the city. It can be observed that the water quality is degraded at the end of the city to the entry point. The BOD of the water at the entry point in summer was 7.5 and has increased to 9.5 at the exit point of the city. A similar trend can be observed for the monsoon and winter seasons. Currently, water quality at the entry and exit points of the city is satisfactory. However, Samastipur and other cities in Bihar are growing rapidly. Different industrial activities are also increasing in these cities. So, there is a requirement for proper supervision of the quality of water and human activities in such cities or towns.

3.3 Impact of duration/season

Table 3 shows the quality of water collected from Burhi Gandak near Sugauli in different months. In North Bihar, heavy rainfall occurs mainly during the monsoon season, which starts from mid-June and remains till mid-September. During this time, flood conditions occur in all the rivers of North Bihar, and it remains till September. Considering this, the results of post- and pre-monsoon are presented in Table 3. It can be observed that the other quality of water is not changing except the amount of the TSSs.

TABLE 3 Variation in different river water quality in different seasons near Sugauli.

S. No.	Parameter	February	March	September	October	November	December
1	Color	<5.0	<5.0	<5.0	<5.0	<5.0	<5.0
2	pH	7.5	7.7	7.6	7.8	8.1	7.9
3	BOD (mg/L)	2.2	2.4	2	2.4	2	2.1
4	COD (mg/L)	16	16	24	16	20	20
5	TSS (mg/L)	24	28	52	12	15	15
6	TDS (mg/L)	245	268	225	190	185	191
7	Cl- (mg/L)	26	28	22	14	12.8	16
8	NH3-N (mg/L)	0.14	0.18	0.28	0.14	0.14	0.28
9	NO3-(mg/L)	0.32	0.42	0.36	0.28	0.32	0.32

During flood conditions, huge amounts of sediments get mixed in the water. Due to this, the total suspended solids increased during the monsoon season, i.e., in September.

The quality of the Burhi Gandak River is influenced by several key pollutants, including the following:

a. Organic matter: the high BOD levels, especially around urban areas like Samastipur, suggest the presence of organic pollutants. These may originate from untreated or poorly treated domestic sewage, agricultural runoff, and effluent discharges from sugar plants.
b. Suspended solids: the monsoon season significantly increases the TSSs due to soil erosion and sediment transport from upstream areas. Industrial discharges, particularly those from sugar plants, can also contribute to suspended solids when not properly managed.
c. Chemical pollutants: fertilizers and pesticides from agricultural runoff are a significant source of nitrates and phosphates in the river. Industrial effluents containing chemicals, especially during the operational season of sugar mills, contribute to TDSs and may carry other pollutants like heavy metals or chemical residues.
d. Pathogenic microorganisms: urbanization leads to higher contamination with pathogenic microorganisms, as seen in areas with inadequate sewage treatment. These pollutants can compromise the biological health of the river, affecting its suitability for drinking, agriculture, and aquatic life. Anthropogenic activities play a crucial role in degrading the water quality of the Burhi Gandak River. The activities that are possibly affecting the quality of water can be summarized below.
e. Industrial discharges: the sugar plants located near the banks of the river, such as those in Sugauli and Lauria, release industrial effluents, particularly during their operational season (November to March). Despite effluent treatment plants, there is still a noticeable degradation in water quality when these industries are active. The discharge from sugar mills adds organic matter, chemicals, and suspended solids to the river, affecting overall water quality.
f. Urbanization and domestic sewage: rapid urbanization in cities like Samastipur has led to the discharge of untreated or partially treated domestic wastewater into the river. The increase in BOD levels as the river flows through urban areas indicates the contribution of organic pollutants from human activities, including sewage and waste disposal.
g. Agricultural runoff: agricultural activities in the region contribute to the river's pollution, especially during the rainy season when runoff carries fertilizers, pesticides, and other chemicals into the river. This runoff increases the levels of dissolved solids and chemical pollutants such as nitrates and phosphates, contributing to the nutrient loading of the river and potential eutrophication.
h. Land use changes and deforestation: land use changes, including deforestation and soil erosion, contribute to sediment deposition in the river, particularly during the monsoon season. This results in increased TSS levels and turbidity, as shown by the higher TSS values during the post-monsoon period.

4 Conclusion

Based on the data collected from the laboratory analyses and relevant literature, the impact of different parameters, location, industrialization, and urbanization, on the water quality of the Burhi Gandak River was investigated. Based on analysis, the following major conclusions can be drawn.

- The quality of the river varies from location to location and heavily depends on the local conditions.
- The water quality gets degraded due to industrial activities. There is a requirement for the supervision of these industries so that the quality of water remains within the desirable limits.
- The urbanization of cities along the bank of the Burhi Gandak River significantly influences the water quality of the river. So, there is a requirement for the supervision of the water quality of rivers near cities and towns as well as the human activities occurring in these cities.
- The impact of the season on water quality is temporary. The Burhi Gandak River is mainly influenced during the monsoon season, which lasts for 2–3 months. So, the impact is for a short duration.

Data availability statement

The raw data supporting the conclusions of this article will be made available by the authors, without undue reservation.

Author contributions

AP: writing–original draft. AR: writing–review and editing. VK: writing–review and editing. AK: writing–review and editing. NK: Writing-review and editing.

Funding

The author(s) declare that no financial support was received for the research, authorship, and/or publication of this article.

Conflict of interest

The authors declare that the research was conducted in the absence of any commercial or financial relationships that could be construed as a potential conflict of interest.

Publisher's note

All claims expressed in this article are solely those of the authors and do not necessarily represent those of their affiliated organizations, or those of the publisher, the editors, and the reviewers. Any product that may be evaluated in this article, or claim that may be made by its manufacturer, is not guaranteed or endorsed by the publisher.

References

Ali, A. M., and Roy, L. B. (2024). Muzaffarpur city land changes and impact on urban runoff and water quality of the river Burhi Gandak. *Int. J. Environ. Sci. Technol.* 21, 2071–2082. doi:10.1007/s13762-023-05008-2

Bhardwaj, V., Singh, D. S., and Singh, A. K. (2010). Water quality of the chhoti Gandak River using principal component analysis, Ganga plain, India. *Sci.* 119, 117–127. doi:10.1007/s12040-010-0007-8

Bhargav, D. S. (1987). Nature and the Ganga. *Envi. Conserv.* 14 (4), 307–318. doi:10.1017/S0376892900016829

DES (2022). Directorate of Economics and Statistics, district-wise rainfall data of Bihar. Available at: https://dse.bihar.gov.in/rainfall.htm.

Dwivedi, S. L., and Pathak, V. (2007). Studies of water quality of Mandakini River in Chitrakoot for irrigation purposes. *Ind. J. Envi. Prot.* 27, 761–764.

India-WRIS (2010). "Ganga Basin report," in *India-WRIS*. Available at: https://www.india-wris.nrsc.gov.in.

Kumar, M. (2018). A geomorphic study of Burhi Gandak drainage basin in Muzaffarpur district. *Int. J. Res. Eng., IT Soci. Sci.* 8 (8), 323–329.

Kumar, N., and Mishra, Y. (2015). Effect of sewage and limnobioloy of Burhi Gandak River near Samastipur urban area. *Int. J. Bio. Sci.* 9 (1), 8–12.

Kumar, S. (2020). Hydrobiological study of Burhi Gandak River near the urban area at Samastipur (Bihar). *Int. J. Environ. Sci.* 11 (1), 5–10. doi:10.53390/ijes.v11i1.2

Kumar, S. (2020). Hydrobiological study of Burhi Gandak River near the urban area at Samastipur (Bihar). *Int. J. Envi. Sci.* 11 (1), 6–10. doi:10.53390/ijes.v11i1.2

Kumar, S., and Prasad, J. (2022). Water quality of Burhi Gandak River near Samastipur town, Bihar. *Int. J. Bio. Sci.* 13 (1), 8–13.

Lantzy, R. J., and Mackenzie, F. T. (1979). Atmospheric trace metals global cycles and assessment of man's impact. *Geochimica Cosmochimica Acta* 43, 511–525. doi:10.1016/0016-7037(79)90162-5

Mishra, D. K. (2018). Revisiting Burhi Gandak breach at begampur in Samastipur district of Bihar-1986. *Dialogue* 19 (3), 70–83.

MOES (2010). Ministry of earth science, 110 Years (1901-2010) monthly rainfall data series for districts, states and met sub-divisions and all India. Available at: https://www.imdpune.gov.in/library/public/e-book110.pdf

Muzaffarpur-District Industrial Potential Survey (2011). *District census handbook, directorate of census operations Bihar village and town directory.*

Nriagu, J. O. (1979). Global inventory of natural and anthropogenic emissions of trace metals to the atmosphere. *Nature* 279, 409–411. doi:10.1038/279409a0

Philip, G., and Gupta, R. P. (2008). Channel pattern transformation of the Burhi-Gandak river, Bihar, India: a study based on multidata sets. *Geocarto Int.* 8 (3), 47–51. doi:10.1080/10106049309354419

Prakash, S., Kumar, A., Prakash, S., and Mishra, B. K. (2020). A survey of the fish fauna of Rapti River, Balrampur (U.P.), India. *Int. J. Bio. Innov.* 2 (1), 76–81. doi:10.46505/IJBI.2020.2110

Ross, S. M. (1994). *Toxic metals in soil-plant systems*. Chichester, U.K: Wiley.

Sharma, D., and Choudhary, S. K. (2014). Evaluation of water quality index for assessment of water quality of the Budhi Gandak River at Khagaria, Bihar. *Pollut. Res.* 33 (4), 81–86.

Sharma, D., and Choudhary, S. K. (2016). A comparative assessment of water quality index of surface (river) water and groundwater along the Budhi Gandak belt using correlation analysis at Khagaria (Bihar). *Ecoscan* 10 (1and2), 7–12.

Singh, D. S., and Singh, I. B. (2005). Facies architecture of the Gandak megafan, Ganga plain, India. *Paleontological Soc. Ind.* 2, 125–140.

Singh, D. S., Tiwari, A. K., and Gautam, P. K. (2018). "The Burhi Gandak: most sinuous river," in *The Indian rivers*. Editor D. S. Singh (Singapore: Springer Hydrogeology. Springer). doi:10.1007/978-981-10-2984-4_17

Sinha, R., and Friend, P. F. (1994). River systems and their sediment flux, Indo-Gangetic plains, Northern Bihar, India. *Sedimentology* 41 (4), 825–845. doi:10.1111/j.1365-3091.1994.tb01426.x

Sinha, S. N., and Dayal, N. (1980). Geomorphological and sedimentological study of a part of lower Ganga basin, district Begusarai. *Bihar. J. Geo. l Soc. Ind.* 21, 348–353.

Trivedi, R. C. (2010). Water quality of the Ganga River – an overview. *Aquatic Eco. Health and Mang* 13 (4), 347–351. doi:10.1080/14634988.2010.528740

Verma, A. K. (2018a). Unsustainable agriculture, environmental ethics, and ecological balance. *HortFlora Res. Spectr.* 7 (3), 239–241.

Verma, A. K. (2018b). Ecological balance: an indispensable need for human survival. *J.Expi. Zool. Ind.* 21 (1), 407–409.

Village and town directory (2011). *Purba champaran village and town wise primary census abstract (PCA), directorate of census operations Bihar village and town directory.*

frontiers | Frontiers in Environmental Science

TYPE Original Research
PUBLISHED 09 December 2024
DOI 10.3389/fenvs.2024.1505480

OPEN ACCESS

EDITED BY
Jahangeer Jahangeer,
University of Nebraska-Lincoln, United States

REVIEWED BY
Michael Tso,
United Kingdom Centre for Ecology and Hydrology (UKCEH), United Kingdom
Jiangjiang Zhang,
Hohai University, China

*CORRESPONDENCE
Michael V. Callaghan,
mcallaghan@aquanty.com

RECEIVED 02 October 2024
ACCEPTED 18 November 2024
PUBLISHED 09 December 2024

CITATION
Callaghan MV, Frey SK, Miller K, Hwang H-T, Zolfaghari R, Hammel K, Berg SJ and Sudicky EA (2024) Development of a fully integrated hydrological fate and transport model for plant protection products: incorporating groundwater, tile drainage, and runoff. *Front. Environ. Sci.* 12:1505480. doi: 10.3389/fenvs.2024.1505480

Development of a fully integrated hydrological fate and transport model for plant protection products: incorporating groundwater, tile drainage, and runoff

Michael V. Callaghan[1]*, Steven K. Frey[1,2], Killian Miller[1], Hyoun-Tae Hwang[1,2], Reza Zolfaghari[3], Klaus Hammel[3], Steven J. Berg[1,2] and Edward A. Sudicky[1,2]

[1]Aquanty Inc., Waterloo, ON, Canada, [2]Department of Earth and Environmental Sciences, University of Waterloo, Waterloo, ON, Canada, [3]Bayer AG, Monheim, Germany

Introduction: Plant protection products (PPPs) such as pesticides and herbicides are experiencing increased use worldwide. In the context of PPP authorization and registration, water exposure assessments (drinking water and aquatic exposure) use numerical modeling to simulate relevant hydrological processes and exposure pathways. A common practice for estimating PPP leaching to groundwater, PPP loading onto surface water via tile drainage, or PPP transport via runoff utilizes multiple one-dimensional models, each representing a separate exposure pathway. Separate analysis of individual exposure pathways can result in disparate assumptions being made that represent relative worst-case scenarios for each pathway, rather than an integrated reasonable worst-case scenario for all pathways.

Methods: The interplay between PPP degradation, leaching to groundwater, transport in tile drainage, and runoff is well-suited for simulation using an integrated surface–subsurface hydrologic and chemical fate and transport model. This study presents functionality added to HydroGeoSphere (HGS), a three-dimensional, fully integrated, surface–subsurface hydrologic model. HGS was verified against other recognized models: PRZM, HYDRUS, PEARL, PELMO, and MACRO. Added features include automatic irrigation, non-linear adsorption, temperature and soil water content-dependent degradation, and solute uptake by plant roots.

Results and Discussion: HGS results for leaching of PPP mass to groundwater showed the highest correlation, lowest error, and lowest bias relative to PEARL model results. Simulation of macropore flow to tile drains in HGS produced an intermittent tile drain flow in summer that resulted in generally lower peak effluent concentrations compared to the MACRO model. Simulation of runoff

Abbreviations: AET, actual evapotranspiration; CN, curve number; DT50, half-life; FOCUS, FOrum for the Co-ordination of pesticide models and their USe; GW, groundwater; Koc, soil organic carbon-water partitioning coefficient; LAI, leaf area index; NRCS, Natural Resources Conservation Service; PET, potential evapotranspiration; PPP, plant protection product; SW, surface water.

in HGS produced a higher total runoff compared to the PRZM model, attributed to lower evapotranspiration in HGS. Use of the integrated HGS model resulted in a greater agreement in water balance components relative to using multiple models to simulate individual hydrologic pathways.

KEYWORDS

pesticide, three-dimensional, reactive transport, HydroGeoSphere, agricultural water, green water

1 Introduction

Sustainable development goals adopted by United Nations Member States in 2015 (UNGA, 2015) include alleviation of hunger, access to clean water, and responsible agricultural production. These goals are at the nexus of the use of plant protection products (PPPs) to improve crop production while simultaneously reducing the potential for negative effects on drinking water and the aquatic environment. Plant protection products are herbicides, insecticides, and fungicides used in agriculture to protect crops from pests and disease. In some of the largest agricultural regions worldwide (the United States, Australia, Canada, and the European Union), PPP sales and active ingredient registrations show a stable or slightly increasing trend through nominally the last 10 years (Eurostat, 2022; Maino et al., 2023; PMRA, 2023), while among low-to-middle income countries, PPP use is increasing steadily (Shattuck et al., 2023). Signatory countries to the UN Convention on Biodiversity have committed to decreasing the risks associated with PPP contaminants in the environment to half by 2030 (CBD, 2022). In light of PPP usage trends that are stable or increasing, improved evaluation of risks to drinking water and the environment, as well as mitigation of those risks, can potentially be realized through increased rigor of PPP exposure assessment. Reliable assessment of the risks associated with PPP application requires concentrations in the environment to be known or estimated and then compared to potential effect thresholds. In the context of PPP authorization, water exposure assessments (drinking water and aquatic exposure) use numerical modeling software to simulate relevant hydrological processes (USEPA, 2023). Models are validated and approved by regulatory authorities and thus provide a benchmark for any new model that might be used for the same purpose (European Commission, 2014).

Leaching of PPPs and their degradates to groundwater (GW) is of concern for direct human or animal consumption of well water (Squillace et al., 2002; Bexfield et al., 2021), as well as transport during groundwater–surface water (GW–SW) exchange (Hintze et al., 2020). Direct loading of surface water (SW) bodies occurs via aerial drift, tile drainage, and runoff with potential resultant effects on aquatic receptors (Kladivko et al., 2001; Silburn, 2023). Increased recognition of the occurrence and persistence of PPPs in the water environment has resulted in an increasing need to improve scientific rigor when modeling the potential fate and transport of PPPs to GW or SW (Gassmann, 2021; Jorda et al., 2021; Pietrzak, 2021). Use of fate and transport modeling as part of the environmental exposure assessment is one tool that serves to inform the environmental risk to GW and SW receptors associated with particular PPP products or active ingredients (Holmes et al., 2009).

The interplay between PPP degradation, leaching to GW, transport in tile drainage, and runoff is well-suited for simulation using an integrated surface–subsurface hydrology and the chemical fate and transport model (Gatel et al., 2019). A common practice for estimating PPP leaching to GW, PPP loading onto SW via tile drainage, or PPP transport via runoff utilizes multiple one-dimensional (1D) models, each representing a separate exposure pathway (FOCUS, 2001; European Commission, 2014). Separate analysis of individual exposure pathways can result in disparate assumptions being made that represent relative worst-case scenarios for each pathway, rather than an integrated reasonable worst-case scenario for all pathways. Additionally, modeling of exposure pathways in multiple models can limit interpretations of overlapping or interrelated hydrological processes. Inherently dependent hydrological processes, such as deep percolation to GW, tile drainage, and surface runoff, can be simulated in a single integrated surface–subsurface hydrologic model while maintaining water and pesticide mass balance. HydroGeoSphere (HGS) is a three-dimensional (3D), fully integrated surface–subsurface hydrological modeling platform (Brunner and Simmons, 2012; Kurtz et al., 2017; Aquanty, 2024), with a tightly coupled formulation (Barthel and Banzaf, 2016). HGS is a flexible fully integrated GW–SW and chemical fate and transport model that supports many conceptualizations of hydrological settings using physically realistic boundary conditions and contaminant source geometries; as such, it is not solely a PPP transport model but a modeling platform well-suited to PPP fate and transport modeling. The general flow formulation of HGS includes variably saturated 3D flow using Richards' equation and the two-dimensional (2D) depth-averaged surface flow using the diffusive-wave approximation of the Saint-Venant shallow water flow equation. HGS is designed to simulate the entire terrestrial water cycle, with a surface boundary condition driven by precipitation and potential evapotranspiration. Actual evapotranspiration is calculated internally in HGS by accounting for soil moisture effects on soil evaporation and plant transpiration and includes open water evaporation.

The HGS model has been successfully benchmarked for variably saturated subsurface and overland flow against several other integrated hydrologic models (Maxwell et al., 2014; Koch et al., 2016; Kollet et al., 2017). In the 2017 flow benchmarking study, HGS produced results indicative of the model ensemble norm for surface flow depth, ponding, and saturated and unsaturated zone storage dynamics. Recent applications of HGS for subsurface water flow include simulation of dynamics of infiltration and vadose zone storage in a karst aquifer using a dual-permeability approach by Bresinsky et al. (2023), quantification of percolation to GW with a fluctuating water table by Gong et al. (2023), and dynamics of

GW–SW flow reversals between small surface water bodies and their connected aquifer by Steidl et al. (2023). Previous modeling of agrichemical fate and transport in GW using HGS has included the simulation of a soluble, non-sorbing hypothetical PPP similar to 2-methyl-4-chlorophenoxyacetic acid, bentazone, metam sodium, clopyralid, and nitrate by Lutz et al. (2013), and of sulfonamide antibiotics by Park et al. (2016). Viscosity effects of liquid manure infiltration into macroporous soil were simulated using HGS by Frey et al. (2012), and variable density effects of saline GW intrusion were simulated using HGS by Paldor et al. (2022). HGS has been used to model tile drainage in several studies using different approaches, ranging from using a single porous medium with seepage nodes to model flow only (de Schepper et al., 2017; Hwang et al., 2019) to dual domain flow representing the soil matrix and macropores including nutrient transport to a discrete tile drain network (Frey et al., 2016).

The overarching objective of this work is to develop a physics-based, 3D, fully integrated chemical fate and transport model for simulating PPP loading on GW and SW and improve PPP mass balance accounting in exposure assessment through the use of a single model that can be used to track water and PPP mass. Toward achieving this objective, the fate and transport routines of the HGS model have been updated to include the addition of non-linear chemical adsorption in both the soil matrix and macropore domains, implementation of temperature and soil moisture-dependent chemical degradation in both the soil matrix and macropore domains, and solute uptake by plant roots. To enhance HGS application in an agricultural setting, automatic irrigation via modeled water content has been added. This manuscript documents the verification of the new HGS functionality against other widely accepted models used for the simulation of PPP leaching to GW. Following verification of subsurface fate and transport functionality, PPP transport to tile drains in macroporous soils is demonstrated, as well as runoff generation.

2 Methods

Upgrades to the capability of HGS to simulate PPP fate and transport in soil and runoff were guided by the existing functionality of multiple separate hydrologic models used for PPP fate and transport simulation in the European Union regulatory context. The PEARL (Leistra et al., 2001) and PELMO (Klein, 2020) models are used within the European Union's FOrum for the Co-ordination of pesticide models and their USe (FOCUS) framework for the simulation of predicted environmental concentrations of PPPs in GW (European Commission, 2014). The MACRO model (Larsbo and Jarvis, 2003) is used within the FOCUS framework to simulate transport of PPPs through macroporous soils to surface water via tile drainage, and the PRZM model (Suarez, 2005) is used to simulate PPP loading to surface water via runoff (Young and Fry, 2019), including both dissolved substances and those adhered to eroded sediment (FOCUS, 2001).

Following guidance on the use of recommended numerical models, the FOCUS GW and SW working groups developed a set of standard scenarios that can be used to evaluate predicted environmental concentrations of PPPs in GW and SW (FOCUS, 2001; European Commission, 2014). The FOCUS scenarios include a set of test substances that are a suite of regulator-accepted and industry-utilized scenarios that have been previously used for model sensitivity analysis by FOCUS (European Commission, 2014), model intercomparison by FOCUS (2001), and model verification by others, as was conducted by Diamantopoulos et al. (2017) with the HYDRUS model (Šimůnek et al., 2012). The FOCUS scenarios were used in the current study for the verification of the HGS model to simulate PPP leaching to GW and demonstrate PPP transport to tile drains and runoff generation.

2.1 Model formulation

2.1.1 Added functionality for irrigation

The HGS model simulates 3D variably saturated subsurface flow in porous media using Richards' equation and solute transport using the advection–dispersion equation and has been under development from early work by Therrien and Sudicky (1996) to present. In addition to simulating flow in variably saturated uniform porous media, HGS also includes optional subsurface flow domains: discrete fractures, wells, tile drains, and a dual domain for simulating flow and transport in macroporous soils or fractured media (Aquanty, 2024). Of the FOCUS GW models, PEARL and PELMO, the subsurface flow functionality of HGS most closely resembles that of the Richards' equation-based PEARL model, rather than the soil moisture capacitance formulation of the PELMO model.

The FOCUS version of the PEARL model FOCUSPEARL (Berg et al., 2019) includes an automated irrigation scheme. The FOCUS GW leaching scenarios include irrigation for some of the location and crop combinations. Therefore, irrigation triggered by soil matric potential was added to HGS to better align with the irrigation scheme within FOCUSPEARL. The new irrigation functionality in HGS applies irrigation over a user-specified duration defined by a table of irrigation depths and soil matric potentials. The drier the soil is, the more irrigation water is added. Irrigation occurs only during the user-specified growing season, and irrigation events can be restricted to occur at fixed time intervals defined by a recurrence interval, e.g., one irrigation event per week.

2.1.2 Added functionality for subsurface PPP fate and transport

The numerical models within the FOCUS framework for modeling PPP fate and transport in soil, namely, PEARL (Leistra et al., 2001), PELMO (Klein, 2020), MACRO (Larsbo and Jarvis, 2003), and PRZM (Suarez, 2005), include soil moisture and temperature-dependent PPP degradation. PPP degradation rates increase with an increase in soil moisture and temperature. New functionality was added to HGS to incorporate soil moisture and temperature-dependent degradation of PPPs for both dissolved and adsorbed phases. Modifications made to the degradation coefficient formulation, including temperature and saturation dependence (Equations 1, 2, respectively), and the inclusion of non-linear adsorption (Equation 3) were updates made to the pre-existing HGS functionality that included non-temperature and non-saturation-dependent degradation and linear adsorption. Therefore, only the updates to the degradation and adsorption formulations are given here, and the reader is referred to Frey et al. (2016) for the governing equations for reactive transport in the

soil matrix and macropore domains in HGS for parent and daughter species. The first-order degradation coefficient, λ_S [T^{-1}], dependent on soil water saturation is given by

$$\lambda_S = \alpha_S \left(\frac{\theta_w}{\theta_r} \right)^{\beta}, \quad (1)$$

where α_S [T^{-1}] is the degradation coefficient determined at reference volumetric soil water content, θ_r [L^3 L^{-3}]; while θ_w [L^3 L^{-3}] is the simulated water content, and β [-] is the shape parameter, modified after Walker (1974).

The first-order degradation coefficient dependent on temperature, λ_T [T^{-1}], is calculated using a modified form of the Arrhenius equation:

$$\lambda_T = \alpha_T \cdot exp\left[\frac{E_a \cdot (T_b - T_r)}{R \cdot T_b \cdot T_r} \right], \quad (2)$$

where α_T [T^{-1}] is the degradation coefficient determined at reference temperature T_r [K], T_b is the bulk soil temperature [K], E_a [M L^2 N^{-1} T^{-2}] is the activation energy of the reaction, and R is the universal gas constant [M L^2 N^{-1} K^{-1} T^{-2}]. An analytical solution to the heat conduction equation was used to calculate the 1D subsurface temperature profile (Schilling et al., 2019), wherein the surface soil temperature boundary condition is user-specified, typically taken to be the average daily air temperature, and the temperature boundary condition at depth is typically taken to be the long-term average air temperature. Degradation is implemented in HGS for straight and branched decay chains.

Numerical models used for modeling PPP fate and transport in the FOCUS framework, namely, PEARL (Leistra et al., 2001), PELMO (Klein, 2020), MACRO (Larsbo and Jarvis, 2003), and PRZM (Suarez, 2005), include the non-linear Freundlich adsorption isotherm. The non-linear Freundlich adsorption isotherm formulation was added to HGS, which relates the amount of adsorbate in equilibrium, X [M M^{-1}], to the solute concentration, C [M L^{-3}], via the empirical relationship:

$$X = K_F \cdot C_0 \left(\frac{C}{C_0} \right)^n, \quad (3)$$

where K_F is the Freundlich adsorption capacity [L^3 M^{-1}], C_0 [M L^{-3}] is the reference concentration, and n [-] is the Freundlich exponent.

The solution distribution coefficient, K' [L^3 M^{-1}], (Equation 4) is defined as the slope of the non-linear Freundlich isotherm:

$$K' = \frac{dX}{dC} = n \cdot K_F \left(\frac{C}{C_0} \right)^{n-1}. \quad (4)$$

PPP mass, M [M], uptake by plant roots has been incorporated into HGS via plant transpiration water flux, q_{trans} [L^3 T^{-1}] (Equation 5), according to Briggs et al. (1982). The mass flux rate for uptake via plant roots is therefore given as

$$\frac{dM}{dt} = q_{trans} f_T C, \quad (5)$$

where f_T [-] is the transpiration stream concentration factor. Plant uptake is typically less than mass available in the plant solution (Leistra et al., 2001); therefore, $f_T \leq 1$ and is typically specified as 0.5 for ionic species (European Commission, 2014).

2.1.3 Macropore flow and transport to tile drains

PPP transport, following application on an agricultural field, via infiltration through soil macropores and then into tile drainage and ultimately into surface water is one of the transport pathways of concern in the FOCUS framework. The methodology employed in the FOCUS (2001) framework utilizes the MACRO (Larsbo and Jarvis, 2003) 1D, dual-permeability model to simulate the preferential flow through a high hydraulic conductivity macropore domain using the kinematic wave approach (Germann, 1985), connected with a lower hydraulic conductivity soil matrix domain. The dual-permeability, variably saturated 3D flow solution in HGS solves two coupled Richards' equations for both the macropore and matrix domains. HGS supports both a common node and dual node approach. The dual node approach, used here, calculates explicit exchange fluxes between the two model domains. For simulating water flow and solute exchange between the two domains, HGS employs the formulation of Gerke and van Genuchten (1993). Dual domain solute transport is simulated in both HGS (Frey et al., 2012; Frey et al., 2016) and MACRO (Larsbo and Jarvis, 2003) using the advection dispersion equation in both models.

Tile drainage in the 1D MACRO model assumes a fully penetrating seepage surface, such as a ditch or highly permeable backfill above the tile drain (Larsbo and Jarvis, 2003). Lateral flow from saturated soil layers to the ditch or tile drain is simulated in MACRO using seepage potential theory (Leeds-Harrison et al., 1986). Tile drainage can be simulated in HGS using two approaches, where one simulates flow and transport in discrete subsurface 1D linear tile drain elements (De Schepper et al., 2015) and the second approach utilizes drain nodes to extract water from the model under saturated conditions at the depth of tile installation (Boico et al., 2023), used for modeling herein.

2.1.4 Runoff generation

HGS utilizes a globally implicit control-volume finite element approach with adaptive time stepping and OpenMP parallelization (Hwang et al., 2014) to solve a coupled set of equations that includes diffusive wave approximation to the 2D depth-averaged Saint-Venant equation for overland flow and 1D Manning's equation for the open channel flow (Aquanty, 2024). Partitioning of rainfall into runoff is simulated implicitly in HGS based on the infiltrability of the subsurface, which can result in either saturation-excess or infiltration-excess overland flow being generated. The soil moisture saturation level and hydraulic conductivity of the subsurface influence whether rainfall will infiltrate or run off.

Runoff generation mechanisms in agricultural settings are controlled by surface attributes including vegetation cover, macro and microtopography, and subsurface conditions such as hydraulic conductivity and soil moisture levels (Appels et al., 2016; Sittig et al., 2020). The effect of topography on runoff generation at multiple scales has been demonstrated using HGS simulations, including wetlands, coastal areas, and upland agricultural landscapes (Frei et al., 2012; Amado et al., 2016; Frey et al., 2021; Paldor et al., 2022). Rain event-induced runoff was separated into rainfall-excess overland flow (13%) and exfiltration-induced overland flow (87%) using HGS by Chen et al. (2023), thus demonstrating the model's ability to quantify mixing of surface and subsurface water in runoff. Transport of PPPs in surface water in HGS currently

TABLE 1 Summary of the nine groundwater scenario locations: climate, soil texture, and soil organic matter, after FOCUS (2000).

Location	Mean annual temperature (°C)	Annual rainfall (mm)	Surface soil texture*	Surface soil organic matter (%)
Châteaudun, FR	11.3	648	Silty clay loam	2.4
Hamburg, DE	9.0	786	Sandy loam	2.6
Jokioinen, DK	4.1	638	Loamy sand	7.0
Kremsmünster, AT	8.6	900	Loam/silt loam	3.6
Okehampton, United Kingdom	10.2	1,038	Loam	3.8
Piacenza, IT	13.2	857	Loam	1.7
Porto, PT	14.8	1,150	Loam	6.6
Sevilla, ES	17.9	493	Silt loam	1.6
Thiva, GR	16.2	500	Loam	1.3

*Soil texture corresponds to the USDA (1975) system.

includes dissolved species only. Advection and diffusion of solutes are simulated both to and from the surface and subsurface domains.

2.2 Verification of PPP leaching to GW

An objective of this study was to verify the new chemical fate and transport functionality added to HGS by using the FOCUS GW scenarios. Soil water balance and PPP leaching to GW simulated using HGS were compared against leaching results from the PEARL, PELMO, and HYDRUS models after Diamantopoulos et al. (2017), for the nine FOCUS GW scenarios summarized in Table 1. Although the HYDRUS model is not currently included within the FOCUS framework, it has been widely applied to simulate PPP fate and transport in soils (Boivin et al., 2006; Cheviron and Coquet, 2009; Köhne et al., 2009; Anlauf et al., 2018). The nine FOCUS GW sites are distributed across the European Union and were estimated to be representative of 65% of the arable area of 27 member states, as of 2014 (European Commission, 2014). The FOCUS GW leaching scenarios span a range of crops and associated parameterized model inputs that effect plant water uptake (e.g., time varying leaf area index [LAI], root growth, and maximum root depth), as well as the timing of planting and PPP application.

The HGS models used for the simulation of PPP leaching to GW were constructed as 1D soil column models comprising a single 1-m square quadrilateral element in the horizontal plane and vertically discretized in uniform 1-cm increments. Modeled soil column depths were 4.5 m, except for the Sevilla model which was 6.0 m deep. HGS model parameterization for the porous media was specified from each FOCUS GW scenario (European Commission, 2014), including soil layering, saturated hydraulic conductivity, saturated volumetric water content, and van Genuchten (1980) soil hydraulic parameters. A potato crop was selected for HGS model verification to align with the methodology of Diamantopoulos et al. (2017). Growth stage timing, maximum LAI, and maximum rooting depth were aligned with the FOCUS scenarios and were used to generate daily LAI and root depth time series for input into the HGS models.

Daily rainfall was applied to the top boundary of the HGS models using FOCUS meteorological datasets for a 20-year period taken from the 1971 to 1996 interval, including a six-year spin-up period. Irrigation was generated internally by HGS in response to soil matric potential for the five FOCUS scenarios that include irrigation: Châteaudun, FR; Piacenza, IT; Porto, PT; Sevilla, ES; and Thiva, GR. Daily potential evapotranspiration (PET) was applied using FOCUS daily reference evapotranspiration for each scenario, which was then internally partitioned into plant transpiration and soil evaporation by HGS using partitioning coefficients based on the method of Kristensen and Jensen (1975). Actual transpiration calculated by HGS is a function of soil matric potential and is calculated using the method of Feddes et al. (1978), whereby transpiration is maximum across a user-specified matric potential range, and then progressively decreases under excessively wet or dry conditions. Soil evaporation is maximum under wet soil conditions and progressively decreases to zero as soil dries, according to user-specified matric potential thresholds, following Allen et al. (1998).

No flow lateral boundary conditions were used in both the surface and subsurface model domains. The bottom boundary conditions were scenario-dependent, as per the HYDRUS models developed by Diamantopoulos et al. (2017). The free drainage boundary condition in HGS is a direct analog to the free drainage boundary condition in HYDRUS, while the specified head boundary condition in HGS is similar to the time varying pressure head boundary condition in HYDRUS. The fluid transfer boundary condition in HGS has the most similarity to the deep drainage boundary condition in HYDRUS and was used for five of the scenarios. The fluid transfer boundary condition in HGS is a flux boundary that is controlled by a user-specified hydraulic conductivity and a reference head value applied over a user-specified distance from the boundary, while the deep drainage boundary condition in HYDRUS uses the water table position and two empirical parameters to define the flux across the boundary. Details of the FOCUS GW model inputs and bottom boundary conditions are included in Supplementary Material.

Four test substances and associated fate and transport parameter values are prescribed in the FOCUS framework for use in model verification. The four test substances were originally developed by

TABLE 2 Summary of FOCUS groundwater leaching test substances after European Commission (2014).

Substance	Description	Substance has a metabolite?
A	Medium persistent, low sorbing, non-volatile (DT50 = 60 d, Koc = 103 L kg^{-1})	No
B	Low persistent, very low sorbing, somewhat volatile (DT50 = 20 d, Koc = 17 L kg^{-1})	No
C	Low persistent, medium sorbing, non-volatile (DT50 = 20 d, Koc = 172 L kg^{-1})	Yes, persistent, low sorbing, and non-volatile (DT50 = 100 d, Koc = 52 L kg^{-1})
D	Low persistent, low sorbing, somewhat volatile (DT50 = 20 d, Koc = 60 L kg^{-1})	No

DT50, half-life; Koc, soil organic carbon–water partitioning coefficient.

the FOCUS GW working group to demonstrate a range of leaching sensitivity across the suite of scenarios (European Commission, 2014). The four test substances and their description are given in Table 2.

A 1D analytical heat conduction model is used in HGS to calculate the vertical soil profile temperature of the bulk porous medium to account for the temperature dependence of PPP degradation (Aquanty, 2024). The thermal diffusivity for calculation of the soil temperature profile was set to 4.0 × 10^{-7} m^2 s^{-1} for all scenarios. For each site, the surface boundary condition for the analytical heat conduction model was taken to be equal to the daily air temperature provided in the FOCUS scenarios, while the background soil temperature at depth was taken to be equal to the 20-year average air temperature.

The dispersion length was set to 0.05 m for all FOCUS GW leaching scenario models, and the molecular diffusion coefficient in water was set to 4.98 × 10^{-10} m^2 s^{-1}. For soil moisture-dependent PPP degradation (Equation 1), the reference soil moisture saturation was specified at −10 kPa for all soils and the shape parameter was set to 0.7 for all substances, as recommended in European Commission (2014). For temperature-dependent degradation, a reference temperature of 20°C and an activation energy of 65.4 kJ mol^{-1} were used in Equation 2. Depth dependency of PPP degradation is included as per the FOCUS framework, which specifies that the degradation rate coefficient is maximum in the plough layer (Ap) and is multiplied by a factor of 0.5 for the layer (B) immediately below the plough layer, by a factor of 0.3 for the subsequent layer (C), and by a factor of 0.0 below 1.0 m depth (European Commission, 2014). The specification of the Freundlich adsorption isotherm in HGS (Equation 3) used a reference concentration of 1 mg L^{-1}, with a Freundlich exponent of n = 0.9 and the adsorption capacity, K_F as the product of Koc and the soil organic carbon content specified for each soil in each FOCUS scenario. The transpiration stream concentration factor for PPP uptake by plant roots was not used for the GW leaching scenarios, to be consistent with the methodology of Diamantopoulos et al. (2017), with which the HGS results are compared. Test PPPs were applied to the HGS models at the soil surface as a specified mass flux of 1 kg ha^{-1}. All test substances (A, B, C, and D) were applied 1 day before crop emergence.

2.3 Demonstration of surface water pathway modeling

Within the FOCUS framework, simulation of PPP transport to surface water (FOCUS, 2001) is prescribed separately from that for GW(European Commission, 2014). Two models are used for the two PPP transport pathways to SW. For simulation of PPP transport off-field via tile drains, the dual permeability MACRO model is specified by FOCUS, while for simulating PPP transport off-field in runoff, the PRZM model is specified. Comparisons are made here between HGS results and the output from the MACRO and PRZM models for a single FOCUS scenario for each model. The comparison between FOCUS model results (MACRO and PRZM) against HGS model results is intended to serve as a demonstration of the current HGS functionality and identify future HGS model development requirements.

FOCUS (2001) SW scenarios cover a range of climate, landscape, land use, and cropping characteristics. To demonstrate the HGS model for SW PPP loading applications, one tile drainage scenario was selected—site D4 in Skousbo, DK—and one runoff scenario was selected—site R3 in Ozzano, Bologna, IT. The basis for selection of these two scenarios was their locations in Northern (D4) and Southern Europe (R3), respectively, thereby representing very broad continental trends in agricultural runoff and drainage. Summary details for the surface water loading scenarios are contained in Supplementary Material.

2.3.1 Tile drainage scenario construction

The FOCUS Surface Water Scenarios Help software program (SWASH) serves as a graphical user interface for the MACRO and PRZM models for FOCUS simulations and includes climate inputs, hydraulic parameters, a database of PPP properties, PPP application timing, and a means to run the suite of FOCUS SW loading scenarios (European Comission, 2024). The SWASH program (SWASH v5.3, Berg et al. (2015)) was used to generate the MACRO tile drainage model for the D4 scenario with a potato crop.

An HGS tile drainage model was constructed for the FOCUS D4 SW loading scenario to demonstrate HGS tile drainage with PPP fate and transport modeling functionality in macroporous soils. The D4 scenario simulation period comprises 7 years and 4 months (1979–1985), with the first 6 years being a model spin-up period, followed by a 16-month analysis period (FOCUS, 2001).

Flow to agricultural tile drains is primarily a 2D process with predominantly vertical infiltration into soil macropores and lateral flow toward the drain (Gerke et al., 2013). The HGS model domain was constructed 5-m wide, which is half of the 10-m tile drain spacing specified in the D4 scenario, thereby taking advantage of symmetry about the midline between tile drains. The thickness of the soil column was set at 1.8 m, with the tile drain at 1.2-m depth, as per the D4 scenario. Surface topography was constructed to be typical of potato ridge and a furrow cropping system with ridges

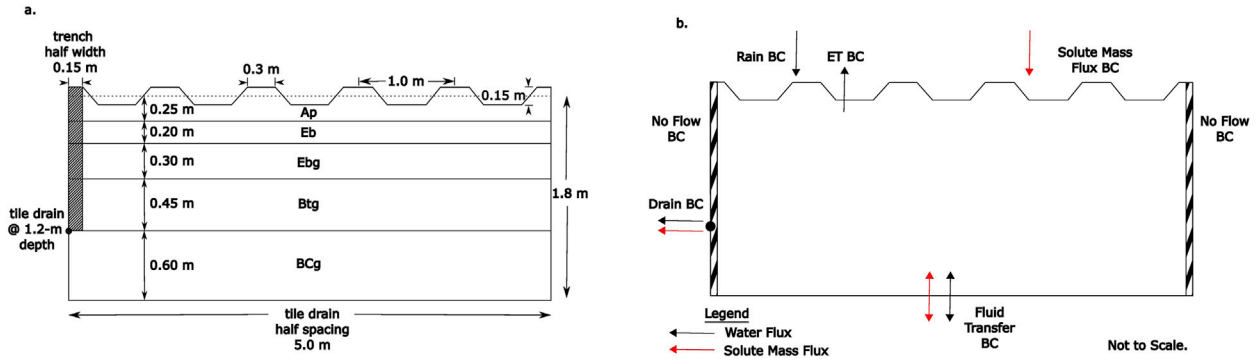

FIGURE 1
Cross section through the HGS tile drain model for the FOCUS surface water D4 scenario, **(A)** showing model geometry, layering, and **(B)** boundary conditions (BCs).

0.15-m high, 0.3-m top width, and an inter-ridge spacing of 1 m (Schock et al., 2013). A surface slope of 1% was applied in the direction of the furrows, which is within the 0.5%–2% range of surface slope for the D4 scenario. The HGS model domain was discretized into rectangular prism elements of 0.05 m on each side, which were deformed within the Ap layer below the furrows to a thickness of 0.025 m to accommodate the difference in furrow topography, with a uniform 0.01-m thick layer of elements added at the soil surface. A dual permeability formulation was used to represent a fast-flowing macropore domain coupled with a slow-flowing soil matrix domain. A cross section through the HGS tile drain model is illustrated in Figure 1.

The vertical profile was subdivided into five soil layers, according to the D4 scenario. The three middle layers were further subdivided for specification of depth-dependent PPP degradation parameters, for a total of eight property layers. Since not all the parameters required for HGS input were given in the D4 tile drainage scenario, some equivalencies were estimated. The bulk saturated hydraulic conductivity from the D4 scenario MACRO model input was split into a saturated macropore and matrix hydraulic conductivity for HGS by assuming a fixed macropore fraction of 2% for the macroporous soil layers above the tile drain depth, which was decreased to 0.1% below the tile drain depth. Unsaturated soil hydraulic parameters, using the van Genuchten (1980) formulation for the HGS model's soil matrix, were calculated using the Rosetta pedotransfer model (Zhang and Schaap, 2017). Percent sand, silt, and clay; wilting point; and bulk density from the D4 scenario were used as input to Rosetta. Macropore hydraulic properties used in the HGS model followed the van Genuchten (1980) formulation and were taken from Frey et al. (2016). Matrix and macropore hydraulic properties used for HGS model input are included in Supplementary Material.

There is no direct guidance in FOCUS (2001) for building 2D or 3D models of tile drainage, such as with HGS. Therefore, some assumptions were required with respect to constructing the D4 tile drainage scenario in HGS. In MACRO, tile drains are assumed to be laid in a trench of highly permeable backfill material (Larsbo and Jarvis, 2003). The highly permeable backfill assumption enables simulation of tile drainage by 1D models, such as MACRO (FOCUS, 1997). To enable comparison of results between the HGS and MACRO models, it was convenient to adopt a similar conceptualization of a well-drained trench in the HGS model. Therefore, a trench backfilled with disturbed, well-drained soils was included in the HGS model to be fully penetrating to just below the tile drain depth (Figure 1). In HGS, the assumption of well-drained soils in the trench required a higher macropore domain hydraulic conductivity than the corresponding undisturbed soil, which is a reasonable assumption. The resultant minimum bulk saturated hydraulic conductivity used for the Ebg and Btg layers of trench backfill material was 80 mm h^{-1}, which is a factor of 10 greater than that of the undisturbed Ebg layer and a factor of 80 greater than that of the undisturbed Btg layer.

Daily rainfall plus irrigation for a potato crop (as a single rainfall time series) was specified for the D4 scenario, as provided in the FOCUS meteorological forcing data. PET calculated by MACRO was used as input to HGS to facilitate an inter-model comparison of water balance components. In the HGS model, a third-type bottom boundary condition was used, which is similar to the "percolation as a function of water table height" boundary condition used in the MACRO model.

Crop growth was included in the HGS model through specification of time-varying LAI and root depth based on crop growth stages from the D4 scenario. The substance properties used in the HGS model were for FOCUS (2001) Test Substance I, a very low sorbing (Koc = 17 L kg^{-1}), low persistence (DT50 = 6 d), and moderately volatile PPP, as recommended for a potato crop from the FOCUS test protocol. A single application per year of Test Substance I was applied at a rate of 3 kg ha^{-1} to the soil surface. Due to the high degree of sensitivity of peak tile drain effluent concentrations to flushing caused by rainfall events, the FOCUS framework includes a set of rules for PPP application timing relative to rainfall. For the D4 potato scenario, the target date for spring PPP application is the crop emergence date minus 1 day, which results in a target application date of 22 May. The pesticide application timing calculator (PAT) within the SWASH program was used to generate the PPP application dates for both the MACRO and HGS models. The basis of the PAT search algorithm is to apply the PPP on days without excessive rainfall but to have an appreciable amount of rainfall in the days following application. The initial rules that the PAT calculator attempts to satisfy are that there should be at

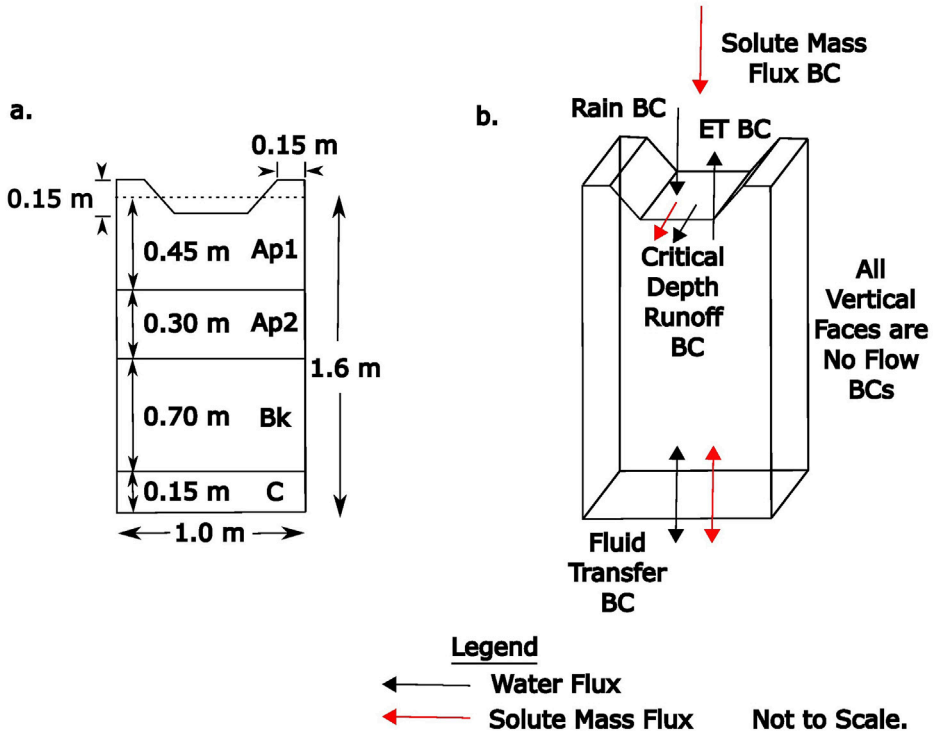

FIGURE 2
Cross section through the HGS runoff model for the FOCUS surface water R3 potato scenario, **(A)** showing model geometry, layering, and **(B)** boundary conditions (BCs).

least 10 mm of rainfall in the 10 days following application and less than 2 mm of rain per day for a 5-day period centered on the application day (FOCUS, 2001). In the model runs, the application date ranged from 14 days prior to 1 day prior to the target date (22 May) for the seven annual PPP applications.

The soil surface boundary conditions for the analytical heat conduction model were assumed to be equal to the daily air temperature provided in the FOCUS D4 scenario, with the background temperature at depth taken to be the 7-year average (1979–1985) of the daily air temperature.

2.3.2 Runoff scenario construction

The SWASH software program was used to generate the PRZM model for the R3 (Bologna, IT) runoff scenario. An HGS model was constructed to demonstrate the utility of a physics-based approach for runoff generation, through comparison to the PRZM model. Currently, the HGS model does not include a specific scheme for mixing shallow PPP-laden soil water with surface runoff nor does HGS include soil erosion and sediment transport of adhered chemicals. Therefore, *in lieu* of comparing PPP transport in runoff between HGS and PRZM, a comparison of runoff generated by both models was made using the R3 scenario with a potato crop to demonstrate similarities and differences between the physics-based approach to runoff generation in HGS and the empirically based runoff generation in PRZM. Surface runoff generation in HGS is primarily controlled by the infiltrability of the subsurface, which controls whether infiltration excess or saturation excess overland flow is produced by the model. Runoff is generated in PRZM using the empirically based Natural Resources Conservation Service (NRCS) curve number (CN) approach (Suarez, 2005). The CN approach was originally conceptualized for watershed-scale, event-based streamflow estimation (Garen and Moore, 2005). CNs tabulated for four hydrologic soil groups are adjusted for land use, soil hydrologic condition, and agricultural practice (Suarez, 2005). The CN tabulated in PRZM is the CN for average antecedent soil moisture conditions and is subsequently adjusted for soil moisture by linear interpolation between a range of values using PRZM's modeled soil moisture (Young and Fry, 2020).

The HGS model surface represents ridge and furrow microtopography, typical of potato cropping, from one ridge centerline to another at a spacing of 1 m (Figure 2). The HGS model comprised four soil layers (Ap1, Ap2, Bk, and C) to a depth of 1.6 m. Node spacing was 0.05 m in the horizontal directions, with node spacing 0.01 m and 0.04 m for the top two rows in the vertical direction and 0.05 m, thereafter, to the bottom of the model. The FOCUS R3 location has a surface slope terraced to 5%, which was applied to the HGS model along the direction of the furrows. Surface slope is not an input to the curve number method used in the 1D PRZM runoff model (Suarez, 2005).

The CN method used in PRZM generates runoff in relation to rainfall, initial abstraction, and soil moisture (Equation 6) (NRCS, 2004):

$$Q = \begin{cases} 0 \text{ for } P \le I_a \\ \dfrac{(P - I_a)^2}{P - I_a + S} \text{ for } P > I_a, \end{cases} \quad (6)$$

where Q [L] is runoff, P [L] is rainfall, S [L] is the potential maximum soil moisture retention, and I_a [L] is initial abstraction before runoff begins. S is related to the CN by $S = 1{,}000/CN - 10$, and within PRZM, I_a is set to 0.2 S. The CN method lumps interception, early infiltration, and surface depression storage into the I_a term (NRCS, 2004), while in contrast, HGS models these processes separately. This presented a challenge to parameterize HGS and PRZM in a similar way; however, some equivalencies were developed to aid in HGS parameterization. Canopy interception was set to zero in HGS as it was in PRZM, according to FOCUS (2001). Therefore, the initial abstraction term was conceptually reduced to include only two processes: early infiltration and surface depression storage. Within HGS, it was necessary to only parameterize the surface depression storage process because the infiltration process is handled separately through hydraulic parameterization of the model subsurface. The bare furrow in the HGS runoff model was assumed to be similar to the fallow condition in the PRZM model, with a CN of 91, which resulted in a calculated initial abstraction of 5 mm. An equivalent surface depression storage in HGS can therefore be assumed to be ≤5 mm. HGS parameterizes surface depression storage through a term called "rill storage," which uses a parabolic representation for surface depressions (Aquanty, 2024). In the demonstration run, a rill storage of 4 mm was assumed, which corresponds to an initial abstraction depth of 3.15 mm of water. Additional parameterization of the HGS surface domain was completed by using a Manning's roughness coefficient of 0.1, adopted from the PRZM model input.

Additional parameterization of the HGS subsurface domain was required since the PRZM model is a soil water capacitance model (i.e., a tipping bucket) and does not include hydraulic parameters used for the discretized form of Richards' equation in HGS, including saturated hydraulic conductivity and the van Genuchten (1980) parameters for variably saturated soils. Soil texture (% sand, % silt, and % clay) is provided for the FOCUS surface water scenarios and was used as an input to the Rosetta pedotransfer function model (Zhang and Schaap, 2017) to generate estimates of saturated hydraulic conductivity. Additional supplemental information provided by FOCUS for the R3 scenario included field capacity and wilting point as percentage of water content by volume and bulk density, which were used as inputs to Rosetta to produce estimates of the van Genuchten parameters.

Daily rainfall plus irrigation (as a single rainfall time series) and potential evaporation for a potato crop were specified for the R3 scenario for 6 years (1975–1980), as provided in the FOCUS meteorological forcing data. Crop growth was included in the HGS model through specification of time-varying LAI and root depth based on crop growth stages from the FOCUS R3 scenario for a potato crop. As per FOCUS (2001), the analysis year for the R3 scenario with spring PPP application was 1980, which was the final year of the simulation. In the HGS model, a third-type bottom boundary condition was used for the subsurface domain, and the surface boundary conditions were no flow on the upslope side, no flow along the two ridges, and critical depth on the downslope side, as illustrated in Figure 2.

3 Results and discussion

3.1 Verification of soil moisture-controlled irrigation

An example comparison of HGS water balance components for a 20-year simulation period (first 6 years removed as spin up) is shown for the FOCUS Châteaudun GW scenario in Figure 3 and is compared to values from the PEARL model output of Diamantopoulos et al. (2017). In addition to 648 mm of average annual precipitation, average annual irrigation simulated using HGS for Châteaudun was 204 mm, compared to 198 mm from PEARL. Average annual combined soil evaporation and plant transpiration simulated using HGS for Châteaudun was 612 mm compared to 637 mm for PEARL. The net result was an average annual bottom outflow simulated using HGS for Châteaudun of 244 mm compared to 210 mm from PEARL. Bar charts of annual water balance components for the other eight FOCUS GW scenarios are included in Supplementary Material.

Irrigation is a specified requirement for the potato test crop for five of the more southerly locations out of the nine FOCUS scenarios (Châteaudun, FR; Piacenza, IT; Porto, PT; Sevilla, ES; and Thiva, GR). Climatic variability resulted in varied crop requirements for irrigation to supplement rainfall for the five irrigated scenarios. Soil moisture-controlled irrigation results produced using HGS were compared to irrigation values from the irrigated FOCUS GW scenarios from PEARL produced by Diamantopoulos et al. (2017). Annual soil moisture-controlled irrigation simulated using HGS is biased high relative to PEARL by 54 mm on average for the ensemble of five FOCUS scenarios shown in Figure 4A and summarized in Table 3. A high degree of sensitivity was noted in the annual irrigation amounts calculated by HGS relative to the pressure head trigger used (data not shown). In HGS, the depth of irrigation water was applied based on a user-specified table of soil matric potentials. The HGS-simulated annual irrigation totals were within a similar range to irrigation amounts reported for the FOCUS scenarios modeled using PELMO, reported by European Commission (2014) (data not shown). Therefore, it was decided that further attempt to calibrate the HGS irrigation scheme to the PEARL model results was not justified. The positive bias in the HGS modeled irrigation amounts is offset by higher evaporation (41 mm on average) in the HGS results compared to PEARL, resulting in generally lower bias (5.8 mm on average) for the model bottom outflow shown in Figure 4B. Given the relatively low bias between the bottom outflow of both models, the irrigation scheme implemented in HGS appears to function sufficiently well.

3.2 Verification of PPP leaching to groundwater

HGS results for leaching to GW for four test substances in the Châteaudun GW scenario for a potato crop are compared to HYDRUS, PEARL, and PELMO results after Diamantopoulos et al. (2017) in Figure 5. Mass flux comparison plots for the other eight FOCUS GW scenarios are included in Supplementary Material.

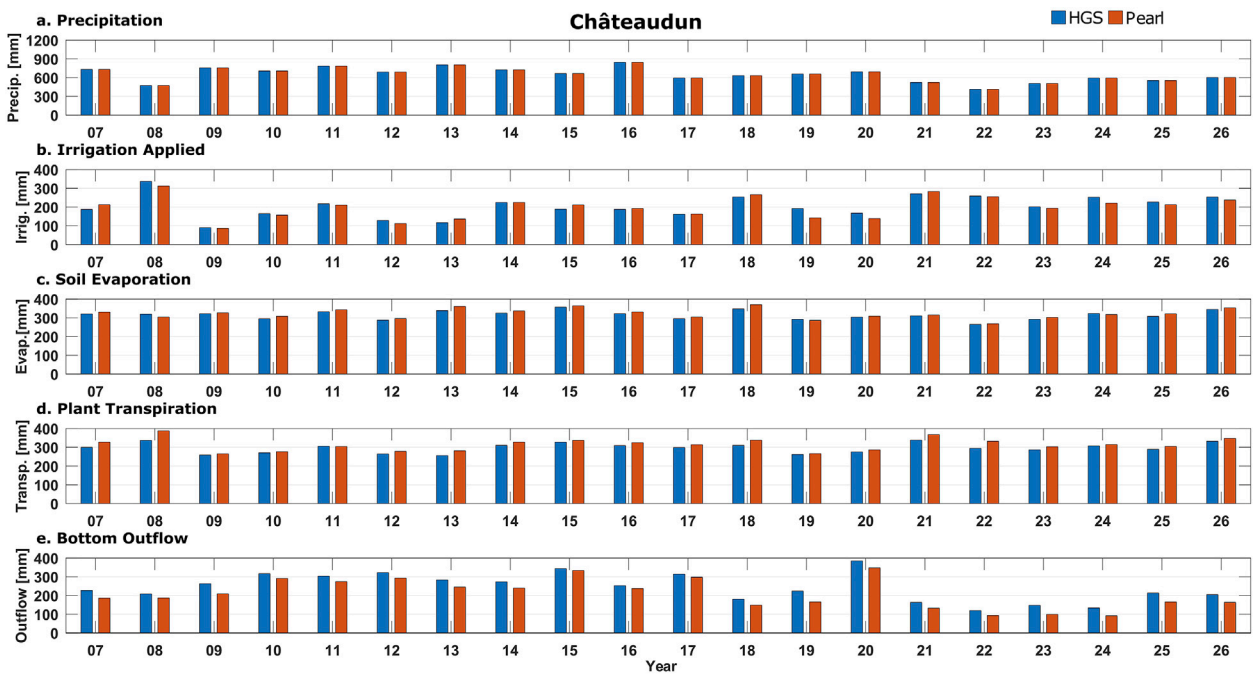

FIGURE 3
Comparison of annual water balance components between the HGS and PEARL models for a 20-year period for the FOCUS Châteaudun groundwater scenario with a potato crop: precipitation **(A)**, irrigation applied **(B)**, soil evaporation **(C)**, plant transpiration **(D)**, and bottom outflow **(E)**. PEARL model results after Diamantopoulos et al. (2017).

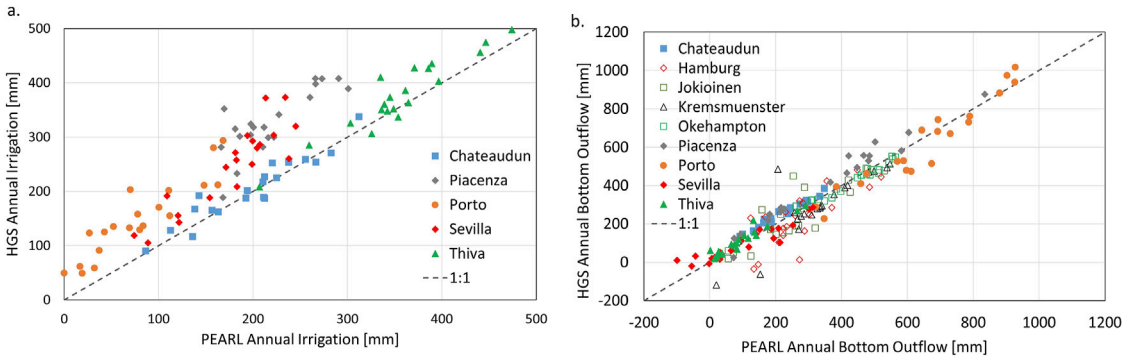

FIGURE 4
Crossplot of simulated moisture-controlled irrigation **(A)** and bottom outflow **(B)** simulated using HGS and PEARL models for the FOCUS groundwater scenarios. PEARL model results after Diamantopoulos et al. (2017). Irrigated sites are indicated with filled symbols, while non-irrigated sites have unfilled symbols.

Statistics comparing modeled annual mass leached from the four models and four test substances are given in Table 4. Crossplots of simulated annual PPP mass leached for the nine FOCUS GW scenarios are included in Supplementary Material. Of the three models' results, the PEARL results for annual mass of PPP leached to GW show the highest degree of linear correlation with HGS, Pearson correlation coefficient (R) = 0.94 to 0.96, across the four test substances, which is higher than the correlation for the two FOCUS models, PEARL vs. PELMO, which has R = 0.84 to 0.92 across the four test substances in Table 4. Additionally, the degree of spread, as quantified by the root mean squared error (RMSE), and the mean bias error (MBE) are both the lowest for HGS vs. PEARL, in comparison to HYDRUS and PELMO. Although HGS mass leaching results for some individual scenarios show higher bias relative to PEARL results compared to other scenarios, the aggregate MBE is lower in magnitude than for PEARL vs. PELMO for test substances A, B, and D but is larger for C-metabolite. Overall, the PPP fate and transport functionality of HGS, including the newly added non-linear sorption and PPP degradation as a function of temperature and soil moisture content, is satisfactorily verified against the three other models across the four test substances.

TABLE 3 Summary of statistics for the comparison of simulated water balance components for a 20-year period for HGS vs. PEARL model results for the FOCUS groundwater scenarios with a potato crop.

Statistic	HGS-PEARL			
	Irrigation	Evaporation	Transpiration	Bottom outflow
n	5	9	9	9
R	0.90	0.81	0.98	0.91
RMSE*	72	59	22	87
MBE*	54	41	−0.54	5.8

*units of mm.

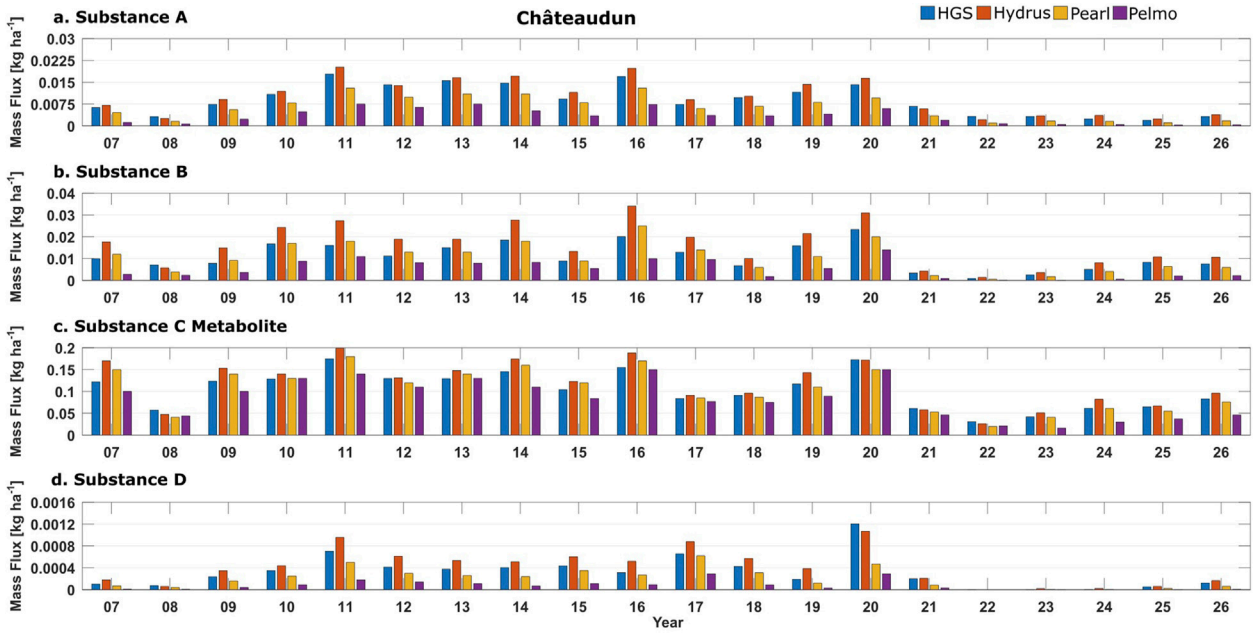

FIGURE 5
Comparison of annual PPP mass flux to groundwater for the FOCUS Châteaudun potato crop scenario simulated using HGS, HYDRUS, PEARL, and PELMO models for test substances: A **(A)**, B **(B)**, C-Metabolite **(C)**, and D **(D)**. HYDRUS, PEARL, and PELMO model results after Diamantopoulos et al. (2017).

3.3 Demonstration of PPP transport via tile drains

Due to differences in the dimensionality between HGS (3D) and MACRO (1D), the comparison of HGS results to MACRO should not be interpreted as a model verification in a strict sense; however, the comparison of tile drainage and PPP transport in HGS to the MACRO results does provide indication of the HGS model capability. As per the guidance of the FOCUS framework, mass balance analysis for PPP mass transported via tile drainage was conducted over the final 16 months of the 7-year simulation, while the preceding 6-year period was regarded as the model spin up. The inclusion of the spin-up period allows buildup of PPP residues between annual application intervals, as may be expected to occur in a repetitional agricultural setting (FOCUS, 2001). HGS and MACRO water balance results for the FOCUS SW D4 potato scenario (Skousbo, DK) for the final year of the simulation (1 May 1985 to April 30, 1986) are given in Table 5. Rainfall + irrigation applied to the two models was essentially identical. Of the remaining water balance components listed in Table 5, percolation, runoff, and storage change show differences between HGS and MACRO on the order of 1% or less when normalized by the rainfall + irrigation total. The two largest differences between the HGS and MACRO results were for AET and tile drain flow. The excess AET in the HGS model results was approximately offset by a lower tile drain flow. If this comparison is extended to the AET subcomponents, plant transpiration accounted for 87% of the difference, soil evaporation accounted for 24%, surface evaporation accounted for 0.2%, and canopy evaporation accounts for −11%. The exact reason for lower plant transpiration in the MACRO model results relative to HGS is unclear.

During the winter period with negligible evapotranspiration, tile drain flows between HGS and MACRO were very similar, as shown in Figure 6A. During summer months, the effect of higher transpiration in HGS vs. MACRO resulted in periods of low to no tile drain flow from HGS, while the MACRO flows showed high response to periods of rain + irrigation. A higher tile drain flow in MACRO during spring and summer resulted in mass flushing of Test Substance I in summer that

TABLE 4 Summary statistics for the comparison of simulated annual mass of PPP leached to groundwater for nine FOCUS groundwater scenarios for a 20-year period for HGS, HYDRUS, PEARL, and PELMO model results.

Test Substance	Statistic	HGS-HYDRUS	HGS-PEARL	HGS-PELMO	HYDRUS-PEARL	HYDRUS-PELMO	PEARL-PELMO
A	R	0.812	0.947	0.913	0.845	0.691	0.841
	RMSE*	1.95E-02	4.16E-03	5.45E-03	1.96E-02	2.21E-02	6.91E-03
	MBE*	−9.88E-03	6.87E-04	1.40E-03	1.06E-02	1.13E-02	7.17E-04
B	R	0.821	0.935	0.792	0.841	0.586	0.844
	RMSE*	3.56E-02	6.15E-03	1.07E-02	3.52E-02	4.23E-02	9.36E-03
	MBE*	−1.91E-02	−9.95E-04	2.41E-03	1.81E-02	2.15E-02	3.41E-03
C-Met.	R	0.899	0.958	0.908	0.931	0.874	0.922
	RMSE*	8.18E-02	3.89E-02	5.15E-02	5.50E-02	6.14E-02	3.47E-02
	MBE*	−5.21E-02	−2.78E-02	−3.47E-02	2.43E-02	1.74E-02	−6.91E-03
D	R	0.843	0.950	0.872	0.805	0.634	0.886
	RMSE*	3.61E-03	4.46E-04	7.85E-04	3.85E-03	4.25E-03	5.58E-04
	MBE*	−1.38E-03	1.09E-04	2.48E-04	1.49E-03	1.63E-03	1.39E-04

*units of kg ha^{-1}.

TABLE 5 Water balance components for the FOCUS surface water D4 potato scenario for HGS and MACRO model runs for analysis year: 1 May 1985 to 30 April 1986.

Model	Rainfall + irrigation (mm)	Drain flow (mm)	AET (mm)	Percolation (mm)	Runoff (mm)	Storage change (mm)
MACRO	826	310	484	27.3	12.3	6.86
HGS	827	191	616	16.2	5.83	1.76
Difference as % of R+I	0.1	14.3	−16.0	1.3	0.8	0.6

R, rainfall; I, irrigation; AET, actual evapotranspiration.

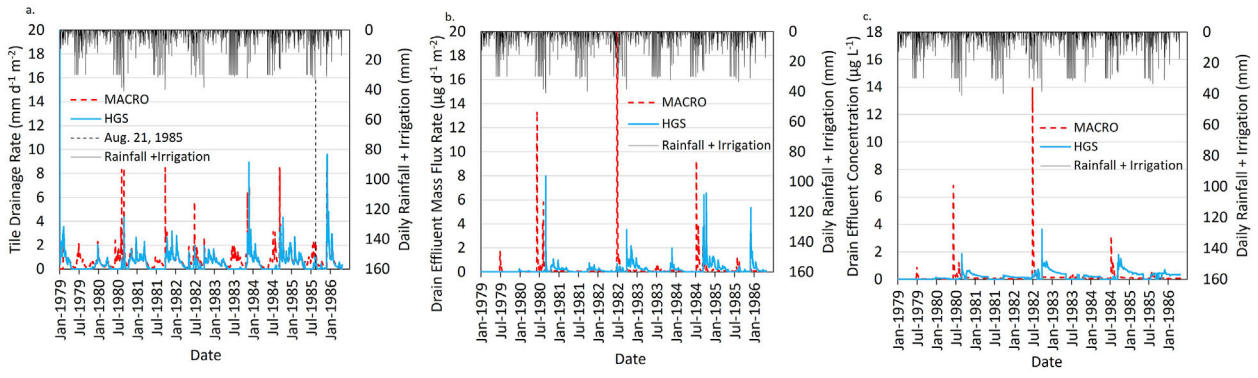

FIGURE 6
Comparison of HGS and MACRO modelling results for the FOCUS surface water D4 scenario as implemented with a potato crop: **(A)** tile drainage rate, **(B)** drain effluent mass flux rate for Test Substance I, and **(C)** tile drainage effluent Test Substance I concentration. For panel **(B)**, mass flux axis was truncated to show additional detail. The peak mass flux rate for MACRO on 29 June 1982 was 78 µg d−1 m^{-2}.

did not occur in HGS until fall. The delay of mass flushing in HGS until fall allowed additional time for degradation to reduce mass in the soil profile, thereby reducing the magnitude of the mass flux rates shown in Figure 6B, and in the peak concentrations shown in Figure 6C. Fall and winter tile drain mass flux and concentrations in the tile drain effluent were higher in HGS compared to MACRO, likely due to two processes;

TABLE 6 Mass balance comparison for Test Substance I between HGS and MACRO for the FOCUS surface water D4 potato scenario for the 16-month period: 1 January 1985 to 30 April 1986.

Model	Applied (mg/m^2)	Lost to drains (mg/m^2)	Leached (mg/m^2)	Degraded (mg/m^2)	Runoff (mg/m^2)	Storage change (mg/m^2)	Plant uptake (mg/m^2)
MACRO	300	0.0410	0.00910	298	9.76E-6	−0.0345	1.57
HGS	300	0.0120	0.00629	291	3.88E-5	−0.101	9.23
Difference as % of mass applied	1.59E-3	−0.0263	9.37E-4	−2.55	−9.67E-6	−0.0221	2.55

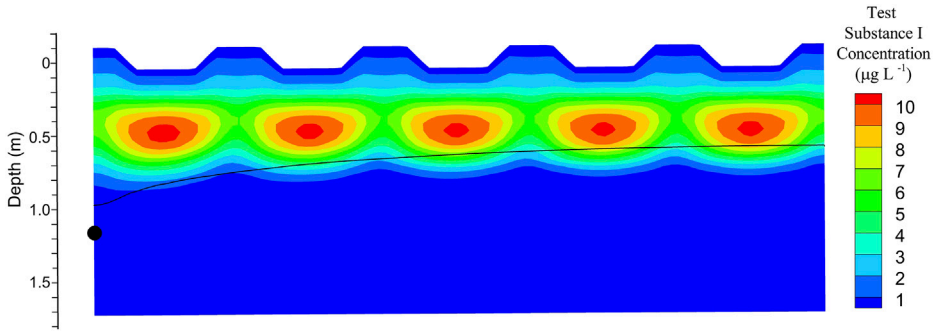

FIGURE 7
Cross section through the FOCUS surface water D4 scenario, as implemented in HGS with a potato crop, showing simulated Test Substance I concentrations within the porous media (micropore) domain in μg L^{-1} on 21 August 1985 with the water table position (black line). The tile drain position is indicated with a black circle. The depth scale is approximate.

one is the mass flushing in MACRO through summer, which depleted the soil column of mass, and the second is the delay in HGS mass flushing, which resulted in deeper penetration of Test Substance I in the soil profile below the degradation extinction depth of 0.5 m. Penetration of mass below the depth of degradation resulted in elevated mass flushing and elevated tile drain concentrations through the winter period in the HGS results.

Mass balance results for the Test Substance I for the final 16 months of the HGS and MACRO tile drainage simulations are given in Table 6. The largest differences between mass balance components between the two models are for the plant uptake and mass degraded. A higher plant uptake simulated in HGS was offset by lower degradation. Plant uptake of Test Substance I in MACRO was 83% lower than that of HGS, for the 16-month period. The lower plant uptake of Test Substance I in MACRO was at least partly attributable to the lower calculated transpiration, which was 64% lower in MACRO than in HGS. The remainder of the difference in plant uptake between the two models may be a result of differences between the models with respect to the domain (matrix or macropore), from where transpiration water is drawn. In HGS, transpiration water is drawn exclusively from the matrix domain (Aquanty, 2024), while in MACRO, at least part of the transpiration stream is drawn from the macropore domain (Larsbo and Jarvis, 2003). The dynamics of Test Substance I concentrations in the MACRO macropore domain would be expected to be more variable than in the soil matrix, thereby introducing a potential difference between the two models' results.

For the D4 potato scenario, Test Substance I was applied uniformly across the top of the HGS model. A cross section of Test Substance I concentrations is plotted in Figure 7 for the date of the summer high-flow event on 21 August 1985. It is notable that the higher Test Substance I concentrations occurred below the bottoms of the furrows, compared to below the ridges, at approximately 0.5-m depth, which is the depth below which no further degradation occurs in the model. This sequence of high and low concentrations laterally across the model demonstrates the effect of the interaction of the 2D flow field developed below the ridge and furrow microtopography. Higher infiltration rates occurred below the furrows, akin to the mechanism of depression-focused recharge (Berthold et al., 2004; Wiebe et al., 2023) but on a smaller scale. The increased rate of flow below the furrows transported PPP mass deeper than under the ridges. Since degradation was specified in the model to decrease with depth, less mass is degraded below the furrows than below the ridges. These higher Test Substance I residual concentrations below the furrows demonstrate that PPP application directly to the potato ridges could reduce mass leaching to depth and into the tile drains. Precision application of PPPs shows potential to reduce losses to the water environment (GW or SW) by targeting application to a smaller footprint, such as to individual plants or rows of plants (Zanin et al., 2022). Thereby, less PPP is applied where it is not readily effective. Precision PPP application is increasing in practice (Anastasiou et al., 2023), and thereby, the need for fate and transport models to simulate PPP application scenarios that are fundamentally 2D or 3D in geometry can also be expected to increase for exposure assessments.

TABLE 7 Water balance components for the FOCUS surface water R3 potato scenario for HGS and PRZM models for 1980.

Model	Rainfall + irrigation (mm)	PET (mm)	AET (mm)	Percolation (mm)	Runoff (mm)	Storage change (mm)
PRZM	934	739	635	189	110	−0.4
HGS	933	739	545	169	231	−13
Difference as % of R+I	−0.1	0.0	−9.6	−2.1	13.0	−1.3

R, rainfall; I, irrigation; PET, potential evapotranspiration; AET, actual evapotranspiration.

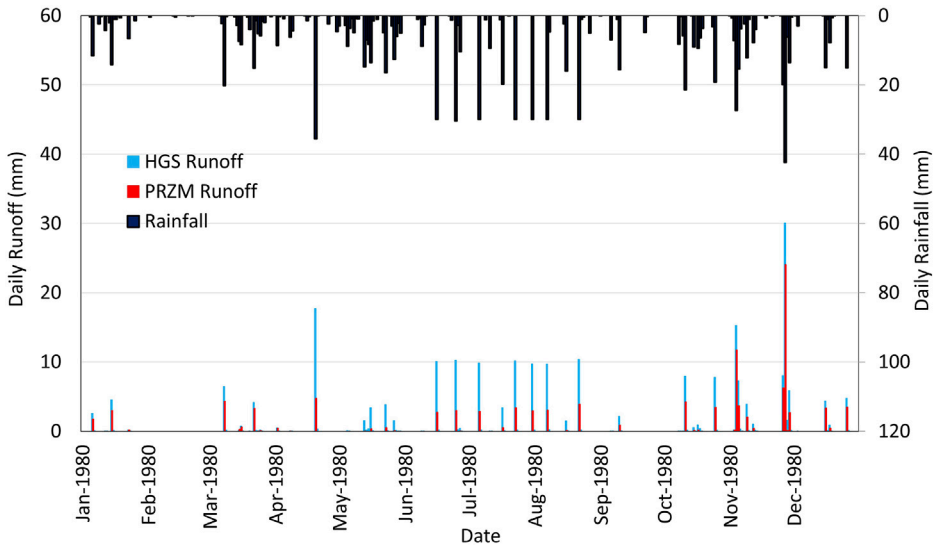

FIGURE 8
Daily runoff simulated by HGS and PRZM for the FOCUS surface water R3 potato scenario with a potato crop for the analysis year 1980.

3.4 Demonstration of surface runoff generation

Surface runoff generated in HGS was compared to runoff generated using the PRZM model for the FOCUS SW R3 scenario with a potato crop (Bologna, IT). Runoff is generated in HGS as either infiltration or saturation excess runoff, depending on soil moisture and variably saturated hydraulic conductivity at the time of a rainfall event. For the PRZM model, runoff behavior is a function of general field conditions, namely, land use, cover treatment, hydrologic condition, and hydraulic soil group, with modifications made to the CN based on the antecedent soil moisture condition prior to rainfall (Suarez, 2005; Young and Fry, 2020). Insights into the differences in runoff generated between HGS and PRZM can be gleaned from examination of the major water balance components for the R3 scenario, for the 1980 analysis year in Table 7. The parameterization scheme for soil hydraulic parameters used in HGS (saturated hydraulic conductivity and the variably saturated hydraulic parameters of the van Genuchten (1980) formulation) resulted in similar annual percolation rates of 189 mm and 169 mm for PRZM and HGS, respectively. The largest difference in the subsurface water balance occurred in AET, calculated in HGS as 545 mm, compared to 635 mm in PRZM. The ET parameters used in the HGS R3 scenario were adopted directly from the HGS models used for the FOCUS GW scenarios. Minor differences in annual water storage between HGS and PRZM were observed, which is to be expected, given the difference in model flow formulation between the Richards' equation-based HGS model and the soil water capacitance-based PRZM model. The net effect on the annual water balance was that for the 1980 analysis year, HGS produced a higher simulated runoff of 231 mm compared to 110 mm for PRZM, a difference of 121 mm, 90 mm of which was attributed to lower modeled AET in the HGS model. The daily PET time series input to both models was equal to the pan evaporation multiplied by a pan factor of 0.9, with annual PET for 1980 of 739 mm, given in Table 7. No attempt was made to adjust the PET input to HGS.

The PRZM AET formulation is soil moisture-based (Suarez, 2005; Young and Fry, 2020) not matric potential-based, as used in HGS (Aquanty, 2024). PRZM does not parameterize a matric potential-based root water uptake function, such as that of Feddes et al. (1978), commonly implemented in Richards' equation-based models such as HGS (Aquanty, 2024), HYDRUS (Šimůnek et al., 2012), and PEARL (Leistra et al., 2001). Therefore, given the differences in flow and AET formulations between PRZM and HGS, it is not surprising that the calculated AET values are substantially different between them. The verification of transpiration values calculated with HGS against the HYDRUS

and PEARL models (Table 3) lends credence to the robustness of the AET formulation used in HGS. Therefore, if AET calculated in HGS was biased low and runoff was biased high relative to PRZM, it is likely that the ET formulation in PRZM was the source of the discrepancy and not the AET calculation within HGS. This relatively large difference in runoff generated between the tipping bucket-style model (PRZM) and the Richards' equation-based model with Feddes' root water uptake function (HGS) highlights the benefits of calculating infiltration and runoff using a single physics-based model, such as HGS. The use of multiple hydrologic models with different numerical formulations to calculate PPP leaching to GW and PPP transport in runoff can lead to discrepancies in the major water balance components, which then contribute to differences in solute mass partitioning to GW and SW pathways. A hydrologic model cannot reasonably be expected to capture surface–subsurface interactions that are not adequately included in its model formulation (Ebel and Loague, 2006). Therefore, there exists a strong use-case for the unification of PPP fate and transport to GW and SW within a single modeling platform to avoid misallocation of PPP mass to GW or SW or vice versa.

The frequency of runoff events was nearly identical between HGS and PRZM, shown in Figure 8, resulting from a close match between depression storage modeled in HGS and the initial abstraction term in PRZM. Differences in the runoff magnitude between the HGS and PRZM models show some seasonal trends. Differences were generally smaller outside of the growing season, reflecting less of an influence of the discrepancy between AET calculated by the two models.

4 Conclusion and future work

New irrigation, soil adsorption, and chemical degradation functionality were added to the HGS 3D fully integrated, surface–subsurface hydrological model. The added functionality has been verified for simulated leaching of PPPs to GW for a suite of four test substances using nine geographically based scenarios across the EU from the FOCUS GW framework (European Commission, 2014). HGS model functionality for PPP transport to SW has been demonstrated using two FOCUS (2001) SW scenarios: one for tile drainage and one for runoff generation. HGS results for a 2D cross-sectional dual permeability model produced reasonable tile drain flows, mass fluxes, and concentrations compared to the MACRO model. Runoff generation in HGS was demonstrated through comparison to the PRZM model, which highlighted the role that subsurface hydrologic conditions play in the generation of runoff, along with the calculation of AET.

Fate and transport modeling of PPP leaching to GW, SW via tile drainage, or transport via runoff is commonly simulated with multiple 1D models, each representing a separate exposure pathway. Inherently dependent hydrological processes such as deep percolation to GW, tile drainage, and surface runoff can be simulated in a single 3D, fully integrated, surface–subsurface HGS model while maintaining water and solute mass balance closure. One-dimensional models, as commonly used for exposure assessments, are also not capable of evaluating complex 2D or 3D PPP application geometries or the effects of multidimensional flow on subsurface PPP concentrations. PPP exposure assessment for GW and SW via the tile drainage pathway can now be extended from the use of uncoupled 1D models to the 3D, fully integrated HGS model, with a goal of reducing total mass of PPP in the water environment through precision application. Thus, HGS models can demonstrate that PPP effectiveness is maintained, while environmental risks to GW and SW are decreased. Recognition of the potential role for 3D PPP fate and transport modeling in the regulatory area has long been present (European Commission, 2014). However, noted lack of modeling technology has limited application of 3D models as potential exposure assessment tools. The verification of HGS for PPP fate and transport modeling against existing models should serve to increase the confidence for the use of HGS in a regulatory context. The implications of this verification of the reactive transport functionality of HGS for PPP fate and transport in soil and GW are not limited to the simulation of PPPs. HGS can be applied to other chemicals of concern with reactive transport properties compatible with the new HGS formulations for chemical adsorption and degradation.

Current limitations in the functionality of HGS to simulate PPP fate and transport relative to the FOCUS GW and SW models include a lack of vapor phase and sediment transport. For the current suite of FOCUS test substances used to verify HGS results for leaching of PPPs to GW, the lack of vapor phase transport did not appear to appreciably affect the HGS results. Future work should investigate the potential implications of vapor phase transport on environmental concentrations of PPPs in GW or SW. The robust physics of subsurface flow and runoff generation and verified PPP fate processes paves the way for continued development of HGS functionality, such as the incorporation of PPP subsurface partitioning to surface runoff and transport of PPPs adhered to eroded sediment.

Data availability statement

The datasets presented in this study can be found in online repositories. The names of the repository/repositories and accession number(s) can be found at: https://zenodo.org/records/13119195.

Author contributions

MC: conceptualization, data curation, formal analysis, investigation, methodology, validation, visualization, writing–original draft, and writing–review and editing. SF: conceptualization, data curation, formal analysis, funding acquisition, investigation, methodology, project administration, validation, visualization, and writing–review and editing. KM: methodology, software, and writing–review and editing. H-TH: methodology, software, and writing–review and editing. RZ: conceptualization, funding acquisition, project administration, and writing–review and editing. KH: conceptualization, funding acquisition, project administration, and writing–review and editing. SB: conceptualization, project administration, and writing–review and editing. ES: conceptualization and writing–review and editing.

Funding

The author(s) declare that financial support was received for the research, authorship, and/or publication of this article. This study, including publishing, was financially supported by Bayer AG, who helped develop the scope of the research and provided valuable feedback on preparation of the manuscript.

Acknowledgments

The authors express their appreciation to Diamantopoulos et al. (2017) who graciously shared their HYDRUS, PEARL, and PELMO modeling results with the authors.

Conflict of interest

Authors MC, SF, KM, H-TH, SB, and ES were employed by Aquanty Inc. Authors RZ and KH were employed by Bayer AG.

Generative AI statement

The author(s) declare that no Generative AI was used in the creation of this manuscript.

Publisher's note

All claims expressed in this article are solely those of the authors and do not necessarily represent those of their affiliated organizations, or those of the publisher, the editors, and the reviewers. Any product that may be evaluated in this article, or claim that may be made by its manufacturer, is not guaranteed or endorsed by the publisher.

Supplementary material

The Supplementary Material for this article can be found online at: https://www.frontiersin.org/articles/10.3389/fenvs.2024.1505480/full#supplementary-material

References

Allen, R. G., Pereira, L. S., Raes, D., and Smith, M. (1998). "Crop evapotranspiration: guidelines for computing crop water requirements," in *FAO irrigation and drainage paper 56* (Rome, Italy: Food and Agriculture Organization of the United Nations).

Amado, A. A., Politano, M., Schilling, K., and Weber, L. (2016). Investigating hydrologic connectivity of a drained prairie pothole region wetland complex using a fully integrated, physically-based model. *Wetlands* 38, 233–245. doi:10.1007/s13157-016-0800-5

Anastasiou, E., Fountas, S., Voulgaraki, M., Psiroukis, V., Koutsiaras, M., Kriezi, O., et al. (2023). Precision farming technologies for crop protection: a meta-analysis. *Smart Agric. Technol.* 5, 100323. doi:10.1016/j.atech.2023.100323

Anlauf, R., Schaefer, J., and Kajitvichyanukul, P. (2018). Coupling HYDRUS-1D with ArcGIS to estimate pesticide accumulation and leaching risk on a regional basis. *J. Environ. Manag.* 217, 980–990. doi:10.1016/j.jenvman.2018.03.099

Appels, W. M., Bogaart, P. W., and van der Zee, S. E. A. T. M. (2016). Surface runoff in flat terrain: how field topography and runoff generating processes control hydrological connectivity. *J. Hydrology* 534, 493–504. doi:10.1016/j.jhydrol.2016.01.021

Aquanty (2024). *HydroGeoSphere theory manual*. Waterloo, ON, Canada: Version 2653. Available at: https://aquanty-artifacts-public.s3.amazonaws.com/hgs/hydrosphere_theory.pdf (Accessed March 8, 2024).

Barthel, R., and Banzhaf, S. (2016). Groundwater and surface water interaction at the regional-scale – a review with focus on regional integrated models. *Water Resour. Manage* 30, 1–32. doi:10.1007/s11269-015-1163-z

Berg, F. van den, Beltman, W. H. J., Adriaanse, P. I., de Jong, A., and te Roller, J. A. (2015). *SWASH manual 5.3, user's guide version 5. The statutory research tasks unit for nature and the environment*. Wageningen, Netherlands: WOT Natuur and Milieu, 58. WOT-technical report 36. Available at: https://edepot.wur.nl/352934

Berg, F. van den, Tiktak, A., van Kraalingen, D. W. G., and Boesten, J. J. T. I. (2019). *User manual for FOCUSPEARL version 5.5.5. The statutory research tasks unit for nature and the environment*. Wageningen, Netherlands: WOT Natuur and Milieu, 76. WOT-technical report 164.

Berthold, S., Bentley, L. R., and Hayashi, M. (2004). Integrated hydrogeological and geophysical study of depression-focused groundwater recharge in the Canadian prairies. *Water Resour. Res.* 40. doi:10.1029/2003WR002982

Bexfield, L. M., Belitz, K., Lindsey, B. D., Toccalino, P. L., and Nowell, L. H. (2021). Pesticides and pesticide degradates in groundwater used for public supply across the United States: occurrence and human-health context. *Environ. Sci. Technol.* 55, 362–372. doi:10.1021/acs.est.0c05793

Boico, V. F., Therrien, R., Fleckenstein, J. H., Nogueira, G., Iversen, B. V., and Petersen, R. J. (2023). 3D surface–subsurface modeling of a bromide tracer test in a macroporous tile-drained field: improvements and limitations. *Soil Sci. Soc Amer J* 87, 462–484. doi:10.1002/saj2.20537

Boivin, A., Šimůnek, J., Schiavon, M., and Van Genuchten, M.T. (2006). Comparison of pesticide transport processes in three tile-drained field soils using HYDRUS-2D. *Vadose Zone J.* 5, 838–849. doi:10.2136/vzj2005.0089

Bresinsky, L., Kordilla, J., Engelhardt, I., Livshitz, Y., and Sauter, M. (2023). Variably saturated dual-permeability flow modeling to assess distributed infiltration and vadose storage dynamics of a karst aquifer – the Western Mountain Aquifer in Israel and the West Bank. *J. Hydrology X* 18, 100143. doi:10.1016/j.hydroa.2022.100143

Briggs, G. G., Bromilow, R. H., and Evans, A. A. (1982). Relationships between lipophilicity and root uptake and translocation of non-ionised chemicals by barley. *Pestic. Sci.* 13, 495–504. doi:10.1002/ps.2780130506

Brunner, P., and Simmons, C. T. (2012). HydroGeoSphere: a fully integrated, physically based hydrological model. *Groundwater* 50, 170–176. doi:10.1111/j.1745-6584.2011.00882.x

Chen, X., Yu, Z., Yi, P., Aldahan, A., Hwang, H.-T., and Sudicky, E. A. (2023). Disentangling runoff generation mechanisms: combining isotope tracing with integrated surface/subsurface simulation. *J. Hydrology* 617, 129149. doi:10.1016/j.jhydrol.2023.129149

Cheviron, B., and Coquet, Y. (2009). Sensitivity analysis of transient-MIM HYDRUS-1D: case study related to pesticide fate in soils. *Vadose Zone J.* 8, 1064–1079. doi:10.2136/vzj2009.0023

Convention on Biological Diversity (CBD) (2022). "Kunming-montreal global biodiversity framework," in Decision Adopted by the Conference of the Parties to the Convention of Biological Diversity. Fifteenth meeting – Part II, Montreal, Canada. Available at: https://www.cbd.int/doc/decisions/cop-15/cop-15-dec-04-en.pdf (Accessed December 19, 2022).

De Schepper, G., Therrien, R., Refsgaard, J. C., and Hansen, A. L. (2015). Simulating coupled surface and subsurface water flow in a tile-drained agricultural catchment. *J. Hydrology* 521, 374–388. doi:10.1016/j.jhydrol.2014.12.035

De Schepper, G., Therrien, R., Refsgaard, J. C., He, X., Kjaergaard, C., and Iversen, B. V. (2017). Simulating seasonal variations of tile drainage discharge in an agricultural catchment. *Water Resour. Res.* 53, 3896–3920. doi:10.1002/2016WR020209

Diamantopoulos, E., Šimůnek, J., Oberdörster, C., Hammel, K., Jene, B., Schröder, T., et al. (2017). Assessing the potential exposure of groundwater to pesticides: a model comparison. *Vadose Zone J.* 16, 1–13. doi:10.2136/vzj2017.04.0070

Ebel, B. A., and Loague, K. (2006). Physics-based hydrologic-response simulation: seeing through the fog of equifinality. *Hydrol. Process.* 20, 2887–2900. doi:10.1002/hyp.6388

European Commission (EC) (2014). Assessing potential for movement of active substances and their metabolites to ground water in the EU. *Rep. FOCUS Ground Water Work Group, EC Document Reference Sanco/13144/2010 Version 3*, 613. Available at: https://esdac.jrc.ec.europa.eu/public_path/projects_data/focus/gw/NewDocs/focusGWReportOct2014.pdf

European Commission (EC) (2024). *SWASH (website)*. Brussels, Belgium: Joint Research Centre, European Soil Data Centre. Available at: https://esdac.jrc.ec.europa.eu/projects/swash (Accessed March 1, 2024).

Eurostat (2022). "Pesticide sales,". Luxembourg: European Commission. Available at: https://ec.europa.eu/eurostat/databrowser/view/aei_fm_salpest09/default/table?lang=en (Accessed on February 23, 2024).

Feddes, R. A., Kowalik, P. J., and Zaradny, H. (1978). *Simulation of field water use and crop yield*. Wiley, 188.

FOCUS (1997). Surface water models and EU registration of plant protection products. Final report of the work of the regulatory modelling working group on surface water models of FOCUS. *Eur. Comm. Doc. 6476/VI/96*. Available at: https://esdac.jrc.ec.europa.eu/public_path/projects_data/focus/docs/sw_en_6476VI96_24Feb1997.pdf.

FOCUS (2000). FOCUS groundwater scenarios in the EU review of active substances. Report of the FOCUS Groundwater Scenarios Working Group. *EC Doc. Ref. Sanco/321/2000 rev.2*, 202pp. Available at: https://esdac.jrc.ec.europa.eu/public_path/projects_data/focus/gw/docs/Generic_guidance_forV1_1.pdf

FOCUS (2001). FOCUS surface water scenarios in the EU evaluation process under 91/414/EEC. Report of the FOCUS working group on surface water scenarios. *EC Doc. Ref. SANCO/4802/2001-rev.2 Version 1.4 (May 2015)*. Available at: https://esdac.jrc.ec.europa.eu/public_path/projects_data/focus/sw/docs/Generic%20FOCUS_SWS_vc1.4.pdf (Accessed on May, 2015).

Frei, S., Knorr, K. H., Peiffer, S., and Fleckenstein, J. H. (2012). Surface micro-topography causes hot spots of biogeochemical activity in wetland systems: a virtual modeling experiment. *J. Geophys. Res.* 117. doi:10.1029/2012JG002012

Frey, S. K., Hwang, H.-T., Park, Y.-J., Hussain, S. I., Gottschall, N., Edwards, M., et al. (2016). Dual permeability modeling of tile drain management influences on hydrologic and nutrient transport characteristics in macroporous soil. *J. Hydrology* 535, 392–406. doi:10.1016/j.jhydrol.2016.01.073

Frey, S. K., Miller, K., Khader, O., Taylor, A., Morrison, D., Xu, X., et al. (2021). Evaluating landscape influences on hydrologic behavior with a fully-integrated groundwater – surface water model. *J. Hydrology* 602, 126758. doi:10.1016/j.jhydrol.2021.126758

Frey, S. K., Rudolph, D. L., Lapen, D. R., and Ball Coelho, B. R. (2012). Viscosity dependent dual-permeability modeling of liquid manure movement in layered, macroporous, tile drained soil. *Water Resour. Res.* 48. doi:10.1029/2011WR010809

Garen, D. C., and Moore, D. S. (2005). Curve number hydrology in water quality modelling: uses, abuses and future directions. *J. Am. Water Resour. Assoc.* 41, 377–388. doi:10.1111/j.1752-1688.2005.tb03742.x

Gassmann, M. (2021). Modelling the fate of pesticide transformation products from plot to catchment scale — state of knowledge and future challenges. *Front. Environ. Sci.* 9, 717738. doi:10.3389/fenvs.2021.717738

Gatel, L., Lauvernet, C., Carluer, N., Weill, S., Tournebize, J., and Paniconi, C. (2019). Global evaluation and sensitivity analysis of a physically based flow and reactive transport model on a laboratory experiment. *Environ. Model. and Softw.* 113, 73–83. doi:10.1016/j.envsoft.2018.12.006

Gerke, H. H., Dusek, J., and Vogel, T. (2013). Solute mass transfer effects in two-dimensional dual-permeability modeling of bromide leaching from a tile-drained field. *Vadose Zone J.* 12, 1–21. doi:10.2136/vzj2012.0091

Gerke, H. H., and Van Genuchten, M. T. (1993). A dual-porosity model for simulating the preferential movement of water and solutes in structured porous media. *Water Resour. Res.* 29, 305–319. doi:10.1029/92WR02339

Germann, P. F. (1985). Kinematic wave approach to infiltration and drainage into and from soil macropores. *Trans. ASAE* 28, 745–0749. doi:10.13031/2013.32331

Gong, C., Cook, P. G., Therrien, R., Wang, W., and Brunner, P. (2023). On groundwater recharge in variably saturated subsurface flow models. *Water Resour. Res.* 59, e2023WR034920. doi:10.1029/2023WR034920

Hintze, S., Glauser, G., and Hunkeler, D. (2020). Influence of surface water – groundwater interactions on the spatial distribution of pesticide metabolites in groundwater. *Sci. Total Environ.* 733, 139109. doi:10.1016/j.scitotenv.2020.139109

Holmes, K. J., Graham, J. A., McKone, T., and Whipple, C. (2009). Regulatory models and the environment: practice, pitfalls, and prospects. *Risk Anal.* 29, 159–170. doi:10.1111/j.1539-6924.2008.01186.x

Hwang, H.-T., Park, Y.-J., Frey, S. K., Callaghan, M. V., Berg, S. J., Lapen, D. R., et al. (2019). Efficient numerical incorporation of water management operations in integrated hydrosystem models: application to tile drainage and reservoir operating systems. *J. Hydrology* 575, 1253–1266. doi:10.1016/j.jhydrol.2019.03.098

Hwang, H.-T., Park, Y.-J., Sudicky, E. A., and Forsyth, P. A. (2014). A parallel computational framework to solve flow and transport in integrated surface–subsurface hydrologic systems. *Environ. Model. and Softw.* 61, 39–58. doi:10.1016/j.envsoft.2014.06.024

Jorda, H., Huber, K., Kunkel, A., Vanderborght, J., Javaux, M., Oberdörster, C., et al. (2021). Mechanistic modeling of pesticide uptake with a 3D plant architecture model. *Environ. Sci. Pollut. Res.* 28, 55678–55689. doi:10.1007/s11356-021-14878-3

Kladivko, E. J., Brown, L. C., and Baker, J. L. (2001). Pesticide transport to subsurface tile drains in humid regions of North America. *Crit. Rev. Environ. Sci. Technol.* 31, 1–62. doi:10.1080/20016491089163

Klein, M. (2020). "PELMO (pesticide leaching model), user manual. Version 5.00," in *Fraunhofer institute for molecular biology and applied Ecology*. Germany: Schmallenberg.

Koch, J., Cornelissen, T., Fang, Z., Bogena, H., Diekkrüger, B., Kollet, S., et al. (2016). Inter-comparison of three distributed hydrological models with respect to seasonal variability of soil moisture patterns at a small forested catchment. *J. Hydrology* 533, 234–249. doi:10.1016/j.jhydrol.2015.12.002

Köhne, J. M., Köhne, S., and Šimůnek, J., 2009. A review of model applications for structured soils: b Pesticide transport. *Journal of Contaminant Hydrology* 104, 36–60. doi:10.1016/j.jconhyd.2008.10.003

Kollet, S., Sulis, M., Maxwell, R. M., Paniconi, C., Putti, M., Bertoldi, G., et al. (2017). The integrated hydrologic model intercomparison project, IH-MIP2: a second set of benchmark results to diagnose integrated hydrology and feedbacks. *Water Resour. Res.* 53, 867–890. doi:10.1002/2016WR019191

Kristensen, K. J., and Jensen, S. E. (1975). A model for estimating actual evapotranspiration from potential evapotranspiration. *Hydrol. Res.* 6, 170–188. doi:10.2166/nh.1975.0012

Kurtz, W., Lapin, A., Schilling, O. S., Tang, Q., Schiller, E., Braun, T., et al. (2017). Integrating hydrological modelling, data assimilation and cloud computing for real-time management of water resources. *Environ. Model. and Softw.* 93, 418–435. doi:10.1016/j.envsoft.2017.03.011

Larsbo, M., and Jarvis, N. (2003). *MACRO 5.0. A model of water flow and solute transport in microporous soil, Technical Description*. Emergo: Swedish University of Agricultural Sciences, Department of Soil Sciences, Division of Environmental Physics. 6 Report.

Leeds-Harrison, P. B., Shipway, C. J. P., Jarvis, N. J., and Youngs, E. G. (1986). The influence of soil macroporosity on water retention, transmission and drainage in a clay soil. *Soil Use Manag.* 2, 47–50. doi:10.1111/j.1475-2743.1986.tb00678.x

Leistra, M., van der Linden, A. M. A., Boesten, J. J. T. I., Tiktak, A., and Berg, F. van den. (2001). PEARL model for pesticide behaviour and emissions in soil-plant system: description of the processes in FOCUS PEARL v 1.1.1. Bilthoven, National Institute of Public Health and the Environment. *Wageningen, Alterra, Green World Res. RIVM Rep. 711401009/Alterra-rapport 013*, 116. Available at: https://edepot.wur.nl/26563

Lutz, S. R., Van Meerveld, H. J., Waterloo, M. J., Broers, H. P., and Van Breukelen, B. M. (2013). A model-based assessment of the potential use of compound-specific stable isotope analysis in river monitoring of diffuse pesticide pollution. *Hydrol. Earth Syst. Sci.* 17, 4505–4524. doi:10.5194/hess-17-4505-2013

Maino, J. L., Thia, J., Hoffmann, A. A., and Umina, P. A. (2023). Estimating rates of pesticide usage from trends in herbicide, insecticide, and fungicide product registrations. *Crop Prot.* 163, 106125. doi:10.1016/j.cropro.2022.106125

Maxwell, R. M., Putti, M., Meyerhoff, S., Delfs, J., Ferguson, I. M., Ivanov, V., et al. (2014). Surface-subsurface model intercomparison: a first set of benchmark results to diagnose integrated hydrology and feedbacks. *Water Resour. Res.* 50, 1531–1549. doi:10.1002/2013WR013725

Natural Resources Conservation Service (NRCS) (2004). *National engineering handbook Part 630: hydrology, chapter 10: estimation of direct runoff from storm rainfall*. Washington DC: Natural Resources Conservation Service, United States Department of Agriculture.

Paldor, A., Stark, N., Florence, M., Raubenheimer, B., Elgar, S., Housego, R., et al. (2022). Coastal topography and hydrogeology control critical groundwater gradients and potential beach surface instability during storm surges. *Hydrol. Earth Syst. Sci.* 26, 5987–6002. doi:10.5194/hess-26-5987-2022

Park, J. Y., Ruidisch, M., and Huwe, B. (2016). Transport of sulfonamide antibiotics in crop fields during monsoon season. *Environ. Sci. Pollut. Res.* 23, 22980–22992. doi:10.1007/s11356-016-7465-8

Pest Management Regulatory Agency (2023). *Pest control product sales report for 2021*. Ottawa, ON: Health Canada. Available at: https://www.canada.ca/en/health-canada/services/consumer-product-safety/reports-publications/pesticides-pest-management/corporate-plans-reports/pest-control-products-sales-report.html.

Pietrzak, D. (2021). Modeling migration of organic pollutants in groundwater — review of available software. *Environ. Model. and Softw.* 144, 105145. doi:10.1016/j.envsoft.2021.105145

Schilling, O. S., Park, Y., Therrien, R., and Nagare, R. M. (2019). Integrated surface and subsurface hydrological modeling with snowmelt and pore water freeze–thaw. *Groundwater* 57, 63–74. doi:10.1111/gwat.12841

Schock, C. C., Wang, F., Flock, R., Eldredge, E., Pereira, A., and Klauzer, J. (2013). "Drip irrigation guide for potatoes," in *Sustainable agriculture techniques*. Corvallis, OR: Oregon State University. Extension Service. EM 8912, Revised Jan. 2013.

Shattuck, A., Werner, M., Mempel, F., Dunivin, Z., and Galt, R. (2023). Global pesticide use and trade database (GloPUT): new estimates show pesticide use trends in low-income countries substantially underestimated. *Glob. Environ. Change* 81, 102693. doi:10.1016/j.gloenvcha.2023.102693

Silburn, D. M. (2023). Pesticide extraction from soil into runoff under a rainfall simulator. *Soil Res.* 61, 468–483. doi:10.1071/SR22115

Šimůnek, J., van Genuchten, M.T., and Šejna, M. (2012). *The HYDRUS software package for simulating two- and three-dimensional movement of water, heat, and multiple solutes in variably-saturated porous media. Technical manual, Version 2.0*. Prague, Czech Republic: PC Progress.

Sittig, S., Sur, R., Baets, D., and Hammel, K. (2020). Consideration of risk management practices in regulatory risk assessments: evaluation of field trials with

micro-dams to reduce pesticide transport via surface runoff and soil erosion. *Environ. Sci. Eur.* 32, 86. doi:10.1186/s12302-020-00362-1

Squillace, P. J., Scott, J. C., Moran, M. J., Nolan, B. T., and Kolpin, D. W. (2002). VOCs, pesticides, nitrate, and their mixtures in groundwater used for drinking water in the United States. *Environ. Sci. Technol.* 36, 1923–1930. doi:10.1021/es015591n

Steidl, J., Gliege, S., Semiromi, M. T., and Lischeid, G. (2023). Groundwater flow reversal between small water bodies and their adjoining aquifers: a numerical experiment. *Hydrol. Process.* 37, e14890. doi:10.1002/hyp.14890

Suarez, L. A. (2005). *PRZM-3, A model for predicting pesticide and nitrogen fate in the crop root zone and unsaturated zones: user manual for release 3.12.2. National exposure research laboratory*. Athens, GA: U.S. Environmental Protection Agency.

Therrien, R., and Sudicky, E. A. (1996). Three-dimensional analysis of variably-saturated flow and solute transport in discretely-fractured porous media. *J. Contam. Hydrology* 23, 1–44. doi:10.1016/0169-7722(95)00088-7

United Nations General Assembly (UNGA) (2015). "Transforming our world: the 2030 agenda for sustainable development," in *Resolution adopted by the general assembly. Seventieth session*. New York, USA. Available at: https://documents.un.org/doc/undoc/gen/n15/291/89/pdf/n1529189.pdf (Accessed October 21, 2015).

United States Department of Agriculture (USDA) (1975). "Soil taxonomy. A basic system of soil classification for making and interpreting soil surveys," in *Agriculture handbook no. 436. Soil conservation Service* (Washington DC: USDA).

United States Environmental Protection Agency (USEPA) (2023). Models for pesticide risk assessment. Available at: https://www.epa.gov/pesticide-science-and-assessing-pesticide-risks/models-pesticide-risk-assessment#aquatic (Accessed April 11, 2024).

van Genuchten, M. T. (1980). A closed-form equation for predicting the hydraulic conductivity of unsaturated soils. *Soil Sci. Soc. Am. J.* 44 (5), 892–898. doi:10.2136/sssaj1980.03615995004400050002x

Walker, A. (1974). A simulation model for prediction of herbicide persistence. *J. Environ. Qual.* 3, 396–401. doi:10.2134/jeq1974.00472425000300040021x

Wiebe, A. J., Menkveld, P. G., and Rudolph, D. L. (2023). Quantifying seasonal, depression focused recharge in the context of public supply well vulnerability. *Hydrol. Process.* 37, e14938. doi:10.1002/hyp.14938

Young, D. F., and Fry, M. M. (2019). Field-scale evaluation of pesticide uptake into runoff using a mixing cell and a non-uniform uptake model. *Environ. Model. and Softw.* 122, 104055. doi:10.1016/j.envsoft.2017.09.007

Young, D. F., and Fry, M. M. (2020). "PRZM5, A model for predicting pesticides in runoff, erosion, and leachate," in *Rev. B. Office of pesticide programs*. Washington DC: U.S. Environmental Protection Agency.

Zanin, A. R. A., Neves, D. C., Teodoro, L. P. R., Da Silva Júnior, C. A., Da Silva, S. P., Teodoro, P. E., et al. (2022). Reduction of pesticide application via real-time precision spraying. *Sci. Rep.* 12, 5638. doi:10.1038/s41598-022-09607-w

Zhang, Y., and Schaap, M. G. (2017). Weighted recalibration of the Rosetta pedotransfer model with improved estimates of hydraulic parameter distributions and summary statistics (Rosetta3). *J. Hydrol.* 547, 39–53. doi:10.1016/j.jhydrol.2017.01.004

frontiers | Frontiers in Water

TYPE Original Research
PUBLISHED 17 December 2024
DOI 10.3389/frwa.2024.1507961

OPEN ACCESS

EDITED BY
Vikram Kumar,
Planning and Development, Government of Bihar, India

REVIEWED BY
Francesco Viola,
University of Cagliari, Italy
Anuj Dwivedi,
Indian Institute of Technology Roorkee, India

*CORRESPONDENCE
Taoufik Hermassi
✉ taoufik.hermassi@ingref.ucar.tn

RECEIVED 08 October 2024
ACCEPTED 27 November 2024
PUBLISHED 17 December 2024

CITATION
Madani AZ, Hermassi T, Taibi S, Dakhlaoui H and Mechergui M (2024) Climate change impacts on the Chiffa basin (northern Algeria) using bias-corrected RCM data. *Front. Water* 6:1507961. doi: 10.3389/frwa.2024.1507961

Climate change impacts on the Chiffa basin (northern Algeria) using bias-corrected RCM data

Amina Zoubida Madani[1,2], Taoufik Hermassi[2]*, Sabrina Taibi[3], Hamouda Dakhlaoui[4,5] and Mohamed Mechergui[6]

[1]Department of Rural Engineering, Water and Forestry, National Agronomic Institute of Tunisia (INAT), University of Carthage (UC), Tunis, Tunisia, [2]National Research Institute for Rural Engineering, Water and Forestry (INRGREF), Ariana, Tunisia, [3]LPPRE, Department of Water and Environment Sciences, University of Saad Dahlab, Blida, Algeria, [4]LMHE, Ecole Nationale d'Ingénieurs de Tunis, Université Tunis El Manar, Tunis, Tunisia, [5]Ecole Nationale d'Architecture et d'Urbanisme, Université de Carthage, Tunis, Tunisia, [6]Department of Rural, Water and Forest Engineering, National Agronomic Institute of Tunisia (INAT), Tunis, Tunisia

Introduction: This study aims to assess the efficacy of Quantile mapping (QM) and Delta change (DC) bias correction methods to improve hydrological simulations of the Chiffa basin in northern Algeria. The main issue addressed is the need for corrected climate data to provide reliable hydrological projections in semi-arid climates.

Methods: Hydrological simulations were conducted using the GR2M conceptual rainfall-runoff model, recognized for its robustness in Mediterranean climates. This model was coupled with precipitation simulations from the Rossby Centre regional atmospheric model RCA4 of the Coordinated Regional Climate Downscaling Experiment (Cordex-Africa) forced by two global circulation models (MPI-ESM-LR and CRNM-CM5). Hydrological projections were produced for the future period 20702099 under RCP 4.5 and RCP 8.5 scenarios, comparing raw and bias-corrected data.

Results and discussion: The findings indicate that raw precipitation data are inadequate for reflecting future rainfall trends and simulating future flows. Bias correction methods significantly improved the models performance, with the coefficient of determination (R^2) increasing from 0.440.53 to 0.830.97. Additionally, regional climate models project a 5 to 8% decrease in annual flows by the end of the 21st century under RCP 4.5 and RCP 8.5 scenarios. These results highlight the importance of bias correction methods for hydrological impact studies, and we recommend implementing specific adaptation measures, such as improved irrigation efficiency, development of water storage infrastructure, and adoption of drought-resistant agricultural practices. Future research should focus on employing multivariate bias correction methods, utilizing higher-resolution climate data (≤10 km), and implementing ensemble modeling approaches to better characterize uncertainties.

KEYWORDS

bias correction, climate change impacts, CORDEX-Africa, Delta change, GR2M, hydrological modelling, northern Algeria, Quantile mapping

Highlights

- Coordinated Regional Climate Downscaling Experiment (CORDEX)-Africa domain climate model data are used to assess the hydrological impacts of climate change on the Chiffa basin in northern Algeria.
- Two bias correction methods are used to improve hydrological simulations.
- Bias correction methods highlight important effects on future flow projections.
- The future flow of the study area will likely decrease by the end of the 21st century.
- This study recommends the implementation of adaptation and mitigation measures to ensure the sustainability of water resources.

1 Introduction

The climate change assessments and the development of adaptation and mitigation strategies are generally based on the projection of Global Circulation Models (GCMs) (Sorland et al., 2018; IPCC et al., 2019; Parthiban and Amit, 2021). However, the outputs from the GCM simulation have a coarse resolution, which is not adequate for hydrological applications.

Regional Climate Models (RCMs) provide a dynamic downscaling to a finer resolution, making them suitable for hydrological impact studies (Smitha et al., 2018; Shin et al., 2019; Dixit et al., 2021). Some studies have shown that using downscaled GCM data through RCMs (RCM-GCM) can introduce significant uncertainties and biases that can significantly reduce the reliability of the results (Smitha et al., 2018; Mendez et al., 2020; Mesta and Kentel, 2021; Mengistu et al., 2021).

The climate variables that are simulated by various RCM-GCMs generally represent an inadequate distribution of the observed data. The gap that exists between simulation and observation, has been identified as bias or error (Dimri, 2021; Chelkeba, 2021). Therefore, bias correction techniques are applied to enhance the accuracy of RCM-GCM simulations (Pastén-Zapata et al., 2020; Miralha et al., 2021; Tamene and Chala, 2021).

There are several methods of bias correction, depending on different approaches. For example, linear scaling (ML) is a method that corrects the monthly average and maintains the variability of climate model-adjusted data consistent with uncorrected data (Teutschbein and Seibert, 2010; Chathuranika et al., 2022).

The Quantile mapping (QM) method is also a bias correction technique that adjusts the cumulative distribution function of a simulated variable to align with the observed distribution function by using a transfer function (Teutschbein and Seibert, 2012; Willkofer et al., 2018; Soriano et al., 2019; Szabó-Takács et al., 2019). Teutschbein and Seibert (2012), found that all bias correction methods are effective; however, Quantile mapping is more reliable, a finding also supported by several studies (White and Toumi, 2013; Foughali et al., 2015; Maraun, 2016; Emami and Koch, 2018; Tan et al., 2020).

Local intensity scaling (LOCI) is a method that corrects both precipitation intensity and frequency (Schmidli et al., 2006; Willkofer et al., 2018; Satiprasad et al., 2019; Szabó-Takács et al., 2019).

The bias correction can also be done through an approach based on power transformation. This method is used to adjust the rainfall variance statistics. The simulated monthly precipitation is powered by a value "b," which guarantees that this approach ensures correspondence between the coefficient of variance (CV) of the simulated daily precipitation and the CV of the observed daily precipitation (Rajab et al., 2020; Szabó-Takács et al., 2019).

The Delta change (DC) method is the simplest method. It does not propose a correction for RCM-GCM simulations; instead, it acts as a perturbation method. It generates future climate projections by adjusting the observed climatic series to reflect the differences between the reference and future raw RCM-GCM simulations (Räty et al., 2018; Eekhout and De Vente, 2018; Beyer et al., 2019). This technique was largely used worldwide, especially in the Mediterranean region (Macias et al., 2018; François et al., 2020). In addition, this method was considered the most efficient compared to other methods of bias correction applied at the level of Turkey (Oruc, 2022).

Several studies propose a comparison of bias correction techniques for different regions of the Mediterranean basin. Marcos et al. (2018) assessed the ability of three bias correction methods two linear (mean bias correction (BC), and linear regression (LR)) and a nonlinear (model output statistic analogs (MOS-analog)) to improve the seasonal feature of precipitation simulated by climate models during the period 1981–2100 in the Boadella reservoir (northwestern Mediterranean). The results suggest that the analogous (MOS-analog) approach to model output statistics and the linear regression method generally perform better than other approaches in late autumn and early winter. They demonstrate the possibility of introducing bias correction methods to improve the seasonal prediction of water resources in the climate services system.

Similarly, Martins et al. (2021) have attempted to compare two bias correction methods: linear and Quantile mapping. These methods were applied to a bias-correct RCM-GCM simulation of temperature and precipitation during the reference period 1989–2005 in the Douro Wine Region, Portugal. The results indicate that the linear method corrects only the location (mean) and the scale (standard deviation) of the empirical probability distribution function (EPDF), while the Quantile mapping corrects the complete EPDF. The first method appears to be less computationally demanding, which makes easier to execute in large sets of data.

In Algeria, only a few studies have addressed bias correction when using climate model outputs. Taibi et al. (2021b) demonstrated that the use of Delta change and Quantile mapping methods for the correction of simulated precipitation from the outputs of the Cordex-Africa regional climate models yields a superior analysis of precipitation in the Oran coastal basin in Algeria. Zeroual et al. (2020) also used the Quantile mapping method to identify climate zones based on the Koppen-Geiger classification for all of Algeria by the end of the century.

The presence of biases in the climate simulations resulting from RCM-GCMs is worth correcting before being used in impact studies to allow a better assessment of climate projections. The response of hydrological systems to climate change can be carried out according to the direct use of runoff simulated by the global climate models of the CMIP5 or regional (Alkama et al., 2013; Zheng et al., 2018).

Conceptual Rainfall-Runoff was widely used in hydrological impact studies of climate change, due to the limited data they require (mainly rain and evapotranspiration). This is true,

especially for developing countries suffering from data scarcity. This approach is most often used, and it has been the subject of many studies. Those studies aimed at simulating future flows at the scale of a watershed, using the outputs of climatic models of rainfall and temperatures as input data to the hydrological model (Ibrahim et al., 2015; Todorovic and Plavsic, 2016; Giuntoli et al., 2018; Al-Safi et al., 2020; Hadour et al., 2020; Sidibe et al., 2020). In Algeria, the GR2M Hydrological model is widely used given its simplicity but also its efficacy in conveniently reproducing the hydrological functioning of Algerian watersheds (Zeroual et al., 2013; Ouhamdouche et al., 2018).

The Chiffa watershed presents specific hydrological challenges characteristic of Mediterranean semi-arid regions. Its complex topography, ranging from mountainous areas to coastal plains, combined with high temporal and spatial variability of precipitation, makes it particularly sensitive to climate model biases. The basin experiences intense seasonal variations, with dry summers and irregular winter rainfall, often resulting in flash floods. These regional characteristics make the bias correction of climate models particularly important, as uncorrected biases could significantly affect the representation of both extreme events and low-flow periods, which are critical for water resource management in the region. In addition, the size of the Chiffa catchment (316 km^2) is smaller than one entire RCM grid cell of CORDEX-Africa (50 km × 50 km = 2,500 km^2). This presents a challenge for using climate model simulations, as they are not designed to capture features at spatial scales smaller than their grid resolution (Dakhlaoui and Djebbi, 2021). Applying a bias correction technique could help downscale climate model outputs to align with the study catchment scale (Hakala et al., 2018; Djebbi and Dakhlaoui, 2023).

The aim of this study is to evaluate some bias correction methods for the improvement of hydrological simulations in the Chiffa watershed. Specifically, we investigate how different bias correction methods can better represent the precipitation patterns and hydrological processes of this semi-arid Mediterranean basin. For this purpose, the precipitation from the Rossby Centre regional atmospheric model RCA4 of the Coordinated Regional Climate Downscaling Experiment (Cordex-Africa) forced by two global circulation models (MPI-ESM-LR and CRNM-CM5) was corrected by two bias correction methods, "Quantile mapping (QM)" and "Delta change (DC)," before being used as input data to the GR2M hydrological model to assess the impact of climate change on the hydrological response of the Chiffa basin by 2100, under two Representative Concentration Pathways (RCP): RCP 4.5 and RCP 8.5.

2 Methods

2.1 Study area and data set

The Chiffa basin is one of the three sub-watersheds of the Mazafran, the most important coastal basin in Algiers. The Chiffa basin is located in northern Algeria between latitudes of 36° 10′ and 36°30′N and longitudes of 2° 30′ and 3° East. It is bounded to the north by Blida, to the west by Hadjout and Djendel, and to the south by Medea (Figure 1). It has an area of approximately 316 km^2 at the Amont des Gorges hydrometric station, with a relatively elongated shape. It has an average altitude of 833 m, with a highest point of 1,629 m.

The Chiffa basin presents a complex geological structure (Figure 1) dominated by Triassic and Cretaceous formations in its central part, with Jurassic and lower Cretaceous deposits in the northern section, while Tertiary outcrops are present in the southern area. This geological diversity significantly influences the basin's hydrogeological behavior, particularly in terms of groundwater storage and surface water-groundwater interactions.

The study area is characterized by a Mediterranean vegetation cover, including various forest formations. These formations are mainly composed of Atlas cedars, Aleppo pines, and Berberis Tuyas (A.P.N.A., 2006). The Chiffa basin belongs to a semi-arid Mediterranean climate with a warm season.

The interannual variability of precipitation in the Chiffa basin is indeed significant (Figure 2). Over the period 1979–2014, annual precipitation varies considerably, ranging from around 400 mm to nearly 1,100 mm, which highlights substantial interannual variability of precipitation. Such variability directly impacts water availability and increases the risk of drought episodes and flood events. On average, the basin receives around 800 mm of annual precipitation, which is characteristic of semi-arid Mediterranean climates. These interannual fluctuations are essential for assessing the basin's resilience to future climate scenarios and underscore the importance of water resource management strategies adapted to extreme conditions.

The average temperature for the reference period (1979–2014) is around 17°C, characterized by marked seasonal contrasts, with hot summers and mild winters contributing to high evapotranspiration rates during the warm season. Additionally, Northern Africa, including the Chiffa basin, has been identified as one of the most vulnerable "hot spots" to climate change. Projections indicate that the region will experience a significant warming trend, with temperatures expected to rise by 0.5°C–2.5°C by the end of the century under emission scenarios, leading to an increase in hydrological drought (IPCC, 2021).

The hydroclimatic data used in this study correspond to the El Hamdania rain gauge and the Amont des Gorges hydrometric gauging station that were collected from the National Water Resources Agency (ANRH). The temperature data correspond to the climate station of Dar el Beida of the National Office of Meteorology (ONM). All hydro-climatic data are available on a monthly scale during the study period 1979–2014 (Table 1).

The estimation of the potential evapotranspiration (PET) over the historical and projection period is based on the Thornthwaite formula given (Thornthwaite and Mather, 1951) in Equation 1.

$$PET(m) = 16 * \left[\frac{10 * \overline{T}(m)}{I}\right]^{a} * F(m,\varphi) \quad (1)$$

Where $PET\ (m)$ is the mean evapotranspiration of month m (m = 1 to 12) in mm, $T(m)$ is the interannual mean temperature of the month in °C and $F\ (m, \phi)$ is the corrective factor for month (m) and latitude, a: 0.016 * I + 0.5, I annual thermal index defined in Equation 2.

$$I = \sum_{m=1}^{12} i(m) \quad i(m) = \left[\frac{\overline{T}(m)}{5}\right]^{1.514} \quad (2)$$

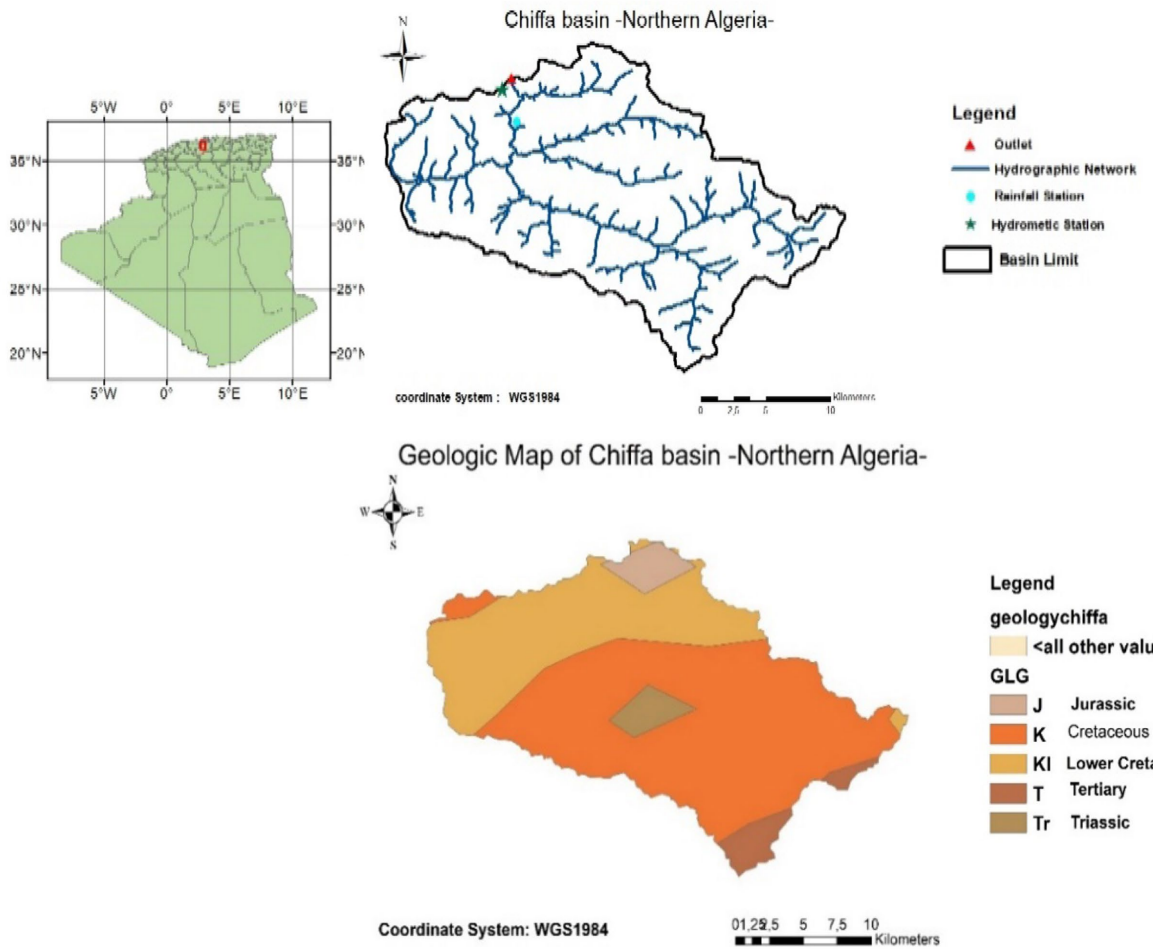

FIGURE 1
Geographical location and geological map of the study area.

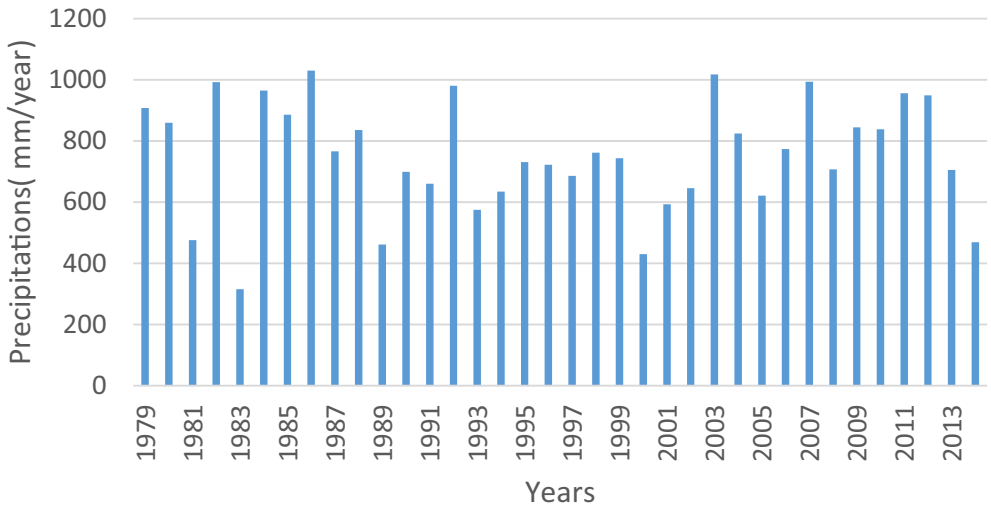

FIGURE 2
The interannual variability of precipitation in the Chiffa basin.

TABLE 1 Geographical and characteristics of the hydro-climatic stations in the study area.

Code	Name	Source	Longitude (°)	Latitude (°)	Altitude (m)	Kind of station	Study period
021126	Amont des Gorges	ANRH	2.76	36.38	290	Hydrometric	1979–2014
021115	El Hamdania	ANRH	2.77	36.36	400	Rainfall	1979–2014
020611	Dar El Beida	ONM	3.15	36.43	25	Climatic	1979–2014

ANRH, National Agency of Water Resources; ONM, National Office of Meteorology.

Drouiche et al. (2019) showed that the study area has experienced an increase in drought episodes characterized by a reduction in annual rainfall of about 16 to 24% during the period 1973–2001. Regarding the temperature, Bouderbala (2019) observed an increase in temperatures of approximately 6 to 30% in the study area between February and June during the period 1974–2010, highlighting potential consequences on the availability of water resources.

To estimate future flows in the study catchment, the projected monthly precipitation and temperature of the RCM-GCMs RCA4-MPI-ESM-LR and RCA4-CNRM-CM5 of the Africa-Cordex project are used. These two climate models were considered suitable for Algeria compared to other available models (Zeroual et al., 2019). Thus, these models offer simulations of climatic variables at a monthly scale during the period 1981–2100, with a horizontal resolution of about 50 km. Two Representative Concentration Pathways are considered: RCP 4.5 and RCP 8.5, which represent, respectively, an optimistic and a pessimistic greenhouse gas emission scenario.

2.2 GR2M hydrological model

In this study, the GR2M conceptual model (Perrin et al., 2007) was selected for simulating hydrological processes in the Chiffa watershed after careful consideration of several factors. Although we acknowledge that more complex models with finer temporal resolutions exist, GR2M's selection was justified by multiple considerations. GR2M's parsimonious structure, requiring only precipitation and PET as inputs, is particularly advantageous in our study context where data availability is limited. This parsimony, combined with its proven robustness, makes it especially suitable for climate change impact studies where the focus is on long-term hydrological changes rather than short-term events.

For our study focusing on long-term climate change impacts, the monthly resolution proves particularly relevant because it better aligns with the reliability of climate projections, whose uncertainties increase significantly at finer time scales (Lehner et al., 2020). This temporal scale also facilitates the better propagation of uncertainties in climate projections while remaining consistent with water resource management and planning scales.

The model has demonstrated remarkable performance in semi-arid Mediterranean contexts, particularly in northern Algeria. Previous studies have successfully applied GR2M to similar watersheds (Zeroual et al., 2013; Sakaa et al., 2015; Hallouz et al., 2018; Hadour et al., 2020; Pulido-Velazquez et al., 2021; Bouguerra and Mansour, 2023; Mahdaoui et al., 2024), achieving satisfactory results in capturing the dominant hydrological processes at the monthly scale. Although we recognize that the monthly time step may not capture certain short-term events, such as flash floods (Bargaoui et al., 2008; Dakhlaoui et al., 2009), this temporal resolution aligns well with our study's primary objective of assessing long-term climate change impacts on water resources.

The model structure consists of two main functions (production and routing) organized around two reservoirs. The production function operates through a soil reservoir, while the transfer function is governed by a gravitational water reservoir. The model also accounts for underground water exchange, which is particularly relevant in our semi-arid context where groundwater contributions can be significant. A detailed description of the model structure and equations is available in Perrin et al. (2007).

Model calibration and validation were performed under the R environment using the airGR package (Gader et al., 2020), which provides comprehensive outputs including monthly simulated flow series, numerical performance criteria, graphical outputs, and internal model variables. The calibration process focused on optimizing the model's two parameters to best represent the watershed's hydrological behavior, with particular attention to both high and low flow periods to ensure robust performance across different hydrological conditions.

2.3 Performance criteria for hydrological model assessment

The estimation of the performance of a hydrological model is one of the most important steps in evaluating the quality of the simulation. It requires a comparison between observed and simulated flows. There is a multitude of criteria to evaluate the performance of the hydrological model. Two performance criteria are used in this study: the Nash criterion (Nash and Sutcliffe, 1970) and Pearson's correlation coefficient.

2.3.1 Nash criterion

This criterion compares the mean square deviation of the flux roots to the variance it has given more precise results compared to the other evaluation criteria. This is confirmed by several studies such as Nounangnonhou et al. (2018), Fathi et al. (2019), Ditthakit et al. (2021a) and Orozco et al. (2021). This criterion is based on the sum of the square errors as defined in Equation 3.

$$Nash = 100^{*}\left[1-\left(\frac{\sum_{i=1}^{N}\left(\sqrt{Q_0}-\sqrt{Q_c}\right)^2}{\sum_{i=1}^{N}\left(\sqrt{Q_0}-\sqrt{\overline{Q}_0}\right)^2}\right)\right] \quad (3)$$

Q_0 observed flows, Q_c simulated flows with the model, $\overline{Q}_0$: average observed flow, N: number of observations.

Where:

If $Nash \leq 0$: the model is no better than the average of the observed flows.

If *Nash* > *0*: the model is better than the average of the observed flows.

If *Nash* = *1*: the model corresponds perfectly to the observed flows.

2.3.2 Pearson's correlation coefficient (*r*)

The linear regression between the calculated and the observed flows, its formulation is as shown in Equation 4.

$$r = \frac{\sum_{i=1}^{N}\left(Q_0 - \overline{Q_0}\right)\left(Q_c - \overline{Q_c}\right)}{\sqrt{\sum_{i=1}^{N}\left(Q_0 - \overline{Q_0}\right)^2}\cdot\sqrt{\sum_{i=1}^{N}\left(Q_c - \overline{Q_c}\right)^2}} \quad (4)$$

Where Q_0 and Q_C are, respectively, the observed and simulated flows for $i = 1\ldots, N$, N the number of inputs $\overline{Q_0}$ and $\overline{Q_c}$ are, respectively, the averages of the observed and simulated flows. The value (r) varies from −1 to 1. If (r) is positive and close to 1, the relationship between the measured flows and the flows calculated by the linear models is increasing, and the scatterplot is concentrated around the regression line, if (r) is negative and close to −1, indicates a perfect negative correlation between the values of observed and predicted flows (Koffi et al., 2011; Charifi, 2018; Ditthakit et al., 2021b).

2.3.3 Kling-Gupta Efficiency (KGE)

The Kling-Gupta Efficiency (KGE), developed by Gupta et al. (2009), was designed to enhance the traditional Nash-Sutcliffe Efficiency (NSE) metric. KGE addresses certain limitations of NSE, particularly its sensitivity to data variability; its formulation is as follows in Equation 5:

$$KGE = 1 - \sqrt{(R-1)^2 + \left(\frac{\sigma_c}{\sigma_0} - 1\right)^2 + \left(\frac{\overline{Q_c}}{\overline{Q_0}} - 1\right)^2} \quad (5)$$

where Q_0 represents the observed flows, Q_c represents the simulated flows, $\overline{Q_0}$ the average of the observed flows, $\overline{Q_c}$ is the average of the simulated flows, R is the Pearson's correlation coefficient, σ_0 is the standard deviation of the observations, and σ_c is the standard deviation of the simulations.

With KGE, a value close to 1 indicates a high agreement between observed and simulated values, while values closer to 0 or negative indicate poor performance.

2.3.4 Root-mean squared error (RMSE)

RMSE is calculated from the observation values and then averaged for all the simulations made with the different models. It measures the difference between simulations and observation flows. The formulation is given as shown in Equation 6:

$$RMSE = \sqrt{\frac{1}{N}\sum_{i=1}^{N}\left(Q_C - Q_0\right)^2} \quad (6)$$

With Q_C. Q_0 is the simulated and observed flow, respectively. For i = 1…N; N is the total number of flow data over the analysis period.

2.4 Performance criteria for climate model assessment

Mostly, climate models have systematic errors in their output. Then, to evaluate the performance of regional climate models, a bias is estimated between simulated and observed rainfall data during the reference period (1981–2010) as shown in Equation 7.

2.4.1 BIAS

$$BIAS = \frac{\overline{P_{sim}} - \overline{P_{obs}}}{\overline{P_{obs}}} \quad (7)$$

Where $\overline{P_{obs}}, \overline{P_{sim}}$ are, respectively, the average observed and simulated rainfall.

2.4.2 Coefficient of determination (R^2)

The coefficient of determination (R^2) represents the proportion of variance in the dependent variable that is predictable from the independent variable(s). In hydrology, it measures how well the simulated flows match the observed flows as shown in Equation 8.

$$R^2 = \left\{\frac{\sum_{i=1}^{N}\left(Q_0^i - \overline{Q_0}\right)\times\left(Q_C^i - \overline{Q_C}\right)}{\sqrt{\sum_{i=1}^{N}\left(Q_0^i - \overline{Q_0}\right)^2}\times\left[\sum_{i=1}^{N}\left(\left(Q_C^i - \overline{Q_C}\right)^2\right)\right]}\right\} \quad (8)$$

With N being the number of observations, for i = 1…N, Q_0^i represents the observed flows on day i, Q_C^irepresents the simulated flows on day i, $\overline{Q_0}$ the average of the observed flows, and $\overline{Q_C}$ the average of the simulated flows.

The R^2 values range from 0 to 1, where:

- $R^2 = 1$ indicates a perfect correlation between observed and simulated flows.
- $R^2 = 0$ indicates no correlation.
- Values above 0.5 generally indicate acceptable model performance.

2.5 Bias correction methods

The bias correction of climate data is a crucial step in assessing the impacts of climate change (Tan et al., 2020). In this study, we have carefully selected two widely used bias correction techniques: the Delta change (DC) method and the Quantile mapping (QM) method. This selection was based on their proven effectiveness in Mediterranean and semi-arid regions (Enayati et al., 2021; Taibi et al., 2021b; Dakhlaoui and Djebbi, 2021; Djebbi and Dakhlaoui, 2023), particularly for their distinct but complementary strengths in handling different aspects of climate data correction.

The DC method was selected for its robust approach to adjusting the observed climatic series based on mean monthly changes between reference and future RCM-GCM simulations (Ruelland et al., 2012). This method is particularly advantageous for preserving the temporal structure of observed data, which is important for hydrological impact studies in semi-arid regions. It effectively captures mean shifts in

climate variables while maintaining the natural variability patterns present in observations, assuming that the regional bias remains constant over time (Beyer et al., 2019). In addition, the DC technique is recognized for its simplicity of application. The DC method is defined by Equations 9 and 10 (Mendez et al., 2020):

$$P_{contr}^{BC}(t) = P_{obs}(t) \tag{9}$$

$$P_{frc}^{BC}(t) = P_{obs}(t).\left[\frac{\mu_m P_{frc}(t)}{\mu_m P_{contr}(t)}\right] \tag{10}$$

Where P_{contr} (t) and $P_{obs}(t)$ are, respectively, the raw simulated and observed precipitation during the control period, $P_{frc}(t)$ is the raw projected time series, $P_{frc}^{BC}(t)$ is the bias-corrected projected time series, and μm is the long-term monthly mean.

The QM method was chosen as a complementary approach due to its efficacy in correcting the entire distribution of climate variables by aligning the cumulative distribution functions (CDFs) of observed and simulated data. This method is particularly valuable for correcting extreme values, which are critical in Mediterranean climates like the Chiffa basin, where precipitation patterns show high variability (Motlagh et al., 2022). The QM method is expressed by Equation 11 (Heo et al., 2019):

$$P_m(t) = F_0^{-1}\left[F_s\left[P_s(t)\right]\right] \tag{11}$$

Where $P_m(t)$ and $P_s(t)$ are, respectively, the corrected and simulated precipitations and F_s and F_0^{-1} are the cumulative distribution function (*CDF*) of the raw precipitation from the RCM and the inverse *CDF* of the observed precipitation.

3 Results and discussion

3.1 Calibration and validation of the GR2M model

Hydrological modeling performance was evaluated through calibration and validation steps, using multiple evaluation criteria to guarantee a robust assessment of the model's capabilities. We employed four performance metrics: Nash-Sutcliffe Efficiency (NSE), Pearson's correlation coefficient (R), Root Mean Square Error (RMSE), and Kling-Gupta Efficiency (KGE), each providing different insights into model performance.

The calibration period (January 1981–December 2000) encompasses various hydrological conditions, including several drought events characteristic of the Mediterranean climate (e.g., in the 1990s). During this period, the model achieved satisfactory performance with an NSE of 77.5% and R of 87.6% (Table 2, Figure 3A). The RMSE of 2.97 mm/month indicates a reasonable level of accuracy in flow prediction, whereas the KGE is 48%.

For the validation period (January 2002–December 2012), using the calibrated parameters (X1 = 347.234 mm and X2 = 0.682 mm), the model showed notably high-performance metrics with an NSE of 99% and R of 99.8% (Table 2, Figure 3B). The RMSE improved to 1.01 mm/month, and the KGE increased to 60%.

The hydrological response presented in Figure 4 demonstrates that the model effectively captures the general flow dynamics driven by precipitation inputs, though with varying performance across different hydroclimatic conditions. The model's performance during both wet and dry periods suggests its capability to simulate the watershed's hydrological behavior under various climatic conditions.

3.2 Evaluation of regional climate models over the reference period

3.2.1 Evaluation of raw RCM-GCM precipitation over the reference period (1981–2010)

The performance of RCM-GCMs during the reference period (1981–2010) was assessed using multiple statistical metrics: bias, Root Mean Square Error (RMSE), and correlation coefficient (R) between observed and simulated precipitation data (Table 3).

On the annual scale, results show that the two raw RCM-GCMs strongly underestimate precipitation. The bias between observations and RCA4-CNRM-CM5 and RCA4-MPI-ESM-LR is, respectively, about −57.03% and −55.92%. This substantial underestimation is further confirmed by high RMSE values of 2102.47 mm and 2061.47 mm, respectively, while the weak correlation coefficients (R = −0.14 and −0.25) indicate poor temporal agreement between simulated and observed precipitation patterns.

The representation of observed and simulated mean monthly precipitation during the control period (1981–2010) shows distinct seasonal patterns. During the wet season (October–May), both models exhibit significant biases, with maximum negative biases occurring in December and January (−71.45% and −66.03%, respectively, for RCA4-CNRM-CM5). These months also show the highest RMSE values (421.91 mm and 394.10 mm, respectively), indicating substantial uncertainty in wet season precipitation simulation. During the dry season (June–September), while relative biases are lower (e.g., −14.5% and −24.5% in June and July for RCA4-CNRM-CM5), the models still struggle to accurately capture the limited rainfall events characteristic of this period, as evidenced by the poor correlation coefficients.

TABLE 2 Performance of GR2M over calibration and validation periods.

Periods	Nash (%)	R (%)	RMSE (mm/month)	KGE (%)
Calibration period (January 1981–December 2000)	77.5	87.6	2.97	48
Validation period (January 2002–December 2012)	99.0	99.8	1.01	60

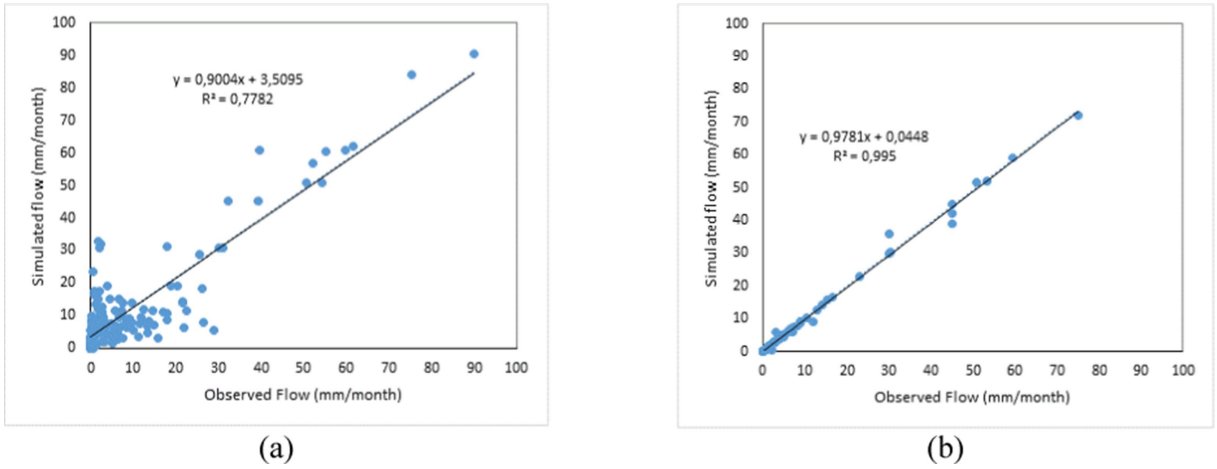

FIGURE 3
Hydrological simulation of the rainfall-runoff process using the GR2M model in the Chiffa basin during the calibration and validation periods.

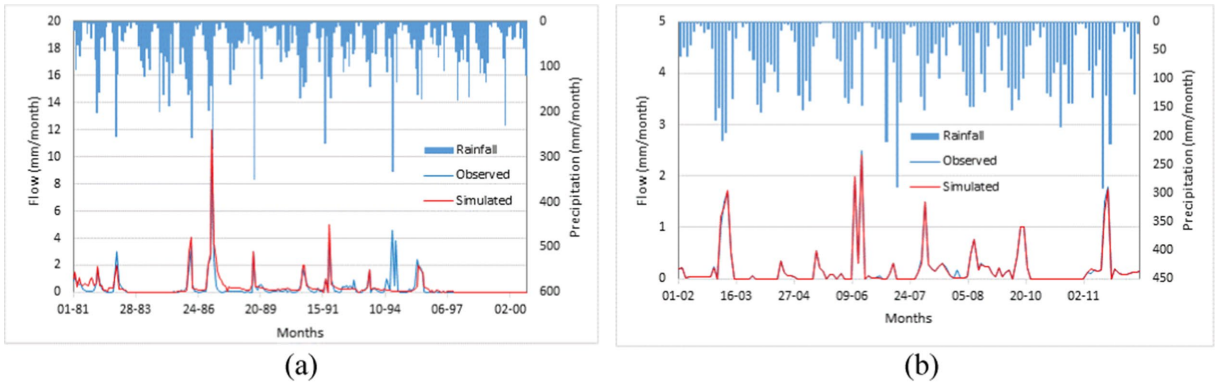

FIGURE 4
Result of hydrological simulation rainfall-runoff of the GR2M model on the Chiffa basin during the **(A)** calibration period (1981–2000), and **(B)** validation period (2002–2012).

TABLE 3 **Estimated bias between observed and simulated monthly and annual rainfall over the reference period 1981–2010.**

	RCA4-CNRM-CM5			RCA4-MPI-ESM-LR		
	BIAS (%)	RMSE (mm)	R	BIAS (%)	RMSE (mm)	R
January	−66.03	394.09	−0.01	−61.50	367.057	0.02
February	−63.36	322.04	0.20	−62.12	315.71	−0.09
March	−34.09	118.12	0.11	−39.65	137.32	−0.25
April	−47.34	166.56	0.00	−64.48	226.87	0.25
May	−56.34	136.88	−0.05	−44.68	108.56	0.04
June	−14.51	9.45	−0.07	−47.92	31.16	0.08
July	−24.49	7.90	−0.01	−62.56	20.19	0.18
August	−61.30	31.71	0.09	−72.56	37.53	0.14
September	−67.98	105.07	0.14	−64.44	99.59	0.21
October	−44.05	124.48	−0.20	−46.22	130.60	0.06
November	−56.96	264.20	−0.10	−47.89	222.20	0.21
December	−71.53	421.90	−0.33	−61.81	364.63	0.07
Annual	−57.03	2102.46	−0.14	−55.92	2061.47	−0.25

The high bias obtained during the dry season can be explained by the low quantity of precipitation in this season. However, for the wet season, the precipitation simulated by the climate models depends on processes represented by each model. Indeed, some studies have highlighted that climate models generally fail to estimate rainfall correctly during wet periods (Taibi et al., 2019, 2022; Dunning et al., 2018). This is because the resolution of climate models makes them not able to consider more phenomena that occur at a spatial scale smaller than the grid size of climate models, such as convective precipitation and orographic rainfall, which are highly dependent on local relief (Ouatiki et al., 2019; Gu et al., 2022). The location of the Chiffa catchment at the Blidean Atlas downstream, which is characterized by its relief, could be one of the origins of such underestimation.

These significant biases and errors in precipitation simulation could substantially affect hydrological forecasts in the Chiffa basin, particularly affecting seasonal water availability predictions, extreme event forecasting, and long-term water resources planning. This is particularly crucial in the semi-arid context of the Chiffa basin, where accurate precipitation estimates are essential for reliable hydrological modeling. According to the results above, both RCM-GCMs, RCA4-CNRM-CM5, and RCA4-MPI-ESM-LR, cannot reproduce correctly rainfall at the Chiffa basin. A bias correction technique is then necessary to improve the rainfall data simulated by the climate models.

3.2.2 Evaluation of raw RCM-GCM temperature over the reference period (1981–2010)

The performance assessment of temperature simulations was conducted using bias, RMSE, and correlation coefficient (R) at both annual and monthly scales (Table 4). At the annual scale, the temperature bias between observations and simulations data of RCA4-CNRM-CM5 and RCA4-MPI-ESM-LR over the reference period (1981–2010) was about −0.8°C and 0.1°C, respectively. The annual RMSE values (52.35°C for RCA4-CNRM-CM5 and 2.21°C for RCA4-MPI-ESM-LR) and correlation coefficients (R = −0.11 and −0.08, respectively) suggest that RCA4-MPI-ESM-LR shows better overall temperature simulation capability.

At the monthly scale, results show that generally, temperature variation simulated by the two RCM-GCMs is almost similar.

The RCA4-CNRM-CM5 model shows good performance in winter months, reproducing exactly the monthly temperatures observed in December, January, and February (Bias = 0°C, RMSE <0.5°C). However, it underestimates temperatures during other months, with estimated biases ranging from −0.2°C to −2.2°C. The highest discrepancies are observed in June and October, with RMSE values of 10.48°C and 12.13°C, respectively, suggesting significant model uncertainty during these seasons.

The RCA4-MPI-ESM-LR model demonstrates more consistent performance across seasons. The analysis shows average biases of about 1°C in winter (December–January–February [DJF]), 0.2°C in spring (March–April–May [MAM]), 0.5°C in summer (June–July–August [JJA]), and −0.6°C in autumn (September–October–November [SON]). The RMSE values are lower compared to RCA4-CNRM-CM5, ranging from 0.05°C in July to 5.38°C in June, indicating better overall temperature simulation capability.

The correlation coefficients of both models exhibit weak to moderate correlations with observed temperatures, varying from −0.41 to 0.33, indicating limitations in capturing temperature variability patterns. This performance variability across seasons and models has important implications for hydrological modeling, particularly for processes sensitive to temperatures such as evapotranspiration and snowmelt in the elevated parts of the catchment. While the biases are smaller than precipitation, temperature corrections might still be necessary to ensure reliable hydrological simulations, especially during seasons with larger discrepancies.

3.2.3 Seasonal analysis of raw RCM-GCM precipitations and temperatures over the reference period (1981–2010)

The analysis of raw RCM-GCM outputs reveals significant systematic biases in both temperature and precipitation simulations across seasons (Figure 5).

TABLE 4 Estimated bias between observed and simulated monthly and annual temperatures over the reference period 1981–2010.

	RCA4-CNRM-CM5			RCA4-MPI-ESM-LR		
	BIAS(°C)	RMSE(°C)	R	BIAS(°C)	RMSE(°C)	R
January	0	0.09	−0.13	0.9	3.95	−0.12
February	0	0.44	0.33	1	4.92	0.31
March	−0.7	3.49	−0.14	0.3	0.82	−0.13
April	−0.7	4.10	−0.09	0.3	1.43	−0.12
May	−1	5.49	0.16	−0.1	0.94	0.16
June	−2	10.48	0.01	−1.2	5.38	−0.01
July	−0.6	3.29	−0.16	0	0.05	−0.13
August	−0.2	1.08	−0.01	0.3	1.27	0.03
September	−1.1	6.03	0.24	−0.2	0.87	0.24
October	−2.2	12.13	−0.19	−1.2	5.35	−0.17
November	−1.3	6.81	−0.40	−0.3	1.90	−0.41
December	0	0.22	−0.17	1	4.20	−0.19
Annual	−0.8	52.35	−0.11	0.1	2.21	−0.08

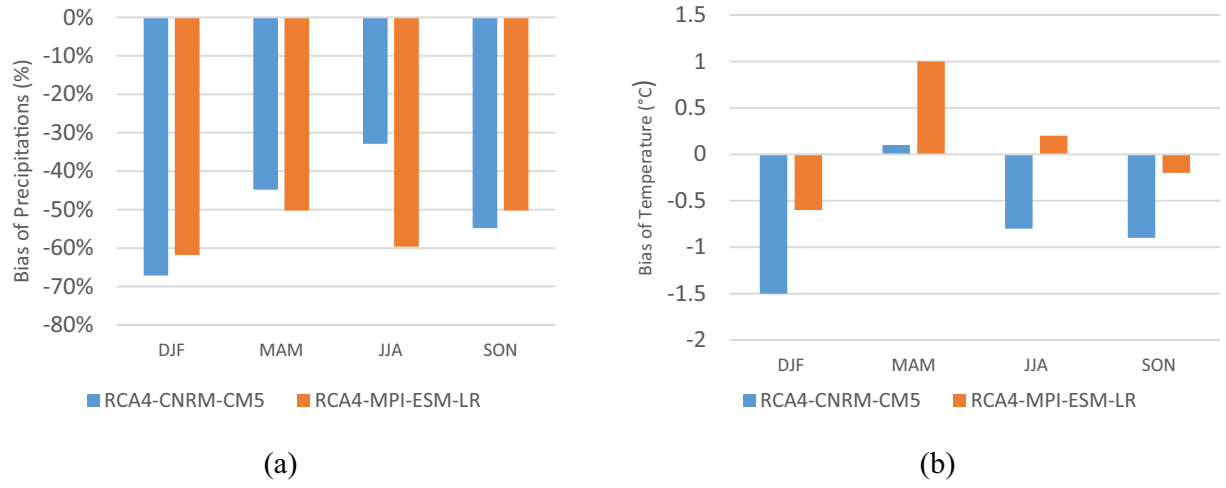

FIGURE 5
Seasonal analysis of raw RCM-GCM **(A)** precipitations and **(B)** temperatures over the reference period (1981–2010).

The precipitation biases are even more substantial (Figure 5A), with both models significantly underestimating rainfall across all seasons. Winter shows the most severe underestimation (up to −60% for RCA4-MPI-ESM-LR), followed by spring (−40% to −50%), while summer and autumn maintain significant negative biases (−30% to −60%).

For temperature, RCA4-CNRM-CM5 shows a consistent cold bias (Figure 5B), particularly pronounced in winter (−1.5°C) and autumn (−1°C), while RCA4-MPI-ESM-LR exhibits a warm bias in spring (+1°C).

These systematic biases underscore the critical need for bias correction in the Chiffa basin context. The substantial precipitation underestimation would lead to unrealistic water availability estimates, and temperature biases would affect evapotranspiration calculations, both important components in semi-arid hydrological modeling. The magnitude of these biases varies seasonally, suggesting that their impact on hydrological responses would be pronounced.

3.3 Hydroclimatic projection

3.3.1 Precipitation changes

The RCA4-CNRM-CM5 and RCA4-MPI-ESM-LR models provide projected precipitation until 2100 for two representative concentration pathways, RCP 4.5 and RCP 8.5. We propose an analysis of the change coefficient of future precipitation over the period 2070–2099 compared to the reference period 1981–2010, calculated at annual and seasonal scales. To highlight the efficiency of the bias correction methods (Quantile mapping and Delta change), a change coefficient was calculated for raw RCM-GCM and bias-corrected RCM-GCM by the two correction methods.

The raw RCA4-CNRM-CM5 model, at the annual scale, projects a decrease of precipitation of more than 60% under both scenarios (RCP 4.5 and RCP 8.5). However, after correcting the bias, the change coefficient of precipitation indicates a future decrease of precipitation that does not exceed 5 and 27% by 2100, respectively, under RCP 4.5 and RCP 8.5 (Figures 6A,B). The two bias correction methods (Quantile mapping and Delta change) reduced the projected change in precipitation by 33 to 55% compared to raw climate models.

At the seasonal scale, the results show a significant future decrease in precipitation of more than 70% in winter (December–January–February [DJF]), according to RCP 4.5 (Figure 6A) and RCP 8.5 (Figure 6B). For the same season, the results from the rainfall corrected by the two bias correction methods—Quantile mapping and Delta change—indicate a future decrease in rainfall that does not exceed 30%, according to RCP 4.5 (Figure 6A), and 49%, according to RCP 8.5 (Figure 6B). For this season, the bias correction methods have favored a correction of error with a percentage of 40%.

In spring (March–April–May [MAM]), the results of the raw climate model show a decrease in precipitation of 49% under RCP 4.5 (Figure 6A) and 59% under RCP 8.5 (Figure 6B). Whereas, after the correction of this rainfall by the two bias correction methods, the results show an increase of the rainfall that exceeds 16%, according to RCP 4.5(Figure 6A), while the RCP 8.5 scenario shows a decrease of no more than 14% (Figure 6B), yet both methods show a correction performance that exceeds 40%.

For the summer season (June–July–August [JJA]), the raw rainfall over the projection period (2070–2099) indicates a decrease of 20%, according to RCP 4.5 and 45%, according to RCP 8.5, while all the results from the Quantile mapping and Delta change-corrected data show an increase in rainfall of more than 80%, according to RCP 4.5(Figure 6A) and RCP 8.5 (Figure 6B).

In autumn (September–October–December [SON]), bias correction methods reduced the climate predictions simulated by the raw RCM-GCM by 42%. Thus, a decrease of 4% is projected after bias correction for RCP 4.5 (Figure 6A) and 21% according to RCP 8.5 (Figure 6B).

The RCA4-MPI-ESM-LR model, RCP 4.5, shows a great decrease in rainfall, which exceeds 60% at the horizon of 2099 compared to the reference period 1981–2010, for the two RCPs (Figures 7A,B). The results obtained after the correction of the biases indicate a reduction in precipitation of about 20% according to RCP 4.5 (Figure 7A) and

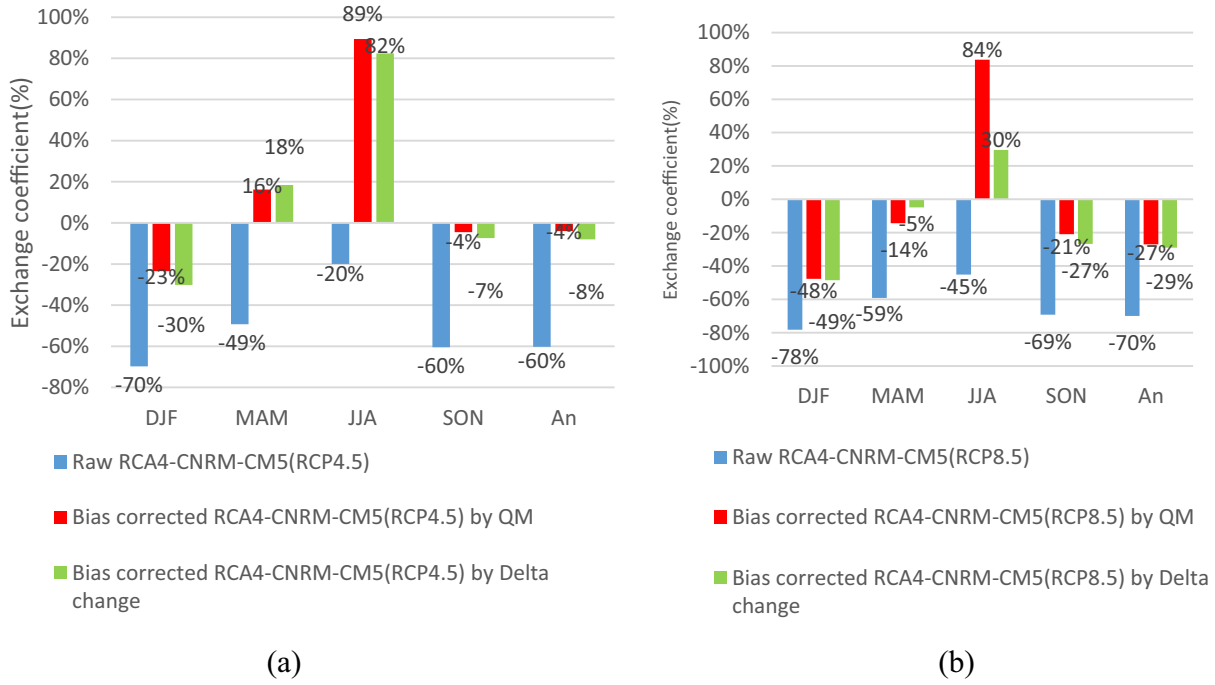

FIGURE 6
Seasonal and annual projected change in precipitation of raw and bias-corrected (Quantile mapping and Delta change) climate model RCA4-CNRM-CM5 according to **(A)** RCP 4.5 and **(B)** RCP 8.5 over the period (2070–2099).

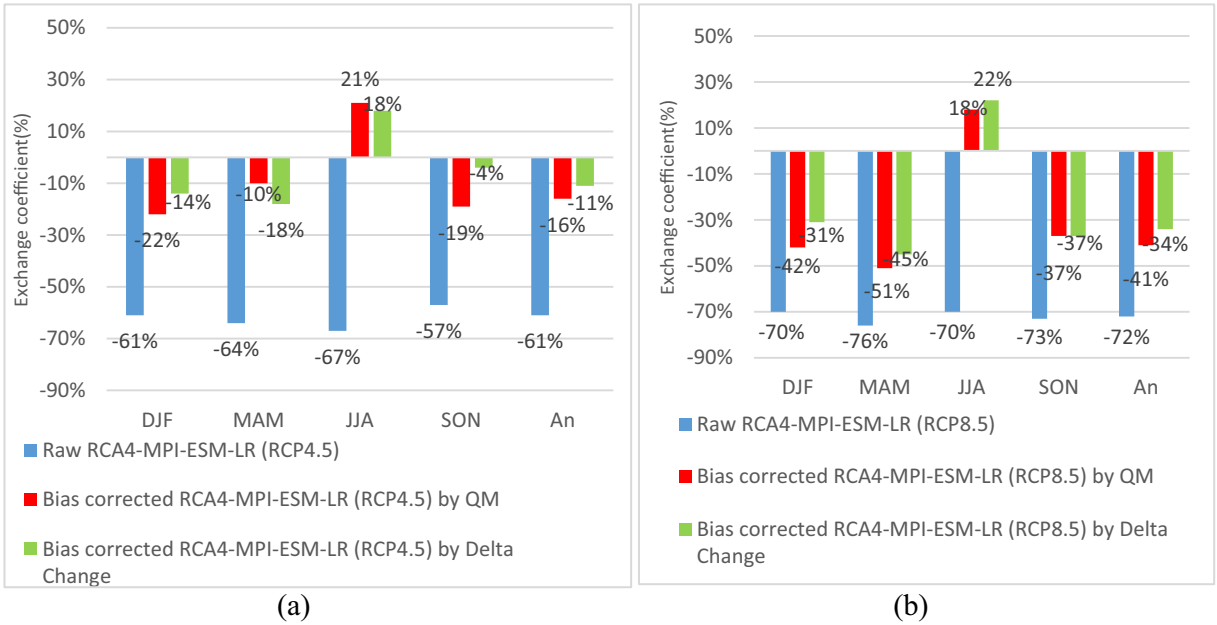

FIGURE 7
Seasonal and annual projected change in precipitation of raw and bias-corrected (Quantile mapping and Delta change) climate models. **(A)** RCA4-MPI-ESM-LR and **(B)** RCA4-MPI-ESM-LR according to RCP 4.5 and RCP 8.5 over the period (2070–2099).

34% according to RCP 8.5 (Figure 7B). These two methods have made it possible to reduce the simulated climatic change by 40% compared with the uncorrected future rainfall.

At the seasonal scale, the projected precipitation with raw RCM-GCM for the period (2070–2099) shows a significant decrease for all seasons, particularly in winter (DJF) which registers a decrease of 61% according to RCP 4.5 (Figure 7A) and 70% according to RCP 8.5 (Figure 7B). After the correction of rainfall by the two bias correction methods (Quantile mapping and Delta change), the projected precipitation shows a decrease of 14% according to RCP 4.5

(Figure 7A) and 31% according to RCP 8.5 (Figure 7B) compared to the reference period. The two bias correction methods have allowed a reduction of 47% of the bias calculated before the correction.

In spring (MAM), the difference between observed and projected raw precipitation over the period (2070–2099) predicts a decrease of the order of 64% according to RCP 4.5 (Figure 7A) and 76% according to RCP 8.5 (Figure 7B). However, after using both bias correction methods, the results indicate a reduction in rainfall of about 20% under the RCP 4.5 scenario (Figure 7A) and 45% under the RCP 8.5 scenario (Figure 7B). Both methods reduced the bias of the RCA4-MPI-ESM-LR model outputs by 31 to 44%.

In summer (JJA), the estimated change in raw precipitation over the projection period shows a decrease of more than 60% under RCP 4.5 and 70% under RCP 8.5. After bias correction, the results show an increase in rainfall of more than 20% under both emission scenarios (Figures 7A,B).

In autumn (SON), the projected raw precipitation over the period (2070–2099) shows a decrease of 57% under the scenario RCP 4.5 (Figure 7A) and 73% under the scenario RCP 8.5 (Figure 7B). After the application of the bias correction methods, the change in precipitation shows a respective decrease of 4 and 37% according to RCP 4.5 and RCP 8.5, which present a respective correction of bias with percentages of 53 and 36%.

3.3.2 Potential evapotranspiration projection

The projected potential evapotranspiration over the period 2070–2099 was obtained using the Thornwaite formula forced by the monthly bias-corrected projected temperature by the two RCM-GCMs.

At the annual scale, the projected PET presents an increase of about 10 to 32% according to RCP 4.5 and RCP 8.5 for the two climate models, compared to the reference period for the 2099 horizon (Figures 8A,B).

At the seasonal scale, the two RCM-GCM (CNRM-CM5 and MPI-ESM-LR) present future change in PET and show an increase for the four seasons of the year over the 2099 horizon under RCP 4.5 and RCP 8.5 (Figures 8A,B).

The RCA4-CNRM-CM5 model shows an increase of PET during winter (DJF) of about 15 to 65%, respectively, for the RCP 4.5 and RCP 8.5 scenarios (Figure 8A). In spring (MAM), the change in PET exceeds +20% according to the two emission scenarios (Figure 8A), while in summer (JJA), the projected PET shows a little increase of 3% according to RCP 4.5 and 36% according to RCP 8.5 (Figure 8A). In autumn (SON), the RCA4-CNRM-CM5 model projects an increase in PET of about 13% according to RCP 4.5 and 27% according to RCP 8.5 (Figure 8A) by 2099.

The future evolution of PET simulated by the MPI-ESM-LR model in winter (DJF) shows an increase of 11% under RCP 4.5 and 17% under RCP 8.5 (Figure 8B). In spring (MAM), PET estimates a small increase of 9%, according to RCP 4.5, and 23% according to RCP 8.5 (Figure 8B). The summer (JJA) and autumn (SON) seasons are characterized by a high increase in PET by 2099, which varies between 12%, according to RCP 4.5and 38%, according to RCP 8.5 (Figure 8B).

3.3.3 Hydrological projection

The projected flows of the Chiffa basin were simulated using the GR2M hydrological model calibrated over the reference period 1981–2000 and forced by RCM-GCMs projected corrected precipitation and PET during the period 2070–2099. The results show that the projected change in mean annual and mean seasonal flows is almost identical from the two used raw RCM-GCM (Figures 9A, 10A) because the simulated precipitation and PET are so close. At the annual scale, both RCM-GCM project an increase in the mean annual flow of about 11% over the 2070–2099 projection period under RCP 4.5 and RCP 8.5 emission scenarios (Figures 9A, 10A),

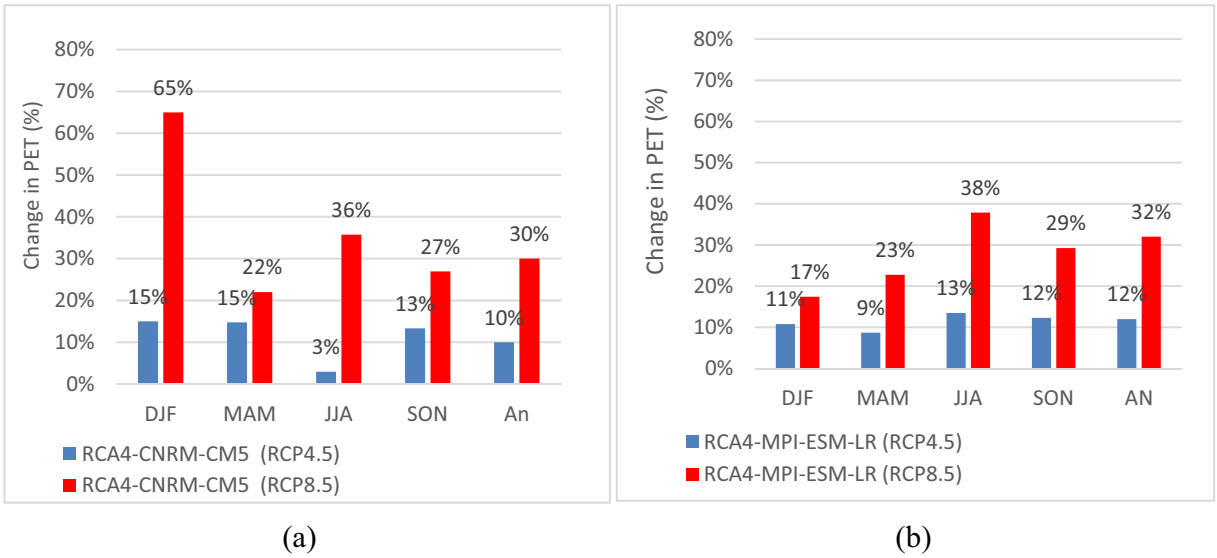

FIGURE 8
Seasonal and annual projected change in bias-corrected potential evapotranspiration according to **(A)** RCA4-CNRM-CM5 and **(B)** RCA4-MPI-ESM-LR, under RCP 4.5 and RCP 8.5 over the period (2070–2099).

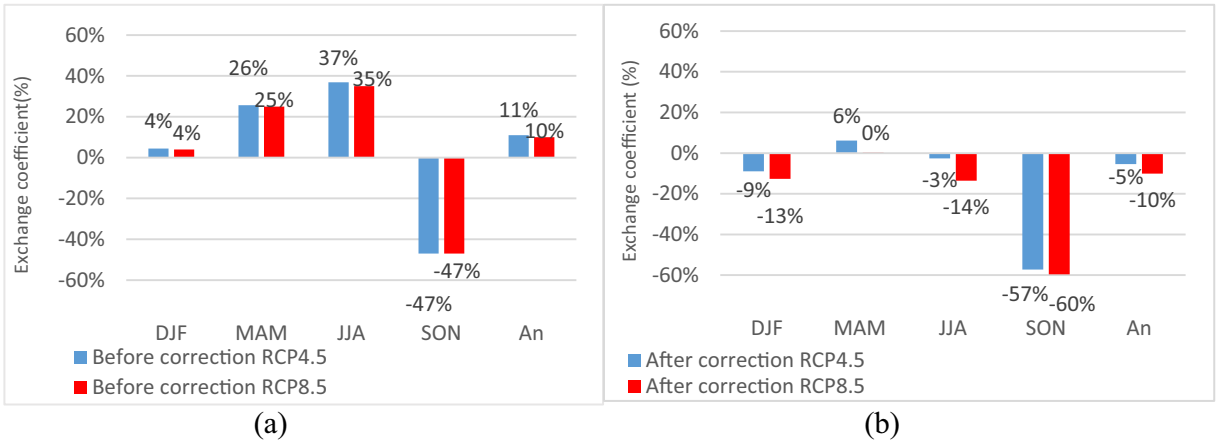

FIGURE 9
Seasonal and annual projected change in flow at the Chiffa catchment of **(A)** raw and **(B)** bias-corrected (Quantile mapping) climate model RCA4-CNRM-CM5 according to RCP 4.5 and RCP 8.5 over the period (2070–2099).

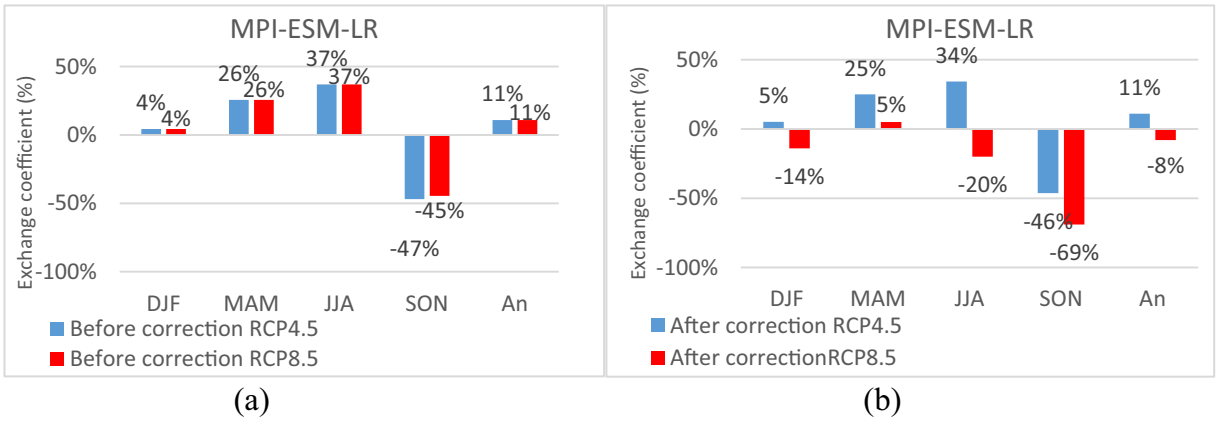

FIGURE 10
Seasonal and annual projected change in flow at the Chiffa catchment of **(A)** raw and **(B)** bias-corrected (Quantile mapping) climate model RCA4-MPI-ESM-LR according to RCP 4.5 and RCP 8.5 over the period 2070–2099.

while the simulated future raw rainfall is decreasing (see section 3.3.1).

At the seasonal scale, the two raw RCM-GCM predict an increase in runoff for three seasons—winter, spring, and summer—of about 4, 26, and 37%, respectively, according to RCP 4.5 and RCP 8.5 by 2099 (Figures 9A, 10A). In autumn (SON), the two raw climate models simulate a similar decrease in runoff of about 47% according to the two emission scenarios (Figures 9A, 10A). From these results, it is clear that the future evolution of flows (increasing trend) according to the raw climate model is consistent with the decreasing trend of precipitation projected by these two raw models (see section 3.3.1).

The projected evolution of annual flows simulated based on the bias correction by the Quantile mapping method, which is judged to be more relevant, indicates a decrease of 5 and 10% at the annual scale, respectively, according to the RCP 4.5 and RCP 8.5 emission scenarios by 2099, based on rainfall from the RCA4-CNRM-CM5 model (Figure 9B). At the seasonal scale, these RCM-GCM projects winter (DJF) a decrease of 9 and 13% of the mean seasonal flows, respectively, according to the two emission scenarios, RCP 4.5 and RCP 8.5 (Figure 9B).

In spring (MAM), the model indicates a little increase of 6% according to RCP 4.5 and no modification of the hydrological regime according to RCP 8.5 (Figure 9B). In summer (JJA), a decrease of 3 and 14% of the runoff is projected by the model under RCP 4.5 and RCP 8.5, respectively (Figure 9B). In autumn (SON), the results indicate a significant decrease in runoff of more than 50% under both RCP 4.5 and RCP 8.5 scenarios (Figure 9B), which is principally due to the significant decrease in runoff in October.

Concerning the RCA4-MPI-ESM-LR model at the annual scale, the projected flows at the horizon 2099 show an increase of 11% according to the RCP 4.5, whereas the RCP 8.5 predicts a decrease of 8% (Figure 10B). At the seasonal scale in winter (DJF), the model predicts a small increase of 5% according to RCP 4.5, while RCP 8.5 simulates a decrease of 14% (Figure 10B). In spring (MAM), the model projects an increase in runoff of 25% according to RCP 4.5 over the period 2070–2099; however, this increase is less important according to RCP 8.5 and does not exceed 5% (Figure 10B). In

TABLE 5 The results of the coefficient of determination (R^2) of raw and corrected (QM) flows from RCM-Cordex models.

Models	Coefficient of determination (R^2)	
	Raw	Corrected (QM)
RCA4-CNRM-CM5 RCP 4.5	0.53	0.95
RCA4-CNRM-CM5 RCP 8.5	0.44	0.89
RCA4-MPI-ESM-LR RCP 4.5	0.45	0.97
RCA4-MPI-ESM-LR RCP 8.5	0.53	0.83

summer (JJA), RCP 4.5 shows an increase in runoff that exceeds 20%, while RCP 8.5 predicts a decrease of 20% (Figure 10B). For the autumn season, the model predicts a significant reduction in runoff of 46 and 69% respectively, according to RCP 4.5 and RCP 8.5 (Figure 10B).

The coefficient of determination (R^2) results (Table 5) demonstrate the significant improvement in model performance achieved through bias correction using the Quantile mapping (QM) method. For the raw RCM-CORDEX models, R^2 values ranged between 0.44 and 0.53, indicating moderate performance in simulating observed flows. However, after applying the QM bias correction method, the R^2 values increased substantially, ranging from 0.83 to 0.97, showing excellent agreement between simulated and observed flows. The most notable improvement was the market for the RCA4-MPI-ESM-LR model under the RCP 4.5 scenario, where R^2 increased from 0.45 to 0.97, followed by RCA4-CNRM-CM5 under the RCP 4.5 with an improvement from 0.53 to 0.95. These results demonstrate the effectiveness of the QM bias correction method in enhancing the reliability of flow projections from RCM-CORDEX models.

4 Discussion

The performance of the GR2M model on the Chiffa basin showed that it was able to reproduce the hydrological response adequately during both calibration and validation periods. This result was in harmony with several previous studies showing successful application of this model in Algerian catchments such as the Kebir Rhumul basin in Eastern Algeria, where a good simulation of flow by the GR2M with a Nash criterion higher than 0.80 is obtained (Sakaa et al., 2015). Hadour et al. (2020) report results showing the high performance of the GR2M model in the Chellif basin (northern Algeria), with a Nash value of 73.6 and 75.8% estimated, respectively, in the calibration and validation periods. In the Mitidja basin (northern Algeria), Hallouz et al. (2018) showed satisfactory results in the validation of the GR2M with a Nash value higher than 60%. The results obtained in this study and previous ones could confirm GR2M as a suitable model for hydrological application in this region of the world.

A notable finding was the model's enhanced performance during the validation period compared to the calibration period (Nash values increasing from 77.5 to 99%). This improved performance can be attributed to the more humid hydrological regime during the validation period compared to the calibration period (1981–2000) and improved data quality. This behavior aligns with previous research demonstrating that rainfall-runoff models calibrated under dry conditions often show improved performance during wetter validation periods (Dakhlaoui et al., 2020; Coron et al., 2012). This pattern suggests the model parameters are robust rather than overfitted to specific climatic conditions, enhancing confidence in its application for future projections.

Overall, the RCA4-CNRM-CM5 and RCA4-MPI-ESM-LR models reproduce correctly the seasonality of temperature over the Chiffa basin during the reference period, which was confirmed by several previous studies that found that temperature does not have a significant spatial variability, and climate models are generally able to reproduce it correctly over the study area and over Algeria (Meddi and Meddi, 2009; Taibi et al., 2013; Bessaklia et al., 2018; Drouiche et al., 2019; Taibi et al., 2019).

For the RCA4-CNRM-CM5 model, the two bias correction methods give similar results in terms of future changes in precipitation. Similar results were found in several previous studies that have compared different methods of bias correction (e.g., Obada et al., 2016; Priyanko et al., 2022).

A detailed comparison of the two bias correction methods revealed distinctive patterns in their effectiveness for precipitation adjustment. For the RCA4-CNRM-CM5 model, both Quantile mapping and Delta methods showed comparable performance, with similar precipitation change patterns.

The Quantile mapping method demonstrated significant bias reduction capabilities, particularly in representing the full range of precipitation distribution, which is important for our catchment-scale analysis. This effectiveness was evidenced in other regions, such as Vietnam, where bias reductions of 3 to 45% were achieved in the regional model (RegCM) of the Cordex-SEA project. This project was piloted by five global climate models (CNRM-CM5, MPI-ESM-MR, EC-Earth, CSIRO, and GFDL-ESM2M) of the CMIP5 phase during the period (2046–2065) (Trinh-Tuan et al., 2018). In the Volta basin, where biases were reduced by −9 to 5% for the precipitation simulated by the raw data under the four Cordex–Africa project models of the RCA4 model forced by four global circulation models (MPI-ESM, CNRM-CM5, HadGEM2-ES, and CCLM4) at the level of the Volta basin (West Africa) on the horizon 2080 (Yeboah et al., 2022).

For the RCA4-MPI-ESM-LR model, the Delta method always shows a greater reduction of the change in precipitation, which is confirmed by previous studies such as Taibi et al. (2021b). They compared two bias correction methods (Quantile mapping and Delta method) on the evolution of precipitation simulated by two models (CNRM-CM5 and MPI-ESM-MR) of the Cordex-Africa project at the level of the Oran coastal basin during the projection period (2075–2099). Their results indicate that the Delta method delivered less biased results of −27% and −47% for the RCA4-MPI-ESM-LR model. Miralha et al. (2021) also found that the Delta method outperformed the other bias correction techniques used in this study (Delta, Linear empirical, Quantile mapping, and Quantile Delta mapping), and was applied to bias correct the four CMIP5 project models (CCSM4, CNRM-CM5, IPSL-CM5A-MR, and MPI-ESM-MR) over the period (2046–2065) on the Maumee River in the United States (Giuntoli et al., 2018).

In our study, the Quantile mapping method was particularly relevant given that the Oued Chiffa catchment (315.68 km^2) is smaller than one RCM grid cell of Cordex-Africa (~50 km × 50 km = 2,500 km^2). This method effectively provided additional statistical downscaling of the RCM output to fit the catchment scale, complementing the dynamical downscaling from the GCM (horizontal grid ~150 km × 150 km) to the RCM grid (~50 km × 50 km), this could explain the important reduction in precipitation change in bias-corrected RCM-GCM compared to raw simulation.

However, we recognize that hydrological modeling in the Chiffa catchment is challenging since RCM-GCM is not designed to represent precipitation features at a spatial scale smaller than their grid (Hakala et al., 2018).

Any bias correction method has limitations. The two bias correction techniques used in this study were univariate ones, which imply temperature and precipitation and have been corrected separately. The technique's limitation is that they do not take into consideration the intervariable dependence between climate variables. We propose the use, in future studies, more sophisticated techniques, such as multivariate bias correction (Cannon et al., 2020), that take into consideration intervariable dependence.

The results of hydro-climatic projection over the Chiffa catchment confirm results obtained by previous studies with different and/or earlier generations of climate models. For the precipitation, the overall results obtained on the future evolution of precipitation are concordant with previous studies in the Mediterranean region, including the Chiffa catchment (Zanis et al., 2008; Coppola and Giorgi, 2010; Ceglar et al., 2014; Babaousmail et al., 2022). Schilling et al. (2020) reported about a −20% to −40% decrease in projected mean precipitation over most parts of the Mediterranean region by the end of the 21st century, especially in Algeria and Morocco. Indeed, Driouech et al. (2020) showed that the Mediterranean area would experience a significant drying up by the end of the 21st century according to RCP 8.5, particularly over the western part of the MENA region, including Algeria. Their results indicate a reduction in total precipitation amounts ranging from −5% to −20% and exceeding −40% in the west of the Atlas Mountains.

For PET, results in the present study show an important increase in the evaporative demand for all seasons, which is in concordance with other studies already done in the Mediterranean basin. Indeed, Aubé (2016) found a 20% increase in PTE in the Rhone Mediterranean and Corsica basin by 2046–2065. Acharki et al. (2019) also showed that the autumn season is characterized by a high increase in evapotranspiration, which is about 60% over the projection period (2021–2050) in northern Morocco. In Algeria, Hadour et al. (2020) highlighted a 35 mm increase in PET by the end of the 21st century for the four seasons of the year in some basins of northwestern Algeria. Taibi et al. (2021a) found an increase in future PET that exceeds 30%, particularly in summer by 2100 in the Ain Dalia catchment located in eastern Algeria.

We recognize that the projected PET by a temperature-based formula as the Thornthwaite formula used in this study, could overestimate the projected increase in PET compared to a physically based formula such as Penman-Monteith that takes into consideration the change in the major physical variables leading to the evaporative demand (air temperature, vapor pressure, net radiation, and wind speed). The Thornthwaite formula's primary limitation lies in its sole reliance on temperature, which may not fully capture the complex interactions between climate variables affecting evapotranspiration, particularly in a changing climate context. This simplification could lead to potential biases in extreme seasons; especially during summer when other factors like wind speed and relative humidity play an important role in the evaporative process. However, several studies showed the low sensitivity of hydrological projection to PET formulation, especially for semi-arid regions (Oudin et al., 2005; Dakhlaoui et al., 2020), which is the case of our study catchment. The seasonal analysis of flow reduction indicates a more pronounced decrease, which is consistent with the projected decrease in precipitation. This seasonal pattern of flow reduction has significant implications for water resource management, particularly for irrigation planning and reservoir operation during the dry season.

For flows, the overall results obtained in this study show a decrease in flows by the end of the 21st century in Oued Chiffa. This reduction shows significant seasonal variations, with more pronounced decreases during the wet season (October–May) compared to the dry season. These seasonal patterns have important implications for water resource management, particularly regarding storage requirements. This projected decrease is in agreement with several studies conducted in several regions of the Mediterranean basin. For example, Nerantzaki et al. (2019) found a 24.2% decrease in flows in Greece by 2100. In Italy, the study by Perra et al. (2018) showed a 31% reduction in flows over the period (2041–2070) in the Rio Mannu catchment in southern Sardinia, while in France, on the Hérault River located in the south of the region that flows into the Mediterranean Sea at Agde, models predict a 7% decrease in flows by 2085. This observed impact is frequently recorded in the Mediterranean basin due to the sensitive vulnerability of this region to variations in rainfall and drier, warmer conditions (Coppens et al., 2020).

The hydrological simulation and projection in Oued Chifa were performed over a monthly time step; however, northern Algeria is well known for its torrential pluvial events. These extreme precipitation events are particularly challenging to model as they can generate significant flash floods and represent a substantial portion of the annual water balance in semi-arid regions. Additionally, it is important to consider resilient precipitation events that persist despite overall trends toward drier conditions, as they can also significantly contribute to the hydrological cycle.

Climate change is likely to affect not only the frequency but also the intensity of these events, potentially leading to more severe flooding episodes despite an overall decrease in annual precipitation. We recognize that any future change in precipitation intensity could have a big impact on the hydrological response and affect the proposed hydrological projection.

To better consider these complex interactions in future studies, we recommend implementing multivariate bias correction methods that can preserve the interdependence between different climate variables (such as temperature, precipitation, and humidity). These methods would be particularly relevant for semi-arid regions where the interaction between extreme and resilient precipitation events strongly influences the hydrological response. Furthermore, the use of high-resolution climate models coupled with event-based hydrological modeling could provide more accurate representations of intense precipitation events and their impacts on flash floods, which are important for water resource management and flood risk assessment in the region.

5 Conclusion

The objective of this study was to assess the impact of climate change on the flows of the Chiffa basin, which necessitates combining a hydrological model with climate model simulations. All the results obtained indicate a decrease in rainfall by 2099 at the scale of our study area.

Initial analysis of raw rainfall simulations from two RCM-GCMs from the Africa-Cordex project (RCA4-MPI-ESM-LR and RCA4-CNRM-CM5) during the reference period (1981–2010) indicates an important bias of 50%. This is primarily due to the models' limitations in representing regional atmospheric processes and local topographic effects characteristic of the Mediterranean region, with particular difficulties in reproducing extreme precipitation events and interannual variability. They are crucial elements for reliable hydrological modeling. These limitations necessitated the implementation of bias correction techniques to improve the reliability of future projections.

Following an application of bias correction, it is found that the difference between the future simulated rainfall corrected by the two bias correction methods (Quantile mapping and Delta change) by 2099 is significantly reduced biases in rainfall simulations compared to the uncorrected rainfall. This is due to the corrected simulated rainfall achieving a closer alignment with observed precipitation patterns. We observed significant improvements in model performance, with the coefficient of determination (R^2) increasing from 0.44–0.53 to 0.83–0.97, demonstrating a better representation of observed flow patterns. This indicates that the two bias correction methods used (Quantile mapping and Delta change) have proven to be effective in adjusting the seasonal and annual mean precipitation simulations (2074–2099) of the RCM (CNRM-CM5 and MPI-ESM-LR) to the observed precipitation values (1981–2010).

However, each correction method presented specific limitations: Quantile mapping occasionally introduced physical inconsistencies in the relationships between variables, while Delta change, although preserving temporal variability, may not fully capture changes in future precipitation distribution patterns. Despite these limitations, both methods substantially enhanced the model outputs' reliability for future projections.

The projected flows from the bias-corrected RCM-GCM during the period (2070–2099) showed a decrease of 5 and 10%, respectively, for RCP 4.5 and RCP 8.5 compared to the reference period, with more pronounced reductions during the winter and autumn seasons. This difference between scenarios (5% vs. 10%) provides a quantifiable measure of the uncertainty in future climate projections.

The methodological uncertainty was also present in our bias correction approach, though it was significantly reduced through the application of multiple correction methods. The seasonal changes in flow patterns have significant implications for water resource management in the Chiffa basin. The projected decrease in winter and autumn flows could particularly impact agricultural activities, since these seasons are crucial for soil moisture recharge and winter crop irrigation. Urban water supply may experience increased pressure during these periods, potentially requiring adaptation measures such as improved storage capacity or demand management strategies. Furthermore, the decreased flows during these seasons could affect ecosystems, particularly for aquatic habitats and riparian vegetation that rely on seasonal flow patterns. These findings suggest the need for integrated water resource management strategies should consider both human water needs and environmental flow requirements.

Therefore, the results obtained in this study are in full agreement with previous studies, strengthening our confidence in our findings conducted at the scale of the North African and Mediterranean regions. For example, De Girolamo et al. (2022) indicate that climate model projections for the period 2030–2059 predict reductions in the mean annual flow of up to 21 and 39% for the Celone River (Southern Italy) under a Mediterranean climate. Similarly, the study by Madani et al. (2024) in North Africa projects flow reductions ranging from 35 to 43%, with more severe impacts under the RCP 8.5 scenario for the period 2069–2099 in the Oued Abid catchment (Northern Tunisia).

Based on our findings, we recommend several directions for future research and water management: the implementation of multivariate bias correction methods (Cannon et al., 2020) would better preserve inter-variable dependencies, particularly between temperature and precipitation; the utilization of higher-resolution climate data (≤10 km) would improve the representation of local topographic effects; and the application of ensemble modeling approaches using multiple GCMs, RCMs, and hydrological models would better characterize uncertainty ranges and provide more robust projections.

For practical water management, our results suggest the need for specific adaptation strategies, including modified reservoir operation rules, drought-resistant crop selection, and enhanced water conservation measures. These strategies should be designed to address the projected seasonal changes in water availability, especially the more pronounced reductions in winter and autumn flows.

In conclusion, this study strengthens the extensive evidence of climate change impacts on North Africa and the Mediterranean region, underscoring the necessity of robust methodological rigor in climate impact assessments. The demonstrated effectiveness of bias correction methods, coupled with a comprehensive understanding of their limitations, provide valuable insights for future climate impact studies. The alignment of our results with other regional studies strengthens confidence in our projections while acknowledging the continuing challenges of accurately representing local-scale processes.

The integration of more sophisticated modeling approaches, combined with robust uncertainty quantification and practical adaptation strategies, will be crucial for effective water resource management in the face of climate change.

In order to enhance the robustness of future climate impact assessments in the region, we strongly recommend the use of multiple climate models and bias correction methods to capture the complete range of uncertainties. This comprehensive approach, combined with detailed analyses of local conditions and specific adaptation requirements, will support better informed decision-making for sustainable water resource management in the Chiffa basin and similar Mediterranean watersheds.

Data availability statement

The data analyzed in this study is subject to the following licenses/restrictions: The National Office of Meteorology (ONM) provides the *in-situ* data, and the Coordinated Regional Climate Research Study on Africa (CORDEX-Africa) provides the National Agency of Water Resources (ANRH). Projected data from the RCA4-MPI-ESM-LR and RCA4-CNRM-CM5 models. Requests to access these datasets should be directed to https://cordex.org/data-access/.

Author contributions

AM: Writing – original draft. TH: Conceptualization, Methodology, Supervision, Validation, Writing – review & editing. ST: Conceptualization, Methodology, Supervision, Validation, Writing – review & editing. HD: Validation, Writing – review & editing. MM: Supervision, Validation, Writing – review & editing.

Funding

The author(s) declare financial support was received for the research, authorship, and/or publication of this article. The author declare that the publication of this paper was supported by ResAllaince Project (101086600 ResAlliance HORIZON-CL6-2022-GOVERNANCE-01), the authors are grateful to the ResAlliance project for funding the article processing charge.

Acknowledgments

The authors wish to express their gratitude to the National Office of Meteorology (ONM) for providing the climate data as well as the National Agency of Water Resources (ANRH) for the rainfall and hydrometric data on which the analyses of this study are based. Our thanks go to the Regional Climate Downscaling Experiment (CORDEX-Africa). The authors are thankful to the National Research Institute for Rural Engineering, Water and Forestry (INRGREF) for its valuable support of this research.

Conflict of interest

The authors declare that the research was conducted in the absence of any commercial or financial relationships that could be construed as a potential conflict of interest.

Generative AI statement

The author(s) declare that no Generative AI was used in the creation of this manuscript.

Publisher's note

All claims expressed in this article are solely those of the authors and do not necessarily represent those of their affiliated organizations, or those of the publisher, the editors and the reviewers. Any product that may be evaluated in this article, or claim that may be made by its manufacturer, is not guaranteed or endorsed by the publisher.

References

A.P.N.A. (2006). Atlas des parcs nationaux algériens (Direction Générale des forêts, Parc national de Théniet El Had. 98) (Atlas of Algerian National Parks (General Directorate of Forests, Theniet El Had National Park). 98).

Acharki, S., Amharref, M., El Halimi, R., and Bernoussi, A. S. (2019). Évaluation par approche statistique de l'impact des changements climatiques sur les ressources en eau: application au périmètre du Gharb (Maroc). *J. Water Sci.* 32, 291–315. doi: 10.7202/1067310ar

Alkama, R., Marchand, L., Ribes, A., and Decharme, B. (2013). Detection of global runoff changes: results from observations and CMIP5 experiments. *Hydrol. Earth Syst. Sci.* 17, 2967–2979. doi: 10.5194/hess-17-2967-2013

Al-Safi, H. I. J., Kazemi, H., and Sarukkalige, P. R. (2020). Comparative study of conceptual versus distributed hydrologic modelling to evaluate the impact of climate change on future runoff in unregulated catchments. *J. Water Clim. Change* 11, 341–366. doi: 10.2166/wcc.2019.180

Aubé, D. (2016). Impacts du changement climatique dans le domaine de l'eau Sur les bassins Rhône-Méditerranée et Corse Bilan actualisé des connaissances (Impacts of climate change in the field of water on the Rhône-Mediterranean and Corsica basins – updated knowledge report). Water & Knowledge, Rhône Mediterranean Corsica Water Agency, 114.

Babaousmail, H., Hou, R., Ayugi, B., Sian, L. K., Ojara, M., Mumo, R., et al. (2022). Future changes in mean and extreme precipitation over the Mediterranean and Sahara regions using Bias-corrected CMIP6 models. *Int. J. Climatol.* 42, 7280–7297. doi: 10.1002/joc.7644

Bargaoui, Z., Dakhlaoui, H., and Houcine, A. (2008). Modélisation Pluie-Débit et Classification Hydroclimatique. *J. Water Sci.* 2008, 123–125. doi: 10.7202/018468ar

Bessaklia, H., Ghenim, A. N., Megnounif, A., and Martin-Vide, J. (2018). Spatial variability of concentration and aggressiveness of precipitation in north-east of Algeria. *J. Water Land Dev.* 36, 3–15. doi: 10.2478/jwld-2018-0001

Beyer, R., Krapp, M., and Manica, A. (2019). A systematic comparison of bias correction methods for paleoclimate simulations. *Clim. Past Discuss.* 30, 1–23. doi: 10.5194/cp-2019-11

Bouderbala, A. (2019). The impact of climate change on groundwater resources in coastal aquifers: case of the alluvial aquifer of Mitidja in Algeria. *Environ. Earth Sci.* 78:698. doi: 10.1007/s12665-019-8702-5

Bouguerra, S. A., and Mansour, B. (2023). Rainfall-flow modeling using a global conceptual model: case of the Beni Bahdel watershed (northwest of Algeria). *J. Water Manag. Model.* 12, 3820–3838.

Cannon, A. J., Piani, C., and Sippel, S. (2020). "Bias correction of climate model output for impact models" in Climate extremes and their implications for impact and risk assessment. eds. J. Sillmann, S. Sippel and S. Russo (Amsterdam, Netherlands: Elsevier), 77–104.

Ceglar, A., Honzak, L., Žagar, N., Skok, G., Žabkar, R., and Rakovec, J. (2014). Evaluation of precipitation in the ENSEMBLES regional climate models over the complex orography of Slovenia. *Int. J. Climatol.* 35, 2574–2591. doi: 10.1002/joc.4158

Charifi, S. (2018). Application du modèle hydrologique GR2M Sur les bassins versants de la Soummam et de l'Isser. Conf on implication of a "potato-green bean" mixed crop system on water and light use efficiencies at: WATMED 4-Algiers.

Chathuranika, I. M., Gunathilake, M. B., Azamathulla, H. M., and Rathnayake, U. (2022). Evaluation of future streamflow in the upper part of the Nilwala River basin (Sri Lanka) under climate change. *Hydrology.* 9:48. doi: 10.3390/hydrology9030048

Chelkeba, B. (2021). Performance assessment of six bias correction methods using observed and RCM data at upper awash basin, Oromia, Ethiopia. *J. Water Clim. Change* 13, 664–683. doi: 10.2166/wcc.2021.181

Coppens, J., Trolle, D., Jeppesen, E., and Beklioğlu, M. (2020). The impact of climate change on a Mediterranean shallow lake: insights based on catchment and lake modelling. *Reg. Environ. Chang.* 20:62. doi: 10.1007/s10113-020-01641-6

Coppola, E., and Giorgi, F. (2010). An assessment of temperature and precipitation change projections over Italy from recent global and regional climate model simulations. *Int. J. Climatol.* 30, 11–32. doi: 10.1002/joc.1867

Coron, L., Andréassian, V., Perrin, C., Lerat, J., Vaze, J., Bourqui, M., et al. (2012). Crash testing hydrological models in contrasted climate conditions: an experiment on 216 Australian catchments. *Water Resour. Res.* 48, 1–17. doi: 10.1029/2011WR011721

Dakhlaoui, H., Bargaoui, Z., and Bardossy, A. (2009). Comparaison de trois méthodes d'usage de la technique des voisins les plus proches en vue d'amélioration de la performance de l'algorithme SCE-UA appliqué pour le calage du modèle pluie-débit HBV. Hydroinformatics in Hydrology, Hydrogeology and Water Resources, IAHS Publ. 331, 139–153.

Dakhlaoui, H., and Djebbi, K. (2021). Evaluating the impact of rainfall-runoff model structural uncertainty on the hydrological rating of regional climate model simulations. *J. Water Clim. Change*. doi: 10.2166/wcc.2021.004

Dakhlaoui, H., Hakala, K., and Seibert, J. (2022). "Hydrological impacts of projected climate change on northern Tunisian headwater catchments—an ensemble approach addressing uncertainties" in Climate change in the Mediterranean and middle eastern region. Climate change management. eds. F. W. Leal and E. Manolas (Cham: Springer).

Dakhlaoui, H., Seibert, J., and Hakala, K. (2020). Sensitivity of discharge projections to potential evapotranspiration estimation in northern Tunisia. *Reg. Environ. Chang.* 20:34. doi: 10.1007/s10113-020-01615-8

De Girolamo, A. M., Barca, E., Leone, M., and Porto, A. L. (2022). Impact of long-term climate change on flow regime in a Mediterranean basin. *J. Hydrol. Regn. Chang.* 41:101061. doi: 10.1007/s10113-020-01641-6

Dimri, A. P. (2021). Bias correction demonstration in two of the Indian Himalayan river basins. *J. Water Clim. Change* 12, 1297–1309. doi: 10.2166/wcc.2020.119

Ditthakit, P., Pinthong, S., Salaeh, N., Binnui, F., Khwanchum, L., and Bao Pham, Q. (2021a). Using machine-learning methods for supporting GR2M model in runoff estimation in an ungauged basin. *Sci. Rep.* 11:19955. doi: 10.1038/s41598-021-99164-5

Ditthakit, P., Pinthong, S., Salaeh, N., Binnui, F., Khwanchum, L., Kuriqi, A., et al. (2021b). Performance evaluation of a two-parameters monthly rainfall-runoff model in the Southern Basin of Thailand. *Water.* 13:1226. doi: 10.3390/w13091226

Dixit, S., Tayyaba, S., and Jayakumar, K. V. (2021). Spatio-temporal variation and future risk assessment of projected drought events in the Godavari River basin using regional climate models. *J. Water Clim. Change* 12, 3240–3263. doi: 10.2166/wcc.2021.093

Djebbi, K., and Dakhlaoui, H. (2023). Evaluating regional climate model simulations at Wadi El Abid catchment (northeastern Tunisia) using HBV rainfall-runoff model. *Arab. J. Geosci.* 16:139. doi: 10.1007/s12517-022-11160-9

Driouech, F., ElRhaz, K., Moufouma-Okia, W., Arjdal, K., and Balhane, S. (2020). Assessing future changes of climate extreme events in the CORDEX-MENA region using regional climate model ALADIN-climate. *Earth Syst. Environ.* 4, 477–492. doi: 10.1007/s41748-020-00169-3

Drouiche, A., Nezzal, F., and Djema, M. (2019). Variabilité interannuelle des précipitations dans la plaine de la Mitidja en Algérie du Nord (Interannual variability of precipitation in the Mitidja plain in Northern Algeria). *J. Water Sci.* 32, 165–177. doi: 10.7202/1065205ar

Dunning, C. M., Black, E., and Allan, R. P. (2018). Later wet seasons with more intense rainfall over Africa under future climate change. *J. Clim.* 31, 9719–9738. doi: 10.1175/JCLI-D-18-0102.1PP

Eekhout, J. P. C., and De Vente, J. (2018). The implications of bias-correction methods and climate model ensembles on soil erosion projections under climate change. *Earth Surf. Process. Landf.* 44, 1137–1147. doi: 10.1002/esp.4563

Emami, F., and Koch, M. (2018). Evaluation of statistical-downscaling/Bias-correction methods to predict hydrologic responses to climate change in the Zarrine River basin, Iran. *Climate.* 6:30. doi: 10.3390/cli6020030

Enayati, M., Bozorg-Haddad, O., Bazrafshan, J., Hejabi, S., and Chu, X. (2021). Bias correction capabilities of quantile mapping methods for rainfall and temperature variables. *J. Water Clim. Change* 12, 401–419. doi: 10.2166/wcc.2020.261

Fathi, M. M., Awadallah, A. G., Abdelbaki, A. M., and Haggag, M. (2019). A new Budyko framework extension using time series SARIMAX model. *J. Hydrol.* 570, 827–838. doi: 10.1016/j.jhydrol.2019.01.037

Foughali, A., Tramblay, Y., Bargaoui, Z., Carreau, J., and Ruelland, D. (2015). Hydrological modeling in northern Tunisia with regional climate model outputs: performance evaluation and Bias-correction in present climate conditions. *Climate.* 3, 459–473. doi: 10.3390/cli3030459

François, B., Vrac, M., Cannon, A. J., Robin, Y., and Allard, D. (2020). Multivariate bias corrections of climate simulations: which benefits for which losses? *Earth Syst. Dynam.* 11, 537–562. doi: 10.5194/esd-11-537-2020

Gader, K., Gara, A., Vanclooster, M., and Slimani, M. (2020). Quantification of predictive uncertainty in climate change context using airGRpackages: case of Medjerda catchment, Tunisia. 3rd Conference of the Arabian Journal of Geosciences (CAJG) In: Webinaire.

Giuntoli, I., Villarini, G., Prudhomme, C., and Hannah, D. M. (2018). Uncertainties in projected runoff over the conterminous United States. *Clim. Chang.* 150, 149–162. doi: 10.1007/s10584-018-2280-5

Gu, J., Liu, S., Zhou, Z., Chalov, S., and Qi, Z. (2022). Stacking ensemble learning model for monthly rainfall prediction in the Taihu Basin, China. *Water.* 14:492. doi: 10.3390/w14030492

Gupta, H. V., Kling, H., Yilmaz, K. K., and Martinez, G. F. (2009). Decom-position of the mean squared error and NSE performance criteria: implications for improving hydrological modelling. *J. Hydrol.* 377, 80–91. doi: 10.1016/j.jhydrol.2009.08.003

Hadour, A., Mahé, G., and Meddi, M. (2020). Watershed based hydrological evolution under climate change effect: an example from North Western Algeria. *J. Hydrol. Reg. Stud.* 28:100671. doi: 10.1016/j.ejrh.2020.100671

Hakala, K., Addor, N., and Seibert, J. (2018). Hydrological modeling to evaluate climate model simulations and their Bias correction. *J. Hydrometeorol.* 19, 1321–1337. doi: 10.1175/JHM-D-17-0189.1

Hallouz, F., Karahacane, H., Meddi, M., Mahé, G., Sadi, F., Benchikh, H., et al. (2018). "Impact of climate variability on hydrology of the Western Mitidja watershed, Algeria" in Recent advances in environmental science from the Euro-Mediterranean and surrounding regions. EMCEI. Advances in science, Technology & Innovation. eds. A. Kallel, M. Ksibi, H. Ben Dhia and N. Khélifi (Cham: Springer), 753–754.

Heo, J. H., Ahn, H., Shin, J. Y., Kjeldsen, T. R., and Jeong, C. (2019). Probability distributions for a quantile mapping technique for a Bias correction of precipitation data: a case study to precipitation data under climate change. *Water.* 11:1475. doi: 10.3390/w11071475

Ibrahim, B., Karambiri, H., and Polcher, J. (2015). Hydrological impacts of the changes in simulated rainfall fields on Nakanbe Basin in Burkina Faso. *Climate.* 3, 442–458. doi: 10.3390/cli3030442

IPCC (2019). "Summary for policymakers" in Climate change and land: an IPCC special report on climate change, desertification, land degradation, sustainable land management, food security, and greenhouse gas fluxes in terrestrial ecosystems. eds. V. P. Masson-Delmotte, A. Zhai, S. L. Pirani, C. Connors, S. Péan, N. Berger, et al. (Geneva: IPCC).

IPCC (2021). "Weather and climate extreme events in a changing climate" in Climate change 2021: The physical science basis. Contribution of working group I to the sixth assessment report of the intergovernmental panel on climate change. eds. V. Masson-Delmotte, P. M. Zhai and A. Piraniet al. (Cambridge and New York: Cambridge University Press), 1513–1766.

Koffi, Y. B., Ayral, P. A., Kouassi, A. M., Johannet, A., and Biemi, J. (2011). Modélisation des débits des rivières en région tropicale humide: application des réseaux de neurones et du modèle Gr2m au bandama blanc (côte d'ivoire) (Modeling of rivers flow in tropical humid area: application of neural networks and the model gr2m to the Bandama Blanc River (Côte d'Ivoire)). *Rev. Ivoir. Sci. Technol.* 17, 151–171. doi: 10.4000/physio-geo.940

Lehner, F., Deser, C., Maher, N., Marotzke, J., Fischer, E. M., Brunner, L., et al (2020). Partitioning climate projection uncertainty with multiple large ensembles and CMIP5/6. *Earth Syst. Dynam.* 11:491508. doi: 10.5194/esd-11-491-2020

Macias, D., Garcia-Gorriz, E., Dosio, A., Stips, A., and Keuler, K. (2018). Obtaining the correct sea surface temperature: bias correction of regional climate model data for the Mediterranean Sea. *Clim. Dyn.* 51, 1095–1117. doi: 10.1007/s00382-016-3049-z

Madani, A. Z., Hermassi, T., Taibi, S., Boudabbous, K., and Mechergui, M. (2024). Climate change impacts on the hydrological behaviour of watershed in northeastern Tunisia (Oued El Abid watershed). *GSC Advanc. Res. Rev.* 20, 175–186. doi: 10.30574/gscarr.2024.20.3.0350

Mahdaoui, K., Chafiq, T., Asmlal, L., and Tahiri, M. (2024). Assessing hydrological response to future climate change in the Bouregreg watershed, Morocco. *Sci. African* 23:e02046. doi: 10.1016/j.sciaf.2023.e02046

Maraun, D. (2016). Bias correcting climate change simulations – a critical review. *Curr. Clim. Chang. Rep.* 2, 211–220. doi: 10.1007/s40641-016-0050-x

Marcos, R., Llasat, M. C., Quintana-Seguí, P., and Turco, M. (2018). Use of bias correction techniques to improve seasonal forecasts for reservoirs – a case study in northwestern Mediterranean. *Sci. Total Environ.* 610, 64–74. doi: 10.1016/j.scitotenv.2017.08.010

Martins, J., Fraga, H., Fonseca, A., and Santos, J. A. (2021). Climate projections for precipitation and temperature indicators in the Douro wine region: the importance of Bias correction. *Agronomy* 11:990. doi: 10.3390/agronomy11050990

Meddi, H., and Meddi, M. (2009). Variabilité des précipitations annuelles du Nord-Ouest de l'Algérie (Variability of annual rainfall in North-West Algeria). *Sci. Planet. Change / Drought.* 20, 57–65. doi: 10.1684/sec.2009.0169

Mendez, M., Maathuis, B., Hein-Griggs, D., and Alvarado-Gamboa, L. F. (2020). Performance evaluation of Bias correction methods for climate change monthly precipitation projections over Costa Rica. *Water* 12:482. doi: 10.3390/w12020482

Mengistu, A. G., Woldesenbet, T. A., and Dile, Y. T. (2021). Evaluation of the performance of bias-corrected CORDEX regional climate models in reproducing Baro–Akobo basin climate. *Theor. Appl. Climatol.* 144, 751–767. doi: 10.1007/s00704-021-03552-w

Mesta, B., and Kentel, E. (2021). Superensembles of raw and bias-adjusted regional climate models for Mediterranean region, Turkey. *Int. J. Climatol.* 42, 2566–2585. doi: 10.1002/joc.7381

Miralha, L., Muenich, R. L., Scavia, D., Wells, K., Steiner, A. L., Kalcic, M., et al. (2021). Bias correction of climate model outputs influences watershed model nutrient load predictions. *Sci. Total Environ.* 759:143039. doi: 10.1016/j.scitotenv.2020.143039

Motlagh, S. B., Honarbakhsh, A., Azizian, A., et al. (2022). Bias correction performance of global precipitation forecasting systems in Poldokhtar watershed in Iran. *Res. Sq.* 1–26. doi: 10.21203/rs.3.rs-1644511/v1

Nash, J. E., and Sutcliffe, J. V. (1970). River flow forecasting through conceptual models part I—A discussion of principles. *J. Hydrol.* 10, 282–290. doi: 10.1016/0022-1694(70)90255-6

Nerantzaki, S. D., Efstathiou, D., Giannakis, G. V., Kritsotakis, M., Grillakis, M. G., Koutroulis, A. G., et al. (2019). Climate change impact on the hydrological budget of a large Mediterranean island. *Hydrol. Sci. J.* 64, 1190–1203. doi: 10.1080/02626667.2019.1630741

Nounangnonhou, T. C., Fifatin, F. X., Lokonon, B. E., Acakpovi, A., and Sanya, E. A. (2018). Modelling and prediction of ouémé (Benin) river flows by 2040 based on gr2m approach. *LARHYSS J.* 33, 71–91.

Obada, E., Adéchina, A., Zandagba, J., Biao, E., Amédée, C., and Abel, A. (2016). Comparative study of seven bias correction methods applied to three regional climate models in Mekrou catchment (Benin, West Africa). *Int. J. Curr. Eng. Technol.* 6, 1831–1840. doi: 10.1016/j.ejrh.2021.100937

Orozco, J. C. C., Aranzana, M. F. G., and Hurtado, S. S. (2021). Hydrological modeling of high jungle area sub-basin, using the GR2M, Temez and Lutz Scholtz models. Congreso Internacional de Innovación y Tendencias en Ingeniería (CONIITI), 1–6. doi: 10.1109/CONIITI53815.2021.9619714

Oruc, S. (2022). Performance of bias corrected monthly CMIP6 climate projections with different reference period data in Turkey. *Acta Geophys.* 70:777. doi: 10.1007/s11600-022-00731-9

Ouatiki, H., Boudhar, A., Ouhinou, A., Arioua, A., Hssaisoune, M., Bouamri, H., et al. (2019). Trend analysis of rainfall and drought over the Oum Er-Rbia River basin in Morocco during 1970–2010. *Arab. J. Geosci.* 12:128. doi: 10.1007/s12517-019-4300-9

Oudin, L., Hervieu, F., Michel, C., Perrin, C., Andréassian, V., Anctil, F., et al. (2005). Which potential evapotranspiration input for a lumped rainfall-runoff model? Part 2: towards a simple and efficient potential evapotranspiration model for rainfall-runoff modelling. *J. Hydrol.* 303, 290–306. doi: 10.1016/j.jhydrol.2004.08.026

Ouhamdouche, S., Bahir, M., Carreira, P. M., and Zouari, K. (2018). Climate change impact on future flows in semi-arid environment, case of Essaouira Basin (Morocco). In: H. Chaminé, M. Barbieri, O. Kisi, M. Chen and B. Merkel (eds) Advances in Sustainable and Environmental Hydrology, Hydrogeology, Hydrochemistry and Water

Resources. Conference of the Arabian Journal of Geosciences, Advances in Science, Technology & Innovation. Springer, Cham

Parthiban, L., and Amit, B. M. (2021). Statistical downscaling using principal component regression for climate change impact assessment at the Cauvery River basin. *J. Water Clim. Change* 12, 2314–2324. doi: 10.2166/wcc.2021.223

Pastén-Zapata, E., Jones, J. M., Moggridge, H., and Widmann, M. (2020). Evaluation of the performance of euro-CORDEX regional climate models for assessing hydrological climate change impacts in Great Britain: a comparison of different spatial resolutions and quantile mapping bias correction methods. *J. Hydrol.* 584:124653. doi: 10.1016/j.jhydrol.2020.124653

Perra, E., Piras, M., Deidda, R., Paniconi, C., Mascaro, G., Vivoni, E. R., et al. (2018). Multimodel assessment of climate change-induced hydrologic impacts for a Mediterranean catchment. *Hydrol. Earth Syst. Sci.* 22, 4125–4143. doi: 10.5194/hess-22-4125-2018

Perrin, C., Claude, M., and Vazken, A. (2007). Modèles hydrologiques du génie rural (GR). Cemagref, UR Hydrosystèmes et Bioprocédés 16.

Priyanko, D., Zhenke, Z., and Hang, R. (2022). Evaluation of four bias correction methods and random forest model for climate change projection in the Mara River basin, East Africa. *J. Water Clim. Change* 13, 1900–1919. doi: 10.2166/wcc.2022.299

Pulido-Velazquez, D., Collados-Lara, A. J., Pérez-Sánchez, J., Segura-Méndez, F. J., and Senent-Aparicio, J. (2021). Climate change impacts on the streamflow in Spanish basins monitored under near-natural conditions. *J. Hydrol. Reg. Stud.* 38:100937. doi: 10.1016/j.ejrh.2021.100937

Rajab, H., Shiru, M. S., Shahid, S., Ismail, T., Bin Harun, S., Al-Ansari, N., et al. (2020). Precipitation projection using a CMIP5 GCM ensemble model: a regional investigation of Syria. *Eng. Appl. Comput. Fluid Mech.* 14, 90–106. doi: 10.1080/19942060.2019.1683076

Räty, O., Räisänen, J., Bosshard, T., and Donnelly, C. (2018). Intercomparison of univariate and joint Bias correction methods in changing climate from a hydrological perspective. *Climate.* 6:33. doi: 10.3390/cli6020033

Ruelland, D., Ardoin-Bardin, S., Collet, L., and Roucou, P. (2012). Simulating future trends in hydrological regime of a large Sudano-839 Sahelian catchment under climate change. *J. Hydrol.* 424–425, 207–216. doi: 10.1016/j.jhydrol.2012.01.002

Sakaa, B., Boulghobra, N., Chaffai, H., Hani, A., and Djabri, L. (2015). Application of GR2M for rainfall-runoff modeling in Kébir Rhumel watershed, north east of Algeria. *World Appl. Sci. J.* 33, 1623–1630. doi: 10.5829/idosi.wasj.2015.33.10.367

Satiprasad, S., Saumava, D., Anirban, D., Debsarkar, A., and Biswajeet, P. (2019). On projected hydrological scenarios under the influence of bias-corrected climatic variables and LULC. *Ecol. Indic.* 106, 1–17. doi: 10.1016/j.ecolind.2019.105440

Schilling, J., Hertig, E., Tramblay, Y., and Scheffran, J. (2020). Climate change vulnerability, water resources and social implications in North Africa. *Reg. Environ. Chang.* 20, 1–12. doi: 10.1007/s10113-020-01597-7

Schmidli, J., Frei, C., and Vidale, P. L. (2006). Downscaling from GCM precipitation: a benchmark for dynamical and statistical downscaling methods. *Int. J. Climatol.* 26, 679–689. doi: 10.1002/joc.1287

Shin, J. Y., Lee, T., Park, T., and Kim, S. (2019). Bias correction of RCM outputs using mixture distributions under multiple extreme weather influences. *Theor. Appl. Climatol.* 137, 201–216. doi: 10.1007/s00704-018-2585-3

Sidibe, M., Dieppois, B., Eden, J., Mahé, G., Paturel, J. E., Amoussou, E., et al. (2020). Near-term impacts of climate variability and change on hydrological systems in west and Central Africa. *Clim. Dyn.* 54, 2041–2070. doi: 10.1007/s00382-019-05102-7

Smitha, P. S., Narasimhan, B., Sudheer, K. P., and Annamalai, H. (2018). An improved bias correction method of daily rainfall data using a sliding window technique for climate change impact assessment. *J. Hydrol.* 556, 100–118. doi: 10.1016/j.jhydrol.2017.11.010

Soriano, E., Mediero, L., and Garijo, C. (2019). Selection of Bias correction methods to assess the impact of climate change on flood frequency curves. *Water.* 11:2266. doi: 10.3390/w11112266

Sorland, S., Schär, C., Lüthi, D., and Kjellström, E. (2018). Bias patterns and climate change signals in GCM-RCM model chains. *Environ. Res. Lett.* 13, 1–10. doi: 10.1088/1748-9326/aacc77

Szabó-Takács, B., Farda, A., Skalák, P., and Meitner, J. (2019). Influence of bias correction methods on simulated Köppen–Geiger climate zones in Europe. *Climate.* 7:18. doi: 10.3390/cli7020018

Taibi, S., Anza, F. Z. H., and Zeroual, S. (2021a). Etude de l'impact des changements climatiques sur la disponibilité des ressources en eau basée sur les simulations du modèle climatique régional RCA4: cas du bassin de Ain DALIA (Algérie). *Algerian J. Environ. Sci. Technol.* 7, 1860–1869.

Taibi, S., Boegh, E., Blyth, E., Hannah, D. M., Hisdal, H., Kunstmann, H., et al (2013). "Evolution et régionalisation des précipitations au nord de l'Algérie (1936–2009)" in Climate and land surface changes in hydrology. eds. E. Boegh, E. Blyth, D. M. Hannah, H. Hisdal, H. Kunstmann, B. Su, et al. (Wallingford: IAHS Publ. 359), 191–197.

Taibi, S., Meddi, M., and Mahe, G. (2019). Seasonal rainfall variability in the southern Mediterranean border: observations, regional model simulations and future climate projections. *Atmosfera* 32, 39–54. doi: 10.20937/ATM.2019.32.01.04

Taibi, S., Zeroual, A., and Meddi, M. (2022). Effect of autocorrelation on temporal trends in air-temperature in northern Algeria and links with teleconnections patterns. *Theor. Appl. Climatol.* 147, 959–984. doi: 10.1007/s00704-021-03862-z

Taibi, S., Zeroual, A., and Melhani, N. (2021b). Evaluation de deux méthodes de correction de biais des sorties de modèles climatiques régionaux Cordex-Africa pour la prévision des pluies: cas du bassin côtier oranais. *Proc. IAHS.* 384, 213–218. doi: 10.5194/piahs-384-213-2021

Tamene, D., and Chala, S. (2021). Assessment of the performance of CORDEX regional climate models in simulating rainfall and air temperature over Southwest Ethiopia. *Heliyon.* 7:e07791. doi: 10.1016/j.heliyon.2021.e07791

Tan, Y., Guzman, S. M., Dong, Z., and Tan, L. (2020). Selection of effective GCM Bias correction methods and evaluation of hydrological response under future climate scenarios. *Climate.* 8:108. doi: 10.3390/cli8100108

Teutschbein, C., and Seibert, J. (2010). Regional climate models for hydrological impact studies at the catchment scale: a review of recent modeling strategies. *Geography* 4, 834–860. doi: 10.1111/j.1749-8198.2010.00357.x

Teutschbein, C., and Seibert, J. (2012). Bias correction of regional climate model simulations for hydrological climate-change impact studies: review and evaluation of different methods. *J. Hydrol.* 456, 12–29. doi: 10.1016/j.jhydrol.2012.05.052

Thornthwaite, C. W., and Mather, J. R. (1951). The role of evapotranspiration in climate. *Arch. Meteorol., Geophys. Bioklimatol., Ser. B* 3, 16–39. doi: 10.1007/BF02242588

Todorovic, A., and Plavsic, J. (2016). The role of conceptual hydrologic model calibration in climate change impact on water resources assessment. *J. Water Clim. Change* 7, 16–28. doi: 10.2166/wcc.2015.086

Trinh-Tuan, L., Matsumoto, J., Tangang, F. T., Juneng, L., Cruz, F., Narisma, G., et al. (2018). Application of quantile mapping bias correction for mid-future precipitation projections over Vietnam. *SOLA.* 15, 1–6. doi: 10.2151/sola.2019-001

White, R. H., and Toumi, R. (2013). The limitations of bias correcting regional climate model inputs. *Geophys. Res. Lett.* 40, 2907–2912. doi: 10.1002/grl.50612

Willkofer, F., Schmid, F. J., Komischke, H., Korck, J., Braun, M., and Ludwig, R. (2018). The impact of bias correcting regional climate model results on hydrological indicators for Bavarian catchments. *J. Hydrol. Reg. Stud.* 19, 25–41. doi: 10.1016/j.ejrh.2018.06.010

Yeboah, K., Akpoti, K., Kabo-Bah, A., Ofosu, E., Siabi, E., Mortey, E., et al. (2022). Assessing climate change projections in the Volta Basin using the CORDEX-Africa climate simulations and statistical bias-correction. *Environ. Challenges* 6:100439. doi: 10.1016/j.envc.2021.100439

Zanis, P., Kapsomenakis, I., Philandras, C., Douvis, K., Nikolakis, D., Kanellopoulou, E., et al. (2008). Analysis of an ensemble of present day and future regional climate simulations for Greece. *Int. J. Climatol.* 29, 1614–1633. doi: 10.1002/joc.1809

Zeroual, A., Assani, A. A., Meddi, M., and Alkama, R. (2019). Assessment of climate change in Algeria from 1951 to 2098 using the Köppen–Geiger climate classification scheme. *Clim. Dyn.* 52, 227–243. doi: 10.1007/s00382-018-4128-0

Zeroual, A., Assani, A. A., Meddi, H., Bouabdelli, S., Zeroual, S., and Alkama, R. (2020). "Assessment of projected precipitations and temperatures change signals over Algeria based on regional climate model: RCA4 simulations" in Water resources in Algeria – part I. The handbook of environmental chemistry. eds. A. M. Negm, A. Bouderbala, H. Chenchouni and D. Barceló, vol. *97* (Cham: Springer), 135–159.

Zeroual, A., Meddi, M., and Bensaad, S. (2013). "The impact of climate change on river flow in arid and semi-arid rivers in Algeria" in Climate and land surface changes in hydrology. eds. E. Boeghet al. (Wallingford: International Association of Hydrological Sciences Publ. 359), 105–110.

Zheng, H., Chiew, F. H. S., Charles, S., and Podger, G. (2018). Future climate and runoff projections across South Asia from CMIP5 global climate models and hydrological modelling. *J. Hydrol.* 18, 92–109. doi: 10.1016/j.ejrh.2018.06.004

frontiers | Frontiers in Water

TYPE Review
PUBLISHED 13 January 2025
DOI 10.3389/frwa.2024.1504492

OPEN ACCESS

EDITED BY
Vikram Kumar,
Planning and Development, Govt. of Bihar, India

REVIEWED BY
Aviva Rahmani,
University of Colorado Boulder, United States
Brian Deal,
University of Illinois at Urbana-Champaign, United States

*CORRESPONDENCE
Nadeem Ahmad
✉ nadeem2008643@st.jmi.ac.in
Quamrul Hassan
✉ qhassan@jmi.ac.in

RECEIVED 30 September 2024
ACCEPTED 17 December 2024
PUBLISHED 13 January 2025

CITATION
Ahmad N and Hassan Q (2025) Ecosystem services linked to nature-based solutions for resilient and sustainable cities in India. *Front. Water* 6:1504492. doi: 10.3389/frwa.2024.1504492

Ecosystem services linked to nature-based solutions for resilient and sustainable cities in India

Nadeem Ahmad* and Quamrul Hassan*

Department of Civil Engineering, Jamia Millia Islamia, New Delhi, India

Rampant urbanization and undervaluing of the natural ecosystem have detrimental impacts on urban spaces – increased flooding risk, increased air and water pollution, water stress, resource inefficiency, loss of biodiversity, and increased risk of ill health. Climate change further exacerbates the adverse impacts of urbanization. Despite the importance of the natural ecosystem, the blue and green spaces of the cities in India have drastically decreased. The present study highlights the degrading natural ecosystem, the negative impacts, and the need for resilience in Indian cities. Eco-centric approaches like nature-based solutions (NBS) are closely related to sustainability and resilience, offering a more efficient and cost-effective approach to urban development than traditional approaches. The paper explores the concept of NBS, focusing on ecosystem services as a 'living' and 'adaptable' tool to make cities resilient and sustainable with many regional implementations. It also focuses on the role of NBS in achieving the United Nations' Sustainable Development Goals (SDGs). The paper critically analyses the five notable NBS projects from different countries (USA, Canada, The Netherlands, China, and Australia) and further addresses the viabilities for NBS intervention in Indian cities. It is observed that the successful adaptation of NBS in urban development necessitates eco-centric policies, collaborative research, adaptive management practices, community engagement, and a strong emphasis on a multi-benefit approach. A proactive focus on ecosystem services is strongly recommended for Indian cities, which includes raising an understanding of the value of nature, introducing NBS at the planning stage, and encouraging investment in ecosystem-based approaches.

KEYWORDS

urbanization, ecosystem services, nature-based solutions, climate change, sustainable development goals, resilient cities

1 Introduction

Cities worldwide are grappling with resilience challenges arising from the complex interplay of climate risks, urbanization, biodiversity loss, diminishing ecosystem services, poverty, and increasing socioeconomic disparities (World Meteorological Organization (WMO), 2022; United Nations Environment Programme (UNEP), 2023). The impact of climate change is projected to lead to more frequent and severe natural hazards and climate-related extremes like floods, droughts, and heat waves. Moreover, urbanization can increase the vulnerability of urban communities and infrastructure to these hazards due to rapidly declining natural land-use land-cover (LULC), i.e., blue (waterbodies) and green (vegetation) spaces (Ghofrani et al., 2017). The combined impacts of rampant urbanization and climate change have become evident at the global scale– nearly 2 billion people lacked access to safe drinking water till 2021, and over 90 billion USD of global economic losses from various

natural disasters in the first half of 2021 alone (United Nations, 2022; United Nations Environment Programme (UNEP), 2023). With the existing trends of rampant urbanization and climate change impacts, urban resilience challenges are anticipated to intensify (World Bank, 2021).

Disaster risk reduction and climate resilience used to focus mainly on grey infrastructure, which may not always be the most cost-effective, resilient, and sustainable option. Grey Infrastructure refers to the engineered assets and built structures like embankments, dams, stormwater drains, and wastewater treatment plants created to manage environmental and hydrological attributes. In recent decades, the significance of nature-based solutions (NBS) has been increasingly acknowledged for urban resilience. NBS is an umbrella concept covering a range of ecosystem-related approaches to address social, economic and environmental challenges while benefiting human well-being and biodiversity (Cohen-Shacham et al., 2016). In other words, the NBS interventions harness the natural elements and processes of healthy ecosystems to effectively address some of the most significant challenges of the present time, like climate change, water security, and natural disasters (Bozovic et al., 2017; Ghofrani et al., 2017; Dorst et al., 2019; Hamel and Tan, 2022). The benefits attained through NBS interventions are commonly referred to as ecosystem services. Numerous international agreements and initiatives, like the Sendai Framework for Disaster Risk Reduction, the Sustainable Development Goals (SDGs) and the Paris Climate Agreement, promote nature-based approaches and align with environmental and risk management goals to address climate risk and environmental degradation and promote investment in disaster risk reduction (Reguero et al., 2020; World Bank, 2021). In the present study, the concept of NBS, including its ecosystem services, has been discussed with various successful case studies across the globe, and the possibilities of adaptation for the development of resilient cities in India have been explored.

2 Declining natural LULC compromising resilience and sustainability of cities in India

2.1 A brief description of land use transition in a few major Indian cities

This section discusses the trend of urbanization and declining natural LULC of a few major Indian cities and their suburbs, emphasizing the need for resilient cities in India. The increase in built-up area in the National Capital Territory (NCT) of Delhi was 162.7 sq. km to 531.2 sq. km from 1993 to 2018 (Bondwal and Bisht, 2019). The same study found that the forest cover in the NCT of Delhi decreased from 155.8 sq. km to 130 sq. km between 1993 and 2018. Land-use transitions are not only limited to the cities but also greatly affect suburban regions (Naikoo et al., 2020). Mumbai city experienced a significant decline in natural land use and land cover (LULC) from 1977 to 2017, with a 60 percent reduction in vegetation and a 65 percent reduction in waterbodies (Udas-Mankikar and Driver, 2021). Another study reported that the built-up area of Mumbai rose from 28 to 57% of the city's total area from 1991 to 2018, and it is projected to reach 66% by 2030 (Naikoo et al., 2023). Similarly, the Chennai Metropolitan Area (CMA) witnessed an increase in built-up areas from 18 to 48% and a decrease in vegetation from 57 to 26% between 1988 and 2017 (Mathan and Krishnaveni, 2020). Developments have taken over 90 per cent of the wetlands of Chennai city (Ahmad and Hassan, 2024). Bengaluru city experienced a significant decrease in the green cover of the city, more than 50% from 2003 to 2021, while the built-up area almost doubled during the same period (Keerthi-Naidu and Chundeli, 2023).

2.2 Need for resilient and sustainable cities in India

The consequences of the rampant land use transition in urban and suburban landscapes in India can be seen as increased urban pressures, i.e., flood risk, water stress, water pollution, urban heat island (UHI) and air pollution. The natural drainage systems in most cities are facing threats from encroachment, inadequate maintenance, poor solid waste management, and lack of adequately designed stormwater drainage infrastructure. For example, Chennai city suffered the most disastrous flood of the century in 2015, causing more than 400 human casualties, nearly 2 million severely affected and about USD 80 billion of estimated loss (Vojinovic, 2015). On the contrary, four years later, in June 2019, the city was unexpectedly hit by 'Day Zero,' and all of its major reservoirs dried up. The city has a minimum of 108 Litre per capita per day (LPCD) of water supply, much less than the WHO minimum criteria of 150 LPCD (Rajaveni et al., 2016). The study confirms the presence of UHI in Chennai with an intensity of 4.5°C in winter and 2.5°C in summer (Rajan and Amirtham, 2021).

The annual economic impact of urban flooding in India is disastrous, ranging from USD 1.1 billion to USD 5 billion (Sharief and Vangipuram, 2022). The highest UHI intensity recorded internationally is as high as 12°C, while the observed maximum UHI intensity in India is 8–9°C. UHI can deteriorate the urban environment in multiple ways – increase in energy and water consumption, higher emissions of pollutants into the atmosphere resulting in the greenhouse effect, heat-related health discomfort, and degradation of water quality in streams, rivers, and other water bodies (Jain and Sarkar, 2017; Veena et al., 2020; Vujovic et al., 2021). Every city and its suburbs face the abovementioned urban pressures with varying intensities depending on the type of city (like coastal city, riverine city, or mountainous city). The lack of effective streamlining, regulation, and monitoring of urbanization processes is a key factor contributing to significant environmental degradation. Taking account of climate change, environmental risks, and socio-economic vulnerability, there is an urgent need for a paradigm shift in urban developments in India and the adaptation of nature-based solutions for the development of resilient cities. NBS strategies optimize the climate-related risks with other objectives to achieve multiple benefits regarding ecological, socio-economic and overall urban well-being (Roumeau et al., 2015; Vojinovic, 2015). The concept of nature-based solutions and the associated ecosystem services have been discussed in detail in the next section.

3 Nature-based solutions (NBS): an approach for resilient cities

3.1 Overview of the NBS concept

The World Bank introduced the NBS concept in the late 2000s to address increasing climate-related risks, promoting

ecosystem-based approaches (World Bank, 2008). The International Union for Conservation of Nature (IUCN) has been taking the lead in conserving the ecosystem and promoting nature-based solutions (NBS) globally by formulating core principles and frameworks for mainstreaming NBS. Figure 1 highlights the timeline of major milestones in developing the NBS concept. In recent years, the definition and scope of nature-based solutions have become vast and diverse. The diversity of concepts and definitions has led to challenges in achieving conceptual clarity, making the term more subjective (European Commission, 2021; Cohen-Shacham et al., 2016; Albert et al., 2017; Dhyani et al., 2020). Table 1 enlists the two most widely accepted definitions of NBS. Fundamentally, NBS is a novel approach that primarily focuses on using ecosystems to address climatic, environmental, and socio-economic challenges (Balian et al., 2014; Cohen-Shacham et al., 2016; Depietri and McPhearson, 2017; Dorst et al., 2019). Figure 2 depicts a distinct range of ecosystem and natural capital-based approaches under the NBS concept (Dhyani et al., 2020). Ecosystems demonstrate a remarkable ability to mitigate the adverse effects of climate-related risks and safeguard communities (Diaz et al., 2015; Lo, 2016).

NBS encompass the use of natural processes and ecosystems to create infrastructure, provide services, and develop comprehensive strategies to enhance urban resilience. World Bank identifies some NBS typologies like urban forests, urban farming, green corridors, river and stream renaturation, river floodplains, bioretention areas, and wetlands (World Bank, 2021). These approaches typically transcend traditional boundaries and necessitate collaborative efforts across various sectors. Nature-based solutions offer diverse advantages for cities, such as mitigating disaster risks, strengthening climate resilience, ensuring food-water security, promoting biodiversity restoration, and overall community well-being. Numerous terminologies under nature-based concepts have been developed in different parts of the world, such as 'green infrastructure' (GI), 'blue-green infrastructure' (BGI), 'natural infrastructure' (NI), 'low impact development' (LID), and 'ecosystem-based adaptation' (EBA). The terms NBS, GI, BGI, LID, EBA and sustainable measures are interchangeably used in the present study.

3.2 Integration of NBS measures across a range of spatial scales

There is a hierarchy of approaches for implementing the NBS umbrella concept as strategic planning, i.e., 'protection and sustainable management of existing natural infrastructure', 'restoration and rehabilitation of degraded one' and then 'creation of new NBS' (Cohen-Shacham et al., 2019). It is essential to consider this hierarchy when identifying and prioritizing nature-based solutions opportunities at a strategic level, such as when evaluating investment options for a city. These three approaches must be applied to plan and prepare NBS projects across various spatial scales. Generally, NBS is implemented at three spatial scales – neighborhood scale, city scale and river basin scale. At each scale, various NBS families can be implemented. For instance, floodplain restoration projects that restore natural hydraulic and hydrological connectivity can effectively mitigate flood hazards at the river basin level, while green roofs and bioswales can be strategically designed for implementation at the neighborhood scale (Liberalesso et al., 2020; Puchol-Salort et al., 2021). Measures (like urban forests, constructed wetlands and rivers and streams renaturation) at the city scale aim to enhance urban land use planning and strengthen the city's disaster risk management. Figure 3 depicts the schematic section of NBS at the neighborhood, city, and river basin scales.

3.3 Methodology

The study presents a constructive exploration of NBS and its associated ecosystem services, featuring a range of successful regional implementations, as shown in Table 2. The reviewed literature included technical reports, project summaries, academic publications, government publications, conference proceedings, and resources from web search engines and academic databases ('Web of Sciences' and 'Scopus') for regional and city-scale NBS interventions. Search keywords include various NBS measures – green corridors, green roofs, urban forests and parks, urban agriculture, bioswales, rain gardens, retention ponds, permeable pavements, natural wetlands, constructed wetlands, stream renaturation and floodplain restoration.

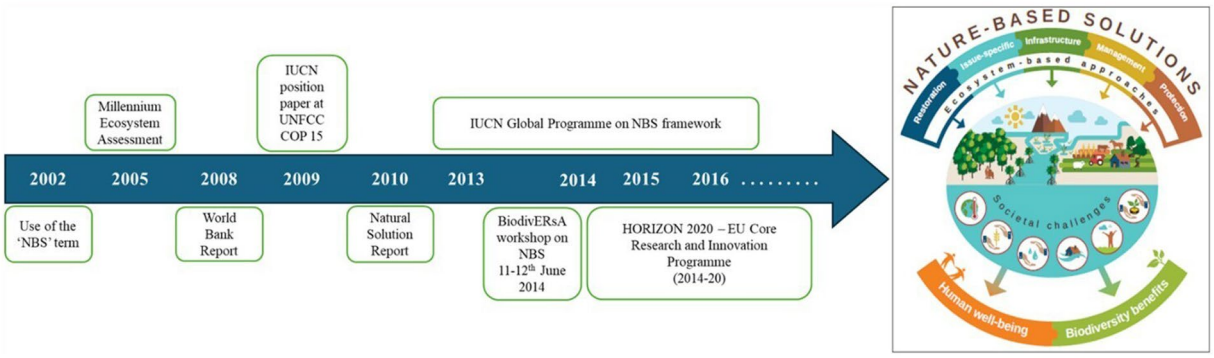

FIGURE 1
Milestones in the development of NBS concept [adapted from Cohen-Shacham et al. (2016)].

TABLE 1 Two most widely accepted definitions of NBS.

Organization name	Definition	References
European Commission (EC)	"Inspired and supported by nature, which are cost-effective, simultaneously provide environmental, social and economic benefits and help build resilience."	European Commission (2021)
International Union for Conservation of Nature (IUCN)	"Actions to protect, sustainably manage and restore natural or modified ecosystems that address societal challenges effectively and adaptively, simultaneously providing human well-being and biodiversity benefits."	Cohen-Shacham et al. (2016)

Further, five long-term city-scale NBS projects were selected to gain a worldwide perspective and foster the development of resilient cities in India (as mentioned in section 3.5). The number of NBS measures adopted simultaneously and the wide range of ecosystem services were used as selection criteria for the city-scale NBS exemplars examined in the study. It is worth mentioning that while no formal surveys were conducted with city officials, the findings still offer valuable insights for future discussions and research in the context of the development of resilient cities in India.

3.4 Ecosystem services and SDGs linked to NBS

The natural ecosystem can deliver multiple environmental and socio-economic benefits, which are called ecosystem services. Figure 4 depicts the pertinent processes related to ecosystem services for urban resilience. A few major ecosystem services related to NBS are briefly discussed below, along with the role of NBS in achieving SDGs.

3.4.1 Stormwater management and flood risk mitigation

Cities worldwide face the challenges of stormwater management and flood risk management (pluvial, fluvial or coastal), depending on the rainfall patterns, urbanization-induced LULC transitions, location (riverine, coastal, mountainous), and population growth. Considering the rise in impervious surfaces and increased extreme weather events, NBS can be implemented in the cities to mitigate the risks due to floods and combined sewer overflow (CSO) events by promoting infiltration and evapotranspiration (U.S. Environmental Protection Agency (USEPA), 2010; Shakya and Ahiablame, 2021; Ahmad and Hassan, 2024). Reducing the volume of stormwater entering the sewer system during rain events can alleviate pressure on the sewer system. A study related to flood regulation in three Australian capital city regions, SEQ, Melbourne and Perth, emphasizes the importance of green open spaces (Victoria State Government (VSG), 2017; Schuch et al., 2017). Similarly, in a study from Taichung City in Taiwan, different NBS measures (infiltration ponds, infiltration swales, and rain barrels) were evaluated using the stormwater management model (SWMM), showing the reduced annual runoff by 43.5–54.5 percent (Lin et al., 2018).

3.4.2 Urban heat island (UHI) mitigation

In urban areas, buildings and paved surfaces change thermal properties and radiative behavior compared to natural surroundings, creating distinct environmental impacts. These surfaces absorb solar radiation, contributing to elevated surface and ambient temperatures in urban areas as compared to rural areas, creating what is known as an "urban heat island" effect (Arrau and Peña, 2011; Killingsworth et al., 2011). The urban heat island phenomenon can lead to health issues such as heat stroke and even death during heat waves (U.S. Environmental Protection Agency (USEPA), 2003). Due to this effect, cities across the globe are becoming warmer than surrounding suburban areas in the summer. Implementing measures like green roofs and trees can lower temperatures through evapotranspiration, helping to mitigate urban heat island effects and improve public health (Killingsworth et al., 2011; Pitman et al., 2015). For instance, a study assessing the benefits and costs of green roofs in Toronto has shown that widespread adoption of green roofs could reduce local ambient air temperatures by 0.5°C to 2°C (Banting et al., 2005).

3.4.3 Improved water quality and groundwater recharge

NBS practices, such as green infrastructure (GI) measures, have proven effective in enhancing the quality of stormwater runoff. GI measures work by slowing down and filtering the polluted runoff before it enters adjacent water bodies such as lakes and rivers (Liu et al., 2015; Brumley et al., 2018; Yu and Li, 2023). Additionally, NBS include a range of measures (shown in Table 2) to improve water quality and promote groundwater replenishment (Brumley et al., 2018; Natural Resource Defence Council (NRDC), 2022). For instance, the restoration project of Genetta Park and Genetta Stream in Montgomery, in the United States, has been creating positive impacts on the Genetta Stream by mitigating downstream floods, improving water quality, enhancing stream biodiversity, and promoting groundwater recharge.

3.4.4 Improved air quality

Nature-based measures (such as green roofs, rain gardens, green facades, and green roads) are vital in mitigating air pollution, reducing emissions, and extending the distance between pollution sources and receptors (Hewitt et al., 2020). Vegetation enhances air quality by filtering out airborne pollutants and toxic gases, such as particulate matter (PM_{10}) and ozone (O_3). Additionally, the adoption of green infrastructure practices under NBS strategies in buildings leads to reduced energy consumption, which in turn helps improve air quality

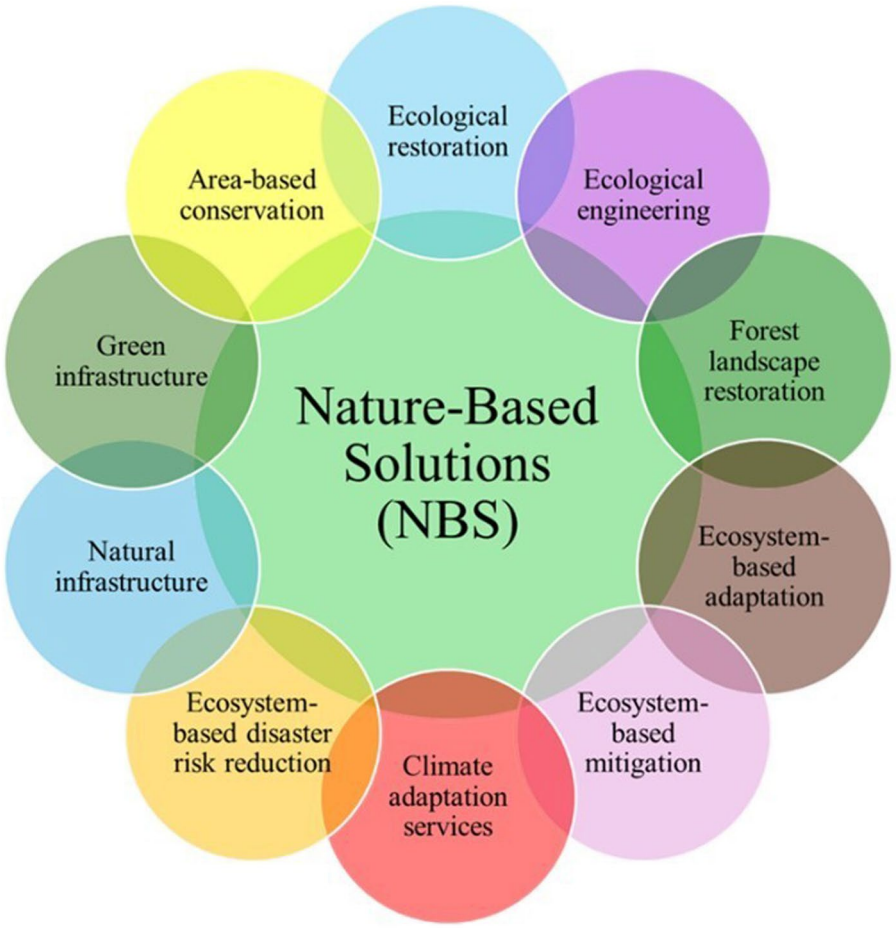

FIGURE 2
Ecosystem-related approaches under the present scope of NBS.

by lowering the emission of sulfur dioxide (SO_2) and nitrogen dioxide (NO_2) (Yang et al., 2005; Wang et al., 2014). The Blue Green Wave is a one-hectare green roof, the largest in the entire Paris region in France, improving air quality with other ecosystem services like stormwater management and UHI mitigation (Brown and Mijic, 2019). Such initiatives have also been seen in Asian countries at different scales, like the Centenary Park in Bangkok, Thailand and 'pocket parks' in Kuala Lumpur, Malaysia (Holmes, 2019; Hamel and Tan, 2022).

3.4.5 Recreation and community well-being

Recent studies highlight the significance of GI measures under NBS strategies in urban areas for providing essential ecosystem services. GI measures use natural processes for infrastructure development and land use planning to promote economic and social development (Osei et al., 2022). Incorporating GI practices like urban parks, forests, green roofs, streams, ponds, swales, wetlands and community gardens into new developments and urban renewal projects to create new green spaces has been proven to enhance community liveability and offer opportunities for recreational activities, thereby contributing to improved public health and well-being (Wolch et al., 2014; Pamukcu-Albers et al., 2021).

3.4.6 Achieving SDG targets through NBS

The effective adaptation of NBS diminishes urban susceptibility to climate-related risks and contributes to attaining the United Nations' SDGs (Mahmoud et al., 2022; Kiribou et al., 2024). Acharya et al. (2020) investigated new methods to improve nature-based approaches to accomplish SDGs while focusing on transformative strategies and outlining responsibilities for communities, private sectors, and government organizations. Lombardía and Gómez-Villarino (2023) conducted a systematic review demonstrating how GI measures can facilitate SDGs in metropolitan regions and emphasized the need for increased support from policymakers and urban planners. Most SDGs are interconnected and mutually reinforce each other in various ways. An Australian study revealed that achieving 100% of the SDGs by 2030 is a significant challenge, but it is projected to achieve 70% (Allen et al., 2019). Table 3 summarizes the role of NBS in achieving all the SDGs and their varying relative importance (High >60%, moderate 30–60%, and low <30%), and each contribution is supported by a range of references. NBS directly contributes to SDG3, SDG6, SDG11, SDG13, and SDG15 by providing multiple cost-effective urban ecosystem services.

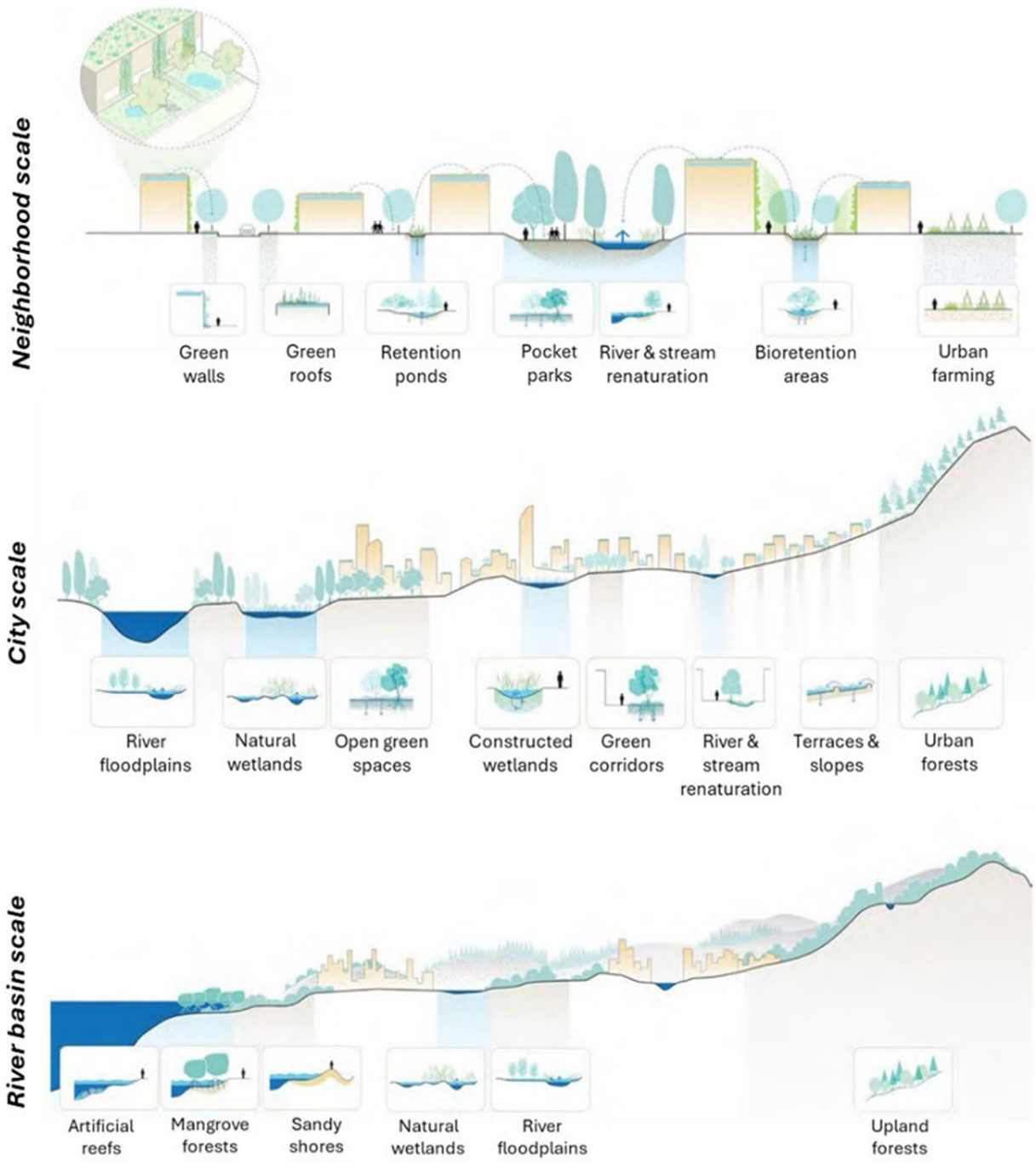

FIGURE 3
Schematic section of NBS at different scales [adapted from World Bank (2021)].

3.5 NBS in practice on the ground: key lessons learnt from the exemplars across the globe

In recent decades, there has been a growing trend toward using nature-based solutions for sustainable and resilient cities. Countries like the United States, the United Kingdom, the Netherlands, Germany, and many more have seen notable success in managing urban pressures through nature-based practices. The European countries have tremendously succeeded in developing the NBS strategies for urban resilience. In Asia, countries like China, Malaysia, Singapore, Japan and Thailand have also been working on the NBS implementation for various urban ecosystem services for a long time. As research into nature-based intervention expands, many such projects have been launched and completed successfully in cities worldwide. Therefore, five NBS projects from different countries (USA, Canada, The Netherlands, China, and Australia) have been selected to understand a worldwide perspective. All the

TABLE 2 NBS measures and some regional implementations and studies.

NBS measures	Ecosystem services	Few regional implementations	References
Green corridors	UHI mitigation, Pluvial flood mitigation, carbon sequestration, water & air quality, biodiversity, recreation and community well-being	• 'The Rail Corridor' -Singapore • 'Green Belt of Vitoria-Gasteiz'-Spain • Street trees, Portland, United States • Many implementations in Europe, the US, Canada, China, Australia	Norton et al. (2015), Lim and Lu (2016), Victoria State Government (VSG) (2017), O'Donnell et al. (2019), and World Bank (2021)
Green roofs	Pluvial flood mitigation, UHI mitigation, water & air quality, biodiversity, and community well-being	• 'Blue Green Wave'-the largest green roof in Paris (France) • 'ABC Programme'-Singapore • 'Eco-Roofs'- Portland, United States • Common examples – London (UK), Brussels (Germany), Seoul (South Korea), Victoria (Australia), Cairo (Egypt)	Mentens et al. (2006), Shafique et al. (2016), Lim and Lu (2016), Victoria State Government (VSG) (2017), Maryati and Humaira (2017), and Brown and Mijic (2019)
Urban forests and parks	Pluvial flood mitigation, UHI mitigation, carbon sequestration, water & air quality, resource efficiency, biodiversity, recreation and community well-being	• 'Centenary Park' – Bangkok (Thailand) • 'Pocket parks'- Copenhagen (Denmark) and Kuala Lumpur (Malaysia) • Urban forests in Toronto, Canada • High Line Park in New York (US)	Surma (2013), Norton et al. (2015), Holmes (2019), United States Department of Agriculture (USDA) Forest Service (2020), Udas-Mankikar and Driver (2021), Puchol-Salort et al. (2021), and Hamel and Tan (2022)
Urban agriculture	Food security, resource efficiency, Pluvial flood mitigation, carbon sequestration, UHI mitigation, and community well-being	• Urban Agriculture Practices in Lima (Peru). • Urban farming with 'Sponge City Program'in Chinese cities • Medium to large-scale practices in Jakarta (Indonesia) • Other examples- New York (US), Mexico City (Mexico); Bologna (Italy), Bangkok (Thailand)	World Bank (2013), Artmann and Sartison (2018), Sanyé-Mengual et al. (2020), Akter and Gupta (2022), and Zhu et al. (2023)
Engineered bioretention areas (bioswales, rain gardens, and retention ponds)	Pluvial and riverine flood mitigation, water quality and sediment management, carbon sequestration, biodiversity, UHI mitigation, recreation and community well-being	• 'Copenhagen Climate Change Adaptation Plan' in Copenhagen Metropolitan Area, Denmark • Many cities in the US like, Seattle, Lincoln, New York, Philadelphia • Bioswales of Riga city in Latvia • Sponge City Program (SCP) for Chinese cities	Sidek et al. (2013), Kato et al. (2017), O'Donnell et al. (2019), Lin et al. (2018), Wang et al. (2019), Hermawan et al. (2020), United States Department of Agriculture (USDA) Forest Service (2020), Natural Resource Defence Council (NRDC) (2022), and Kondratenko et al. (2024)
Green parking lots and Permeable pavements	Pluvial flood mitigation, UHI mitigation, water & air quality,	• 'Green Street Program' of Portland, US • Montgomery in Maryland, US • 'SCP-permeable pavements' in Wuhan, China • Taichung city of Taiwan • Many cities of US, UK, Australia, Indonesia	U.S. Environmental Protection Agency (USEPA) (2008), Montgomery County Planning Commission (MCPC) (2011), Li et al. (2017), O'Donnell et al. (2019), Puchol-Salort et al. (2021), and Natural Resource Defence Council (NRDC) (2022)
Natural wetlands and Constructed wetlands	Pluvial and riverine flood mitigation, water quality and sediment management, biodiversity, UHI mitigation, carbon sequestration, resource efficiency, recreation and community well-being	• Wetlands in Mississippi river basin, US • 'Qunli National Wetland' in Qunli, China • Natural wetlands in city of Columbia, Sri Lanka • Natural wetlands in Phnom Penh (Cambodia) • Constructed inland wetlands in Beijing (China), Bangkok (Thailand)	United States Army Corps of Engineers (USACE) (2012), Irvine et al. (2015), Holmes (2019), Agaton and Guila (2023), Shah et al. (2023), and Ganapathi et al. (2024)
Stream renaturation and floodplain restoration	Pluvial and riverine flood mitigation, water quality and sediment management, resource efficiency, carbon sequestration, UHI mitigation biodiversity, recreation and community well-being	• Odra River floodplain project (2007–20) in Wroclaw city (Poland) • Rio Bogota Environmental Flood Control Project (2011–21) in Bogota (Colombia) • Mississippi floodplain restoration (USA) • 'Room for the River' program in Nijmegen City (The Netherlands)	United States Army Corps of Engineers (USACE) (2012), Schindler et al. (2014), European Environmental Agency (EEA) (2017), European Environmental Agency (EEA) (2018), Steger et al. (2019), World Bank (2021), and Ahmad and Hassan (2021)

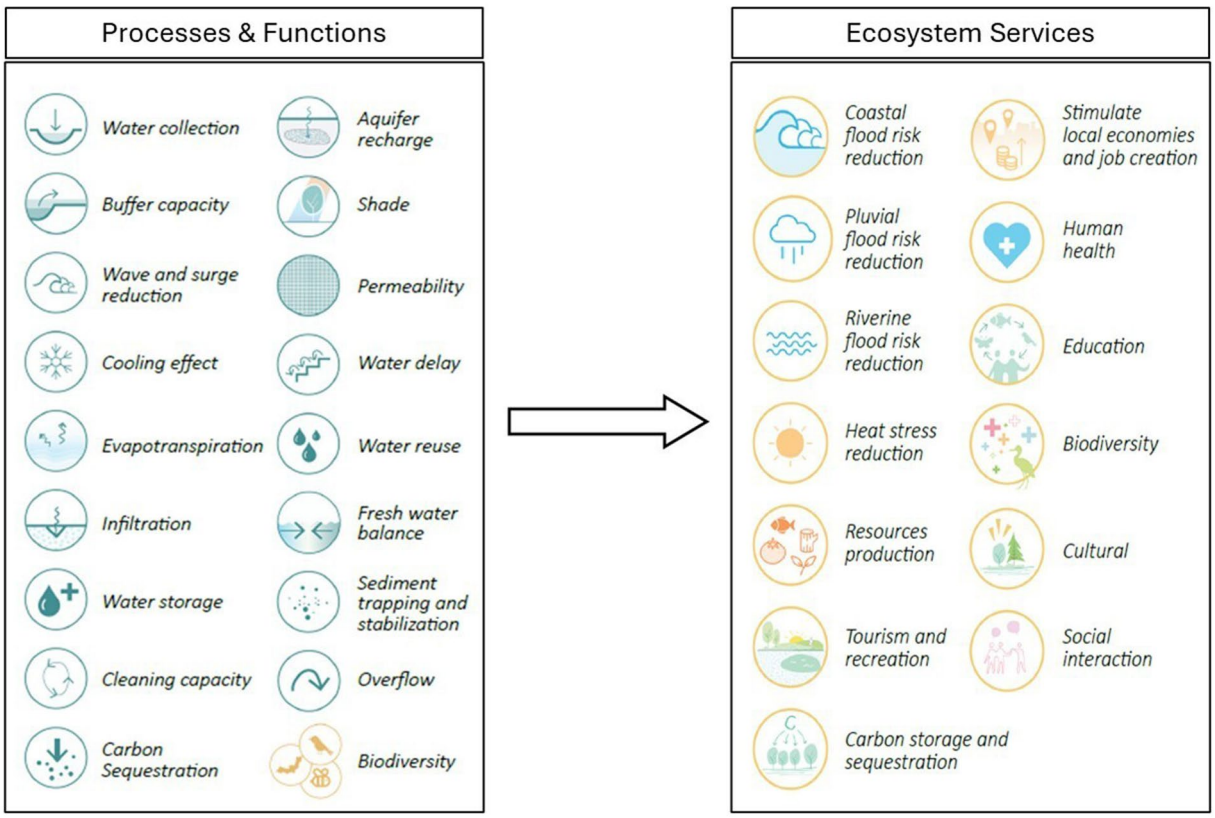

FIGURE 4
Relevant processes and ecosystem services of NBS concerning urban resilience.

selected projects have been critically analyzed, and their major objectives and the key lessons learnt have been presented in Table 4. The key learnings from these city-scale NBS projects include the effective combination of green and grey infrastructure to optimize urban water management and enhance urban resilience, implementing adaptive management practices, community engagement and awareness, and a strong emphasis on a multi-benefit approach.

4 Addressing the viabilities for NBS implementation in Indian cities

4.1 Challenges in NBS intervention in the cities of India

As the demand for resilient cities grows and NBS intervention plans are being developed, several challenges have emerged in implementing NBS in urban areas. These challenges span technical, social, and institutional factors. Indian cities face unique urban pressures due to their diverse socio-economic culture, demography, and climate. Despite the vital role of blue and green spaces for the environment and community well-being, these natural spaces are decreasing, and impermeable surfaces are rising in the cities. Analyzing the factors responsible for increasing urban pressures in Indian cities, some of the major challenges in NBS intervention that need to be addressed are as follows.

4.1.1 Degrading natural landscapes in cities and limited space

Rapid and unplanned urbanization has reduced the blue and green spaces (waterbodies and vegetation) in many Indian cities over time. The older cities (like Delhi, Mumbai, Chennai, Kolkata, and Bengaluru) have grappled with rampant urbanization and high population density. These factors create urban pressures like UHI and declined natural urban drainage, posing significant challenges for the existing combined sewer system. Designing and remodeling separate sewer systems with sustainable drainage measures or any NBS measures at the city scale in high-density areas will be intricate. This limitation of natural spaces hinders the integration of various nature and ecosystem-based measures such as urban parks, gardens, lakes, retention ponds, and wetlands within the city. Furthermore, implementing NBS at the building scales (like blue-green roofs, urban agriculture and rainwater harvesting measures) for other urban ecosystem services is also quite challenging due to unplanned settlements within and around the cities.

4.1.2 Climate and hydrology

Specific BGI measures can exhibit performance limitations due to varying climatic and hydrological behavior in different parts of the country. For instance, coastal cities with shallow groundwater levels will face challenges in implementing infiltration-based GI measures like bioswales and rain gardens. Cities with a minor rainy season and limited water resources may increase their water demand due to the

TABLE 3 Sustainable development goals (SDGs) through the NBS.

SDG title	NBS contributions to SDGs	Relevance order
No poverty (SDG1)	• Community gardens historically helped alleviate poverty in Europe and provided food for factory workers during the war and industrial revolution (Cabral et al., 2017). • It also helps developing nations in building resilience, where urban agriculture is essential due to unemployment and increasing food demand (De Bon et al., 2009; Douglas, 2018).	High
Zero hunger (SDG2)	• NBS can enhance crop production in urban regions to meet the food demand, promoting resilience (Cassman and Grassini, 2020). • Urban agriculture improves food security in developed and developing nations, ensuring access to food for vulnerable communities (Besthorn, 2013; Kahane et al., 2013; Clark and Nicholas, 2013).	High
Good health and well-being (SDG3)	• Green plants can remove major air pollutants like NO_2, improving urban air quality. • NBS can also enhance the water and soil quality of cities. • It could provide sustainable development with good health and overall well-being (Dora et al., 2015; Panagopoulos et al., 2016).	Moderate
Quality education (SDG4)	• NBS practices like urban agriculture not only impart knowledge to children and seniors but also equip low-income workers with new skills (Sterling et al., 2017) • Many studies elucidate the potential of GI to promote environmental education and social and professional growth, offering experiential learning opportunities for individuals of all ages (Cohen and Reynolds, 2015).	Low
Gender equality (SDG5)	• In developed countries, the practice of small-scale organic agriculture by urban women is undeniably growing with a primary motivation of factors such as lifestyle choice, self-dependent, and a strong sense of social commitment and education (Jarosz, 2011).	Low
Clean water and sanitation (SDG6)	• NBS practices like GI can potentially enhance water quality by removing pollutants like heavy metals. • Reinforcing urban drainage systems with GI measures can mitigate social and environmental risks (Dong et al., 2017).	Moderate
Affordable and clean energy (SDG7)	• GI measures like green roofs, green facades, and urban parks facilitate cities for low-energy consumption (Safikhani et al., 2014; Besir and Cuce, 2018).	Moderate
Decent work and economic growth (SDG8)	• NBS has the potential to create more urban jobs and increase property values in green regions of urban areas (Maes and Jacobs, 2017). Many studies have validated that GI measures, especially urban forests, to cater the socio-economic needs of the cities (Capotorti et al., 2015).	Moderate
Industry, innovation, and infrastructure (SDG9)	• Research indicates that by adopting green strategies, cities can achieve resilience. • Establishing a green infrastructure network could empower social, economic, and environmental systems to exhibit resistance, recoverability, and robustness – the key attributes of resilient socio-ecological systems (Grafton et al., 2019).	Moderate
Reduced inequalities (SDG10)	• Ecosystem-based practices like urban agriculture foster social cohesion and cooperation (Corcoran and Kettle, 2015). It helps in creating an inclusive and equal society with policies based on social justice.	Low
Sustainable cities and communities (SDG11)	• An integrated approach to GI measures with existing grey infrastructures promotes sustainable cities (Corbett and Mellouli, 2017). • GI measures provide multiple cost-effective ecosystem services, such as reduced flood risks, improved water and air quality, UHI mitigation, and overall well-being (Keeler et al., 2019).	High
Responsible consumption and production (SDG12)	• Local food production from urban agriculture can sustainably facilitate consumption and production cycles (Olsson et al., 2016; Pigford et al., 2018). • Vacant land in urban and suburban regions could be utilized for biofuel production to support energy demand sustainably (Niblick et al., 2013).	Moderate
Climate action (SDG13)	• There is growing evidence of NBS facilitating climate change adaptation by CO_2 sequestration and UHI mitigation (Wang and Zacharias, 2015; Wang et al., 2016). • Land-use transition with adequately integrated GI measures could enhance carbon sequestration from 5 to 30% (Roe et al., 2019); therefore, urban vegetation can reduce global emissions (Kulak et al., 2013; Macreadie et al., 2019).	High
Life below water (SDG14)	• Ecosystem-based approaches foster sustainability in coastal regions by enhancing ecosystem services, reducing flood risk, improving water storage, minimizing marine pollution, and promoting biodiversity in oceans (Keesstra et al., 2018b; Thacker et al., 2019). • Constructed wetlands and restoring the natural wetlands enable coastal areas to exhibit resilience.	Moderate

(Continued)

10.3389/frwa.2024.1504492

TABLE 3 (Continued)

SDG title	NBS contributions to SDGs	Relevance order
Life on land (SDG15)	• NBS conserves and enhances soil productivity, and also facilitates biodiversity conservation (Keesstra et al., 2016; Keesstra et al., 2018a). • Urban GI measures provide a network for urban wildlife, pollinators and microorganisms while also impacting the socio-economic sector and human well-being (Hou et al., 2014; Hall et al., 2017; Akinsemolu, 2018). • These measures can greatly contribute to sustainability by providing an ecosystem for biodiversity.	High
Peace, justice and strong institutions (SDG16)	• Adequate integration of NBS in urban regions leads to a sustainable and resilient city, which can be reflected in the governance perspective. • It ultimately strengthens socio-economic and environmental institutions and promotes a peaceful, inclusive society (Wamsler et al., 2013; Maes et al., 2019)	Moderate
Partnerships for the goals (SDG17)	• Proper implementation of the NBS in urban spaces requires collaboration among decision-makers and other stakeholders (Murphy et al., 2019). • Public-private entities and citizens can collaborate to enhance the existing urban ecosystem and develop strategies for ecosystem-based adaptations (Fritz et al., 2019).	Moderate

water requirements of the crops, thereby limiting the use of green roofs, urban farming, and other vegetation-based infrastructures.

4.1.3 Limited NBS research and uncertainties

Due to the existing knowledge gaps and limited research on nature-based solutions in India, there are uncertainties regarding the hydrologic and ecologic performance of NBS. The lack of understanding and research regarding the adaptation of ecosystem-based approaches in India might result in initial resistance from urban planners and local authorities, who might overlook the potential ecosystem services linked to green infrastructure and other ecosystem-based strategies. Limited research with insufficient data also hinders NBS intervention on a city or river basin scale, creating uncertainty regarding the effectiveness of NBS, i.e., which approach would yield immediate versus sustained results.

4.1.4 Socio-economic constraints

Recent studies have provided more useful insights into the socio-economic constraints of non-traditional measures in urban development (Almaaitah et al., 2021; Mumtaz, 2021). Lack of community awareness and challenges in the economic valuation of the ecosystem services can create difficulties in justifying investments in nature-based approaches, especially compared to traditional methods. Apart from a social reluctance to support novel practices due to the lack of awareness, implementing NBS measures (like green roofs, urban agriculture, and rainwater harvesting) can be costly and challenging for retrofitting in dense urban agglomerations.

4.1.5 Lack of enforceable standards at the policymaking and planning level

The Government of India has taken significant steps to tackle urban transformation through the "Atal Mission for Rejuvenation and Urban Transformation" (AMRUT) program. The program focuses on enhancing urban infrastructure in 500 cities, emphasizing areas such as stormwater drainage, water supply, sewerage, green spaces, and public transport (Gupta, 2020). 'Smart City Mission' is also an initiative emphasizing sustainable solutions for urban development. Nevertheless, there remains a need for enforceable standards for incorporating NBS with proper specifications at the planning and policy-making stage. The government needs to create a statutory body by institutionalizing the NBS framework, which will ensure the implementation of the projects at the local level with specific standards.

4.2 Overcoming the challenges in NBS intervention in India from a global perspective

Various studies have been conducted worldwide to develop strategies to address the challenges (social, institutional and technical) associated with NBS interventions. Financial constraints are recognized as an institutional challenge. Studies highlight that social and institutional barriers tend to outweigh technical barriers (O'Donnell et al., 2017; Thorne et al., 2018; O'Donnell et al., 2021). Case studies of numerous cities emphasize the importance of a comprehensive approach to overcome these challenges. It is crucial to raise awareness, secure diverse funding sources, integrate green infrastructures into new developments,

TABLE 4 Some exemplary NBS projects in five major cities worldwide and key lessons learnt.

NBS projects	Metropolis	Population/Area (km^2)	Major objectives	Key lessons	References
NYC Green Infrastructure Plan (2010–2030)	New York (USA)	1,95,67,410 (34,490 km^2)	• To reduce CSO through sustainable stormwater management practices, target 1.5 billion gallons per year • To implement GI such as green roofs, right-of-way bioswales, green streets, and street trees for urban water management with additional UES	• Integration of Green and Grey Infrastructure to optimize water management and improve urban resilience • Adaptive management practices allowing flexibility based on performance and conditions • Community engagement and awareness • Focus on multi-benefit approach	Department of Environmental Protection (DEP) (2010), McPhearson et al. (2014), Culligan (2019), and Shakya and Ahiablame (2021)
Sponge City Program (2013-present)	Wuhan (China) – 30 pilot cities	6,31,486 (114 km^2)	• To absorb 60–85% of annual precipitation by 2030 and manage pluvial floods • To meet the sponge city standards by 2030 • To improve water quality, ensure water security and mitigate UHI through the NBS intervention	• Utilizes NBS measures for effective FRM and improved water quality • GI supportive policies and regulations • Developed localized strategies and technical standards tailored to specific urban contexts • Community and stakeholder engagement in the planning and implementation	Fenner (2020), Chen et al. (2021), Udas-Mankikar and Driver (2021), Qi et al. (2021), and Peng and Reilly (2021)
Green Infrastructure Vision 2050 (2020–2050)	Amsterdam (The Netherlands)	11,82,000 (220 km^2)	• To develop green routes for a 10-min walk from your front door to a park • To transform pavements into green spaces, wherever feasible, for the natural environment • To increase public green areas like parks and urban forests social well-being, climate adaptation, health, and biodiversity	• Emphasizing GI-integrated holistic urban planning • Developing climate resilience in extreme weather conditions • Long-term economic benefits through cost reduction in stormwater management, energy consumption, and healthcare • Community awareness and sensitization toward NBS	Paulin et al. (2019), Carbon Neutral Cities (2020), Department of Planning and Sustainability (DPS) (2020), and Kottari (2021)
Rain City Strategy (2020–2050)	Vancouver (Canada)	1,06,00,000 (8,494 km^2)	• To transform Vancouver into a resilient city and enhance its livability through GI measures • To improve the City's water quality • Increase greeneries, UHI mitigation and rainwater harvesting • To invest in education and capacity building to increase ecosystem-based adaptations	• Focus on integrating GI across public and private properties for effective rainwater management • Maximizes the investment in NBS through a multi-benefit approach • Community engagement and education • Establishes clear performance standards, adaptive management and regular monitoring	Rain City Strategy (2019) and Udas-Mankikar and Driver (2021)
30-Year Plan for Greater Adelaide (2010–2040)	Greater Adelaide (Australia)	15,15,491 (10,873 km^2)	• To transform the city into a sustainable and resilient one against climate risks by 2040 • To maintain and improve livability through NBS • Promoting public transport, cycling and walking • To protect, restore and enhance the natural environment	• Focus on creating compact urban forms to preserve the natural landscapes and reduce urban agglomeration • Promoting the sustainable transportation • Emphasizing the integration of GI in urban planning • Participation of residents in planning helps to foster a sense of responsibility for the natural landscape	Living Adelaide (2017), Australian Bureau of Statistics (ABS) (2021), and Greater Adelaide Regional Plan (GARP) (2021)

10.3389/frwa.2024.1504492

and increase overall funding for nature-based projects within cities (Iojă et al., 2018; O'Donnell et al., 2021). Drawing insights from multiple studies and frameworks addressing the challenges in NBS intervention in urban areas worldwide (O'Donnell et al., 2017; Melville-Shreeve et al., 2018; Amaral et al., 2021; Toxopeus and Polzin, 2021; Suleiman, 2021; Castelo et al., 2023), six key steps have been identified for formulating strategies to tackle the implementation challenges in India. These steps include – (a) amending legislation and developing the policies to establish guidelines for nature-based measures with specific standards, (b) highlighting and promoting the numerous co-benefits of NBS-integrated multifunctional spaces, (c) encouraging collaborative efforts from research and planning to execution (d) increasing awareness through education, community events, and activities, (e) securing sustainable funding by involving the private sector (f) promoting the advanced scientific research on retrofitting NBS measures in existing urban settings and creating new ones.

Researchers also presented the strategies at various stakeholder levels to conceptualize and streamline the framework for NBS intervention (Qiao et al., 2018; Landscape Institute and the Construction Industry Council (LI and CIC), 2019; O'Donnell et al., 2020). Similarly, the stakeholders can be selected to institutionalize the NBS in the urban landscapes in India. It will define a framework at each stakeholder level to overcome these challenges. These stakeholders include the central government, state governments, academia, practitioners, and individuals. The central government should acknowledge the benefits of NBS and promote its nationwide adoption by revising legislation, establishing technical standards, empowering states to create regional policies, and facilitating collaborative research. State governments should promote the benefits of blue-green infrastructures at the local level, invest in outreach programs to educate communities, develop policies for adoption and maintenance, and secure funding through private-sector collaboration.

Taking on financial constraints and investing in blue-green infrastructure necessitates a proactive approach, including conducting a thorough cost–benefit analysis. For example, developing a robust framework to assess the socioeconomic impact of a flood event can provide valuable insights for comparing the economic benefits of blue-green infrastructure to the local community and the investors. The role of academia and practitioners in the development of strategies to overcome technical and financial issues is inevitable. The academia should enhance scientific understanding of the nature-based approaches through rigorous collaborative research with international organizations to fill the knowledge gaps and provide evidence regarding the hydrological and ecological performance of NBS. Researchers can also advocate for policy changes that support the implementation of NBS by publishing the research outcomes. With the collaboration of academia, practitioners need to develop low-maintenance blue-green infrastructure measures, assess their suitability for regional environments, create open-source toolkits to assess and monetize the ecosystem services and raise public awareness about the co-benefits. Assessing the ecosystem services and further monetizing them will also draw the attention of the private sector to invest in nature-based projects for urban sustainability and resilience.

Citizen engagement can facilitate cities through the problem-based model to identify the local challenges, connect people with nature and increase the sense of ownership of NBS-intervened places to overcome the challenges. Communities working with natural processes and systems can facilitate better adaptability of nature-based projects (Brown and Mijic, 2019). Individuals should take part in local stewardship efforts for nature conservation, actively engage in the ongoing NBS projects, provide valuable support, and strive for sustainable development. Encouraging behavior change among fellow citizens is also important, as it raises awareness about the multifaceted NBS-integrated urban spaces.

5 Conclusion

The study emphasizes the declining natural LULC in Indian urban landscapes and the urgent need for sustainable and resilient cities. NBS has gained recognition for enhancing urban resilience, addressing environmental and climate challenges, and promoting community well-being and biodiversity. NBS offers various ecosystem services (such as flood risk mitigation, improved water and air quality, urban heat island mitigation, and resource efficiency). The present study provides a detailed analysis of the ecosystem services linked to NBS, focusing on how these ecosystem-based strategies can facilitate SDGs.

To explore the potential integration of NBS in India, five exemplary NBS projects from different countries have been analyzed – NYC Green Infrastructure Plan (USA), Sponge City Program (China), Green Infrastructure Vision (The Netherlands), Rain City Strategy (Canada), 30-Year Plan for Greater Adelaide (Australia). Learning from global initiatives can be a significant step toward developing ecosystem-based strategies to understand and address the resilience challenges against the increasing urban pressures in Indian cities. The valuable insights drawn from these city-scale projects highlight the integration of green and traditional infrastructure for improved urban water management and enhanced urban resilience. Additionally, these projects emphasize the significance of employing adaptive management techniques, fostering community involvement and awareness, and prioritizing a multi-faceted approach to achieve multiple benefits.

Various challenges (technical, social, and institutional) related to NBS intervention in Indian cities have also been discussed. Limited research exists to compare the effectiveness of NBS with traditional grey infrastructure alternatives. Comprehensive research on nature-based solutions, particularly implementation and suitability consideration frameworks, is very much needed in India. It will be instrumental in quantifying the environmental benefits, facilitating urban water management, and developing climate change adaptation and mitigation strategies. It will also support the formulation of ecosystem-based policies and encourage investment from the private sector. Moreover, introducing NBS during the planning and policymaking phase, setting clear standards for NBS deliverables, encouraging stakeholders' participation and collaborative efforts, and ensuring practical implementation can maximize ecosystem services,

enhancing sustainable development, economic growth, and urban resilience.

Author contributions

NA: Conceptualization, Formal analysis, Methodology, Resources, Writing – original draft, Writing – review & editing. QH: Supervision, Writing – review & editing.

Funding

The author(s) declare that no financial support was received for the research, authorship, and/or publication of this article.

Acknowledgments

The authors would like to thank all the reviewers for their constructive comments.

Conflict of interest

The authors declare that the research was conducted in the absence of any commercial or financial relationships that could be construed as a potential conflict of interest.

Generative AI statement

The authors declare that no Gen AI was used in the creation of this manuscript.

Publisher's note

References

Acharya, P., Gupta, A. K., Dhyani, S., and Karki, M. (2020). "New pathways for NbS to realise and achieve SDGs and post 2015 targets: transformative approaches in resilience building" in Nature-based solutions for resilient ecosystems and societies. Disaster Resilience and Green Growth. eds. S. Dhyani, A. Gupta and M. Karki (Singapore: Springer).

Agaton, C. B., and Guila, P. M. C. (2023). Ecosystem services valuation of constructed wetland as a nature-based solution to wastewater treatment. *Earth* 4, 78–92. doi: 10.3390/earth4010006

Ahmad, N., and Hassan, Q. (2021). An engineered and sustainable solution for flood and sediment Management in Kosi River, India. *J Ecol Nat Resour* 5:258. doi: 10.23880/jenr-16000258

Ahmad, N., and Hassan, Q. (2024). "Enhancing blue-green infrastructures for flood and water stress management: A case study of Chennai" in Recent developments in water resources and transportation engineering. TRACE 2022. Lecture Notes in Civil Engineering. eds. N. Nagabhatla, Y. Mehta, B. K. Yadav, A. Behl and M. Kumari, vol. *353* (Singapore: Springer).

Akinsemolu, A. A. (2018). The role of microorganisms in achieving the sustainable development goals. *J. Clean. Prod.* 182, 139–155. doi: 10.1016/j.jclepro.2018.02.081

Akter, S., and Gupta, B. (2022). Case studies in urban agriculture – A monograph by sustainable urban food systems class/group (2021–22). Available online at: https://www.researchgate.net/publication/360354060

Albert, C., Spangenberg, J. H., and Schröter, B. (2017). Nature-based solutions: criteria. *Nature* 543:315. doi: 10.1038/543315b

Allen, C., Metternicht, G., Wiedmann, T., and Pedercini, M. (2019). Greater gains for Australia by tackling all SDGs but the last steps will be the most challenging. *Nat Sustain* 2, 1041–1050. doi: 10.1038/s41893-019-0409-9

Almaaitah, T., Appleby, M., Rosenblat, H., Drake, J., and Joksimovic, D. (2021). The potential of blue-green infrastructure as a climate change adaptation strategy: a systematic literature review. *Blue-Green Syst.* 3, 223–248. doi: 10.2166/bgs.2021.016

Amaral, M. H., Benites-Lazaro, L. L., de Almeida, A., Sinisgalli, P., da Fonseca, P., Alves, H., et al. (2021). Environmental injustices on green and blue infrastructure: urban nexus in a macrometropolitan territory. *J. Clean. Prod.* 289:125829. doi: 10.1016/j.jclepro.2021.125829

Arrau, C. P., and Peña, M. A. (2011). The urban Heat Island (UHI) Effect. Available online at: http://www.urbanheatislands.com/

Artmann, M., and Sartison, K. (2018). The role of urban agriculture as a nature-based solution: A review for developing a systemic assessment framework. *Sustain. For.* 10:1937. doi: 10.3390/su10061937

Australian Bureau of Statistics (ABS). (2021). Greater Adelaide Census Data, South Australia. Available online at: https://www.abs.gov.au/census/

Balian, E., Eggermont, H., and Le Roux, X. (2014). BiodivERsA: BiodivERsA workshop on nature-based solutions. Available online at: http://www.biodiversa.org/671

Banting, D., Doshi, H., Li, J., Missios, P., Au, A., Currie, B. A., et al. (2005). Report on the environmental benefits and costs of green roof Technology for the City of Toronto; City of Toronto and Ontario Centres of excellence—Earth and environmental technologies. Toronto, ON: Ryerson University.

Besir, A. B., and Cuce, E. (2018). Green roofs and facades: a comprehensive review. *Renew. Sust. Energ. Rev.* 82, 915–939. doi: 10.1016/j.rser.2017.09.106

Besthorn, F. H. (2013). Vertical farming: social work and sustainable urban agriculture in an age of global food crises. *Aust. Soc. Work.* 66, 187–203. doi: 10.1080/0312407X.2012.716448

Bondwal, R. S., and Bisht, N. S. (2019). A temporal data analysis to identify land cover change trends in NCT Delhi. 2019. International conference on machine learning, big data, cloud and parallel computing (COMITCon).

Bozovic, R., Maksimovic, C., Mijic, A., Smith, K. M., Suter, I., and Van Reeuwijk, M. (2017) Blue green solutions. A systems approach to sustainable, resilient and cost-efficient urban development.

Brown, K., and Mijic, A. (2019). Integrating green and blue spaces into our cities: Making it happen. Grantham institute briefing paper, no 30. London: Imperial College London.

Brumley, J., Marks, C., Chau, A., Lowrance, R., Huang, J., Richardson, C., et al. (2018). The influence of green infrastructure practices on groundwater quality: the state of the science. Washington, DC: U.S. Environmental Protection Agency.

Cabral, I., Keim, J., Engelmann, R., Kraemer, R., Siebert, J., and Bonn, A. (2017). Ecosystem services of allotment and community gardens: a Leipzig, Germany case study. *Urban For. Urban Green.* 23, 44–53. doi: 10.1016/j.ufug.2017.02.008

Capotorti, G., Mollo, B., Zavattero, L., Anzellotti, I., and Celesti-Grapow, L. (2015). Setting priorities for urban forest planning. A comprehensive response to ecological and social needs for the metropolitan area of Rome (Italy). *Sustainability* 7, 3958–3976. doi: 10.3390/su7043958

Carbon Neutral Cities. (2020). https://carbonneutralcities.org/wp-content/uploads/2020/09/Amsterdam-Green-Infrastructure-Vision-2050toegankelijk02092020.pdf

Cassman, K. G., and Grassini, P. (2020). A global perspective on sustainable intensification research. *Nat Sustain* 3, 262–268. doi: 10.1038/s41893-020-0507-8

Castelo, S., Amado, M., and Ferreira, F. (2023). Challenges and opportunities in the use of nature-based solutions for urban adaptation. *Sustain. For.* 15:7243. doi: 10.3390/su15097243

Chen, S., van de Ven, F. H. M., Zevenbergen, C., Verbeeck, S., Ye, Q., Zhang, W., et al. (2021). Revisiting China's Sponge City planning approach: lessons from a case study on Qinhuai District, Nanjing. *Front. Environ. Sci.* 9:748231. doi: 10.3389/fenvs.2021.748231

Clark, K. H., and Nicholas, K. A. (2013). Introducing urban food forestry: a multifunctional approach to increase food security and provide ecosystem services. *Landsc. Ecol.* 28, 1649–1669. doi: 10.1007/s10980-013-9903-z

Cohen, N., and Reynolds, K. (2015). Resource needs for a socially just and sustainable urban agriculture system: Lessons from new York City. *Renew Agric Food Syst* 30, 103–114. doi: 10.1017/S1742170514000210

Cohen-Shacham, E., Andrade, A., Dalton, J., Dudley, N., Jones, M., Kumar, C., et al. (2019). Core principles for successfully implementing and upscaling nature-based solutions. *Environ. Sci. Pol.* 98, 20–29. doi: 10.1016/j.envsci.2019.04.014

Cohen-Shacham, E., Walters, G., Janzen, C., and Maginnis, S. (Eds.) (2016). Nature-based solutions to address global societal challenges. Gland, Switzerland: IUCN, xiii.

Corbett, J., and Mellouli, S. (2017). Winning the SDG battle in cities: how an integrated information ecosystem can contribute to the achievement of the 2030 sustainable development goals. *Inf. Syst. J.* 27, 427–461. doi: 10.1111/isj.12138

Corcoran, M. P., and Kettle, P. C. (2015). Urban agriculture, civil interfaces and moving beyond difference: the experiences of plot holders in Dublin and Belfast. *Local Environ.* 20, 1215–1230. doi: 10.1080/13549839.2015.1038228

Culligan, P. J. (2019). Green infrastructure and urban sustainability: A discussion of recent advances and future challenges based on multiyear observations in New York City. *Sci. Technol. Built Environ.* 25, 1113–1120. doi: 10.1080/23744731.2019.1629243

De Bon, H., Parrot, L., and Moustier, P. (2009). Sustainable urban agriculture in developing countries: A review. *Sustain Agric* 30, 619–633. doi: 10.1007/978-90-481-2666-8_38

Department of Environmental Protection (DEP). (2010). NYC green infrastructure plan: A sustainable strategy for clean waterways. Available online at: https://www1.nyc.gov/assets/dep/downloads/pdf/water/stormwater/green-infrastructure/nyc-green-infrastructure-plan-2010.pdf

Department of Planning and Sustainability (DPS). (2020). Amsterdam green infrastructure vision 2050 – A liveable city for people, plants, and animals. City of Amsterdam, The Netherlands. Available online at: https://www.amsterdam.nl/en/policy/policy-green-space

Depietri, Y., and McPhearson, T. (2017). "Integrating the grey, green, and blue in cities: nature-based solutions for climate change adaptation and risk reduction" in Nature-based solutions to climate change adaptation in urban areas. eds. N. Kabisch, H. Korn, J. Stadler and A. Bonn (New York: Springer), 91–109.

Dhyani, S., Karki, M., and Gupta, A. K. (2020). "Opportunities and advances to mainstream nature-based solutions in disaster risk management and climate strategy" in Nature-based solutions for resilient ecosystems and societies. eds. S. Dhyani, A. Gupta and M. Karki (Singapore: Disaster Resilience and Green Growth, Springer).

Diaz, S., Demissew, S., Joly, C., Lonsdale, W. M., and Larigauderie, A. (2015). A Rosetta stone for nature's benefits to people. *PLoS Biol.* 13:e1002040. doi: 10.1371/journal.pbio.1002040

Dong, X., Guo, H., and Zeng, S. (2017). Enhancing future resilience in urban drainage system: green versus grey infrastructure. *Water Res.* 124, 280–289. doi: 10.1016/j.watres.2017.07.038

Dora, C., Haines, A., Balbus, J., Fletcher, E., Adair-Rohani, H., Alabaster, G., et al. (2015). Indicators linking health and sustainability in the post-2015 development agenda. *Lancet* 385, 380–391. doi: 10.1016/S0140-6736(14)60605-X

Dorst, H., van der Jagt, S., Raven, R., and Runhaar, H. (2019). Urban greening through nature-based solutions—key characteristics of an emerging concept. *Sustain. Cities Soc.* 49:101620. doi: 10.1016/j.scs.2019.101620

Douglas, I. (2018). The challenge of urban poverty for the use of green infrastructure on floodplains and wetlands to reduce flood impacts in intertropical Africa. *Landsc. Urban Plan.* 180, 262–272. doi: 10.1016/j.landurbplan.2016.09.025

European Commission (2021). Evaluating the impact of nature-based solutions: a handbook for practitioners. Luxembourg: Publications office of the European Union.

European Environmental Agency (EEA). (2017). Green infrastructure and flood management: Promoting cost-efficient flood risk reduction via green infrastructure solutions. Copenhagen: European Environmental Agency. Available online at: https://www.eea.europa.eu/publications/green-infrastructure-and-flood-management

European Environmental Agency (EEA). (2018). The Dutch make Room for the river. Interview with Willem Jan Goossen. Ministry of Infrastructure and Water Management. The Hague, Netherlands. Available online at: https://www.eea.europa.eu/signals/signals-2018-content-list/articles/interview-2014-the-dutch-make

Fenner, R. (2020). Urban flood resilience – philosophical transactions of the Royal Society A. London: The Royal Society Publishing.

Fritz, S., See, L., Carlson, T., Haklay, M., Oliver, J. L., Fraisl, D., et al. (2019). Citizen science and the United Nations sustainable development goals. *Nat Sustain* 2, 922–930. doi: 10.1038/s41893-019-0390-3

Ganapathi, H., Awasthi, S., and Vasudevan, P. (2024). "Wetlands as a nature-based solution for urban water management" in Nature-based solutions for circular Management of Urban Water. Circular Economy and Sustainability. eds. A. Stefanakis, H. V. Oral, C. Calheiros and P. Carvalho (Cham: Springer).

Ghofrani, Z., Sposito, V., and Faggian, R. (2017). A comprehensive review of blue-green infrastructure concepts. *Int J Environ Sustain* 6, 15–36. doi: 10.24102/ijes.v6i1.728

Grafton, R. Q., Doyen, L., Béné, C., Borgomeo, E., Brooks, K., Chu, L., et al. (2019). Realising resilience for decision-making. *NatSustain* 2, 907–913. doi: 10.1038/s41893-019-0376-1

Greater Adelaide Regional Plan (GARP) (2021). Greater Adelaide Data, 2021, South Australia. Available online at: https://plan.sa.gov.au/regional-planning-program/

Gupta, K. (2020). Challenges in developing urban flood resilience in India. *Phil. Trans. R. Soc. A* 378:20190211. doi: 10.1098/rsta.2019.0211

Hall, D. M., Camilo, G. R., Tonietto, R. K., Ollerton, J., Ahrné, K., Arduser, M., et al. (2017). The city as a refuge for insect pollinators. *Conserv. Biol.* 31, 24–29. doi: 10.1111/cobi.12840

Hamel, P., and Tan, L. (2022). Blue-green infrastructure for flood and water quality management in Southeast Asia: evidence and knowledge gaps. *Environ. Manag.* 69, 699–718. doi: 10.1007/s00267-021-01467-w

Hermawan, A. A., Talei, A., Salamatinia, B., and Chua, L. H. C. (2020). Seasonal performance of stormwater biofiltration system under tropical conditions. *Ecol. Eng.* 143:105676. doi: 10.1016/j.ecoleng.2019.105676

Hewitt, C. N., Ashworth, K., and MacKenzie, A. R. (2020). Using green infrastructure to improve urban air quality (GI4AQ). *Ambio* 49, 62–73. doi: 10.1007/s13280-019-01164-3

Holmes, D. (2019). Chulalongkorn University Centenary Park—green infrastructure for the city of Bangkok. World Landscape Architecture. Available online at: https://worldlandscapearchitect.com/chulalongkorn-centenary-park-green-infrastructure-for-the-city-of-bangkok/#.Yg3IpThBzIU

Hou, Y., Zhou, S., Burkhard, B., and Müller, F. (2014). Socioeconomic influences on biodiversity, ecosystem services and human well-being: a quantitative application of the DPSIR model in Jiangsu, China. *Sci. Total Environ.* 490, 1012–1028. doi: 10.1016/j.scitotenv.2014.05.071

Iojă, I. C., Osaci-Costache, G., Breuste, J., Hossu, C. A., Grădinaru, S. R., Onose, D. A., et al. (2018). Integrating urban blue and green areas based on historical evidence. *Urban Forestry Urban Green.* 34, 217–225. doi: 10.1016/j.ufug.2018.07.001

Irvine, K., Sovann, C., Suthipong, S., Kok, S., and Chea, E. (2015). Application of PCSWMM to assess wastewater treatment and urban flooding scenarios in Phnom Penh, Cambodia: a tool to support eco-city planning. *J. Water Manag Model.* doi: 10.14796/jwmm.c389

Jain, G., and Sarkar, S. (2017). Urban Heat Island: causes effects and mitigating strategies. *Imp. J. Interdiscip. Res.* 3, 2098–2103.

Jarosz, L. (2011). Nourishing women: toward a feminist political ecology of community supported agriculture in the United States. *Gend. Place Cult.* 18, 307–326. doi: 10.1080/0966369X.2011.565871

Kahane, R., Hodgkin, T., Jaenicke, H., Hoogendoorn, C., Hermann, M., Dyno Keatinge, J. D. H., et al. (2013). Agrobiodiversity for food security, health and income. *Agron. Sustain. Dev.* 33, 671–693. doi: 10.1007/s13593-013-0147-8

Kato, S., Hishiyama, K., Darmadi, A. K., Ngurah, A., and Suprapta, D. (2017). Changing roles of traditional small urban green spaces (Telajakan) in Bali, Indonesia. *Open J Ecol* 7, 1–11. doi: 10.4236/oje.2017.71001

Keeler, B. L., Hamel, P., McPhearson, T., Hamann, M. H., Donahue, M. L., Meza Prado, K. A., et al. (2019). Social-ecological and technological factors moderate the value of urban nature. *Nat Sustain* 2, 29–38. doi: 10.1038/s41893-018-0202-1

Keerthi-Naidu, B., and Chundeli, F. A. (2023, 2023). Assessing LULC changes and LST through NDVI and NDBI spatial indicators: a case of Bengaluru, India. *GeoJournal* 88, 4335–4350. doi: 10.1007/s10708-023-10862-1

Keesstra, S. D., Bouma, J., Wallinga, J., Tittonell, P., Smith, P., Cerda, A., et al. (2016). The significance of soils and soil science towards realisation of the United Nations sustainable development goals. *Soil* 2, 111–128. doi: 10.5194/soil-2-111-2016

Keesstra, S., Mol, G., de Leeuw, J., Okx, J., Molenaar, C., de Cleen, M., et al. (2018a). Soil-related sustainable development goals: four concepts to make land degradation neutrality and restoration work. *Land* 7. doi: 10.3390/land7040133

Keesstra, S., Nunes, J., Novara, A., Finger, D., Avelar, D., Kalantari, Z., et al. (2018b). The superior effect of nature based solutions in land management for enhancing ecosystem services. *Sci. Total Environ.* 610-611, 997–1009. doi: 10.1016/j.scitotenv.2017.08.077

Killingsworth, B., Lemay, L., and Peng, T. (2011). The urban Heat Island effect and Concrete's role in mitigation. Available online at: http://www.nrmca.org/members/ConcreteInFocus/Enviro%20Library/NRC-S0511_urban.pdf

Kiribou, R., Djene, S., Bedadi, B., Ntirenganya, E., Ndemere, J., and Dimobe, K. (2024). Urban climate resilience in Africa: a review of nature-based solution in African cities' adaptation plans. *Discov. Sustain.* 5:94. doi: 10.1007/s43621-024-00275-6

Kondratenko, J., Boogaard, F. C., Rubulis, J., and Maļinovskis, K. (2024). Spatial and temporal variability in bioswale infiltration rate observed during full-scale infiltration tests: case study in Riga Latvia. *Water* 16:2219. doi: 10.3390/w16162219

Kottari, M. (2021). "Amsterdam's pathway to climate neutrality: creating an enabling environment" in The Palgrave encyclopedia of urban and regional futures (Cham: Palgrave Macmillan).

Kulak, M., Graves, A., and Chatterton, J. (2013). Reducing greenhouse gas emissions with urban agriculture: a life cycle assessment perspective. *Landsc. Urban Plan.* 111, 68–78. doi: 10.1016/j.landurbplan.2012.11.007

Landscape Institute and the Construction Industry Council (LI and CIC) (2019). Achieving Sustainable drainage: A Review of delivery by Lead Local Flood Authorities, January 2019 London, UK. Available online at: https://landscapewpstorage01.blob.core.windows.net/wwwlandscapeinstitute-org/2019/01/11689_LI_SuDS-Report_v4a-Web.pdf (Accessed September 06, 2024)

Li, Y. H., Tung, C. P., and Chen, P. Y. (2017). Stormwater management toward water supply at the community scale – a case study in northern Taiwan. *Sustain. For.* 9:1206. doi: 10.3390/su9071206

Liberalesso, T., Cruz, C. O., Silva, C. M., and Manso, M. (2020). Green infrastructure and public policies: an international review of green roofs and green walls incentives. *Land Use Policy* 96:104693. doi: 10.1016/j.landusepol.2020.104693

Lim, H. S., and Lu, X. X. (2016). Sustainable urban stormwater management in the tropics: an evaluation of Singapore's ABC waters program. *J. Hydrol.* 538, 842–862. doi: 10.1016/j.jhydrol.2016.04.063

Lin, J.-Y., Chen, C.-F., and Ho, C.-C. (2018). Evaluating the effectiveness of green roads for runoff control. *J. Sustain. Water Built. Environ.* 4:4018001. doi: 10.1061/JSWBAY.0000847

Liu, A., Goonetilleke, A., and Egodawatta, P. (2015). Role of rainfall and catchment characteristics on urban Stormwater quality. Singapore: Springer.

Living Adelaide. (2017). The 30-year plan for greater Adelaide 2017 update. Department of Planning, Transport and Infrastructure (DPTI) Government of South Australia. Available online at: https://livingadelaide.sa.gov.au/

Lo, V. (2016). *Synthesis report on experiences with ecosystem-based approaches to climate change adaptation and disaster risk reduction, technical series no.85*. Secretariat of the convention on biological diversity, Montreal, 106.

Lombardía, A., and Gómez-Villarino, M. T. (2023). Green infrastructure in cities for the achievement of the un sustainable development goals: a systematic review. *Urban Ecosyst.* 26, 1693–1707. doi: 10.1007/s11252-023-01401-4

Macreadie, P. I., Anton, A., Raven, J. A., Beaumont, N., Connolly, R. M., Friess, D. A., et al. (2019). The future of blue carbon science. *Nat. Commun.* 10, 1–13. doi: 10.1038/s41467-019-11693-w

Maes, J., and Jacobs, S. (2017). Nature-based solutions for Europe's sustainable development. *Conserv. Lett.* 10, 121–124. doi: 10.1111/conl.12216

Maes, M. J. A., Jones, K. E., Toledano, M. B., and Milligan, B. (2019). Mapping synergies and trade-offs between urban ecosystems and the sustainable development goals. *Environ. Sci. Pol.* 93, 181–188. doi: 10.1016/j.envsci.2018.12.010

Mahmoud, I. H., Morello, E., Rizzi, D., and Wilk, B. (2022). "Localizing sustainable development goals (SDGs) through co-creation of nature-based solutions (NBS)" in The Palgrave encyclopedia of urban and regional futures (Cham: Palgrave Macmillan).

Maryati, S., and Humaira, A. N. S. (2017). Implementation of green infrastructure concept in citarum watershed. In: Proceedings of the AIP conference proceedings. College Park, MD: American Institute of Physics Inc., 20031.

Mathan, M., and Krishnaveni, M. (2020). Monitoring spatio-temporal dynamics of urban and peri-urban land transitions using ensemble of remote sensing spectral indices—a case study of Chennai metropolitan area, India. *Environ. Monit. Assess.* 192:15. doi: 10.1007/s10661-019-7986-y

McPhearson, T., Hamstead, Z., and Kremer, P. (2014). Urban ecosystem Services for Resilience Planning and Management in new York City. Ambio;43:502–515.

Melville-Shreeve, P., Cotterill, S., Grant, L., Arahuetes, A., Stovin, V., Farmani, R., et al. (2018). State of SuDS delivery in the United Kingdom. *Water Environ. J.* 32, 9–16. doi: 10.1111/wej.12283

Mentens, J., Raes, D., and Hermy, M. (2006). Green roofs as a tool for solving the rainwater runoff problem in the urbanized 21st century? *Landsc. Urban Plan.* 77, 217–226. doi: 10.1016/j.landurbplan.2005.02.010

Montgomery County Planning Commission (MCPC) (2011). Planning by design: green parking lots. Montgomery County, the state of Maryland, United States of America (USA). Available online at: https://www.montcopa.org/DocumentCenter/View/3017/GreenParking08292011

Mumtaz, M. (2021). Role of civil society organizations for promoting green and blue infrastructure to adapting climate change: evidence from Islamabad city, Pakistan. *J. Clean. Product.* 309:127296. doi: 10.1016/j.jclepro.2021.127296

Murphy, A., Enqvist, J. P., and Tengö, M. (2019). Place-making to transform urban social–ecological systems: insights from the stewardship of urban lakes in Bangalore India. *Sustain. Sci.* 14, 607–623. doi: 10.1007/s11625-019-00664-1

Naikoo, M. W., Rihan, M., Ishtiaque, M., and Shahfahad, M. (2020). Analyses of land use land cover (LULC) change and built-up expansion in the suburb of a metropolitan city: Spatio-temporal analysis of Delhi NCR using landsat datasets. *J. Urban Manag.* 9, 347–359. doi: 10.1016/j.jum.2020.05.004

Naikoo, M. W., Shahfahad, Talukdar, S., das, T., Ahmad, M., Ishtiaque, M., et al. (2023). "Land use land cover change modeling and future simulation in Mumbai City by integrating cellular automata and artificial neural network" in Advancements in urban environmental studies. GIScience and geo-environmental modelling. eds. A. Rahman, S. Sen Roy and S. Talukdar (Cham: Springer).

Natural Resource Defence Council (NRDC) (2022). Green infrastructure: how to manage water in a sustainable way. Available online at: https://www.nrdc.org/stories/green-infrastructure-how-manage-water-sustainable-way

Niblick, B., Monnell, J. D., Zhao, X., and Landis, A. E. (2013). Using geographic information systems to assess potential biofuel crop production on urban marginal lands. *Appl. Energy* 103, 234–242. doi: 10.1016/j.apenergy.2012.09.036

Norton, B. A., Coutts, A. M., Livesley, S. J., Harris, R. J., Hunter, A. M., and Williams, N. S. G. (2015). Planning for cooler cities: a framework to prioritise green infrastructure to mitigate high temperatures in urban landscapes. *Landsc. Urban Plan.* 134, 127–138. doi: 10.1016/j.landurbplan.2014.10.018

O'Donnell, E. C., Lamond, J. E., and Thorne, C. R. (2017). Recognising barriers to implementation of blue-green infrastructure: a Newcastle case study. *Urban Water J.* 14, 964–971. doi: 10.1080/1573062X.2017.1279190

O'Donnell, E. C., Maskrey, S., Skenderian, M., O'Brien, H., and Vann, J. (2020). Overcoming barriers to innovation in urban flood risk management. *Blue–Green Cities*, 15–35. doi: 10.1680/bgc.64195.015

O'Donnell, E. C., Netusil, N. R., Chan, F. K. S., Dolman, N. J., and Gosling, S. N. (2021). International perceptions of urban blue-green infrastructure: a comparison across four cities. *Water* 13:544. doi: 10.3390/w13040544

O'Donnell, E. C., Thorne, C., and Yeakley, J. A. (2019). Managing urban flood risk in blue-green cities: the clean water for all initiative. *J. Flood Risk Manag.* 12. doi: 10.1111/jfr3.12513

Olsson, E. G. A., Kerselaers, E., Kristensen, L. S., Primdahl, J., Rogge, E., and Wästfelt, A. (2016). Peri-urban food production and its relation to urban resilience. *Sustainability* 8, 1–21. doi: 10.3390/su8121340

Osei, G., Pascale, F., Delle-Odeleye, N., and Pooley, A. (2022). "Green infrastructure" in The Palgrave encyclopedia of urban and regional futures. ed. R. C. Brears (Cham: Palgrave Macmillan).

Pamukcu-Albers, P., Ugolini, F., La Rosa, D., et al. (2021). Building green infrastructure to enhance urban resilience to climate change and pandemics. *Landsc. Ecol.* 36, 665–673. doi: 10.1007/s10980-021-01212-y

Panagopoulos, T., González Duque, J. A., and Bostenaru Dan, M. (2016). Urban planning with respect to environmental quality and human wellbeing. *Environ. Pollut.* 208, 137–144. doi: 10.1016/j.envpol.2015.07.038

Paulin, M., Remme, R., and De Nijs, T. (2019). Amsterdam's green infrastructure valuing Nature's contributions to people. 2019. RIVM letter report 2019-0021. National institute for public health and the environment – RIVM, The Netherlands. Available online at: http://hdl.handle.net/10029/623099

Peng, Y., and Reilly, K. (2021). Grow green-using nature to reshape cities and live with water: An overview of the Chinese sponge city programme and its implementation in Wuhan. Etterbeek: IUCN European Regional Office.

Pigford, A. A. E., Hickey, G. M., and Klerkx, L. (2018). Beyond agricultural innovation systems? Exploring an agricultural innovation ecosystems approach for niche design and development in sustainability transitions. *Agric. Syst.* 164, 116–121. doi: 10.1016/j.agsy.2018.04.007

Pitman, S. D., Daniels, C. B., and Ely, M. E. (2015). Green infrastructure as life support: urban nature and climate change. *Trans. R. Soc. S. Aust.* 139, 97–112. doi: 10.1080/03721426.2015.1035219

Puchol-Salort, P., O'Keeffe, J., Reeuwijk, M., and Mijic, A. (2021). An urban planning sustainability framework: systems approach to blue green urban design. *Sustain. Cities Soc.* 66:102677. doi: 10.1016/j.scs.2020.102677

Qi, Y., Chan, F. K. S., O'Donnell, E. C., Feng, M., Sang, Y., Thorne, C. R., et al. (2021). Exploring the development of the sponge city programme (SCP): the case of Gui'an new district, Southwest China. *Front. Water* 3:676965. doi: 10.3389/frwa.2021.676965

Qiao, X. J., Kristoffersson, A., and Randrup, T. B. (2018). Challenges to implementing urban sustainable stormwater management from a governance perspective: a literature review. *J. Clean. Prod.* 196, 943–952. doi: 10.1016/j.jclepro.2018.06.049

Rain City Strategy. (2019). A green rainwater infrastructure and rainwater management initiative. City of Vancouver, Canada. Available online at: https://vancouver.ca/files/cov/rain-city-strategy.pdf

Rajan, E. H. S., and Amirtham, L. R. (2021, 2021). Urban heat island intensity and evaluation of outdoor thermal comfort in Chennai, India. *Environ. Dev. Sustain.* 23, 16304–16324. doi: 10.1007/s10668-021-01344-w

Rajaveni, S. P., Nair, I. S., and Elango, L. (2016). Evaluation of impact of climate change on seawater intrusion in a coastal aquifer by finite element modelling. *J. Clim Change* 2, 111–118. doi: 10.3233/JCC-160022

Reguero, B. G., Beck, M. W., Schmid, D., Stadtmüller, D., Raepple, J., Schüssele, S., et al. (2020). Financing coastal resilience by combining nature-based risk reduction with insurance. *Ecol. Econ.* 169:106487. doi: 10.1016/j.ecolecon.2019.106487

Roe, S., Streck, C., Obersteiner, M., Frank, S., Griscom, B., Drouet, L., et al. (2019). Contribution of the land sector to a 1.5 °C world. *Nat. Clim. Chang.* 9, 817–828. doi: 10.1038/s41558-019-0591-9

Roumeau, S., Seifelislam, A., Jameson, S., and Kennedy, L. (2015). Water governance and climate change issues in Chennai, USR 3330 "Savoirs et Mondes Indiens" working papers series no. 8. 2015, 1–34.

Safikhani, T., Abdullah, A. M., Ossen, D. R., and Baharvand, M. (2014). A review of energy characteristic of vertical greenery systems. *Renew. Sust. Energ. Rev.* 40, 450–462. doi: 10.1016/j.rser.2014.07.166

Sanyé-Mengual, E., Specht, K., Vávra, J., Artmann, M., Orsini, F., and Gianquinto, G. (2020). Ecosystem Services of Urban Agriculture: perceptions of project leaders, Stakeholders and the General Public. *Sustainability* 12:10446. doi: 10.3390/su122410446

Schindler, S., Sebesvari, Z., Damm, C., Euller, K., Mauerhofer, V., Schneidergruber, A., et al. (2014). Multifunctionality of floodplain landscapes: relating management options to ecosystem services. *Landsc. Ecol.* 29, 229–244. doi: 10.1007/s10980-014-9989-y

Schuch, G., Serrao-Neumann, S., Morgan, E., and Choy, D. L. (2017). Water in the city: green open spaces, land use planning and flood management—an Australian case study. *Land Use Policy* 63, 539–550. doi: 10.1016/j.landusepol.2017.01.042

Shafique, M., Reeho Kim, R., and Lee, D. (2016). The potential of green-blue roof to manage storm water in urban areas. *Nat Environ Pollution Technol* 15.

Shah, A. M., Liu, G., Chen, Y., Yang, Q., Yan, N., Agostinho, F., et al. (2023). Urban constructed wetlands: assessing ecosystem services and disservices for safe, resilient, and sustainable cities. *Front. Eng. Manag.* 10, 582–596. doi: 10.1007/s42524-023-0268-y

Shakya, R., and Ahiablame, L. (2021). A synthesis of social and economic benefits linked to green infrastructure. *Water* 13:3651. doi: 10.3390/w13243651

Sharief, M. A. J., and Vangipuram, B. (2022). "Assessment of socio-economic impact of urban flooding in Hyderabad due to climate change" in A system engineering approach to disaster resilience. Lecture notes in civil engineering. eds. C. Ghosh and S. Kolathayar, vol. *205* (Singapore: Springer).

Sidek, L. M., Muha, N. E., Noor, N. A. M., and Basri, H. (2013). Constructed rain garden systems for stormwater quality control under tropical climates. *IOP Conf. Ser.* 16:012020. doi: 10.1088/1755-1315/16/1/012020

Steger, K., Fiener, P., Marvin-DiPasquale, M., Viers, J. H., and Smart, D. R. (2019). Human-induced and natural carbon storage in floodplains of the Central Valley of California. *Sci. Total Environ.* 651, 851–858. doi: 10.1016/j.scitotenv.2018.09.205

Sterling, E. J., Filardi, C., Toomey, A., Sigouin, A., Betley, E., Gazit, N., et al. (2017). Biocultural approaches to well-being and sustainability indicators across scales. *Nat Ecol Evol* 1, 1798–1806. doi: 10.1038/s41559-017-0349-6

Suleiman, L. (2021). Blue green infrastructure, from niche to mainstream: challenges and opportunities for planning in Stockholm. *Technol. Forecast. Soc. Chang.* 166:120528. doi: 10.1016/j.techfore.2020.120528

Surma, M. (2013). Green infrastructure planning as a part of sustainable urban development–case studies of Copenhagen and Wroclaw. *Proc. Latv. Univ. Agric.* 2013, 22–32.

Thacker, S., Adshead, D., Fay, M., Hallegatte, S., Harvey, M., Meller, H., et al. (2019). Infrastructure for sustainable development. *Nat Sustain* 2, 324–331. doi: 10.1038/s41893-019-0256-8

Thorne, C. R., Lawson, E. C., Ozawa, C., Hamlin, S. L., and Smith, L. A. (2018). Overcoming uncertainty and barriers to adoption of blue-green infrastructure for urban flood risk management. *J. Flood Risk Manag.* 11, S960–S972. doi: 10.1111/jfr3.12218

Toxopeus, H., and Polzin, F. (2021). Reviewing financing barriers and strategies for urban nature-based solutions. *J. Environ. Manag.* 289:112371. doi: 10.1016/j.jenvman.2021.112371

U.S. Environmental Protection Agency (USEPA) (2003). Cooling summertime temperatures: Strategies to reduce urban Heat Islands; publication number: 430-F-03-014; United States Environmental Protection Agency. Washington, DC: U.S. Environmental Protection Agency, 2003.

U.S. Environmental Protection Agency (USEPA) (2008). Green parking lot resource guide—February 2008. Cincinnati, OH: National Service Center for Environmental Publications (NSCEP), United States.

U.S. Environmental Protection Agency (USEPA) (2010). Green infrastructure case studies: Municipal policies for managing Stormwater with green infrastructure; EPA-841-F-10-004. Washington, DC: Office of Wetlands, oceans and watersheds, 2010.

Udas-Mankikar, S., and Driver, B. (2021). Blue-green infrastructure: an opportunity for Indian cities. ORF occasional paper no. 317, May 2021, observer research foundation

United Nations (2022). The sustainable development goals report 2022. New York: USA, United Nations. Available online at: https://unstats.un.org/sdgs/report/2022/The-Sustainable-Development-Goals-Report-2022.pdf

United Nations Environment Programme (UNEP) (2023). Nature-based infrastructure: how natural infrastructure solutions can address sustainable development challenges and the triple planetary crisis. Geneva: United Nations Environment Programme.

United States Army Corps of Engineers (USACE). (2012). ROOM FOR THE RIVER: Preparedness, response, recovery and mitigation – summary report of the 2011 Mississippi River flood and successful operation of the Mississippi River and tributaries system.

United States Department of Agriculture (USDA) Forest Service (2020). Urban forest systems and green stormwater infrastructure. *FS* 1146.

Veena, K., Parammasivam, K. M., and Venkatesh, T. N. (2020). Urban Heat Island studies: current status in India and a comparison with the international studies. *J. Earth Syst. Sci.* 129:85. doi: 10.1007/s12040-020-1351-y

Victoria State Government (VSG) (2017). Planning a green-blue city: A how-to guide for planning urban greening and enhanced stormwater management in Victoria, February 2017. Treasury Place: Department of Environment, Land, Water and Planning, Victoria, Australia.

Vojinovic, Z. (2015). Floor risk: The holistic perspective—From integrated to interactive planning for flood resilience, vol. *14*. London: The International Water Association (IWA) Publishing.

Vujovic, S., Haddad, B., Karaky, H., Sebaibi, N., and Boutouil, M. S. (2021). Urban Heat Island: Causes, Consequences, and Mitigation Measures with Emphasis on Reflective and Permeable Pavements. *CivilEng.* 2, 459–484. doi: 10.3390/civileng2020026

Wamsler, C., Brink, E., and Rivera, C. (2013). Planning for climate change in urban areas: from theory to practice. *J. Clean. Prod.* 50, 68–81. doi: 10.1016/j.jclepro.2012.12.008

Wang, Y., Bakker, F., De Groot, R., and Wörtche, H. (2014). Effect of ecosystem services provided by urban green infrastructure on indoor environment: A literature review. *Build. Environ.* 2014, 88–100.

Wang, Y., Berardi, U., and Akbari, H. (2016). Comparing the effects of urban heat island mitigation strategies for Toronto, Canada. *Energ. Buildings* 114, 2–19. doi: 10.1016/j.enbuild.2015.06.046

Wang, J., Chua, L. H. C., and Shanahan, P. (2019). Hydrological modeling and field validation of a bioretention basin. *J. Environ. Manag.* 240, 149–159. doi: 10.1016/j.jenvman.2019.03.090

Wang, Y., and Zacharias, J. (2015). Landscape modification for ambient environmental improvement in central business districts – A case from Beijing. *Urban For. Urban Green.* 14, 8–18. doi: 10.1016/j.ufug.2014.11.005

Wolch, J. R., Byrne, J., and Newell, J. P. (2014). Urban green space, public health, and environmental justice: the challenge of making cities 'just green enough'. *Landsc. Urban Plan.* 125, 234–244. doi: 10.1016/j.landurbplan.2014.01.017

World Bank (2008). Biodiversity, climate change, and adaptation: Nature-based solutions from the World Bank portfolio. Washington, DC: World Bank.

World Bank (2013). "Urban agriculture: findings from four city case studies (English)" in Urban development series knowledge papers, vol. *18* (Washington D.C: World Bank Group).

World Bank (2021). A catalogue of nature-based solutions for urban resilience. Washington, DC: World Bank Group.

World Meteorological Organization (WMO) (2022). State of the global climate in 2021. Geneva: World Meteorological Organization.

Yang, J., McBride, J., Zhou, J., and Sun, Z. (2005). The urban forest in Beijing and its role in air pollution reduction. *Urban For. Urban Green.* 2005, 65–78.

Yu, Q., and Li, N. (2023). "Assessment of green infrastructures performance for water quality management" in Proceedings of the 5th international symposium on water resource and environmental management. WREM 2022. Environmental Science and Engineering. ed. H. Xu (Cham: Springer).

Zhu, Z., Wang, J., Chan, F. K. S., Xu, Y., Li, G., Xu, M., et al. (2023). Urban agriculture as nature-based solutions: three key strategies to tackle emerging issues on food security in Chinese cities under climatic and non-climatic challenges. *Front. Eng. Manag.* 10, 736–741. doi: 10.1007/s42524-023-0262-4

frontiers | Frontiers in Water

TYPE Original Research
PUBLISHED 22 January 2025
DOI 10.3389/frwa.2025.1500086

OPEN ACCESS

EDITED BY
Vikram Kumar,
Government of Bihar, India

REVIEWED BY
Anuj Dwivedi,
Indian Institute of Technology Roorkee, India
Rituraj Shukla,
University of Guelph, Canada

*CORRESPONDENCE
Shams Quamar
✉ s.quamar4u@gmail.com

RECEIVED 22 September 2024
ACCEPTED 09 January 2025
PUBLISHED 22 January 2025

CITATION
Quamar S, Kumar P and Singh HP (2025) Streamflow and sediment simulation in the Song River basin using the SWAT model. *Front. Water* 7:1500086.
doi: 10.3389/frwa.2025.1500086

Streamflow and sediment simulation in the Song River basin using the SWAT model

Shams Quamar[1]*, Pradeep Kumar[2] and Harendra Prasad Singh[1]

[1]Department of Civil Engineering, Central University of Jharkhand, Ranchi, India, [2]Division of Environmental Hydrology, National Institute of Hydrology, Roorkee, India

This study assesses the performance of the Soil and Water Assessment Tool (SWAT) in simulating streamflow and sediment for the Song River watershed, with a focus on calibration, validation, and sensitivity analysis. Thirteen parameters were selected for calibration, with eight identified as highly sensitive, reflecting key hydrological processes of the area. The model was calibrated for the period 1974–1995 and validated from 1996 to 2004, with additional testing using field data collected in 2022–2023 through Acoustic Doppler Current Profiler (ADCP) measurements. Key model adjustments, such as the baseflow recession constant (ALPHA_BF) and channel roughness coefficient (CH_N2), were set to 0.05 and 0.04, respectively, to capture the area's groundwater dynamics and channel characteristics. The calibration results indicated a strong fit, with R^2 values of 0.77, NSE of 0.70, and PBIAS of 17.06, demonstrating good agreement between observed and simulated streamflow. Validation showed slightly lower but acceptable performance, with R^2 of 0.75 and NSE of 0.68. Further ADCP validation from field data showed R^2 values of 0.79 and 0.78 for two monitoring sites, confirming the model's reliability. Sediment yield simulations at site-2 yielded R^2 values of 0.70 and 0.59 for calibration and validation, with NSE values of 0.53 and 0.52, indicating the model's capability to simulate both streamflow and sediment accurately. These results demonstrate SWAT's practical utility for water resource management in similar data-limited regions.

KEYWORDS

rainfall-runoff modelling, streamflow, sediment, SWAT, calibration, validation

1 Introduction

Accurate estimation of streamflow and sediment generation is crucial for effective water resources management. Hydrological models serve as fundamental tools for simulating these processes and have been extensively utilized for both change detection and attribution in catchment systems (Folton et al., 2015; Hassan et al., 2010; Vandenberghe et al., 2006). Inappropriate application of these models may result in erroneous understanding and suboptimal policy recommendations. Daggupati et al. (2015) assert that the requisite modeling accuracy may vary for different applications, contingent upon the risk associated with actions that follow model implementation (e.g., explanatory, planning and/or regulatory).

Surface water resources, particularly rivers, are essential for sustaining ecosystems, human settlements, and economic activities worldwide (Mishra and Saxena, 2024; Kumar and Sen, 2023). Global warming-induced changes in weather patterns, urban expansion, industrial growth, and agricultural chemical use are transforming water resources (Joseph et al., 2018; Kaur and Sinha, 2019). Numerous areas face freshwater shortages or contamination issues. Hydrological elements such as evaporation, transpiration, soil moisture, and runoff are highly responsive to slight changes in temperature and precipitation (Brutsaert and Parlange, 1998;

Seneviratne et al., 2010). Consequently, addressing water resource challenges, including the effects of urban development, alternative management approaches, and future climate variations on streamflow and water quality, necessitates a comprehensive understanding and accurate modeling of Earth surface processes at the catchment level (Kumar and Paramanik, 2020; Iwanaga et al., 2020; Gassman et al., 2014; Koltsida et al., 2023). Examining various components of the hydrological process is necessary to evaluate and quantify sediment and auricular chemical yields (Ghoraba, 2015).

Due to the complexity of hydrological processes, various models have been developed over time to facilitate the comprehension of the hydrological system (Arnold and Allen, 1996; Sahu et al., 2016). These hydrological models are essential tools for evaluating catchment behavior, informing decisions on water resource projects, flood control, pollution management, and numerous other applications (Gupta et al., 2024; Pérez-Sánchez et al., 2019; Kumar and Sen, 2024). Among these, semi-distributed hydrological models can simulate water balance spatially by accounting for various soils, land uses, topographical features, and climate conditions (Rafiei Emam et al., 2017). The semi-distributed hydrologic model SWAT is renowned for providing detailed information on water resources in a river basin and projecting the impact of land use changes and management practices on water quantity and quality (Janjić and Tadić, 2023; Gelete et al., 2023; Narsimlu et al., 2015). Researchers have applied the SWAT model across various regions, from arid and semi-arid to humid and tropical (Nguyen and Kappas, 2015; Samimi, 2020). Schuol et al. (2008) assessed the distribution of blue and green water in Africa; Phuong et al. (2014) utilized SWAT to estimate surface runoff and soil erosion in a small part of Vietnam. Understanding runoff and sediment yield dynamics in watersheds is crucial for effective management, especially in data-scarce regions such as the Western Himalayan area. Jain et al. (2010) employed SWAT to estimate runoff and sediment yield in the Suni to Kasol watershed, achieving satisfactory R^2 coefficients for both daily and monthly values. Similarly, Agrawal et al. (2011) simulated surface runoff and sediment yield in the Chhokranala watershed, emphasizing the impact of calibrated Manning's "n" values on sediment yield. Aawar and Khare (2020) utilized the SWAT model to analyze the climate change impact on the streamflow of the Kabul River; Bouslihim et al. (2016) opted for the SWAT model to access the hydrological components of the Sebou watershed (Morocco). The SWAT model can also simulate basin hydrology in terms of both quantity and quality by incorporating agricultural practices, point sources, and non-point sources. Thus, the primary objective of this study is to apply the SWAT model to simulate the hydrological processes and sediment yield in the Song River watershed.

2 Methods

2.1 Study area

The Song River, originating from various small streams in the Dhanolti mountain range and merging with Sahastradhara streams, flows down to the Doon valley basins before eventually joining the Ganga River. Known for its picturesque surroundings, the Song River in Dehradun is particularly renowned for its plentiful natural sulphur springs. These springs emerge from mountain fissures and feed into the main watercourse, enriching the river with sulphur. Visitors flock to immerse themselves in the mineral-rich waters, as sulphur baths are thought to alleviate various health issues, particularly skin conditions. Situated at 30°28′ latitude and 78°8′ longitude, the Song River is vital to the communities of Raiwala, Doiwala, Chiddarwala, and Lacchiwala, serving as their primary water source along its 107 km journey. It converges with the Ganga River at 78° 14′ 54″ longitude and 30° 02′ 02″ latitude, just upstream of Haridwar near the Satyanarayan G&D station maintained by CWC, after passing through the Satyanarayana area (Figure 1).

A significant tributary of the Song River is the Suswa River, which originates in the clayey depression of the Mussoorie range. It drains the eastern part of Dehradun city and joins the Song River southeast of Doiwala. The catchment area includes two major urban settlements: Dehradun and Doiwala. The Rispana and Bindal, two primary drainage networks, carry municipal sewage from these urban areas and discharge into the Song River via the Suswa River. The region experiences an average annual rainfall of approximately 1,451 mm, with about 1,181 mm (81%) occurring during the monsoon season. Consequently, July and August are the wettest months of the year.

2.2 Model input

2.2.1 Spatial database

Digital Elevation Model (DEM) are critical tools in hydrological modeling as they provide detailed topographical data necessary for analyzing basin characteristics (Figure 3A). DEM are utilized to generate key hydrological parameters, including flow direction, flow accumulation, stream networks, and watershed boundaries. In this study, the FABDEM (Forest and Buildings Removed Copernicus DEM), a state-of-the-art dataset available at a 1 arc-second resolution (approximately 30 m), was employed (Figure 3B). This dataset, freely accessible through the University of Bristol website, offers refined elevation data critical for accurate terrain analysis. Alongside the DEM, Land Use Land Cover (LULC) and soil maps were utilized as essential inputs for hydrological modeling using the SWAT model. The LULC map was developed using Landsat 8 satellite imagery at a 30 m resolution, sourced from the USGS Earth Explorer platform. A supervised classification technique, specifically the Maximum Likelihood Classification method, was applied using ERDAS IMAGINE software to categorize the basin into five land cover classes: water bodies, forest, built-up areas, agricultural land, and riverbed/wasteland. Validation of the LULC map was conducted using ground truth data collected via portable GPS devices during field surveys, revealing that 68% of the catchment is forested and 14% is under agricultural use (Figure 3C).

The soils property data were obtained from the Harmonized World Soil Database (HWSD) version 1.2, available from the Food and Agriculture Organization (FAO). Based on this data, soils in the basin were classified as clay loam and loam, providing crucial information for modeling soil-water interactions (Figure 3D). Additionally, Figure 2 illustrates the hydrological modeling framework of the study area, demonstrating the interaction of inputs such as precipitation and land use with watershed attributes like soil, topography, and river systems. This flow diagram emphasizes how these elements converge to generate outputs such as streamflow and sediment yield, as simulated by the SWAT model, offering an integrated perspective on the hydrological dynamics of the Song River watershed (Figure 3).

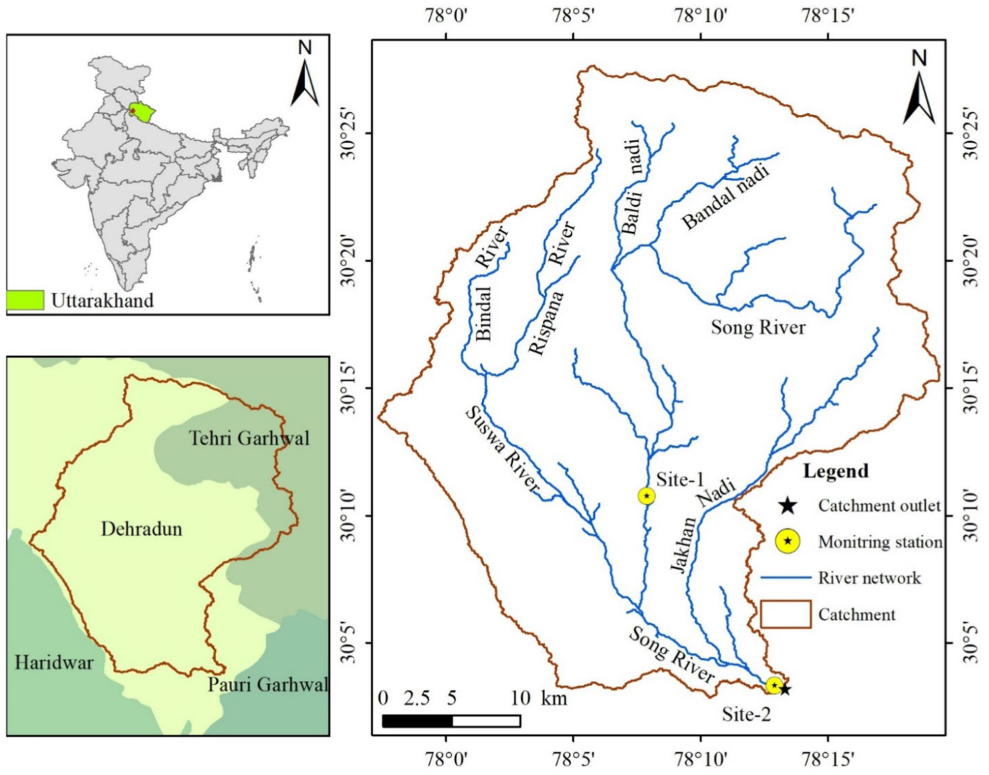

FIGURE 1
Map of Song River basin, drainage network and selected sites.

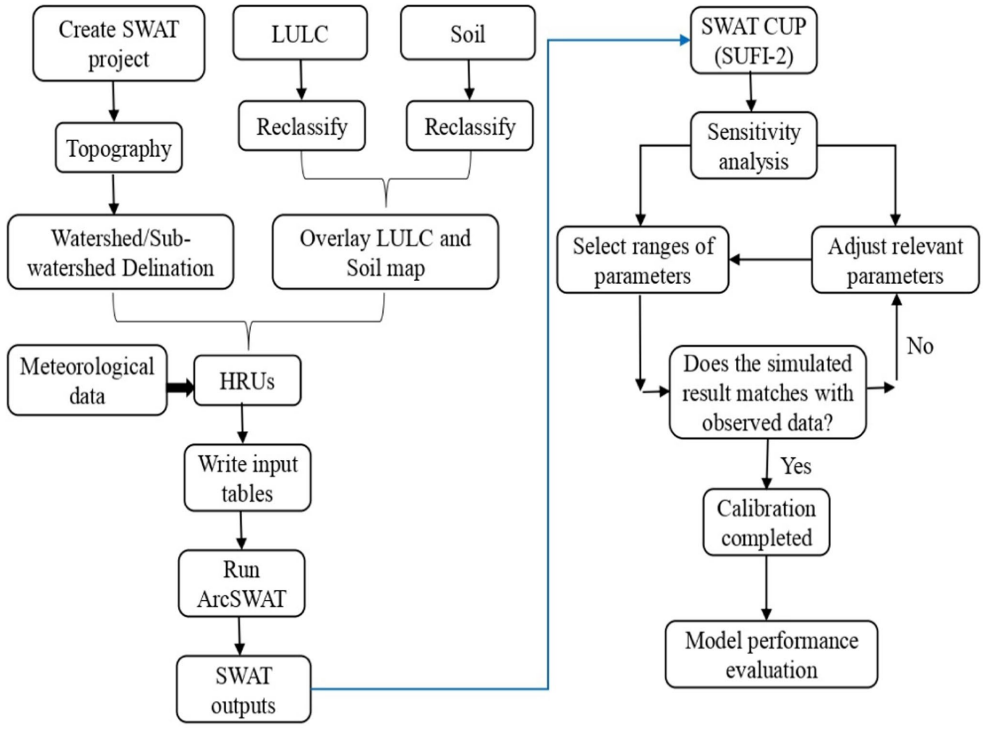

FIGURE 2
Flow diagram emphasizing the essential elements and processes involved in the hydrological modelling for the study area.

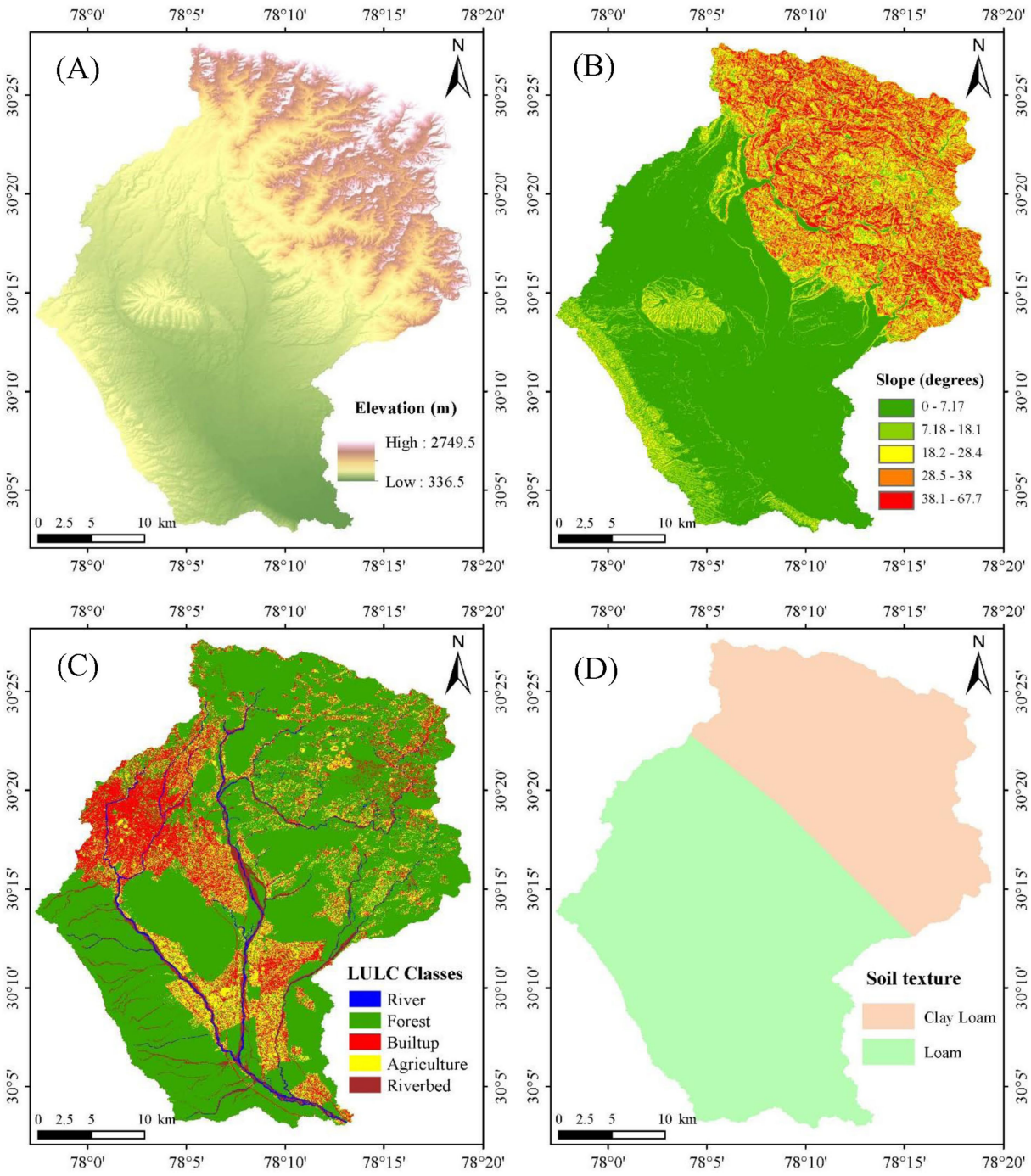

FIGURE 3
(A) Digital elevation model (DEM) map; **(B)** Slope map; **(C)** Land cover map; **(D)** Soil map used as topographical and spatial input for SWAT model.

2.2.2 Hydro-meteorological database

In hydrological modeling, precipitation and air temperature are the fundamental meteorological datasets required for model setup. This study utilized gridded precipitation and minimum and maximum air temperature data on a daily scale, obtained from the India Meteorological Department (IMD), with spatial resolutions of 0.25° x 0.25° and 1° x 1°, respectively.

The observed streamflow data required for calibrating the SWAT hydrological model. The Central Water Commission (CWC), India's central water resource management organization maintained a Gauging and Discharge (G&D) station on the Song River until 2004 at Satyanarayana, located just before the song river's confluence with the Ganga near Rishikesh. For this study, daily streamflow data spanning 44 years (1971–2004) was obtained from the CWC's Satyanarayana gauging site, designated as site-2.

Accurately simulating streamflow and sediment dynamics in recent scenario, a weekly monitoring program was conducted at Site 1 and Site 2 over a period of two monsoon years (June 2022 to

November 2023). During this period, weekly discharge measurements were carried out using an Acoustic Doppler Current Profiler (ADCP) instrument to ensure high accuracy. Additionally, one-liter water samples were collected during each site visit for laboratory analysis. Water quality analyses were performed at the National Institute of Hydrology, Roorkee water quality laboratory to determine Total Suspended Solids (TSS) concentrations, expressed in mg/L. These analyses provided critical data for calibrating and validating the suspended sediment component of the SWAT model (Table 1).

2.2.3 Field survey and investigation

In the present study, discharge data were available only up to 2004. To address this data gap and validate the model's applicability for recent conditions, river discharge measurements were conducted for more recent periods, specifically 2022–2023. The process of site selection and the methodology employed for discharge measurement are delineated in sections 3.1.4 and 3.1.5. This approach was essential to ensure that the model's predictions remain relevant and accurate for contemporary river conditions, considering potential changes in discharge patterns over time.

2.2.4 Design of monitoring programme

The Song River and its primary tributary, the Suswa River, were monitored across two monsoon seasons (June 2022 to November 2023) at two strategically selected sites along the Song River. These stations were situated upstream and downstream of the confluence of the Suswa River, adjacent to road bridges, ensuring accessibility during the monsoon season. Discharge measurements were conducted weekly during the monsoon (June to September), biweekly during the post-monsoon period (October to November), and monthly during the lean seasons (December to May). Table 2 provides details of the monitoring stations.

2.2.5 Observed streamflow and sediment data

Flow velocity and discharge measurements were conducted using two instruments: the SonTek FlowTracker2 and the Acoustic Doppler current profiler (ADCP). The SonTek FlowTracker2, an Acoustic Doppler Velocimeter (ADV), utilizes the Doppler effect to measure velocities ranging from 0.001 to 4 m/s. For low-flow conditions, the ADV was employed to measure velocity, while the mid-section method was utilized to calculate river discharge. In flood scenarios, a boat-mounted ADCP was deployed to measure both velocity and discharge (Figure 4).

Water samples for sediment analysis were collected during each site visit. At all monitoring locations, river water samples were collected using the grab sampling technique. One liter of river water sample was collected in high-density polyethylene (HDPE) containers and transport to the National Institute of Hydrology, Roorkee water quality lab for examination. To ensure uniformity, the collected samples were vigorously agitated. Subsequently, one liter of each sample was filtered through a 0.45-micron gridded cellulose nitrate membrane using an electric vacuum pump to extract suspended sediments. The filter paper containing the captured sediments was then dried in a hot oven to determine the total suspended sediment (TSS) concentration. The TSS concentration in the water sample was calculated by measuring the dry weight difference of the filter paper before and after the filtration process.

2.3 Model setup

The eco-hydrological model Soil and Water Assessment Tool (SWAT) is a versatile hydrological model capable of simulating diverse environmental conditions and scales (Arnold et al., 1998). The establishment of a SWAT model requires spatially distributed data, including Digital Elevation Models (DEMs), soil data, land use land cover maps, and weather data. The model operates exclusively on this data and does not necessitate prior knowledge of catchment behavior or flow processes. SWAT simulates water balance, a fundamental driver of watershed processes, to accurately predict runoff, sediment, and nutrient movement. The model comprises two primary components: the land phase and the routing phase. For surface runoff estimation, the Curve Number method is utilized.

2.4 Model calibration and validation and sensitivity analysis

The SWAT model encompasses numerous hydrological parameters whose effectiveness is affected by variables such as soil type, slope, and land cover. To identify the most influential parameters and reduce the number needed for calibration, sensitivity analysis is essential. This research employed the SUFI-2 algorithm within the SWAT-CUP interface to perform sensitivity analysis on 13 crucial parameters, including ALPHA_BF (baseflow alpha factor),

TABLE 1 Summary of the dataset used in this study.

Data set	Source	Scale/Time series	Data description/Properties
DEM	FABDEM V1-0	30 m	https://data.bris.ac.uk/data/dataset/25wfy0f9ukoge2gs7a5mqpq2j7
Land cover	Landsat 8	30 m	https://earthexplorer.usgs.gov/
Soil	FAO/HWSDv1.2	1:1,000,000	https://www.fao.org/soils-portal/data-hub/soil-maps-and-databases/harmonized-world-soil-database-v12/en/
Rainfall (mm)	IMD Gridded	Daily (0.25° × 0.25°)	Rainfall data (1971–2023)
Temperature (°C)	IMD Gridded	Daily (1°x1°)	Max. and Min. temperature (1971–2023)
Discharge	CWC Observed data	Daily/(1971–2004) Weekly/(2022–2023)	CWC Satyanarayana site. Weekly discharge measured using ADCP and FlowTracker2 instrument.
Suspended sediment	Observed data	Weekly/(2022–2023)	–

TABLE 2 Descriptive characteristics of the selected monitoring stations.

Name	Station code	Sampling site location name	Stream	Latitude (decimal degrees)	Longitude (decimal degrees)	Elevation (m)
Song U/S	Site-1	Song Bridge, Doiwala	Song	30.17915	78.13162	486.32
Song D/S	Site-2	Song Bridge, Nepali Farm, Raiwala	Song	30.05506	78.21517	346.35

FIGURE 4
Discharge measurement using **(A)** Flow-Tracker2 in low flow condition **(B)** ADCP in high flow condition.

CH_K2 (hydraulic conductivity in the main channel alluvium), CH_N2 (Manning's "n" for the main channel), as well as GWQMN, SOL_AWC, ESCO, and SURLAG. The impact of these parameters on hydrological components like discharge, infiltration, baseflow, groundwater flow, evaporation, and transpiration were examined by methodically altering one parameter at a time while keeping others constant. The relationship between parameters and hydrological responses was quantified using sensitivity coefficients. To enhance the model's accuracy, both manual and automated calibration techniques were utilized. Manual calibration involved visually adjusting parameters based on observed and simulated flow patterns, considering catchment characteristics. Automated calibration, facilitated by SWAT-CUP, systematically optimized uncertain parameters by comparing model outputs with measured data through an interactive interface. This combined approach ensured effective parameter optimization and improved the SWAT model's ability to simulate hydrological processes.

2.5 Performance evaluation

There are multiple efficacy measures that can be used to assess the model's performance. These efficacy metrics show how the model-simulated values and the observed values are reconciled. Nash-Sutcliffe Efficiency (NSE) (Equation 1), coefficient of determination (R^2) (Equation 2) and PBIAS (Equation 3) are the most widely utilized metrics among them (Sane et al., 2020; Swain et al., 2022).

Nash-Sutcliffe efficiency (NSE) (Nash and Sutcliffe, 1970),

$$\mathrm{NSE} = 1 - \frac{\sum_{i=1}^{n}\left(O_i - P_i\right)^2}{\sum_{i=1}^{n}\left(O_i - \bar{O}\right)^2} \tag{1}$$

Percent bias (PBIAS) (Moriasi et al., 2007),

$$PBIAS = \frac{\left(\sum_{i=1}^{n}\left(O_i - P_i\right)\times 100\right)}{\left(\sum_{i=1}^{n} O_i\right)} \tag{2}$$

Coefficient of determination (R^2) (Suryavanshi et al., 2017),

$$R^2 = \left[\frac{\sum_{i=1}^{n}\left(O_i + \bar{O}\right)\left(P_i - \bar{P}\right)}{\sum_{i=1}^{n}\left(O_i - \bar{O}\right)^2 \sum_{i=1}^{n}\left(P_i - \bar{P}\right)^2}\right]^2 \tag{3}$$

P_i and O_i are the simulated and observed values of discharge; n is the sample number,

$\overline{P}$ and $\overline{O}$ are the average of simulated and observed discharge.

3 Results and discussion

3.1 Model calibration and validation and sensitivity analysis

This research utilized previous studies to guide parameter selection for calibration, examining 13 parameters in total, with 8 identified as sensitive at a 0.05 significance level. Table 3 outlines the range, fitted values, t-statistics, significance levels, and sensitivity rankings for these parameters. The study employed a three-year warm-up period (1971–1973), with calibration and validation periods spanning 1974–1995 and 1996–2004, respectively. The dotty plots generated in SWAT-CUP indicate that the baseflow recession constant (ALPHA_BF) and Channel roughness (CH_N2) are the most sensitive parameters. This conclusion is evident from the noticeable variation in the model's performance metrics corresponding to changes in their values. The ALPHA_BF was calibrated to 0.05, suggesting a contribution of groundwater to streamflow, during low-flow periods is a critical factor in accurately simulating streamflow. CH_N2 was set at 0.04, indicative of a dredged channel, while effective hydraulic conductivity (CH_K2) was calibrated to 121.15 mm/h, signifying high-permeability conditions. The return flow threshold depth (GWQMN) was set at 735 mm, and soil water capacity (SOL_AWC) showed a 47% decrease, indicating reduced plant-available water. The groundwater "revap" coefficient (GW_REVAP) was calibrated to 0.07, suggesting limited water movement to the root zone. Manning's coefficient (OV_N) was determined to be 0.83, and deep aquifer percolation (REVAPM) required 404.5 mm of shallow aquifer water. Soil evaporation compensation (ESCO) was set at 0.12, indicating high demand from lower soil layers. Surface runoff lag time (SURLAG) was calibrated to 2.33, and plant uptake compensation (EPCO) decreased to −0.29, demonstrating reduced uptake in lower soil layers. Groundwater delay (GW-DELAY) was established at 472.5 days, indicating a slow aquifer response, while lateral flow travel time (LAT_TTIME) was set at 22.14 days, representing lateral flow dynamics within the hydrological response units (HRUs). These calibrated parameters significantly enhanced model performance and improved the simulation of hydrological processes.

3.2 Model performance evaluation

The study employed daily observations from 1974 to 2004, with Figure 5 illustrating the temporal comparison between observed and simulated discharge during both calibration and validation phases. Model effectiveness was assessed using R^2, NSE, and PBIAS metrics, as presented in Table 4. The observed and simulated flows showed strong correlation, with R^2 values of 0.79 and 0.66 for calibration and validation, respectively. During calibration, both baseflow and peak flows aligned well between observed and simulated data. Although the validation period showed underestimated goodness of fit, the results remained satisfactory. The NSE reached 0.7 during calibration and 0.62 during validation. PBIAS values fell within acceptable ranges for both periods, measuring 17.06 for calibration and 19.60 for validation.

The weekly average simulated and observed flow for the 1974–2004 period is depicted in Figure 5 as a time series plot. This graph reveals a high degree of similarity between the simulated and observed discharge, with the model successfully capturing overall flow trends, including seasonal fluctuations and high-flow events. The simulated flow closely tracks the observed data during the calibration phase, demonstrating the model's precision in replicating both low-flow conditions and peak discharge occurrences. Although the validation period exhibits minor underestimations of some peak flows, the general trend remains aligned, indicating satisfactory model performance across the extended timeframe. This sustained consistency underscores the model's dependability for long-term hydrological flow simulations.

Figure 6 presents a scatter plot depicting the weekly mean simulated versus observed flow during the calibration and validation periods. The plot demonstrates a strong linear relationship between the simulated and observed flow data, with the majority of points clustering in close

TABLE 3 Fitted values of the SWAT parameter and statistics of sensitivity analysis.

Parameter name	Min. value	Max. value	Fitted Value	*t*-stat	*P*-value	Rank
V__ALPHA_BF.gw	0.0	1.0	0.05	−47.66	0.00	1
V__CH_N2.rte	0.0	0.1	0.04	21.53	0.00	2
V__CH_K2.rte	51.0	127.0	121.15	14.65	0.00	3
V__GWQMN.gw	0.0	5000.0	735.00	−11.80	0.00	4
R__SOL_AWC(..).sol	−0.5	0.2	−0.47	10.31	0.00	5
V__GW_REVAP.gw	0.0	0.2	0.07	−10.30	0.00	6
R__OV_N.hru	0.0	1.0	0.83	3.42	0.00	7
V__REVAPMN.gw	0.0	500.0	404.50	2.10	0.04	8
V__ESCO.bsn	0.0	1.0	0.12	1.25	0.21	9
V__SURLAG.bsn	0.1	24.0	2.33	1.02	0.31	10
R__EPCO.bsn	−0.5	1.0	−0.29	−0.37	0.71	11
V__GW_DELAY.gw	0.0	500.0	472.50	0.33	0.74	12
R__LAT_TTIME.hru	0.0	180.0	22.14	−0.18	0.86	13

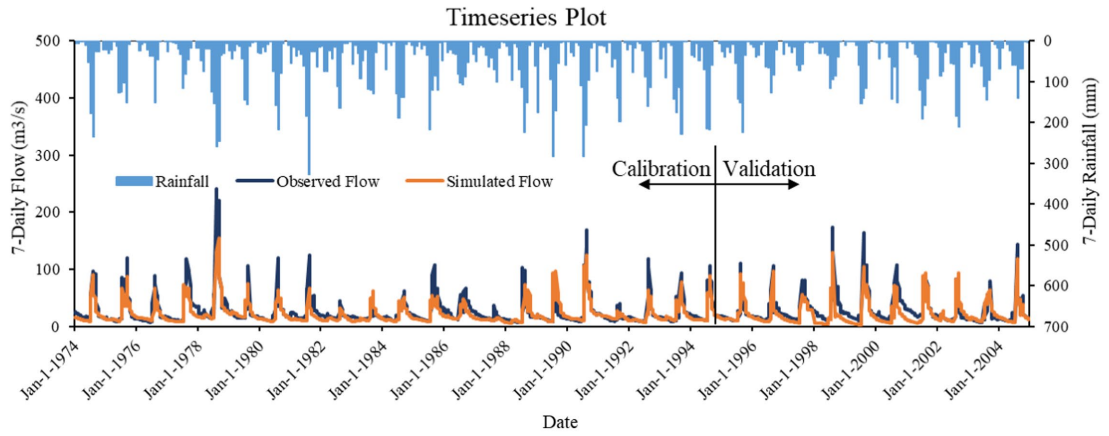

FIGURE 5
Time series plot of weekly mean observed and simulated flow (1974–2004) at site 2 maintained by CWC.

TABLE 4 Model performance statistics.

Time series	R^2	NSE	PBIAS
Calibration (1974–1995)	0.77	0.70	17.06
Validation (1996–2004)	0.75	0.68	19.60

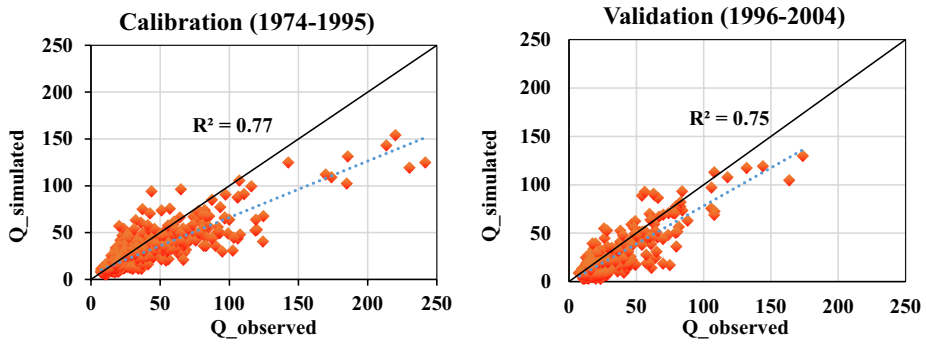

FIGURE 6
Scatter plot of weekly mean simulated and observed flow during calibration and validation.

proximity to the 1:1 line, indicating a high degree of accuracy in the model's predictions. During the calibration period, the scatter plot exhibits a tight correlation, reflecting the model's efficacy in capturing the observed flow dynamics. Although the validation period displays a slight dispersion from the 1:1 line, the overall alignment remains satisfactory, confirming the model's robustness in simulating streamflow across diverse hydrological conditions.

3.3 Model performance evaluation with field survey data

The model's applicability to the study area was evaluated by comparing its simulated flows with ADCP-measured discharges obtained during a field survey. A strong correlation was observed between the simulated flows and observed discharge data at both upstream (site-1) and downstream (site-2) locations. The model's performance was quantified using statistical indicators R^2, NSE, and PBIAS, with results presented in Table 5, demonstrating its robust performance. The R^2 values, ranging from 0.78 to 0.79, indicated a strong correlation, while NSE values of 0.79 upstream and 0.68 downstream showed high agreement between simulated and observed flows. PBIAS values of 0.04 upstream and − 16.20 downstream fell within acceptable ranges, further confirming the model's reliability. A time series plot comparing weekly mean simulated flows with observed flows for 2022–2023 at both sites is shown in Figure 7. The plot reveals exceptional alignment at the upstream site, where the model accurately captures flow variations and peak flows. Although minor discrepancies are noted at the downstream site, the overall flow patterns are well-represented, highlighting the model's ability to accurately simulate flow conditions in the Song River basin under diverse field conditions.

Figure 8 presents a scatter plot depicting the relationship between weekly mean simulated flow and field survey observed flow at both the upstream and downstream sections of the Song River. The plot demonstrates a strong correlation between the simulated and observed data, with data points closely aligned with the line of perfect

TABLE 5 Performance of calibrated model with field survey data.

Sites	Coefficient of determination (R^2)	NSE	PBIAS
Song upstream	0.79	0.79	0.04
Song downstream	0.78	0.68	−16.20

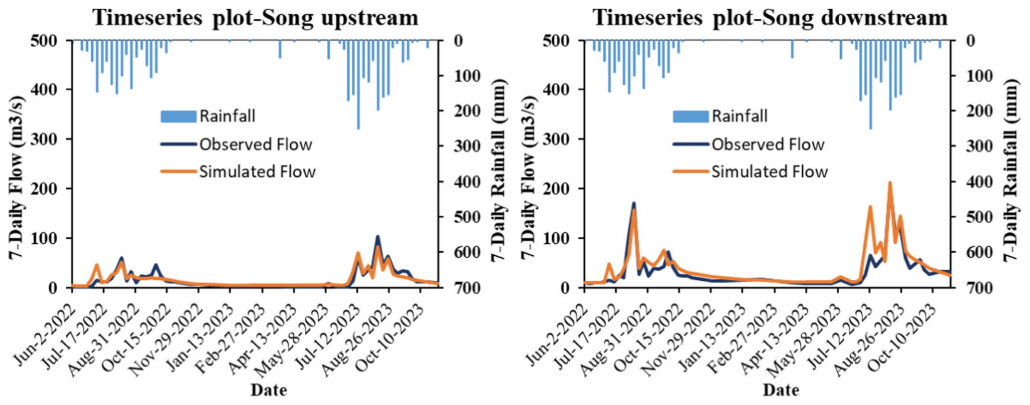

FIGURE 7
Time series plot of the weekly mean simulated flow and field survey observed flow (2022–2023) at the upstream and downstream sections of the Song River.

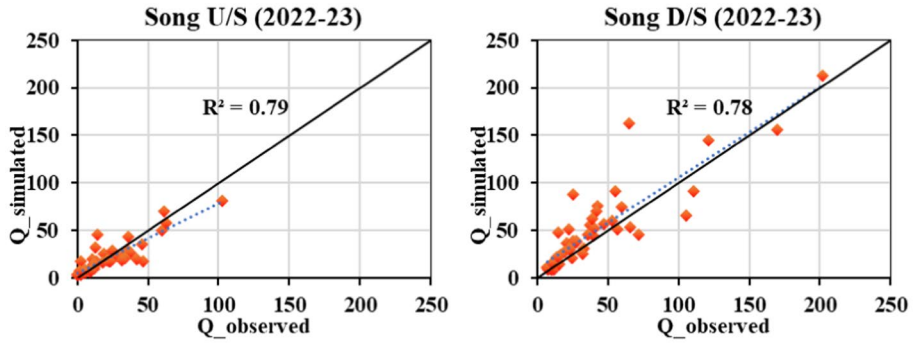

FIGURE 8
Scatter plot of weekly mean simulated flow and field survey observed flow at upstream and downstream of Song River.

agreement. The upstream section exhibits a marginally higher degree of concordance, indicating superior model accuracy in this region, while the downstream section, despite displaying some dispersion, still demonstrates robust predictive performance. In aggregate, the scatter plot corroborates the model's efficacy in replicating observed flow conditions across distinct sections of the river.

3.4 Model calibration and validation for weekly sediment load

The pre-calibrated runoff model was subsequently utilized for sediment load calibration. Four additional parameters Channel erodibility factor (CH_EROD), Peak rate adjustment factor for sediment routing in the subbasin (ADJ_PKR), USLE equation support practice (P) factor (USLE_P) and Linear parameter for calculating the maximum amount of sediment (SPCON) added in SWAT-CUP using SUFI2 algorithm for calibrate and validate Sediment load, at daily time scale (Table 6). The results of the best simulation (based on efficacy measures on daily scale) and its comparison with respect to the observed sediment load along with the observed discharge at weekly scale for 2 years, i.e., 2023–2024 are presented in Figure 9. The statistical performance indicators for the calibration period (2022) revealed that the model achieved an R^2 value of 0.70 and a Nash-Sutcliffe Efficiency (NSE) of 0.53. For the validation period (2023), the model demonstrated an R^2 of 0.59 and an NSE of 0.52.

Figure 9, comparing observed and simulated daily sediment yields at site 2 during the 2022 calibration and 2023 validation periods, elucidates both the efficacy and limitations of the SWAT model. In the 2022 calibration period, observed sediment yields exhibit substantial peaks in September and October, with loads reaching up to 1,800 tonnes per day. While the SWAT model captures the overall seasonal pattern, including the pronounced increase during the monsoon and subsequent decline, it underestimates the magnitude of these peaks, particularly during high-flow events. Similarly, during the 2023 validation period, the observed

TABLE 6 Fitted values of the SWAT parameter for sediment analysis.

Parameter name	Definition	Min. value	Max. value	fitted value
V_CH_EROD.rte	Channel erodibility factor	0.0	0.304	0.007
V_ADJ_PKR.bsn	Peak rate adjustment factor for sediment routing in the subbasin	0.5	1.0	0.79
V_USLE_P.mgt	USLE equation support practice (P) factor	0.6	1.0	0.76
V_SPCON.bsn	Linear parameter for calculating the maximum amount of sediment	0.0001	0.01	0.003

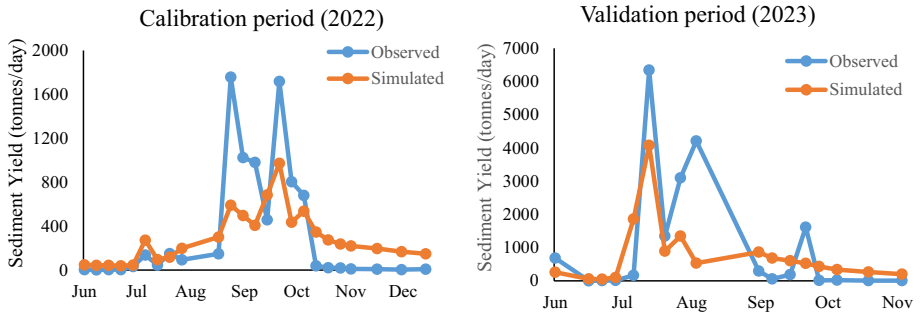

FIGURE 9
Sediment load calibration and validation plot at Song D/S.

sediment yield peaks in July, exceeding 6,000 tonnes per day, followed by a rapid decline and smaller peaks in subsequent months. The simulated sediment yield generally follows this trend but significantly underestimates the July peak, reaching only approximately 4,000 tonnes per day, and fails to capture some of the acute fluctuations observed in the following months. These results demonstrate the model's capacity to replicate the general seasonal dynamics of sediment transport but also underscore challenges in accurately simulating extreme events. To enhance the model's performance, particularly during high-flow periods, further refinement of parameters or the incorporation of additional factors may be necessary.

4 Conclusion

The present study demonstrates the efficacy of the SWAT model in simulating streamflow and sediment yield within the Song River watershed, establishing its reliability for hydrological modelling in comparable basins. A comprehensive runoff calibration and validation process refined 13 critical parameters, with 8 identified as highly sensitive, significantly enhancing the model's accuracy. During the calibration phase (1974–1995), the model achieved an R^2 of 0.79 and a NSE of 0.70, indicating a robust correlation between simulated and observed discharge capture both baseflow and peak flow dynamics with high precision. Although a slight decrease in performance occurred during the validation period (1996–2004), with R^2 and NSE values of 0.66 and 0.62, demonstrating its robustness across varying conditions suggesting the model maintains efficacy under changing conditions, such as alterations in land use and climate. The Percent Bias (PBIAS) values of 17.06% during calibration and 19.60% during validation indicated underestimate the model. Furthermore, real-time observed field data from 2022–2023 reinforced the model's accuracy, with strong correlations (R^2 = 0.79 upstream and 0.78 downstream), validating its applicability for watershed management and planning.

In addition to streamflow, the model was evaluated for sediment transport, successfully capturing seasonal trends in sediment dynamics. The R^2 and NSE value for weekly sediment yield at site 2 was obtained as 0.70 and 0.53, respectively, for the calibration period and 0.59 and 0.52, respectively, for the validation period. However, the model underestimated sediment yields at site 2 during high-flow events, indicating the necessity for further refinement to enhance predictions under extreme weather conditions, such as floods. Notwithstanding this limitation, the model's capability to simulate sediment transport remains valuable for comprehending sediment dynamics and addressing sediment-related issues in watershed management.

The calibration and validation results indicate that the model performs well in simulating streamflow and provides satisfactory results for sediment transport. However, the limited availability of observed suspended sediment data remains a significant challenge for achieving a more reliable and persuasive model application. The calibrated model has also been utilized to simulate nonpoint source pollution loads in the Song River catchment. With ongoing refinement and the incorporation of additional field data, the model exhibits substantial potential to improve hydrological modelling and support more effective water resource management strategies in the future.

Data availability statement

The raw data supporting the conclusions of this article will be made available by the authors, without undue reservation.

Author contributions

SQ: Writing – original draft, Writing – review & editing. PK: Writing – review & editing. HS: Writing – original draft.

Funding

The author(s) declare financial support was received for the research, authorship, and/or publication of this article. This study was supported by the National Institute of Hydrology Roorkee, Uttarakhand, India.

Acknowledgments

The authors are thankful to the National Institute of Hydrology Roorkee, Uttarakhand as well as Central University of Jharkhand, Ranchi-India for providing necessary laboratory work to conduct the research work.

Conflict of interest

The authors declare that the research was conducted in the absence of any commercial or financial relationships that could be construed as a potential conflict of interest.

Publisher's note

Supplementary material

The Supplementary material for this article can be found online at: https://www.frontiersin.org/articles/10.3389/frwa.2025.1500086/full#supplementary-material

References

Aawar, T., and Khare, D. (2020). Assessment of climate change impacts on streamflow through hydrological model using SWAT model: a case study of Afghanistan. *Modeling Earth Syst. Environ.* 6, 1427–1437. doi: 10.1007/s40808-020-00759-0

Agrawal, N., Verma, M. K., and Tripathi, M. P. (2011). Hydrological modelling of chhokranala watershed using weather generator with SWATmodel. *Ind. J. Soil Conserv.* 39, 89–94.

Arnold, J. G., and Allen, P. M. (1996). Estimating hydrologic budgets for three Illinois watersheds. *J. Hydrol.* 176, 57–77. doi: 10.1016/0022-1694(95)02782-3

Arnold, J. G., Srinivasan, R., Muttiah, R. S., and Williams, J. R. (1998). Large area hydrologic modeling and assessment part I: model development 1. *JAWRA* 34, 73–89. doi: 10.1111/j.1752-1688.1998.tb05961.x

Bouslihim, Y., Kacimi, I., Brirhet, H., Khatati, M., Rochdi, A., Pazza, N. E. A., et al. (2016). Hydrologic modeling using SWAT and GIS, application to subwatershed Bab-Merzouka (Sebou, Morocco). *J. Geogr. Inf. Syst.* 8, 20–27. doi: 10.4236/jgis.2016.81002

Brutsaert, W., and Parlange, M. B. (1998). Hydrologic cycle explains the evaporation paradox. *Nature* 396:30. doi: 10.1038/23845

Daggupati, P., Pai, N., Ale, S., Douglas-Mankin, K. R., Zeckoski, R. W., Jeong, J., et al. (2015). A recommended calibration and validation strategy for hydrologic and water quality models. *Trans. ASABE* 58, 1705–1719. doi: 10.13031/trans.58.10712

Folton, N., Andréassian, V., and Duperray, R. (2015). Hydrological impact of forest-fire from paired-catchment and rainfall–runoff modelling perspectives. *Hydrol. Sci. J.* 60, 1213–1224. doi: 10.1080/02626667.2015.1035274

Gassman, P. W., Sadeghi, A. M., and Srinivasan, R. (2014). Applications of the SWAT model special section: overview and insights. *J. Environ. Qual.* 43, 1–8. doi: 10.2134/jeq2013.11.0466

Gelete, G., Nourani, V., Gokcekus, H., and Gichamo, T. (2023). Ensemble physically based semi-distributed models for the rainfall-runoff process modeling in the data-scarce Katar catchment, Ethiopia. *J. Hydroinform.* 25, 567–592. doi: 10.2166/hydro.2023.197

Ghoraba, S. M. (2015). Hydrological modeling of the Simly dam watershed (Pakistan) using GIS and SWAT model. *Alex. Eng. J.* 54, 583–594. doi: 10.1016/j.aej.2015.05.018

Gupta, A., Hantush, M. M., Govindaraju, R. S., and Beven, K. (2024). Evaluation of hydrological models at gauged and ungauged basins using machine learning-based limits-of-acceptability and hydrological signatures. *J. Hydrol.* 641:131774. doi: 10.1016/j.jhydrol.2024.131774

Hassan, M. A., Church, M., Yan, Y., and Slaymaker, O. (2010). Spatial and temporal variation of in-reach suspended sediment dynamics along the mainstem of Changjiang (Yangtze River), China. *Water Res. Res.* 46:9228. doi: 10.1029/2010WR009228

Iwanaga, T., Partington, D., Ticehurst, J., Croke, B. F., and Jakeman, A. J. (2020). A socio-environmental model for exploring sustainable water management futures: participatory and collaborative modelling in the lower Campaspe catchment. *J. Hydrol. Reg. Stu.* 28:100669. doi: 10.1016/j.ejrh.2020.100669

Jain, S. K., Tyagi, J., and Singh, V. (2010). Simulation of runoff and sediment yield for a Himalayan watershed using SWAT model. *J. Water Res. Prot.* 2, 267–281. doi: 10.4236/jwarp.2010.23031

Janjić, J., and Tadić, L. (2023). Fields of application of SWAT hydrological model—a review. *Earth* 4, 331–344. doi: 10.3390/earth4020018

Joseph, J., Ghosh, S., Pathak, A., and Sahai, A. K. (2018). Hydrologic impacts of climate change: comparisons between hydrological parameter uncertainty and climate model uncertainty. *J. Hydrol.* 566, 1–22. doi: 10.1016/j.jhydrol.2018.08.080

Kaur, T., and Sinha, A. K. (2019). Pesticides in agricultural run offs affecting water resources: a study of Punjab (India). *Agric. Sci.* 10, 1381–1395. doi: 10.4236/as.2019.1010101

Koltsida, E., Mamassis, N., and Kallioras, A. (2023). Hydrological modeling using the soil and water assessment tool in urban and peri-urban environments: the case of Kifisos experimental subbasin (Athens, Greece). *Hydrol. Earth Syst. Sci.* 27, 917–931. doi: 10.5194/hess-27-917-2023

Kumar, V., and Paramanik, S. (2020). Application of high-frequency spring discharge data: a case study of Mathamali spring rejuvenation in the Garhwal Himalaya. *Water Supply* 20, 3380–3392. doi: 10.2166/ws.2020.223

Kumar, V., and Sen, S. (2023). Hydrometeorological field instrumentation in lesser Himalaya to advance research for future water and food security. *Environ. Monit. Assess.* 195:1162. doi: 10.1007/s10661-023-11625-8

Kumar, V., and Sen, S. (2024). Rating curve development and uncertainty analysis in mountainous watersheds for informed hydrology and resource management. *Front. Water* 5:1323139. doi: 10.3389/frwa.2023.1323139

Mishra, R. R., and Saxena, S. (2024). "Cities and rivers: a symbiotic relationship" in Managing Urban Rivers (Amsterdam: Elsevier), 3–24.

Moriasi, D. N., Arnold, J. G., Van Liew, M. W., Bingner, R. L., Harmel, R. D., and Veith, T. L. (2007). Model evaluation guidelines for systematic quantification of accuracy in watershed simulations. *Trans. ASABE* 50, 885–900. doi: 10.13031/2013.23153

Narsimlu, B., Gosain, A. K., Chahar, B. R., Singh, S. K., and Srivastava, P. K. (2015). SWAT model calibration and uncertainty analysis for streamflow prediction in the Kunwari River basin, India, using sequential uncertainty fitting. *Environ. Process.* 2, 79–95. doi: 10.1007/s40710-015-0064-8

Nash, J. E., and Sutcliffe, J. V. (1970). River flow forecasting through conceptual models' part I—A discussion of principles. *J. Hydrol.* 10, 282–290. doi: 10.1016/0022-1694(70)90255-6

Nguyen, H. Q., and Kappas, M. (2015). Modeling surface runoff and evapotranspiration using SWAT and beach for a tropical watershed in North Vietnam, compared to MODIS products. *Int. J. Adv. Remote Sens. GIS* 4, 1367–1384. doi: 10.23953/cloud.ijarsg.124

Pérez-Sánchez, J., Senent-Aparicio, J., Segura-Méndez, F., Pulido-Velazquez, D., and Srinivasan, R. (2019). Evaluating hydrological models for deriving water resources in peninsular Spain. *Sustain. For.* 11:2872. doi: 10.3390/su11102872

Phuong, T. T., Thong, C. V. T., Ngoc, N. B., and Van Chuong, H. (2014). Modeling soil erosion within small mountainous watershed in Central Vietnam using GIS and SWAT. *Resour. Environ* 4, 139–147. doi: 10.5923/j.re.20140403.02

Rafiei Emam, A., Kappas, M., Linh, N. H. K., and Renchin, T. (2017). Hydrological modeling and runoff mitigation in an ungauged basin of Central Vietnam using SWAT model. *Hydrology* 4:16. doi: 10.3390/hydrology4010016

Sahu, M., Lahari, S., Gosain, A. K., and Ohri, A. (2016). Hydrological modeling of Mahi basin using SWAT. *J. Water Res. Hydraulic Eng.* 5, 68–79. doi: 10.5963/JWRHE0503001

Samimi, M. (2020). Adaptive agricultural water resources Management in a Desert River Basin: Insights from hydrologic modeling. Stillwater, OK: Oklahoma State University.

Sane, M. L., Sambou, S., Leye, I., Ndione, D. M., Diatta, S., Ndiaye, I., et al. (2020). Calibration and validation of the SWAT model on the watershed of Bafing River, Main upstream tributary of Senegal River: checking for the influence of the period of study. *Open J. Modern Hydrol.* 10, 81–104. doi: 10.4236/ojmh.2020.104006

Schuol, J., Abbaspour, K. C., Yang, H., Srinivasan, R., and Zehnder, A. J. (2008). Modelling blue and green water availability in Africa. *Water Resour. Res.* 44:6609. doi: 10.1029/2007WR006609

Seneviratne, S. I., Corti, T., Davin, E. L., Hirschi, M., Jaeger, E. B., Lehner, I., et al. (2010). Investigating soil moisture–climate interactions in a changing climate: a review. *Earth Sci. Rev.* 99, 125–161. doi: 10.1016/j.earscirev.2010.02.004

Suryavanshi, S., Pandey, A., and Chaube, U. C. (2017). Hydrological simulation of the Betwa River basin (India) using the SWAT model. *Hydrol. Sci. J.* 62, 960–978. doi: 10.1080/02626667.2016.1271420

Swain, S., Mishra, S. K., Pandey, A., Pandey, A. C., Jain, A., Chauhan, S. K., et al. (2022). Hydrological modelling through SWAT over a Himalayan catchment using high-resolution geospatial inputs. *Environ. Challenges* 8:100579. doi: 10.1016/j.envc.2022.100579

Vandenberghe, V., Van Griensven, A., Bauwens, W., and Vanrolleghem, P. A. (2006). Effect of different river water quality model concepts used for river basin management decisions. *Water Sci. Technol.* 53, 277–284. doi: 10.2166/wst.2006.322

frontiers | Frontiers in Water

TYPE Original Research
PUBLISHED 07 February 2025
DOI 10.3389/frwa.2025.1540703

OPEN ACCESS

EDITED BY
Jahangeer Jahangeer,
University of Nebraska-Lincoln, United States

REVIEWED BY
Sivakumar Karthikeyan,
Alagappa University, India
Padam Jee Omar,
Babasaheb Bhimrao Ambedkar University, India

*CORRESPONDENCE
Mumtaz Ali Khan
✉ mumtazkhan@bui.edu.pk
Muhammad Shahab
✉ shahabgeo07@gmail.com

RECEIVED 06 December 2024
ACCEPTED 27 January 2025
PUBLISHED 07 February 2025

CITATION
Muneer M, Khan MA, Shinwari FU, Ahmed I, Siyar SM, Alshehri F and Shahab M (2025) Assessment of groundwater intrinsic vulnerability using GIS-based DRASTIC method in district Karak, Khyber Pakhtunkhwa, Pakistan.
Front. Water 7:1540703.
doi: 10.3389/frwa.2025.1540703

Assessment of groundwater intrinsic vulnerability using GIS-based DRASTIC method in district Karak, Khyber Pakhtunkhwa, Pakistan

Muhammad Muneer[1], Mumtaz Ali Khan[2]*, Fayaz Ullah Shinwari[3], Ijaz Ahmed[4], Syed Mamoon Siyar[5], Fahad Alshehri[6] and Muhammad Shahab[6]*

[1]Department of Geology, Khushal Khan Khattak University, Karak, Pakistan, [2]Department of Earth and Environmental Sciences, Bahria University Islamabad, Islamabad, Pakistan, [3]Researches Organization for Development (ROD), Kabul, Afghanistan, [4]Université du Québec en Abitibi-Témiscamingue (UQAT), Québec City, QC, Canada, [5]Department of Geology, University of Malakand, Chakdara, Pakistan, [6]Department of Geology and Geophysics, College of Science, King Saud University, Riyadh, Saudi Arabia

The Study area lies in the southern Kohat deformed fold and thrust belt. This part of the Kohat plateau, borders the southern extension of the Himalayan deformation, with the Salt range to the south most. The research is based on DRASTIC model. Anthropogenic activities have the potential to pollute groundwater. An essential component of managing groundwater is vulnerability mapping. This study used the DRASTIC model to analyze aquifer vulnerability and identify the hydrogeological condition in the southern portion of the Karak, Khyber Pakhtunkhwa. For the models, the information layers were provided via geographic information systems (GIS). The DRASTIC model uses seven environmental parameters. Vulnerability index concentrations were found to be 0.78% for Very Low vulnerability, 9.57% for Low vulnerability, 24.96% for Moderate vulnerability, 54.01% for High vulnerability, and 10.68% for Very High vulnerability, according to the results. A total 164.446 km^2 of the total 1,540 km^2 area is covered by the Very High vulnerable zone. The highest Nitrate concentration recorded in the area is 11 ppm and lowest is 4.4 ppm. Around 45% of the samples surpassed the approved limit of PSQWA (Pakistan Standards and Quality Control Authority) and NSQWQ (National Standards for Quality of Water) standard. The concentration of Nitrate >10 ppm represent that some human action has contributed toward the highest concentration.

KEYWORDS

groundwater pollution, contamination, groundwater vulnerability assessment, DRASTIC model, geographic information system (GIS)

1 Introduction

The most crucial resource for life on Earth to survive and flourish, according to Kahlown et al. (2005) is water. There is no denying that subsurface water reservoirs are among the most important and necessary sources of freshwater on the planet (Madsen, 1995). Groundwater resources are more severely impacted by pollution than surface water resources because of the relatively tighter regulation of pollution on them, and as a result, they are rapidly running out of water. Groundwater is regarded as a "major drinking water resource" because of its low susceptibility to contamination (EPA, 1985). Though it is nearly impossible to estimate the

precise volume of subsurface water present in aquifers all over the world, a rough calculation indicates that the planet's reservoirs hold between 15.2 and 60 million cubic meters of water. The amount of fresh groundwater in this system, according to Mishra (2023), is between 8 and 10 million cubic meters, with the remaining volume being brackish and salty. Given its accessibility and superior quality to surface water, groundwater is crucial for daily activities. In daily life, groundwater is used for many things, including domestic, industrial, and agricultural uses. This transforms it into a tactical resource.

According to Abbas et al. (2012) 4,430 km^3 of groundwater is pumped out of the earth each year, with about 70% of that volume being used for agriculture. The remaining 25 and 5% of the pumped groundwater are used for domestic and industrial purposes, respectively. The combined annual withdrawal across the globe, according to Eurostat data from 2011, is estimated to be around 1,000 km3 (or 22% of all groundwater pumps globally). Nearly 2 billion people are thought to rely solely on groundwater resources for their daily needs. The needs of nations all over the world are met by 273 of these groundwater resources that cross national boundaries (Richts et al., 2011). According to a UN report from UNDESA and UNECLAC (2015), the planet's population, which was estimated to be 6.9 billion people in 2010, is growing quickly and is anticipated to reach 8.3 billion people by 2030. There is no proof that socioeconomic or ecological factors will have an impact on that number, and rapid population growth puts the world's freshwater reserves beneath the earth's surface in grave danger. Subsurface water supplies are burdened and pressed by industrial growth, urbanization, and agriculture, which lessens their overall dominance. The primary source of fresh water, groundwater, is used to supply a variety of domestic, commercial, and agricultural needs. There are more aquifers in that region that are susceptible to groundwater pollution from anthropogenic, domestic, industrial, and agricultural activities, all of which have a short-term impact on the water. Remediation is a pricy and difficult task to prevent long-term losses or damages from groundwater contamination (Secunda et al., 1998). Globally, the quality of subsurface waters has significantly declined as a result of accelerating industrialization, urbanization, and anthropogenic pressures (Khatri and Tyagi, 2015). In addition to harming direct and indirect ecosystem processes, subsurface aquifers with contaminated groundwater disrupt the ecosystem and pose a health risk (Danielopol et al., 2003). Chemical (chloride, nitrates, sulfates, etc.), physical (turbidity, odor, taste), and biological (e.g., bacteria) factors are just a few of the many causes of groundwater contamination. We must consider all the major contributing factors, such as chemical, physical, and biological factors, when evaluating the quality of subsurface water (Alley, 1993). The chemical factor has become more important in groundwater quality development as a result of the increased penetration hazards, ease of pollution, and various anthropogenic activities that result in a significant amount of harmful and poisonous chemical elements being discharged into groundwater. The management of subsurface water places more emphasis on these chemical parameters. When groundwater is supplied to homes and used for drinking water while containing hazardous materials, inorganic contaminants, and heavy metal residues, human lives are put in danger. Due to poor management practices and drinking water evolution, infections linked to contaminated groundwater are frequent in developing and third world nations. According to estimates from the WHO (2008), about 3.3 million people die each year in third-world nations due to insufficient access to clean water, unsanitary living conditions, or poor sanitation systems. A large portion of these deaths are thought to be caused by drinking subsurface water that has been contaminated with pathogens. Since underground aquifers are more prone to contamination than surface-water bodies, this fact primarily contributes to diseases linked to groundwater. Subsurface water is regarded as a reliable water source in Pakistan. In addition to drinking water and farming, it is used in a number of different industrial fields. About 35% of what is needed for agriculture comes from groundwater. Furthermore, it is acknowledged that underground water is one of Pakistan's most important sources of drinking water (Daud et al., 2017). Population growth brought about unexpected and ill-managed urbanization, industrialization, and agricultural development. Pakistan's groundwater quality is in danger due to these adverse consequences of the growing population. Due to the unchecked disposal of sewage, industrial, and solid wastes as well as the use of insecticides, herbicides, and chemical fertilizers in agriculture, it is now more likely that groundwater will become polluted. According to Kurwadkar et al. (2020) numerous shallow aquifers, particularly in urban areas, are reportedly affected by the widespread groundwater pollution caused by sewage dumping in Pakistan. In the nation's major cities and metropolitan areas, industrial waste is the main cause of groundwater contamination. Groundwater in industrialized areas and states like Lahore, Gujranwala, and Faisalabad is susceptible to pollution because of the large amount of unprocessed toxic waste present. Additionally, the drinking water of the locals is contaminated by waste from nearby industries like textile, sporting goods, tanneries, paper, pharmaceuticals, leather, and chemical (Mahmood et al., 2011). The groundwater in the Karak region has been contaminated by the toxic waste from numerous businesses.

The health of people is impacted by the decline in groundwater quality and quantity, which also disturbs the natural equilibrium of every biota. Several organizations have already started. They take groundwater pollution very seriously and work to mitigate its effects for the benefit of society (Li et al., 2012; Mogaji et al., 2013; Yin et al., 2013; Wu et al., 2014; Jin and Ray, 2014; Shabbir and Ahmad, 2016; Tan and Duan, 2017; Kozłowski and Sojka, 2019; Li and Merchant, 2013). Subsurface water must be protected from contamination by all necessary precautions because it serves as the primary source of drinking water for the majority of people on earth. Additionally, the likelihood of contamination must be assessed (Dixon, 2005; Huan et al., 2012; Neshat et al., 2014; Pacheco et al., 2015; Shahzad et al., 2018; Mohan et al., 2018).

In the Karak district of Khyber Pakhtunkhwa, Pakistan, managing groundwater resources poses a considerable challenge due to multiple concerns regarding water quality. Javed et al. (2019) indicated that the groundwater in this area is largely impacted by high levels of sodium (Na^+) and chloride (Cl^-), resulting in 84% of the samples being deemed unsuitable for drinking according to WHO standards. Additionally, the study observed that groundwater quality varies spatially, with the majority of samples falling under the C3-S2, C4-S2, and C3-S3 classes, which reflect differing levels of salinity and sodicity that affect agricultural effectiveness. This situation is further complicated by contamination from heavyTamil Nadu, India, but also discov metals, as highlighted by Khan et al. (2021a, 2021b), who discovered that groundwater in Karak contains elevated concentrations of lead (Pb), silver (Ag), iron (Fe), and chromium (Cr), which pose further health hazards. Furthermore, the impact of tectonic activity is

an important yet under-researched aspect of groundwater quality. Khattak et al. (2014) noted that radon levels in drinking water sources within the Karak Thrust region often exceed the EPA's recommended safe thresholds, raising concerns about potential long-term health implications. Besides the quality concerns, fluctuations in water table depth have been recorded, with certain regions, particularly around Sur Dag and Takht-e-Nasrati, showing a downward trend, largely due to excessive extraction (Khan et al., 2021a). The overall rise in groundwater withdrawal, combined with insufficient recharge, intensifies these issues, indicating that sustainable groundwater management practices, such as constructing small dams for aquifer recharge, are essential for maintaining the long-term availability of groundwater resources in the district.

The methods and models used to assess the vulnerability of subsurface water contamination include GOD, SINTACS, MODFLOW, and DRASTIC. This study involved identifying areas that are vulnerable to contamination and used the DRASTIC model, which is based on GIS (Akib et al., 2013; Guler and Ali, 2013; Neshat et al., 2014; Ghosh et al., 2015; Pacheco et al., 2015; Feola et al., 2015; Baghapour et al., 2016; Qadir et al., 2016). The GIS-based DRASTIC model, developed by the United States Environmental Protection Agency USEPA (1994) of the USA, provides support for the assessment of groundwater vulnerability assessment and mapping on a global scale (Sener and Davraz, 2013; Ghosh et al., 2015). The acronym DRASTIC, which stands for "Disruptive, Rapid, and Strategic," is made up of the first seven letters of the word. The elements are (D) water table depth, (R) net recharge, (A) aquifer media, (S) soil media, (T) topography, (I) vadose zone impact, and (C) hydraulic conductivity. The DRASTIC model includes a ranking scheme. Any hydrogeological setup can be given a numerical value by using weights, ratings, and rankings with an additive model to determine susceptibility to groundwater effusion (Jama et al., 2018; Jin and Ray, 2014; Kozłowski and Sojka, 2019; Shahzad et al., 2018; Yin et al., 2013).

The DRASTIC model was chosen for this research because it is well-suited to the hydrogeological and environmental conditions present in Karak District. In comparison to other models such as SINTACS (Subjectivity, Uncertainty, and Numeric Theme for assessing vulnerability of aquifers to surface contamination), AVI (Aquifer Vulnerability Index), or GOD (Groundwater Occurrence, Overlying Lithology, and Depth to Water Table), DRASTIC strikes a good balance between simplicity and depth, making it effective for evaluating groundwater vulnerability in semi-arid regions like Karak. The inclusion of seven environmental parameters in the model corresponds effectively with the varying topography, soils, and aquifer characteristics observed in the study area, ensuring that essential factors influencing groundwater vulnerability are considered.

Furthermore, DRASTIC's GIS-based application facilitates detailed spatial mapping of vulnerability, which is crucial in light of the differences in groundwater recharge and contamination risks throughout the region. The model's standardized framework for weighting and rating, although recognized globally, was also a suitable choice due to the accessibility of the required data and the scale of the study area.

In the southernmost region of district's Karak Khyber Pakhtunkhwa Pakistan's, this research was conducted. The main objective of this study is to use the GIS-based DRASTIC model to address groundwater pollution issues. Investigate how the influencing factors affect how sensitive the groundwater is to pollution. To address this, information has been gathered from a variety of private, public, and semi-public organizations. After going through a quality check, the data was integrated into ArcGIS to produce thematic maps of the DRASTIC model's components. Finally, a map of the groundwater vulnerability index has been developed. The results of this study have been calibrated using the field data on groundwater nitrate concentration. The results of this study will be used to manage groundwater resources and identify potential groundwater risk areas. This map will help administrative department's better serve the public and supply them with clean groundwater in the future by lowering the threat posed by polluted aquifers.

The Karak district was chosen as the focus area for DRASTIC modeling because of its distinct hydrogeological and environmental traits. This region primarily experiences arid and semi-arid conditions, resulting in scarce groundwater resources essential for agriculture, drinking water, and domestic uses. The rising human activities, including urban expansion and intensive agriculture, significantly threaten groundwater quality. Despite the critical nature of these resources, there is insufficient comprehensive research on groundwater vulnerability in the district, resulting in a lack of understanding of potential contamination risks. Previous studies have not sufficiently explored the combination of hydrogeological factors with contamination indicators like nitrate concentration to support vulnerability evaluations. By concentrating on Karak, this study seeks to fill these gaps and provide a scientific foundation for sustainable groundwater management and protective strategies that are adapted to the district's unique circumstances.

In other regions where the DRASTIC model has been implemented, such as the Kherran Plain in Iran, our research reveals a consistent trend of increased hazard in areas characterized by shallow water tables, permeable soils, and significant human activity (Kumar et al., 2009; Chitsazan and Akhtari, 2009). Simultaneously, the study conducted in Kakamigahara Heights, Japan, emphasized that net recharge and geological media are the two primary factors influencing aquifer vulnerability, findings that align with our own research (Babiker et al., 2005). This study not only supports the conclusions drawn by Kumar et al. (2009) in Tamil Nadu, India, but also discovered a notable correlation between nitrate concentrations and zones of high susceptibility as indicated by the DRASTIC model. Conversely, our analysis revealed that the relationship between nitrate levels was more delicate, suggesting that the DRASTIC index highlights local contamination rather than widespread pollution. This difference underscores the need for susceptibility assessments to take into account the unique hydrogeological and anthropogenic ecological aspects of the specific area being investigated in order to accurately create an effective risk map.

2 Study area

The district of Karak is situated in the Kohat Division of Pakistan's Khyber Pakhtunkhwa province (Figure 1). The study area is situated in the westernmost region of the main Himalayan foreland fold and thrust belt, the Kohat Plateau. The Kurram strike-slip fault and the Indus River separate it from the Potwar plateau in the west and east, respectively. Both the major boundary thrust in the north and the Shinghar range in the south encircle it. District

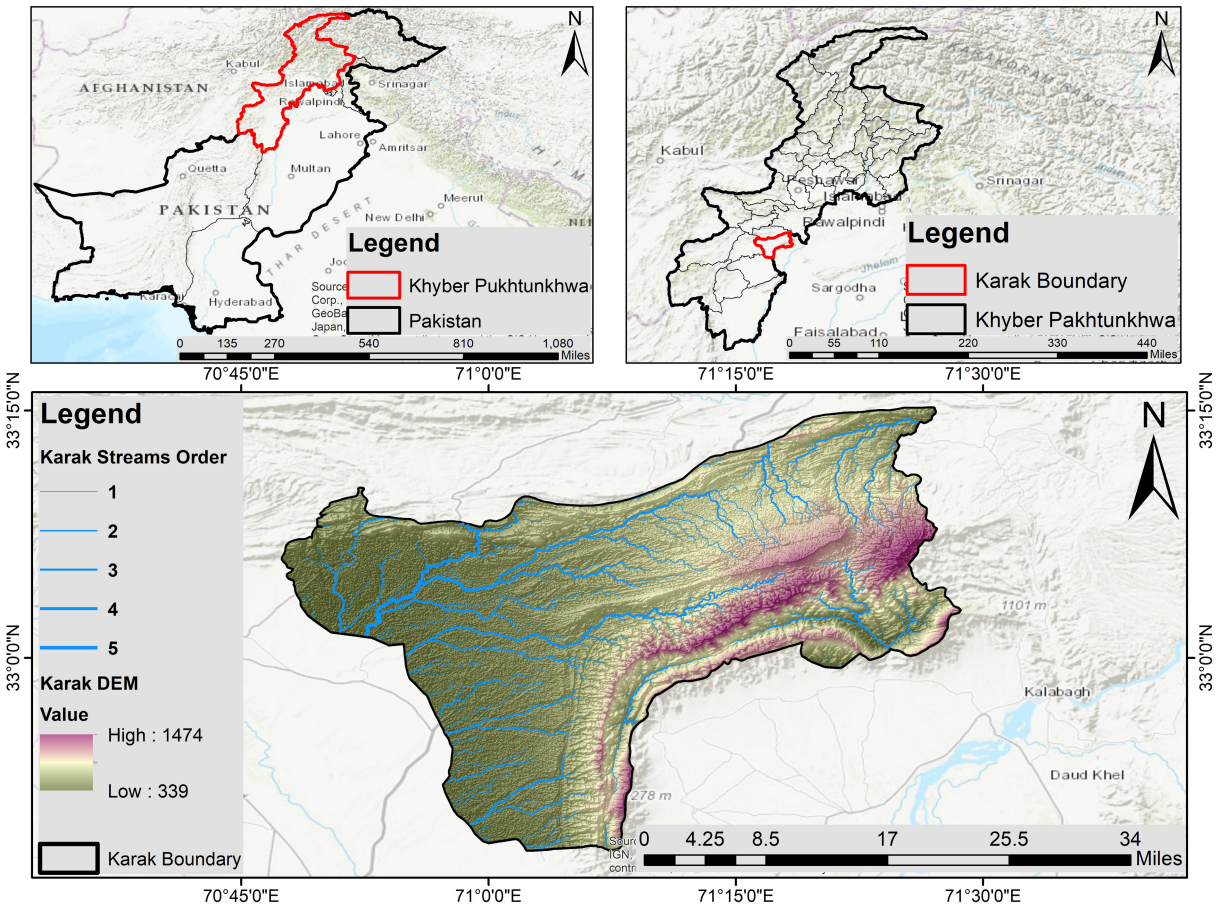

FIGURE 1
Location map of District Karak.

Karak is comprised of three tehsils, which are further subdivided into 23 union councils. Karak is a plain and hilly region that is 548 meters (1,798 feet) above sea level. In 1982, Karak was regarded as a district.

The socio-economic conditions in Karak, shaped by local industries and farming practices, have a direct impact on the quality and availability of groundwater. In the beekeeping industry, for instance, research conducted in Karak, Bannu, and Kohat shows that many beekeepers are young and have limited educational backgrounds, facing difficulties such as pest problems and diseases (Jamil et al., 2023). These challenges, combined with a significant reliance on groundwater, contribute to the overall water stress in the region. The socio-economic effects of this water scarcity are significant, as illustrated by a study on the repercussions of water crises in Karak, which indicates that communities experience conflicts over water allocation, forced migration, and economic difficulties, especially for women who are tasked with water collection (Rasool et al., 2020). Additionally, research on drinking water quality in the region indicates that although many water sources meet safety regulations, some contain higher levels of sodium and heavy metals like iron and chromium, which could pose health risks (Ahmad et al., 2020). These socio-economic and industrial dynamics highlight the intricate connection between groundwater quality and the wellbeing of the community, underscoring the necessity for holistic water resource management to enhance both human and environmental health in Karak.

The Digital Elevation Model (DEM) of the Karak District reveals a varied topography, with elevations spanning from 339 meters in the low-lying areas to 1,474 meters in the highlands. The western and central regions, which feature lower elevations, primarily consist of plains and gently rolling terrains, whereas the rugged mountainous landscapes are found in the higher elevations located in the eastern and southeastern regions. The accompanying map (Figure 1) depicts a clearly defined dendritic drainage system, where first-order streams merge into higher-order streams, highlighting the impact of different slopes and structural influences. The variability in topography indicates that areas with high relief are more likely to experience enhanced runoff, erosion, and sediment transport, while lower regions may act as zones for sediment deposition. This varied landscape significantly affects groundwater recharge, soil stability, and land use planning, presenting vital considerations for hydrological and geological research in the region.

Karak experiences a highly fluctuating climate throughout the year, marked by hot summers and minimal annual rainfall, especially in the Thal zone, which receives <500 mm of rain each year (Khan et al., 2015). During June and July, temperatures can soar to 46°C, and the predominantly sandy soil in this area is conducive to agriculture, with crops depending on either rainfall or water from tube wells. In

contrast, the northeastern Tehsil Karak receives annual rainfall between 500 and 750 mm and is characterized by medium clay soil (Khan et al., 2021b). These climatic and soil conditions are crucial in influencing the agricultural potential and water availability throughout the district.

The surface hydrology in Karak consists of seasonal flood streams that flow during or following precipitation, especially during the monsoon months of March–April and July–August. These streams contribute to downstream flow, with annual rainfall serving as the key source for aquifer recharge. The semi-arid region faces limited and sporadic rainfall, concentrated in brief rainy periods, leaving the majority of the year dry. High temperatures accompanied by heavy rainfall frequently result in substantial water loss through evaporation and runoff (Farid, 2019). Rainfall patterns indicate that 68% of the annual precipitation takes place between June and November, with summer rains being intense but short, in stark contrast to the extended, low-intensity winter showers (Khan et al., 2021b). Summers are characterized by extreme heat and monsoons in May and June, while winters are extremely cold due to the influence of western winds. The drainage system is predominantly active during flood seasons, underscoring the significant role of surface hydrology in regional water resource management.

The soil map of Karak District indicates the presence of two primary soil types: clayey and loamy. Clayey soil is found mainly in the southwestern and southeastern regions, where it retains moisture and is suitable for water-demanding crops, though it necessitates adequate

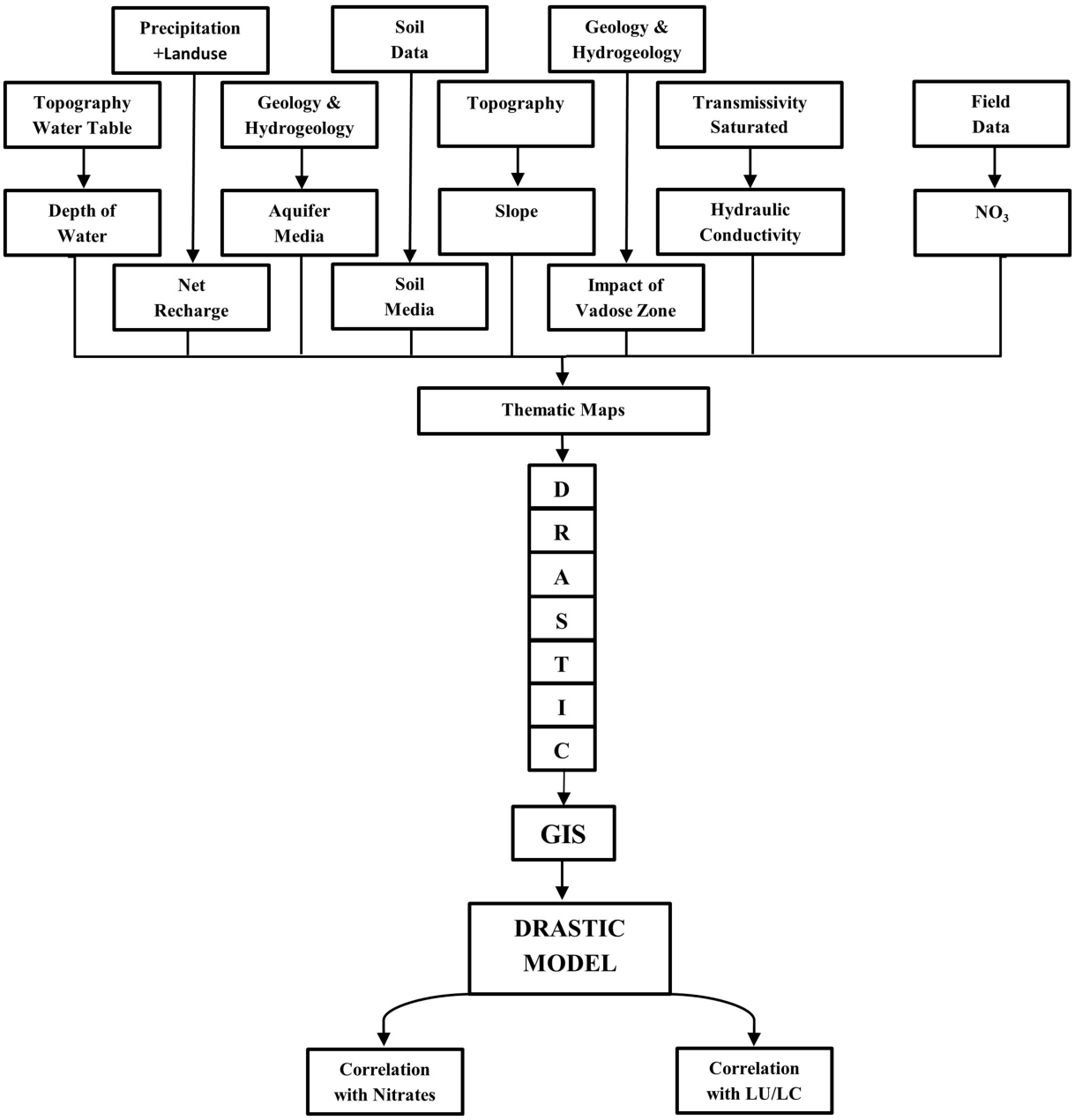

FIGURE 2
Flowchart of methodology.

drainage (Hatiye et al., 2016). Loamy soil, which spans the majority of the district, is highly fertile and accommodates a variety of crops due to its balanced mix of sand, silt, and clay (Zhao et al., 2019). The distribution of these soil types mirrors the area's topography and climate, influencing agricultural methods and water management strategies.

3 Materials and methods

DRASTIC modeling serves as a commonly utilized method for evaluating groundwater vulnerability by integrating various hydrogeological elements to identify areas at risk. Just as climate variations and shifts in land use influence environmental factors such as temperature and air quality, DRASTIC sheds light on the geographical differences in groundwater conditions. For example, the analysis of precipitation and temperature trends in Patna Gupta et al. (2022a) illustrates how evolving climatic patterns, including reduced rainfall and increased temperatures, can affect local groundwater conditions, potentially worsening vulnerabilities. In addition, the anticipated rise in temperatures in the River Ganges basin due to climate change may lead to alterations in groundwater recharge and evaporation rates, affecting both groundwater quality and availability

TABLE 1 Type and nature of data collected from various organizations.

Number	Layer	Data format	Source/Organization
1	Depth to water table	Field data, strata/lowering charts, MS excel sheet	Field surveys, PHED
2	Net recharge	TRMM raster data, land use shape file	NASA, literature review
3	Aquifer media	Well log, strata/lowering charts	PHED
4	Soil media	Map raster data	Soil survey of Pakistan
5	Topography	DEM	SRTM
6	Impact of vadose zone	Well log, strata/lowering charts	PHED
7	Hydraulic conductivity	MS Excel File	PHED

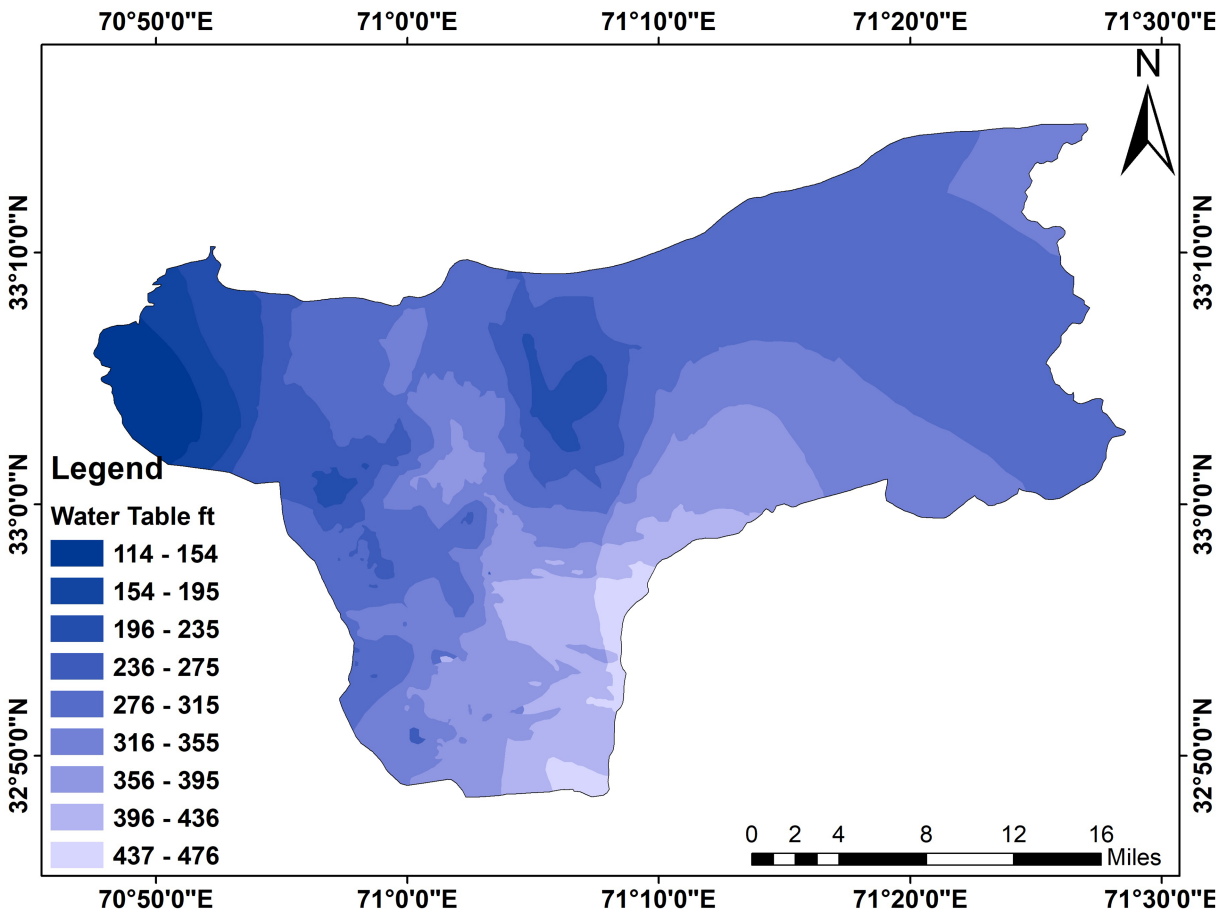

FIGURE 3
Depth to water table map of the study area.

(Gupta et al., 2022b). Furthermore, shifts in land use, such as urban expansion and deforestation, have been found to impact air quality and local environmental health (Jodhani et al., 2024), factors that can indirectly influence groundwater through modifications in infiltration rates and contamination risks. The decrease in wetland areas in Varanasi (Das et al., 2020) also underscores how changes in land use and urbanization can diminish groundwater replenishment, which is a crucial element in DRASTIC assessments. Additionally, research on air pollutants (Srivastava et al., 2023) highlights how pollutants like SO2 and NO2 may compromise groundwater quality through acidification processes. By merging these environmental alterations, DRASTIC modeling can aid in developing strategies to alleviate risks and safeguard groundwater resources in an environment that is rapidly evolving.

One of the most popular models for determining how vulnerable groundwater is to possible pollutants is DRASTIC (Akhter and Hasan, 2016; Awawdeh et al., 2014; Fritch et al., 2000; Knox et al., 1993; Nawafleh et al., 2011; Piscopo, 2001; Secunda et al., 1998; Tan and Duan, 2017). The GIS-based DRASTIC method used seven parameters, including hydraulic conductivity, aquifer media, soil media, topography, net recharge, and groundwater table depth. Spatial datasets are combined for each of these parameters (Navulur and Engel, 1998). Each parameter is given a numerical rating in accordance with Aller et al. (1987) and USEPA (1994). The DRASTIC model specifies that each weight must be multiplied by each rating before the results are added to produce the DRASTIC index (Knox et al., 1993). Every parameter is categorized into separate groups, and each group is assigned a rating based on how significant it is. These weights were determined through expert opinion and a review of relevant literature, adhering to established protocols (Aller et al., 1987). Greater weights were given to depth to water, recharge area, and aquifer conductivity because of their considerable impact on groundwater movement and the transportation of contaminants. The other parameters received weights based on their estimated importance within the study area. The weights for each parameter were determined to be between 1 and 5, and the rate ranged from 1 to 10. According to Aller et al. (1987) based on the relative significance of each parameter (Fortin et al., 1997; Fritch et al., 2000; Jang et al., 2017; Knox et al., 1993; Mohan et al., 2018). The region's net recharge was determined in this study by combining and analyzing data on the mean annual precipitation, land use, and other variables. The DRASTIC Index is calculated using the following Equation 1 (Nurfahasdi et al., 2023).

$$\text{DRASTIC Index (DI)} = \text{Dr.Dw} + \text{Rr.Rw} + \text{Ar.Aw} + \text{Sr.Sw} + \text{Tr.Tw} + \text{Ir.Iw} + \text{Cr.Cw} \quad (1)$$

D = Depth to the water table.

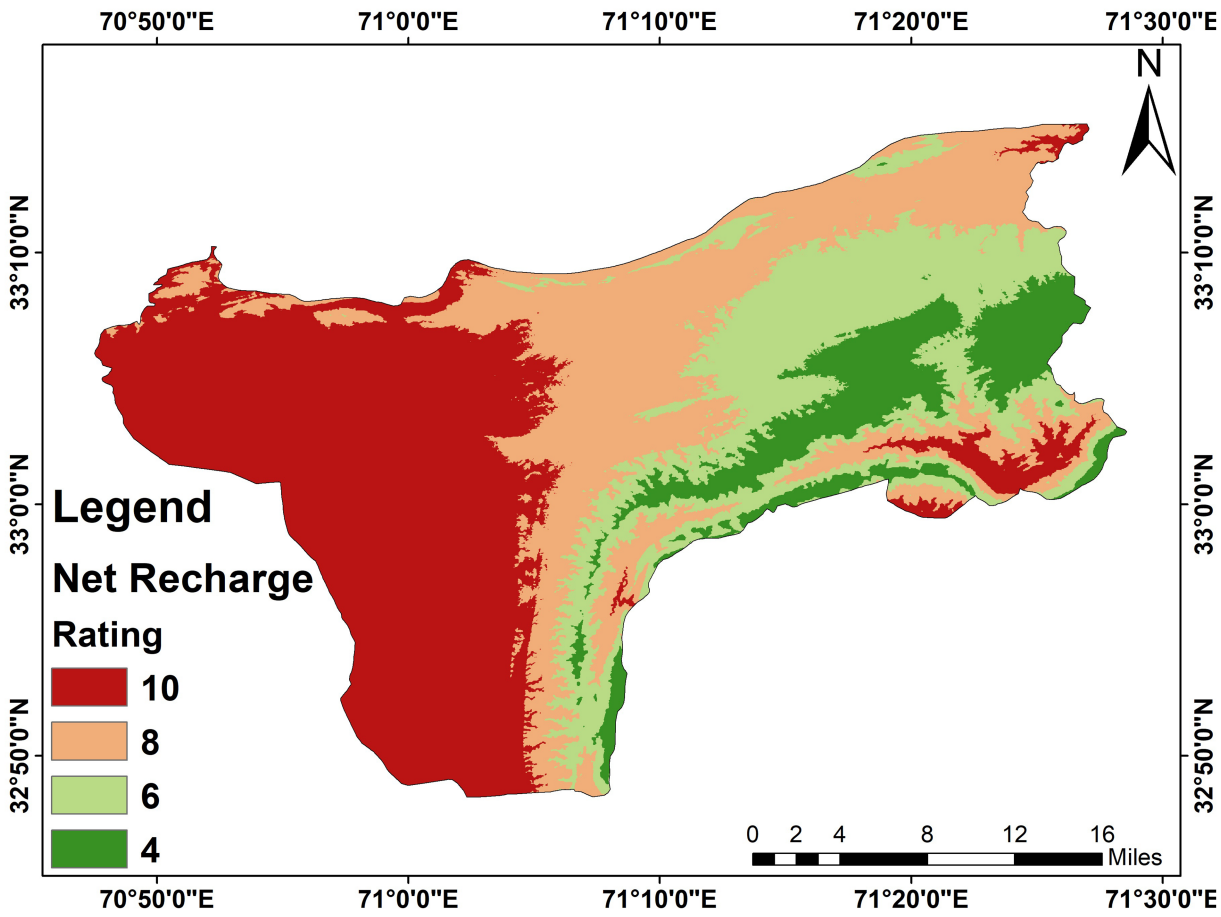

FIGURE 4
Net recharge map of the study area.

R = Net recharge.
A = Aquifer media.
S = Soil media.
T = Topography.
I = Impact of Vadose Zone.
C = Conductivity of Water.
r = Rating.
w = Weight.

Each parameter is divided into classes, and each class is given a rating based on its significance. The ratings range from 1 to 10, with each indicating the relative susceptibility of the groundwater to contamination. Different government, semi-government, and private organizations provided various types of data for various parameters. To gather data and to confirm data obtained from secondary sources, thorough field surveys were conducted. The research utilized ESRI's ArcGIS 10.4 to digitize the maps, process the data through interpolation, and create the final susceptibility map (Figure 2).

The factors and their corresponding classes are given weights and ratings in this study based on the Delphi method. These ratings have been used all over the world and are clearly defined. For the purpose of determining the level of vulnerability, the Delphi method considers the expertise and actions of experts (Khan et al., 2016). Table 1 lists each DRASTIC factor's data type, format, and source.

3.1 Water table depth

The groundwater's susceptibility to pollution is significantly influenced by the depth of the groundwater table. Less vulnerability to pollution results from a deeper water table, and vice versa. In the research area of the district Karak has a water table that is relatively deeper, with a range of 34–145 meters (Figure 3).

3.2 Recharge

The net recharge makes it possible for pollutants to enter the aquifer in addition to diluting the contaminant. As a result, the susceptibility to contamination directly correlates with the amount of recharge, with higher recharge resulting in higher ratings (Abdullahi, 2009; Davis et al., 2002). The recharge was calculated in this study by stacking the parts. Using information on the study area, local precipitation, and land cover to perform a weighted overlay analysis. Figures 2, 3 displays maps of mean land cover, annual precipitation, and mean temperatures. The resulting map shows that district Karak's populated areas have a lower recharge rate due to their buildup zones and slight elevation (Figure 4).

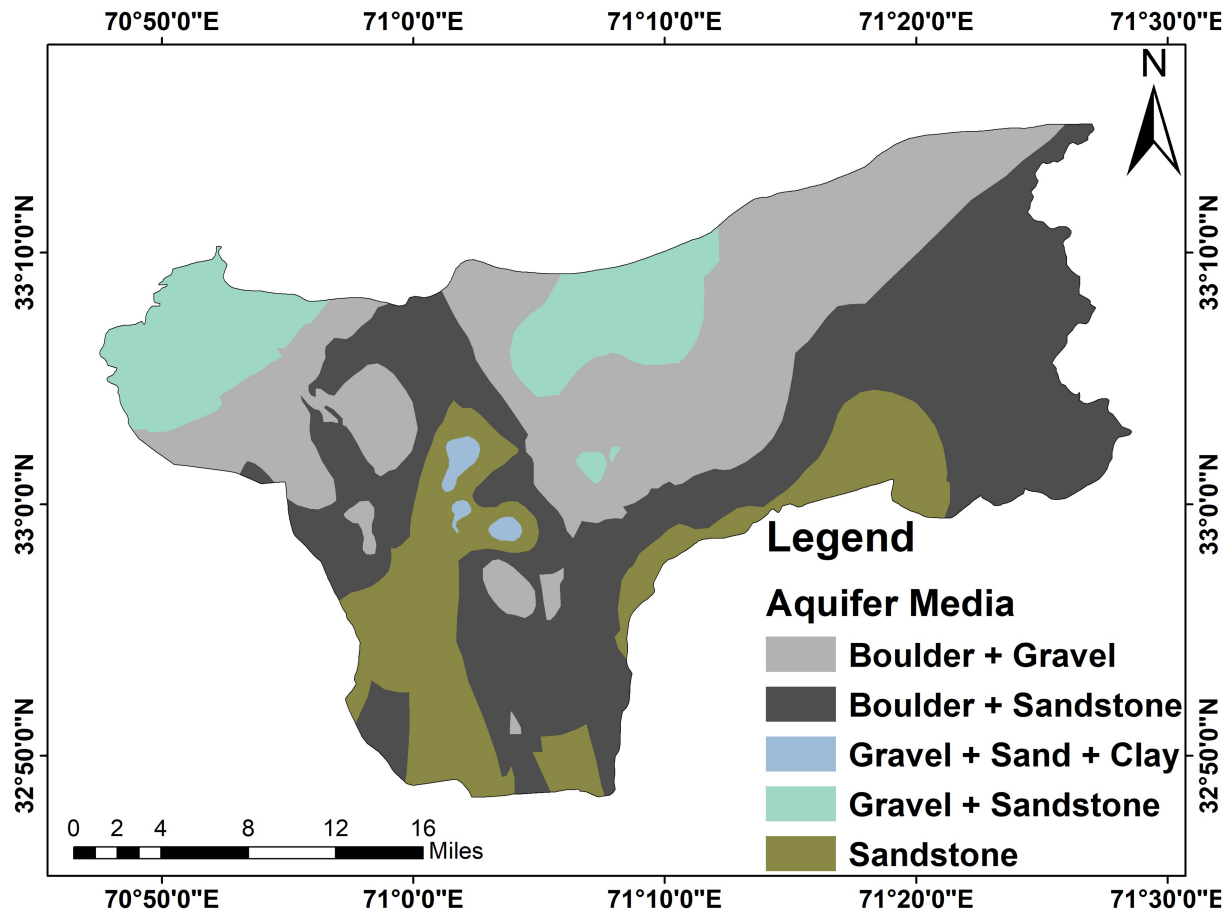

FIGURE 5
Aquifer media map of the study area.

3.3 Aquifer media

In terms of aquifer media, permeability affects susceptibility to pollution and vice versa. Aquifers with large grained sediment have a greater propensity for pollution, whereas unfractured fine-grained aquifers have a lower propensity for it (Hearne et al., 1992). The aquifers in the study area have a relatively high permeability rating (Figure 5).

3.4 Soil media

The vadose zone's uppermost portion, known as the soil media, is a crucial component because it acts as a barrier for contaminants on their way to the aquifer. The loamy soil makes up the bulk of the research area (Figure 6).

3.5 Topography

When determining the area's susceptibility to pollution, the topography is crucial because it affects how quickly water runs off. Water and consequently contaminants are retained for a shorter period of time the steeper the slope (Figure 7).

3.6 Impact of vadose zone

The material in the vadose zone, which is situated between the ground surface and the aquifer, can have a big impact on the vulnerability assessment because it either limits the contamination or makes it easy for it to pass. With increasing grain size, the water below the vadose zone becomes safer (Figure 8).

3.7 Hydraulic conductivity

Hydraulic conductivity is the ability of aquifer rock to conduct and pass fluid. Despite carrying somewhat less weight, it is still a significant factor. The permeability of an aquifer determines its conductivity, which in turn depends on the grain size; i.e., the hydraulic conductivity will increase with finer grain size and vice versa (Figure 9).

In Figures 3–9 the spatial distributions of each parameter are displayed. Table 2 lists the parameters' ranges, rankings, and weights. In order to determine the amount of nitrate, laboratory testing of water samples was done. After that, a map (Figure 10) illustrating the distribution of nitrate concentration was produced using interpolation of the data. Arc-GIS was used to perform a weighted overlay analysis to create a final DRASTIC index map using Equation 1. Figure 11 depicts the DRASTIC index map. The DRASTIC index map was subsequently

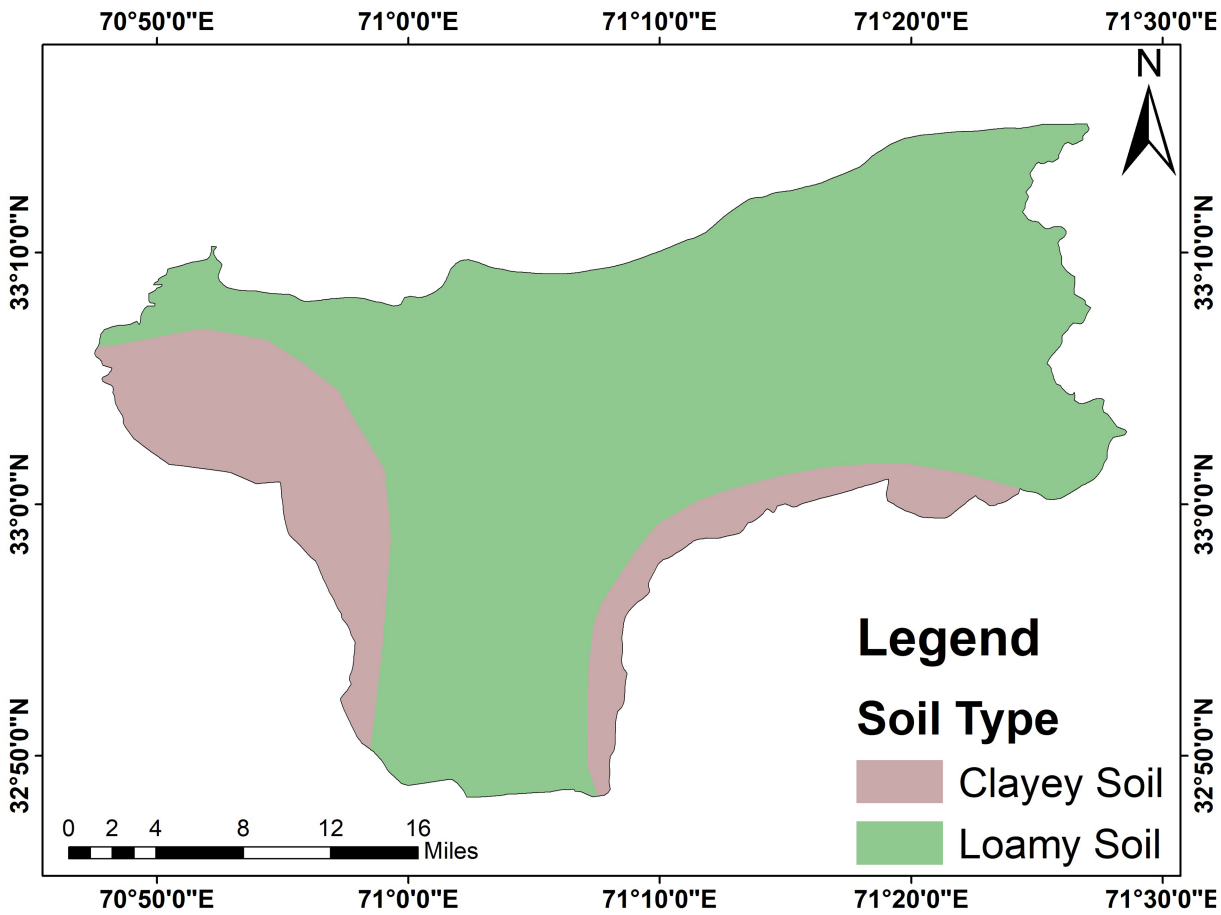

FIGURE 6
Soil media map of the study area.

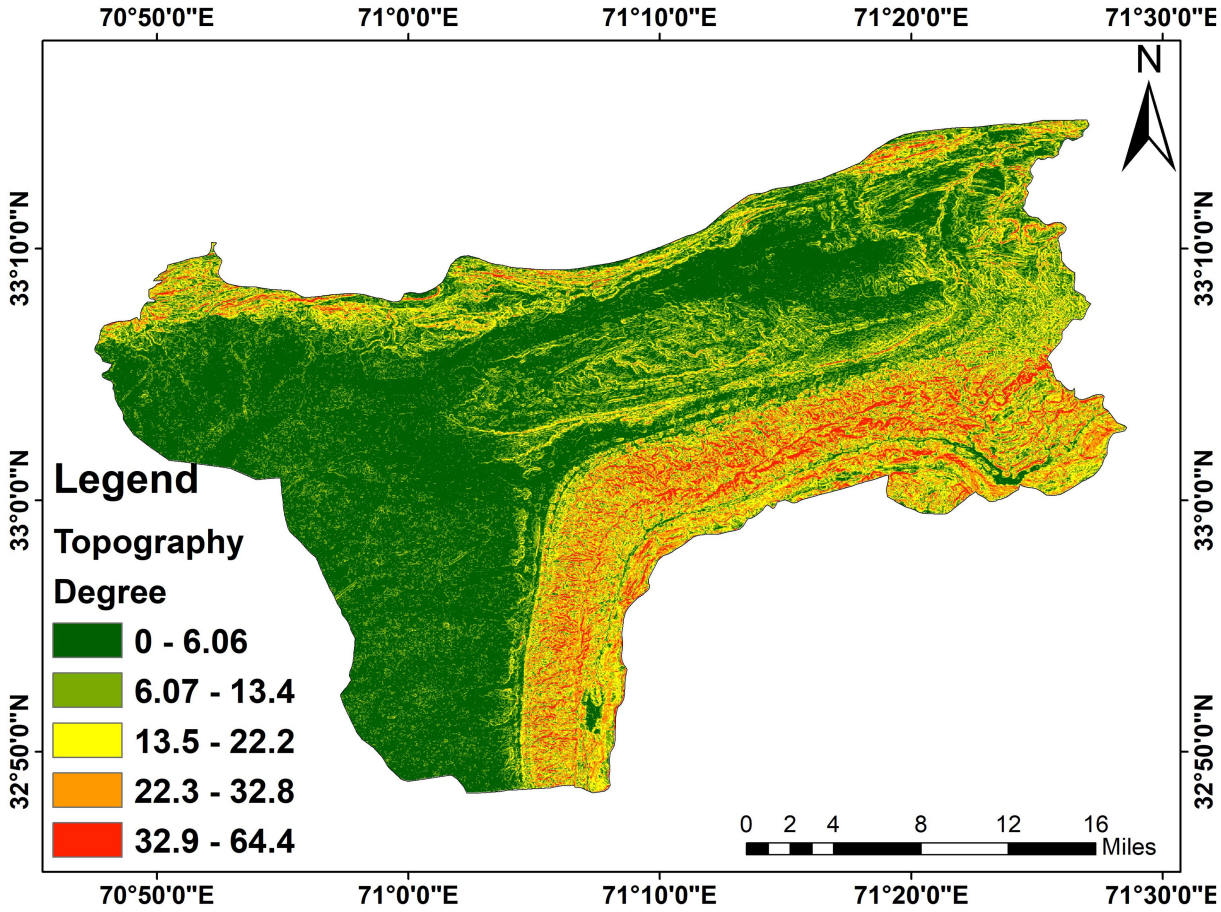

FIGURE 7
Topography of the study area.

calibrated with nitrate (Figure 12). This study utilized ESRI's ArcGIS 10.8 to collect, present, extrapolate from, and analyze the information gathered from various sources. The WGS 1984 projection system was used to create each map in ESRI's ArcGIS software.

4 Results and discussion

Southern Karak District has a DRASTIC vulnerability index. Data were then interpolated following that. Modifications were made to the GIS-based DRASTIC as is customary. In past studies, the GIS-based DRASTIC model frequently had aquifer or environmental parameters added to it or subtracted from it, depending on the specific research objectives and study themes. Changes to ratings and the addition of new parameters are the key modifications. Rather than the customary classes, the vulnerability index values in this study were divided into five classes: very low, low, moderate, high, and very high. The map of the DRASTIC index uses nitrate concentration as its reference point. A map of the research area is needed to measure the impact of anthropogenic activities and to portray pollution susceptibility more accurately.

The results showed the DRASTIC index values ranging from 325 to 950. A lower DRASTIC index value means that pollution is less likely to occur. According to Table 3, there are five categories for the DRASTIC index values: Very Low, Low, Moderate, High and Very High. The values of the DRASTIC index can be categorized using a variety of methods, such as classification based on a histogram's valleys (Kumar et al., 2016, 2017a, 2017b, 2020), quantile classification (Rahman, 2008), and using natural breaks, Jenks, to classify the values of the DRASTIC index (Kumar and Pramod Krishna, 2019). However, classes in this study were split into equal intervals (Kaliraj et al., 2014; Maqsoom et al., 2020; Rajput et al., 2020).

A large section of the study area is covered by the highly vulnerable zone which 831.795 square kilometers and it captivates 54.01% of the total area of the study area. On the DRASTIC index map, the Very Low vulnerable zone is less evenly distributed and takes up 16.06 square kilometers less territory. Which make up 0.78 percent of the entire region. The Low vulnerable zone covers 147.359 square km area which is 9.475 of the total area, Moderate zone covers 384.327 square km area which is 24.965 of the total area and the Very high vulnerable zone covers 164.446 square km area which make up to 10.68% of the total study area.

The most significant factor in the research area is the depth of the water table. In the study area, the water table is at its deepest point (450 feet). When the water table is deeper, the region is less vulnerable to contaminants seeping below. The research region receives very little recharge, which lessens its susceptibility to contamination from the surface. This is the second important component. Due to the investigated area's high level of impermeability, pollution is less likely to affect it. The area's fine particles coat the surface and keep contaminants

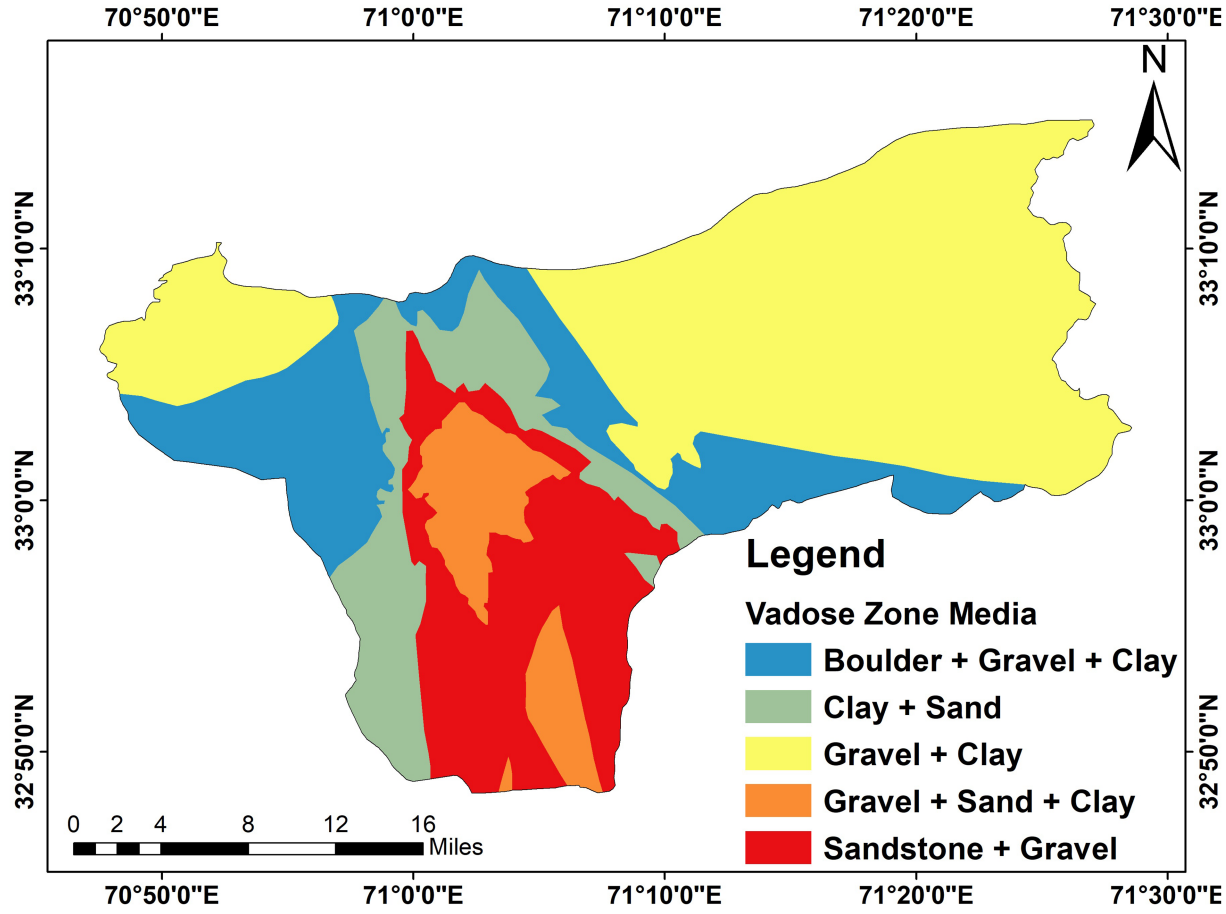

FIGURE 8
Vadose Zone media map of the study area.

from penetrating. The minute grain-size particles filter the water and stop pollutants from flowing downward. The area is generally unpopulated, lies in a medium-vulnerable zone, has a shallow water table, is clayey on the surface, and has a small amount of soil. Low permeability causes a contaminated particle to migrate only little downhill. Large, extremely porous sandstone and gravel particles make up the aquifer media in this zone, which can allow for groundwater contamination. The high sensitivity is caused by a number of variables. One of the main reasons for the high vulnerability zone is that it receives a lot more recharging than other research locations. These areas also have strong vadose zones, high hydraulic conductivity, and very permeable aquifer media. These factors make the area more vulnerable, based on the weight and rating that each range is given. Even though this zone's slope is fairly steep, Aller et al. (1987) gave it a minimum weight of "1," therefore it is insufficient to reduce susceptibility.

Human activities like intensive farming, inadequate waste management, industrial processes, and urban development can greatly affect groundwater quality by contaminating it with pollutants including nitrates, pesticides, and heavy metals. Human activities like extensive farming methods, inadequate waste management, industrial operations, and urban development can greatly affect groundwater quality by releasing contaminants such as nitrates, pesticides, and heavy metals.

Most studies either employ a map of annual precipitation or a map of the distribution of rainfall (Ghosh et al., 2015; Kumar and Pramod Krishna, 2019; Saha and Alam, 2014), in order to compute recharge. According to some studies (Awawdeh et al., 2014), the Net Recharge can be calculated using rainfall patterns and soil permeability. The DRASTIC index map and information on land use and land cover are sometimes combined to create updated DRASTIC maps (Awawdeh et al., 2014). However, in this study, the land use map is combined. Because of the importance of both of these factors in influencing how much an aquifer recharges, net recharge can be computed using mean annual precipitation.

To reduce risks in areas with high vulnerability, it is vital to employ strategies that are both targeted and specific to the context. In regions prone to groundwater pollution, the establishment of localized water purification systems like reverse osmosis or advanced filtration methods is essential for providing safe drinking water. Moreover, it is important to implement controlled practices for groundwater extraction to avoid further depletion and contamination of resources. The use of GIS and remote sensing technologies can facilitate real-time tracking of groundwater quality and levels, thus offering early warning systems for potential risks. Additionally, enforcing more stringent land-use regulations, especially in recharge zones, along with encouraging

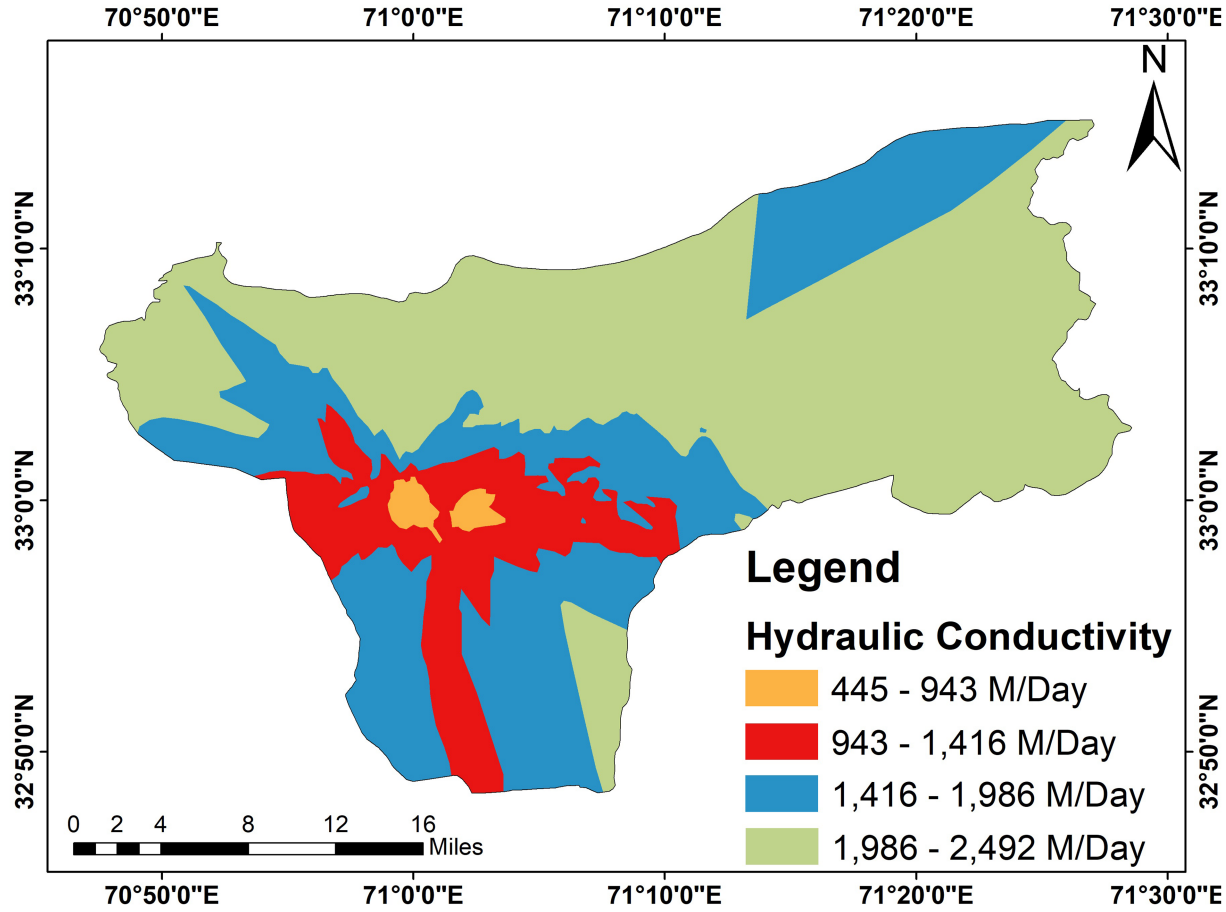

FIGURE 9
Hydraulic conductivity map of the study area.

sustainable farming methods through incentives, will lessen the strain on groundwater supplies. These approaches, customized to fit the distinct conditions of each high-risk area, are crucial for effectively addressing risks and fostering long-term water sustainability.

4.1 Correlation of the DRASTIC map with nitrate concentration

A map (Figure 11) of Nitrate concentration was created to calibrate and confirm the DRASTIC vulnerability map. Forty samples from the study area's accessible zone were taken and the nitrate parameter was examined to create this map. The permissible level established by Pakistan Standard Quality Control Authority (PSQCA) and National Standard for Drinking Water Quality (NSDWQ) is 10 ppm, but the average value over the entire region is 8.67 ppm. The lowest and highest concentrations that were measured were 4.4 ppm and 11 ppm, respectively. The permitted limit of PSQWA and NSQWQ standard was exceeded by about 45% of the samples. Figure 10 identifies the area of district Karak where nitrate is concentrated. The Regression analysis (Figure 12) showed a very weak correlation between DRASTIC model and the Nitrate concentration in the karak region with the R^2 0.058.

Nitrate concentrations more than 10 ppm indicate that human activity has played a role in the highest concentration (Spalding and Exner, 1993). After the preparation of both the DRASTIC index map and the nitrate concentration map it showed that in the areas where the nitrate concentration is higher the DRASTIC index values are also higher in those areas.

4.2 Correlation of the DRASTIC map with land use/land cover

To explore the relationship between Land Use/Land Cover (LULC) and the DRASTIC index, a point sampling approach was utilized. A series of points were randomly created within the study region. For each point, the LULC category was identified by superimposing the point onto the LULC map. After that, the relevant DRASTIC index value was obtained from the DRASTIC index map at each point's location. The gathered LULC categories and corresponding DRASTIC index values for all the randomly generated points were then organized into a table.

TABLE 2 The weight and rating assigned of each influencing DRASTIC parameters.

Parameter	Ranges	Rating	Weight
Depth to water table (ft)	114–235	10	20
	236–315	7	
	316–395	4	
	396–476	2	
Net recharge	High	10	15
	Moderate	8	
	Low	6	
	Very Low	4	
Aquifer media	Boulder + Gravel	10	10
	Boulder + Sandstone	8	
	Gravel + Sandstone	6	
	Sandstone	4	
	Gravel + Sand + Clay	2	
Soil	Loamy Soil	8	15
	Clayey Soil	3	
Topography	0–6.06	10	20
	6.07–13.4	8	
	13.5–22.2	6	
	22.3–32.8	4	
	32.9–64.4	2	
Vadose zone	Sandstone + Gravel	10	10
	Boulder + Gravel + Clay	8	
	Gravel + Sand + Clay	6	
	Gravel + Clay	4	
	Clay + Sand	2	
Hydraulic conductivity	445–943 M/Day	10	10
	943–1,416 M/Day	8	
	1,416–1,986 M/Day	6	
	1,986–2,492 M/Day	4	

Based on the gathered data (Table 4), an assessment was performed to comprehend the connection between land use/land cover (LULC) and groundwater vulnerability. This assessment included computing summary statistics (mean, standard deviation, minimum, maximum) for DRASTIC index values corresponding to each LULC category. The findings showed that crop areas had the highest average DRASTIC index value, indicating a greater vulnerability of groundwater. Urban regions also demonstrated considerable vulnerability with a high average DRASTIC index. In comparison, areas with tree cover had the lowest average DRASTIC index value, suggesting a reduced vulnerability of groundwater. Barren land presented an intermediate average DRASTIC index. These results imply that crops and urban zones may necessitate more rigorous land management strategies to reduce the risk of groundwater pollution. Conversely, tree-covered areas could function as a natural barrier, minimizing the risks associated with groundwater pollution.

The analysis indicates that among the land-use and land-cover (LULC) categories, agricultural crops have the highest average DRASTIC index value (838.93), indicating a relatively high vulnerability to groundwater issues. Urban regions also show considerable vulnerability with an elevated average DRASTIC index (809.41). On the other hand, areas covered by trees have the lowest average DRASTIC index value (587.82), implying they have a lower vulnerability to groundwater issues compared to agricultural crops and urban regions. Barren land presents a moderate average DRASTIC index (691.77). These results imply that agricultural crops and urban areas may require more rigorous land management strategies to reduce the risks of groundwater contamination. Possible measures could include proper waste management, regulated use of fertilizers and pesticides, and rainwater harvesting techniques. In contrast, maintaining tree coverage can serve as a natural barrier that lessens the risks of contaminating groundwater. Therefore, it is advantageous to preserve and enhance tree cover for the protection of groundwater resources.

4.3 Implications of the DRASTIC index map

The DRASTIC index map clearly showed that the water table depth, slope, vadose zone material, presence of surface water bodies, and net recharge are the main elements influencing groundwater vulnerability. There are differences in these elements between the high and low through the moderate index zones. Care must be taken when doing so because it is normal practice in many places to dispose of waste and effluents in surface water bodies, which are given higher indices and provide an excellent recharge for groundwater. The most vulnerable discovery was the discovery of the highly contaminated surface streams in the Hattar area. The industrial garbage that was dumped there poisoned the nearby waterway. The highlands, where there is more precipitation and groundwater flowing from north to south, are where the majority of recharge occurs in the research area. This further demonstrates why the places on the map have a higher vulnerability score. In light of this, it is suggested that improving the state of crises should start with the more vulnerable places, particularly in the southern regions where facilities like the Shanawa nuclear facility and the area around it that are drained by those effluents. These further require specific duties to use appropriate technological solutions for disposal of these effluents in order to rehabilitate and recover the contaminated ecosystem. Additionally, it is advised that efforts for health risk monitoring be started right once to guarantee the safety of the areas and the people who live there.

5 Conclusion

This research employed the GIS-based DRASTIC model to assess groundwater vulnerability in the Karak District, indicating that 54.01% of the land is classified as high vulnerability zones and 10.68% as very high vulnerability, primarily attributed to shallow water tables, high rates of recharge, and permeable aquifer materials. In contrast, areas identified as low and very low vulnerability constitute only 9.57 and 0.78% of the region, respectively, linked to deeper water tables and lower permeability. These results highlight the urgent need for specific measures, such

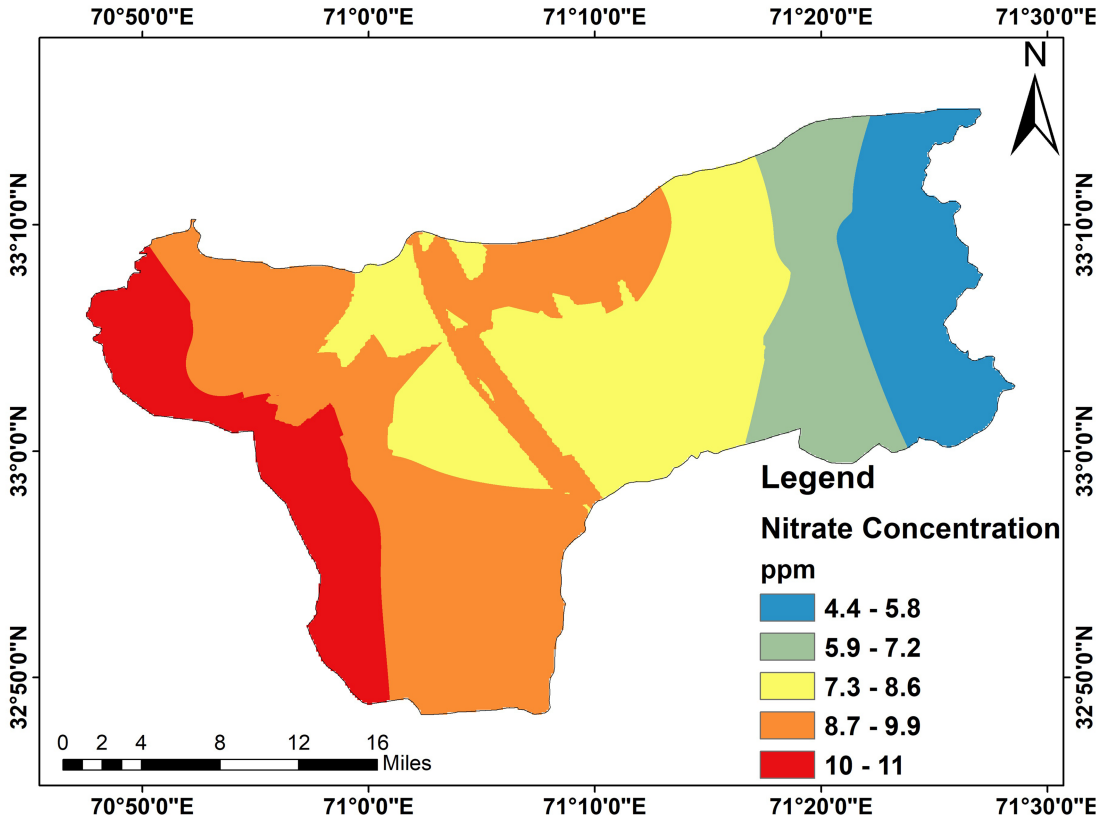

FIGURE 10
Spatial distribution of nitrates in the study area.

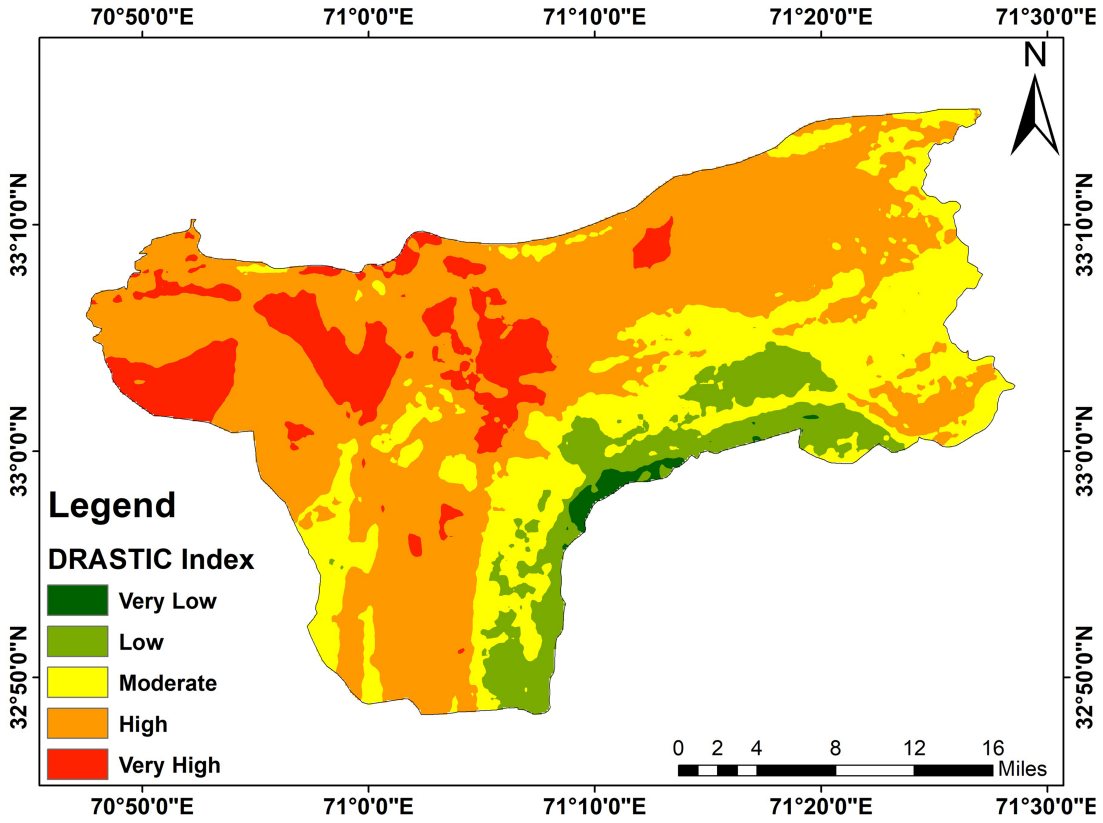

FIGURE 11
DRASTIC vulnerability index map.

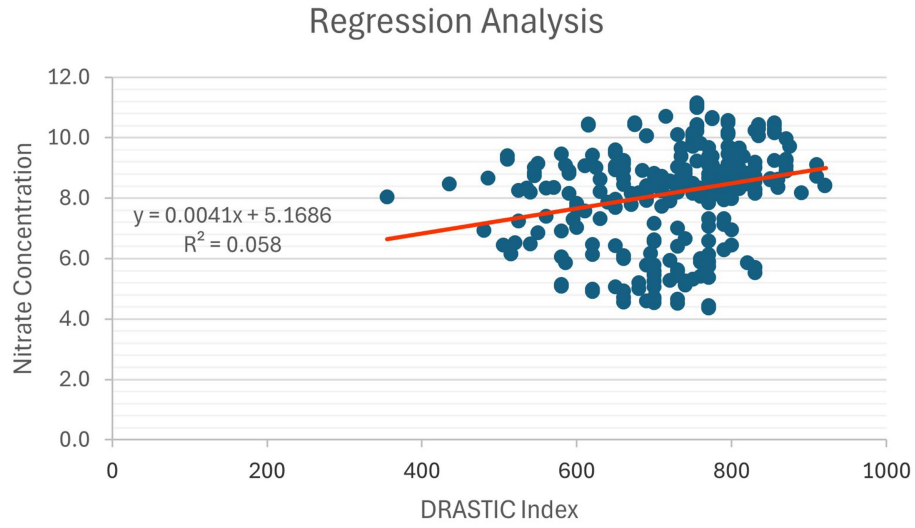

FIGURE 12
Regression analysis between DRASTIC index and nitrate concentrations.

TABLE 3 Statistical distribution of the DRASTIC map.

DRASTIC index	Range	Area sq km	Percent	Color
325–450	Very Low	12.060	0.78	
451–575	Low	147.359	9.57	
576–700	Moderate	384.327	24.96	
701–825	High	831.795	54.01	
826–950	Very High	164.446	10.68	
Total		1539.987	100.00	

TABLE 4 Correlation of LULC with DRASTIC index.

LULC class	Count	Mean	Standard deviation	Minimum	Maximum
Trees	10	587.82	117.12	411.11	831.75
Crops	22	838.93	32.19	801.73	903.01
Urban	45	809.41	51.24	703.89	906.85
Barren	48	691.77	103.84	477.62	862.46

as encouraging sustainable farming practices, improving wastewater treatment facilities, and enforcing land-use regulations to safeguard recharge zones and reduce contamination risks from fertilizers, urban runoff, and industrial waste. Although the DRASTIC model offers a solid basis for vulnerability assessment, it has limitations, including the omission of dynamic contamination sources and reliance on indirect indicators of pollutants, which require validation through direct monitoring of contaminants. Future studies should integrate additional factors, like real-time data on nitrate concentrations, and investigate machine learning techniques to enhance predictive precision. The conclusions drawn from this study provide a scientific foundation for effective policymaking and sustainable management of groundwater resources that considers the specific circumstances of semi-arid regions like Karak.

Data availability statement

The original contributions presented in the study are included in the article/supplementary material, further inquiries can be directed to the corresponding author/s.

Author contributions

MM: Investigation, Methodology, Writing – original draft. MK: Conceptualization, Resources, Supervision, Writing – review & editing. FS: Formal analysis, Software, Writing – original draft. IA: Data curation, Validation, Writing – review & editing. SS: Data curation, Writing – review &

editing. FA: Funding acquisition, Project administration, Writing – review & editing. MS: Funding acquisition, Writing – review & editing.

Funding

The author(s) declare that financial support was received for the research, authorship, and/or publication of this article. The authors extend their appreciation to Researchers Supporting Project Number (RSP2025R327), King Saud University, Riyadh, Saudi Arabia.

Conflict of interest

The authors declare that the research was conducted in the absence of any commercial or financial relationships that could be construed as a potential conflict of interest. The authors declare no conflict of interest.

Generative AI statement

The author(s) declare that no Gen AI was used in the creation of this manuscript.

Publisher's note

All claims expressed in this article are solely those of the authors and do not necessarily represent those of their affiliated organizations, or those of the publisher, the editors and the reviewers. Any product that may be evaluated in this article, or claim that may be made by its manufacturer, is not guaranteed or endorsed by the publisher.

References

Abbas, J. I., Kiyani, S. G., Ahsan, M. S., and Akram, H., &. Iqbal. (2012). Spatio-temporal analysis of water table within Rawalpindi municipal jurisdiction. NUST. Islamabad.

Abdullahi, U. (2009). Evaluation of models for assessing groundwater vulnerability to pollution in Nigeria. *Bayero J. Pure Appl. Sci.* 2, 138–142. doi: 10.4314/bajopas.v2i2.63801

Ahmad, S., Faisal, S., Ali, F., Ullah, S., Ullah, R., Khan, M. A., et al. (2020). Assessment of drinking water quality and human health risks in Karak and adjoining areas, southeastern Kohat Basin, Pakistan. *J. Himalayan Earth Sci.* 53:126.

Akhter, G., and Hasan, M. (2016). Determination of aquifer parameters using geoelectrical sounding and pumping test data in Khanewal District, Pakistan. *Open Geosci.* 8:71. doi: 10.1515/geo-2016-0071

Akib, S., Shirazi, S. M., Imran, H. M., Yusop, Z., and Harun, Z. B. (2013). Groundwater vulnerability assessment in the Melaka state of Malaysia using DRASTIC and GIS techniques. *Environ. Earth Sci.* 70, 2293–2304. doi: 10.1007/s12665-013-2360-9

Aller, L., Lehr, J., Petty, R., Bennett, T., and Hackett, G. (1987). DRASTIC: A standardized system for evaluating groundwater pollution potential using hydrogeologic settings. *Nat. Water Well Assoc.* 29, 23–37. doi: 10.17491/jgsi/1987/290112

Alley, W. M. (Ed.) (1993). Regional ground-water quality. New York, NY: John Wiley & Sons.

Awawdeh, M., Obeidat, M., and Zaiter, G. (2014). Groundwater vulnerability assessment in the vicinity of Ramtha wastewater treatment plant, North Jordan. *Appl. Water Sci.* 5, 321–334. doi: 10.1007/s13201-014-0194-6

Babiker, K. I. S., Mohamed, M. A., Hiyama, T., and Kato, K. (2005). A GIS-based DRASTIC model for assessing aquifer vulnerability in Kakamigahara Heights, Gifu prefecture, Central Japan. *Sci. Total Environ.* 345, 127–140. doi: 10.1016/j.scitotenv.2004.11.005

Baghapour, M. A., Nobandegani, A. F., Talebbeydokhti, N., Bagherzadeh, S., Nadiri, A. A., Gharekhani, M., et al. (2016). Optimization of DRASTIC method by artificial neural network, nitrate vulnerability index, and composite DRASTIC models to assess groundwater vulnerability for unconfined aquifer of shiraz plain, Iran. *J. Environ. Health Sci. Eng.* 14:13. doi: 10.1186/s40201-016-0254-y

Chitsazan, Y. M., &. Akhtari, Y. (2009). A GIS-based DRASTIC model for assessing aquifer vulnerability in Kherran plain, Khuzestan, Iran. *Water Resour. Manag.*, 23, 1137–1155, doi: 10.1007/s11269-008-9319-8

Danielopol, J., Griebler, C., Gunatilaka, A., Notenboom, J., Griebler, C., and Gunatilaka, A. (2003). Present state and future prospects for groundwater ecosystems. *Environ. Conserv.* 30, 104–130. doi: 10.1017/S0376892903000109

Das, N., Ohri, A., Agnihotri, A. K., Omar, P. J., and Mishra, S. (2020). Wetland dynamics using geo-spatial technology. *Adv. Water Res. Eng. Manage. Select Proc. TRACE* 39, 237–244. doi: 10.1007/978-981-13-8181-2_18

Daud, S. J., Nafees, M., Ali, S., Rizwan, M., Bajwa, R. A., and Shakoor, M. B. (2017). Drinking water quality status and contamination in Pakistan. *Biomed. Res. Int.* 2017, 1–18. doi: 10.1155/2017/7908183

Davis, A. D., Long, A. J., and Wireman, M. (2002). KARSTIC: a sensitivity method for carbonate aquifers in karst terrain. *Environ. Geol.* 42, 65–72. doi: 10.1007/s00254-002-0531-1

Dixon, B. (2005). Applicability of neuro-fuzzy techniques in predicting ground water vulnerability: a sensitivity analysis. *J. Hydrol.* 309, 17–38. doi: 10.1016/j.jhydrol.2004.11.010

EPA (1985). Compilation of air pollution emission factors, AP-42. New York, NY: US Environmental Protection Agency.

Farid, H. U. (2019). Assessing seasonal and long-term changes in groundwater quality due to over-abstraction using geostatistical techniques. *Environ. Earth Sci.* 78:386. doi: 10.1007/s12665-019-8373-2

Feola, G., Lerner, A. M., Jain, M., Joseph, M., Montefrio, F., and Nicholas, K. A. (2015). Researching farmer behavior in climate change adaptation and sustainable agriculture: lessons learned from five case studies. *J. Rural. Stud.* 39, 74–84. doi: 10.1016/j.jrurstud.2015.03.009

Fortin, M., Thomson, K., and Edwards, G. (1997). The role of error propagation for integrating multisource data within spatial models: The case of the DRASTIC groundwater vulnerability model. London: Earth Surface Remote Sensing, 358–361.

Fritch, T., Yelderman, J. C., and Arnold, J. G. (2000). An aquifer vulnerability assessment of the Paluxy aquifer, Central Texas, USA, using GIS and a modified DRASTIC approach. *J. Environ. Manag.* 25, 337–345.

Ghosh, A., Tiwari, A. K., and Das, S. (2015). A GIS based DRASTIC model for assessing groundwater vulnerability of Katri watershed, Dhanbad, India. *Modeling Earth Systems Environment* 1:2. doi: 10.1007/s40808-015-0009-2

Guler, C., and Ali, M. (2013). Assessment of groundwater vulnerability to nonpoint source pollution in a Mediterranean coastal zone Mersin, Turkey under conflicting land use practices. *Ocean Coastal Manage.* 71, 141–152. doi: 10.1016/j.ocecoaman.2012.10.010

Gupta, N., Mahato, P. K., Patel, J., Omar, P. J., and Tripathi, R. P. (2022a). Understanding trend and its variability of rainfall and temperature over Patna (Bihar). *Curr. Directions Water Scarcity Res.* 7, 533–543. doi: 10.1016/B978-0-323-91910-4.00030-3

Gupta, N., Patel, J., Gond, S., Tripathi, R. P., Omar, P. J., and Dikshit, P. K. S. (2022b). Projecting future maximum temperature changes in river Ganges Basin using observations and statistical downscaling model (SDSM). River dynamics and flood hazards: Studies on risk and mitigation. Singapore: Springer Nature Singapore, 561–585.

Hatiye, S. D., Hari Prasad, K. S., Ojha, C. S., and Adeloye, A. J. (2016). Estimation and characterization of deep percolation from rice and berseem fields using lysimeter experiments on sandy loam soil. *J. Hydrol. Eng.* 21:05016006. doi: 10.1061/(ASCE)HE.1943-5584.0001365

Hearne, G., Wireman, M., Campbell, A., Turner, S., and Ingersoll, G. (1992). Vulnerability of the uppermost ground water to contamination in the greater Denver area. New York, NY: US Geological Survey, Water-Resources Investigations Report.

Huan, H., Wang, J., and Teng, Y. (2012). Science of the total environment assessment and validation of groundwater vulnerability to nitrate based on a modified DRASTIC model: a case study in Jilin City of Northeast China. *Sci. Total Environ.* 440, 14–23. doi: 10.1016/j.scitotenv.2012.08.037

Jama, R., Ikram, M., and Khan, K. (2018). Physicochemical properties of soil and water along Haro River and Khanpur dam, Haripur, Pakistan. *Int. J. Econ. Environ. Geol.* 9, 54–61.

Jamil, H., Akif, M., Khan, F., Shah, N. U., Nabi, E. U., Haris, M., et al. (2023). Socio-economic analysis of beekeeping: A case study of District Karak, Bannu, and Kohat. *Journal of Xi'an Shiyou University, Natural Science Edition*, 19, 1159–1169.

Jang, W., Engel, B., Harbor, J., and Theller, L. (2017). Aquifer vulnerability assessment for sustainable groundwater management using DRASTIC. *Water* 9:792. doi: 10.3390/w9100792

Javed, T., Sarwar, T., Ullah, I., Ahmad, S., and Rashid, S. (2019). Evaluation of groundwater quality in district Karak Khyber Pakhtunkhwa, Pakistan. *Water Sci.* 33, 1–9. doi: 10.1080/11104929.2019.1626630

Jin, S., and Ray, C. (2014). Using fuzzy logic analysis for siting decisions of infiltration trenches for highway runoff control. *Sci. Total Environ.* 493, 44–53. doi: 10.1016/j.scitotenv.2014.05.121

Jodhani, K. H., Gupta, N., Parmar, A. D., Bhavsar, J. D., Patel, H., Patel, D., et al. (2024). Synergizing google earth engine and earth observations for potential impact of land use/land cover on air quality. *Results Eng.* 22:102039. doi: 10.1016/j.rineng.2024.102039

Kahlown, M. A., Majeed, A., Ashraf, M., and Tahir, M. A. (2005). Drinking water quality in Pakistan: a case study of Islamabad and Rawalpindi cities. Pakistan Council of Research in Water Resources, Islamabad, Pakistan, 245–253.

Kaliraj, S., Chandrasekar, N., Peter, T., Selvakumar, S., and Magesh, N. (2014). Mapping of coastal aquifer vulnerable zone in the south west coast of Kanyakumari, South India, using GIS-based DRASTIC model. *Environ. Monit. Assess.* 187:1. doi: 10.1007/s10661-014-4073-2

Khan, A., Ahmad, S., and Noman, M. (2015). Sustainability of groundwater resources in semi-arid regions using integrated hydrological modeling and remote sensing: a case study from Pakistan. *Environ. Earth Sci.* 74, 4443–4456. doi: 10.1007/s12665-015-4641-3

Khan, A., Hassan, M., and Rasheed, M. (2021a). Evaluation of groundwater quality and vulnerability to contamination in the Lahore region of Pakistan. *Environ. Earth Sci.* 80:438. doi: 10.1007/s12665-021-08904-0

Khan, R., Islam, S., and Singh, R. (2016). Methods of estimating groundwater recharge. *Int. J. Eng. Assoc.* 5, 1047–1057.

Khan, A., Naeem, M., Zekker, I., Arian, M. B., Michalski, G., Zeeshan, S., et al. (2021b). Multivariate statistical analysis of heavy metals and physico-chemical parameters in the groundwater of Karak District, Khyber Pakhtunkhwa, Pakistan. *Proc. Estonian Acad. Sci.* 70, 297–306. doi: 10.3176/proc.2021.3.08

Khatri, S. N., &. Tyagi, S. (2015). Influences of natural and anthropogenic factors on surface and groundwater quality in rural and urban areas. *Front. Life Sci.*, 8, 23–39, doi: 10.1080/21553769.2014.933716

Khattak, N. U., Khan, M. A., Shah, M. T., and Ali, N. (2014). Radon concentration in drinking water sources of the region adjacent to a tectonically active Karak thrust, southern Kohat plateau, Khyber Pakhtunkhwa, Pakistan. *J. Radioanal. Nucl. Chem.* 302, 315–329. doi: 10.1007/s10967-014-3257-0

Knox, R. C., Sabatini, D. A., and Canter, L. W. (1993). Subsurface transport and fate processes. New York, NY: Lewis Publishers.

Kozłowski, M., and Sojka, M. (2019). Applying a modified DRASTIC model to assess groundwater vulnerability to pollution: a case study in Central Poland. *Pol. J. Environ. Stud.* 28, 1223–1231. doi: 10.15244/pjoes/84772

Kumar, A., and Pramod Krishna, A. (2019). Groundwater vulnerability and contamination risk assessment using GIS-based modified DRASTIC-LU model in hard rock aquifer system in India. *Geocarto Int.* 35, 1149–1178. doi: 10.1080/10106049.2018.1557259

Kumar, S. K., Rammohan, V., Sahayam, J. D., and Jeevanandam, M. (2009). Assessment of groundwater quality and hydrogeochemistry of Manimuktha River basin, Tamil Nadu, India. *Environ. Monitor. Assessment* 159, 341–351. doi: 10.1007/s10661-008-0633-7

Kumar, P., Thakur, P., Bansod, B., and Debnath, S. (2016). Groundwater vulnerability assessment of Fatehgarh Sahib District. Punjab: India International Science Festival (IISF) - Young Scientists' Conclave (YSC).

Kumar, P., Thakur, P., Bansod, B., and Debnath, S. (2017a). Groundwater: a regional resource and a regional governance. *Environ. Dev. Sust.* 20, 1133–1151. doi: 10.1007/s10668-017-9931-y

Kumar, P., Thakur, P., Bansod, B., and Debnath, S. (2017b). Multicriteria evaluation of hydro-geological and anthropogenic parameters for the groundwater vulnerability assessment. *Environ. Monit. Assess.* 189:564. doi: 10.1007/s10661-017-6267-x

Kumar, P., Thakur, P., Bansod, B., and Debnath, S. (2020). Groundwater vulnerability assessment and mapping using DRASTIC model. London: CRC Press.

Kurwadkar, A. S., Kanel, S. R., and Nakarmi, A. (2020). Groundwater pollution: occurrence, detection, and remediation of organic and inorganic pollutants. *Water Environ. Res.* 92, 1659–1668. doi: 10.1002/wer.1415

Li, Y., Li, J., Chen, S., and Diao, W. (2012). Establishing indices for groundwater contamination risk assessment in the vicinity of hazardous waste landfills in China. *Environ. Pollut.* 165, 77–90. doi: 10.1016/j.envpol.2011.12.042

Li, R., and Merchant, J. W. (2013). Modeling vulnerability of groundwater to pollution under future scenarios of climate change and biofuels-related land use change: a case study in North Dakota, USA. *Sci. Total Environ.* 447, 32–45. doi: 10.1016/j.scitotenv.2013.01.011

Madsen, E. L. (1995). Impacts of agricultural practices on subsurface microbial ecology. *Adv. Agron.* 54, 1–67. doi: 10.1016/S0065-2113(08)60897-4

Mahmood, B. S. Q., Baig, S. A., Nawab, B., Shafqat, M. N., Pervez, A., &. Zeb, B. S. (2011). Development of low cost household drinking water treatment system for the earthquake affected communities in northern Pakistan. *Desalination*, 273, 316–320. doi: 10.1016/j.desal.2011.01.052

Maqsoom, A., Aslam, B., Khalil, U., Ghorbanzadeh, O., Ashraf, H., Faisal Tufail, R., et al. (2020). A GIS-based DRASTIC model and an adjusted DRASTIC model (DRASTICA) for groundwater susceptibility assessment along the China–Pakistan economic corridor (CPEC) route. *ISPRS Int. J. Geo Inf.* 9:332. doi: 10.3390/ijgi9050332

Mishra, R. K. (2023). Fresh water availability and its global challenge. *Br. J. Multidisciplinary Adv. Stu.* 4, 1–78. doi: 10.37745/bjmas.2022.0208

Mogaji, K. A., Lim, H. S., and Abdullah, K. (2013). Modeling groundwater vulnerability prediction using geographic information system GIS-based ordered weighted average OWA method and DRASTIC model theory hybrid approach. *Arab. J. Geosci.* 7, 5409–5429. doi: 10.1007/s12517-013-1163-3

Mohan, C., Western, A. W., Wei, Y., and Saft, M. (2018). Predicting groundwater recharge for varying land cover and climate conditions. A global meta-study. *Hydrol. Earth Syst. Sci.* 22, 2689–2703. doi: 10.5194/hess-22-2689-2018

Navulur, K. C. S., and Engel, B. A. (1998). Groundwater vulnerability assessment to non-point source nitrate pollution on a regional scale using GIS. *Trans. ASAE* 41, 1671–1678. doi: 10.13031/2013.17343

Nawafleh, A., Awawdeh, M., and Salameh, E. (2011). Assessment of groundwater vulnerability to contamination in Irbid governorate, North Jordan. *DIRASAT* 38, 122–133.

Neshat, A. R., Pradhan, B., and Dadras, M. (2014). Groundwater vulnerability assessment using an improved DRASTIC method in GIS. *Resour. Conserv. Recycl.* 86, 74–86. doi: 10.1016/j.resconrec.2014.02.008

Nurfahasdi, S. M., Zega, A. Y., Silalahi, A. M. E., Singh, D. R., and Babayev, A. (2023). Mapping groundwater vulnerability using drastic method. *E3S Web Conf.* 434:03019. doi: 10.1051/e3sconf/202343403019

Pacheco, F. A. L., Pires, L. M. G. R., Santos, R. M. B., and Fernandes, L. F. S. (2015). Factor weighting in DRAS-TIC modeling. *Sci. Total Environ.* 505, 474–486. doi: 10.1016/j.scitotenv.2014.09.092

Piscopo, G. (2001). *Groundwater vulnerability map explanatory notes—Castlereagh Catchment*. NSW Department of Land and Water Conservation.

Qadir, A., Ahmad, Z., et al. (2016). A spatio-temporal three-dimensional conceptualization and simulation of Dera Ismail Khan alluvial aquifer in visual MODFLOW: a case study from Pakistan. *Arab. J. Geosci.* 9:2069. doi: 10.1007/s12517-015-2069-z

Rahman, A. (2008). A GIS based DRASTIC model for assessing groundwater vulnerability in shallow aquifer in Aligarh, India. *Applied Geography* 28, 32–53. doi: 10.1016/j.apgeog.2007.07.008

Rajput, H., Goyal, R., and Brighu, U. (2020). Modification and optimization of DRASTIC model for groundwater vulnerability and contamination risk assessment for Bhiwadi region of Rajasthan, India. *Environ. Earth Sci.* 79:8874. doi: 10.1007/s12665-020-8874-z

Rasool, A., Saeed, S., and Shah, R. (2020). Water crisis and its impact on the socio-economic condition of local people of district Karak, Khyber Pakhtunkhwa, Pakistan. *Islamabad J. Soc. Sci.* 1, 39–50.

Richts, M. A, Struckmeier, W. F, and Zaepke, H. (2011). "WHYMAP and the groundwater resources map of the world 1: 25,000,000," in *Sustaining Groundwater Resources: A Critical Element in the Global Water Crisis*, 159–173.

Saha, F. D., & Alam, F. (2014). Groundwater vulnerability assessment using DRASTIC and pesticide DRASTIC models in intense agriculture area of the Gangetic plains, India. *Environ. Monit. Assess.*, 186, 8741–8763, doi: 10.1007/s10661-014-4041-x

Secunda, S., Collin, M., and Melloul, A. (1998). Groundwater vulnerability assessment using a composite model combining DRASTIC with extensive agricultural land use. *Environ. Manag.* 54, 39–57.

Sener, E., and Davraz, A. (2013). Assessment of groundwater vulnerability based on a modified DRASTIC model, GIS and an analytic hierarchy process AHP method: the case of Egirdir Lake basin Isparta, Turkey. *Hydrogeol. J.* 21, 701–714. doi: 10.1007/s10040-012-0947-y

Shabbir, R., and Ahmad, S. S. (2016). Water resource vulnerability assessment in Rawalpindi and Islamabad, Pakistan using analytic hierarchy process (AHP). *J. King Saud Univ. Sci.* 28, 293–299. doi: 10.1016/j.jksus.2015.09.007

Shahzad, S. M., Jianxin, L., Shahzad, A., Raza, M. S., Ya, S., and Meryem, F. (2018). Groundwater potential zone identification in unconsolidated aquifer using geophysical techniques around tarbela ghazi, district haripur, Pakistan. *International Journal of Geological and Environmental Engineering*, 12, 475–482.

Spalding, R., and Exner, M. (1993). Occurrence of nitrate in groundwater–a review. *J. Environ. Qual.* 22, 392–402. doi: 10.2134/jeq1993.00472425002200030002x

Srivastava, S., Omar, P. J., Shekhar, S., and Gupta, S. (2023). Study of acidic air pollutant (SO2 and NO2) tolerance of microalgae with sodium bicarbonate as growth stimulant. *AQUA—Water Infrastr. Ecosyst. Soc.* 72, 739–749. doi: 10.2166/aqua.2023.013

Tan, M., and Duan, Z. (2017). Assessment of GPM and TRMM precipitation products over Singapore. *Remote Sens.* 9:720. doi: 10.3390/rs9070720

UNDESA and UNECLAC (2015). Water for a sustainable World. Santiago: UNDESA and UNECLAC.

USEPA (1994). An determination of metals and trace elements in water and wastes by inductively coupled plasma-atomic emission spectrometry. Washington, DC: USEPA.

WHO (Ed.) (2008). World health statistics 2008. Geneva: World Health Organization.

Wu, W., Yin, S., Liu, H., and Chen, H. (2014). Groundwater vulnerability assessment and feasibility mapping under reclaimed water irrigation by a modified DRASTIC model. *Water Resour. Manag.* 28, 1219–1234. doi: 10.1007/s11269-014-0536-z

Yin, L., Zhang, E., Wang, X., Wenninger, J., Dong, J., Guo, L., et al. (2013). A GIS-based DRASTIC model for assessing groundwater vulnerability in the Ordos plateau, China. *Environ. Earth Sci.* 69, 171–185. doi: 10.1007/s12665-012-1945-z

Zhao, X., Yuan, G., Wang, H., Lu, D., Chen, X., and Zhou, J. (2019). Effects of full straw incorporation on soil fertility and crop yield in rice-wheat rotation for silty clay loamy cropland. *Agronomy* 9:133. doi: 10.3390/agronomy9030133

frontiers | Frontiers in Water

TYPE Original Research
PUBLISHED 10 February 2025
DOI 10.3389/frwa.2025.1502169

OPEN ACCESS

EDITED BY
Jahangeer Jahangeer,
University of Nebraska-Lincoln, United States

REVIEWED BY
Balaji Etikala,
Yogi Vemana University, India
Sunitha Vangala,
Yogi Vemana University, India

*CORRESPONDENCE
Hanaa A. Megahed
✉ hanaa.ahmed@narss.sci.eg;
✉ hanaanarss@yahoo.com
Antonio Scopa
✉ antonio.scopa@unibas.it

RECEIVED 26 September 2024
ACCEPTED 20 January 2025
PUBLISHED 10 February 2025

CITATION
Megahed HA, Farrag AE-HA, Mohamed AA, Darwish MH, AbdelRahman MAE, El-Bagoury H, D'Antonio P, Scopa A and Saad MAA (2025) GIS-based modeling and analytical approaches for groundwater quality suitability for different purposes in the Egyptian Nile Valley, a case study in Wadi Qena. *Front. Water* 7:1502169. doi: 10.3389/frwa.2025.1502169

GIS-based modeling and analytical approaches for groundwater quality suitability for different purposes in the Egyptian Nile Valley, a case study in Wadi Qena

Hanaa A. Megahed[1]*, Abd El-Hay A. Farrag[2], Amira A. Mohamed[2], Mahmoud H. Darwish[3], Mohamed A. E. AbdelRahman[4], Heba El-Bagoury[5], Paola D'Antonio[6], Antonio Scopa[6]* and Mansour A. A. Saad[7]

[1]Division of Geological Applications and Mineral Resources, National Authority for Remote Sensing and Space Sciences (NARSS), Cairo, Egypt, [2]Geology Department, Faculty of Science, Assiut University, Assiut, Egypt, [3]Geology Department, Faculty of Science, New Valley University, El Kharga, Egypt, [4]Division of Environmental Studies and Land Use, National Authority for Remote Sensing and Space Sciences (NARSS), Cairo, Egypt, [5]Geography Department, Faculty of Arts, Port Said University, Port Said, Egypt, [6]Dipartimento di Scienze Agrarie, Forestali, Alimentari ed Ambientali (DAFE), Università degli Studi della Basilicata, Potenza, Italy, [7]Higher Institute of Literary Studies, Higher Institutes in King Mariout (KMA), Alexandria, Egypt

Availability in Egypt is minimal due to a real restriction on the quantity and quality of acceptable water; it is also increasingly in demand, particularly since the reduction in the share in the Nile following the construction of the Renaissance Dam in Ethiopia. At the same time, the need for water increases due to population growth, industrial development and the cultivation of desert land. The country depends significantly on its water supply on the groundwater. Wadi Qena represents one of the most promising valleys, on which the government depends for land reclamations and developments. This study aims to assess groundwater quality for drinking and irrigation purposes by integrating quantitative analyses and GIS techniques. To achieve this goal, 17 groundwater samples were collected from the Quaternary and Nubian aquifer from the middle and southern part of the Wadi. Chemical analysis of the major cations and anions was carried out at Assuit's Regional Soil Fertility Laboratory. Maps of chemical variables are created using statistical tools by combining observations with interpolation models that can incorporate simple process relations. Major ions, total salinity, Na%, SAR, EC, RSC, PI, MH, KR, SSP, TH, and Cl^- were used to assess the groundwater for drinking and irrigation purposes. Schoeller's, Stiff's, and Piper's, diagrams were used to determine the hydrochemical facies of groundwater in the area. The hydrochemical composition reflects that Sodium–Chloride is the main water type in the study area, and in the sequence of the cations and anions, 100% of the groundwater samples are in the order $Na^+ > Ca^{2+} > Mg^{2+}/Cl^- > SO_4^{2-} > HCO_3^-$. Comparative analysis against standard quality guidelines indicated that most groundwater samples exceeded safe levels for major constituents, TDS, TH, pH, and EC, making them unsuitable for drinking but potentially suitable for irrigation of high salt-tolerant crops. The results of hydrochemical analysis maps and analytical diagrams of groundwater samples revealed that the water was characterized by natural to alkali and the total dissolved solids (TDS) increasing from the Nubian to Quaternary and high ranges of sodium absorption (SAR). The GIS-spatial model indicated that the southwest

part and northwest part represented the highest and lowest suitability, respectively, for drinking water purposes. In contrast, the northwest part and southwest parts represented the highest and lowest suitability, respectively, for irrigation purposes. This is confirmed by the values of Na^+, SAR, EC, RSC, PI, MH, KR, SSP, TH, and Cl^-. The values of Na^+, SAR, EC, RSC, PI, MH, KR, SSP, TH, and Cl confirm this. The study lists corrective measures to improve groundwater quality using monitoring systems, efficient irrigation techniques, localized desalination, artificial recharge projects, stricter waste management and agricultural policies that will minimize sources of contamination. This study's proposed model offers a promising and potentially universal tool for water quality assessment in the Nile basin and similar settings worldwide with the innovative model presented in this study.

KEYWORDS

hydrogeochemistry, modeling, groundwater assessment, GIS, Wadi Qena, Egypt

1 Introduction

Groundwater plays a crucial role in the Earth's hydrological cycle and is a valuable resource that must be conserved. Availability of water of acceptable quality in Egypt is limited and getting even more restricted where the country relies heavily on groundwater with increasing population growth, industrial development, and the cultivation of desert lands. Wadi Qena, located in the Egyptian Eastern Desert, is a vast valley extending from the town of Qena south to the Galala Plateau in the north, west of the Gulf of Suez. The main objective of this research is to assess groundwater quality for various purposes using Geographic Information System (GIS) techniques. Like the study area, arid-semi-arid regions rely heavily on groundwater for their water supply. The chemical properties, water quality characteristics, and evolutionary patterns of groundwater are closely related to the surrounding environment. They are mainly influenced by hydrogeological conditions, water-rock interactions, and other natural factors, as well as human activities and misuse of groundwater (Jiang et al., 2015; Ren and Zhang, 2020; Xiao et al., 2023; Gong et al., 2023). Human actions, dissolution of soluble salts, evaporation and weathering of silicate minerals are the main influences on the development of groundwater (Yidana et al., 2018; Pazand et al., 2018; Metwaly et al., 2022). Assessing groundwater quality and monitoring groundwater levels is essential for effective management of groundwater sources (Metwaly et al., 2022; Haghizadeh et al., 2017; Honarbakhsh et al., 2019). It is crucial to preserve groundwater resources through innovative approaches, especially considering the increasing global population and scarcity of fresh water. Given its diverse applications, water is recognized as a precious natural good, and the provision of clean and accessible water is fundamental for all individuals (Ferreira dos Santos and Cunha-Santino, 2015). The increase in population, the objectives of agricultural, and industrial progress and the growing needs for water could potentially lead to the depletion of water reserves and the degradation of their quality (Simonetti et al., 2019). Groundwater quality can be influenced by a multitude of factors, including geological formations that contain water, human activities, environmental conditions, agricultural practices, irrigation methods, and the use of fertilizers in agriculture (Belkhiri et al., 2010; Darwish and Galal, 2020; Galal and Darwish, 2022; El-Rawi et al., 2020). The increasing demand for water has necessitated an immediate need for water as a supplement for various purposes. This issue has received increased attention through the implementation of new reclamation initiatives and development efforts, particularly in regions characterized by aridity and semi-aridity (Darwish et al., 2023; AbdelRahman et al., 2018). Groundwater hydrochemistry is primarily influenced by processes such as rock weathering, mineral dissolution, and ion exchange (Yuan et al., 2024).

The integration of modeling software and a geographic information system (GIS) facilitates the creation of a holistic representation of groundwater quality (Mohamaden et al., 2024; Wang et al., 2008; Megahed et al., 2023). The use of a finite element model in conjunction with numerical modeling of groundwater flows can be very effective in assessing the influence of climate on cropping patterns and optimizing irrigation water management (Sanaullah et al., 2023). Groundwater chemical constituents can serve as indicators of water quality attributes and provide insight into the chemical composition of groundwater in the designated research region (Kreins et al., 2015). The major factors contributing to soil fertility, optimal plant development, and abundant agricultural yield in each region can be attributed mainly to the use of superior quality irrigation water (Giri et al., 2021).

The hydrochemical composition of groundwater is influenced by both sedimentary conditions and human activities (Mester et al., 2022). Groundwater pollution is mainly caused by agricultural activities, industrial discharges, domestic wastewater and overexploitation, which contribute to the degradation of water quality. Among these factors, agricultural runoff represents a significant contributor to contamination. Another concern is the presence of hazardous disinfection byproducts (DBPs) that can occur during the disinfection process. Finally, the overall environmental impact must also be taken into consideration when assessing the quality of drinking water (Han and Currell, 2017; Srivastav et al., 2020). Water quality management requires continuous assessment and sustained monitoring to ensure its safe use for various purposes (Wali et al., 2022). Many analytical techniques are used to analyze groundwater evolution processes. Various analytical methods are used to characterize groundwater evolution processes (Zhang et al., 2022; Abu Salem et al., 2022).

Application of water quality entropy weight index (EWQI) along with multivariate statistical methods proves to be very beneficial for water quality assessment and improvement of monitoring approaches (Han et al., 2024). Sustainable land use planning and appropriate agricultural management practices are essential for establishing new communities, particularly in arid

regions. A comprehensive assessment of soil and irrigation water characteristics is essential, as the quantitative parameters used can be identified through monitoring temporal variations in arid areas and assessing water properties in relation to management strategies and environmental risks (Megahed et al., 2022). Assessing groundwater quality in desert systems poses a significant challenge, primarily due to the paucity of hydrological data and the isolated nature of desert oases. To deal with future obstacles faced by arid and semi-arid regions, the use of a geographic information system (GIS) model becomes essential (Megahed et al., 2023).

This research aims to assess groundwater quality in Wadi Qena, Egypt using GIS techniques. Groundwater quality is influenced by hydrogeological conditions, water-rock interactions, natural factors, human activities, and misuses. The study highlights the importance of continued evaluation and monitoring for safe use. Factors affecting drinking water quality include anthropogenic contaminants, conventional treatment processes, and hazardous disinfection byproducts. Sustainable land use and agricultural management practices are essential for establishing new communities in arid regions.

2 Materials and methods

2.1 Description of the study area

Wadi Qena is one of Egypt's largest wadies, on which the government depends for land reclamations and developments. It is located northeast of Qena city between latitudes 26°00′ and 28°20′N and longitudes 32°00′ and 33°00′E, covering approximately 16,000 km^2. The study area includes the southern part of the Wadi (Figure 1A). Wadi Qena has extreme aridity, with deficient and unpredictable rainfall, high evaporation rates, and high summer temperatures.

Geologically, the area of study from Wadi Qena is formed of a sedimentary succession from base to top: Nubia Sandstone (Pre-Campanian), Quseir Shale (Campanian-Maestrichtian), Duwi

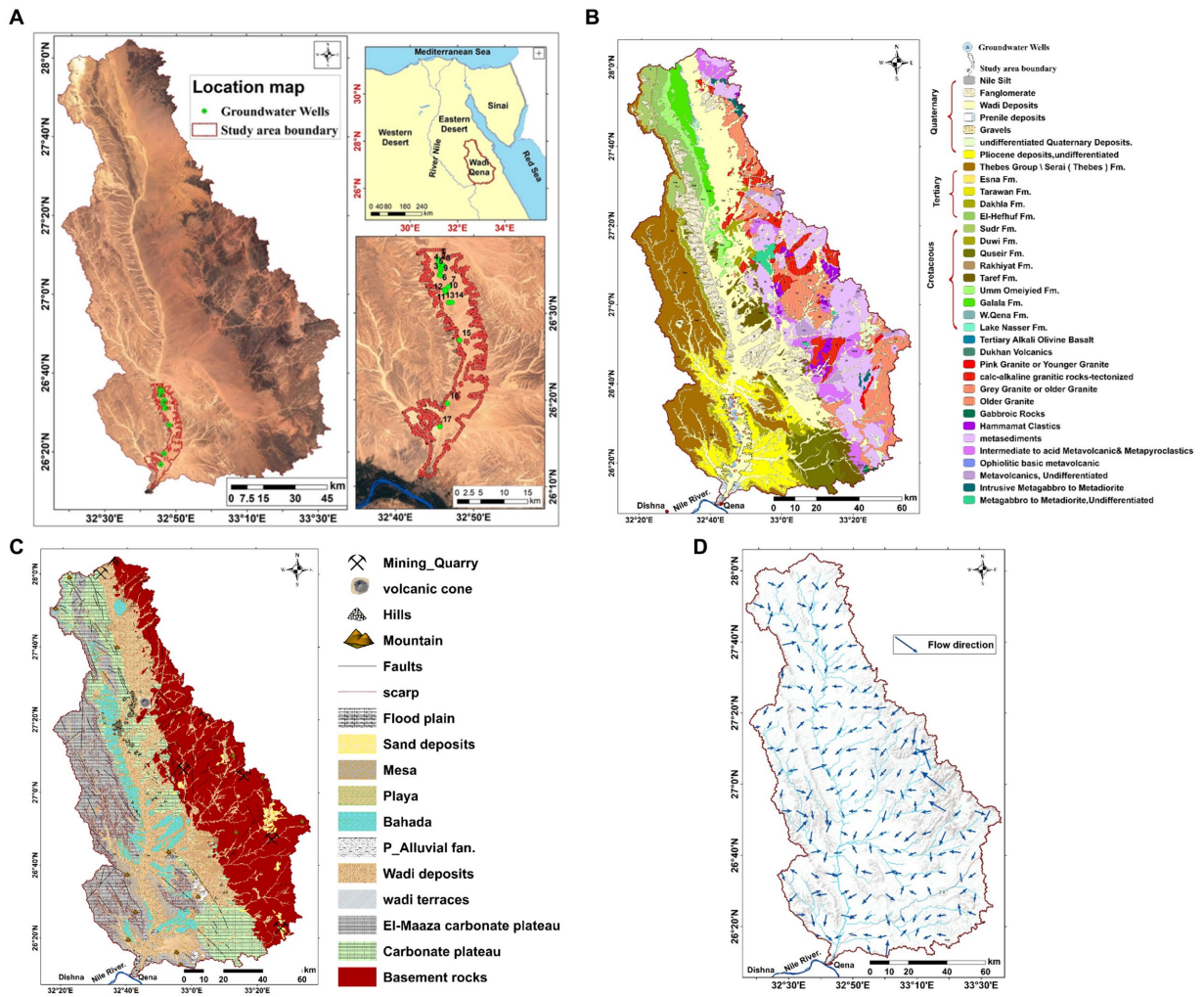

FIGURE 1
(A) Location map with monitoring wells. **(B)** Geological map [Modified after (Conoco, 1987; Egyptian Geological Survey and Mining Authority (EGSMA), 1983; Egyptian Geological Survey and Mining Authority (EGSMA), 2006)]. **(C)** Geomorphological units (derived from topographic map 1:500,000 and Google Earth). **(D)** Slope map indicating groundwater flow direction (derived from DEM, 30 m) of Wadi Qena.

Formation (Maestrichtian), Dakhla Shale (Maestrichtian-Landenian), Tarawan Chalk (Landenian), and Esna Shale (Landenian Early Ypresian) (Figure 1B). The age of different formations was assigned after (Abd El Razik and Razvaliaev, 1972; Faris, 1974). The Nubia Sandstone is overlain by a shaly sequence of Quseir Shale, which is intercalated in its lower part with two phosphorites. The Duwi Formation was composed of three phosphorite beds intercalated with shale, marl, and sandstone, a succession of siliciclastics from Dakhla Shale and Esna Shale divided by the Tarawan Chalk. The Lower Eocene limestone represents the upper part of Esna Shale, which forms the surface of the plateau (Ahmed, 1983). Overall, the study area encompasses the Quaternary in its northwestern part, as well as the Nubian sandstone aquifers, each with different conditions. The shallow Quaternary aquifer, mainly composed of sand and gravel, is very susceptible to contamination because it is quite shallow and well permeable. Groundwater from the deeper Nubian aquifer, mainly composed of sandstone with interbedded shales, causes higher mineralization due to a longer water-rock contact.

The Wadi Qena area has an overall geomorphology comprising several key geomorphological units important in controlling groundwater distribution and quality (Figure 1C). These include the wadi channel and bed, which are predominantly alluvial in nature, consisting of sand, gravel and silt, which serve as a reservoir for the alluvial aquifer recharged by seasonal runoff. Alluvial fans form at the mouths of the tributary channels, where sediments are deposited, contributing to the recharge of the shallow aquifer and providing fertile land for agriculture. The floodplains, covered with fine sediments such as clay and silt, are periodically inundated by the overflow of the wadi, temporarily storing surface water but with limited contribution to groundwater recharge. The Red Sea Mountains are composed of granite and metamorphic rocks, forming a major watershed. It influences drainage patterns and contributes its weathering products to groundwater chemistry. Beneath the alluvial deposits of the southern part of the wadi, the Nubian Sandstone forms a confined aquifer. This is a major source of groundwater for agricultural and drinking purposes, mainly in the deeper layers. All these geomorphic units together contribute to the groundwater dynamics in Wadi Qena; changes in sediment types, permeability, and recharge potential control water quality and quantity. Topography in relation to the elevation gradient and underlying geological structures is one of the major controlling factors that can influence the direction of groundwater flow. Geomorphology and surface features have contributed greatly to groundwater movement in this region. They generally occur downstream from mountainous recharge areas through wadi channels and alluvial fans to discharge areas at lower elevations. The slope map shown in Figure 1D is a good way to visualize the direction of groundwater flow because it graphically represents the gradient of the land surface to which groundwater movement is directly related. The slope map was obtained from DEM data in the study area using GIS techniques. Water generally flows to lower elevation areas and gradually accumulates in aquifers or flows into surface water systems.

Hydrogeologically, Wadi Qena's can be divided into four aquifers: a Quaternary aquifer (QAS), a Nubian sandstone aquifer (NSAS), a fractured limestone aquifer; and a fractured crystalline (basement) aquifer. The QAS and NSAS are considered the most water-bearing aquifers in terms of their thickness and water quantity (Abdel Moneim, 2005). The thickness of the QAS of alluvial deposits varies from place to place in the area; it is formed of sand, gravel, and boulders with depths ranging from a few meters to more than 80 m; the average thickness of the NSAS varies by location and is about 350 m, with a depth reaching 300–500 m underground. The groundwater in this aquifer occurs under confined conditions overlying the impermeable Quseir Shale, and the flow of the groundwater in the NSAS in Wadi Qena is defined to be from the northeast to the southeast (Abdel Moneim et al., 2015). As for the structural area in Wadi Qena, it is preferable to connect the QAS with the NSAS below it (Elewa and Abu El Ella, 2011; Elewa et al., 2000; Elewa et al., 2006).

The research analyzes the hydrogeological situation in the study area using field observations and data. GPS and GIS techniques are used to convert field data into a set of maps that depict groundwater conditions. Rockwork and EXCEL were used to represent hydrochemical data. Seventeen Quaternary and Nubian aquifer samples were collected from water wells scattered throughout the study area. Stakeholders drilled these wells, and their abundance grew in tandem with agricultural activity in the region.

All collection equipment was thoroughly washed with deionized water before and after each collection. Samples were stored in high-density polyethylene bottles that had been previously rinsed with the groundwater to be collected. For consistency, duplicate samples will be collected at each location in June 2024. The variation between each set of duplicates was compared to verify accuracy. Field measurements of pH, electrical conductivity, and temperature were performed using field-calibrated meters to ensure real-time accuracy. Samples were rapidly cooled to 4°C to minimize chemical changes before transport to the laboratory. Chemical analyses were performed in an ISO-certified laboratory using conventional titrimetric, gravimetric, and spectrophotometric methods. Standard solutions were used for this purpose and equipment was calibrated regularly to ensure accuracy. Groundwater samples, as well as blanks, standards and spiked samples, were analyzed to monitor for possible contamination or analytical errors. The IBE was calculated to verify the analytical precision to ensure that it was within the acceptable limit of ±5%. To prevent a change in the partial pressure of CO_2, the samples were packed in clean plastic bottles that were filled with water and contained no air. In Assiut's Regional Soil Fertility Laboratory, water samples were analyzed. CL^-, HCO_3^-, Ca^{2+}, and Mg^{2+} were measured by titration, while SO_4^{2-} was estimated by turbidity, and Na^+ and K^+ were analyzed by flame photometer.

Sodium adsorption ratio (SAR), sodium percentage (Na%), residual sodium carbonate (RSC), soluble sodium percentage (SSP), permeability index (PI), Kelly's ratio (KR), magnesium hazard (MH), and total hardness (TH) are the quality parameters of irrigation (Table 1). By comparing the results and based on the physicochemical analyses with water guideline values, the acceptability of groundwater sources for drinking and agricultural applications will be assessed.

Accordingly, GIS modeling integrated the AHP results using the weighted overlay method to spatially analyze and visualize groundwater quality in the study area. In addition, individual layers were created for each hydrochemical parameter and quality index; therefore, a spatial interpolation technique was applied to fill the gaps in data coverage. The geospatial database built in ArcGIS 9.1 included layers for hydrochemical parameters and quality indices that allowed generating detailed groundwater adequacy maps. These maps are useful for identifying spatial patterns of areas most and least suitable for consumption and irrigation.

According to the methods adopted by Rainwater and Thatcher (1960) and Fishman and Friedman (1989), pH, electrical conductivity (EC), and temperature were measured *in situ* using a portable field kit. Collection of the geological and hydrogeological data of the study area from previous works and internal reports is done. Using a topographic map (scale 1: 100,000) for the preparation of the base map of the studied area, all the graphical representations and maps for the analytical results through creating a geospatial database was built using Arc GIS 9.1 (ESRI, 2006) and Surfer 8 for Windows for analysis the hydrochemical data and visualization of the results.

2.2 Groundwater quality assessment

Various factors were evaluated to assess the suitability of groundwater in the research area for both human consumption and irrigation. The water quality was verified by analyzing its chemical properties against the guidelines set by the Egyptian High-Water Committee (Egypt Standard, 2007) and the World Health Organization (WHO Guidelines, 2004), as shown in Table 2. Other classifications of groundwater suitability for drinking are based on total dissolved solids (TDS) (College of Agricultural Sciences, 2002; Hem, 1970), as listed in Tables 3, 4.

Also, the suitability of water for agriculture depends upon many factors, such as effective salinity hazard, sodium adsorption ratio (SAR) (College of Agricultural Sciences, 2002; US Salinity Laboratory Staff (USSL), 1954), residual sodium carbonate (RSC) (Eaton, 1950), as listed in Tables 5, 6.

TABLE 1 Groundwater quality indices for irrigation.

Index	Mathematical equation	References
SAR	$SAR = Na + /\sqrt{(Ca + Mg)/2}$ all ions in meq L^{-1}	Wilcox (1955)
Na%	$Na\% = Na^{+}+K^{+}/Ca^{2+} + Mg^{2+} + Na^{+} + K^{+} \times 100$	Doneen (1964)
RSC	$RSC = (HCO_3^{-} + CO_3^{2-}) - (Ca^{2+} + Mg^{2+})$ all ions in meq L^{-1}	Richards (1954)
SSP	$SSP = (Na^{+} + K^{+})/(Ca^{2+} + Mg^{2+} + Na^{+} + K^{+}) \times 100$	Wilcox (1955)
PI	$PI = \frac{Na^{+} + \sqrt{HCO_3^{-}}}{Ca^{2\aleph} + Ma^{2} + Na} \times 100$	Doneen (1964)
MH	$MH = \frac{Mg}{(Ca + Mg)} \times 100$	Raghunath (1987)
KR	$KR = \frac{Na +}{(Ca + Mg)} \times 100$	Kelly (1940) and Paliwal (1972)
TH	$TH = 2.497\ Ca^{2+} + 4.115\ Mg^{2+}$ ions in meq L^{-1}	Todd and Mays (2004)

3 Results

3.1 Hydrochemical classification

Rockwork and Excel programs are used to examine the chemical composition of collected samples, with the aim of understanding their hydrochemical properties. The diagram provides a visual representation of the results (Piper, 1944; Stiff, 1951; Schoeller, 1962). The chemical composition of the groundwater in the area was examined using the Schoeller diagram, constructed using Excel software version 2016. By plotting the data on this diagram, a comparison of the major ion analyses, especially for groundwater samples with high salinity, can be facilitated. The resulting chemical data are shown in Figure 2A, with the chemical analysis of the groundwater samples represented in equivalents per million (meq/L). One of the advantages of this diagram over the more commonly used trilinear diagram is that it provides the actual concentrations of the parameters. Major ions are represented on the graph by straight lines connecting the different ions, and if these lines have approximately equal slopes, this indicates an identical relationship between the correlated analyses. According to this diagram, the following general patterns were recognized: $Na^{+} > Cl^{-} > SO_4^{2-} > Ca^{2+} > Mg^{2+} > HCO_3^{-}$, this reflects a high concentration of sodium, chloride, and sulfate ions, indicating that the dominant salts are sodium chloride and sodium sulfate. Several factors can be attributed to these high concentrations of sodium, calcium, magnesium, potassium and other ions in the groundwater of the study area. From a geological perspective, the high ion concentrations in the groundwater could be caused by the dissolution of minerals such as halite, gypsum, calcite, dolomite,

TABLE 2 WHO Guidelines (2004) and Egypt Standard (2007) for drinking water quality.

Parameter		WHO Guidelines (2004)	Egypt Standard (2007)	Present study
Bicarbonate (HCO_3^{-})	mg/L	500	No guideline	24.4–91.5
Calcium (Ca^{2+})		75–200	200	30–100
Chloride (Cl^{-})		250	250	887.5–1,775
Conductivity (EC)	(mS/cm)	No guideline	No guideline	3,600–13,800
Total Hardness (TH)	mg/L	200	500	155.032–390.056
Magnesium (Mg^{2+})		300	150	14.64–34.16
pH	–	6.5–8	6.5–8.5	7.5–8
Potassium (K^{+})	mg/L	12	No guideline	
Sodium (Na^{+})		200	200	690–1,265
Sulfate (SO_4^{2-})		250	250	240–597
Total Dissolved Solids (TDS)		600	1,000	2,304–8,832

10.3389/frwa.2025.1502169

feldspars and micas. Long-term water-rock interaction, especially for deeper aquifers such as the Nubian Sandstone, increases the dissolution of minerals and increases the ion concentration. High evaporation rates in this low-precipitation region tend to further concentrate dissolved ions, mainly sodium and chloride. Anthropogenic activities such as agricultural runoff containing fertilizers and improper disposal of industrial and domestic wastewater add large amounts of potassium and magnesium. The hydrochemical processes involved include cation exchange, whereby sodium replaces calcium and magnesium in the aquifer matrix, reshaping the chemical composition of this groundwater. All these factors therefore combine to explain the variations in ion concentrations observed in the study area.

In the Stiff plot, TDS values of groundwater samples are plotted on the horizontal axes at constant intervals. The plotted dots form a distinctive pattern that reflects the composition of the representative sample. By examining the resulting polygon, we can identify similarities or differences in overall water chemistry. The width of the polygon serves as an approximation of the total ion content. Based on the plotted results, it can be inferred that the proximity of groundwater samples is determined by the prevalence of sodium cations and chloride anions (Figure 2B).

Cations and anions are shown separately in ternary plots in the Piper diagram. The peaks of the anion plot represent sulfate, chloride, and carbonate anions as well as hydrogen carbonate anions, while the peaks of the cation plot represent calcium, magnesium, and sodium as well as potassium cations. These two ternary plots are then projected onto a diamond, which is a mathematical transformation of a graph representing anions (sulfate + chloride/total anions) and cations (sodium + potassium/total cations). Typically, water samples located in the upper triangle exhibit secondary salinity characteristics, where sulfate and chloride levels exceed those of sodium and potassium. Conversely, samples found in the lower triangle indicate primary alkalinity properties, with higher levels of calcium and magnesium than carbonates and bicarbonates. In the current investigation, the anion triangular zone in the Piper diagram reveals that approximately 100% of the groundwater samples are in the chloride zone. On the other hand, the cation triangular area of the Piper diagram shows that all the groundwater samples belong to the sodium and potassium categories. The data represented as a diamond of the Piper diagram indicates that all samples belong to the Sodium–Potassium–Chloride–Sulfate category in the specified area (Figure 2C). The diagrams indicate that the groundwater chemistry of the region is primarily influenced by the dissolution and alteration of silicate and sulfate minerals.

TABLE 3 Classification of water according to its TDS value (Hem, 1985).

TDS values in mg L^{-1}	Water categories	Present study
<1,000	Freshwater	–
From 3,000 to 10,000	Moderately saline water	All samples (100%)
From 10,000 to 35,000	Very saline water	–
>35,000	Brine water	–

TABLE 4 Classification of water according to hardness (Hem, 1970).

Classification	Hardness concentration as $CaCO_3$ mg L^{-1}	Present study
Soft	0–60	–
Moderately hard	61–120	–
Hard	121–180	15 samples (88.23%)
Very hard	≥180	2 samples (11.77%)

3.2 Hadrochemical facies and water types

Based on the levels of cations and anions found in groundwater samples from the research site, the predominant orders of ions and resulting chemical classifications are as follows. The hydrochemical composition indicates that sodium chloride is the main water type in the study area. In terms of cation and anion sequence, all groundwater samples are classified in the order $Na^+ > Ca^{2+} > Mg^{2+} > K^+/Cl^- > SO_4^{2-} > HCO_3^-$, as detailed in Table 7. In the study area, the main water type is sodium chloride, as indicated by the hydrochemical composition. The cations and anions in the groundwater samples follow a specific order, with $Na^+ > Ca^{2+} > Mg^{2+} > K^+/Cl^- > SO_4^{2-} > HCO_3^-$ being the sequence observed in all samples, as presented in Table 7.

TABLE 5 Classification of irrigation water based on SAR values, College of Agricultural Sciences (2002) and US Salinity Laboratory Staff (USSL) (1954).

Level	SAR	Quality	Class	Hazard	Use of water for irrigation	Present study
S1	0–10	Low sodium	Excellent	No harmful effect from sodium	In all types of soil	–
S2	10–18	Medium sodium	Good	Problems on fine texture soils sodium sensitive plants, especially under low-leaching conditions, but could be used on sandy soils with good permeability.	In coarse-texture soils with high permeability and rich in organic matter	–
S3	18–26	High sodium	Fair	Harmful effects could be anticipated in most soils and amendments such as gypsum would be necessary to exchange sodium ions	Requires good drainage and chemical amendments	Wells no. 9, 10, 11 and 17
S4	>26	Very high sodium	Poor	Generally unsatisfactory for irrigation	It is very poor for irrigation and requires low salinity water.	Most samples (Wells no. 1 to 8, and 12 to 16)

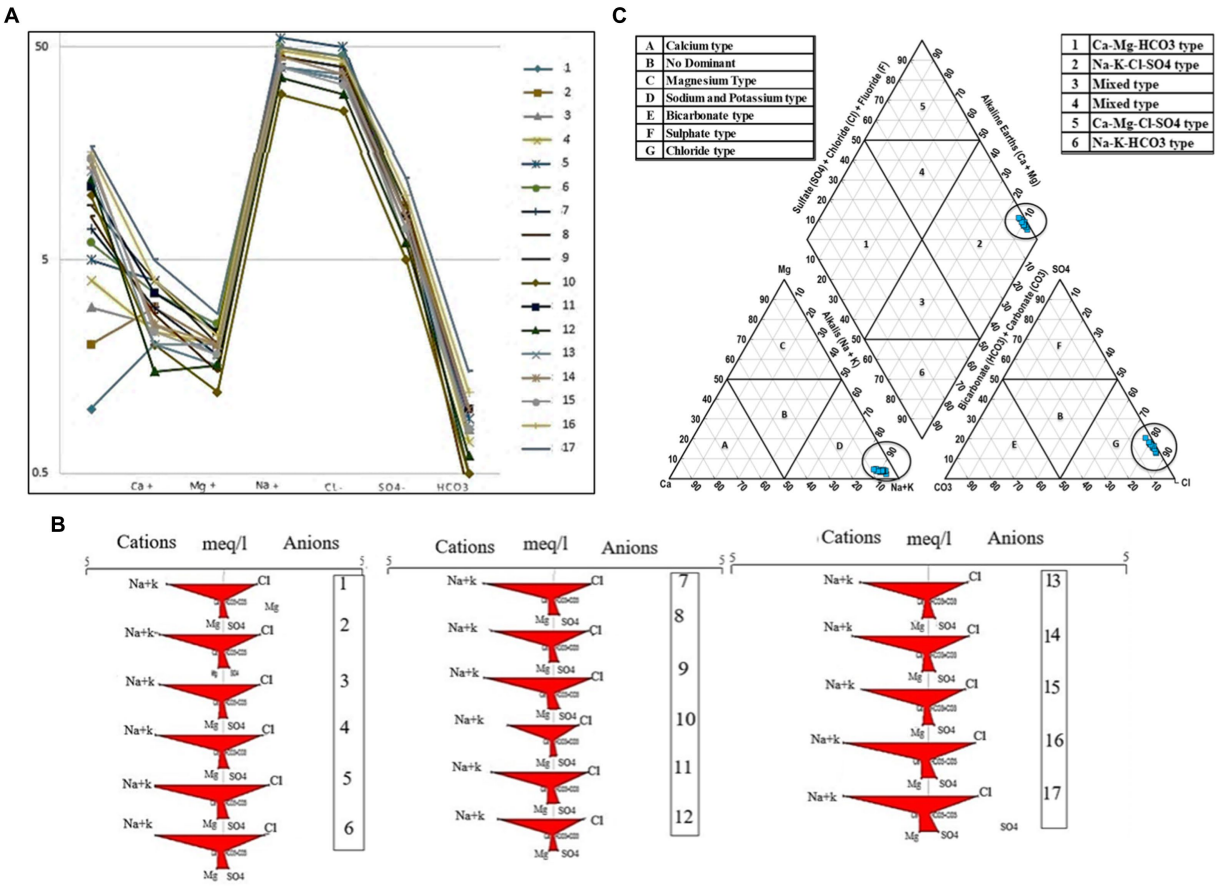

FIGURE 2
(A) Semi-logarithmic representation (Schoeller Diagram). **(B)** Stiff Diagram. **(C)** Piper triangle diagram of groundwater samples in the study area.

TABLE 6 Classification of irrigation water based on RSC values (Eaton, 1950).

RSC	Hazard	Present study
<0	None	All samples (100%)
0–1.25	low, with some removal of calcium and magnesium from irrigation water	–
1.25–2.50	Medium, with appreciable removal of calcium and magnesium from the irrigation water	–
>2.50	High, with most calcium and magnesium removal leaving sodium to accumulate	–

3.3 Groundwater quality

3.3.1 Groundwater quality for drinking purposes

Tables 8, 9 and Figures 3A–C, 4A–C present the results of the analysis performed on groundwater samples, including ion concentrations and distribution maps of the chemical analysis results. These results comply with the standards set by Egyptian regulations and the World Health Organization (WHO) for the quality of drinking water. pH levels are between 7.5 and 8, indicating a slightly acidic to slightly alkaline nature, which corresponds to the recommended pH range of 6.5–8.5 by Egyptian standards and those of the WHO. However, the range of electrical conductivity (EC) values recorded was between 3,600 and 13,800 µS/cm, exceeding the permissible limits for drinking water, as defined by WHO and Egyptian guidelines. The total dissolved solids (TDS) ranged from 2,304 mg/L at well sample no. 8 to 8,832 mg/L at well sample no. 17. The TDS distribution map in the area d of the study reveals an increase toward the southern part of the wadi, with the salinity of the QAS being higher than that of the NSAS. This southward increase in salinity can be attributed to the direction of groundwater flow in this area, indicating the influence of leaching effects from aquifers and potentially continued recharge by precipitation. By the standards set by Egyptian and WHO regulations, none of the groundwater samples analyzed meet acceptable TDS levels for drinking water. Additionally, the total hardness (TH) of groundwater samples exceeds 120 mg/L, making the groundwater unsuitable for drinking. Sodium levels in the area ranged between 690 and 1,265 mg/L (highest in Well 5), exceeding acceptable limits for drinking water. It should be noted that sodium concentrations increased downstream, indicating the presence of water-soluble alkalis. In the QAS, sodium levels steadily increased northward, while in the NSAS, they peaked further south. Calcium concentrations generally remained within drinking water limits, ranging from 40 to 100 mg/L (highest in well 17). Unlike sodium, calcium levels showed an increase from north to south in both aquifers, peaking at the southernmost point. The magnesium content, naturally present in groundwater due to interactions between clays

10.3389/frwa.2025.1502169

TABLE 7 Ion's dominance sequences and groundwater type in the study area.

Sample no.	(%)			(%)			Water type	
	$Na^+ + K^+$	Ca^{2+}	Mg^{2+}	Cl^-	SO_4^{2-}	HCO_3^-		
1	91.7	4.6	3.7	82.6	15.6	1.8	$Na^+ > Ca^{2+} > Mg^{2+} > K^+$/ $Cl^- > SO_4^{2-} > HCO_3^-$	Sodium–Chloride
2	90	6	4	80	18	2		
3	91.3	5.1	3.6	85.5	12.8	1.7		
4	91.8	4.4	3.8	83.2	15.5	1.3		
5	89.7	6.5	3.8	84.9	13.6	1.5		
6	89.3	6.2	4.5	83.6	14.9	1.5		
7	90.4	6	3.6	82.5	16.5	1		
8	90.2	6.4	3.4	82.5	16.5	1		
9	88.3	7.8	3.9	80.3	18.1	1.6		
10	90.4	6	3.6	82	16.4	1.6		
11	87.4	7.6	5	79.5	18.2	2.3		
12	92.1	3.8	4.1	82	16.4	1.6		
13	90.9	4.6	4.5	80	18.2	1.8		
14	91	4.6	4.4	80.4	17.4	2.2		
15	91	5.5	3.5	81	17.2	1.8		
16	89	7.1	3.9	79.3	18.5	2.2		
17	86.5	8.7	4.8	76.9	20.5	2.6		

TABLE 8 Chemical analyses of the groundwater samples in the study area.

Well no.	pH	EC (µS/cm)	TDS (mg/L)	Major cations (mg/L)				Major anions (mg/L)			TH (mg/L)
				Na^+	K^+	Ca^{2+}	Mg^{2+}	HCO_3^-	Cl^-	SO_4^{2-}	
1	7.8	6,500	4,160	920	4	40	19.52	48.8	1,313.5	336	180.032
2	7.8	9,000	5,760	1,035	5	60	24.4	61	1,420	432	250.04
3	7.5	6,000	3,840	1,035	5	50	21.96	48.8	1,420	288	214.913
4	7.6	6,000	3,840	1,104	5.1	46	24.4	42.7	1,526.5	384	215.04
5	8	11,500	7,360	1,265	5.4	80	28.06	54.9	1,775	384	315.046
6	7.7	7,500	4,800	1,150	7.9	70	30.5	48.8	1,597.5	384	300.05
7	7.8	5,200	3,328	1,035	11.3	60	21.96	30.5	1,420	384	240.036
8	7.6	3,600	2,304	920	10.4	56	18.3	24.4	1,242.5	336	215.03
9	7.8	7,300	4,672	1,035	7.9	80	24.4	48.8	1,420	432	300.04
10	7.6	3,700	2,545	690	9.9	40	14.64	30.5	887.5	240	160.024
11	7.8	8,000	5,120	920	8.8	70	28.06	61	1,242.5	384	290.046
12	7.7	4,500	2,880	828	9	30	19.52	36.6	1,065	288	155.032
13	7.9	6,700	4,288	920	8.5	40	24.4	48.8	1,242.5	384	200.04
14	7.8	6,800	4,352	1,035	8	50	24.4	61	1,313.5	384	225.04
15	7.6	5,000	3,200	920	6.5	46	21.96	48.8	1,171.5	336	205.036
16	7.8	11,000	7,040	1,150	11.1	80	26.84	73.2	1,526.5	480	310.044
17	8	13,800	8,832	1,150	12.5	100	34.16	91.5	1,597.5	576	390.056

and minerals, varied between 14.64 and 34.16 mg/L (highest in well 17). It is interesting to note that the distribution of magnesium followed the direction of the flow, increasing toward the north in the QAS and toward the south in the NSAS. Bicarbonate levels were within the acceptable range for drinking water, ranging from 24.4 to 91.5 mg/L (highest in Well 17), with a southward increase observed in both aquifers and a general decrease in the northern region. Chloride levels in the area ranged from 887.5 mg/L (well no. 10) to 1775 mg/L (well no. 5), while sulfate levels ranged from 240 mg/L (well no. 10) to 576 mg/L (well no. 17). Chloride concentrations showed a clear trend: increasing southward in the QAS and northward in the NSAS. Sulfate content followed a similar trend, reflecting the salinity levels of each

TABLE 9 The maximum acceptable concentration for drinking water according to WHO Guidelines (2004) and Egypt Standard (2007).

Constituent		World Health Organization (WHO Guidelines, 2004)	Egyptian maximum permissible limits (Egypt Standard, 2007)	Present study
pH		6.5–8.5	6.5–8.5	7.5–8
EC	mS/cm	1.5	1.5	3,600–13,800
TDS	mg/L	1,000	1,000	2,304–8,832
Na^+		200	200	690–1,265
K^+		12	12	12.5–4
Ca^+		200	200	30–100
Mg^{2+}		150	150	14.64–34.16
Cl-		250	250	887.5–1,597.5
SO_4^{2-}		400	–	240–597
HCO_3^-		200	250	24.4–91.5

aquifer. According to standard limits for drinking water, all groundwater samples from the study area are deemed unfit for consumption. Dissolution and weathering of silicate and sulfate minerals in the study area are the main processes that determine groundwater chemistry. Silicate minerals, mainly feldspar and quartz, and sulfate minerals such as gypsum are abundant in these geological formations: sandstone, shale, and carbonate rocks. Weathering of feldspar, a potassium and aluminum silicate, contributes K^+, Ca^{2+}, and Mg^{2+} ions to the groundwater, resulting in high concentrations of these elements and increased water hardness. Similarly, dissolution of gypsum ($CaSO_4$) and other sulfate minerals in the Nubian aquifer leads to high levels of calcium (Ca^{2+}) and sulfate (SO_4^{2-}), further influencing water mineralization. These processes lead to higher TDS and hardness, making the water less suitable for drinking but possibly suitable for irrigation, particularly for salt-tolerant crops. Greater interaction of groundwater with these rocks in the deeper Nubian aquifer leads to higher mineral content compared to the shallower Quaternary aquifer; this explains the variation in groundwater quality across the region.

3.3.2 Groundwater quality for irrigation purposes

3.3.2.1 Sodium adsorption rate (SAR)

The composition of minerals presents in water impacts soil structure and permeability, which has an indirect effect on plant growth. The suitability of groundwater for irrigation can be assessed using the sodium adsorption rate (SAR), which is determined by the concentration of dissolved solids in the groundwater. Table 10 classifies irrigation water into four main categories based on SAR values. In the case of the groundwater samples studied, the SAR values range from 23 to 32, as shown in Table 11. Figure 5 illustrates the spatial arrangement of the SAR and RSC values of the samples collected at the research site. According to the SAR index, most water samples are considered unsuitable for irrigation. The RSC index, which assesses soil alkalinity risk, was used for irrigation water and soil water assessments (Eaton, 1950; Das and Nag, 2015) categorized irrigation water based on its carbonate and bicarbonate content, introducing the residual value of sodium carbonate as a measure of the relationship between concentrations of bicarbonate, carbonate, calcium, and magnesium in water (meq/L).

3.3.2.2 Residual sodium carbonate (RSC)

The RSC values calculated for groundwater samples from the studied area vary from −2.5 to −6.3 meq/L (Table 11). This range suggests that the water quality is excellent, safe, and suitable for irrigation purposes, according to the RSC index. Irrigation water quality standards established by US Salinity Laboratory Staff (USSL) (1954) and Wilcox (1955) are used to assess water quality effectively and efficiently through graphical representation of irrigation water quality.

3.3.2.3 Chemical analysis

The EC and SAR values of the groundwater samples are plotted on the Wilcox plot using Excel 2016 software (Figure 6). The classification of groundwater samples belongs to category (S4C4), indicating that the water is generally unsuitable for irrigation under normal circumstances but can be used occasionally under specific conditions. To use this water source, the soil must be permeable, adequate drainage must be ensured, excessive irrigation must be applied to allow leaching, and crops with high salt tolerance must be selected.

3.3.2.4 Sodium percentage (Na%)

The soluble sodium content of water, denoted Na%, serves as a parameter that reveals sodium risk and determines the suitability of water for irrigation purposes. The interaction between soil and sodium results in a reduction in soil permeability (Wilcox, 1955). Soil alkalinity results from high levels of sodium present in irrigation water, causing calcium and magnesium to be displaced by sodium. As a result, soil permeability decreases, leading to poor drainage (Collins and Jenkins, 1996). If the concentration of Na% in water exceeds 60%, the physical characteristics of the soil will be compromised (Porter and Marek, 2006). The groundwater in this study has a sodium percentage ranging from 86.5 to 92%. Based on the sodium percentage and electrical conductivity values of the samples in the specified area (as presented in Table 12) and their representation in the Wilcox diagram (Figure 6), it is evident that all samples d of the groundwater in the study area are not suitable for irrigation purposes. High sodium concentrations in groundwater can lead to an exchange of sodium with calcium (Ca^{2+}) and magnesium (Mg^{2+}) in the soil, resulting in reduced permeability and poor soil drainage.

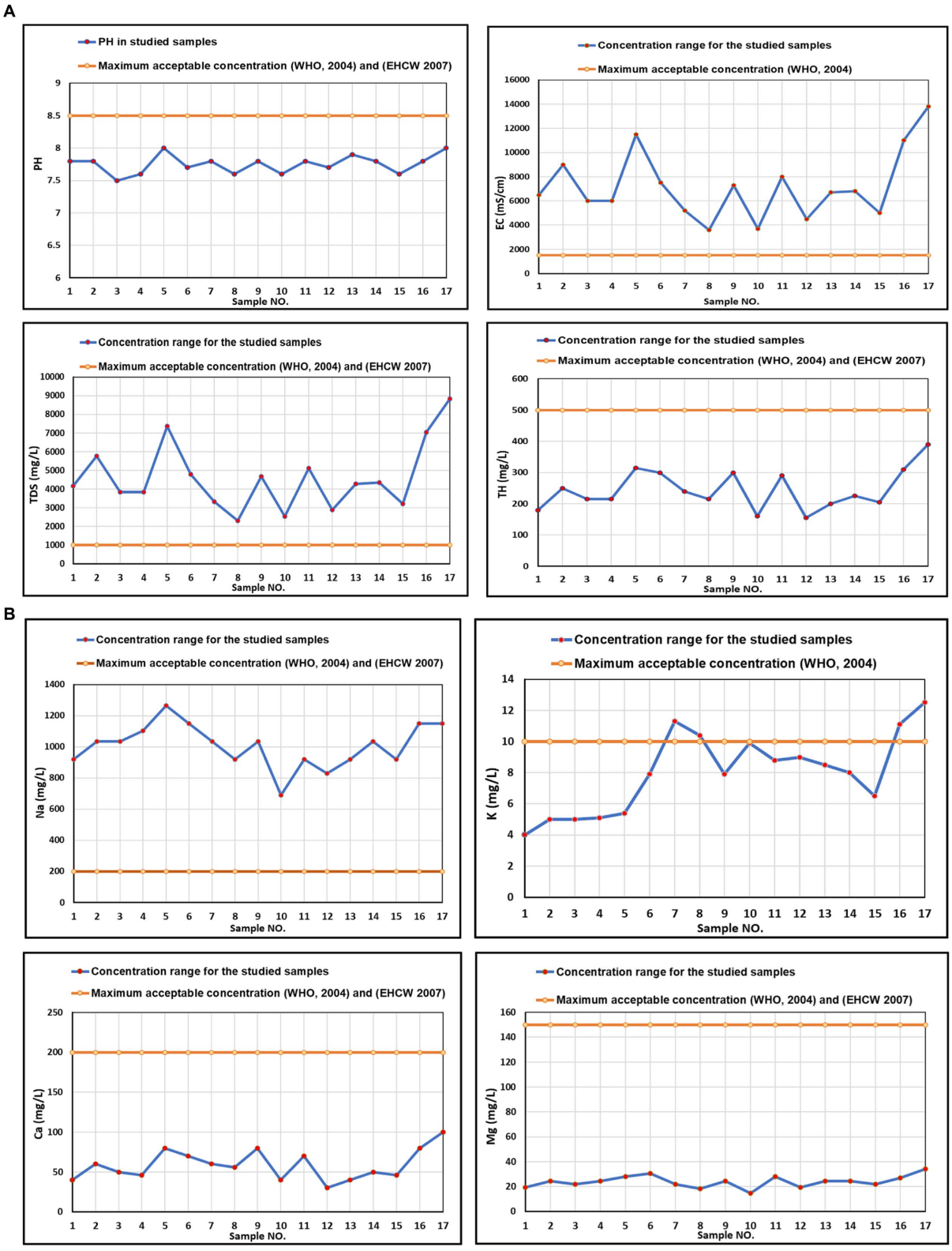

FIGURE 3 (Continued)

3.3.2.5 Permeability index (PI)

Excessive levels of Na^+, Ca^{2+}, Mg^{2+}, and HCO_3^- in irrigation water have been shown to impact soil permeability due to the widespread use of irrigation water (Gautam et al., 2015).

The groundwater in the present study has a PI percentage ranging from 90.3 to 95%. The classification of irrigation water is determined by the PI value, where a value greater than 75% is classified as class I, 25–75% as class II, and less than 25% as class III. This classification

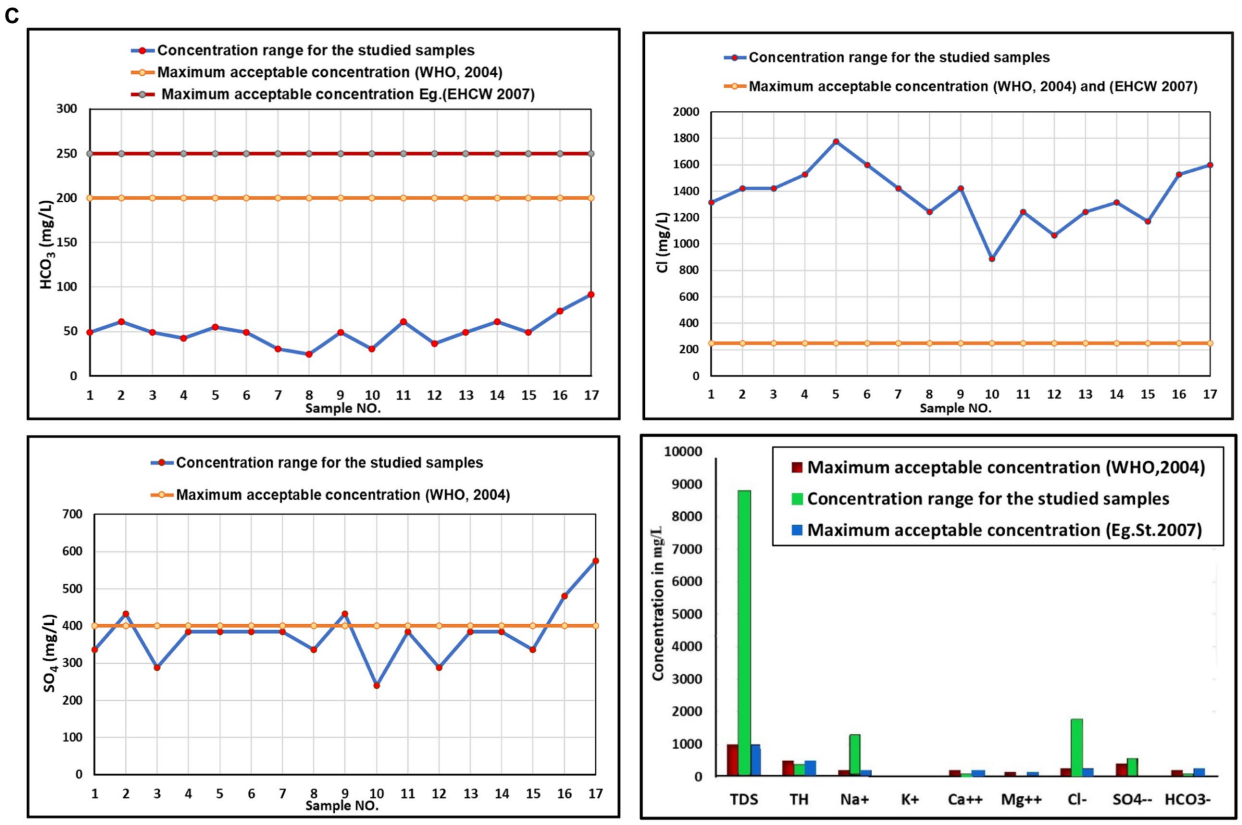

FIGURE 3
(A) pH, EC, TDS, and TH values. **(B)** Major ion (cations) concentrations. **(C)** Major ion (anions) concentrations in the groundwater samples, along with their comparison to WHO (WHO Guidelines, 2004) and EHCW (Egypt Standard, 2007) standards.

takes into account the soil contents of Na^+, Ca^{2+}, Mg^{2+}, and HCO_3^-. IP values were observed in the study area range from 90.3 to 95%, as shown in Table 12. Based on these IP values in the study area, all samples fall under Class I, which indicates that the water is highly unsuitable for irrigation.

3.3.2.6 Magnesium hazard (MH)

A significant concentration of Mg^{2+} in irrigated soils can be attributed to the existence of exchangeable Na^+. Paliwal (1972) proposed a crucial ratio that plays a key role in preserving the balance between calcium and magnesium in the majority of water sources, known as the balance risk index. Crop productivity is negatively affected as the soil becomes increasingly alkaline when the risk value of magnesium exceeds 50% (Raghunath, 1987; Gupta and Gupta, 1987). The groundwater values obtained in this study show a range of 33.3–51.6% for MH. It is clear from these values that the majority of groundwater samples, with the exception of sample 12, are below the 50% threshold. Therefore, these samples can be considered suitable for irrigation purposes, based on the MH values shown in Table 12.

3.3.2.7 Kelly's ratio (KR)

Irrigation water quality is influenced by various factors, including the Kelly ratio (KR). This particular parameter is determined by the levels of Na^+, Ca^{2+}, and Mg^{2+} in the groundwater. When the KR value exceeds one (KR > 1), it indicates an excessive amount of sodium, making the water unsuitable for irrigation. Conversely, a KR value less than one means sodium deficiency (Kelly, 1940). In the present investigation, the KR values vary between 6.4 and 11.6 meq/L, which indicates that all groundwater samples possess values greater than 1. Therefore, this means an excessive presence of sodium, making the water unsuitable for irrigation (Table 12).

3.3.2.8 Soluble sodium percentage (SSP)

The presence of high concentrations of sodium, magnesium, calcium, and bicarbonate in the soil leads to a reduction in its permeability. The suitability of water for irrigation purposes can be determined using the sodium adsorption rate (SAR). The soil saturation percentage (SSP) values obtained in this study vary from 87 to 94% (Table 12). These high SSP values indicate that the soil has a high capacity to interact with sodium, resulting in a reduction in permeability. As a result, groundwater becomes unsuitable for irrigation.

3.3.2.9 Chloride (Cl^-)

Plants need a certain level of chlorine for growth, but high concentrations can be harmful to sensitive crops. Chloride levels below 70 mg L^{-1} are generally safe for all plants, while levels between 70 and 140 mg/L can damage sensitive plants. Moderately tolerant plants can show damage at chloride concentrations ranging from 141 to 350 mg L^{-1}, and levels exceeding 350 mg/L can cause serious problems (Bauder et al., 2011). The study area shows chloride concentrations between 887.5 and 1,775 mg L^{-1}, indicating that most groundwater samples in the area have levels above 350 mg/L, making them unsuitable for irrigation (Table 12).

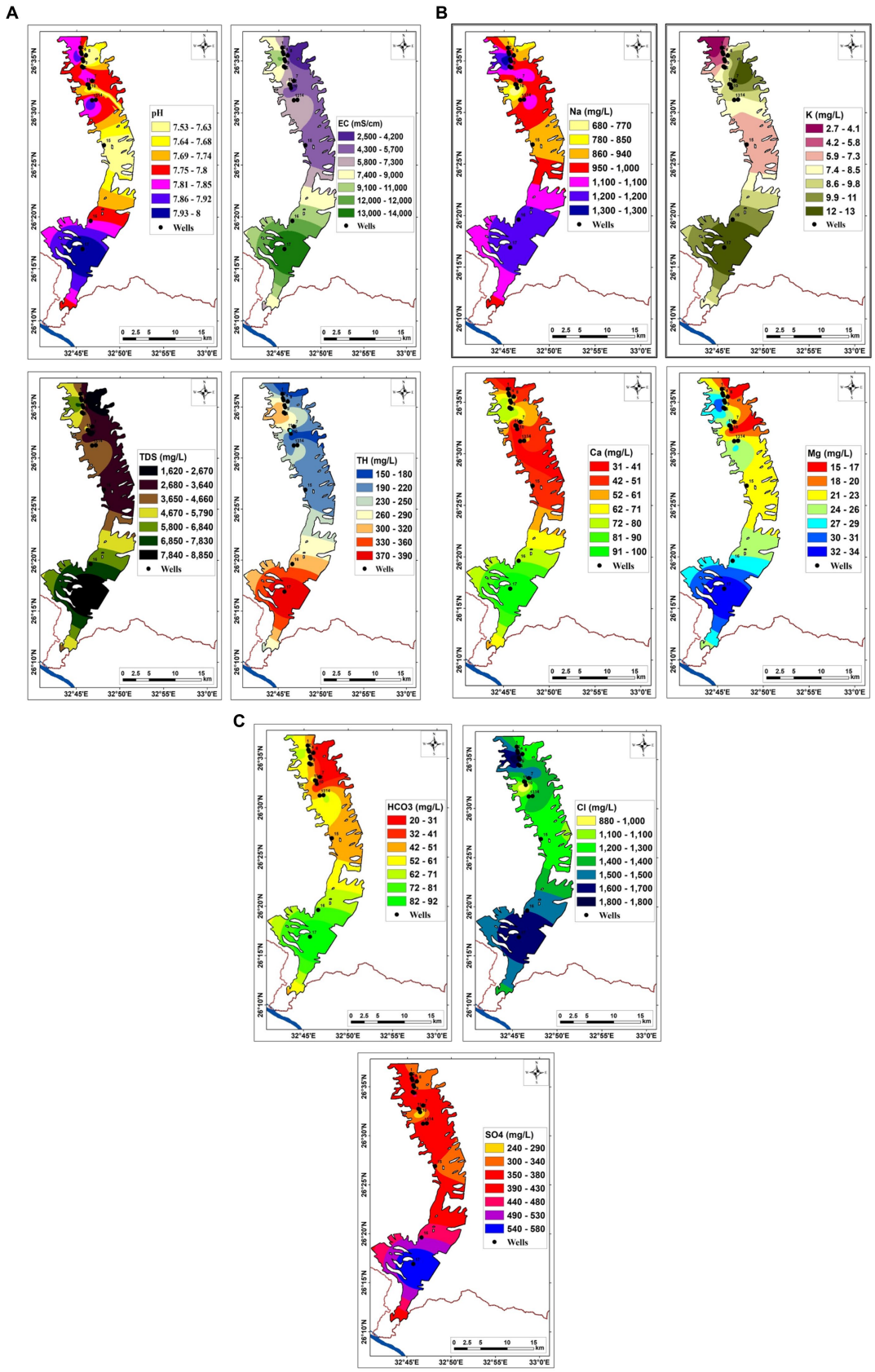

FIGURE 4
(A) Distribution maps of pH, EC, TDS, and TH. **(B)** Distribution maps of major ions (cations) concentrations. **(C)** Distribution maps of major ions (anions) concentrations of the groundwater samples in the study area.

TABLE 10 Irrigation water classes according to SAR.

Level	SAR	Quality	Class	Hazard	Use of water for irrigation	Present study
S_1	0–10	Low sodium	Excellent	No harmful effects from sodium	In all types of soil	–
S_2	10–18	Medium sodium	Good	Problems on fine texture soils sodium sensitive plants, especially under low-leaching conditions, but could be used on sandy soils with good permeability.	In coarse textural soils with high permeability and rich in organic matter	–
S_3	18–26	High sodium	Fair	Harmful effects could be anticipated in most soils and amendments such as gypsum would be necessary to exchange sodium ions.	Requires good drainage and chemical amendments.	Wells no. 9,10,11, 17
S_4	>26	Very high sodium	Poor	Generally unsatisfactory for irrigation.	Very poor for irrigation, requires low salinity water, good drainage, and the addition of gypsum.	Most samples (Wells no. 1 to 8, and 12 to 16)

3.4 Groundwater suitability map

Different chemical quality standards have been established for evaluating the suitability of water for drinking and irrigation uses. The groundwater quality in the studied area can be distinguished from the concentration of the major constituents obtained from the results of chemical analysis of the groundwater samples, (TDS), (TH), (SAR), and (RSC). As well as from its physical properties such as (pH), and (EC), which are indicators of water salinity. Abd El Hameed et al. (2017) concluded that the groundwater in Wadi Qena is unsuitable for drinking and other domestic uses and could be used for irrigation under certain conditions.

3.4.1 Groundwater suitability map for drinking purposes

The groundwater suitability map was produced through the integration of raster maps depicting different parameters (such as pH, EC, TDS, Na^+, Ca^{2+}, Mg^{2+}, Cl^-, SO_4^-, and HCO_3^-) using a GIS spatial model used in Arc GIS 8.1 software. The model results classified the entire research area into the low relevance class (see Figure 7). This suggests that the quality of groundwater throughout the region is deemed unfit for drinking.

3.4.2 Groundwater suitability map for irrigation purposes

Agricultural viability of groundwater (GW) depends on various factors, including Na%, PI, MH, KR, SSP, and Cl^-, SAR, RSC, Cl^-, TH, and soil properties such as permeability, porosity, and texture. A spatial groundwater model was created to identify optimal areas for irrigation planning, taking these factors into account. The model results are divided into two relevance categories: low and moderately low (Figure 8). The groundwater quality suitability for irrigation map revealed that all groundwater samples were deemed unsuitable for irrigation due to their low quality for typical crops, but moderately low suitability for highly salt tolerant crops.

TABLE 11 SAR, RSC, and TH for groundwater samples in the study area.

Well. no	SAR (meq/L)	RSC	TH (mg/L)	Ion balance (%)
1	29.814	−2.8	180.032	−1.4
2	28.4604	−4	250.04	0
3	30.6897	−3.5	214.913	2.6
4	32.7357	−3.6	215.04	0.5
5	30.9889	−5.4	315.046	2
6	28.8675	−5.2	300.05	2
7	29.047	−4.3	240.036	1.3
8	27.2797	−3.9	215.03	2.2
9	25.98	−5.2	300.04	1.2
10	23.717	−2.7	160.024	4.2
11	23.4888	−4.8	290.046	2
12	28.9158	−2.5	155.032	3.3
13	28.284	−3.2	200.04	0.2
14	30	−3.5	225.04	3.6
15	27.9372	−3.3	205.036	3.9
16	28.398	−5	310.044	1.8
17	25.3184	−6.3	390.056	−0.6

4 Discussion

The hydrochemical classification of groundwater samples is analyzed using Rockwork and Excel programs. The Schoeller diagram, constructed using Excel version 2016 software, provides a visual representation of the results, allowing comparison of major ion analyses, especially for high salinity samples. The diagram identifies a high concentration of sodium, chloride and sulfate ions, indicating that the dominant salts are sodium chloride and sodium sulfate. The Stiff plot shows the TDS values of the groundwater samples, indicating similarities or differences in the overall water chemistry. Cations and anions are presented separately in ternary plots in the Piper diagram, with peaks representing sulfate, chloride, carbonate, hydrogen carbonate anions and calcium, magnesium, sodium and potassium cations. The diamond-shaped data in the Piper diagram indicate that all samples fall into the sodium–potassium–chloride–sulfate category within the specified area. The hydrochemical composition indicates that sodium chloride is the main type of water in the study area (Hamma et al., 2024; Nayak

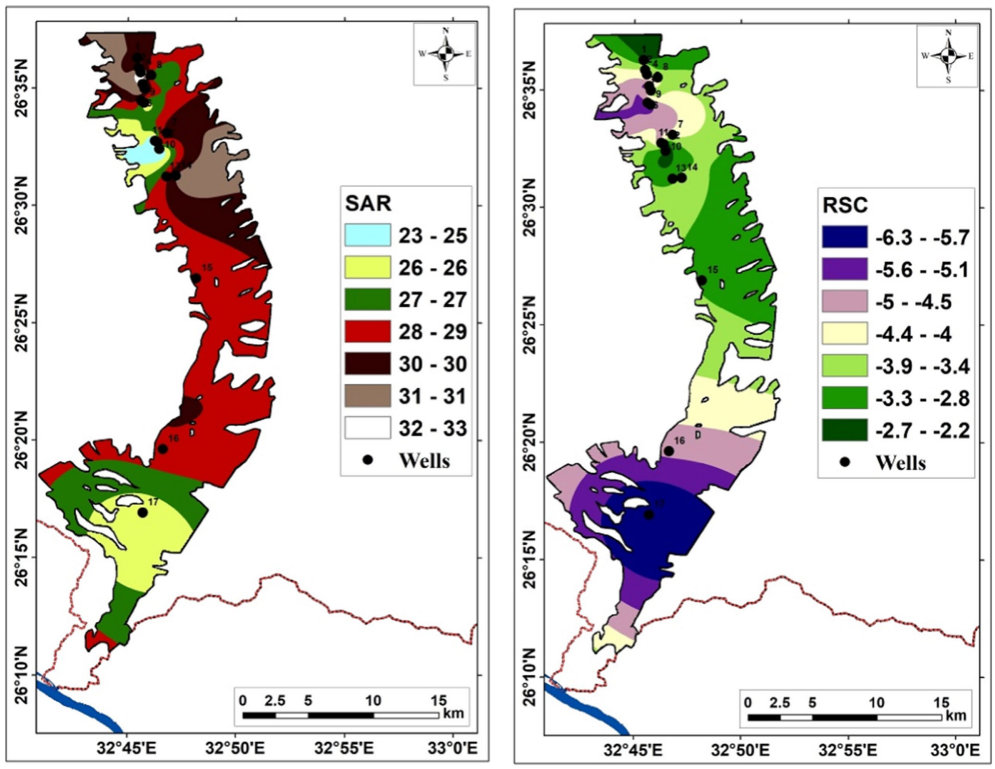

FIGURE 5
SAR, and RSC distribution maps in the study area.

et al., 2023; Ali et al., 2024; Hou et al., 2023; Belkhiri and Mouni, 2012; Bu et al., 2020; Soltan, 1998).

The high salinity rate in general and chemical elements such as sodium, calcium, and other elements are due to two main factors, which are the nature and type of rocks not only in the study area but also all the rocks carrying groundwater from their source which is very far from the study area and it is the second main factor in the high salinity rates in the study area as these elements dissolve from the rocks they pass through. The study area is one of the desert areas and the only source of water is groundwater which includes a Quaternary aquifer (QAS), a Nubian sandstone aquifer (NSAS), a fractured limestone aquifer; and a fractured crystalline (basement) aquifer and the water source of these reservoirs in addition to the geological nature are the factors causing the high rates of various chemical elements in the study area.

The study analyzes groundwater samples, revealing pH levels between 7.5 and 8, which corresponds to the recommended pH range of 6.5–8.5 by Egyptian and WHO standards. However, the electrical conductivity range exceeds the permissible limits for drinking water, according to WHO and Egyptian guidelines. Total dissolved solids (TDS) range from 2,304 to 8,832 mg/L, with an increase toward the southern part of the wadi. The water is considered hard due to the presence of industrial waste (agricultural processing, textile industries, chemical manufacturing and salt production) and sewage, exceeding the permissible limits. Sodium levels range from 690 to 1,265 mg/L, with an increase in QAS and NSAS. Calcium concentrations remain within drinking water limits, while magnesium levels increase from north to south in both aquifers. Bicarbonate levels are within acceptable limits, while chloride and sulfate levels vary. All groundwater samples are considered unsafe for drinking, indicating that dissolution and weathering of silicate and sulfate minerals are having a significant impact on the groundwater chemistry of the region (Chegbeleh et al., 2020; Al Saleh and Nehaba, 2024; Rawat et al., 2018; Soomro et al., 2024; S et al., 2022; Islam and Mostafa, 2022; El-Amier et al., 2021; Osman, 2018).

The suitability of groundwater for irrigation is determined by various factors including sodium adsorption rate (SAR), residual sodium carbonate (RSC), permeability index (PI), magnesium risk (MH), Kelly coefficient (KR) and soil saturation percentage (SSP). The SAR index classifies irrigation water into four main categories based on its dissolved solids concentration in groundwater. Most water samples are considered unsuitable for irrigation due to their high sodium content, which can lead to soil alkalinity and poor drainage (Shaaban, 2024; Yıldız and Karakuş, 2020).

The RSC index indicates that the water quality is excellent, safe and suitable for irrigation. However, soluble sodium (Na%), which is the interaction between soil and sodium, leads to reduced soil permeability, resulting in poor drainage. The Permeability Index (PI) classifies irrigation water based on its Na^+, Ca^{2+}, Mg^{2+}, and HCO_3^- levels. PI values range from 90.3 to 95%, with all samples classified as Class I, indicating that the water is highly unsuitable for irrigation (Khan et al., 2022; Zaman et al., 2018; Badr et al., 2023; Megahed, 2020).

The Equilibrium Risk Index (MH) measures the concentration of exchangeable Na^+ in irrigated soils, which negatively affects crop productivity when the risk value of magnesium exceeds 50%. The majority of groundwater samples, except sample 12, are below the 50%

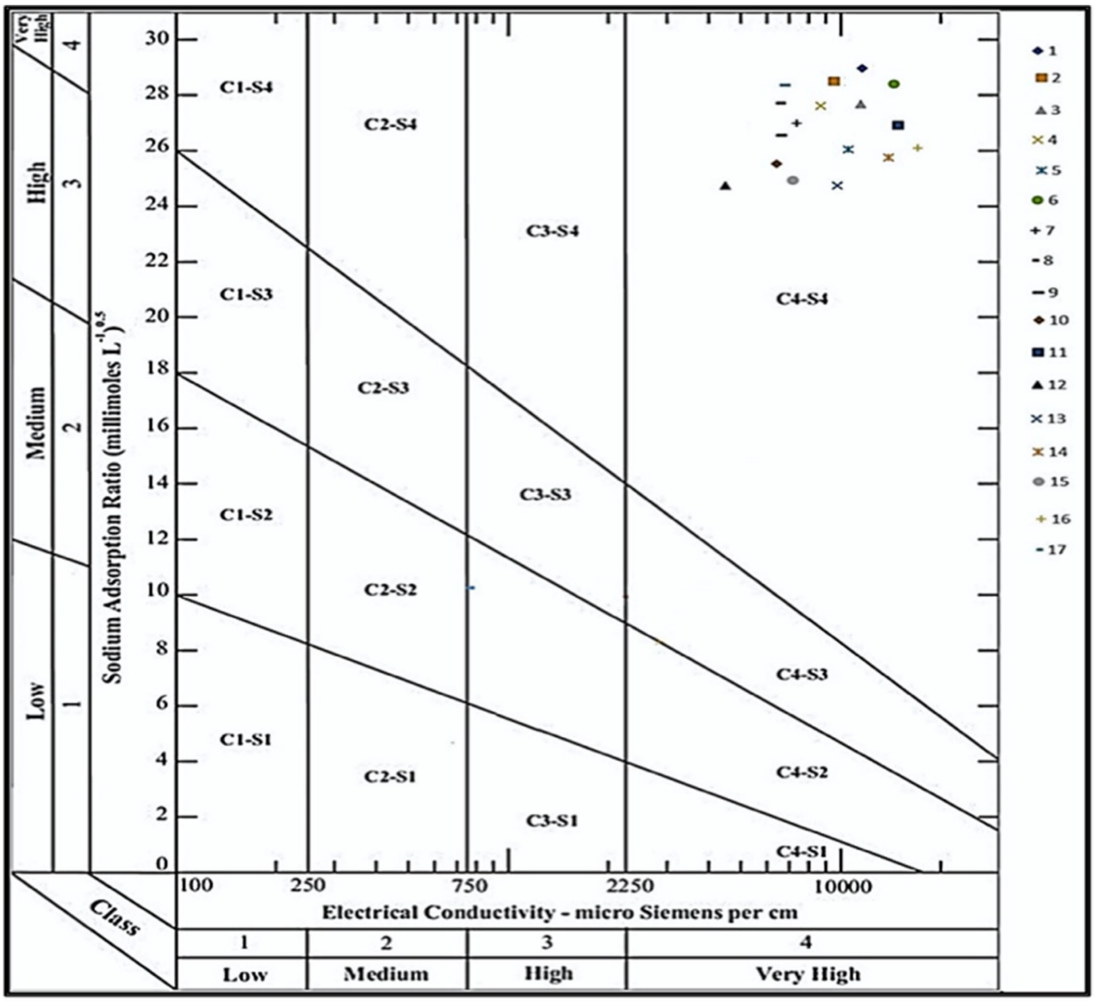

FIGURE 6
Groundwater suitability for irrigation for groundwater samples according to U.S. Lab. Classification.

threshold, making them suitable for irrigation (Osman, 2018; Shaaban, 2024; Yıldız and Karakuş, 2020; Khan et al., 2022; Zaman et al., 2018; Badr et al., 2023; Megahed, 2020).

Another parameter influencing the quality of irrigation water is the Kelly coefficient (KR). When the KR value exceeds 1, it indicates excess sodium, making the water unsuitable for irrigation. Soil saturation percentage (SSP) values range from 87 to 94%, indicating that the soil has a high capacity to interact with sodium, resulting in reduced permeability. Chloride concentrations can be harmful to sensitive plants, and the study area has chloride concentrations greater than 350 mg/L, making most groundwater samples unsuitable for irrigation (Khan et al., 2022; Zaman et al., 2018; Badr et al., 2023; Megahed, 2020).

The groundwater suitability map for drinking and irrigation in Wadi Qena was created using a spatial GIS model. The map incorporated raster maps of various parameters including pH, electrical conductivity, TDS, Na^+, Ca^{2+}, Mg^{2+}, Cl^-, SO_4^{2-}, and HCO_3^-. The results classified the entire research area into a low suitability class, indicating that the groundwater quality is not suitable for drinking. The model also identified suitable areas for irrigation planning, revealing that all groundwater samples were unsuitable for typical crops, but moderately low for highly salt-tolerant crops (Moubark and Abdelkareem, 2018; Yan et al., 2024; Worku et al., 2024; El Osta et al., 2022). In addition, the delineation of the potential groundwater recharge area is underway to improve the quality and quantity of water available in the Wadi Qena watershed. However, there are opportunities for further improvements through the introduction of sustainable agricultural practices and the modernization of wastewater treatment as well as water conservation and pollution control campaigns (El Osta et al., 2022; Saraswat et al., 2023; Kumar et al., 2022; Balaji et al., 2017). The Qena Governorate has developed an environmental action plan that includes environmental awareness raising for residents and government employees, and also includes plans for improving solid waste management, water supply, and water quality.

A GIS map produced classified the area into a low suitability class, and recommended sustainable agricultural practices (AbdelRahman and Arafat, 2020; AbdelRahman et al., 2018), installation of wastewater treatment facilities, as well as campaigns for public awareness on water conservation and prevention of pollution (Megahed et al., 2023).

10.3389/frwa.2025.1502169

TABLE 12 Na%, PI, MH, KR, SSP, and Cl^- parameters values in the study area.

Sample no.	PI	MH	KR	SSP	Na	Cl^-
	%	%	Meq/L	%	%	mg/L
1	94.6	44.4	11.11	94	91.7	1,313.5
2	93.2	40	9	90	90	1,420
3	94.1	41.7	10.5	91	91.3	1,420
4	94.6	46.5	11.2	92	91.8	1,526.5
5	92.7	36.5	10.4	90	89.7	1,775
6	92.5	41.6	8.3	89	89.3	1,597.5
7	93.2	37.5	9.4	90	90.4	1,420
8	93	34.9	9.3	90	90.3	1,242.5
9	91.5	33.3	9	88	88.2	1,420
10	93.4	37.5	9.4	90	90.4	887.5
11	91.1	39.6	6.9	87	87.3	1,242.5
12	95	51.6	11.6	92	92	1,065
13	94.2	50	10	91	90.9	1,242.5
14	94	44.4	10	91	90.9	1,313.5
15	93.8	43.9	9.8	91	90.7	1,171.5
16	92.2	35.5	8.1	89	88.9	1,526.5
17	90.3	35.9	6.4	87	86.5	1,597.5

5 Conclusion

The study area is entirely encompassed by sedimentary rocks ranging from the Precambrian to the Quaternary. The NSAS and QAS are the main sources of groundwater. Chemical analyses carried out on the groundwater samples reveal that they have an acidic to slightly alkaline character. Groundwater quality and suitability for drinking and agricultural uses were assessed using a spatial model and hydrochemical analysis of existing groundwater wells. The results indicated high values of total dissolved solids (TDS) in the north–south section of the Quaternary aquifer in the study area, with sulfate content in the Quaternary aquifer samples increasing toward the south. Conversely, sulfate content increases northward in samples from the Nubian aquifer, which can be attributed to increased agricultural activities and pumping rates.

The quality of groundwater in the region is characterized by a range of values for various parameters. Total Dissolved Solids (TDS) range of 2,304–8,832 mg/L, Total Hardness (TH) of 155.03–390.06 mg/L, Electrical Conductivity (EC) of 3,600–13,800 µS/cm, sodium adsorption ratio (SAR) from 23.49 to 32.74 meq/L, sodium percentage (Na%) from 86.5 to 92%, residual sodium carbonate (RSC) from −2.5 to −5.4 meq/L, permeability index (PI) from 90.3 to 94.6%, magnesium risk (MH) from 33.3 to 51.6%, Kelly ratio (KR) from 6.4 to 11.6 meq/L, sodium saturation percentage (SSP) 87–94%, and chloride (Cl^-) 887.5–1,775 mg/L. The results indicate that all groundwater samples from the study area are unsuitable for drinking

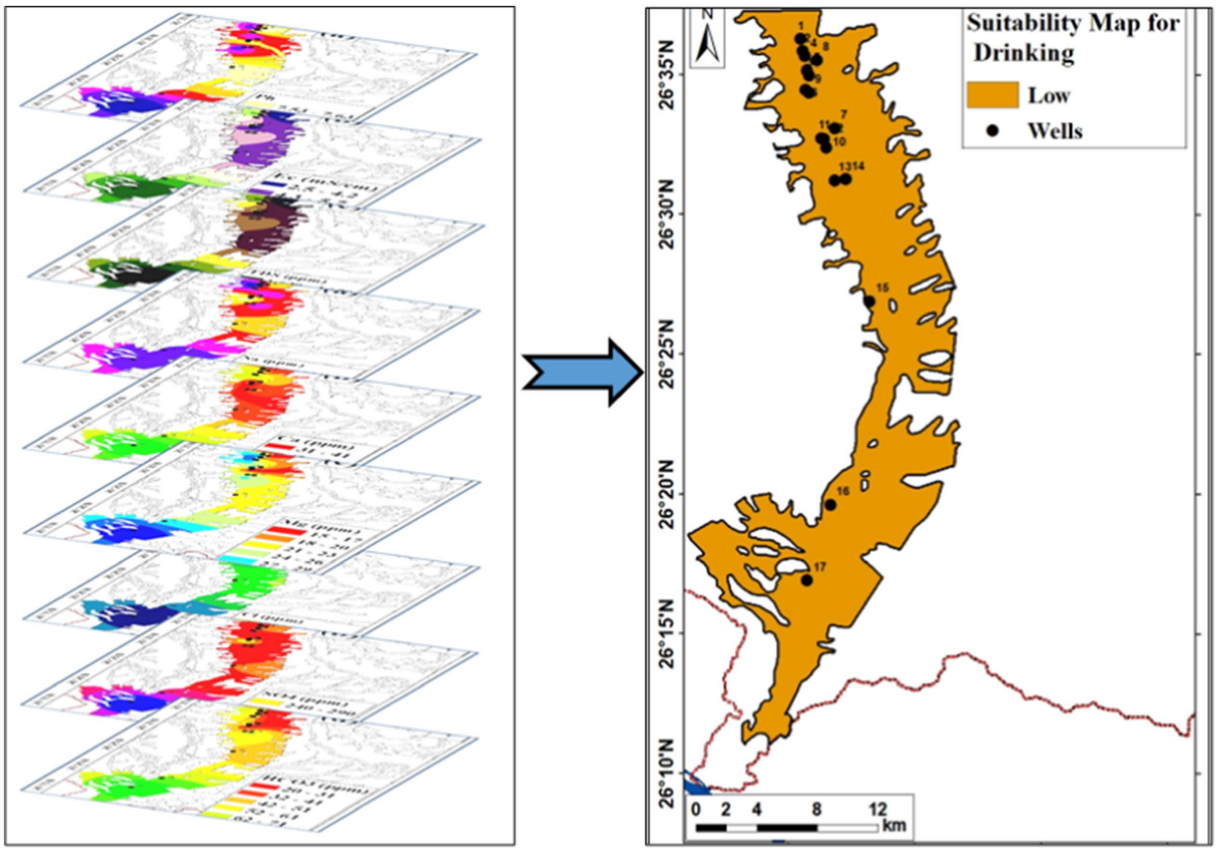

FIGURE 7
Groundwater suitability map for drinking purposes in the study area.

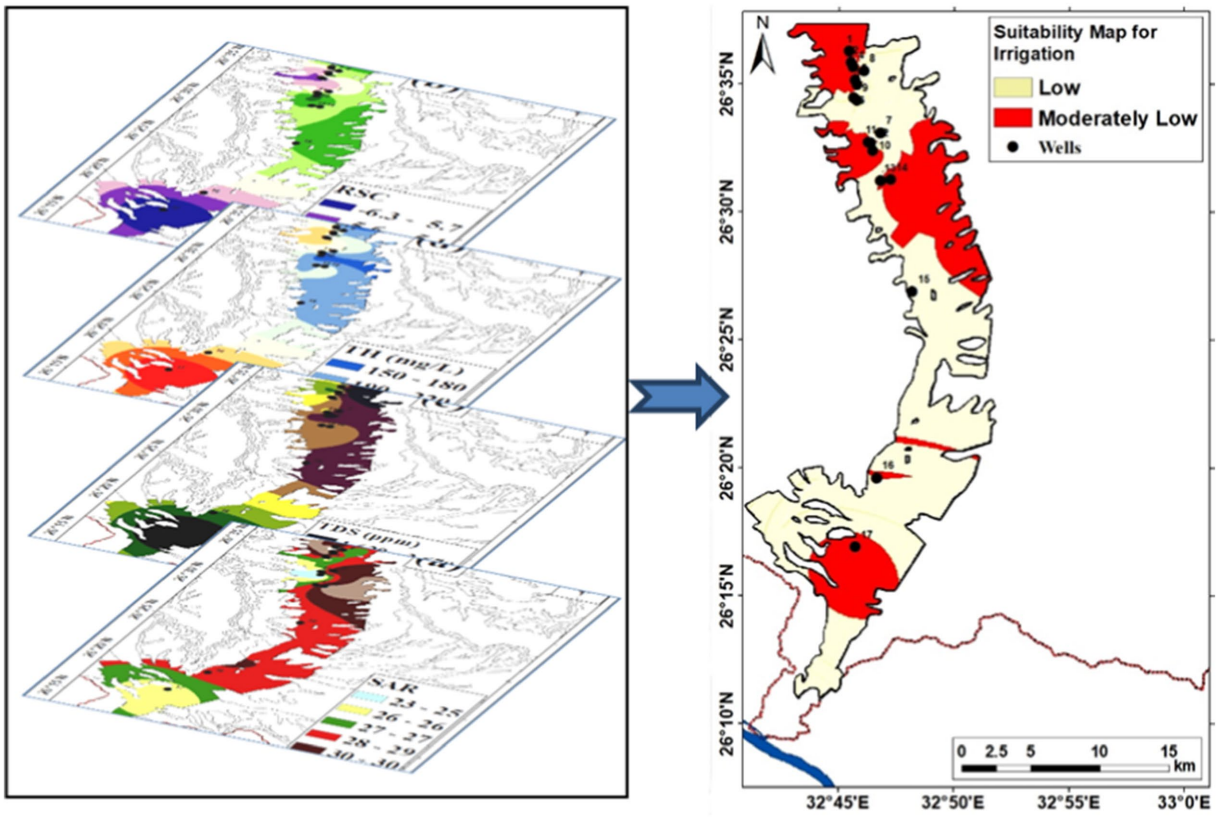

FIGURE 8
Groundwater suitability map for irrigation purposes.

and irrigation. The quality maps further confirm that groundwater is not suitable for these uses. The Schoeller, Stiff, and Piper diagrams suggest that NaCl is the dominant water type in the region. The sequence of cations and anions in groundwater samples shows a predominance of $Na^+ > Ca^{2+} > Mg^{2+}/Cl^- > SO_4^{2-} > HCO_3^-$. These plots, along with multi-analytical analysis, indicate that the dissolution and weathering of silicate and sulfate minerals play an important role in controlling groundwater chemistry in the region. The study highlights remedial measures for improving groundwater quality, such as establishing monitoring and GIS-based management systems to track groundwater quality, promoting efficient irrigation techniques to reduce soil salinity and prevent groundwater contamination, exploring localized desalination and treatment technologies for enhanced water quality, implementing artificial recharge projects using treated wastewater or surplus surface water to improve aquifer storage, and enforcing stricter policies on waste management, industrial effluents, and agricultural practices to minimize contamination sources. To improve groundwater management, it is recommended to stop their use for agricultural purposes due to their unsuitability and instead focus on their use for livestock or poultry farming depending on their quality. Groundwater from the Nubian aquifer can be used to grow crops compatible with its quality and the region's soil conditions, using modern irrigation techniques to conserve this non-renewable resource. Regular monitoring and assessment of changes in water quality in the region is essential. An effective groundwater management plan is needed for the region, and the results of this study can provide valuable information to policy makers involved in managing groundwater quality in the region.

Data availability statement

The original contributions presented in the study are included in the article/supplementary material, further inquiries can be directed to the corresponding authors.

Author contributions

HM: Writing – original draft, Writing – review & editing, Conceptualization, Data curation, Formal analysis, Funding acquisition, Investigation, Methodology, Project administration, Resources, Software, Supervision, Validation, Visualization. AF: Conceptualization, Data curation, Formal analysis, Funding acquisition, Investigation, Methodology, Project administration, Resources, Software, Supervision, Validation, Visualization, Writing – original draft, Writing – review & editing. AM: Conceptualization, Data curation, Formal analysis, Funding acquisition, Investigation, Methodology, Project administration, Resources, Software, Supervision, Validation, Visualization, Writing – original draft, Writing – review & editing. MD: Conceptualization, Data curation, Formal analysis, Funding acquisition, Investigation, Methodology,

Project administration, Resources, Software, Supervision, Validation, Visualization, Writing – original draft, Writing – review & editing. MA: Conceptualization, Data curation, Formal analysis, Funding acquisition, Investigation, Methodology, Project administration, Resources, Software, Supervision, Validation, Visualization, Writing – original draft, Writing – review & editing. HE-B: Data curation, Writing – original draft. PD'A: Conceptualization, Data curation, Funding acquisition, Methodology, Resources, Software, Validation, Visualization, Writing – original draft, Writing – review & editing. AS: Conceptualization, Data curation, Funding acquisition, Resources, Software, Validation, Visualization, Writing – original draft, Writing – review & editing. MS: Validation, Writing – original draft.

Funding

The author(s) declare that no financial support was received for the research, authorship, and/or publication of this article.

Acknowledgments

The authors acknowledge support given by National Authority for Remote Sensing and Space Sciences, Assiut University, Assiut, New Valley University, and Dipartimento di ScienzeAgrarie, Forestali, Alimentari ed. Ambientali (SAFE), Università degli Studi della Basilicata, which is not covered by the author contribution or funding sections.

Conflict of interest

The authors declare that the research was conducted in the absence of any commercial or financial relationships that could be construed as a potential conflict of interest.

Generative AI statement

The authors declare that no Generative AI was used in the creation of this manuscript.

Publisher's note

References

Abd El Hameed, A. G., El-Shayeb, H. M., El-Araby, N. A., and Hegab, M. G. (2017). Integrated geoelectrical and hydrogeological studies on Wadi Qena, Egypt. *NRIAG J. Astron. Geophys.* 6, 218–229. doi: 10.1016/j.nrjag.2017.03.003

Abd El Razik, T. M., and Razvaliaev, A. V. (1972). On the tectonic origin of the Nile Valley between Idfu and Qena, Egypt. *Egypt. J. Geol.* 16, 235–244.

Abdel Moneim, A. A. (2005). Overview of the geomorphological and hydrogeological characteristics of the eastern desert of Egypt. *Hydrogeol. J.* 13, 416–425. doi: 10.1007/s10040-004-0364-y

Abdel Moneim, A. A., Seleem, E. M., Zeid, S. A., Abdel Samie, S. G., Zaki, S., and Abu El-Fotoh, A. (2015). Hydrogeochemical characteristics and age dating of groundwater in the quaternary and Nubian aquifer systems in Wadi Qena, eastern desert, Egypt. *Sustain. Water Resour. Manag.* 1, 213–232. doi: 10.1007/s40899-015-0018-3

AbdelRahman, M. A. E., and Arafat, S. M. (2020). An approach of agricultural courses for soil conservation based on crop soil suitability using geomatics. *Earth Syst. Environ.* 4, 273–285. doi: 10.1007/s41748-020-00145-x

AbdelRahman, M. A. E., Shalaby, A., and Essa, E. F. (2018). Quantitative land evaluation based on fuzzy-multi-criteria spatial model for sustainable land-use planning. *Model. Earth Syst. Environ.* 4, 1341–1353. doi: 10.1007/s40808-018-0478-1

AbdelRahman, M. A. E., Shalaby, A., and Mohamed, E. S. (2018). Comparison of two soil quality indices using two methods based on geographic information system. *Egypt. J. Remote Sens. Space Sci.* 22, 127–136. doi: 10.1016/j.ejrs.2018.03.001

Abu Salem, H. S., Gemail, K. S., Junakova, N., Ibrahim, A., and Nosair, A. M. (2022). An integrated approach for deciphering hydrogeochemical processes during seawater intrusion in coastal aquifers. *Water* 14:1165. doi: 10.3390/w14071165

Ahmed, E. A. (1983). Sedimentology and tectonic evolution of Wadi Qena area, Egypt. (Ph.D thesis). Assiut, Egypt: Geology Dept., Assuit University, 136.

Al Saleh, H. A. A., and Nehaba, S. S. (2024). Evaluating groundwater vulnerability and assessing its quality for sustainable management. *South African J. Chem. Eng.* 50, 291–298. doi: 10.1016/j.sajce.2024.09.001

Ali, S., Verma, S., Agarwal, M. B., Islam, R., Mehrotra, M., Deolia, R. K., et al. (2024). Groundwater quality assessment using water quality index and principal component analysis in the Achnera block, Agra district, Uttar Pradesh, Northern India. *Sci. Rep.* 14:5381. doi: 10.1038/s41598-024-56056-8

Badr, E.-S. A., Tawfik, R. T., and Alomran, M. S. (2023). An assessment of irrigation water quality with respect to the reuse of treated wastewater in Al-Ahsa Oasis, Saudi Arabia. *Water* 15:2488. doi: 10.3390/w15132488

Balaji, E., Nagaraju, A., Sreedhar, Y., Thejaswi, A., and Sharifi, Z. (2017). Hydrochemical characterization of groundwater in around Tirupati area, Chittoor District, Andhra Pradesh, South India. *Appl Water Sci* 7, 1203–1212. doi: 10.1007/s13201-016-0448-6

Bauder, T. A., Waskom, R., Sutherland, P., Davis, J., Follett, R., and Soltanpour, P. (2011). Irrigation water quality criteria: Colorado State University Extension Publication, Crop series/irrigation. Fact sheet no. 0.506, Fort Collins, CO, USA. 4.

Belkhiri, L., Boudoukha, A., Mouni, L., and Baouz, T. (2010). Application of multivariate statistical methods and inverse geochemical modeling for characterization of groundwater - a case study: Ain Azel plain (Algeria). *Geoderma* 159, 390–398. doi: 10.1016/j.geoderma.2010.08.016

Belkhiri, L., and Mouni, L. (2012). Hydrochemical analysis and evaluation of groundwater quality in El Eulma area, Algeria. *Appl. Water Sci.* 2, 127–133. doi: 10.1007/s13201-012-0033-6

Bu, J., Liu, W., Pan, Z., and Ling, K. (2020). Comparative study of hydrochemical classification based on different hierarchical cluster analysis methods. *Int. J. Environ. Res. Public Health* 17:9515. doi: 10.3390/ijerph17249515

Chegbeleh, L. P., Akurugu, B. A., and Yidana, S. M. (2020). Assessment of groundwater quality in the Talensi District, northern Ghana. *Sci. World J.*:8450860:24. doi: 10.1155/2020/8450860

College of Agricultural Sciences (2002). Irrigation water quality. State College, USA: Pennsylvania State University.

Collins, R., and Jenkins, A. (1996). The impact of agricultural land use on stream chemistry in the Middle Hills of the Himalayas, Nepal. *J. Hydrol.* 185, 71–86. doi: 10.1016/0022-1694(95)03008-5

Conoco (1987). Geological map of Egypt, scale 1:500,000, sheet NG36NE Quseir, NG36NW Asyut. Cairo, Egypt: The Egyptian General Petroleum Corporation.

Darwish, M. H., and Galal, W. F. (2020). Spatiotemporal effects of wastewater ponds from a geoenvironmental perspective in the Kharga region, Egypt. *Prog. Phys. Geogr. Earth Environ.* 44, 376–397. doi: 10.1177/0309133319879321

Darwish, M. H., Sayed, A. G., and Hassan, S. H. (2023). Assessment of water for different uses at some localities of the Dakhla Oasis, Western Desert, Egypt. *Water Air Soil Pollut.* 234:516. doi: 10.1007/s11270-023-06458-7

Das, S., and Nag, S. K. (2015). Deciphering groundwater quality for irrigation and domestic purposes - a case study in Suri I and II blocks, Birbhum District, West Bengal, India. *J. Earth Syst. Sci.* 124, 965–992. doi: 10.1007/s12040-015-0583-8

Doneen, L. (1964). Notes on water quality in agriculture, water science and engineering paper 4001. Davis, USA: Dept. of Water. Science and Engineering, Univ. of California.

Eaton, F. M. (1950). Significance of carbonates in irrigation waters. *Soil Sci.* 69, 123–134. doi: 10.1097/00010694-195002000-00004

Egypt Standard. (2007). Higher committee for water Egyptian standers for drinking water and domestic uses (in Arabic).

Egyptian Geological Survey and Mining Authority (EGSMA) (1983). Geological Map of Egypt, Scale 1: 2,000,000. Cairo, Egypt: Egyptian Geological Survey and Mineral Authority.

Egyptian Geological Survey and Mining Authority (EGSMA) (2006). Geological map of Abu had quadrangle. Egypt, Scale 1:100,000. Cairo, Egypt: Egyptian Geological Survey and Mineral Authority.

El Osta, M., Masoud, M., Alqarawy, A., Elsayed, S., and Gad, M. (2022). Groundwater suitability for drinking and irrigation using water quality indices and multivariate modeling in Makkah Al-Mukarramah Province, Saudi Arabia. *Water* 14:483. doi: 10.3390/w14030483

El-Amier, Y. A., Kotb, W. K., Bonanomi, G., Fakhry, H., Marraiki, N. A., and Abd-ElGawad, A. M. (2021). Hydrochemical assessment of the irrigation water quality of the El-Salam Canal, Egypt. *Water* 13:2428. doi: 10.3390/w13172428

Elewa, H. H., and Abu El Ella, E. M. (2011). Numerical modeling for the Nubian aquifer development in Wadi Qena, eastern desert, Egypt. *Egypt. J. Geol.* 55, 105–125. Available at: http://scholar.google.com/scholar_lookup?&title=Groundwater%20potential%20of%20the%20southern%20part%20of%20Wadi%20Qena%20basin%2C%20Eastern%20Desert%20of%20Egypt%20using%20remote%20sensing%20techniques&journal=Egypt%20J%20Remote%20Sens%20Space%20Sci&volume=3&pages=135-152&publication_year=2000&author=Elewa%2CHH&author=Fathy%2CRG&author=Zaghloul%2CEA

Elewa, H. H., Fath, R. G., and Zaghloul, E. A. (2006). Possibility of the agricultural expansion based on land and water resources potentialities at the southern part of Wadi Qena, central Eastern Desert, Egypt. *Egypt. J. Soil Sci.* 46, 153–174. Available at: http://scholar.google.com/scholar_lookup?&title=Possibility%20of%20the%20agricultural%20expansion%20based%20on%20land%20and%20water%20resources%20potentialities%20at%20the%20Southern%20Part%20of%20Wadi%20Qena%2C%20Central%20Eastern%20Desert%2C%20Egypt&journal=Egypt%20J%20Soil%20Sci&volume=46&issue=2&pages=153-174&publication_year=2006&author=Elewa%2CHH&author=Fath%2CRG&author=Zaghloul%2CEA

Elewa, H. H., Fathy, R. G., and Zaghloul, E. A. (2000). Groundwater potential of the southern part of Wadi Qena basin, eastern desert of Egypt using remote sensing techniques. *Egypt. J. Remote Sens. Space Sci.* 3, 135–152. Available at: http://scholar.google.com/scholar_lookup?&title=Groundwater%20potential%20of%20the%20southern%20part%20of%20Wadi%20Qena%20basin%2C%20Eastern%20Desert%20of%20Egypt%20using%20remote%20sensing%20techniques&journal=Egypt%20J%20Remote%20Sens%20Space%20Sci&volume=3&pages=135-152&publication_year=2000&author=Elewa%2CHH&author=Fathy%2CRG&author=Zaghloul%2CEA

El-Rawi, M., AbdelRahman, M. A. E., and Ismail, E. (2020). Integrated use of pollution indices and geomatics to assess soil contamination and identify soil pollution source in El-Minia governorate, upper Egypt. *J. Eng. Sci. Technol.* 15, 2223–2238. Available at: https://jestec.taylors.edu.my/Vol%2015%20issue%204%20August%202020/15_4_7.pdf

ESRI. (2006). ArcGIS 9.1, GIS, and mapping software. Redlands, CA: Environmental Systems Research Institute.

Faris, M. (1974). The contact of the cretaceous and Eocene rocks in Tramsa-Tukh areal Qena, upper Egypt. *Bull. Inst. Oceanogr. Fish.* 28, 73–85. doi: 10.3406/bie.1945.3774

Ferreira dos Santos, C., and Cunha-Santino, M. B. (2015). Monitoramento da qualidade da água do rio monjolinho: a limnologia como uma ferramenta para a gestão ambiental. *Revista de Estudos Ambientais* 16, 27–37. doi: 10.7867/1983-1501.2014V16N1P27-37

Fishman, M. J., and Friedman, L. C. (1989). Methods for determination of inorganic substances in water and fluvial sediments. Reston, VA, USA: US Department of the Interior, Geological Survey.

Galal, W. F., and Darwish, M. H. (2022). Geoenvironmental assessment of the Mut wastewater ponds in the Dakhla Oasis, Egypt. *Geocarto Int.* 37, 3293–3311. doi: 10.1080/10106049.2020.1856197

Gautam, S. K., Maharana, C., Sharma, D., Singh, A. K., Tripathi, J. K., and Singh, S. K. (2015). Evaluation of groundwater quality in the Chotanagpur plateau region of the Subarnarekha River basin, Jharkhand state, India. *Sustain. Water Qual. Ecol.* 6, 57–74. doi: 10.1016/j.swaqe.2015.06.001

Giri, S., Mahato, M. K., Singh, P. K., and Singh, A. K. (2021). Non-carcinogenic health risk assessment for fluoride and nitrate in the groundwater of the Mica Belt of Jharkhand, India. *Hum. Ecol. Risk Assess.* 27, 1939–1953. doi: 10.1080/10807039.2021.1934814

Gong, Z., Tian, X., Fu, L., Niu, H., Xia, Z., Ma, Z., et al. (2023). Chemical characteristics and controlling factors of groundwater in Chahannur Basin. *Water* 15:1524. doi: 10.3390/w15081524

Gupta, S. K., and Gupta, I. (1987). Management of saline soils and waters. New Delhi, India: Oxford & IBH Publishing Co., 399.

Haghizadeh, A., Moghaddam, D. D., and Pourghasemi, H. R. (2017). GIS-based bivariate statistical techniques for groundwater potential analysis (an example of Iran). *J. Earth Syst. Sci.* 126, 1–17. doi: 10.1007/s12040-017-0888-x

Hamma, B., Alodah, A., Bouaicha, F., Bekkouche, M. F., Barkat, A., and Hussein, E. E. (2024). Hydrochemical assessment of groundwater using multivariate statistical methods and water quality indices (WQIs). *Appl Water Sci* 14:33. doi: 10.1007/s13201-023-02084-0

Han, D., and Currell, M. J. (2017). Persistent organic pollutants in China's surface water systems. *Sci. Total Environ.* 580, 602–625. doi: 10.1016/j.scitotenv.2016.12.007

Han, X., Tang, F., and Liu, A.-L. (2024). Drinking water quality evaluation in supply systems in Wuhan, China: application of entropy weight water quality index and multivariate statistical analysis. *Environ. Sci. Pollut. Res.* 31, 280–292. doi: 10.1007/s11356-023-31212-1

Hem, J. D. (1970). Study and interpretation of the chemical characteristics of natural water. *2nd* Edn: U. S. Geological survey. Water supply, papers 1473, 363.

Hem, J. D. (1985). Study and interpretation of the chemical characteristics of natural water. United States Geol. Survey/water supply, paper 2254. Washington DC., USA: United States Geol. Survey.

Honarbakhsh, A., Azma, A., Nikseresht, F., Mousazadeh, M., Eftekhari, M., and Ostovari, Y. (2019). Hydro-chemical assessment and GIS-mapping of groundwater quality parameters in semi-arid regions. *J. Water Supply Res. Technol. Aqua* 68, 509–522. doi: 10.2166/aqua.2019.009

Hou, Q., Pan, Y., Zeng, M., Wang, S., Shi, H., Huang, C., et al. (2023). Assessment of groundwater hydrochemistry, water quality, and health risk in Hainan Island, China. *Sci. Rep.* 13:12104. doi: 10.1038/s41598-023-36621-3

Islam, M. S., and Mostafa, M. G. (2022). Comparison of classical and developed indexing methods for assessing the groundwater suitability for irrigation. *J. Sustain. Agric. Environ.* 1, 226–239. doi: 10.1002/sae2.12027

Jiang, L., Yao, Z., Liu, Z., Wang, R., and Wu, S. (2015). Hydrochemistry and its controlling factors of rivers in the source region of the Yangtze River on the Tibetan plateau. *J. Geochem. Explor.* 155, 76–83. doi: 10.1016/j.gexplo.2015.04.009

Kelly, W. (1940). Permissible composition and concentration of irrigated waters. *Proc. ASCF* 66:607. doi: 10.1055/s-0028-1121592

Khan, A., Khan, M. S., Egozcue, J. J., Shafique, M. A., Nadeem, S., and Saddiq, G. (2022). Irrigation suitability, health risk assessment and source apportionment of heavy metals in surface water used for irrigation near marble industry in Malakand, Pakistan. *PLoS One* 17:e0279083. doi: 10.1371/journal.pone.0279083

Kreins, P., Henseler, M., Anter, J., Herrmann, F., and Wendland, F. (2015). Quantification of climate change impact on regional agricultural irrigation and groundwater demand. *Water Resour. Manag.* 29, 3585–3600. doi: 10.1007/s11269-015-1017-8

Kumar, S., Kumar, A., Prashant Jha, V. N., Sahoo, S. K., and Ranjan, R. K. (2022). Groundwater quality and its suitability for drinking and irrigational purpose in Bhojpur district: middle Gangetic plain of Bihar, India. *Water Supply* 22, 7072–7084. doi: 10.2166/ws.2022.317

Megahed, H. A. (2020). GIS-based assessment of groundwater quality and suitability for drinking and irrigation purposes in the outlet and central parts of Wadi El-Assiuti, Assiut governorate, Egypt. *Bull. Natl. Res. Cent.* 44:187. doi: 10.1186/s42269-020-00428-3

Megahed, H. A., Farrag, A. E.-H. A., Mohamed, A. A., D'Antonio, P., Scopa, A., and AbdelRahman, M. A. E. (2023). Groundwater recharge potentiality mapping in Wadi Qena, eastern desert basins of Egypt for sustainable agriculture base using geomatics approaches. *Hydrology* 10:237. doi: 10.3390/hydrology10120237

Megahed, H. A., GabAllah, H. M., AbdelRahman, M. A. E., D'Antonio, P., Scopa, A., and Darwish, M. H. (2022). Geomatics-based modeling and hydrochemical analysis for groundwater quality mapping in the Egyptian Western Desert: a case study of El-Dakhla Oasis. *Water* 14:4018. doi: 10.3390/w14244018

Megahed, H. A., GabAllah, H. M., Ramadan, R. H., AbdelRahman, M. A. E., D'Antonio, P., Scopa, A., et al. (2023). Groundwater quality assessment using multi-criteria GIS modeling in drylands: a case study at El-Farafra oasis, Egyptian Western Desert. *Water* 15:1376. doi: 10.3390/w15071376

Mester, T., Szabo, G., Sajtos, Z., Baranyai, E., Szabo, G., and Balla, D. (2022). Environmental hazards of an unrecultivated liquid waste disposal site on soil and groundwater. *Water* 14:226. doi: 10.3390/w14020226

Metwaly, M. M., AbdelRahman, M. A. E., and Abdellatif, B. (2022). Heavy metals and micronutrients assessment in soil and groundwater using geospatial analyses under agricultural exploitation in dry areas. *Acta Geophys.* 71, 1937–1965. doi: 10.1007/s11600-022-00979-1

Mohamaden, M., Araffa, S. A. S., Taha, A., AbdelRahman, M. A. E., El-Sayed, H. M., and Sharkawy, M. S. (2024). Geophysical techniques and geomatics-based mapping for groundwater exploration and sustainable development at Sidi Barrani area, Egypt. *Egypt. J. Aquatic Res.* 50, 36–51. doi: 10.1016/j.ejar.2023.12.001

Moubark, K., and Abdelkareem, M. (2018). Characterization and assessment of groundwater resources using hydrogeochemical analysis, GIS, and field data in southern Wadi Qena, Egypt. *Arab. J. Geosci.* 11:598. doi: 10.1007/s12517-018-3931-6

Nayak, A., Matta, G., and Uniyal, D. P. (2023). Hydrochemical characterization of groundwater quality using chemometric analysis and water quality indices in the

foothills of Himalayas. *Environ. Dev. Sustain.* 25, 14229–14260. doi: 10.1007/s10668-022-02661-4

Osman, K. T. (2018). "Saline and sodic soils" in Management of soil problems (Cham: Springer).

Paliwal, K. V. (1972). Irrigation with saline water. New Delhi, India: Water Technology Centre, Indian Agriculture Research Institute, 198.

Pazand, K., Khosravi, D., Ghaderi, M. R., and Rezvanianzadeh, M. R. (2018). Identification of the hydrogeochemical processes and assessment of groundwater in a semi-arid region using major ion chemistry: a case study of Ardestan basin in Central Iran. *Groundw. Sustain. Dev.* 6, 245–254. doi: 10.1016/j.gsd.2018.01.008

Piper, A. M. (1944). A graphic procedure in the geochemical interpretation of water-analyses. *EOS Trans. Am. Geophys. Union* 25, 914–928. doi: 10.1029/TR025i006p00914

Porter, D. O., and Marek, T. (2006). "Irrigation management with saline water" in Proceedings of the 2006 central plains irrigation conference (Colby, KS, USA: Colorado State University), 21–22.

Raghunath, H. M. (1987). Ground water: Hydrogeology, ground water survey and pumping tests, rural water supply and irrigation systems. New York, NY, USA: John Wiley & Sons Ltd.

Rainwater, F. H., and Thatcher, L. L. (1960). Methods for collection and analysis of water samples (No. 1454-1458). Washington, DC, USA: US Government Printing Office.

Rawat, K. S., Singh, S. K., and Gautam, S. K. (2018). Assessment of groundwater quality for irrigation use: a peninsular case study. *Appl Water Sci* 8:233. doi: 10.1007/s13201-018-0866-8

Ren, C., and Zhang, Q. (2020). Groundwater chemical characteristics and controlling factors in a region of northern China with intensive human activity. *Int. J. Environ. Res. Public Health* 17:9126. doi: 10.3390/ijerph17239126

Richards, L. A. (1954). Diagnosis and improvement of saline alkali soils, agriculture, 160, handbook 60. Washington DC, USA: US Department of Agriculture.

S, C., M, V. P., S, V., M, N., K, P., Panda, B., et al. (2022). Groundwater quality assessment for irrigation by adopting new suitability plot and spatial analysis based on fuzzy logic technique. *Environ. Res.* 204:111729. doi: 10.1016/j.envres.2021.111729

Sanaullah, M., Wang, X., Ahmad, S. R., Mirza, K., Mahmood, M. Q., and Kamran, M. (2023). Optimized irrigated water management using numerical flow modeling coupled with finite element model: a case study of Rechna doab, Pakistan. *Water* 15:4193. doi: 10.3390/w15234193

Saraswat, A., Nath, T., Omeka, M. E., Unigwe, C. O., Anyanwu, I. E., Ugar, S. I., et al. (2023). Irrigation suitability and health risk assessment of groundwater resources in the Firozabad industrial area of north-Central India: an integrated indexical, statistical, and geospatial approach. *Front. Environ. Sci.* 11:1116220. doi: 10.3389/fenvs.2023.1116220

Schoeller, H. (1962). Les eaux souterraines (the underground networks). Paris: Mason and Cie, 64.

Shaaban, M. (2024). "Salt-affected soils" in Frontier studies in soil science. ed. A. Núñez-Delgado (Cham: Springer).

Simonetti, V. C., da Cunha, D. C., and Rosa, A. H. (2019). Análise da influência das atividades antrópicas sobre a qualidade da água da APA Itupararanga (SP), Brasil. *Geosul* 34, 01–27. doi: 10.5007/1982-5153.2019v34n72p01

Soltan, M. E. (1998). Characterisation, classification, and evaluation of some ground water samples in upper Egypt. *Chemosphere*, 37, 735–745. doi: 10.1016/S0045-6535(98)00079-4

Soomro, S. A., Hao, L., Memon, G. A., Junejo, A. R., Niu, W., Channa, Z. A., et al. (2024). Comprehensive analysis of groundwater suitability for irrigation in rural Hyderabad, Sindh, Pakistan. *Agronomy* 14:1072. doi: 10.3390/agronomy14051072

Srivastav, A. L., Patel, N., and Chaudhary, V. K. (2020). Disinfection by-products in drinking water: occurrence, toxicity and abatement. *Environ. Pollut.* 267:115474. doi: 10.1016/j.envpol.2020.115474

Stiff, H. A. (1951). The interpretation of chemical water analysis by means of patterns. *J. Pet. Technol.* 3, 15–13. doi: 10.2118/951376-G

Todd, D. K., and Mays, L. W. (2004). Groundwater hydrology. New York, NY, USA: John Wiley & Sons Ltd.

US Salinity Laboratory Staff (USSL) (1954). Diagnosis and improvement of saline and alkali soils, Agric, handbook 60, USDA. Washington, DC, USA: US Government Printing Office.

Wali, S. U., Alias, N. B., Harun, S. B., Umar, K. J., Gada, M. A., Dankani, I. M., et al. (2022). Water quality indices and multivariate statistical analysis of urban groundwater in semi-arid Sokoto Basin, Northwestern Nigeria. *Groundwater Sustain. Dev.* 18:100779. doi: 10.1016/j.gsd.2022.100779

Wang, S., Shao, J., Song, X., Zhang, Y., Huo, Z., and Zhou, X. (2008). Application of MODFLOW and geographic information system to groundwater flow simulation in North China plain, China. *Environ. Geol.* 55, 1449–1462. doi: 10.1007/s00254-007-1095-x

WHO Guidelines (2004). "Global drinking water index development and sensitivity analysis report" in United Nations Environment Programme (UNEP)/Global Environment Monitoring System (GEMS)/Water Programme. eds. C. Rickwood and G. Curr, Burlington, Ontario, Canada: NEP GEMS/Water Programme. 8–101.

Wilcox, L. (1955). The quality of water for irrigation use. Washington, DC, USA: US Department of Agriculture, Technical Bulletin No. 962, 1–40.

Worku, D., Boja, A., and Fantu, A. (2024). Evaluation of land suitability areas for irrigation using GIS and AHP-based tools in the case of Zenti River catchment, Gofa district, Ethiopia. *Cogent Eng.* 11. doi: 10.1080/23311916.2024.2345519

Xiao, Y., Zhang, J., Long, A., Xu, S., Guo, T., Gu, X., et al. (2023). Hydrochemical characteristics and formation mechanism of quaternary groundwater in Baoshan basin, western Yunnan, China. *Water* 15:2736. doi: 10.3390/w15152736

Yan, Y., Zhang, Y., Yao, R., Wei, C., Luo, M., Yang, C., et al. (2024). Groundwater suitability assessment for irrigation and drinking purposes by integrating spatial analysis, machine learning, water quality index, and health risk model. *Environ. Sci. Pollut. Res.* 31, 39155–39176. doi: 10.1007/s11356-024-33768-y

Yidana, S. M., Bawoyobie, P., Sakyi, P., and Fynn, O. F. (2018). Evolutionary analysis of groundwater flow: application of multivariate statistical analysis to hydrochemical data in the Densu Basin, Ghana. *J. African Earth Sci.* 138, 167–176. doi: 10.1016/j.jafrearsci.2017.10.026

Yıldız, S., and Karakuş, C. B. (2020). Estimation of irrigation water quality index with development of an optimum model: a case study. *Environ. Dev. Sustain.* 22, 4771–4786. doi: 10.1007/s10668-019-00405-5

Yuan, Z., Jian, Y., Chen, Z., Jin, P., Gao, S., Wang, Q., et al. (2024). Distribution of groundwater hydrochemistry and quality assessment in Hutuo River drinking water source area of Shijiazhuang (North China plain). *Water* 16:175. doi: 10.3390/w16010175

Zaman, M., Shahid, S. A., and Heng, L. (2018). "Irrigation water quality" in Guideline for salinity assessment, mitigation and adaptation using nuclear and related techniques (Cham: Springer).

Zhang, X., Zhao, R., Wu, X., and Mu, W. (2022). Hydrogeochemistry, identification of hydrogeochemical evolution mechanisms, and assessment of groundwater quality in the southwestern Ordos basin, China. *Environ. Sci. Pollut. Res.* 29, 901–921. doi: 10.1007/s11356-021-15643-2

Frontiers in Water

Transforming our approach to water research and its applications

A journal dedicated to exploring challenges facing freshwater systems, including demand and supply of water resources, extreme weather events and climate change.

Discover the latest Research Topics

See more →

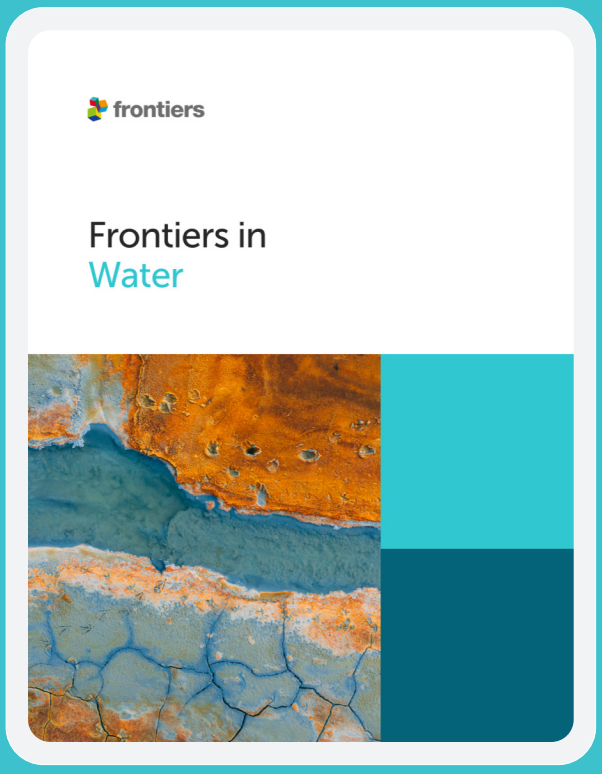

Frontiers

Avenue du Tribunal-Fédéral 34
1005 Lausanne, Switzerland
frontiersin.org

Contact us

+41 (0)21 510 17 00
frontiersin.org/about/contact